Beyond Born-Oppenheimer: Non-Adiabatic Interactions of Diatomic Molecules for High Resolution Spectroscopy

Ryan P. Brady

A dissertation submitted in partial fulfillment
of the requirements for the degree of
Doctor of Philosophy
of
University College London.

Department of Physics & Astronomy
University College London

July 24, 2025

I, Ryan P. Brady, confirm that the work presented in this thesis is my own. Where information has been derived from other sources, I confirm that this has been indicated in the work.

Abstract

Spectroscopy is essential for understanding a wide range of scientific phenomena, making the production of accurate spectroscopic data crucial. The demand for such data has grown significantly, particularly in astrophysics, where the recent deployment of the James Webb Space Telescope requires accurate and comprehensive line lists for effective data analysis. To meet this need, the thesis introduces SOLIS, an infrared and visible line list for the sulfur monoxide (SO) radical. Generated using variational calculations and refined with empirically determined energy levels and experimental uncertainties, SOLIS is expected to be valuable for studying exoplanetary atmospheres, stellar formation regions, the interstellar medium, and shock zones. Notably, it has already been applied in the analysis of JWST data, with the results discussed in this thesis.

The ultraviolet spectra of molecules are especially important for studying astrophysical environments like planetary atmospheres. Accurately describing the highly excited electronic states of molecules is vital. However, many molecules exhibit complex electronic structures due to non-adiabatic interactions from the breakdown of the Born-Oppenheimer approximation. The limitations of this approximation are evident in an increasing number of molecules, where non-adiabatic effects play a significant role.

To address this challenge, this thesis reformulates existing diabatisation theory in a rovibronic context, implementing non-adiabatic modules within the variational rovibronic code Duo. This allows the full incorporation of non-adiabatic effects in generating molecular line lists. Additionally, novel diabatisation methodologies are developed to construct accurate and practical diabatic spectroscopic representations, where non-adiabatic couplings vanish, facilitating the construction of accurate contracted vibronic basis sets.

This thesis also presents the first demonstration of adiabatic-diabatic rovibronic equivalence for an arbitrary number of coupled electronic states, applied to YO, CH, N_2, and a synthetic 10-state system. Duo serves as a powerful tool to benchmark the importance of different non-adiabatic effects on computed spectroscopy.

Impact Statement

The reformulation of existing diabatisation theory within the rovibronic context will greatly benefit future rovibronic studies aiming to incorporate non-adiabatic effects in computed diatomic spectroscopy. All important aspects of the theory are discussed, with useful relations, functional forms, and benchmarks relevant to solving the rovibronic problem. The development of our novel diabatisation method, HyAP, developed in this thesis, allows for the construction of accurate and practical diabatic representations for contracted vibronic basis sets in general N-electronic state systems. This improvement of the molecular spectroscopic model directly enhances the final computed line list/spectra, which is essential to the ExoMol project's production of high-accuracy line lists for high-resolution spectroscopy. This is especially true for the UV description of molecules, where non-adiabatic effects are increasingly relevant, as seen in molecules like C_2, CN, N_2, SiC, Si_2, CO, SO, and YO.

This thesis demonstrates that a diabatic model can be crucial in obtaining accurate diatomic spectroscopy, as applied to the YO and CO molecules. With the full adiabatic and diabatic modules in our rovibronic code Duo, it now serves as a unique and powerful tool to benchmark the effect of different non-adiabatic terms in the nuclear kinetic energy, providing a novel and powerful tool for model selection before computing molecular spectroscopy.

The high-resolution IR/vis sulfur monoxide (SO) line list, SOLIS, presented here is essential to support future spectroscopic studies of SO in various astrophysical environments, particularly the interstellar medium, exoplanets, atmospheric and environmental chemistry, industry, and stars. The SOLIS line list has already been used in analysis of James Webb Space Telescope (JWST) spectral data. Notably, the SOLIS line list has contributed to the detection of sulfur dioxide (SO_2) in the exoplanet WASP-39b, marking a major milestone as the first clear observation of UV-driven sulfur photochemistry in a hot exoplanet atmosphere. Furthermore, the mid-infrared fundamental band feature of SO was identified in WASP-39b, and it has been recognised as a prominent molecular species in the oxygen/silicon/sulfur neon-burning zones within supernova. The abundance of SO has also been shown to be sensitive to the interstellar medium cosmic ray ionization rate, which can then be subsequently constrained.

Acknowledgements

I would like to express my sincere gratitude to my supervisors, Sergey Yurchenko and Jonathan Tennyson, for their invaluable guidance, support, and mentorship throughout this research. Their encouragement of my research interests and their commitment to fostering a positive research environment made my PhD experience thoroughly enjoyable.

I am particularly grateful to Professor Yurchenko for his dedication to rapidly implementing the methods and modules we discussed in our weekly meetings into the Duo code. This work was absolutely essential to obtaining the main results presented in this thesis.

I would also like to thank Oleksiy Smola for his insightful discussions on Lie theory and inverse Monte Carlo transform sampling, and for his daily lunch companionship. I am equally grateful to Charles Bowesman, Andrei Sokolov, Kyriaki Kefala, Armando Perri, Jinxin Zhang, Tony Lynas-Gray, Bridgette Cooper, Alec Owens, Mikhail Semenov, Marco Pezzella, Georgi Mitev, Elizabeth Guest, Wilfrid Somogyi, Apoorva Upadhyay, Thomas Mellor, Qinghe Ni, and Charlie Drury for their advice, camaraderie, coffee breaks, and good company.

I would like to thank all the co-authors and collaborators involved in the projects I undertook during my PhD. In particular, I am grateful to Jeanna Buldyreva and Nayla El-Kork, with whom I've had the pleasure of engaging in many valuable discussions, participating in extracurricular activities, and attending conferences. I also wish to thank University College London for providing the resources essential to this research – especially the Myriad High Performance Computing Facility (Myriad@UCL) and its associated support services – which played a key role in the completion of my PhD.

I am deeply grateful to my parents for their enduring support and constant belief in me throughout the years.

Finally, I offer a special thanks to my fiancée, Leanne Mays, for her unwavering support, love, and patience. I am especially grateful for her willingness to listen to countless discussions about quantum chemistry and for accompanying me to several molecular spectroscopy conferences.

Research Publications

I have (co)authored in the following list of publications, which are listed from most to least recent. Ticks by the publication indicate they have been discussed in this thesis.

✓ 1. **Brady, R. P** and Yurchenko, S. N. Exact Rovibronic Equivalence of the Adiabatic and Diabatic Representations of *N*-Coupled State Diatomic Systems", Journal of Computational Chemistry 46, no. 20 (2025): e70181, 10.1002/jcc.70181. *Material adapted for our proposed N-state diabatisation methodolgy and numerical equivalence discussions in Chapters 2 and 3.*

✓ 2. **Brady, R. P** (2025). A Strict and Internally Consistent Diabatic Representation for Coupled N-state Diatomics: A Hybrid Asymptotic-Property-Based diabatisation Method. J. Chem. Phys. 7 May 2025; 162 (17): 174105. 10.1063/5.0260594. *Material adapted for our proposed N-state diabatisation and regularisation methodolgies in Chapters 2 and 3..*

✓ 3. R. Hassaine, D. Talbi, **R. P. Brady**, J. Zs. Mezei, J. Tennyson, I. F. Schneider. Theoretical study of the excited states of NeH^+ and of their non-adiabatic couplings: A preliminary for the modeling of the dissociative recombination of NeH^+. J. Chem. Phys. 7 April 2025; 162 (13): 134302. 10.1063/5.0261152. *Material adapted on discussion of the DDR procedure in Section 2.2.2 of Chapter 2.*

✓ 4. Khalil, M.; Mahmoud, S.; **Brady, R. P.**; Almehairbi, M.; Gacesa, M.; Yurchenko, S. N.; Tennyson, J.; Al Ghaferi, A.; El-Kork, N. Theoretical investigation of the A1–X1+, B1+–X1+, C1+–X1+, and E1–X1+ transitions of the CO molecule. Phys. Chem. Chem. Phys. 2025, 27, 2783–2801. doi: 10.1039/D4CP03418J. *Material adapted for Chapter 3, Section 3.9.2.*

5. Tennyson, J.; Yurchenko, S. N.; Zhang, J.; Bowesman, C. A.; **Brady, R. P.**; Buldyreva, J.; Chubb, K. L.; Gamache, R. R.; Gorman, M. N.; Guest, E. R.; Hill, C.; Kefala, K.; Lynas-Gray, A.; Mellor, T. M.; McKemmish, L. K.; Mitev, G. B.; Mizus, I. I.; Owens, A.; Peng, Z.; Perri, A. N.; Pezzella, M.; Polyansky, O. L.; Qu, Q.; Semenov, M.; Smola, O.; Solokov, A.; Somogyi, W.; Upadhyay, A.; Wright, S. O.; Zobov, N. F. The 2024 release of the ExoMol database: Molecular line lists for exoplanet and other hot atmospheres. Journal of Quantitative Spectroscopy and Radiative Transfer 2024, 326, 109083. doi:10.1016/j.jqsrt.2024.109083.

✓ 6. **Brady, R. P.**; Drury, C.; Yurchenko, S. N.; Tennyson, J. Numerical Equivalence of Diabatic and Adiabatic Representations in Diatomic Molecules. Journal of Chemical Theory and Computation 2024, 20, 2127–2139, PMID: 38171539. doi:10.1021/acs.jctc.3c01150. *Material adapted for Chapter 3.*

✓ 7. Buldyreva, J.; **Brady, R. P.**; Yurchenko, S. N.; Tennyson, J. Collisional broadening of molecular rovibronic lines. Journal of Quantitative Spectroscopy and Radiative Transfer 2024, 313, 108843. doi: 10.1016/j.jqsrt.2023.108843. *Discussion on ab initio calculations and pressure broadening parameters adapted for Chapter 5.*

✓ 8. Powell, D.; Feinstein, A. D.; Lee, E. K. H.; Zhang, M.; Tsai, S.-M.; Taylor, J.; Kirk, J.; Bell, T.; Barstow, J. K.; Gao, P.; Bean, J. L.; Blecic, J.; Chubb, K. L.; Crossfield, I. J. M.; Jordan, S.; Kitzmann, D.; Moran, S. E.; Morello, G.; Moses, J. I.; Welbanks, L.; Yang, J.; Zhang, X.; Ahrer, E.-M.; Bello-Arufe, A.; Brande, J.; Casewell, S. L.; Crouzet, N.; Cubillos, P. E.; Demory, B.-O.; Dyrek, A.; Flagg, L.; Hu, R.; Inglis, J.; Jones, K. D.; Kreidberg, L.; López-Morales, M.; Lagage, P.-O.; Meier Valdés, E. A.; Miguel, Y.; Parmentier, V.; Piette, A. A. A.; Rackham, B. V.; Radica, M.; Redfield, S.; Stevenson, K. B.; Wakeford, H. R.; Aggarwal, K.; Alam, M. K.; Batalha, N. M.; Batalha, N. E.; Benneke, B.; Berta-Thompson, Z. K.; **Brady, R. P.**; Caceres, C.; Carter, A. L.; Désert, J.-M.; Harrington, J.; Iro, N.; Line, M. R.; Lothringer, J. D.; MacDonald, R. J.; Mancini, L.; Molaverdikhani, K.; Mukherjee, S.; Nixon, M. C.; Oza, A. V.; Palle, E.; Rustamkulov, Z.; Sing, D. K.; Steinrueck, M. E.; Venot, O.; Wheatley, P. J.; Yurchenko, S. N. Sulfur dioxide in the mid-infrared transmission spectrum of WASP-39b. Nature 2024, 626, 979–983. doi:10.1038/s41586-024-07040-9. *Applications of our SOLIS line list are discussed in Chapter 4 Section 4.16.*

✓ 9. Tsai, S.-M.; Lee, E. K. H.; Powell, D.; Gao, P.; Zhang, X.; Moses, J.; Hébrard, E.; Venot, O.; Parmentier, V.; Jordan, S.; Hu, R.; Alam, M. K.; Alderson, L.; Batalha, N. M.; Bean, J. L.; Benneke, B.; Bierson, C. J.; **Brady, R. P.**; Carone, L.; Carter, A. L.; Chubb, K. L.; Inglis, J.; Leconte, J.; Line, M.; López-Morales, M.; Miguel, Y.; Molaverdikhani, K.; Rustamkulov, Z.; Sing, D. K.; Stevenson, K. B.; Wakeford, H. R.; Yang, J.; Aggarwal, K.; Baeyens, R.; Barat, S.; de Val-Borro, M.; Daylan, T.; Fortney, J. J.; France, K.; Goyal, J. M.; Grant, D.; Kirk, J.; Kreidberg, L.; Louca, A.; Moran, S. E.; Mukherjee, S.; Nasedkin, E.; Ohno, K.; Rackham, B. V.; Red- field, S.; Taylor, J.; Tremblin, P.; Visscher, C.; Wallack, N. L.; Welbanks, L.; Young- blood, A.; Ahrer, E.-M.; Batalha, N. E.; Behr, P.; Berta-Thompson, Z. K.; Blecic, J.; Casewell, S. L.; Crossfield, I. J. M.; Crouzet, N.; Cubillos, P. E.; Decin, L.; Désert, J.-M.; Feinstein, A. D.; Gibson, N. P.; Harrington, J.; Heng, K.; Henning, T.; Kempton, E. M.- R.; Krick, J.; Lagage, P.-O.; Lendl, M.; Lothringer, J. D.; Mansfield, M.; Mayne, N. J.; Mikal-Evans, T.; Palle, E.; Schlawin, E.; Shorttle, O.; Wheatley, P. J.; Yurchenko, S. N. Photochemically produced SO2 in the atmosphere of WASP-39b. Nature 2023, 617, 483–487.

oi:10.1038/s41586-023-05902-2. *Applications of our SOLIS line list are discussed in Chapter 4 Section 4.16.*

✓ 10. **Brady, R. P.**; Yurchenko, S. N.; Tennyson, J.; Kim, G.-S. ExoMol line lists – LVI. The SO line list, MARVEL analysis of experimental transition data and refinement of the spectroscopic model. Monthly Notices of the Royal Astronomical Society 2023, 527, 6675–6690. doi:10.1093/mnras/stad3508. *Material adapted for discussion on the generation of the SOLIS line list in Chapter 4.*

✓ 11. Liljegren, S.; Jerkstrand, A.; Barklem, P. S.; Nyman, G.; **Brady, R.**; Yurchenko, S. N. The molecular chemistry of Type Ibc supernovae and diagnostic potential with the James Webb Space Telescope. Aston. and Astr. 2023, 674, A184. doi:10.1051/0004-6361/202243491. *Applications of our SOLIS line list are discussed in Chapter 4 Section 4.16.*

✓ 12. Yurchenko, S. N.; **Brady, R. P.**; Tennyson, J.; Smirnov, A. N.; Vasilyev, O. A.; Solomonik, V. G. ExoMol line lists – LIII: empirical rovibronic spectra of yttrium oxide. Monthly Notices of the Royal Astronomical Society 2023, 527, 4899–4912. doi:10.1093/mnras/stad3225. *Material adapted for discussion on the applications of our diabatisation methods to diatomic line list generation in Chapter 3 Section 3.9.*

✓ 13. **Brady, R. P.**; Yurchenko, S. N.; Kim, G.-S.; Somogyi, W.; Tennyson, J. An ab initio study of the rovibronic spectrum of sulphur monoxide (SO): diabatic vs. adiabatic representation. Phys. Chem. Chem. Phys. 2022, 24, 24076–24088. doi:10.1039/D2CP03051A. *Material adapted for discussion on two-state diabatisation in Chapter 2 and in the generation of the SOLIS line list in Chapter 4*

14. Niculescu-Duvaz, M.; Barlow, M. J.; Bevan, A.; Wesson, R.; Milisavljevic, D.; De Looze, I.; Clayton, G. C.; Krafton, K.; Matsuura, M.; **Brady, R. P.**. Dust masses for a large sample of core-collapse supernovae from optical emission line asymmetries: dust formation on 30-year time-scales. Monthly Notices of the Royal Astronomical Society 2022, 515, 4302–4343. doi:10.1093/mnras/stac1626.

Pending Publications

I list here the current publications under the submission process which are suspected to be published soon.

✓ 1. **Brady, R. P.**, Yurchenko, S. N (2024). Spin-Orbit Induced Non-Adiabatic Dynamics: A True Ω-Representation. [Manuscript in preparation for submission to PRL]. *Material adapted for discussions on the Ω-representation of nuclear motion and ongoing work in Chapter 5.*

2. **Brady, R. P.**, Yurchenko, S. N (2025), 'Diabatisation of Diatomic Molecules: Book Chapter'. [Currently in preparation]. *Material adapted from this thesis will form the book chapter on diabatisation*.

Abbreviations & Notes

This is a list of frequently used abbreviations and their meanings, provided for the reader's quick reference.

- **NAC**: Non-Adiabatic Coupling.
- **DDR**: nuclear coordinate derivative coupling terms which act on the electronic wavefunctions. DDR is also the name of the procedure in MOLPRO which computes NACs from transition densities. DDR means $\frac{d}{dr}$.
- **DBOC**: Diagonal Born-Oppenheimer Correction.
- **AtDT**: Adiabatic to Diabatic Transformation.
- **DC**: Diabatic Coupling, also known as an off-diagonal diabatic potential coupling.
- **HyAP**: Hybrid Asymptotic Property based diabatisation procedure.
- **BOA**: Born-Oppenheimer Approximation.
- **HFT**: Hellmann-Feynman Theorem.
- **DoF**: Degree of Freedom.
- **CASSCF**: Complete Active Space Self-Consistent Field.
- **MRCI**: Multi-Reference Configuration Interaction.
- **CCSD(T)**: Coupled Cluster with Singles, Doubles, and perturbative Triples.
- **DVR**: Discrete Variable Representation.

Note: Unless otherwise stated, the first-person plural terms 'we' and 'our' refer to collaborative work undertaken with supervisors, collaborators, group members, and/or students. Where such terms are absent (either in passive voice or first person singular), the work described is understood to be my own individual contribution.

Contents

Chapter 1

Introduction

The Born-Oppenheimer (BO) approximation and, later, the related adiabatic approximation have been pivotal to the treatment of photodynamical processes since the 1927 seminal paper by Born and Oppenheimer[2]. The BO approximation distinguishes between fast moving electrons and slowly moving nuclei, where coupling between the electronic and nuclear degrees of freedom through the nuclear kinetic energy operator, called non-adiabatic couplings (NACs) or derivative couplings (DDRs), are neglected. Within the BO approximation, electronic adiabatic states are realised where their associated potential energy curves [1] (PECs) have no mass dependence, and evolve on single decoupled curves. These electronic eigenstates effectively diagonalise the electronic Hamiltonian and are approximate solutions to the stationary Schrödinger equation for atomistic systems. Their existence has been both paramount to the understanding of many aspects of chemistry and physics and unanimous to a wide range of experimental studies; such as in chemical reactions where bonding is understood by electronic configurations gluing nuclei together[3]; in photodynamics where photodissociation can be understood by a radiative transition from a single bound electronic state potential to a repulsive PEC[3–7]; and in astronomy and atmospheric chemistry where collisionally induced dynamics of atoms and molecules are governed by the electronic states involved[8–10]. The adiabatic approximation then introduces mass-dependence into the PECs by inclusion of the well-known diagonal BO correction (DBOC, the diagonal second DDRs). Generally, BO-PECs are good for predicting near-equilibrium properties for many molecules[11], but become increasingly less accurate upon approach of (degenerate) electronic states of the same-symmetry, which cannot cross, and exhibit so-called avoided crossings (first established by Neumann and Wigner[12]) where the DDRs

[1] Here the Born-Oppenheimer approximation is discussed in the context of diatomic molecules, and so this thesis refers to molecular properties as curves as opposed to surfaces for the polyatomic case.

become singular and therefore must not be neglected. Figure 1.1 illustrates an example avoided crossing between two adiabatic $^1\Pi$ states of sulfur monoxide and their corresponding NAC[13] (see Chapter 4 for details). In cases of electronically degenerate states, molecular (photo)dynamics occurs on multiple adiabatic potential surfaces opposed to just one, where introduction of these DDR coupling terms brings the treatment of molecular systems beyond BO.

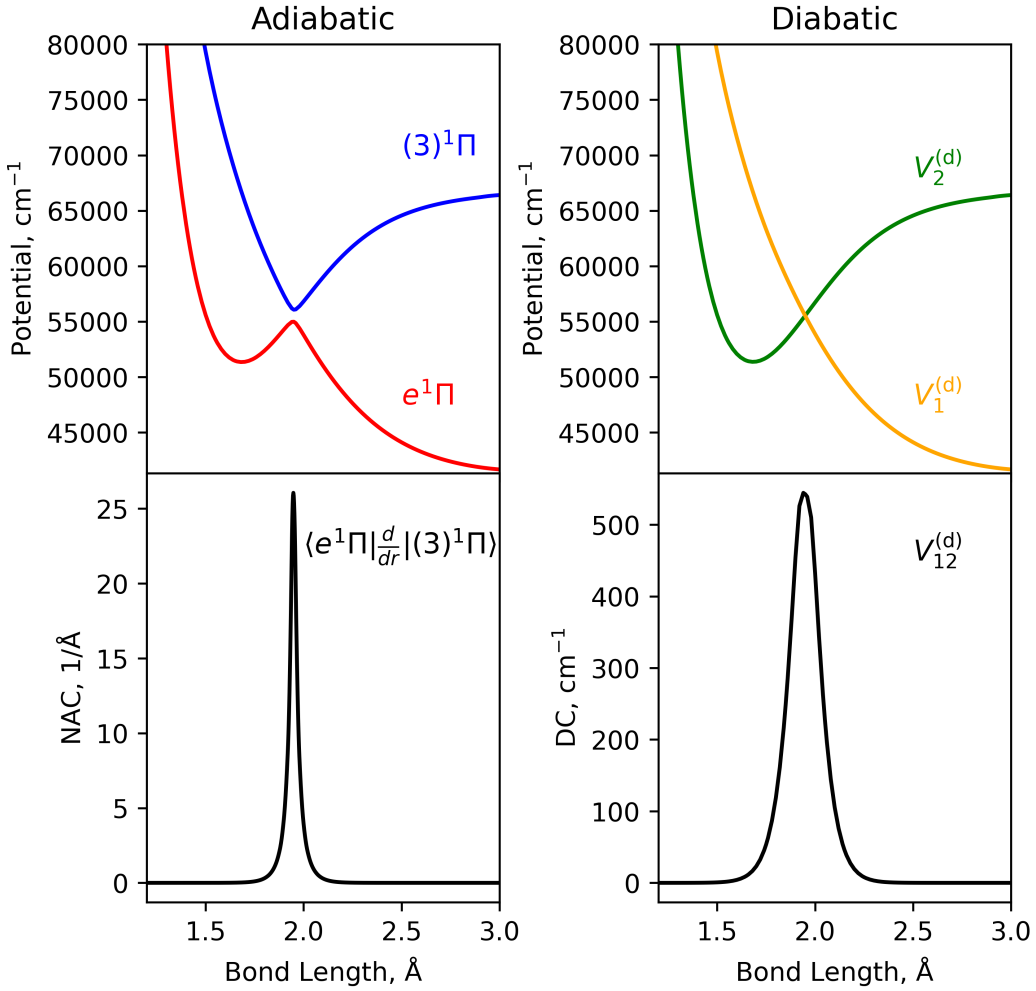

Figure 1.1: Illustration of the avoided crossing adiabatic PECs of the $e\,^1\Pi$ and $(3)\,^1\Pi$ states of sulfur monoxide and the corresponding NAC (left panels). The right panels show their diabatisation, producing a set of smooth diabatic PECs which cross and are coupled by the diabatic coupling (bottom right). The NAC is strongest at the avoided crossing geometry, showing cusp-like behaviour.

Because the realisation of BO-PECs has been useful in explaining numerous chemophysical processes, it is expected that non-adiabatic interactions should also play a significant role in their understanding. Indeed, proper treatment of non-adiabatic interactions has been shown to be important for numerous photochem-

ical processes[14–18,11,19] where the electronic structure of molecules, and consequentially nuclear motion, is altered. Furthermore, non-adiabatic interactions are important in astronomy and atmospheric chemistry where collisions of free radicals and open shell molecules with degenerate electronic states are often seen[20–24]. Modelling electronically non-adiabatic processes has also been effective in explaining the bonding in dications such as BF^{2+}[25] and strongly ionic molecules, such as LiF[26] and NaCl[27], whose $^1\Sigma^+$ states show non-adiabatic behaviour.

The primary focus of non-adiabatic interactions in this thesis concerns nuclear motion calculations. As such, this work will predominantly centre on the treatment and exploration of these processes, emphasising their role in molecular dynamics and spectroscopy. The importance of DDR couplings are expected to be crucial for the accurate calculation of molecular rovibronic energies. Many studies have investigated this importance for small hydrogen bearing molecules because of the cheap computational cost within quantum chemistry calculations due to few correlating electrons. For example, a series of papers by Wolniewicz, Dressler, and co-workers[28–34] investigated the excited electronic states of molecular hydrogen. Early studies used the adiabatic approximation, but NACs were progressively introduced for more excited states, proving essential for accurately reproducing rovibronic energies and spectra, as confirmed by experiment. Similarly, Ralph Jaquet showed that including DDRs are critical for accurate spectroscopy of small hydrogen-bearing molecules such as H_2^+, D_2^+, H_3^+, and H_2[35]. Pachucki and Komasa[36,37] further demonstrated the importance of NACs through a nonadiabatic perturbation theory for H_2, achieving accurate rovibronic energies via perturbative corrections. It is expected for small molecules that kinetic energy coupling (DDRs) to be important since the $-\hbar^2/2\mu$ factor in the nuclear kinetic energy is large, where μ is the reduced mass of the diatom. However, more recently we showed[38] (for the first time in nuclear motion calculations) that omission of any DDR terms lead to significant changes in the molecular spectral properties, even for heavier molecules, where we study the YO ($B\,^2\Sigma^+$, $D\,^2\Sigma^+$) and CH ($C\,^2\Sigma^+$, $2\,^2\Sigma^+$) diatomic systems, where inclusion of all DDRs is shown to be crucial for high-resolution applications. Even the DBOC, often omitted in practical applications, was shown to be of central importance in the adiabatic rovibronic solution. Like the previously mentioned studies, as more molecular systems are investigated experimentally and by *ab initio* treatments, it is clear that the BO approximation cannot be satisfied in most regions of the molecular configuration space.

In an attempt to simplify the problem of treating nuclear motion non-BO, in 1960 Hober and Weber[39] first discussed a transformation which removes com-

pletely the DDR couplings from the nuclear kinetic energy. As a fortunate consequence, nuclear motion can be calculated either in the adiabatic representation, consisting of BO-PECs, DBOCs, and off-diagonal NACs, or a diabatic representation consisting of a diagonal kinetic energy matrix (no DDRs) and crossing PECs coupled by off-diagonal potential couplings called diabatic couplings (DCs)[40–42]. The diabatic representation is recovered through a unitary transformation of the adiabatic electronic wavefunctions[43–50,42,40,41,51] (herein the adiabatic to diabatic transformation; AtDT), and has the property that the diagonal and off-diagonal DDRs are simultaneously removed (see, e.g. Mead and Truhlar[40]) at the cost of introducing a DC within the potential matrix, allowing the PECs to cross. Whilst the adiabatic representation diagonalises the electronic Hamiltonian, the diabatic representation diagonalises instead the nuclear kinetic energy. Figure 1.1 illustrates the diabatisation of the $e\,^1\Pi$ and $(3)\,^1\Pi$ states of sulfur monoxide. The main reason that one would choose the diabatic representation is because of the smooth molecular property curves such as potentials and dipole moments[13,52] (see also Figure 1.1), allowing for a simpler spectroscopic model – by which analytical forms can be easily utilised – which is crucial if one wants to refine these curves to better match experimental data (see, e.g. the works by the ExoMol project[53–55]). In the adiabatic representation, the cusp-like behaviour of the PECs and the singular nature of the DDRs in the region of degeneracy[40,41,20,56] can make integrating, fitting with analytical forms, and thus the production of both a physically meaningful and accurate spectroscopic model for the desired system, very difficult. Because of the complex adiabatic topology in this representation the physics of the desired system will be sensitive to small changes in the property curves near the avoided crossing geometries, which is undesirable for theoretical models. The diabatic representation then provides a simple and stable model which does not influence the physics strongly with small variations in the topology of its property curves, and can be effectively parameterised by simple analytical functions. Equivalency between the two-state adiabatic and diabatic representations has only been shown recently by us[38] for the computed rovibronic energies of the $B\,^2\Sigma^+$ and $D\,^2\Sigma^+$ states of YO and the $C\,^2\Sigma^+$ and $2\,^2\Sigma^+$ states of CH. This equivalence has also been extended to the general N-state case in our recent work[57,58], which includes the $1\,^1\Sigma_g^+$, $2\,^1\Sigma_g^+$, and $3\,^1\Sigma_g^+$ states of N_2; the $C\,^2\Sigma^+$, $2\,^2\Sigma^+$, $3\,^2\Sigma^+$, and $4\,^2\Sigma^+$ states of CH; and an artificial 10-state model system. Therefore, the diabatic representation is desirable choice for many molecules, especially when the NACs are strong.

A multitude of methods can be employed to compute the AtDT and are typically categorised into one of a few classifications, indirect diabatisa-

tion[20,59–68], direct diabatisation[26,69–75,61,49,43–48,50,42,40,41,76–81], or ansatz diabatisation[82–86,68,87,88]. This thesis incorporates relevant diabatisation literature throughout, aiming to provide context for the presented work wherever possible. For additional context and detailed discussions, readers are directed to the reviews by Yarkony[11], Shu et al.[89], Domcke et al.[90], Köppel et al.[91], Baer[46], Dobbyn and Knowles[63], O'Malley[92].

Indirect diabatisation, known as a property-based diabatisation, optimises an AtDT by maximizing the smoothness of diabatic molecular properties, such as the diabatic PECs, dipole moment curves (DMCs), or wavefunctions. Usually, the AtDT is constrained by forcing the diabatic molecular properties to coincide with the adiabatic curves either side of an avoided crossing and vary smoothly across this region. Property-based diabatisation is desirable due to its simplicity and ability to use any Hermitian operator to construct a diabatisation. Prototypical examples include the ionic and covalent structures of alkali hydrides[92,93] which can be distinguished by the dipole moment[26] and represent natural diabatic states. For example, Werner and Meyer[26] form diabatic states of LiH by computing mixing angles which ensure the (linear) ionic component of the dipole moment passes smoothly through the adiabatic DMCs.

Direct diabatisation instead diabatises each point in the molecular configuration space independently of the surrounding points either directly from the adiabatic electronic wavefunctions without NACs, calculation of diabatic molecular orbitals in which the molecular properties are computed, or via solution of matrix-differential equations involving the NAC matrix[76–79]. The NAC matrix is then often obtained *ab initio* through the DDR procedure of MOLPRO[94]. Diabatisations involving molecular orbitals, on the other hand, are sometimes referred to as orbital-dependent diabatisations[69–74]. The direct diabatisation scheme is typically the most accurate diabatisation method since it aims to exactly remove NACs obtained from *ab initio* electronic structure methods. The drawback of this method (which is discussed extensively in this thesis) is that the resulting diabatisation is not guaranteed to yield a simple or useful representation.

Ansatz diabatisation is widely used in block-diagonalization schemes[83,89,82,87,88,81], and involves fitting the eigenvalues of a predetermined diabatic model to adiabatic electronic structure data. This ansatz-block-diagonalization method has proven to reproduce well the dynamics of ultrafast nonadiabatic processes, but struggles to represent all regions of the adiabatic PECs accurately[85]. This thesis explores the ansatz diabatisation scheme mostly for two-state systems, but also provides insight and formulae for the N-state case.

In this thesis, I develop a novel hybrid property-based and direct orbital-independent diabatisation approach for general N-state coupled diatomic systems. As demonstrated in this thesis and previous works[95,96,76,97], solving the AtDT directly from the NACs of systems with three or more coupled states is inherently non-local, requiring knowledge of diabatisation at surrounding points. This is typically addressed using an evolution method. However, even with a numerically exact solver, diabatisation remains non-trivial because the AtDT solution depends on the choice of initial boundary conditions. As a result, the AtDT is unique only up to its boundary value, leading to an infinite set of AtDT solutions and, consequently, an infinite set of diabatic representations all of which are equivalent to a given adiabatic representation. The AtDT solution does not inherently guarantee the simultaneous satisfaction of multiple boundary conditions for a given set of NACs. Furthermore, inconsistencies between the NACs and other adiabatic properties (e.g., potentials or dipoles) can hinder the construction of a physically meaningful diabatisation that is exactly equivalent to the adiabatic representation, often resulting in undesirable asymptotic behaviour and irregular topologies of the diabatic properties. This then complicates the interpretation and application of these diabatic states.

A limitation of these direct diabatisation methods is that they – often relying solely on NACs – exclude molecular properties such as potentials and dipoles. A primary motivation in this thesis is to bridge this gap by achieving the accuracy characteristic of direct methods while yielding physical diabatic states consistent with property-based approaches. By doing so, it becomes possible to test on the importance of different DDR terms on the computed rovibronic spectroscopy as in the method of Brady et al.[38], but for N-state systems. Furthermore, I also aim to construct diabatic representations which allow for the construction of efficient and accurate contracted vibronic basis sets, which will motivate the development of my novel diabatisation method.

Diabatisation is routinely used to treat the avoided crossings of molecular PECs for the aforementioned reasons, but it is rarely discussed in the literature the numerical equivalence of adiabatic and diabatic energy level terms. Equivalence implies that two representations, like coordinate frames, should yield identical observables such as energy eigenvalues. Establishing this (rovibronic) equivalence would benefit researchers aiming to benchmark their nuclear motion codes and provide deeper insights into the roles of various terms in both the adiabatic and diabatic Hamiltonians such that appropriate approximations can be made. Therefore, adiabatic and diabatic solutions of the nuclear motion Schrödinger equation should coincide[46] with suitable accuracy of the calculation, e.g by using increasingly larger

basis sizes. While equivalence is frequently assumed, it is rarely demonstrated, and only a few studies have thoroughly investigated the convergence between adiabatic and diabatic states. For example, Shi et al.[98] used a sinc-DVR method to evaluate numerical convergence rates of adiabatic and diabatic energy eigenvalues and demonstrated equivalency. This required using a complete adiabatic model and a conical intersection (avoided crossing) at high energy. Zimmerman and George[99] investigated the numerical convergence of transition probability amplitudes for adiabatic and diabatic states in collisions involving collinear atom–diatom systems. Their findings confirmed the convergence to equivalence of the states in question, illustrating that the diabatic representation converges significantly faster than its adiabatic counterpart. However, our recent study[38] showed that for systems where NACs are weak, at least for the isolated two state case (where DCs are large), then the adiabatic representation showed faster convergence of the rovibronic energies than in the diabatic representation. Therefore, it is not immediately clear whether the adiabatic or diabatic representation is more suitable for the target diatomic system. Moreover, it remains uncertain whether approximation by neglecting various DDR couplings or DCs will yield meaningful spectroscopic results. Thus, a theoretical and algorithmic framework where one can test the importance of different coupling terms in the adiabatic and diabatic representation of nuclear motion would be powerful tool. In this thesis I layout the theory and technical details involved in the adiabatic to diabatic transformation, where derivations are presented and discussed. I do not claim to invent the wheel, but rather provide a collation of theory, make clear my own contributions, and provide a consistent and complete framework tailored for use in nuclear motion codes such as Duo.

An additional context in which the equivalence between adiabatic and diabatic representations is applied, beyond nuclear motion calculations, is in scattering calculations, where this equivalence is often assumed[76]. For example, Little and Tennyson[100] study the dissociative recombination of N_2^+[101] and partially model the electronic structure of N_2 diabatically for their multichannel quantum defect theory calculations. It was shown by Volkov et al.[102] that both adiabatic and diabatic representations of multichannel coulomb scattering calculations for the mutual neutralisation reaction $H^+ + H^- \rightarrow H_2^* \rightarrow H(1) + H(n)$ produced equivalent results. Relevant to this thesis, the second DDR term was demonstrated to be important for producing accurate cross-sections, an interesting result which showcases the need for accurate representation of non-adiabatic dynamics.

As part of the ExoMol group, my PhD research contributes to the production of diatomic molecular “line lists”, a (often semi-empirical) spectroscopic dataset

which is essential in the analysis of exoplanet atmospheres. To fully recover the information embedded in the transit spectrum of an exoplanet one must have a solid foundation of spectroscopic characterisation for many molecules which are expected to be present in such environments. In particular, spectroscopic characterisation over a wide range of conditions, such as temperature and pressure. It is the aim of the ExoMol project[53–55] to provide such data, where the core methodology is in the variational calculation of molecular rovibronic energy terms and transition strengths – the "line list" – from which a spectrum can be simulated for different temperatures and pressures. As previously discussed, the accurate treatment of non-adiabatic interactions within nuclear motion calculations, particularly in rovibronic energy levels, plays a crucial role in improving the precision of these line lists, aiding applications ranging from exoplanet atmospheres to cool stars and beyond.

This thesis is structured as follows. Chapter 2 presents the theory and methodology used to develop a diatomic line list, with a particular focus on incorporating non-adiabatic effects in the calculation of diatomic spectra. Beginning with the Born-Oppenheimer approximation, the chapter builds a theoretical framework for treating non-adiabatic couplings arising from the decoupling of electronic and nuclear motions. It then introduces different approaches for handling these NACs in the generation of an AtDT for systems with different numbers of coupled states. Our novel regularization method, HyAP, is also described, which aims to construct accurate and practical diabatic representations for the development of efficient vibronic basis sets through correction to the NACs. The chapter also includes a discussion of the variational treatment of nuclear motion, implemented in the Duo program. Chapter 3 applies the diabatisation theory outlined in Chapter 2 to several systems: the two-state YO and CH molecules, the three-state N_2 system, the four-state CH system, and an artificial 10-state system. It demonstrates, for the first time, numerical rovibronic equivalence between adiabatic and diabatic representations in both two-state and general N-state cases. Chapter 3 also showcases the application of diabatic spectroscopic models to the YO and CO molecules, resulting in the generation of accurate line lists. Chapter 4 describes the creation of an accurate IR/Vis line list for the SO radical, covering *ab initio* calculations of molecular property curves, inversion and validation of experimental transition frequencies, the development of a spectroscopic network for rovibronic energies and uncertainties, and refinement of the *ab initio* model based on the aforementioned empirical energy levels. Chapter 5 highlights additional research activities, collaborative projects, and unpublished preliminary results. While these do not constitute the core focus of the thesis, they represent significant contributions and offer potential avenues

for future exploration. Finally, Chapter 6 summarises the results of this thesis and outlines directions for future work.

Chapter 2

Theory & Methodology

The basis of this thesis lies primarily in the production of diatomic molecular line lists. A line list contains a set of molecular energy levels with corresponding quantum number assignments, their transitions, and associated transition strengths from which a spectrum can be simulated. The production of a line list requires quantum mechanical calculations of first the electronic structure (often in the Born-Oppenheimer approximation) *a priori* to nuclear motion calculations yielding rovibronic energy terms, wavefunctions, and transition strengths (see Section 2.3 for details). This thesis heavily uses the general purpose variational (open access[1]) code Duo[103] that solves the rovibronic Schrödinger equation for diatomic molecules using a detailed spectroscopic model as input. The model contains potential energy curves, couplings (e.g. spin-orbit, electronic angular momenta, e.t.c.), (transition) dipole moments, and higher order moments.

Initially, the molecular property curves input to nuclear motion codes are often obtained from *ab initio* using quantum chemistry programs such as `MOLPRO`[104], `ORCA`[105], and `Psi4`[106]. The *ab initio* spectroscopic model often serves as a baseline for refinement to empirical energy levels – determined from experimental transition data – and intensities. The refinement process involves iteratively adjusting the property curves until the computed rovibronic energies have the best agreement to the empirical energies. This approach underpins the ExoMol project's production of high-accuracy line lists for applications in high-resolution spectroscopy. Therefore, any work that attempts to improve the description of the molecular spectroscopic model is directly aiming to improve the final computed line list/spectra. This thesis aims to do this by incorporating non-adiabatic effects which are becoming more and more relevant for different molecular systems, especially in their UV description. Key theoretical aspects of Duo's methodology are summarised in Section

[1] github.com/Exomol

2.3, with non-adiabatic coupling theory and related methods covered in Sections 2.1 through 2.8.

As part of my PhD research, I reformulated existing diabatisation theory to enable systematic benchmarking of non-adiabatic effects within the nuclear motion code Duo. Throughout this chapter, I will clearly distinguish my original contributions from established theory, citing relevant sources where appropriate.

2.1 The Born-Oppenheimer Approximation

The non-relativistic Hamiltonian for the diatomic molecule is first considered, which reads in the body-fixed center of mass frame [107–112]

$$\left[\hat{H}_{\text{vib}} + \hat{H}_{\text{rot}} + \hat{H}_{\mu} + \hat{H}_{e}\right] |\Psi\rangle = |\Psi\rangle E, \tag{2.1}$$

where $|\Psi\rangle$ is the total electronic + nuclear wavefunction and E is the associated rovibronic energy eigenvalue. $\hat{H}_e$ is the electronic Hamiltonian given by

$$\hat{H}_e = \underbrace{-\sum_{i}^{n_e} \frac{\hbar^2}{2m_i} \nabla_i^2}_{\hat{T}_e} + V(\xi, r), \tag{2.2}$$

where the sum is over all n_e electrons, m_i are the electron masses, ∇_i^2 is the Laplacian for the i^{th} electron, $\hat{T}_e$ is the electronic kinetic energy operator, and $V(\xi, r)$ is the total Coulomb electrostatic potential between all particles (electron-electron, electron-nuclei, nuclei-nuclei) and is a function of the electron and nuclear coordinates ξ and r, respectively, given by

$$V(\xi, r) = \underbrace{\sum_{i<j}^{n_e} \frac{e^2}{4\pi\varepsilon_0} \frac{1}{|\vec{\xi}_i - \vec{\xi}_j|}}_{V_{\text{ee}}} + \underbrace{\frac{Z_1 Z_2 e^2}{4\pi\varepsilon_0} \frac{1}{|\vec{r}_1 - \vec{r}_2|}}_{V_{NN}} - \underbrace{\frac{1}{2} \sum_{i}^{2} \sum_{j}^{n_e} \frac{Z_i e^2}{4\pi\varepsilon_0} \frac{1}{|\vec{r}_i - \vec{\xi}_j|}}_{V_{Ne}}. \tag{2.3}$$

Here, Z_i is the atomic number of the i^{th} nuclei, e is the electron charge, ε_0 is the permittivity of free space, $|\vec{r}_i - \vec{r}_j|$ is the internuclear separation, $|\vec{r}_i - \vec{\xi}_j|$ is the electron nuclei separation, and $|\vec{\xi}_i - \vec{\xi}_j|$ are the inter-electron distances. V_{ee} is then the electron-electron repulsion potential, V_{NN} is the nuclei-nuclei repulsion potential, and V_{Ne} is the electron-nuclei attraction potential. The mass polarization term, $\hat{H}_{\mu}$, arises when separating the center-of-mass (COM) motion from the internal motion of the particles [113]. It originates from the correlated motion of electrons and nuclei. In many cases, the COM is approximated as the COM of the nuclei, neglecting the

small electronic contribution, which results in the appearance of the mass polarization term as a correction. $\hat{H}_\mu$ is not a physical effect, but rather an artifact of the choice of coordinates. In all practical applications it is negligible since it depends on the inverse of the total molecular mass, and will not be explored in this thesis. $\hat{H}_{\text{vib}}$ is the nuclear vibrational kinetic energy Hamiltonian given by

$$\hat{H}_{\text{vib}} = -\frac{\hbar^2}{2\mu}\frac{d^2}{dr^2}, \tag{2.4}$$

where $\mu = M_1^{-1} + M_2^{-1}$ is the reduced mass of the two nuclei and r is the internuclear separation, or bond length. $\hat{H}_{\text{rot}}$ is the nuclear rotational kinetic energy Hamiltonian and can be expressed in terms of the body-fixed rotational angular momentum operator $\hat{R}$ as

$$\hat{H}_{\text{rot}} = \frac{\hbar^2}{2\mu r^2}\hat{R}^2. \tag{2.5}$$

It is clear that analytically solving Eq.(2.1) for the total wavefunction $|\Psi\rangle$ and energy E is impossible beyond the simplest system, the Hydrogen atom, because of the coupling between the electronic and nuclear motion. Consequently, this equation is not separable into electronic and nuclear degrees of freedom, if it was then one may solve it. It is exactly this thought upon which the Born-Oppenheimer approximation is built, and goes as follows: consider the electron nuclear mass ratio $m_e/m_n \ll 1$, which is very small even for the hydrogen atom ($m_e/m_p \approx 1/1837$), this means the electrons are assumed to move very quickly compared to the slowly moving nuclei. As a result, when solving for the electronic motion, one can ignore the nuclear kinetic energy $\hat{H}_{\text{vib}} + \hat{H}_{\text{rot}}$ because of the $1/\mu$ term. This can be understood in two ways: (1) electrons effectively have time to relax as the nuclei move; (2) the uncertainty in the nuclei positions can be ignored and assumed fixed as the electrons move. Thus, under the Born-Oppenheimer approximation, the nuclear positions are treated as fixed parameters when solving the electronic Schrödinger equation (discussed below). As a result, in the molecule fixed frame, the electronic wavefunctions can be expressed as depending parametrically on the nuclear coordinate as

$$|\varphi\rangle \approx |\varphi(\xi; r)\rangle, \tag{2.6}$$

where $|\varphi\rangle$ are the electronic wavefunctions and r represents the internuclear distance. Thus, for each fixed r, a different electronic eigenfunction is obtained. During these electronic structure calculations, the molecule is placed in a fixed orientation, typically with the internuclear axis aligned along the z-axis in the molecular

(body-fixed) frame. Rotational degrees of freedom are therefore excluded from the electronic problem and are treated separately at the nuclear motion stage (see Section 2.3). As a result, the rotational degrees of freedom are 'frozen' during the electronic step, similarly to the vibrational coordinates, where we assume the electronic energies are not altered by the slow molecular rotations.

The total wavefunction can then be expressed by the Born-Huang expansion as[114,2]

$$|\Psi(\xi, r, \theta, \phi)\rangle = \sum_{i=1}^{\infty} |\varphi_i(\xi; r)\rangle \, |\chi_i(r, \theta, \phi)\rangle \tag{2.7}$$

where $|\chi_i(r, \theta, \phi)\rangle$ are the nuclear wavefunctions, with $\{\theta, \phi\}$ denoting the Euler angles that describe the molecular orientation. In our nuclear motion code Duo, the total nuclear wavefunction is represented in a product basis comprising vibrational, spin, and rotational components. The rotational part depends implicitly on the Euler angles and is constructed using eigenfunctions of the molecular-fixed rotational angular momentum operators (see Section 2.3). This expansion is exact if all possible adiabatic states are included. However, practical calculations require truncating the sum, limiting it to a finite number of terms. This truncation of the electronic Hilbert space introduces an approximation error (associated with the Born-Oppenheimer approximation), as higher energy states, which contribute marginally to the ground state energy, are neglected in practice. The Born-Oppenheimer approximation[2] then assumes the electronic Hamiltonian only acts on $|\varphi_i\rangle$ and the nuclear part on $|\chi_i\rangle$, yielding a static description of the electronic structure. From this, the electronic Hamiltonian eigenvalue equation is obtained, and the electronic motion computed by clamping the nuclei

$$\left[\hat{T}_e + V\right] |\varphi_\alpha(\xi; r)\rangle = |\varphi_\alpha(\xi; r)\rangle \, E^e_\alpha(r), \tag{2.8}$$

Here it is realised that the E^e_α term is the BO-PEC for the α electronic state and is a function of the internuclear separation r. Thus, for each nuclear configuration the electronic motion can be solved, producing a set of PECs over an entire grid of internuclear separations. $E^e(r)$ and the corresponding electronic wavefunctions are commonly solved using *ab initio* methods, such as Hartree-Fock[115,116], complete active space self-consistent field (CASSCF)[117,118], multi-reference configuration interaction (MRCI)[119,120], or coupled cluster[121,122] theories.

Currently, only electronic motion has been considered, which alone will not yield accurate molecular energy terms. The remaining task is to solve the following nuclear Hamiltonian where the final molecular energies are computed incorporating

both nuclear and electronic motion

$$\left[\hat{H}_{\text{vib}} + \hat{H}_{\text{rot}} + E^e_\alpha(r)\right] |\chi_i(r,\theta,\phi)\rangle = |\chi_i(r,\theta,\phi)\rangle\, E_i^{rvr}, \tag{2.9}$$

where E_i^{rvr} are the rovibronic energies. The BO-PEC for the α electronic state approximates the nuclear motion extremely well for many molecules, especially near the equilibrium geometry[11]. As discussed in the introduction, the BO-approximation has been highly successful in many areas of photochemistry and molecular physics. In particular, BO-PECs often reproduce molecular dynamics/spectroscopy with high accuracy and are supported by a (i.e., energy levels computed from PECs correspond to observable transitions in molecular spectra). For many physical processes, nuclear motion occurs on energy scales approximately 3-4 orders of magnitude lower than electronic excitations, making the use of a single, uncoupled PEC a very effective approximation for many systems.

2.2 Beyond Born-Oppenheimer: Non-Adiabatic Couplings

Despite the successes of the BO-approximation (see Sections 1 and 2.1) it cannot be satisfied in all regions of the molecular configuration space for many molecules. When same symmetry electronic eigenvalues – $E^e_\alpha(r)$ of Eq.(2.9) – become degenerate, non-adiabatic couplings become singular and the PECs exhibit an avoided crossing such as in Figure 1.1. The non-adiabatic couplings are commonly neglected under the BO-approximation, which assumes the nuclear kinetic energy operator $\hat{H}_{\text{vib}}$ does not act on the electronic wavefunctions. More precisely, the electronic wavefunctions are assumed to vary smoothly with nuclear coordinates, so that the derivative couplings (DDRs) vanish, i.e.

$$\hat{H}_{\text{vib}} |\varphi\rangle \begin{cases} = 0, & \text{Born-Oppenheimer approximation} \\ \neq 0, & \text{beyond Born-Oppenheimer.} \end{cases} \tag{2.10}$$

Consequently, the BO approximation treats nuclear motion as evolving independently on single, uncoupled potential energy curves given by the electronic eigenvalues $E^e_\alpha(r)$ of Eq.(2.9). Technically, it is the Born–Oppenheimer framework itself that gives rise to nonadiabatic couplings, as they emerge from retaining the nuclear kinetic energy operator acting on the total wavefunction. However, in the standard BO treatment of molecular dynamics, these couplings are assumed to be negligible and are therefore typically omitted.

The DDR terms as presented in many other works[123,49,48,41,47] are now derived, providing a complete derivation of all terms for the general N-state case, explaining their significance. A quick note, from herein the term 'adiabatic' refers to the representation where all DDR couplings are included in the nuclear kinetic energy, where the electronic Hamiltonian is diagonalised with eigenvalues being the avoided crossing potentials. Furthermore, the work during my PhD and therefore in this thesis concerns removal of the *radial* DDR coupling terms, where the angular part is ignored. Angular DDRs arise from the dynamical electron nuclear coupling as the molecule rotates, and couples states of different angular-momenta projections[40,47] ($\Delta\Lambda = \pm 1$).

The adiabatic nuclear kinetic energy Hamiltonian is now derived. The operator $\hat{H}_{\text{vib}}$ is first left- and right-multiplied by the Born–Huang wavefunction element (see Eq. (2.7)), $|\Psi^{(\text{a})}_{i,\text{tot}}\rangle = |\varphi^{(\text{a})}_i\rangle\,|\chi^{(\text{a})}_i\rangle$, yielding the kinetic energy elements

$$\begin{aligned}\langle\chi^{(\text{a})}_\alpha|\,\langle\varphi^{(\text{a})}_\alpha|\,\hat{H}^{(\text{a})}_{\text{vib}}\,|\varphi^{(\text{a})}_\beta\rangle\,|\chi^{(\text{a})}_\beta\rangle &= -\frac{\hbar^2}{2\mu}\,\langle\chi^{(\text{a})}_\alpha|\,\langle\varphi^{(\text{a})}_\alpha|\,\frac{d^2}{dr^2}\,|\varphi^{(\text{a})}_\beta\rangle\,|\chi^{(\text{a})}_\beta\rangle \\ &= -\frac{\hbar^2}{2\mu}\,\langle\chi^{(\text{a})}_\alpha|\left[\langle\varphi^{(\text{a})}_\alpha|\,\frac{d^2}{dr^2}\,|\varphi^{(\text{a})}_\beta\rangle + 2\,\langle\varphi^{(\text{a})}_\alpha|\,\frac{d}{dr}\,|\varphi^{(\text{a})}_\beta\rangle\,\overrightarrow{\frac{d}{dr}} + \langle\varphi^{(\text{a})}_\alpha|\varphi^{(\text{a})}_\beta\rangle\,\overrightarrow{\frac{d^2}{dr^2}}\right]|\chi^{(\text{a})}_\beta\rangle\end{aligned} \tag{2.11}$$

where in the second line the Laplacian identity for the product $|\varphi^{(\text{a})}_\beta\rangle\,|\chi^{(\text{a})}_\beta\rangle$ was used, the direction of the derivative is specified – to explicitly show they act on the nuclear wavefunctions – and will be important for our algorithmic formulation later, and the superscript '(a)' means properties are taken in the adiabatic representation. Terms appear where the derivative in the nuclear coordinates act on the electronic wavefunction, these are exactly the DDR (derivative) coupling terms and when assumed zero brings the Hamiltonian into the BO-approximation where adiabatic potentials are realised and assumed to evolve on single uncoupled surfaces. The above equation can be simplified by introducing matrix notation for the electronic properties

$$\langle\chi^{(\text{a})}_\alpha|\,\langle\varphi^{(\text{a})}_\alpha|\,\hat{H}^{(\text{a})}_{\text{vib}}\,|\varphi^{(\text{a})}_\beta\rangle\,|\chi^{(\text{a})}_\beta\rangle = -\frac{\hbar^2}{2\mu}\,\langle\chi^{(\text{a})}_\alpha|\left[\mathbf{W}^{(2)} + 2\mathbf{W}^{(1)}\,\overrightarrow{\frac{d}{dr}} + \mathbf{I}\,\overrightarrow{\frac{d^2}{dr^2}}\right]|\chi^{(\text{a})}_\beta\rangle\,, \tag{2.12}$$

where the orthogonality in the electronic wavefunctions is used to introduce the identity matrix $\mathbf{I}$. The different DDR terms are now examined. First, the second

derivative coupling is considered.

$$W^{(2)}_{\alpha,\beta} = \langle \varphi^a_\alpha | \frac{d^2}{dr^2} | \varphi^a_\beta \rangle , \tag{2.13}$$

where $|\varphi^a\rangle$ are the adiabatic electronic basis wavefunctions and $W^{(2)}_{\alpha,\beta}$ are the second DDR derivative coupling elements. The NAC, or first DDR term, is well known and defined as the matrix elements of the first derivative operator

$$W^{(1)}_{\alpha,\beta} = \begin{cases} \langle \varphi^a_\alpha | \frac{d}{dr} | \varphi^a_\beta \rangle = - \langle \varphi^a_\beta | \frac{d}{dr} | \varphi^a_\alpha \rangle & \text{if } \alpha \neq \beta \\ 0 & \text{if } \alpha = \beta \end{cases} , \tag{2.14}$$

where the NAC matrix $\mathbf{W}^{(1)}$ is anti-Hermitian. Multiple studies[124,125,46] have used the following identity to relate the first and second DDR coupling elements via

$$\frac{d}{dr} \langle \varphi^a_\alpha | \frac{d}{dr} | \varphi^a_\beta \rangle = \left\langle \frac{d\varphi^a_\alpha}{dr} \middle| \frac{d\varphi^a_\beta}{dr} \right\rangle + \langle \varphi^a_\alpha | \frac{d^2}{dr^2} | \varphi^a_\beta \rangle \rightarrow W^{(2)}_{\alpha,\beta} = \frac{dW^{(1)}_{\alpha,\beta}}{dr} - K_{\alpha,\beta} , \tag{2.15}$$

where the diagonal elements of the $\boldsymbol{K}$ matrix, when multiplied by the kinetic energy factor, $-\frac{\hbar^2}{2\mu} K_{\rho,\rho}$, are the well-known DBOCs. The off-diagonal elements of $\boldsymbol{K}$ form further second DDR couplings for systems with $N > 3$ coupled adiabatic states. The DBOCs can then be added to the BO-PECs to describe non-adiabatic perturbation in the potential energies (or the contribution to electronic structure due to nuclear motion) in the region of avoided crossing. Historically, the use of the above identity was to avoid the cumbersome computation of $\mathbf{W}^{(2)}$ by only having to evaluate $\mathbf{W}^{(1)}$ and its derivative, and is identical to the g-, h-, and k- notation by Lengfield & Yarkony[124] and Saxe & Yarkony[125] with $h = \frac{dg}{dr} - k$. The above relation shows $\mathbf{W}^{(2)}$ to have both diagonal and off-diagonal components. But first, Eq.(2.15) is further simplified by introducing a resolution of the identity between the bra and ket of the $K_{\alpha,\beta}$ element within the adiabatic basis, yielding

$$K_{\alpha,\beta} = \left\langle \frac{d\varphi^a_\alpha}{dr} \middle| \frac{d\varphi^a_\beta}{dr} \right\rangle = \sum_\kappa^N \left\langle \frac{d\varphi^a_\alpha}{dr} \middle| \varphi^a_\kappa \right\rangle \left\langle \varphi^a_\kappa \middle| \frac{d\varphi^a_\beta}{dr} \right\rangle = - \sum_\kappa^N W^{(1)}_{\alpha,\kappa} W^{(1)}_{\kappa,\beta} \tag{2.16}$$

where the summation, in principle, should be over all adiabatic states ($N = \infty$) – another source of error from the BO-approximation which strictly requires all infinite states to be treated. It turns out that the $\boldsymbol{K}$ matrix can be computed simply via the

squared NAC matrix as

$$\mathbf{K} = -\mathbf{W}^{(1)} \cdot \mathbf{W}^{(1)}, \tag{2.17}$$

and that all DDRs are completely defined in terms of the NAC only. In conjunction of Eqs.(2.15-2.17) and other theoretical results[46,50,47], a simple and powerful expression for the matrix element of the second DDR term $\mathbf{W}^{(2)}$ is obtained

$$\mathbf{W}^{(2)} = \frac{d\mathbf{W}^{(1)}}{dr} + \left(\mathbf{W}^{(1)}\right)^2. \tag{2.18}$$

Since the derivative of $\mathbf{W}^{(1)}$ is skew-symmetric, it is useful to reformulate Eq.(2.18) such that the final rovibronic Schrödinger equation is Hermitian (therefore producing real valued energy eigenvalues). This is not the first time it has been done[126], but I continue the derivation for clarity using the defined symbols from this section. First, the derivative of $\mathbf{W}^{(1)}$ is re-expressed in terms of directional derivatives. This can be done by considering the following matrix-operator

$$\left(\frac{\overrightarrow{d}}{dr}\mathbf{W}^{(1)}(r)\right)|\chi_i(r)\rangle\,, \tag{2.19}$$

where $\frac{\overrightarrow{d}}{dr}$ means the derivative acts on the ket state (and $\frac{\overleftarrow{d}}{dr}$ on the bra state), and $|\chi_i(r)\rangle$ is a column vector of nuclear wavefunctions in which the NAC matrix $\mathbf{W}^{(1)}$ acts on. Using the chain rule of differentiation, the following is obtained in operator form,

$$\left(\frac{\overrightarrow{d}}{dr}\mathbf{W}^{(1)}(r)\right)|\chi_i(r)\rangle = \left(\frac{d\mathbf{W}^{(1)}(r)}{dr} + \mathbf{W}^{(1)}(r)\frac{\overrightarrow{d}}{dr}\right)|\chi_i(r)\rangle\,. \tag{2.20}$$

Eq.(2.20) shows that the differentiation operator does not commute with $\mathbf{W}^{(1)}$, yielding the commutator relation

$$\left[\frac{\overrightarrow{d}}{dr}, \mathbf{W}^{(1)}(r)\right] = \frac{d\mathbf{W}^{(1)}(r)}{dr}. \tag{2.21}$$

Now, using the anti-Hermiticity of the first derivative operator, inversion of the derivative direction on the left hand side of Eq.(2.20) is possible assuming the left multiplication of a bra state (to induce an integral in r), introducing a minus sign.

Rearranging for the derivative of $\mathbf{W}^{(1)}$ gives, again in operator form

$$\left(\frac{d\mathbf{W}^{(1)}}{dr}\right)|\chi_i(r)\rangle = -\left(\frac{\overleftarrow{d}}{dr}\mathbf{W}^{(1)} + \mathbf{W}^{(1)}\frac{\overrightarrow{d}}{dr}\right)|\chi_i(r)\rangle\,. \tag{2.22}$$

Inserting this into eq.(2.18) yields the symmetric, Hermitian reformulation of the second DDR term

$$\mathbf{W}^{(2)} = -\left(\frac{\overleftarrow{d}}{dr}\mathbf{W}^{(1)} + \mathbf{W}^{(1)}\frac{\overrightarrow{d}}{dr}\right) + \left(\mathbf{W}^{(1)}\right)^2. \tag{2.23}$$

Inserting $\mathbf{W}^{(2)}$ above into Eq.(2.12) yields the adiabatic nuclear kinetic energy matrix elements

$$\langle\chi_\alpha^{(a)}|\langle\varphi_\alpha^{(a)}|\hat{H}_{\text{vib}}^{(a)}|\varphi_\beta^{(a)}\rangle|\chi_\beta^{(a)}\rangle = -\frac{\hbar^2}{2\mu}\langle\chi_\alpha^{(a)}|\left(-\left[\frac{\overleftarrow{d}}{dr}\mathbf{W}^{(1)} - \mathbf{W}^{(1)}\frac{\overrightarrow{d}}{dr}\right] + \left(\mathbf{W}^{(1)}\right)^2 + \frac{\overrightarrow{d^2}}{dr^2}\right)|\chi_\beta^{(a)}\rangle\,,$$

In matrix-operator form, the adiabatic nuclear kinetic energy (vibrational) Hamiltonian reads

$$\hat{\mathbf{H}}_{\text{vib}}^{(a)} = -\frac{\hbar^2}{2\mu}\left(\frac{\overrightarrow{d^2}}{dr^2} + \left(\mathbf{W}^{(1)}\right)^2 - \left[\frac{\overleftarrow{d}}{dr}\mathbf{W}^{(1)} - \mathbf{W}^{(1)}\frac{\overrightarrow{d}}{dr}\right]\right). \tag{2.24}$$

This concludes the extension of the Born-Oppenheimer (BO) approximation considered in this thesis and establishes the adiabatic (vibrational) nuclear kinetic energy Hamiltonian used throughout my nuclear motion calculations. This formulation is fundamental to the rovibronic treatment, as it allows all non-adiabatic effects to be defined solely in terms of the NAC matrix $\mathbf{W}^{(1)}$. This significantly simplifies *ab initio* DDR calculations (see Section 2.2.2 for more details), as only the first derivative of the electronic wavefunctions is required, eliminating the need for second derivative DDR couplings.

Moreover, in this symmetric representation, the nuclear kinetic energy remains Hermitian even when truncating the electronic Hilbert space, in contrast to the conventional formulation in Eq.(2.12) where such truncations can introduce anti-Hermitian terms[126]. This means it is safe to extend the non-adiabatic rovibronic treatment to any number of coupled states, and will be explored extensively throughout this thesis. The directional derivatives also emphasise their direct implementation within our nuclear motion code Duo[110]. The NAC term $\mathbf{W}^{(1)}$ thus fully governs the non-adiabatic dynamics that arise when relaxing the BO approximation, rein-

forcing the practical and theoretical advantages of this formulation in rovibronic modelling. In Chapter 3, I demonstrate that benchmarking the effects of different DDR terms in Eq. (2.24) is now straightforward. This formulation ensures that Hermiticity is preserved even when selectively deactivating individual coupling terms.

2.2.1 Hellmann-Feynman Formalism of the NAC

To better understand the NAC, many studies have used Hellmann-Feynman theorem (HFT)[127,128] to evaluate the NAC terms[129–132] via the Hamiltonian gradient, or "force". For completeness I will re-derive the HFT form of the NAC and discuss its implications. To this end, consider the following eigenvalue equation

$$\hat{H}_{\mathrm{e}}^{(a)} \left|\varphi_\beta^a\right\rangle = E_\beta^{(\mathrm{a})}(r) \left|\varphi_\beta^a\right\rangle, \tag{2.25}$$

where $\hat{H}_{\mathrm{e}}^{(a)}$ is the adiabatic electronic Hamiltonian and $E_\beta^{(\mathrm{a})}(r)$ are the adiabatic PECs. Enclosing by a bra (electronic) state $\langle\varphi_\alpha^a|$ (omitting the r dependence in the potential energy term) yields

$$\langle\varphi_\alpha^a|\hat{H}_e^{(\mathrm{a})}\left|\varphi_\beta^a\right\rangle = E_\beta^{(\mathrm{a})}\langle\varphi_\alpha^a|\varphi_\beta^a\rangle = E_\beta^{(\mathrm{a})}\delta_{\alpha,\beta}, \tag{2.26}$$

where $\delta_{\alpha,\beta}$ is the Kroncker delta since $|\varphi^a\rangle$ form an orthonormal basis. Considering the off-diagonal terms, or Born-Oppenheimer corrections (DDR couplings), and differentiating with respect to internuclear separation

$$\begin{aligned}
&\frac{d}{dr}\langle\varphi_\alpha^a|\hat{H}_e^{(\mathrm{a})}\left|\varphi_\beta^a\right\rangle = 0 \\
\rightarrow\ &\left\langle\frac{d\varphi_\alpha^a}{dr}\middle|\hat{H}_e^{(\mathrm{a})}\middle|\varphi_\beta^a\right\rangle + \left\langle\varphi_\alpha^a\middle|\frac{d\hat{H}_e^{(\mathrm{a})}}{dr}\middle|\varphi_\beta^a\right\rangle + \left\langle\varphi_\alpha^a\middle|\hat{H}_e^{(\mathrm{a})}\middle|\frac{d\varphi_\beta^a}{dr}\right\rangle \\
\rightarrow\ &E_\beta\left\langle\frac{d\varphi_\alpha^a}{dr}\middle|\varphi_\beta^a\right\rangle + \left\langle\varphi_\alpha^a\middle|\frac{d\hat{H}_e^{(\mathrm{a})}}{dr}\middle|\varphi_\beta^a\right\rangle + E_\alpha\left\langle\varphi_\alpha^a\middle|\frac{d\varphi_\beta^a}{dr}\right\rangle = 0,
\end{aligned} \tag{2.27}$$

Where the product rule was used in the second line and the Hermiticity of the Hamiltonian was used in the last line to act $\hat{H}_e^{(\mathrm{a})}$ on the bra state yielding the E_α term. Recognising $\left\langle\varphi_\alpha^a\middle|\frac{d\varphi_\beta^a}{dr}\right\rangle$ as the NAC element $W_{\alpha,\beta}^{(1)}$, rearranging for the NAC, the off-diagonal HFT emerges,

$$W_{\alpha,\beta}^{(1)} = \frac{1}{E_\beta - E_\alpha}\left\langle\varphi_\alpha^a\middle|\frac{d\hat{H}_e^{(\mathrm{a})}}{dr}\middle|\varphi_\beta^a\right\rangle. \tag{2.28}$$

This shows that the NAC depends on the inverse energy gap between the coupled electronic states. When the states α and β are sufficiently well separated –

$|E_\beta - E_\alpha| \gg 1$ – then the NAC between these states is small $W^{(1)}_{\alpha,\beta} \ll 1$. In contrast, when the energy gap is small, the NAC grows large. Interestingly, the term $\left\langle \varphi^a_\alpha \middle| \frac{d\hat{H}^{(a)}_e}{dr} \middle| \varphi^a_\beta \right\rangle$ corresponds to a "force" on the electronic structure due to nuclear motion in the diatomic molecule. This force plays a critical role in time-dependent non-adiabatic molecular dynamics[133,134,130,135], where transitions between different potential energy surfaces (quantum states) are allowed through the NAC and therefore become more probable when the NAC is large. As the energy gap between surfaces narrows, these transitions (or "surface hops") become more likely, allowing the molecule to evolve on multiple potential energy surfaces. This dynamic behavior, enabled by the NAC, goes beyond the scope of the Born-Oppenheimer approximation, which assumes separation of nuclear and electronic motion (see Chapter 1 and Section 2.1 for details). HFT then plays an important role in understanding how the NACs influence the complex nuclear dynamics of molecules through the forces and energy separation in the BO-PECs.

Importantly, the Hellmann-Feynman Theorem justifies the truncation of the number of (BO) adiabatic states considered, as the coupling between states diminishes significantly when their energy separation is large. As a result, transitions between well-separated states become negligible, allowing the focus to remain on a smaller region of the total molecular electronic Hilbert space covering energetically relevant states. Furthermore, the truncated molecular wavefunction approximates well the full Born-Huang expansion in Eq.(2.7).

2.2.2 The DDR Procedure

As will be used extensively throughout this thesis, a computational method for calculating non-adiabatic coupling (NAC) terms from electronic structure quantum chemistry calculations is essential. One such method is implemented in the quantum chemistry package MOLPRO[136], known as the DDR procedure.[2] This procedure approximates the NAC terms $\langle \psi_i | d/dr | \psi_j \rangle$ (see Eq.(2.14)) using a finite-difference approach to estimate the derivative of the electronic wavefunction with respect to the nuclear coordinate.

The NAC terms are computed from the electronic wavefunctions $|\psi_i(r)\rangle$ using

[2]For further details on the DDR procedure, please refer to the MOLPRO manual.

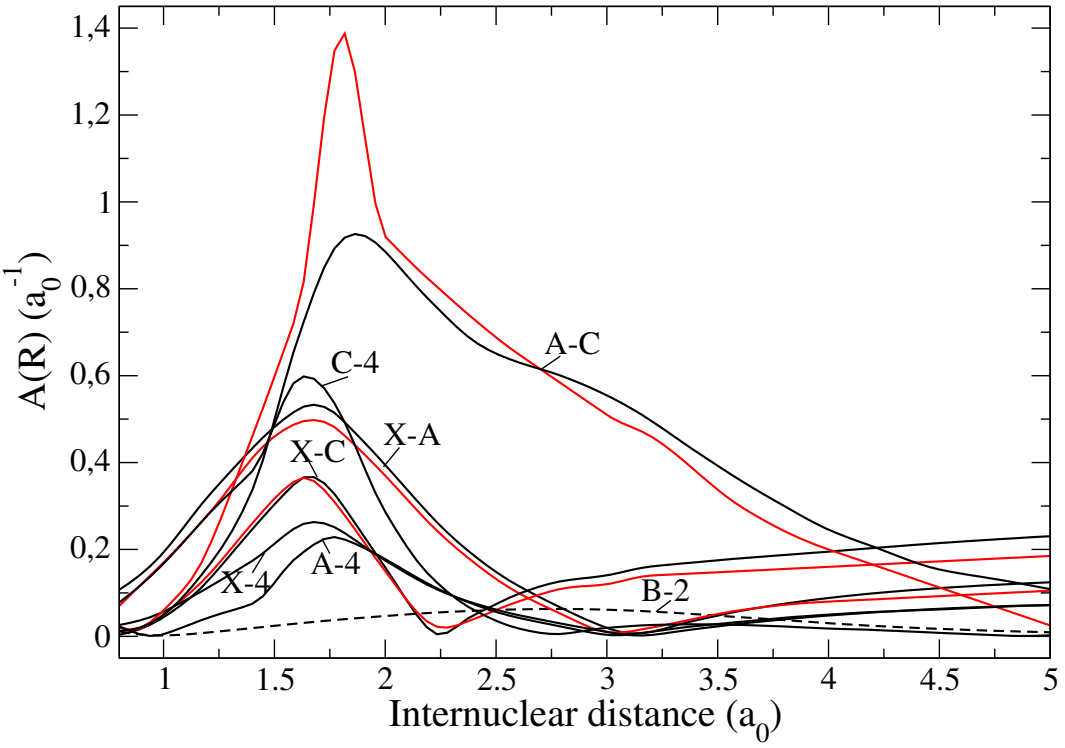

Figure 2.1: Illustration of our computed *ab initio* radial NACs for the $^2\Sigma^+$ manifold of the NeH^+ cation. The DDR procedure was used with the MOLPRO quantum chemistry package.

the central three-point finite difference formula

$$\begin{aligned} W_{ij}^{(1)} = \langle \psi_i(r)|\frac{d}{dr}|\psi_j(r)\rangle &\approx \langle \psi_i(r)|\frac{|\psi_j(r+\Delta r)\rangle - |\psi_j(r-\Delta r)\rangle}{2\Delta r} \\ &\approx \frac{\langle \psi_i(r)|\psi_j(r+\Delta r)\rangle - \langle \psi_i(r)|\psi_j(r-\Delta r)\rangle}{2\Delta r} \\ &\approx \frac{1}{2\Delta r}\left(\rho_{ij}^{+} - \rho_{ij}^{-}\right). \end{aligned} \tag{2.29}$$

Here, $\rho_{ij}^{\pm}$ are the transition densities (i.e., overlaps) between the i^{th} and j^{th} electronic states, evaluated at nuclear geometries displaced positively or negatively by Δr. These overlaps can be directly computed using MOLPRO, enabling straightforward evaluation of the NAC terms. Typically, we have seen a value of 0.01 Å to be suitable for the geometry displacement.

An example application of the DDR procedure can be found in our recent theoretical study of the NeH^+ cation[137]. Figure 2.1 shows the ab initio radial NACs computed for NeH^+ using this approach.

2.3 Variational Calculations: Nuclear Motion

Having established the Born-Oppenheimer theory of electronic states, potential energy curves, and the nuclear Schrödinger equation in both adiabatic and diabatic representations, this section will summarise the general theory of nuclear motion calculations for determining rovibronic energy terms and wavefunctions. In particular, the Duo solution of the nuclear motion Schrödinger equation will be discussed.

The variational principle[116] states that an upper bound for the energy eigenvalue of a Hamiltonian can be calculated by optimisation of the corresponding wavefunction. It was first demonstrated by Frank Boys[138] that molecular energy terms and wavefunctions could be evaluated using the variational method, and so begun the development of what is now an extremely powerful tool in the calculation of a molecules spectroscopy. Unlike in effective Hamiltonian methods (see, e.g. Martin-Drumel et al.[139], Heays et al.[140], Burkholder et al.[141]) whereby energy functionals are parameterised in terms of quantum numbers and fit to experimentally measured spectra [3], variational methods rely on use of the potential energy curves/surfaces and associated couplings arising from the BO-approximation to compute energy levels and transition strengths [4]. For example, the early series of papers Tennyson and Sutcliffe[142,143,144], Miller and Tennyson[145] showed that indeed a variational approach to the calculation of the H_3^+ spectroscopy led to its detection in Jupiter's atmosphere[146]. More recently the variational treatment of the diatomic sulfur-monoxide (SO)[13] (see Chapter 4) led to its detection in the exoplanet WASP-39b[147] and aided in the detection of SO_2 in the same object[148]. There are a wealth of example use-cases of the variational method for molecular spectroscopy, in particular the work by the MoLLIST project[149] implements an interesting hybrid effective Hamiltonian variational approach, and the ever increasing line list productions by the ExoMol project[53–55].

Duo computes diatomic rovibronic energy terms, wavefunctions, and transition strengths from a set of property curves defined on a grid of internuclear seperations, r. Initially, the molecular property curves (potentials and couplings) input to nuclear motion codes are often obtained *ab initio* using quantum chemistry programs such as `MOLPRO`[104], `ORCA`[105], and `Psi4`[106]. These curves can be defined with analytical forms (see Chapter 4 for examples of functional forms used to model different property curves), which are then computed on the sinc-DVR grid[150,150,151] (see Section 2.3.1 for details) in which the fully coupled rovibronic Schrödinger equation

[3] Whereby a highly accurate but local description of the molecular spectroscopy is determined.

[4] Whereby a complete spectroscopy is determined, and can be made accurate through refinement of the spectroscopic model to empirical energy levels.

is solved. Alternatively, the property curves can be represented in a grid format, which are mapped onto the sinc-DVR grid r via cubic splines. To then compute rovibronic energies and wavefunctions one requires a set of boundary conditions upon which the nuclear motion Schrödinger equation is solved, usually the setting of eigenstate wavefunctions and their derivative with bond length, r, to zero at the "simulation border". This is achieved in Duo by introducing a potential barrier of infinite height at the 'right hand' side of the simulation region at bond length r_c – the so-called particle in a box problem. Whilst this methodology is fully defined for solving bound rovibronic states which come as solutions to the nuclear motion inside potential wells, it does not provide a complete solution to the continuum region where states are unbound (such as those for electronic states which are repulsive). Since a finite simulation box size is utilised, the continuum is truncated to the solutions which satisfy the boundary conditions and consequently the continuum is effectively discretised. If one could solve the nuclear motion for an infinite simulation box size, i.e. $r_c \to \infty$, then the infinite rovibronic solutions are reconstructed for the unbound problem. A description of this discretisation method of solving nuclear motion can be found in the works Hazi and Taylor [152], Mandelshtam et al. [153], and Bacic and Simons [154], which discuss its implementations for stabilisation methods.

The strengths of the variational method is that, provided one has defined potentials and couplings which cover the spectroscopic region of interest, a complete description of the molecular energy levels, and therefore a complete spectroscopy, is easily achieved. For example, rovibronic terms can be computed up to dissociation including all the relevant effects such as level splitting and resonances. However, the quality of the computed spectroscopy relies on the accuracy of the property curves input to nuclear motion, which are often not to high-resolution standard before refinement of the curves to data. For example, errors in the vibrational band heads computed from *ab initio* curves at the MRCI level of theory can be as high as tens, or even hundreds, of wavenumbers. Of course, depending on the system, the accuracy of the *ab initio* calculations depends particularly on the number electrons to be treated. Regardless, the potentials and various coupling curves can be fitted iteratively such that the computed rovibronic energies agree with empirically determined ones. Empirical energy levels can be computed from experimentally derived spectroscopic constants using programs like PGOPHER [155], or directly through inversion of experimental transition frequencies via the MARVEL method [156] (see Chapter 4 for details). As a result, the fitted spectroscopic model can be made to reproduce the molecular spectroscopy to near-experimental accuracy. However, due to limitations in experimental technique, every rovibronic line, and therefore every

energy level, for the system of interest can not be feasibly measured. Consequently, refinement of the spectroscopic model is limited to the experimental coverage of the system and only parts of the model are refined. Typically only transitions involving the lowest lying rovibronic levels and (vertical) states in the Frank-Condon region of the ground state are measured, and so the potential minima are often fitted. The quality of high lying rovibronic energy levels, which are not experimentally characterised, are determined by the unrefined parts of the property curves. One then hopes extrapolation of their spectroscopic model beyond the refined region is sensible. An attempt to preserve the physics of the system in these unrefined regions is to weight the property curves to the *ab initio* forms during refinement. This then minimises the deviation of the fitted property curves from the quantum chemical predictions.

2.3.1 The Duo Solution to the Nuclear Motion Schrödinger Equation

The nuclear motion code Duo solves the following total[5] non-relativistic molecular rovibronic Schrödinger equation in the body-fixed COM frame, with Hamiltonian given by Eq.(2.1) (see Section 2.1 for details), which reads in the adiabatic representation

$$\begin{aligned}&\left[\hat{\mathbf{H}}_{\text{vib}}+\hat{\mathbf{H}}_{\text{rot}}+\boldsymbol{V}+\hat{\mathbf{H}}_c\right]\vec{\chi}\\&=\left[-\frac{\hbar^2}{2\mu}\left(\frac{\overrightarrow{d^2}}{dr^2}+\hat{\mathbf{H}}_W\right)+\frac{\hbar^2}{2\mu r^2}\hat{\mathbf{R}}^2+\boldsymbol{V}+\hat{\mathbf{H}}_c\right]\vec{\chi}=E_i\vec{\chi},\end{aligned}\tag{2.30}$$

where E_i is the i^{th} rovibronic energy eigenvalue and $\vec{\chi}$ is a vector of rovibronic wavefunctions (vectorised by the electronic labelling). The first term is the vibrational Hamiltonian studied in Sections 2.2 and 2.4, $\hat{\mathbf{H}}_W$ is the Hamiltonian associated with non-adiabatic interactions and is given by (see Eq.(2.24))

$$\hat{\mathbf{H}}_W=\left(\mathbf{W}^{(1)}\right)^2-\left[\frac{\overleftarrow{d}}{dr}\mathbf{W}^{(1)}-\mathbf{W}^{(1)}\frac{\overrightarrow{d}}{dr}\right],\tag{2.31}$$

with $\mathbf{W}^{(1)}$ being the NAC matrix. The non-adiabatic kinetic energy couplings in $\hat{\mathbf{H}}_W$ are now fully implemented in a new module in Duo. We discuss the usage, underlying theory, adiabatic/diabatic equivalence, and convergence tests in our recent publications[38,57,58]. Chapter 3 reports on the results of this work and its importance

[5] We ignore the mass-polarisation term. See Section 2.1 for details.

in spectroscopic modelling.

The second term of Eq.(2.30) is the rotational Hamiltonian associated with the body-fixed rotational angular momentum (AM) operator $\hat{\mathbf{R}}$. In general, $\hat{\mathbf{R}}$ can be expressed in terms of the total AM $\hat{\mathbf{J}}$, the electron orbital AM $\hat{\mathbf{L}}$, and the electron spin angular AM $\hat{\mathbf{S}}$ as $\hat{\mathbf{R}} = \hat{\mathbf{J}} - \hat{\mathbf{L}} - \hat{\mathbf{S}}$. Its eigenvalues for a $^1\Sigma$ state are $BJ(J+1)$ where B is the rotational constant and therefore corresponds to rotational levels with total AM quantum number J. Introducing the ladder operators $\hat{\mathbf{J}}_\pm = \hat{\mathbf{J}}_x \pm i\hat{\mathbf{J}}_y$, $\hat{\mathbf{L}}_\pm = \hat{\mathbf{L}}_x \pm i\hat{\mathbf{L}}_y$, and $\hat{\mathbf{S}}_\pm = \hat{\mathbf{S}}_x \pm i\hat{\mathbf{S}}_y$, the rotational Hamiltonian becomes

$$\hat{\mathbf{H}}^{\text{el}}_{\text{rot}} = \frac{\hbar^2}{2\mu r^2}\left[(\hat{\mathbf{J}}^2 - \hat{\mathbf{J}}_z^2) + (\hat{\mathbf{L}}^2 - \hat{\mathbf{L}}_z^2) + (\hat{\mathbf{S}}^2 - \hat{\mathbf{S}}_z^2) \right.$$
$$\left. + (\hat{\mathbf{J}}_+\hat{\mathbf{S}}_- - \hat{\mathbf{J}}_-\hat{\mathbf{S}}_+) + (\hat{\mathbf{J}}_+\hat{\mathbf{L}}_- - \hat{\mathbf{J}}_-\hat{\mathbf{L}}_+) + (\hat{\mathbf{S}}_+\hat{\mathbf{L}}_- - \hat{\mathbf{S}}_-\hat{\mathbf{L}}_+)\right]. \quad (2.32)$$

Strictly speaking, the rotational Hamiltonian operator in Eq.(2.32) is defined prior to the integration over electronic coordinates; however, once this integration is performed, the resulting operator matrix is incorporated into Eq.(2.30).

Lastly, $\boldsymbol{V}$ in Eq.(2.30) is the adiabatic (diagonal) potential energy matrix with diagonal elements being the electronic energy eigenvalues solved in the BO-approximation *a priori* to nuclear motion (see Section 2.1). The nomenclature here corresponds to that in Section 2.1 via $V_{\text{state}} \equiv E^e_\alpha(r)$, where 'state' counts over different electronic states.

The $\hat{\mathbf{H}}_c$ term in Eq.(2.30) is a Hamiltonian containing additional coupling operators to be added in construction of the fully coupled Hamiltonian matrix (see discussion below). For example, the Breit-Pauli spin-orbit (SO) operator[157,158,108] gives rise to the fine structure of rovibronic energy levels. SO terms can couple electronic states of the same spatial symmetry Λ (diagonal terms) or different Λ (off-diagonal) provided the total AM projection $|\Omega|$ is the same for both bra and ket states. One can see that for states of large total AM Ω, then a given rovibronic level may be split into many sub-levels. For example, a $^3\Pi$ state has 6 spin-orbit components, since computing the total AM projection gives $\Omega = 0, \pm 1, \pm 2$, where $\Omega = 0$ is twice degenerate. Additional operator terms include the phenomenological spin-spin (SS) couplings and the empirical spin-rotation (SR) couplings[159,107]. The SS couplings have the same effect as the SO couplings, which also give rise to Ω splitting and are usually used as empirical terms of the Hamiltonian. The SR couplings instead give rise to an empirical energy correction linear in the total AM quantum number J. Lastly, for non Σ states with $|\Lambda| \geq 1$, asymmetrical perturbations of different parity states are induced because of off-diagonal elements of the rota-

tional and spin-orbit Hamiltonian's, known as Λ-doubling. Empirical Λ-doubling couplings can be employed in Duo, and come in three flavours 'opq', '$p2q$', and 'q' [160]. A detailed discussion of the different coupling terms, corresponding matrix elements, and examples are provided by Kato [107].

A complete description of the Duo methodology can be found in Yurchenko et al. [103], but a brief description is provided here for reference in following sections. Duo begins to solve the total rovibronic Schrödinger equation of Eq.(2.30) by first solving the pure (uncoupled) vibronic part $\hat{\mathbf{H}}_{\text{vib}} + \boldsymbol{V}$ (in the case of the diabatic representation, without the DCs) using the numerical sinc-DVR method [150,150,151], yielding a set of vibronic energies E_v and wavefunctions $|\text{state}, v\rangle$ with vibrational quantum number $v = 0, 1, 2, 3, \ldots$. The vibrational wavefunctions are optimised on the PECs, and so it is to be expected that different representations of the electronic states (and therefore potentials) will influence the character, physicality, and convergence properties of the contracted vibronic basis in solution to the fully coupled problem (see discussion in Section 2.5.2). The vibronic wavefunctions are then used to construct the full rovibronic basis set $|n\rangle$ given by

$$|n\rangle \equiv |\text{state}, J, \Omega, \Lambda, S, \Sigma, v\rangle = |\text{state}, \Lambda, S, \Sigma\rangle\, |\text{state}, v\rangle\, |J, \Omega, M_J\rangle\,, \tag{2.33}$$

where the electronic states are labeled by the $|\text{state}, \Lambda, S, \Sigma\rangle$ basis with $\Lambda = 0, \pm 1, \pm 2, \ldots$ and $\Sigma = 0, \pm 1/2, \pm 1, \ldots$ being the projections of $\hat{\mathbf{L}}$ and $\hat{\mathbf{S}}$ on the internuclear axis, $S = 0, 1/2, 1, \ldots$ is the total electronic spin, and the 'state' label counts over different electronic curves. $\Omega = \Lambda = \Sigma$ is the total AM projection onto the internuclear axis, whereas M_J is the projection of total AM on the space-fixed Z-axis which is important when considering external fields. In the representation of angular momentum operators, the basis set $|J, \Omega, M_J\rangle$ implicitly contains the dependence on the Euler angles describing the molecular orientation and thus fully describes the rotational motion of the molecule. Moreover, the $|J, \Omega, M_J\rangle$ basis can be used to reconstruct spherical harmonics, explicitly capturing the wavefunction's dependence on these Euler angles.

The rovibrational basis set in Eq.(2.33) are used to solve the fully coupled rovibronic Schrödinger equation Eq.(2.30) to compute a full set of rovibronic energy terms and wavefunctions for the electronic states of interest. Particularly, the basis set in Eq.(2.33) correspond to Hund's case (a) functions [161,162]. To construct the full Hamiltonian matrix in the basis of Eq.(2.33), one can add any number of different coupling terms such as the aforementioned DDR, SO, SS, SR, and Λ-doubling coupling terms in the $\hat{\mathbf{H}}_c$ Hamiltonian of Eq.(2.30). Diagonalisation of

the final Hamiltonian then yields the rovibronic energy terms E_i and wavefunctions for the good quantum numbers J (total AM), and τ (parity) given by the following expansion in the basis set of Eq.(2.33)

$$\varphi_i^{J,\tau} = \sum_n C_i^{J,\tau} |n\rangle , \tag{2.34}$$

where i is the energy enumeration counting number and $C_i^{J,\tau}$ are the expansion coefficients. As stated, only J and τ are good quantum numbers; other quantum numbers $\Omega, \Lambda, \Sigma, \Omega, v$, and 'state' are assigned on the basis of the largest coefficient $C_i^{J,\tau}$ in the basis set. A complete spectroscopy for the system in question is then obtained by use of the eigenfunctions to compute transition line strengths and Einstein A coefficients from (transition) moment couplings. All computed rovibronic states are outputted into a .STATES file which contains the enumerator, i, quantum numbers, and energy. The computed transitions are provided as a .TRANS file which contains the upper and lower states of the transition given by enumerators i (initial) and f (final), the Einstein A coefficient, and transition frequency ν.

2.4 Conditions for a Strictly Diabatic Representation

I begin with the strict diabatic basis, a framework in which both the off-diagonal DDR and DBOC couplings vanish simultaneously[163]. In this diabatic representation, the diatomic molecular Hamiltonian consists of a purely diagonal kinetic energy operator and an electronic potential matrix with non-zero off-diagonal elements, known as diabatic couplings (DCs)[40,41].

While the diabatic representation introduces coupling within the electronic potential, the adiabatic representation places coupling within the kinetic energy. In the diabatic framework, potential energy curves (PECs) are allowed to cross and property operator curves, such as dipoles, are smooth functions of the nuclear coordinates. My goal is to explore the diabatic and adiabatic Hamiltonians similarly to the work of Köppel et. al.[91] who developed a Hamiltonian for the two-coupled electronic state problem. The nuclear vibronic diatomic molecular Schrödinger equation in the diabatic representation, neglecting spin and rotational angular momenta, is given by

$$\left(\hat{\mathbf{H}}_{\text{vib}}^{(\text{d})} + \mathbf{V}^{(\text{d})}\right) \vec{\chi}(r) = E_v \vec{\chi}(r), \tag{2.35}$$

where r is the internuclear distance and $\vec{\chi}(r)$ is a N-dimensional vector of nuclear vibronic wavefunctions. The Born-Huang $N \times N$ nuclear (vibrational) kinetic en-

ergy Hamiltonian reads

$$\hat{\mathbf{H}}^{(\mathrm{d})}_{\mathrm{vib}} + \mathbf{V}^{(\mathrm{d})} = -\frac{\hbar^2}{2\mu}\begin{pmatrix} \frac{d^2}{dr^2} & 0 & \cdots \\ 0 & \frac{d^2}{dr^2} & \cdots \\ \vdots & \vdots & \ddots \end{pmatrix} + \begin{pmatrix} V^d_1 & V^d_{1,2} & \cdots \\ V^d_{1,2} & V^d_2 & \cdots \\ \vdots & \vdots & \ddots \end{pmatrix}, \tag{2.36}$$

where the superscript 'd' denotes operators/matrices in the diabatic representation, $\mathbf{H}^{(\mathrm{d})}_{\mathrm{vib}}$ is the *diagonal* nuclear kinetic energy matrix, and $\mathbf{V}^{(\mathrm{d})}$ is the *non-diagonal* diabatic electronic potential matrix with elements $V^d_{i\neq j}$ being the DC between states i and j. The diabatic pure vibronic Hamiltonian is notably much simpler compared to its adiabatic representation in Eq.(2.24).

It has been shown by Mead and Truhlar[40] that transformation to diabatic representation, whereby the first and second DDR couplings and the DBOC term are reduced simultaneously, is possible through the action of a unitary transformation $\boldsymbol{U}$ on the adiabatic Hamiltonian matrix. This r-dependent unitary transformation effectively rotates the adiabatic electronic wavefunctions to yield diabatic states via

$$\psi^{(\mathrm{d})}_j(\boldsymbol{\xi};r) = \sum_{i=1}^{N} U_{ij}(r)\,\psi^{(\mathrm{a})}_i(\boldsymbol{\xi};r), \tag{2.37}$$

where $\boldsymbol{\xi}$ are the electronic coordinates. Then, one requires the derivatives of the diabatic electronic states with respect to the nuclear coordinate, r, to be zero (or negligible). After performing this transformation, one finds to completely remove the radial DDR terms, diagonalising the nuclear kinetic energy. To determine the condition required to achieve this strict diabatic basis, Eq.(2.36) is transformed back to the adiabatic representation via the inverse unitary transformation $\mathbf{U}^\dagger$, the adiabatic to diabatic transformation (AtDT)[51,43–46,40,48,89]. This change of basis to the diabatic representation can be thought to mix the electronic basis functions through a rotation by the mixing angle(s)[164–166,20,89,48], i.e. $\vec{\Psi}^{(\mathrm{d})} = \mathbf{U}^\dagger\vec{\Psi}^{(\mathrm{a})}$. For the two state cases, the AtDT takes the form of a simple rotation matrix

$$\mathbf{U} = \begin{pmatrix} \cos(\beta(r)) & -\sin(\beta(r)) \\ \sin(\beta(r)) & \cos(\beta(r)) \end{pmatrix} \tag{2.38}$$

where $\beta(r)$ is the scalar mixing angle. A detailed discussion on two-state diabatisation is given in Sections 2.5.1 and 2.5.2.

The diabatic nuclear kinetic energy Hamiltonian matrix $\mathbf{U}\boldsymbol{H}^{(\mathrm{d})}_{\mathrm{vib}}\mathbf{U}^\dagger$ is now trans-

formed to obtain the adiabatic matrix elements, yielding

$$\langle \chi_\alpha^{(\mathrm{a})} | \mathbf{U} \boldsymbol{H}_{\mathrm{vib}}^{(\mathrm{d})} \mathbf{U}^\dagger | \chi_\beta^{(\mathrm{a})} \rangle = -\frac{\hbar^2}{2\mu} \langle \chi_\alpha^{(\mathrm{a})} | \mathbf{U} \frac{d^2}{dr^2} \mathbf{U}^\dagger | \chi_\beta^{(\mathrm{a})} \rangle \,. \tag{2.39}$$

Before evaluating the above matrix elements, a minus sign and change in the direction of one of the first derivative components of the second derivative is introduced via a Hermitian conjugation under integration of nuclear coordinates. This is shown below explicitly via the following integration by parts in wavefunction notation,

$$\begin{aligned} -\frac{\hbar^2}{2\mu} \langle \chi_\alpha^{(\mathrm{a})} | \mathbf{U} \frac{d^2}{dr^2} \mathbf{U}^\dagger | \chi_\beta^{(\mathrm{a})} \rangle &= -\frac{\hbar^2}{2\mu} \int_0^\infty dr \, \chi_\alpha^{(\mathrm{a})*} \mathbf{U} \frac{d^2}{dr^2} \mathbf{U}^\dagger \chi_\beta^{(\mathrm{a})} \\ &= -\frac{\hbar^2}{2\mu} \left[\left[\chi_\alpha^{(\mathrm{a})*} \mathbf{U} \frac{d}{dr} \mathbf{U}^\dagger \chi_\beta^{(\mathrm{a})} \right]_0^\infty - \int_0^\infty dr \, \frac{d(\chi_\alpha^{(\mathrm{a})*} \mathbf{U})}{dr} \frac{d(\mathbf{U}^\dagger \chi_\beta^{(\mathrm{a})})}{dr} \right] . \end{aligned} \tag{2.40}$$

Since the wavefunction vanishes for $r \to 0$ and $r \to \infty$, then $\left[\chi_\alpha^{(\mathrm{a})*} \mathbf{U} \frac{d}{dr} \mathbf{U}^\dagger \chi_\beta^{(\mathrm{a})} \right]_{-\infty}^{\infty} = 0$, simplifying the above expression to be

$$-\frac{\hbar^2}{2\mu} \langle \chi_\alpha^{(\mathrm{a})} | \mathbf{U} \frac{d^2}{dr^2} \mathbf{U}^\dagger | \chi_\beta^{(\mathrm{a})} \rangle \equiv -\frac{\hbar^2}{2\mu} \left[-\left\langle \frac{d\chi_\alpha^{(\mathrm{a})}}{dr} \mathbf{U} \middle| \frac{d\mathbf{U}^\dagger \chi_\beta^{(\mathrm{a})}}{dr} \right\rangle \right] . \tag{2.41}$$

As noticed by Römelt in 1983 [126], the Hermitian conjugation of the first derivatives will lead to an adiabatic Hamiltonian being in its obviously Hermitian/symmetric form, where the conditions for a strict diabatic representation are obvious. Evaluating the derivatives using the product rule and expanding Eq.(2.41) leads to the following adiabatic matrix elements,

$$\begin{aligned} \left\langle \frac{d\chi_\alpha^{(\mathrm{a})}}{dr} \mathbf{U} \middle| \frac{d\mathbf{U}^\dagger \chi_\beta^{(\mathrm{a})}}{dr} \right\rangle &= \left[\left\langle \frac{d\chi_\alpha^{(\mathrm{a})}}{dr} \middle| \mathbf{U} + \langle \chi_\alpha^{(\mathrm{a})} | \frac{d\mathbf{U}}{dr} \right] \left[\frac{d\mathbf{U}^\dagger}{dr} | \chi_\beta^{(\mathrm{a})} \rangle + \mathbf{U}^\dagger \middle| \frac{d\chi_\beta^{(\mathrm{a})}}{dr} \right\rangle \right] \\ &= \left\langle \frac{d\chi_\alpha^{(\mathrm{a})}}{dr} \middle| \mathbf{U} \frac{d\mathbf{U}^\dagger}{dr} | \chi_\beta^{(\mathrm{a})} \rangle + \left\langle \frac{d\chi_\alpha^{(\mathrm{a})}}{dr} \middle| \mathbf{U}\mathbf{U}^\dagger \middle| \frac{d\chi_\beta^{(\mathrm{a})}}{dr} \right\rangle \right. \\ &\quad \left. + \langle \chi_\alpha^{(\mathrm{a})} | \frac{d\mathbf{U}}{dr} \frac{d\mathbf{U}^\dagger}{dr} | \chi_\beta^{(\mathrm{a})} \rangle + \langle \chi_\alpha^{(\mathrm{a})} | \frac{d\mathbf{U}}{dr} \mathbf{U}^\dagger \middle| \frac{d\chi_\beta^{(\mathrm{a})}}{dr} \right\rangle . \end{aligned} \tag{2.42}$$

Currently, the above equation looks complicated and dissimilar to the adiabatic nuclear kinetic energy in Eq.(2.24). Instead, the symmetries of the matrix products can be used whereby the diagonal and off-diagonal terms are recognised. To this

end, consider the derivative matrix product $\frac{d\mathbf{U}\mathbf{U}^\dagger}{dr}$

$$\frac{d\mathbf{U}\mathbf{U}^\dagger}{dr} = \frac{d\mathbf{U}}{dr}\mathbf{U}^\dagger + \mathbf{U}\frac{d\mathbf{U}^\dagger}{dr} = \mathbf{0},$$

since $\mathbf{U}\mathbf{U}^\dagger$ is the identity its derivative is the zero matrix. This infers that the products $\frac{d\mathbf{U}}{dr}\mathbf{U}^\dagger$ and $\mathbf{U}\frac{d\mathbf{U}^\dagger}{dr}$ are skew-symmetric since the product of a skew-symmetric matrix and its Hermitian conjugate is zero (i.e $\mathbf{S}+\mathbf{S}^\dagger = 0$). Hence,

$$\begin{aligned} \frac{d\mathbf{U}}{dr}\mathbf{U}^\dagger = \mathbf{S}^\dagger \quad &\rightarrow \quad \frac{d\mathbf{U}}{dr} = \mathbf{S}^\dagger\mathbf{U} \\ \mathbf{U}\frac{d\mathbf{U}^\dagger}{dr} = \mathbf{S} \quad &\rightarrow \quad \frac{d\mathbf{U}^\dagger}{dr} = \mathbf{U}^\dagger\mathbf{S}. \end{aligned} \tag{2.43}$$

Therefore, the derivative matrix product $\frac{d\mathbf{U}}{dr}\frac{d\mathbf{U}^\dagger}{dr}$ is given in terms of the skew-symmetric matrix $\mathbf{S}$ via

$$\frac{d\mathbf{U}}{dr}\frac{d\mathbf{U}^\dagger}{dr} = \mathbf{S}^\dagger\mathbf{U}\mathbf{U}^\dagger\mathbf{S} = -\mathbf{S}^2. \tag{2.44}$$

In fact, the matrix product $\mathbf{U}\frac{d\mathbf{U}^\dagger}{dr}$ being skew-symmetric highlights an important connection to the properties of rotation matrices. Similar to classical mechanics, where the angular frequency matrix $\boldsymbol{\Omega}$ is related to a time-dependent rotation matrix $\mathbf{R}$ via $\mathbf{R}\frac{d\mathbf{R}^{\mathrm{T}}}{dt} = \boldsymbol{\Omega}$, here the skew-symmetric matrix encodes information about how two coordinate systems are related through a dynamic rotation. Additionally, the skew-symmetric matrix is the matrix operator of the cross-product, highlighting the connection to the rotational dynamics between different coordinate systems. Finally, inserting Eqs.(2.43,2.44) into the adiabatic kinetic energy matrix elements of Eq.(2.42) yields

$$-\frac{\hbar^2}{2\mu}\langle\chi_\alpha^{(\mathrm{a})}|\mathbf{U}\frac{d^2}{dr^2}\mathbf{U}^\dagger|\chi_\beta^{(\mathrm{a})}\rangle = -\frac{\hbar^2}{2\mu}\left[\langle\chi_\alpha^{(\mathrm{a})}|\left(-\frac{\overleftarrow{d}}{dr}\mathbf{I}\frac{\overrightarrow{d}}{dr}+\mathbf{S}^2\right)|\chi_\beta^{(\mathrm{a})}\rangle - \langle\chi_\alpha^{(\mathrm{a})}|\left[\frac{\overleftarrow{d}}{dr}\mathbf{S}+\mathbf{S}^\dagger\frac{\overrightarrow{d}}{dr}\right]|\chi_\beta^{(\mathrm{a})}\rangle\right]. \tag{2.45}$$

$\mathbf{I}$ is the identity matrix and the directions of derivatives have been specified – which is how we program the adiabatic nuclear kinetic energy coupling elements in our nuclear motion code Duo– concluding the transformation of the kinetic energy Hamiltonian to the adiabatic representation.

The transformation of the diabatic potential matrix via action of the AtDT simply diagonalises it, yielding a set of adiabatic electronic eigenvalues which are the

avoided crossing potentials (such as those in Figure 1.1)

$$\mathbf{V}^{(\mathrm{a})} = \mathbf{U}\mathbf{V}^{(\mathrm{d})}\mathbf{U}^{\dagger}. \tag{2.46}$$

Finally, performing another Hermitian conjugation on the left acting derivative of the $\overleftarrow{\frac{d}{dr}}\mathbf{I}\overrightarrow{\frac{d}{dr}}$ term in Eq.(2.45), then combining with the adiabatic potential matrix yields, in matrix form, the adiabatic vibronic diatomic Hamiltonian

$$\hat{\mathbf{H}}^{(\mathrm{a})} = -\frac{\hbar^2}{2\mu}\left(\overrightarrow{\frac{d^2}{dr^2}} + \mathbf{S}^2 - \left[\overleftarrow{\frac{d}{dr}}\mathbf{S} - \mathbf{S}\overrightarrow{\frac{d}{dr}}\right]\right) + \mathbf{V}^{(\mathrm{a})}. \tag{2.47}$$

Comparing the above adiabatic vibronic Hamiltonian to the one derived from electronic structure in Eq.(2.24), the condition for a strict diabatic representation is easily identified as

$$\mathbf{S} = \mathbf{U}\frac{d\mathbf{U}^{\dagger}}{dr} = \mathbf{W}^{(1)}. \tag{2.48}$$

Therefore, if the AtDT is chosen to satisfy the above condition, then it is guaranteed that all radial DDR coupling terms will vanish in the diabatic Hilbert space. Indeed, $\mathbf{S}$ is skew-symmetric as is the NAC matrix $\mathbf{W}^{(1)}$, and $\mathbf{S}^2$ contains the DBOCs and further second DDR coupling terms.

2.5 Computing the AtDT

Section 2.4 established that a strictly diabatic representation, in which the (*radial*) DBOCs and DDR couplings vanish simultaneously, is achievable for diatomic systems whereby solution of the following first-order, ordinary, linear differential equation is required in determination of the AtDT

$$\frac{d\mathbf{U}}{dr} = -\mathbf{W}^{(1)}\mathbf{U}. \tag{2.49}$$

Since Eq.(2.49) is a linear differential equation, any linear combination of the columns of $\mathbf{U}$ is also a solution, i.e. making any r-independent unitary transformation of $\mathbf{U}$ also satisfy Eq.(2.49). This will be used later in the treatment of $N > 2$ coupled electronic states.

As briefly discussed in Section 2.4, equations of this form highlight the connections between rotational dynamics and coordinate system transformations. Such equations appear in various fields, including computer graphics, robotics, and kinematics[167–169], where the NAC matrix is analogous to an angular frequency matrix, and the AtDT represents a time-varying rotation matrix that describes a particle's

motion. In this context, $\mathbf{W}^{(1)}$ can be interpreted as the $r-$dependent "angular frequency" matrix of the diabatic frame's motion within the electronic Hilbert space relative to the adiabatic frame as the diatomic molecule stretches. Thus, the diabatic frame effectively operates as a quasi-inertial [6] frame where radial non-adiabatic couplings – or electron-nuclear momentum coupling – are eliminated.

The angle-axis representation of this abstract rotation of the electronic Hilbert space can be derived from the eigenvalues and eigenvectors of $\mathbf{W}^{(1)}$. For skew-symmetric matrices, eigenvalues come in imaginary pairs $\pm i\lambda_n$ and or are zero if the dimension of the matrix is odd. The eigenvector corresponding to the zero eigenvalue identifies the axis of rotation, while the eigenvalue pair λ_n is the angular frequency about that axis. In higher-dimensional systems, each unique eigenvalue pair characterises rotations within orthogonal planes.

For a three-state system, $\mathbf{W}^{(1)}$ is represented as a 3×3 matrix with the following instantaneous axis of rotation $\vec{n}$ and angular frequency ω are expressed as follows

$$\vec{n}(r) = \frac{1}{\omega(r)} \begin{pmatrix} -W_{23}^{(1)}(r) \\ W_{13}^{(1)}(r) \\ -W_{12}^{(1)}(r) \end{pmatrix}, \quad \omega(r) = \sqrt{\sum_{i<j}^{3} \left(W_{ij}^{(1)}(r) \right)^2}. \tag{2.50}$$

If $\vec{n}$ is not constant, direct integration to obtain the angular position as a function of bond length is not feasible because of the non-commutativity of rotations (angles do not form a vector space). This implies $\mathbf{W}^{(1)}$ does not commute with its integral, rendering solution to Eq.(2.49) non-local and non-analytic generally. While the angle-axis representation of the NACs and AtDT highlights the complexities associated with solving Eq.(2.49), it is important to note it does not universally imply that all solutions will be non-analytic. Rather, it illustrates the inherent difficulties in addressing such differential equations. Nevertheless, the solutions presented in the subsequent sections are well-established in the literature, making them a reasonable choice for representation in this context.

This thesis first demonstrates the simpler 2-state solution before discussing the details of treating N-state systems in Section 2.6.

[6] Although electronic angular momentum and molecular rotation still introduce non-inertial effects in the total molecular Hilbert space, ignoring these, it is nice to conceptualise the strict diabatic electronic Hilbert space as an inertial frame with respect to radial electron-nuclear momentum coupling.

2.5.1 The 2-State Problem

In the special case where one deals with an isolated 2-state system[7], $\mathbf{W}^{(1)}$ and $\mathbf{U}$ are represented by 2×2 matrices, where an analytical solution to Eq.(2.49) exists. Since for a 2 dimensional system the axis of rotation remains fixed (always points orthogonal to the plane of rotation), then direct integration of the NAC gives exactly the mixing angle of the adiabatic to diabatic basis. Therefore, the 2-state problem will serve as a simple introduction to the AtDT and the generation of diabatic molecular properties before progressing to the general N-state case.

The AtDT is conveniently represented by the following exponential matrix (which will be useful in later sections)

$$\mathbf{U} = e^{-\boldsymbol{\beta}} = \exp\left(-\begin{bmatrix} 0 & \beta_{12}(r) \\ -\beta_{12}(r) & 0 \end{bmatrix}\right), \tag{2.51}$$

where $\boldsymbol{\beta} \in \mathfrak{so}(2)$ is the so-called generator (Lie algebra) of the AtDT (Lie group) and linearizes $\mathbf{U} \in SO(2)$ in the tangent space of rotation matrices (see Appendix B for details on generators). Equivalently, the 2-state AtDT can be written as a rotation matrix in the Euler angle β_{12} as in Eq.(2.38). Inserting Eq.(2.51) into Eq.(2.49) yields the following solution to the AtDT

$$\mathbf{U}\frac{d\mathbf{U}^\dagger}{dr} = \mathbf{U}\mathbf{U}^\dagger\frac{d\boldsymbol{\beta}}{dr} = \frac{d\boldsymbol{\beta}}{dr} = \mathbf{W}^{(1)}, \tag{2.52}$$

where $\beta_{12}(r)$ is the mixing angle and is therefore related to the NAC via [164–166,20]

$$\frac{d\beta_{12}(r)}{dr} = W_{12}^{(1)} \quad \rightarrow \quad \beta_{12}(r) = \beta_{12}(r_0) + \int_0^r W_{12}^{(1)} dr, \tag{2.53}$$

where r_0 is a reference geometry and is usually chosen as such that one can define the physical condition which ensures the mixing angle is equal to $\pi/4$ at the diabatic crossing point (r_c). Then, in the 2-state case, the NACs can be interpreted as an angular velocity of the diabatic frame in the electronic Hilbert space with respect to the molecular stretching coordinate. Thus, the solution of the 2-state AtDT is

$$\mathbf{U}(r) = \exp\left(-\boldsymbol{\beta}(r_0) - \int_0^r \mathbf{W}^{(1)} dr\right) = \begin{pmatrix} \cos(\beta_{12}(r)) & -\sin(\beta_{12}(r)) \\ \sin(\beta_{12}(r)) & \cos(\beta_{12}(r)) \end{pmatrix}. \tag{2.54}$$

[7] Of course this is an approximation, where treatment of all infinite adiabatic states is required for the Born-Huang expansion of the wavefunction in Eq.(2.7) to be exact. However, if the two states are energetically well separated from the rest of the electronic state manifold, it is often argued using HFT (see Section 2.2.1) that the two states are effectively isolated.

If one chooses to model the NACs with analytical integrals, then the AtDT can be found analytically. It has been shown that the Lorentzian provides a good description of the NAC around the crossing point[170,171,165,166], and is given by

$$W_{12}^{(1)} = \frac{1}{2}\frac{\gamma}{\gamma^2 + (r - r_c)^2}, \tag{2.55}$$

where γ is the FWHM, r_c is the peak position (crossing point geometry), has total area of $\pi/2$, and is illustrated in Figure 2.2. Then, the mixing angle can be obtained via Eq.(2.53) as

$$\beta_{12} = \frac{\pi}{4} + \frac{1}{2}\arctan\left(\frac{r - r_c}{\gamma}\right) \in \left[0, \frac{\pi}{2}\right]. \tag{2.56}$$

When the mixing angle equals zero ($r \ll r_c$) the adiabatic and diabatic frames coincide with zero mixing, at the crossing point ($r = r_c$) the mixing angle equals $\pi/4$ meaning equal mixture of the two adiabatic states, and at large stretches ($r \gg r_c$) the mixing angle equals $\pi/2$ meaning a complete swap of the adiabatic states. This is illustrated in figure 2.2, where a mixing angle computed via Eq.(2.56) corresponding to a Lorentzian NAC with FWHM $\gamma = 0.019$ and centroid $r_0 = 1.95$ Å is plotted. As a result, the diabatic PECs will cross. This is, of course, an idealised approximation of the NAC, ensuring a well-behaved mixing angle and, consequently, a meaningful diabatic representation. In general, the NAC is not strictly required to satisfy the proposed normalisation, as discussed in detail in Sections 2.5.2 and 2.7.

As used in our spectroscopic works on sulfur monoxide[13,172], yittrium oxide[52,38], and carbon monohydride[38], a powerful theoretical tool can be obtained for modelling complex adiabatic potentials and NACs for the 2-state system by first transforming the adiabatic potential matrix. The diabatic potential energy functions $V_1^{\mathrm{d}}(r)$ and $V_2^{\mathrm{d}}(r)$ and the DC function $V_{12}^{\mathrm{d}}(r)$ are then given by

$$\begin{aligned}\mathbf{V}^{\mathrm{d}}(r) = \mathbf{U}^{\dagger}\mathbf{V}^{\mathrm{a}}(r)\mathbf{U} &= \begin{pmatrix} V_1^{\mathrm{d}}(r) & V_{12}^{\mathrm{d}}(r) \\ V_{12}^{\mathrm{d}}(r) & V_2^{\mathrm{d}}(r) \end{pmatrix} \\ &= \begin{bmatrix} V_1^{\mathrm{a}}\cos^2\beta_{12} + V_2^{\mathrm{a}}\sin^2(\beta_{12}) & \frac{1}{2}(V_2^{\mathrm{a}} - V_1^{\mathrm{a}})\sin(2\beta_{12}) \\ \frac{1}{2}(V_2^{\mathrm{a}} - V_1^{\mathrm{a}})\sin(2\beta_{12}) & V_1^{\mathrm{a}}\sin^2(\beta_{12}) + V_2^{\mathrm{a}}\cos^2(\beta_{12}) \end{bmatrix}.\end{aligned} \tag{2.57}$$

The adiabatic representation of an isolated two-electronic state diatomic system is fully defined by the three functions $V_1^{\mathrm{a}}(r)$, $V_2^{\mathrm{a}}(r)$ and $W_{12}^{(1)}(r)$, and, in turn, the diabatic representation is fully defined by the three functions $V_1^{\mathrm{d}}(r)$, $V_2^{\mathrm{d}}(r)$ and $V_{12}^{\mathrm{d}}(r)$.

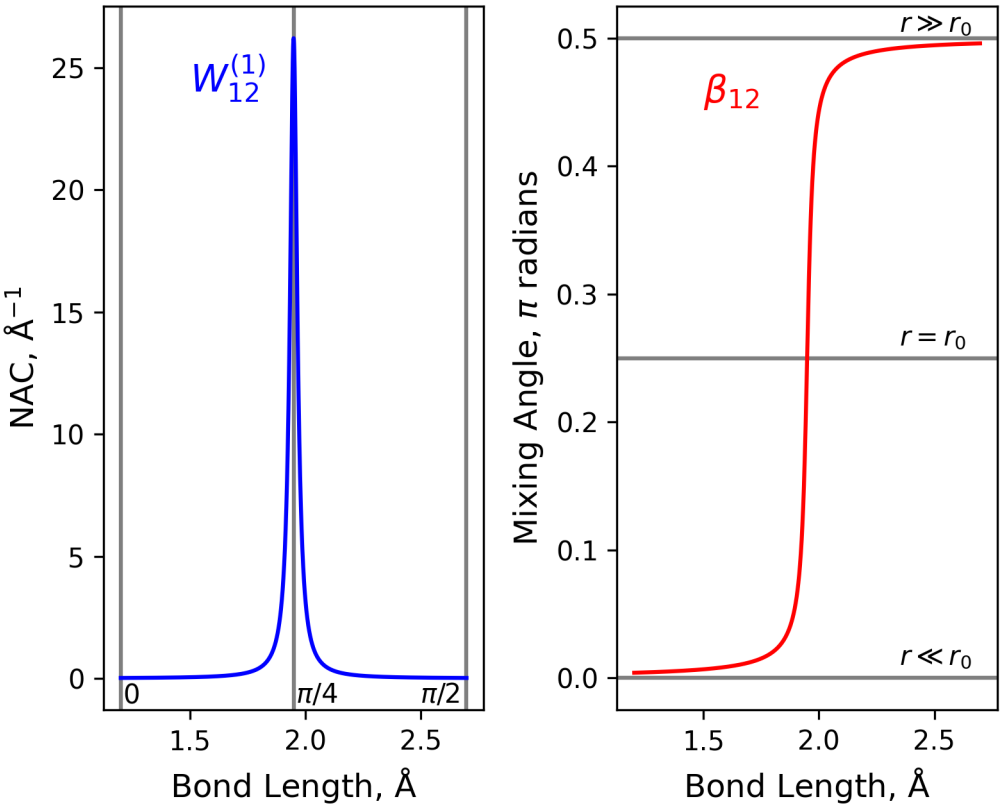

Figure 2.2: Illustration of the diabatising mixing angle computed via Eq.(2.56) (right panel) corresponding to a Lorentzian NAC with FWHM $\gamma = 0.019$ and centroid $r_0 = 1.95$ Å (left panel). The grey lines indicate regions of interest, where the numbers by the vertical lines in the NAC plot indicate the mixing angle at that geometry, and the bond lengths by the horizontal lines in the mixing angle plot.

In fact, both representations can be fully described by a combination of any three functions from the set $V_1^{\mathrm{a}}(r)$, $V_2^{\mathrm{a}}(r)$, $W_{12}^{(1)}(r)$, $V_1^{\mathrm{d}}(r)$, $V_2^{\mathrm{d}}(r)$ and $V_{12}^{\mathrm{d}}(r)$[38]. For modelling of the spectroscopic models, we showed that it is convenient to choose $V_1^{\mathrm{d}}(r)$, $V_2^{\mathrm{d}}(r)$ and $W_{12}^{(1)}(r)$. This is because the diabatic PECs $V_1^{\mathrm{d}}(r)$, $V_2^{\mathrm{d}}(r)$ are expected to have smooth shapes by construction and are easy to parameterize, which explains our choice, while $W_{12}^{(1)}(r)$ has also a rather simple, easy-to-parameterize cusp-like shape[26,40,41,20,56], often modelled using a Lorentzian in Eq.(4.5). I repeat Figure 1.1 in Figure 2.3 here for ease of the reader, which shows that indeed the diabatic PECs are simple functions of bond length, representing a Morse-Oscillator like bound state and a standard repulsive hyperbolic curve while the NAC is seen to show Lorentzian character. The other three functions are constructed from $V_1^{\mathrm{d}}(r)$, $V_2^{\mathrm{d}}(r)$ and $W_{12}^{(1)}(r)$ as follows.

The diabatising mixing angle $\beta(r)$ is first computed via Eq.(2.53) to generate

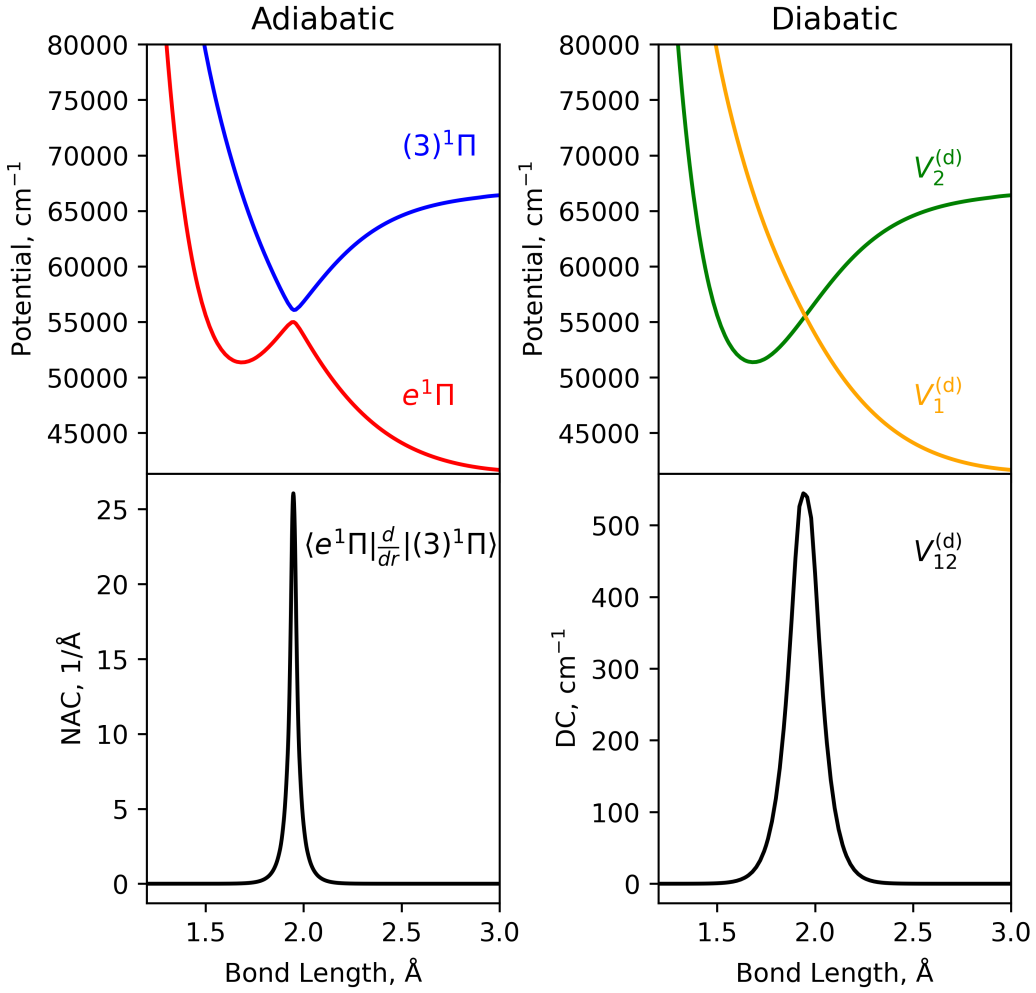

Figure 2.3: Illustration of the avoided crossing adiabatic PECs of the $e\,^1\Pi$ and $(3)\,^1\Pi$ states of sulfur monoxide and the corresponding NAC (left panels). The right panels show their diabatisation, producing a set of smooth diabatic PECs which cross and are coupled by the diabatic coupling (bottom right). The NAC is strongest at the avoided crossing geometry, showing cusp-like behaviour.

the AtDT. Then, by transforming the diabatic potential matrix $\mathbf{V}^{\mathrm{d}}(r)$ in Eq.(4.4) back to the adiabatic representation via action of the inverse transformation $\mathbf{U}^{\dagger}$, the DC can be determined from the following condition on the off-diagonal elements of the adiabatic potential matrix

$$\sin\beta(r)\cos\beta(r)\left(V_1^{\mathrm{d}}-V_2^{\mathrm{d}}\right)+\left(\cos\beta(r)^2-\sin\beta(r)^2\right)V_{12}^{\mathrm{d}}=0, \tag{2.58}$$

which is required to be zero since $\mathbf{V}^{\mathrm{a}}(r)=\mathbf{U}\mathbf{V}^{\mathrm{d}}(r)\mathbf{U}^{\dagger}$ in Eq.(2.24) is diagonal by definition. Hence, rearranging for the DC gives (similarly to the work by Macias

and Riera[64])

$$V_{12}^{\mathrm{d}} = \frac{1}{2}\tan\left(2\beta(r)\right)\left(V_2^{\mathrm{d}} - V_1^{\mathrm{d}}\right). \tag{2.59}$$

The adiabatic functions $V_1^{\mathrm{a}}(r)$ are $V_2^{\mathrm{a}}(r)$ can be then constructed as eigenvalues of the diabatic potential energy matrix (second term in Eq.(2.36)):

$$V_1^{\mathrm{a}}(r) = \frac{V_1^{\mathrm{d}}(r)+V_2^{\mathrm{d}}(r)}{2} - \frac{1}{2}\sqrt{[V_1^{\mathrm{d}}(r)-V_2^{\mathrm{d}}(r)]^2+4V_{12}^2(r)}, \tag{2.60}$$

$$V_2^{\mathrm{a}}(r) = \frac{V_1^{\mathrm{d}}(r)+V_2^{\mathrm{d}}(r)}{2} + \frac{1}{2}\sqrt{[V_1^{\mathrm{d}}(r)-V_2^{\mathrm{d}}(r)]^2+4W_{12}^2(r)}, \tag{2.61}$$

or, equivalently, via the inverse unitary transformation $\mathbf{U}$:

$$\mathbf{V}^{\mathrm{a}}(r) = \mathbf{U}\mathbf{V}^{\mathrm{d}}(r)\mathbf{U}^{\dagger} = \begin{pmatrix} V_1^{\mathrm{a}}(r) & 0 \\ 0 & V_2^{\mathrm{a}}(r) \end{pmatrix} = \begin{bmatrix} V_1^{\mathrm{d}}\cos^2\beta + V_2^{\mathrm{d}}\sin^2\beta & 0 \\ 0 & V_1^{\mathrm{d}}\sin^2\beta + V_2^{\mathrm{d}}\cos^2\beta \end{bmatrix}. \tag{2.62}$$

We have seen that transformation of the PECs to the diabatic representation is desirable due to its smooth and simplified nature, essential for accurate modelling. However, diabatisation applies not only to the PECs but also to the entire molecular Hamiltonian, which includes other properties like dipoles, spin-orbit couplings, and angular momenta which are also transformed by the AtDT. In the adiabatic representation, like the potentials, steep gradients in the properties around the region of avoided crossing are also seen[13,38], and so diabatisation should be expected to make them smooth also. Figure 2.4 illustrates the diabatisation of the spin-orbit couplings connecting the $e\,^1\Pi$ and $(3)\,^1\Pi$ states in Figure 2.3 to the $X\,^3\Sigma^-$ ground state of sulfur monoxide[13], where the diabatic curves are seen to be smooth and simple functions of the nuclear geometry, which is ideal for modelling and parameterisation. The adiabatic SOCs, however, are seen to have steep gradients around the avoided crossing region r_c, corresponding to the avoided crossing position in the PECs of Figure 2.3. Furthermore, since diabatic property curves vary smoothly without abrupt topological changes, the spectroscopy of the studied system is less sensitive to variations in the diabatic spectroscopic model. In contrast, the adiabatic representation is highly sensitive to small changes in model topology, requiring strict consistency in the non-adiabatic region across all curves—an inherently difficult task. This sensitivity extends to the accuracy of *ab initio* calculations, where even slight shifts in crossing positions can induce significant topological changes in the resulting couplings. Consequently, for diatomic systems exhibiting strong non-adiabatic interactions, the diabatic representation provides a more robust and practical choice.

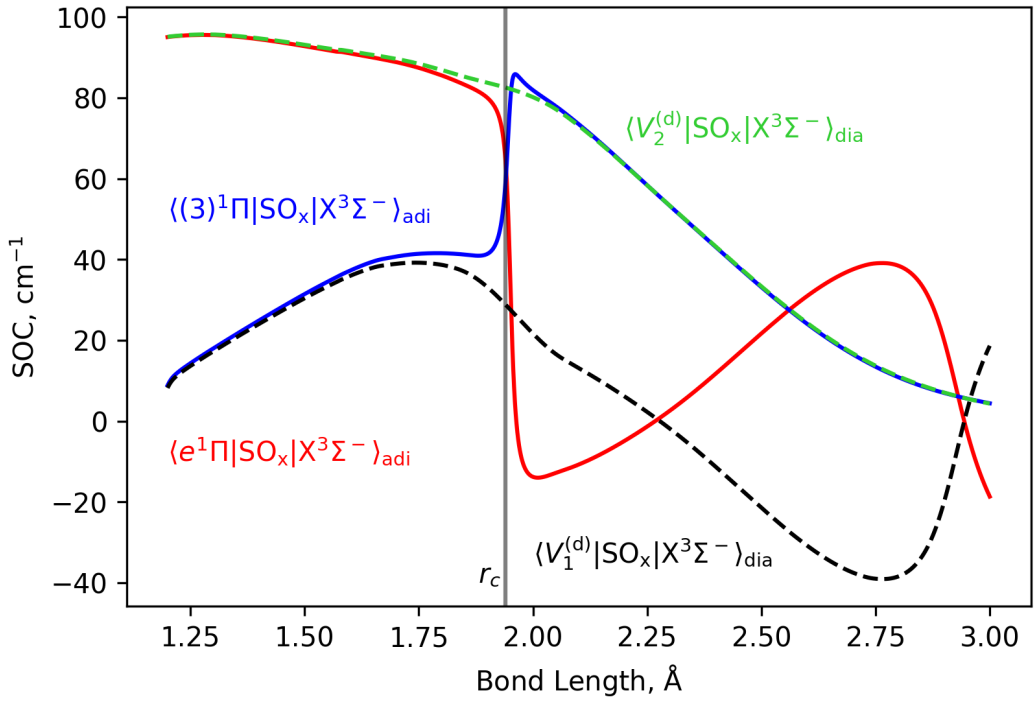

Figure 2.4: Example diabatisation of the adiabatic $\langle e\,^1\Pi|\mathrm{SO_x}|\mathrm{X}\,^3\Sigma^-\rangle$ (red) and $\langle (3)\,^1\Pi|\mathrm{SO_x}|\mathrm{X}\,^3\Sigma^-\rangle$ (blue) SOCs which are seen to have steep topology at the region of avoided crossing r_c highlighted by the vertical line. The corresponding diabatic SOCs (black and green dotted lines) are seen to have smooth topology, and are simple curves of nuclear geometry, ideal for modelling.

2.5.2 Optimal Diabatisation for Efficient Rovibronic Basis Construction

Constructing a contracted rovibronic basis typically involves two steps (see Section 2.3 for details): (1) calculating bound state energies and wavefunctions from individual electronic potentials (e.g., using a DVR method[103]) in the construction of a contracted vibrational basis, and (2) using this uncoupled solution as a basis to solve the fully coupled problem. The shapes of the PECs are then expected to influence the efficiency of the contracted basis in describing the fully coupled rovibronic solution. Thus, adiabatic and diabatic representations are likely to converge with the size of the contracted basis differently within rovibronic calculations[38], as demonstrated in Chapter 3. This section extends this by considering optimal diabatic representations for constructing efficient representations of a molecule's spectroscopy, where the ideal case features diagonal diabatic potentials that are clearly either bound or repulsive.

As used in discussion of the two-state problem in Section 2.5.1, an ideal di-

abatic potential set – smoothly crossing the avoided crossing region while aligning with adiabatic curves at both the united atom and dissociation limits – can be achieved by constraining the mixing angle $\beta(r)$ to transition smoothly from 0 at short bond lengths to $\pi/2$ at dissociation. This ensures the AtDT evolves from the identity matrix $\mathbf{I}$ at short bond lengths to a permutation matrix $\mathbf{P}$ at large stretches, allowing diabatic PECs to coincide with adiabatic PECs outside of the avoided crossing (see, e.g. Figure 2.3). Property-based diabatisation methods enforce this by parameterizing the NAC (e.g., with a Lorentzian function) to optimise the mixing angle $\beta(r)$ via Eq.(2.53), yielding smooth, Morse-like or repulsive diabats suitable for efficient contracted vibronic basis construction.

Ensuring diabatic PECs coincide with adiabatic PECs near equilibrium improves control over spectroscopically relevant regions. Since adiabatic curves, computed *ab initio* within the Born-Oppenheimer approximation, accurately describe equilibrium properties[11], maintaining this structure in the diagonal diabatic electronic Hamiltonian naturally preserves spectroscopic control in rovibronic calculations.

Equilibrium electronic structure is central to theoretical spectroscopy methods (e.g., variational approaches, effective Hamiltonians) as it dictates key rovibronic dynamics – electronic transitions depend on the minimum energy, rotational transitions on equillibrium bond length, and vibrational transitions on well width. Thus, well-behaved diabatic potentials in this regime are desirable. For example, Morse oscillator functions effectively model adiabatic PECs, with parameters directly linked to spectroscopic properties. This approach, widely used in the ExoMol project[53,54,173], refines spectroscopic models against experimental data for accurate rovibronic computations.

Constructing smooth diabatic PECs with an AtDT evolving from $\mathbf{I}$ to $\mathbf{P}$ enables simple analytical modelling and minimises DCs, thereby improving the diagonal diabatic PECs as initial approximations for the coupled rovibronic problem and facilitating efficient contracted vibronic basis sets. Conversely, large DCs degrade these approximations. Empirically, aligning diabatic and adiabatic PECs at dissociation is beneficial since dissociation energies are well defined. Together, these AtDT conditions support efficient and practical spectroscopic computations.

While rovibronic calculations using adiabatic PECs with optimised NACs and their corresponding (equivalent) diabatic representations yield identical rovibronic energies[38], NACs derived from these property-based methods remain approximate. In contrast, integration of *ab initio* NACs (computed with, e.g., the DDR procedure, see Section 2.2.2) enable an exactly equivalent diabatic representation but

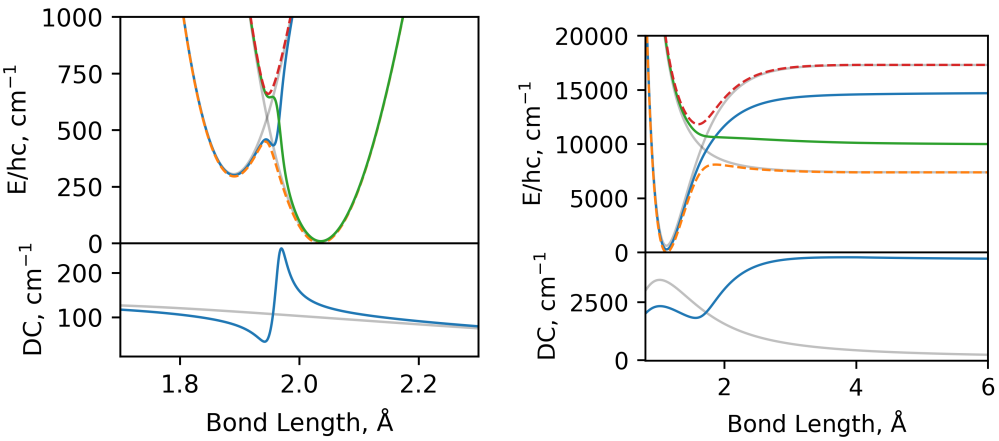

Figure 2.5: diabatisation of the two-state YO system (left) and CH system (right) presented in Brady et al.[38] (and Chapter 3), where the grey lines indicate their diabatisation, and the solid coloured lines the corresponding diabatisation when modifying their NACs (see text for details). The bottom panels plot the DCs derived in both diabatisations.

does not necessarily produce desirable diabatic properties. Furthermore, inconsistencies arise if NACs and adiabatic PECs are computed using different *ab initio* methods, as their predicted crossing points may not align, leading to nonphysical oscillations in the diabatic PECs and DCs. This effect is illustrated in the left panel of Figure 2.5, where shifting the NAC by 0.02 Å in the two-state YO model of Brady et al.[38] yields undesirable diabatic curves (solid colored lines) compared to the original diabatisation (grey lines). Additionally, if the NAC integral fails to reach $\pi/2$ as $r \to \infty$, meaning the AtDT does not converge to a permutation matrix, the diabatic potentials correlate to different dissociation asymptotes with large DCs. This is shown in the right panel of Figure 2.5, where scaling the NAC in the two-state CH model of Brady et al.[38] by $2/3$ causes the mixing angle to approach $\pi/3$ at dissociation. As a result, the bound diabatic potential well is shallower, supporting fewer bound states in the contracted vibronic basis set.

Detailed discussion on the motivations behind enforcing the AtDT to evolve from the identity to a (signed) permutation matrix $\mathbf{P}$ can be found in Section 2.7. While this is trivial to enforce for two-state systems, extension to the general N-state case is not obvious and is the main motivation behind the development of my novel diabatisation method in Section 2.6.4.

2.6 The N-State Diabatisation Problem

In the general case where $\mathbf{W}^{(1)}$ does not commute with its integral (i.e., when the number of electronic states is greater than two), an analytic solution to Eq.(2.49) – and thus the AtDT – appears intractable within the current theoretical framework detailed in this thesis. Instead, a non-local solver can be employed, i.e. the AtDT at one point on the bond length grid depends on knowledge of neighboring points, and the solution is constructed from an accumulated rotation starting from a boundary point. These types of solutions are known as evolution-type methods, with Euler integration being one of the earliest examples. However, because $\mathbf{U}$ is not a linear object (its elements do not form a flat vector space), standard numerical integration methods cannot be directly applied to solve Eq.(2.49). Doing so would yield an innaccurate solution that deviates from unitarity (see Section 2.8). Many studies[46,49,97] have utilised evolution methods to solve Eq.(2.49), often referred to as the line-integral approach. For completeness, the formal exponential line-integral propagator is derived below.

Starting with the definition of the derivative, Eq.(2.49) becomes, at some point $r+\Delta r$,

$$\lim_{\Delta r\to 0} \mathbf{U}(r+\Delta r)\frac{\mathbf{U}^{\dagger}(r+\Delta r)-\mathbf{U}^{\dagger}(r)}{\Delta r} = \mathbf{W}^{(1)}(r+\Delta r), \tag{2.63}$$

which holds in the limit $\Delta r \to 0$ since unitary matrices/rotations become linearised operations in this limit. Rearranging yields

$$\lim_{\Delta r\to 0} \left(\mathbf{U}(r+\Delta r)\mathbf{U}^{\dagger}(r) = \boldsymbol{I} - \Delta r\cdot\mathbf{W}^{(1)}(r+\Delta r)\right), \tag{2.64}$$

where the unitarity of $\mathbf{U}$ allows use of $\mathbf{U}(r+\Delta r)\mathbf{U}^{\dagger}(r+\Delta r) = \boldsymbol{I}$. The right hand side of the equation corresponds to the first-order Taylor expansion of the following matrix exponential,

$$\exp\left(-\Delta r\cdot\mathbf{W}^{(1)}\right) \approx \boldsymbol{I} - \Delta r\cdot\mathbf{W}^{(1)}. \tag{2.65}$$

In the limit of small changes in bond length, $\Delta r \to 0$, the exponent approximates the integral of the NAC matrix (endpoint approximation using Riemann sums),

$$\exp\left(-\int_{r}^{r+\Delta r}\mathbf{W}^{(1)}dr\right) \approx \exp\left(-\Delta r\cdot\mathbf{W}^{(1)}\right). \tag{2.66}$$

Substituting Eqs.(2.65,2.66) into Eq.(2.64) and solving for the AtDT $\mathbf{U}(r+\Delta r)$

gives the formal exponential line-integral propagator

$$\mathbf{U}(r+\Delta r) = \lim_{\Delta r \to 0} \exp\left(-\int_{r}^{r+\Delta r} \mathbf{W}^{(1)} dr \right) \mathbf{U}(r). \tag{2.67}$$

where $\mathbf{U}(r+\Delta r)$ is the AtDT matrix to be solved at the current grid point, $\mathbf{U}(r)$ is the AtDT at the previous point, and $-\int_{r}^{r+\Delta r} \mathbf{W}^{(1)} dr$ is the exponential mapping representing the change in AtDT over the interval $[r, r+\Delta r]$. Thus, definition of an initial matrix $\boldsymbol{M}$ at a point r_0 in the nuclear configuration space

$$\mathbf{U}(r_0) \equiv \boldsymbol{M}, \tag{2.68}$$

determines the full solution of $\mathbf{U}$ from Eq.(2.67). Notably, now that the evolution of the AtDT through bond length is done via many infinitesimal rotations as opposed to linear transformations, the unitarity of the final solution is maintained. The choice of the initial unitary matrix $\boldsymbol{M}$ is not unique and depends on the physical or computational context. Typically, $\boldsymbol{M}$ is chosen to diagonalise the electronic Hamiltonian at r_0, thereby aligning the adiabatic basis with the diabatic one at that point. This choice and its implications are discussed in detail throughout this thesis, particularly in Section 2.7.

The challenges with this solution are: (1) finding the integral of $\mathbf{W}^{(1)}$, which can be analytic for some NAC models or done numerically; (2) computing the exponential matrix (see discussion in Appendix A.1); (3) ensuring asymptotic solutions at multiple points in the nuclear configuration space (see discussion in Section 2.6.1).

Appendix A summarises the technical aspects of the programmatic implementation of the two- and N-state diabatisation methods presented in this thesis. This includes, for example, the construction of an efficient adaptive geometry grid for evolving the AtDT in Eq.(2.67), the matrix exponentiation techniques employed, and relevant Lie theory which is discussed further in Appendix B.

2.6.1 The Asymptotic Solutions of Evolution

A novel contribution of this thesis is the establishment of a connection between inconsistent/improper non-adiabatic couplings (NACs) and nonphysical diabatic representations. After establishing the problem, I present a novel methodology for regularising the NACs such that a physically-meaningful diabatic representation that is exactly equivalent to the N-state adiabatic representation can be generated. A central aim to this method is to bridge the gap between accurate direct-diabatisation

methods and practical property-based diabatisation schemes without additional *ab initio* calculations or repeated evaluations of the AtDT evolution Eq.(2.67). Consequently, this method aims to enhance the accuracy, practicality, and efficiency of diabatic models in quantum dynamics calculations of diatomic nuclear motion with N-coupled states, particularly in the construction of contracted vibronic basis sets (see discussion in Section 2.5.2). The results presented in the remainder of this Section and Section 2.7 are adapted from our recent publication[57].

A challenge with evolution solutions to linear differential equations, like Eq.(2.67), is in satisfying multiple boundary conditions simultaneously. Since the solution is uniquely determined by its initial value, $\mathbf{U}(r_0) = \mathbf{M}$, and the NACs along its trajectory, enforcing a second boundary condition, $\mathbf{U}(r_1) = \mathbf{N}$, at a different bond length is not guaranteed. This follows from the invariance of the solution, $\mathbf{U}$, to linear combinations in its columns, where the following r-independent unitary transformation also satisfies Eq.(2.49)

$$\mathscr{U}(r) = \mathbf{U}(r)\mathbf{U}^{\dagger}(r_1)\mathbf{N}. \tag{2.69}$$

Thus, unless $\mathbf{U}(r_1) = \mathbf{N}$ (i.e. $\mathscr{U}(r) \equiv \mathbf{U}(r)$) then a unitary matrix which simultaneously satisfies the conditions $\mathbf{U}(r_0) = \mathbf{M}$ and $\mathbf{U}(r_1) = \mathbf{N}$ is not related by a constant unitary transformation and is therefore not a solution to Eq.(2.49), i.e. is not consistent with the defined NAC matrix $\mathbf{W}^{(1)}$. This has some consequences on the computed AtDT:

1. Due to the arbitrary choice in the boundary value of evolution, there exists infinitely many solutions to Eq.(2.49) which are related by a single constant unitary transformation. Therefore, an infinite number of diabatic representations exist which are equivalent to the adiabatic representation.

2. The AtDT solution is fixed once the initial boundary condition is specified, with its trajectory dictated solely by the NACs. As a result, satisfying a secondary boundary condition at a different point is not guaranteed.

3. Diabatisation depends on both the chosen boundary condition and NAC topology. A sensible choice in the boundary condition and a specific set of NACs should yield a physically-meaningful diabatic representation with smooth diabatic properties (e.g. potentials and dipoles), desirable asymptotic behavior, and allows the construction of a contracted rovibronic basis that accurately describes the spectroscopy near equilibrium (see discussion in Sections 2.5.2, 2.6.2, and 2.7). However, since molecular property curves do not enter the

AtDT evolution, inconsistencies between NACs and adiabatic property curves can hinder the construction of this physical diabatic representation that is *exactly* equivalent to the adiabatic representation.

The first challenge in solving Eq.(2.49) is selecting appropriate boundary conditions for the AtDT. As noted in point 1, any boundary condition can, in principle, be used with my diabatisation method (see Section 2.6.4). Here, I choose boundary conditions that serve a pragmatic goal: constructing a practical diabatic representation that ensures efficient contracted rovibronic basis sets while remaining exactly equivalent to the adiabatic representation. The rationale behind these choices is detailed in Sections 2.5.2 and 2.7. With an equivalent set of adiabatic and diabatic spectroscopic models established, one can systematically test the impact of non-adiabatic effects on rovibronic solutions, extending the approach of our two-state paper Brady et al.[38] to general N-state coupled systems.

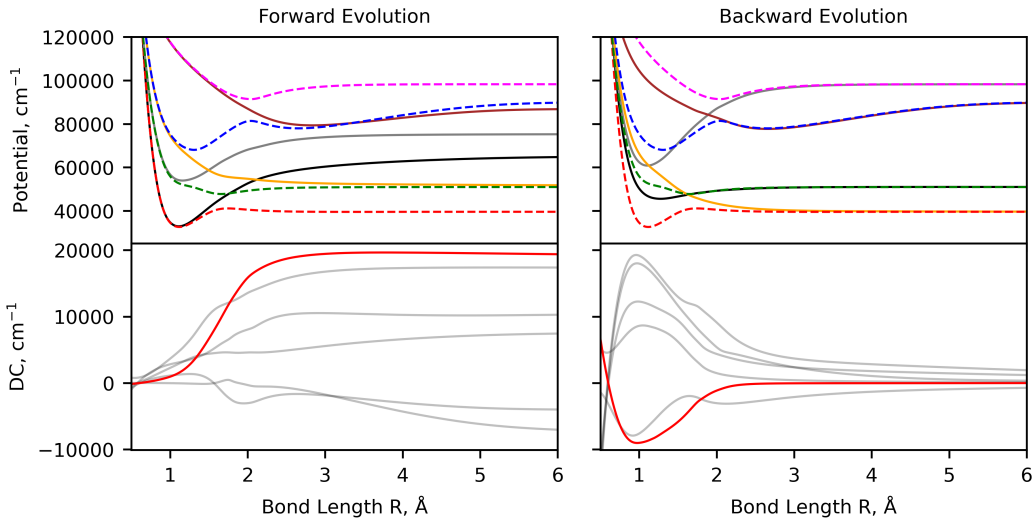

Figure 2.6: Illustration of the diabatic PECs and DCs resulting from a forwards (left) or backwards (right) evolution of the AtDT. It is clear that the diabatic representations, although rovibronically equivalent, are very different in nature. Curves of the same colour correspond to the same matrix element of the electronic Hamiltonian, where only the $d_{1,2}$ DC component (coupling the black and orange diabats) is highlighted for clarity.

2.6.2 Enforcing Multiple Boundary Conditions on the AtDT

To fulfill my pragmatic goal, I aim to enforce the short- and long-stretch AtDT boundary conditions discussed in Sections 2.5.2, 2.7.3, and 2.7.1. The boundary

conditions are defined as:

$$\mathbf{U} = \begin{cases} \mathbf{I}, & r = r_L \text{ (left-boundary, short stretches)} \\ \mathbf{P}, & r = r_R \text{ (right-boundary, long stretches)} \end{cases} \tag{2.70}$$

where $\mathbf{I}$ is the identity matrix and $\mathbf{P}$ is a signed permutation matrix.

The AtDT can be easily constrained to satisfy one of the boundary conditions in Eq.(2.70) by evolution from the boundary using Eq.(2.49). I define forward evolution ($r_\mathrm{L} \rightarrow r_\mathrm{R}$) as propagation from the identity matrix at short bond lengths, while backward evolution ($r_\mathrm{L} \leftarrow r_\mathrm{R}$) refers to propagation from a signed permutation matrix at large bond lengths. Both solutions are exact and equivalent, since they remove the same set of NACs, and so are conveniently related by a single constant unitary transformation via Eq.(2.69). This means both solutions can be constructed via a single evolution of the AtDT through Eq.(2.67). In all subsequent computations, I perform forward evolution to fix the AtDT solution $\mathbf{U}_\mathrm{f}(r)$, to which a backward evolution is immediately constructed via

$$\mathbf{U}_\mathrm{b}(r) = \mathbf{U}_\mathrm{f}(r)\mathbf{U}_\mathrm{f}^\dagger(r_\mathrm{R})\mathbf{P}, \tag{2.71}$$

and is still referred to as a backward evolution solution herein.

Extensive testing shows that forward and backward evolution solutions do not necessarily coincide and are related by a non-identity unitary transformation, $\mathbf{U}_\mathrm{f}^\dagger(r_\mathrm{R})\mathbf{P}$, in general. This leads to topologically different yet equivalent diabatic representations. Figure 2.6 illustrates this for a four-state CH (carbon monohydride) system coupled by six NACs (see Section 3.6.2), where only the DC component $d_{12}(r)$ is highlighted for clarity.

As shown in Figure 2.6, these differences result in distinct diabatic PECs and DCs, confirming the non-uniqueness of AtDT solutions (see point 1 in Section 2.6.1). The forward-evolved AtDT produces a diabatic representation with undesirable dissociation, where PECs deviate from adiabatic atomic limits and DCs approach a constant as $r \rightarrow \infty$. However, it accurately captures the electronic structure near equilibrium, making it suitable for constructing a contracted vibronic basis for spectroscopy calculations, except near dissociation where the DCs are large (see Sections 2.5.2 and 2.7).

Conversely, the backward-evolved AtDT coincides with the adiabatic dissociation limits with minimised DCs but exhibits strong mixing (large DC) at short and intermediate bond lengths, potentially leading to poor control over equilibrium

structure and spectroscopy. As discussed in Section 2.5.2, the diagonal diabatic potentials will be a worse first-order approximations to the dominant rovibronic spectroscopy near equilibrium. Thus, the two diabatic representations, while exactly equivalent, differ topologically, each with distinct advantages and disadvantages for rovibronic calculations.

To confidently attribute the discrepancy between the forward and backward evolved AtDT to the ambiguities of Eq.(2.67) and the NACs, it is crucial to demonstrate the accuracy of the evolution solver and rule out the influence of accumulated numerical error. To rigorously assess the accuracy of the numerically solved AtDT, the residual kinetic energy matrix is computed by transforming the adiabatic kinetic energy Hamiltonian of Eq.(2.24) through left- and right-multiplying by $\mathbf{U}^\dagger$ and $\mathbf{U}$, respectively, yielding

$$\boldsymbol{T}_{\text{res}} = -\frac{\hbar^2}{2\mu}\left(-\frac{d\mathbf{U}^\dagger}{dr}\frac{d\mathbf{U}}{dr} - \mathbf{U}^\dagger\mathbf{K}\mathbf{U} - \left[\frac{d\mathbf{U}^\dagger}{dr}\mathbf{W}^{(1)}\mathbf{U} - \mathbf{U}^\dagger\mathbf{W}^{(1)}\frac{d\mathbf{U}}{dr}\right]\right), \tag{2.72}$$

where the subscript 'res' denotes the residual matrix. For an exact AtDT solution, $\boldsymbol{T}_{\text{res}}$ would equal the zero matrix, indicating complete removal of all radial DDR couplings. Then, the matrix (Frobenius) norm can be used to reduce the dimensionality of the kinetic energy error matrix above via

$$\|\boldsymbol{T}_{\text{res}}\|_{\text{F}} = \sqrt{\sum_{ij}|\boldsymbol{T}_{\text{res,ij}}|^2}, \tag{2.73}$$

computed at each grid point. As shown in Figure 2.7, the error in the computed AtDT matrix, in terms of DDR coupling, is numerically eliminated to within 10^{-11} cm^{-1}. Further refinement of the grid spacing can reduce this residual even further.

Since the solver in Eq.(2.67) is numerically exact with appropriate grid spacing, the observed differences between forward and backward evolutions cannot arise from numerical errors. Instead, adopting the approximate solution whereby all boundary conditions are fullfilled reveals internal inconsistencies between the NACs and adiabatic property curves – obscured in the adiabatic picture but evident in the diabatic representation – that prevent the desired AtDT from being obtained through a single evolution. These inconsistencies, arising from improper NACs input to the solver, lead to asymptotic misbehavior, topological non-smoothness of diabatic properties (see Sections 2.5.2 and 2.7.4), and non-coincidence of AtDT boundary conditions. Possible sources of these NAC inconsistencies are discussed in Section 2.6.3.

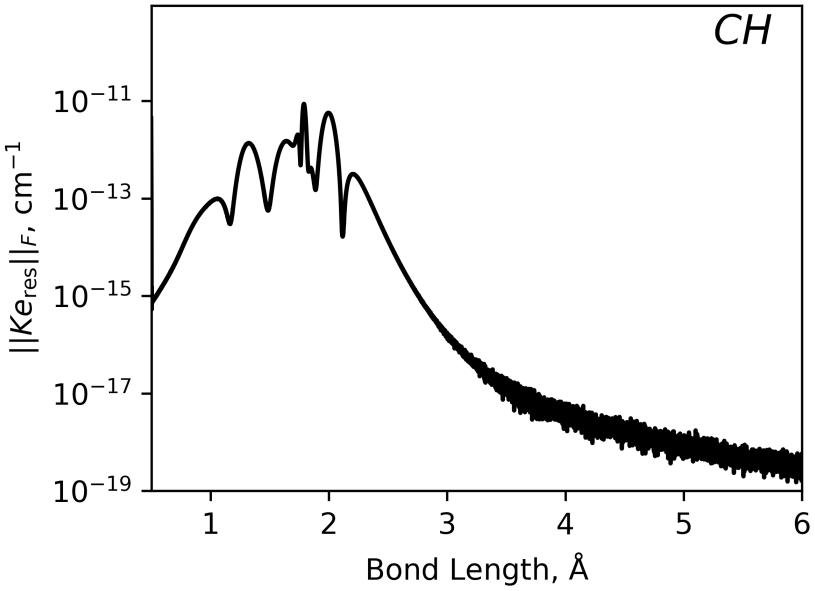

Figure 2.7: The Frobenius norm of the residual (radial) kinetic energy coupling matrix after transformation by the AtDT as a function of bond length. It is clear that all radial DDR couplings have been numerically removed *exactly*.

As seen in the two-state example (Section 2.5.2), modifying the NACs allows the AtDT to connect both boundary conditions and yield a practical diabatic representation. While I do not claim fundamental correctness, if these modified NACs closely match the *ab initio* curves, they provide a pragmatic solution for constructing a physically meaningful diabatic representation and an efficient contracted vibronic basis.

2.6.3 Sources of Inconsistency within NACs

A possible source of inconsistency is at the *ab initio* calculation stage, where NACs are usually computed at a lower level of theory, typically CASSCF[136], than the corresponding adiabatic properties which can be as high as coupled cluster. The NACs will therefore not be positioned at the correct avoided crossing position relative to the adiabatic potentials, and will contain errors in their magnitude. It is therefore expected that if one wants to use a diabatised spectroscopic model computed *ab initio* at a high level of theory, then the NACs must be modified to avoid non-physical features in the resulting diabatic representation[172].

The relative phase of electronic eigenstates must be carefully considered when constructing a set of *ab initio* NACs for subsequent diabatisation. In quantum chemistry calculations, the phase of electronic eigenfunctions is arbitrary and can vary across different nuclear geometries, leading to apparent random sign changes in

NACs. To address this, a common approach ensures phase consistency by selecting a reference point, fixing the NAC signs at that point, and then smoothing the NACs as functions of nuclear geometry. In this thesis, phase consistency in the NAC models are ensured wherever possible.

Another source of inconsistency can occur at the post-processing stage of the *ab initio* calculations. Adjustments made to the NACs and other property curves will introduce further inconsistencies. Such adjustments include the fitting of functional forms or interpolation/extrapolation over non-converged grid points. One can argue that if there is spectroscopic data to fit the spectroscopic model to, then one may absorb these errors in reproduction of the experiment. However, maintaining consistency between the NACs and model is typically very difficult because of the cusp-like nature of the NACs, making them sensitive to small variations in the spectroscopic model.

A permanent source of error in the computed NACs comes from the fundamental Born Oppenheimer approximation of *ab initio* electronic structure. In order to achieve an exact calculation of the electronic wavefunction, all infinite adiabatic states must be treated in the BO approximation. However, the infinite series is truncated to energetically important regions of the molecular Hilbert space in all practical applications. The resulting truncation errors are therefore always present, despite the level of theory used to compute electronic structure, and consequently NACs. However, Hellmann-Feynman theorem[174,175] – which states NACs are inversely proportional to the potential energy difference of the coupled states (see Section 2.2.1) – is usually used to argue for this truncation. Not only will this influence the accuracy of the NACs, but incompleteness of the coupled system, leading to fewer coupled states, will also directly influence the solved AtDT and diabatisation.

2.6.4 A Hybrid Asymptotic Property Based diabatisation

I present a method for regularising NACs outside both *ab initio* quantum-chemistry calculations and evolution of the AtDT, ensuring internal consistency with a given set of adiabatic property curves (such as PECs or dipoles; see section 2.6.1). The presented method aims to find a regularising correction to the NACs by connecting the forward and backward evolved AtDT solutions through application of switching functions to the associated generator matrices (see discussion below and in Section B). I term this method 'Hybrid Asymptotic Property-Based diabatisation' (HyAP) herein.

Any set of boundary conditions on the AtDT can be enforced in conjunction

with the HyAP method, where a regularising correction to the NACs will be computed such that the resulting forward- and backward-evolved AtDT solutions are connected in a single trajectory of the AtDT.

The AtDT is represented via the following exponential map

$$\mathbf{U} = e^{\boldsymbol{\beta}}, \tag{2.74}$$

where $\boldsymbol{\beta}$ is a real and skew-symmetric $N \times N$ matrix known as the generator of the rotation $\mathbf{U}$. For a thorough analysis of these generator matrices and their properties with regards to Lie theory, see Section B.2. However, a concise summary of the theory and motivations behind this generator/exponential-mapping representation of $\mathbf{U}$ are provided below. Since $\boldsymbol{\beta}$ is skew-symmetric, i.e. $\boldsymbol{\beta}^T = -\boldsymbol{\beta}$, and $\boldsymbol{\beta}$ commutes with its transpose $[\boldsymbol{\beta}^T, \boldsymbol{\beta}] = 0$ then $\mathbf{U}$ is guaranteed to be unitary since

$$\mathbf{U}\mathbf{U}^T = e^{\boldsymbol{\beta}} e^{\boldsymbol{\beta}^T} = e^{\boldsymbol{\beta}+\boldsymbol{\beta}^T} = e^{\boldsymbol{\beta}-\boldsymbol{\beta}} = \mathbf{I}. \tag{2.75}$$

This exponential map representation offers several advantages. It enables the use of switching functions to create a regularised AtDT via a linear combination of the forward and backward evolved generator elements, $\boldsymbol{\beta}_{\mathrm{f}}$ and $\boldsymbol{\beta}_{\mathrm{b}}$ respectively. Furthermore, the dimensionality of the parameter space is significantly reduced from N^2 to $N(N-1)/2$ unique terms. Finally, any adjustments made to these elements will yield a unitary AtDT by construction, and substitution into Eq.(2.49) will yield a set of regularised NACs that, together with the regularised AtDT, *exactly* satisfies the criteria for a strictly diabatic basis.

In the two-state case (Eq.(2.54)), the exponential map elements correspond directly to Euler mixing angles. In the N-state case, however, the generator $\boldsymbol{\beta}$ provides a more general parameterisation with a relationship to the NACs being less direct. My proposed method leverages this parameterisation to regularise the NACs.

The HyAP regularization scheme is as follows. Firstly, a forward-solution, $\mathbf{U}_{\mathrm{f}}$, is evolved from the identity at the left boundary $\mathbf{U}_{\mathrm{f}}(r_L) = \mathbf{I} \rightarrow \mathbf{U}_{\mathrm{f}}(r_{\mathrm{R}}) \approx \mathbf{P}$, where the backward-evolved solution $\mathbf{U}_{\mathrm{b}}(r_L) \approx \mathbf{I} \leftarrow \mathbf{U}_{\mathrm{b}}(r_{\mathrm{R}}) = \mathbf{P}$ is recovered via Eq.(2.71) (see Section 2.70 for details). Figure 2.6 illustrates that the imposed boundary conditions of the AtDT are not always satisfied, where it can be assumed that modification to the NACs connects the $\mathbf{U}_{\mathrm{f}}$ and $\mathbf{U}_{\mathrm{b}}$ solutions. This work proposes the following linear combination of forward- and backward-evolved generator matrices

$$\tilde{\mathbf{U}} = \exp\left(\boldsymbol{F} \circ \boldsymbol{\beta}_{\mathrm{b}} + (\mathbf{1} - \boldsymbol{F}) \circ \boldsymbol{\beta}_{\mathrm{f}}\right), \tag{2.76}$$

where $\tilde{\mathbf{U}}$ is the regularised AtDT, $\circ$ is the element-wise (Hadamard) product, $\mathbf{1}$ is a matrix with every element equaling 1, $\boldsymbol{\beta} = \ln(\mathbf{U})$ is a generator matrix, and $\boldsymbol{F}$ acts as a switching function between $\boldsymbol{\beta}_\mathrm{b}$ and $\boldsymbol{\beta}_\mathrm{f}$. Sigmoid functions are used to model the elements of the switching matrix $\boldsymbol{F}$

$$\boldsymbol{F}_{ij}(r;\gamma_{ij},r_{0,ij}) = \left(1+e^{-\gamma_{ij}(r-r_{0,ij})}\right)^{-1}, \tag{2.77}$$

where $\boldsymbol{F}_{ij}\colon \mathbb{R} \to (0,1)$, $r_{0,ij}$ is the reference geometry at which $\boldsymbol{F}_{ij} = \frac{1}{2}$, and γ_{ij} is the slope parameter of the sigmoid where a larger value means a steeper change in the function value near $r_{0,ij}$. Therefore, the exponent in Eq.(2.76) represents a generator matrix which gradually transitions from $\boldsymbol{\beta}_\mathrm{f}$ at short bond lengths to $\boldsymbol{\beta}_\mathrm{b}$ at longer bond lengths. By construction, the asymptote/boundary-problem is fixed, where $\tilde{\mathbf{U}}$ evolves from $\mathbf{I} \to \mathbf{P}$ and $\mathbf{I} \leftarrow \mathbf{P}$, and the desired asymptotes of the diabatic properties are ensured.

Despite solving the asymptote/boundary-condition problem, the resulting diabatic properties are not guaranteed to be smooth functions of the nuclear coordinate r. The trajectory of the AtDT with molecular bond length therefore needs to be optimised to ensure a physical diabatisation. As discussed above, the AtDT trajectory is conveniently parameterised by the generator matrices through which the optimisation is performed. To this end, further flexibility in the shape of $\boldsymbol{F}_{ij}$ is introduced by morphing the constant γ_{ij} parameter of Eq.(2.77) to a Šurkus-like expansion [176,177] via

$$\gamma_{ij} = \gamma_{ij}^{ref} \sum_{i=0}^{N} B_i z^i(r)(r-\xi_p) + \xi_p B_\infty, \tag{2.78}$$

where $\gamma_{ij}^{\mathrm{ref}}$ is a constant reference slope-parameter in which the morphing is applied, $\xi_p(r)$ is the so-called Šurkus variable [178] given by

$$\xi_p(r) = \frac{r^p - r_{\mathrm{ref}}^p}{r^p + r_{\mathrm{ref}}^p}, \tag{2.79}$$

where p is an integer parameter that adjusts the responsiveness of the polynomial, while r_{ref} is a reference geometry for the expansion in Eq.(4.21) and here it is set to $r_{0,ij}$ from Eq.(2.77). B_i are the expansion coefficients corresponding to different orders of the polynomial, where B_∞ is usually taken as zero in order to allow the expansion to not diverge towards $r \to \infty$. Lastly, z is a damped displacement coordinate given by

$$z(r) = (r-r_\mathrm{e})\exp[-\beta_2(r-r_\mathrm{e})^2 - \beta_4(r-r_\mathrm{e})^4], \tag{2.80}$$

where β_2 and β_4 are damping constants, preventing large oscillations at bond lengths far from the reference geometry. This, in particular, is quite useful for the HyAP method as it can be used to preserve the dynamics near the boundary conditions and concentrate the regularization to the region of strong-non-adiabatic interaction.

To complete the HyAP method, the parameters $\gamma_{ij}(r)$ and $r_{0,ij}$ must be optimised for each element ($F_{i<j}$) to achieve the smoothest-possible diabatic properties. Through extensive testing, the following cost function was identified as consistently yielding robust and reliable results when minimised

$$\sqrt{\sum_k \|\mathscr{D}(r_k)^2\|_\Delta{}^2} \to 0 \tag{2.81}$$

where $\mathscr{D}^2$ is the second-derivative matrix of the diabatic property (e.g. diabatic potential matrix, dipole matrix, e.t.c.) for the dynamics induced by action of $\mathbf{U}$ only. For instance, consider the adiabatic and diabatic property matrices $\mathscr{L}^{\mathrm{a}}$ and $\mathscr{L}^{\mathrm{d}} = \mathbf{U}^\dagger \mathscr{L}^{\mathrm{a}} \mathbf{U}$, then $\mathscr{D}^2$ can be computed via

$$\begin{aligned}\mathscr{D}^2 &= \frac{d^2\mathbf{U}^\dagger}{dr^2}\mathscr{L}^{\mathrm{a}}\mathbf{U} + 2\frac{d\mathbf{U}^\dagger}{dr}\mathscr{L}^{\mathrm{a}}\frac{d\mathbf{U}}{dr} + \mathbf{U}^\dagger\mathscr{L}^{\mathrm{a}}\frac{d^2\mathbf{U}}{dr^2} \\ &= \frac{d^2\mathscr{L}^{\mathrm{d}}}{dr^2} + \mathscr{O}\left(\frac{d^n\mathscr{L}^{\mathrm{a}}}{dr^n}\right).\end{aligned} \tag{2.82}$$

This approach avoids penalizing dynamics that arise from the derivatives of the adiabatic properties, eliminating the need to handle the noisy numerical derivatives commonly encountered in *ab initio* data. Lastly, $\|\cdot\|_\Delta$ is defined here to be the Frobenius-norm operator for the upper-triangle and diagonal elements defined by

$$\|\boldsymbol{M}\|_\Delta = \sqrt{\sum_{i\leq j} |\boldsymbol{M}_{ij}|^2}, \tag{2.83}$$

where the Frobenius norm would sum over all elements, however, when $\boldsymbol{M}$ is Hermitian, double counting of the off-diagonal elements would occur.

The regularising correction to the NACs can then be computed by inserting $\tilde{\mathbf{U}}$ of Eq.(2.76) into Eq.(2.49) via

$$\tilde{\mathbf{U}}\frac{d\tilde{\mathbf{U}}^\dagger}{dr} = \mathbf{W}^{(1)} + \Delta = \mathbf{W}^{(1)}_{\mathrm{reg}} \tag{2.84}$$

where Δ is the skew-symmetric regularising correction matrix and $\mathbf{W}^{(1)}_{\mathrm{reg}}$ is the regularised NAC matrix. The regularising correction then ensures the AtDT to cor-

rectly evolve between two imposed boundary conditions and the NACs to be internally consistent with the adiabatic property (PECs, dipoles, e.t.c.) such that the resulting diabatic representation is smooth. Using these NACs in rovibronic calculations means the associated diabatic representation induced by action of $\tilde{\mathbf{U}}$ is an exact transformation by construction since the regularised NAC matrix and $\tilde{\mathbf{U}}$ satisfy Eq.(2.49). However, this method's limitations lie in the choice of cost function and the functional form of the switching functions, both of which introduce a degree of artificiality into the regularised NACs. The impact of this artificial regularization on the rovibronic solution is discussed in Chapter 3.

2.7 Motivations for the Chosen AtDT Boundary Conditions

The process of diabatisation, particularly for complex multi-state systems, presents numerous challenges tied to the non-uniqueness of the AtDT, its boundary conditions, and inconsistencies between NACs and adiabatic property curves. It has been discussed that modifying the NACs by a regularising correction (and will be demonstrated in Chapter 3) can ensure an AtDT that satisfies the imposed boundary conditions and produces a smooth diabatic representation. My choice of boundary conditions was guided by a pragmatic aim to construct a physically meaningful and spectroscopically useful diabatic model that is exactly equivalent to the adiabatic representation. This section discusses the motivations behind these boundary condition choices.

2.7.1 Constraining the AtDT at the Dissociation Limit

A natural boundary condition for diabatisation can be established at molecular dissociation, enforcing coincidence between the adiabatic and diabatic representations when the atoms are far separated. In this limit, the diabatic states exhibit zero electronic coupling (DC) and dissociate into the adiabatic channels describing isolated fragments. The AtDT in this framework corresponds to a (signed) permutation matrix, $\mathbf{P}$, which effectively swaps the adiabatic states – in line with diabatic states that cross. As $r \to \infty$, the AtDT approaches the constant matrix $\mathbf{P}$, and the NACs are required to vanish, as demonstrated by inserting a constant AtDT into Eq. (2.49).

However, Dalgarno et al.[179] showed that if at least one atom dissociates into a state with non-zero angular momentum (e.g., non-S states), electronic-nuclear coupling cannot be neglected. Later, Butler[180] derived that NACs remain non-zero when two electronic states correlate to atomic orbitals differing in angular momentum by 1, due to dipole-like contributions. For example, *ab initio* calculations have

shown non-zero NACs in H_2 persisting up to bond lengths of 80 Bohr[181,182] and up to 40 Å in my *ab initio* calculations of KH (see Section 5.3).

Subsequent studies[183–186] concluded that these non-vanishing NACs are fictitious, arising from the use of undesirable electronic coordinate frames within the Born-Oppenheimer framework. This issue, known as the electron momentum transfer problem, occurs because the Born-Oppenheimer approximation neglects dynamical electron translation effects, leading to a static view of electronic structure and preventing the electron clouds from dynamically following nuclear motion[187,188]. Thus, NACs computed this way are coordinate frame dependent. Solutions to this problem include incorporating electron translation factors (ETFs) or using scattering coordinates to account for electron position and momentum, thereby removing non-vanishing NACs and ensuring accurate descriptions of slow atomic collisions[42,183,185]. More recently, Bian et al.[188] adopted a semi-classical phase-space approach to address this electron-inertia issue.

For simplicity, we ignore long-range interactions between electronic states that correlate to degenerate monomer states in the asymptotic region, which would otherwise split the dissociation channel and introduce further electronic coupling[20,180]. The persistence of non-vanishing NACs poses challenges for constructing diabatic states and defining the AtDT boundary condition. Such diabatic states fail to align with adiabatic ones and continue intercrossing as $r \to \infty$[189], as discussed in Section 2.7.2. When NACs do not vanish at the separated atom limit, the construction of useful diabatic states becomes impossible[190].

In this thesis, non-vanishing NACs are assumed to have been removed during the *ab initio* stage using one of the aforementioned methods, ensuring the validity of the AtDT boundary condition, $\mathbf{P}$. The focus of the ExoMol project is typically on bound-state molecular dynamics in the spectroscopically relevant region of intermediate bond lengths. Thus, non-vanishing NACs in the separated atom limit are not pertinent to our objectives. Assuming vanishing NACs as $r \to \infty$, along with the considerations presented here, is sufficient to achieve my practical goals.

2.7.2 Special Case AtDT – Constant NAC Limit at Long Stretches

As discussed in Section 2.7.1, NACs may persist in the seperated atom limit. For the case of a constant NAC matrix ($d\mathbf{W}^{(1)}/dr = 0$), Eq. (2.49) yields the following solution for $\mathbf{U}$

$$\mathbf{U} = e^{-r\mathbf{W}^{(1)}}, \tag{2.85}$$

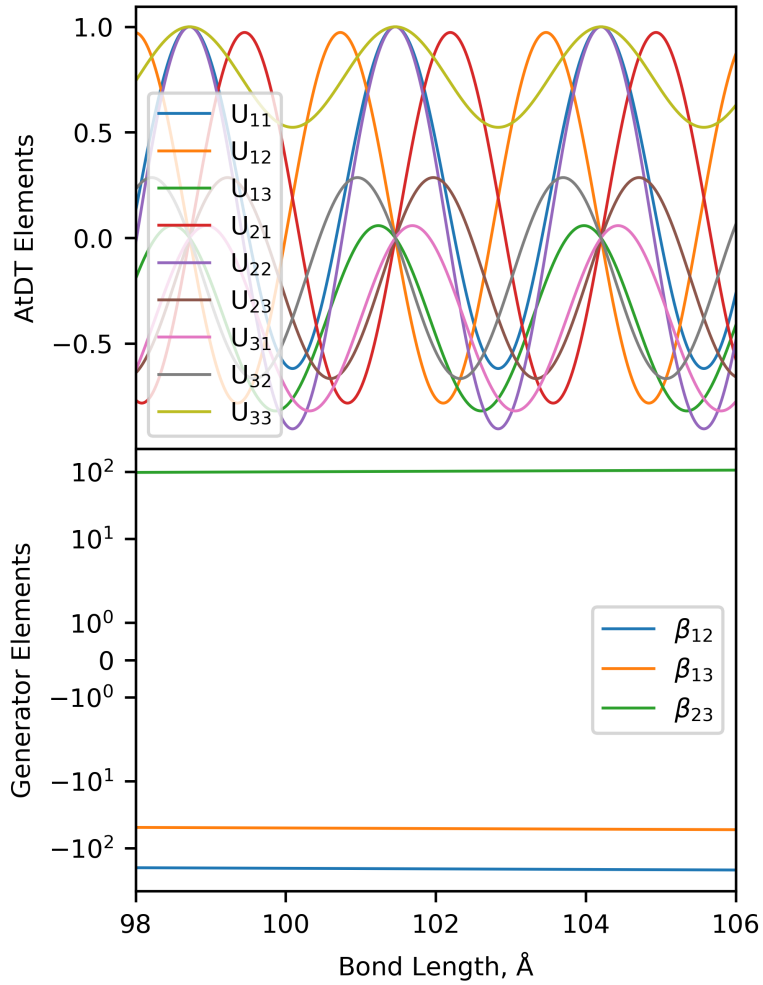

Figure 2.8: Illustration of the AtDT and generator matrix elements from the solution in Eq.(2.85 for an artificial three-state system ($W_{12} = 2$, $W_{13} = 0.5$, $W_{23} = -1$). The top panel depicts the long range behavior of the AtDT matrix elements when NACs tend to a constant limits, and are seen to be oscillatory in behavior. The bottom panel showcases the corresponding generator matrix elements, which are linear functions indicative of a rotation of the diabatic configuration space at a constant angular-frequency.

which is easily verifiable by directly differentiating

$$\frac{d}{dr}\mathbf{U}^{\dagger} = \frac{d}{dr}e^{r\mathbf{W}^{(1)}} = e^{r\mathbf{W}^{(1)}}\mathbf{W}^{(1)}, \tag{2.86}$$

therefore,

$$\mathbf{U}\frac{d\mathbf{U}^{\dagger}}{dr} = e^{-r\mathbf{W}^{(1)}}e^{r\mathbf{W}^{(1)}}\mathbf{W}^{(1)} = \mathbf{W}^{(1)}, \tag{2.87}$$

satisfying condition Eq.(2.49).

Figure 2.8 illustrates this, where the generator elements, $\boldsymbol{\beta} = ln(\mathbf{U})$, are seen to be linear with bond length and represent constant velocities of the evolution (see Appendix B for more details). The AtDT matrix will represent a rotation with constant angular frequency given by the magnitude of the constant NACs. Therefore, towards the limit $r \to \infty$, for systems with NACs that asymptotically approach a constant, the diabatic configuration space will rotate about axes, planes, or manifolds (depending on the dimension of the system studied) with fixed angular-velocities, meaning the diabatic properties will oscillate between adiabatic properties and their mixtures.

The top panel of Figure 2.8 plots the matrix elements of the AtDT, $\mathbf{U}$, in this seperated atom limit, where the elements are seen to be oscillatory and periodically pass through the identity. The axes/planes/manifolds of rotation and the angular-velocities are determined from the eigenvalues and eigenvectors of the constant $\mathbf{W}^{(1)}$ matrix, or could be understood from the Schur-decomposition as described in section A.1.2.

2.7.3 Constraining the AtDT Toward Short-Stretches

This section focuses on constraining the AtDT at short internuclear separations (united atom limit, $r \to 0$) and at spectroscopically important regions, particularly the equilibrium geometry.

Toward the united atom limit $r \to 0$, NACs are not well defined since adiabatic states will approach degeneracy at high energies. Macias et al.[191] showed that, except for single-electron heteronuclear molecules, NACs can vanish in this limit only when the electronic coordinate origin coincides with the nuclear charge center. Additionally, Kim et al.[190] demonstrated that, similarly to the dissociation limit, NACs may not vanish for coupled states correlating to atomic orbitals with an angular momentum difference of 1. Despite this, Kim et al.[190] diabatise their 7-state LiH system by initializing their evolution by setting the AtDT to the identity matrix ($\mathbf{U} = \mathbf{I}$) at $r \to 0$. Using the adiabatic atomic states as a reference, this ensures a smooth transition of the diabatic states into intermediate bond lengths, making them

physically meaningful and sensibly ordered (see discussion below). This diabatisation is sufficient for rovibronic calculations as the high energies in this region do not significantly impact lower-lying bound states, and so the characterisation of the NACs for $r \to 0$ are not spectroscopically important.

The equilibrium geometry is central to molecular spectroscopy, as it controls the dominant rovibronic energy level structure: electronic transitions depend on the equilibrium energy, rotational transitions on the bond length, and vibrational transitions on the potential well width. Consequently, the equilibrium electronic structure, thus well-constrained by spectroscopic data, is central to theoretical treatments like variational or effective Hamiltonian approaches. This representation is typically accurate within the adiabatic framework, usually computed *ab initio* using the Born-Oppenheimer approximation which holds well near equilibrium for most molecules[11]. A diabatic representation that deviates significantly from this equilibrium structure [8] may compromise control over spectroscopically important regions. For example, Morse oscillator functions effectively model adiabatic potential energy curves, with parameters directly controlling spectroscopic properties like minimum energy, bond length, and well width. This approach is extensively used to refine spectroscopic models to experimental data in the ExoMol project[53,54,173], enabling computation of an accurate and comprehensive rovibronic spectroscopy.

I aim to generate a diabatic representation that provides accurate control over dominant molecular spectroscopy, which approximately coincides with the adiabatic representation near equilibrium geometry. This approach, central to many property-based diabatisation methods[20,59–68], constructs diabatic potential energy curves (or properties like dipoles) that match adiabatic curves outside avoided crossings while remaining smooth within them. For example, in two-state diabatisations (see Section 2.5.1), the diabatic curves cross at the avoided crossing and coincide with the adiabatic curves elsewhere, with the NAC integral (mixing angle) typically set to $\pi/4$ at the crossing point and $\pi/2$ at dissociation[38,13,165,170,26]. In this formalism, the AtDT starts as the identity matrix at short internuclear separations – where NACs are assumed to vanish – and evolves into a signed permutation matrix at dissociation, where diabatic states swap energy enumeration.

Considering the arguments presented here, I wish to adopt the boundary condition on the AtDT which equals the identity in the limit $r \to 0$ in line with property-based diabatisation approaches.

[8] While equivalent if generated by an AtDT satisfying Eq. (2.49), significant deviations are corrected by the DCs.

i	j	$argmax(W_{ij}^{(1)})$	r_c^{f}	r_c^{b}
1	2	1.653		
1	3	1.380	2.168	1.606
1	4	1.797		
2	3	1.326	1.504	1.083
2	4	1.658		1.913
3	4	2.000		

Table 2.1: The maximum positions of the NACs and the diabatic crossing geometries, r_c, between states i and j are shown. The superscripts 'f' and 'b' refer to the diabatic crossing geometries using the forward and backward AtDT scheme, respectively. It is clear that the relationship between the position of the NACs and the diabatic crossing geometries are non-trivial for the general N-state coupled system.

2.7.4 Smoothness of the Diabatic Representation

In Section 2.6.1, I demonstrate that satisfying multiple boundary conditions on the AtDT is non-trivial. The connection of NACs and smoothness of the diabatic properties is now discussed, which is unclear in the CH model presented in Figure 2.6. The non-uniqueness of diabatisation means the relationship between NACs and the character of the diabatic representation is inherently complicated. For N-state systems ($N > 2$), establishing this connection requires selecting a boundary condition and calculating the AtDT, adding additional complexity absent in two-state systems. In the latter, one can easily sketch a diabatic representation and model a consistent NAC since the diabatic crossing position typically coincides with the NAC centroid[38,13,165,170,26] with only the NAC width primarily controlling diabatic smoothness. A simple test illustrates that shifting the NAC away from the optimal avoided crossing position introduces steep gradients in the two-state diabatic PECs, which is shown in Figures 2.5 and 2.12.

For N-state systems, the non-uniqueness of the diabatisation and the increased dimensionality and interdependence of states make this process significantly more challenging. For instance, Table 2.1 shows that for the CH model in Figure 2.6, the NAC peak positions and diabatic crossing geometries differ significantly between forward and backward AtDT evolution schemes. Thus, to ensure a smooth diabatic representation a non-linear optimisation of potentially many coupled parameters is likely required (see Section 2.7.5).

In summary, NACs fundamentally shape the diabatic properties, but their influence is non-linear and mediated by the AtDT and its boundary conditions. Understanding this relationship requires careful consideration of NACs and the AtDT constraints. However, inconsistency between the NACs and the adiabatic PECs will

hinder the construction of a smooth diabatic representation.

2.7.5 Artificialness and Reproducibility in Property-Based diabatisation

As discussed in Section 2.7.4, the relationship between NACs and the character of the diabatic representation is ambiguous due to the non-uniqueness of diabatisation via the evolution method. Property-based diabatisation methods aim to ensure smooth diabatic properties by optimising the AtDT. This can be achieved by either minimising a cost function defining diabatic smoothness (method A) or modelling smooth diabatic properties that reproduce adiabatic ones upon diagonalisation (method B, known as ansatz diabatisation[83,89,82,87,88,81]). Both approaches face challenges with reproducibility and artificiality due to their reliance on optimisation and functional parameterisation. Sections 2.8.4 and 2.8.5 discuss these methods in more detail.

A popular approach in both methods is to use simple functions like Lorentzians to represent NACs[170,171,165,166]. While holding well in the strong interaction region, this parameterisation can introduce artificiality, as seen in the systems studied here where NACs exhibit more complex structures. Furthermore, method B, while successful for two-state systems[38,172], struggles with N-state systems ($N > 2$) due to the difficulty of ensuring singularity-free adiabatic PECs and DCs. Even with conditions to determine DCs from diabatic properties and NACs[38] (see Section 2.8.4 for a general condition), constructing a consistent set of NACs and a diabatic representation with singularity-free DCs and adiabatic properties remains challenging. Optimisation in both methods is computationally expensive, requiring repeated AtDT evolutions. Alternatively, optimising the DCs directly such that diagonalisation with sketched diabatic PECs is equally challenging, as there is no guarantee that a consistent set of DCs exists to exactly reproduce the adiabatic PECs. This ansatz diabatisation scheme has been shown to reproduce well the dynamics of ultrafast nonadiabatic processes, but struggles to represent all regions of the adiabatic PECs accurately[85]. Internal tests confirm that this approach is highly inefficient for accurately reconstructing adiabatic PECs globally and demands careful functional parameterisation and selection of initial diabatic PECs.

The HyAP method (see Section 2.6.4) attempts to address these limitations by eliminating repeated AtDT evolutions and minimising artificiality through a regularising correction. This correction, derived from optimised switching functions (see Section 2.6.4), while artificial, are shown in Chapter 3 to introduce minimal changes to the original NACs of N_2 and results in rovibronic energy differences within the

expected error of *ab initio* calculations. Efforts are made to keep the switching function as flexible as possible, ensuring the final AtDT remains guided by the underlying electronic structure data. While some modification of NACs is necessary to address inconsistencies in the spectroscopic model, these corrections are minimal compared to the artificiality introduced by other property-based diabatisation methods, which may disregard electronic structure data entirely. Furthermore, a detailed analysis of HyAP's sensitivity to boundary conditions and switching functions is a promising avenue for future research to further enhance the method's robustness and accuracy.

2.8 Other Methods for Computing the AtDT

This section presents several different methods to determine the AtDT. First, two direct-diabatisation[76–79] approaches in solution to Eq.(2.49) are compared to the formal exponential line-integral propagator approach discussed in Section 2.6. Next, non-direct diabatisation approaches are discussed, namely property-based[20,59–68] and ansatz[83,89,82,87,88,81] methods, where their usefulness and implications are discussed.

Although the analysis presented here on the linear propagator and perturbative approaches to solving the AtDT has not been published, it forms an important part of the methodological development undertaken during my PhD. These approaches represent well-established and broadly representative methods that were explored as part of a comprehensive evaluation of possible solutions, prior to ultimately adopting the line-integral method. Notably, to the best of my knowledge, the perturbative solution proposed here is the first of its kind in its specific application to solving for the AtDT. These methods are included to document and compare their performance with the selected approach, offering insight into the decision-making process that led to the development of the HyAP method. While a more detailed comparative study remains outside the scope of this thesis, it represents a valuable direction for future work.

2.8.1 Linear Propagators: Euler's Method

As a straightforward approach to solving Eq.(2.49), one could use the standard and widely used Euler method which aims to solve first-order initial-value differential equation of the form

$$\frac{dy}{dx} = f(x,y), \quad \text{where } y(x_0) = y_0, \tag{2.88}$$

where y_0 is the initial-value of the function to be solved, $y(x)$, known *a priori* to computation, and $f(x,y)$ is a function of the independent variable x and $y(x)$. Euler's method, also known as first-order Runge-Kutta, is desirable since the computation of high-order derivatives is not required, like in Taylor series solutions, but instead only the functional value is needed. For example, the Euler method solution to Eq.(2.88) can be written in the simple linear form

$$y(x+h) = y(x) + \underbrace{hf(x,y(x))}_{\text{linear-propagator}} . \tag{2.89}$$

The main drawback of the Euler method, and other linear propagator solutions like higher order Runge-Kutta methods (a.k.a RK2, RK3, and most commonly RK4), is that it relies on the solved object to posses addition algebra. It is known that the AtDT belongs to the (Lie) group SO(N) which is not a group under the addition operation (see Appendix B for a thorough discussion). Therefore, the resulting solution will not be an object of SO(N), and will be expected to lose orthogonality. Despite this, one may expect that a dense-enough grid, by which the AtDT is solved, may overcome this problem where the propagated error will be small enough for practical applications.

Here the formula of the Euler method in the context of solving Eq.(2.49) is stated. Eulers method, the simplest of all predictor-corrector methods, will serve to represent linear-propagator type method for comparison in this section. Euler's formula is then given by

$$\mathbf{U}^{\dagger}(r+h) = \mathbf{U}^{\dagger}(r) + \underbrace{h\mathbf{U}^{\dagger}(r)\mathbf{W}^{(1)}(r)}_{\text{linear-propagator}} . \tag{2.90}$$

2.8.2 A Perturbative Approach

A perturbative approach is now introduced, where the aim is to directly evaluate the (skew-symmetric) generator matrix of Eqns.(2.51,A.1,B.6) by some recursive formulae in solution Eq.(2.49). Consider the Taylor series of the exponential generator matrix $\mathbf{U} = \exp(-\boldsymbol{\kappa})$

$$U = e^{-\kappa} = \sum_n \frac{(-1)^n}{n!}\kappa^n \tag{2.91}$$

where $\boldsymbol{\kappa}$ is a real skew-symmetric matrix, $\boldsymbol{\kappa} = -\boldsymbol{\kappa}^{\dagger}$, and $\mathbf{U}$ is the AtDT. Inserting the above into Eq.(2.49), using the Taylor series expansion for the exponential and

its derivative, yields the following formulae

$$e^{-\kappa}\frac{de^{\kappa}}{dr} = \kappa' + \frac{1}{2}\left[\kappa', \kappa\right] + \frac{1}{6}\left[\left[\kappa', \kappa\right], \kappa\right] + \frac{1}{24}\left[\left[\left[\kappa', \kappa\right], \kappa\right], \kappa\right] + \cdots = \mathbf{W}^{(1)}. \tag{2.92}$$

Here $\kappa' = \frac{d\kappa}{dr}$, where this series of nested commutators is equivalent to the Baker–Campbell–Hausdorff formula[192,193] (BCH) for matrix products of non-commuting matrix exponents. It turns out that the BCH formula shows that the Lie algebra determines the Lie groups structure (see Appendix B for more details). This is because the Lie algebras and Lie bracket operators (commutators) define how the product of two Lie groups equals another Lie group, i.e. product $\exp(\mathbf{A})\exp(\mathbf{B}) = \exp(\mathbf{C})$. This result is promising as the formal exponential line-integral propagator method produces sensible solutions for the AtDT and its generator representation is a natural choice.

If κ and κ' commute, i.e. $[\kappa', \kappa] = 0$, then one can pull-out the κ' term on either the left or right hand side, where the above expression reduces to $\kappa' = W^{(1)}$. This solution is equivalent to the two-state problem in Section (2.5.1) where this commutativity holds. In general, only the two-coupled state AtDT has this property, where solution to Eq.(2.49) reduces to computing the scalar mixing angle from the cumulative integral of the single NAC term – Eq.(2.53).

To solve for κ, which can not be done analytically for the above mentioned reasons, and one can use a perturbative treatment. κ is now expanded in a power series of the small perturbation parameter ε,

$$\kappa = \sum_{i=1} \varepsilon^i \kappa_i, \tag{2.93}$$

and then choose as the leading order solution to align with the 'two-state' like problem, yielding

$$\kappa_1 = \frac{1}{\varepsilon}\int W^{(1)} dr. \tag{2.94}$$

The N^{th} order term can be evaluated by the following expression

$$\kappa_N = -\int \left(\frac{1}{2} \sum_{i=1}^{N-1} \mathscr{C}_1(i) + \frac{1}{6} \sum_{i=1}^{N-2} \sum_{j=1}^{N-1-i} \mathscr{C}_2(i,j) + \frac{1}{24} \sum_{i=1}^{N-3} \sum_{j=1}^{N-2-i} \sum_{k=1}^{N-1-i-j} \mathscr{C}_3(i,j,k) + \cdots + \frac{1}{N!} \mathscr{C}_N(1,1,1,\cdots,1) \right) dr, \tag{2.95}$$

where $\mathscr{C}_N(i,j,k,\cdots)$ is the N^{th}–nested commutator defined by

$$\mathscr{C}_N(i,j,k,\cdots) = \left[\left[\left[\cdots \left[\kappa_i', \kappa_j \right], \kappa_k \right], \cdots \right], \kappa_{N-i-j-k-\cdots} \right]. \tag{2.96}$$

For example, the first, second, and third nested terms are given by

$$\begin{aligned} \mathscr{C}_1(i) &= \left[\kappa_i', \kappa_{N-i} \right] \\ \mathscr{C}_2(i,j) &= \left[\left[\kappa_i', \kappa_j \right], \kappa_{N-i-j} \right] \\ \mathscr{C}_3(i,j,k) &= \left[\left[\left[\kappa_i', \kappa_j \right], \kappa_k \right], \kappa_{N-i-j-k} \right] \end{aligned} \tag{2.97}$$

	N	γ	r_c
$W_{12}^{(1)}$	1.000	0.027	2.319
$W_{13}^{(1)}$	0.095	0.140	2.340
$W_{23}^{(1)}$	-1.000	0.048	2.108

Table 2.2: Lorentzian function parameters in Eq.(4.5) used to model simplified NACs for testing different methods in solution of Eq.(2.49) for the AtDT. The NACs are modelled after the 3-state N_2 NACs described in Section 3.6.1.

2.8.3 Comparison of Methods in Solution of the AtDT

I now compare the formal exponential line-integral propagator method (FELIP), the Euler method (section 2.8.1), and the perturbative method (P_N, where N is the perturbative order; see section 2.8.2) in solution to Eq.(2.49) for the AtDT. A 3-state system representing a simplified version of the N_2 model described in Section 3.6.1 of Chapter 3 is used in the comparison. The three NACs are modelled here using the Lorentzian function of Eq.(4.5), where Table 2.2 presents the functional parameters and Figure 2.9 plots them as a function of bond length. The N_2 NACs are simplified as Lorentzian functions since their integral is analytic and is given by Eq.(2.56). Hence, the error due to integrating the NAC in the FELIP and perturbative methods is removed. Therefore, since the Euler method does not require integrals of the

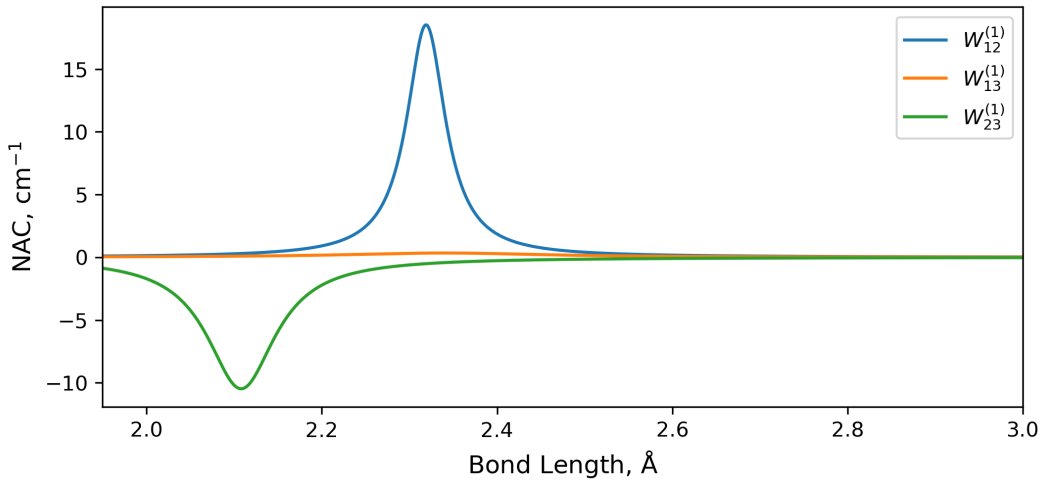

Figure 2.9: Illustration of three NACs computed using Lorentzian functions in Eq.(4.5) with parameters given in Table 2.2. The NACs are simplified models of the N_2 NACs presented in Section 3.6.1.

NAC matrix, its comparison with the other methods measures the characteristics of the solution due to the method applied only.

In order to study the effectiveness of the different solution methods, three metrics are compared. Firstly, the solution error is determined by the Frobenius norm of the residual kinetic energy matrix in Eqns.(2.72,2.73) as described in Section 2.6.1. Secondly, the orthogonality (unitarity) of the AtDT is computed by the Frobenius norm of the difference matrix

$$||\mathbf{U}_s^\dagger \mathbf{U}_s - \mathbf{I}||, \tag{2.98}$$

where $\mathbf{U}_s$ is the solved AtDT and $\mathbf{I}$ is the identity matrix. Larger values of the orthogonality metric in Eq.(2.98) correspond to greater differences from orthogonality, where zero means $\mathbf{U}_s^\dagger \mathbf{U}_s$ coincides with the identity.

Figure 2.10 illustrates orthogonality and residual kinetic energy metrics across the three solution methods, where perturbative orders of 1, 2, 4, 7 and 10 are considered. The `JULIA` programming language was used to facilitate calculations, where the grid of internuclear stretches had a spacing of 10^{-4} Å. Both the FELIP and the perturbative approaches maintain orthogonal AtDT solutions, as demonstrated by the stability of $||\mathbf{U}_s^\dagger \mathbf{U}_s - \mathbf{I}||$, which remains within the precision limit of `Float64` in `JULIA` (approximately 16 significant decimal digits). By contrast, the Euler method shows substantial drift from orthogonality, with the metric reaching 12 orders of magnitude greater than the other methods. This is to be expected since linear propagation of the AtDT will introduce non-orthogonality in the final solution.

The bottom panel displays residual kinetic energy couplings, demonstrat-

ing FELIP's numerical exactness across all nuclear geometries considered. Interestingly, the perturbative method shows increased error at low expansion orders, with the $10^{\text{th}}-$order solution error surpassing that of Euler's method at extended stretches. This result suggests that exact AtDT solutions cannot be well-represented by low-order perturbations of the two-state-like case (see Sections 2.8.2 and 2.5.1). Corrections are needed for the non-commutativity intrinsic to general N-dimensional rotations, which are substantial in this 3D example, indicating that a perturbative approach may be unsuitable for capturing the complex non-commutative behavior. The Euler method, with residual kinetic energy couplings at 10^{-3} cm^{-1}, lacks the precision needed for high-resolution spectroscopy.

In this section, I have demonstrated that linear-propagator solutions, at least for the simplistic Euler method, do not maintain orthogonality and produce poor accuracy in the final result of the AtDT. However, as long as the AtDT varies smoothly, and the grid is dense enough, higher accuracy results may be obtained.

2.8.4 Ansatz/Block-diagonalisation diabatisation

Ansatz-based diabatisation methods[83,89,82,87,88,81], also known as block diagonalisation, prioritise practicality and often employ optimisation strategies. Unlike the direct approaches discussed above, these methods operate in the reverse transformation direction, effectively performing an 'adiabatisation'. The methods begin by diagonalising the diabatic potential matrix

$$\mathbf{V}^{(\mathrm{a})} = \mathbf{U}\,\mathbf{V}^{(\mathrm{d})}_{\text{ansatz}}\mathbf{U}^{\dagger}, \tag{2.99}$$

where I note that $\mathbf{U}$ here is now used to diagonalise the diabatic representation as opposed to diabatising the adiabatic one. The associated eigenvalues of the ansatz $\mathbf{V}^{(\mathrm{d})}_{\text{ansatz}}$ are then identified as the adiabatic potential energies. The diabatic PECs are often sketched to be smooth functions of the nuclear geometries and chosen to coincide with the adiabatic potentials far from the avoided crossings. Then, the DCs are optimised to ensure that upon diagonalisation with the diabatic potentials, the (*ab initio*) adiabatic potentials are reconstructed from the eigenvalues. In practice this method has been shown to reproduce well the dynamics of ultrafast nonadiabatic processes, but struggles to represent all regions of the adiabatic PECs accurately[85]. Particularly why this is is because the exact functional form of the DCs are unknown, but will be heavily influenced by the topology of the potentials and NACs. It is also not guaranteed that a set of DCs exist such that diagonalisation with a sketched set of diabatic potentials will yield the desired set of adiabatic PECs,

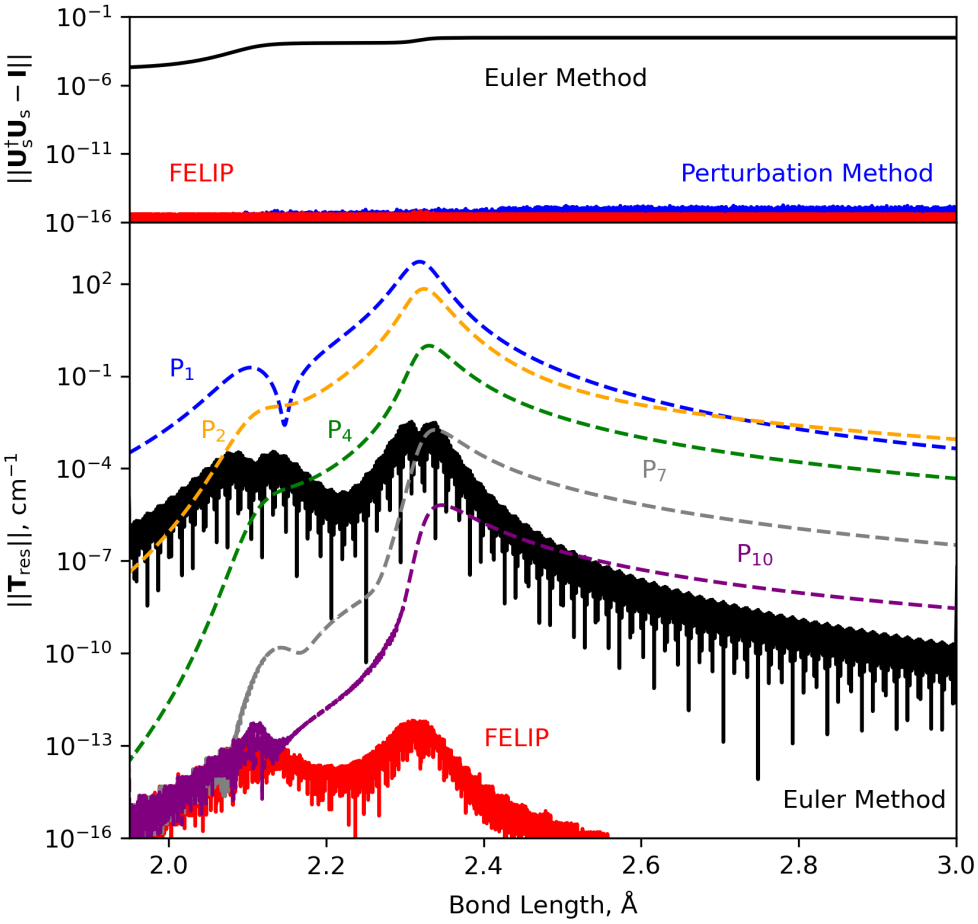

Figure 2.10: Comparison between different methods in solution to Eq.(2.49). The top panel illustrates the deviation from orthogonality (see text for details) of the solved AtDT – $\mathbf{U}_s$ – through Eq.(2.98), where 0 means exact orthogonality. The bottom panel illustrates the residual kinetic energy after transformation by the solved AtDT. Labels with P_n refer to perturbative methods of order n and FELIP means 'Formal Exponential Line-Integral Propagator'.

and will also require the simultaneous optimisation of the diabatic potentials. For N-state systems, many highly-correlated parameters are often required to be optimised, where convergence whilst maintaining a sensible diabatic representation over all regions of the configuration space is very difficult.

For two-state systems, however, this method is practical and well defined. Section 2.5.1 shows how the two-state DC can be recovered from definition of two simple crossing diabatic potentials and a NAC centered on the crossing geometry, and is given by Eq.(2.59). This gives a handle on representing the equilibrium geometry and the shape of the avoided crossing 'hump', requiring no knowledge of the DC functional form. The diabatic potentials are then constructed with simple Morse oscillator functions or repulsive curves and the NAC by a simple Lorentzian with

its position fixed. We have used this ansatz-procedure to fit the adiabatic potential energy curves of multiple molecular systems (YO[52], CH (internal testing), AlH (internal testing), and SO[194]) to experimental transition data.

Extension of condition 2.59 to the N-state case can be achieved by comparing the resulting off-diagonal elements of the transformed matrix $\mathbf{U}^{\dagger}\mathbf{V}^{(\mathrm{d})}\mathbf{U}$ which, by definition, should be zero in the adiabatic representation. This will provide constraints on the DCs to ensure an exact diagonalisation by $\mathbf{U}$ and a modelled set of diabatic potentials. The vector of $N(N-1)/2$ DCs, $\vec{\mathscr{D}}$, is then given by

$$\vec{\mathscr{D}}_{\mu} = -\sum_{\lambda} \mathscr{A}^{-1}_{\mu\lambda} \cdot \vec{F}_{\lambda}. \tag{2.100}$$

$\vec{F}$ is a vector of transformed diabatic PECs defined by

$$\vec{F}_{\mu} = \sum_{m,k} \mathbf{U}_{im}\mathbf{U}^{\dagger}_{kj}\tilde{\boldsymbol{V}}^{(\mathrm{d})}_{mk} \quad \mu \leftarrow i \neq j, \tag{2.101}$$

where μ is the vectorising index generated by "stacking rows" for $i \neq j$, and $\tilde{\boldsymbol{V}}^{(\mathrm{d})}$ is the diabatic potential matrix with only the diagonal elements being non-zero. The matrix $\mathscr{A}$ is defined by

$$\mathscr{A}_{\mu\lambda} = \mathbf{U}_{im}\mathbf{U}^{\dagger}_{kj} \;\; i \neq j \in \mu, m \neq k \in \lambda. \tag{2.102}$$

This provides a way to compute the DCs which ensure the diabatic electronic Hamiltonian $\mathbf{V}^{(\mathrm{d})}$ is diagonalised upon action of a diabatising unitary matrix solved through Eq.(2.49) and N diabatic PECs. We are not aware of any such formulae in the literature which mixes the representations in construction of a set of avoided crossing adiabatic PECs, similarly to the presented 2-state methodology discussed in 2.5.1, using a mixture of diabatic potentials and NACs.

Equation (2.100) does not explicitly impose a condition analogous to the two-state case[38] (Eq.(2.59)), where the NAC integral must equal $\pi/4$ at the diabatic crossing point. While one could attempt to derive conditions on the AtDT elements from Eq.(2.100), their direct correlation with the NACs remains unclear. This is because the AtDT is inherently non-unique (it depends on the chosen boundary conditions) and highly nonlinear in the NAC terms.

Numerical tests show that Eq.(2.100) yields the required diabatic couplings (DCs), enabling their diagonalisation with the modeled diabats through $\mathbf{U}$. However, using Eq. (2.100) often results in DCs and adiabatic potential energy curves

(PECs) with steep gradients when the NACs (and thus **U**) are not well-defined. Figure 2.11 illustrates an example ansatz/block-diagonalisation diabatisation for the simplified N_2 system discussed in Section 3.6.1 of Chapter 3. A set of ansatz diabatic PECs are modeled with Morse oscillator functions and are sketched to coincide with the *ab initio* adiabatic PECs and cross smoothly through the avoided crossings. A forward-evolved AtDT, **U**, is computed from the Lorentzian NACs in Figure 2.9 and used in conjunction with the ansatz diabatic PECs to compute the resulting DCs via Eq.(2.100). The DCs are seen to become discontinuous where the eigenvalues of the ansatz diabatic potential matrix become degenerate. These eigenvalues are observed to be significantly different to the desired *ab initio* curves in dashed lines, showing large gradients at the avoided crossings, becoming degenerate which is impossible for true (adiabatic) Born-Oppenheimer states, and do not coincide with the adiabatic curves far from the avoided crossings (at the asymptotes). The latter point is probably due to the forward-evolved AtDT not coinciding with a permutation matrix at the separated atom limit, highlighting the ambiguities in choosing a good boundary condition. It is clear that this method, while being practical, is sensitive to the ansatz and complicates modelling a set of adiabatic PECs.

It would be valuable to explore the application of the HyAP method alongside constraints on the AtDT elements derived from Eq.(2.100). Unfortunately, time constraints during my PhD prevented further investigation. Nevertheless, I believe this approach *could* enable an efficient hybrid ansatz-block-diagonalisation/property-based diabatisation method. The main challenge, however, lies in selecting appropriate boundary conditions for computing **U**. As demonstrated in Section 2.6.4 and the simple test above, achieving adiabatic-diabatic coincidence at both asymptotic limits is not guaranteed, particularly when using simplified NAC functions to generate **U**, typical of practical diabatisation methods. Consequently, regardless of the ansatz quality, the proposed method cannot ensure adiabatic-diabatic coincidence at both asymptotes and thus global reconstruction of the adiabatic PECs through diagonalisation of the model diabats.

A potential solution could be leveraging the HyAP method to optimise the generator matrix trajectory to minimise the residuals between the eigenvalues of the ansatz model and the *ab initio* adiabatic potentials – opposed to maximising the smoothness of the resulting diabatic properties when diabatising the adiabatic representation (see HyAP method in Section 2.6.4). The advantage of the latter (and which the HyAP method is built on), is that the resulting diabatic representation is *exactly* equivalent with the (*ab initio*) adiabatic representation, whereas the former

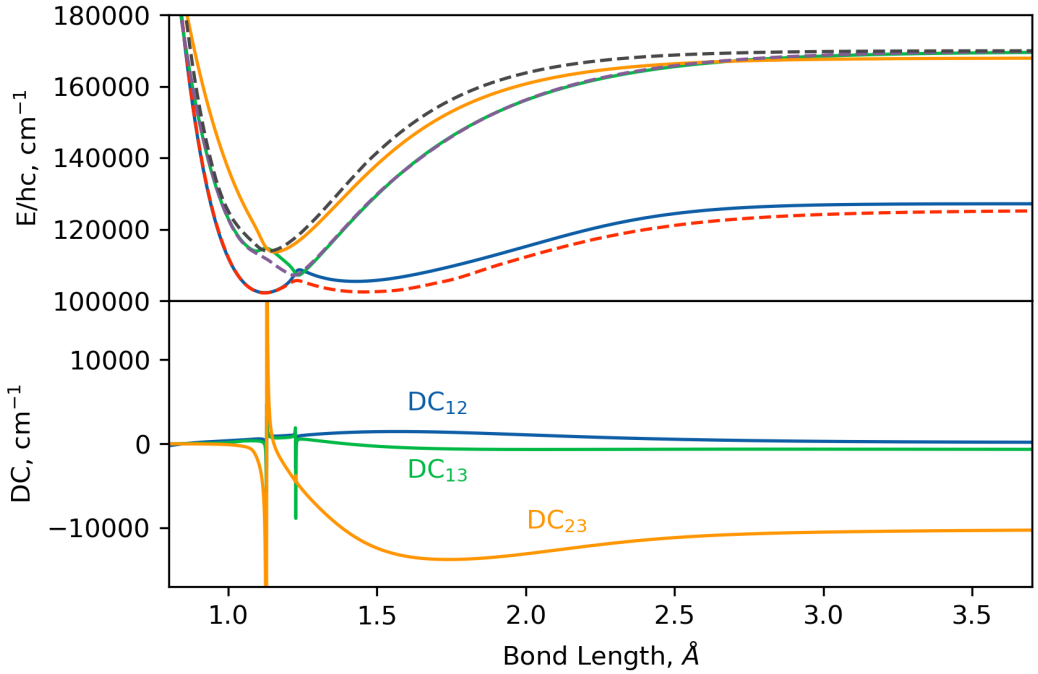

Figure 2.11: Illustration of an ansatz/block-diagonalisation diabatisation for the simplified N_2 system. A forward-evolved AtDT, $\mathbf{U}$, is computed from the Lorentzian NACs in Figure 2.9 and used with ansatz diabatic PECs to compute the resulting DCs via Eq.(2.100) which are shown in the bottom panel. The ansatz diabats are modelled with Morse oscillator functions and are sketched to coincide with the *ab initio* adiabatic PECs (plotted with dashed lines) and cross smoothly through the avoided crossings. The eigenvalues of the ansatz diabatic potential matrix are then plotted as solid lines.

approximates the adiabatic representation in favour of a desirable sketched diabatic representation.

2.8.5 Property-Based diabatisation

Property-based diabatisation[20,59–68] is built upon the pragmatic goal of constructing diabatic property curves (or surfaces) which are smooth functions of the nuclear coordinates which are both simpler to represent analytically and easier to treat numerically (avoiding careful integration in regions of strong variations in the topology gradient). This is motivated by the heuristic that a physical – or rather, sensible – representation should efficiently yield physics which are not sensitive to the representation. In this heuristic, the derived diabatic property curves are twice differentiable due to the properties of the wave function and derivatives. If the wavefunction, and/or property curves such as dipoles, exhibit steep gradients then the computed spectroscopy – which often relies on integrating these functions – will be sensitive to the topology of the associated spectroscopic model, with poten-

tially poor convergence properties. Multiple studies[38,99,98] have shown the adiabatic representation, which exhibits steep gradients in the coupling and potential energy landscape close to the avoided crossings, to have poor convergence properties exactly due to this.

The construction of (smooth) diabatic states through their properties constrains the AtDT. The early work by Macias and Riera[64] present a formal analysis on the variation of molecular properies in the vicinity of avoided crossings, and show that a significant reduction of strong NAC can be done by constructing smooth molecular properties, and thus (near) diabatic states, in this region. Similar procedures have been utilised in the literature, examples include the ionic and covalent structures of alkali hydrides[92,93] which can be distinguished by the dipole moment[26] and represent natural diabatic states. For example, Werner and Meyer[26], similarly to Macias and Riera[64], form diabatic states of LiH by computing mixing angles which ensure the (linear) ionic component of the dipole moment passes smoothly through the adiabatic DMCs.

These examples demonstrate that a simple optimisation procedure can be defined by which the AtDT is computed, even without NACs computed *a priori*. Consider some Hermitian matrix $\mathscr{L}$ corresponding to some molecular property, such as the potential or dipole moment, the diabatic property matrix is then constructed by the transformation

$$\mathscr{L}^{(\mathrm{d})} = \mathbf{U}^{\dagger}\, \mathscr{L}^{(\mathrm{a})}\mathbf{U}, \tag{2.103}$$

where the superscripts '(a)' and '(d)' indicate the adiabatic and diabatic representation, respectively, and $\mathbf{U}$ is the AtDT. In this strictly property-based approach, one then parameterises the AtDT in terms of the NACs. For a simple example, consider modelling the ij^{th} NAC $W^{(1)}_{ij}$ with a characteristic position r^{c}_{ij} and width parameter γ_{ij}, then one parameterises the AtDT as

$$\mathbf{U}(r;\{r^{c}_{ij}\},\{\gamma_{ij}\}). \tag{2.104}$$

Computing the AtDT from the NAC matrix $\mathbf{W}^{(1)}$ for a two-state system is simple and is detailed in Section 2.5.1, however for an N-state system an evolution scheme is required (e.g., see Sections 2.6 and 2.8.1). Then, with this parameterisation the AtDT can be optimised to ensure the elements of the diabatic property matrix $\mathscr{L}^{(\mathrm{d})}$ are smooth, and could be approximately defined to minimise the following cost

function from Section 2.6.3

$$\sqrt{\sum_k \|\mathscr{D}^2(r_k;\{r_{ij}^c\},\{\gamma_{ij}\})\|_\Delta{}^2} \to 0 \tag{2.105}$$

where $\mathscr{D}^2$ is the second-derivative matrix of the diabatic property $\mathscr{L}^{(\mathrm{d})}$, and $\|\cdot\|_\Delta$ is defined as the Frobenius-norm operator in Eq.(2.83).

The optimisation itself is easy to achieve using any commonly available optimisation libraries. Throughout this thesis I use the Julia programming language and the open-source Optim library's `Optim.minimiser` function to minimise loss functions using the Nelder-Mead method[195,196]. Figure 2.12 demonstrates the

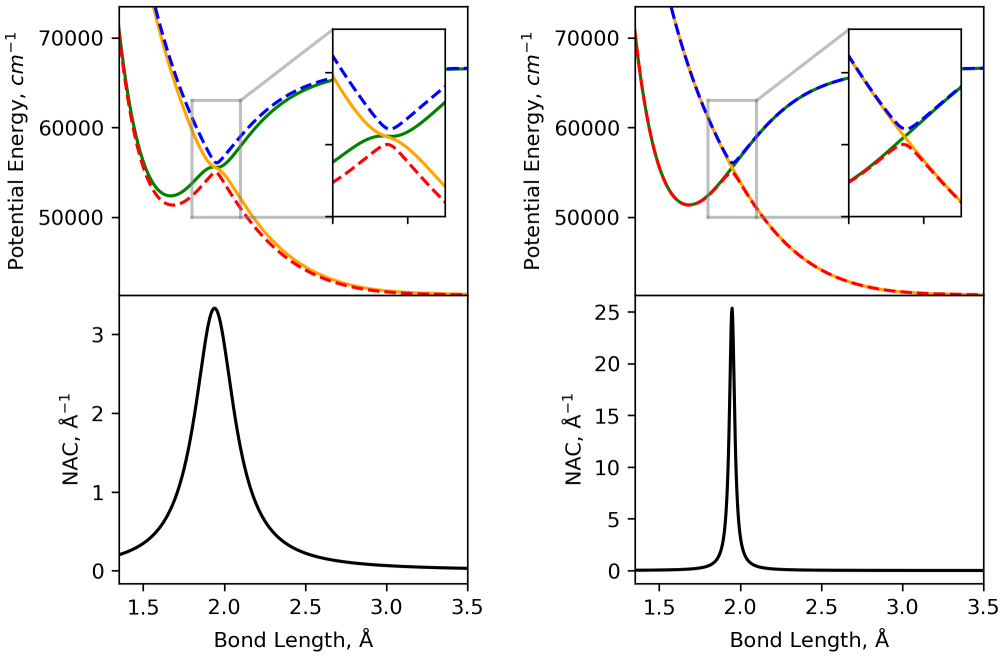

Figure 2.12: Illustration of the optimisation of the AtDT as parameterised by the NAC using Eqns.(2.103,2.104,2.105). The two-state $^1\Pi$ system of sulfur monoxide presented in Figure 2.3 is used as a test model to demonstrate the property-based diabatisation method. The dashed and solid lines are the adiabatic and diabatic PECs, respectively, where the bottom panels show the corresponding NAC. The left plot shows diabatisation by an initial, un-optimised AtDT with a guessed NAC whereas the right hand plots then show the diabatisation after optimising the NAC (thence AtDT). Consequently, the diabats are made to be smooth functions of r. A Lorentzian function is used to model the NAC.

effect of optimisation involved in property-based diabatisation as applied to the two-state system presented in Section 2.5.1. The left plot illustrates how with an initial, guessed NAC, diabatisation yields a set of diabatic PECs which exhibit a kink at the avoided crossing, which is undesireable. However, the NAC coupling these

states (and thence AtDT) is then optimised to ensure the diabats are smooth and is illustrated in the right panel. This figure showcases how improper NACs will yield non-physical diabatisations, where property-based methods aim to build a set of NACs consistent with a smooth set of diabatic moelcular property curves.

To perform a similar optimisation but for an N-state system, repeated evaluations of the AtDT evolution would be required after updating the NACs. This would be computationally expensive, inefficient, and does not take into account the issue with diabatic asymptotes. Instead, the proposed HyAP method in Section 2.6.4 in conjunction with a set of simple Lorentzian NACs centred on the avoided crossing geometries – possibly fitted to two-state diabatisations within the N-state model – would be more practical and efficient. Alternatively, an ansatz method may be better suited, and is discussed in Section 2.8.4.

Chapter 3

The Numerical Equivalence of Adiabatic and Diabatic Representations in Nuclear Motion Calculations

3.1 Introduction

As discussed and mathematically shown in Chapters 1 and 2, non-adiabatic couplings (NACs) are a result of relaxing the Born-Oppenheimer approximation, and arise due to the subsequent coupling of electronic and nuclear motion in molecules. These derivative couplings (DDRs), particularly near avoided crossings or conical intersections[1] become singular, and therefore must not be neglected. As discussed in Chapter 1, these couplings are critical for describing physicochemical processes such as photodissociation, non-radiative transitions, and collision dynamics. The adiabatic representation diagonalises the electronic Hamiltonian, where NACs manifest as derivative terms within the vibrational nuclear kinetic energy operator (see Eq.(2.30)), which is non-diagonal in this frame. By contrast, the diabatic representation was shown in Section 2.4 to eliminate both first- and second-order DDR couplings through a unitary transformation of the molecular Hamiltonian. In this diabatic representation, the vibrational nuclear kinetic energy operator is now diagonalised at the cost of introducing off-diagonal diabatic couplings (DC) within the electronic Hamiltonian. The diabatic representation was shown to be desirable since PECs of the same symmetry are allowed to cross, where (it is assumed) property curves become smooth. This chapter focuses on the numerical equivalence of these

[1] Avoided crossings and conical intersections arise in regions of the molecular configuration space where potential energy curves/surfaces of states of the same symmetry near degeneracy.

two representations within nuclear motion calculations, where rovibronic energies and wavefunctions are shown to be preserved whilst the different representations offer distinct computational advantages depending on the system.

Despite the routine use of diabatisation to treat avoided crossings in molecular PECs, few studies have rigorously examined the numerical equivalence of adiabatic and diabatic representations. Such an investigation would be valuable not only for benchmarking nuclear motion codes but also to better understand the individual contributions of terms in the adiabatic and diabatic Hamiltonians. Numerical equivalence refers to the principle that both representations should yield identical physical observables, such as energy eigenvalues.

The solution of the rovibronic Schrödinger equation should be independent of whether the adiabatic or diabatic representation is employed[46]. In practical numerical applications, equivalence is expected to emerge as calculations become more precise, for example, by increasing the size of the basis set or number of points in the solution grid. However, this equivalence, often assumed, is rarely demonstrated. Studies investigating convergence between the two representations are scarce. For instance, Zimmerman and George[99] performed numerical convergence tests on transition probability amplitudes for collisions in collinear atom–diatom systems. They demonstrated equivalence but found that convergence behavior of the diabatic representation to be much faster. Similarly, Shi et al.[98] examined the convergence of energy eigenvalues and eigenfunctions in adiabatic and diabatic representations using a sinc-DVR method. While equivalence was ultimately achieved, it required a complete adiabatic model and a conical intersection at high energy.

The following section demonstrates the numerical equivalence between the adiabatic and diabatic representations within nuclear motion calculations for several diatomic molecules. The results presented in this chapter are based on our recent publications[38,197], where we apply the diabatisation methods detailed in Chapter 2 to the yttrium oxide (YO), carbon monohydride (CH), molecular nitrogen (N_2), and a synthetic 10-state diatomic systems. The presented numerical equivalence of the adiabatic and diabatic representations within nuclear motion calculations is the first, where our recent article[38] also demonstrated that vibronic energy convergence rates was faster diabatically for the strongly NAC coupled YO system but initially faster adiabatically for the weakly coupled CH system, illustrating the importance of choosing an appropriate frame. This Chapter also demonstrates that a regularising correction to the NACs, through computation via the HyAP method (see Section 2.6.4 of Chapter 2), ensured their internal consistency between different DDR components and adiabatic PECs while minimally influencing the rovibronic solution

within the expected error of *ab initio* calculations – a first regularisation of this type to the best of my knowledge (see Section 2.6.4 for details). The combined results of this chapter and Chapter 2 have built a robust set of methods in the rovibronic treatment of NAC terms and production of a practical and accurate diatomic line lists, essential for the computation of high resolution molecular spectra in line with the ExoMol project.

YO exhibits avoided crossings between the $B\,^2\Sigma^+$, $D\,^2\Sigma^+$ and $A\,^2\Pi$, $C\,^2\Pi$ electronic states as described by Brady et al.[172] in the production of a semi-empirical line list. YO is of significant scientific interest due to its broad range of applications and astrophysical sightings. YO has been observed in stellar spectra, typically of cool stars[198–201], utilised in high-temperature solar furnaces[202,203] where its spectra has been used to probe high temperature materials[204], and explored in the development of magneto-optical traps, showcasing its potential in quantum control and ultracold physics[205–208]. The complex electronic structure of YO is characterised by multiple low-lying electronic states which exhibit avoided crossings, making it a valuable target for accurate theoretical modelling.

CH is one of the most extensively studied free radicals, known for its occurrence in a wide array of environments. CH has been detected in flames[209,210], making it of interest to industrial application. Non-terrestrially, CH has been observed both in solar spectra and stellar atmospheres[211–213]. It is also observed in cometary spectra[214], the interstellar medium (ISM)[215–218], and in molecular clouds[219] highlighting its importance for astrochemical studies. This Chapter studies the non-adiabatic interactions between the $C\,^2\Sigma^+$, $2\,^2\Sigma^+$. $3\,^2\Sigma^+$, and $4\,^2\Sigma^+$ states of CH, where the analysis begins at the two-state system [$C\,^2\Sigma^+$,$2\,^2\Sigma^+$] which are coupled by a weak NAC[38], and then increases the complexity to the four-state system where equivalence and the HyAP method are tested.

N_2 is a spectroscopically important molecule since it makes up nearly 78 percent of Earth's atmosphere, yet its strong triple bond renders it highly inert, posing challenges for chemical utilisation[220] and also spectroscopic detection. This is because of both its weak rovibrational lines and the scarcity of any tracer gases. Despite this, N_2 is indispensable across biological, agricultural, and industrial processes such as in the nitrogen cycle and the production of ammonia via the Haber-Bosch process[221,222]. N_2 has also been observed within our solar system in the UV[223–225] and the ISM[226]. The electronic structure of N_2 exhibits a highly complex web of avoided crossings across multiple electronic states[227–229]. The work in this Chapter is particularly interested in the avoided crossings between the [$1\,^1\Sigma_g^+$, $2\,^1\Sigma_g^+$, $3\,^1\Sigma_g^+$] states which are strongly bound and exhibit significant non-adiabatic

coupling, which will be used to test the HyAP diabatisation method (see Section 2.6.4).

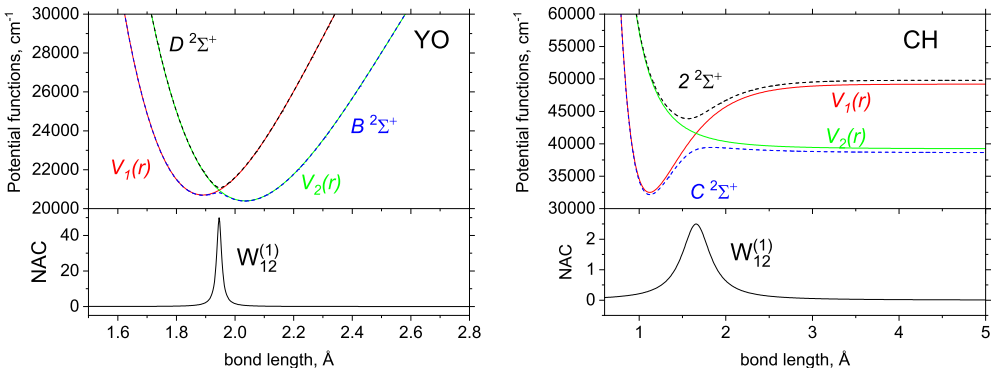

Figure 3.1: Illustration of the $[D\,^2\Sigma^+, B\,^2\Sigma^+]$ and $[\mathrm{C}\,^2\Sigma^+, 2\,^2\Sigma^+]$ avoided crossing systems ([black, blue] lines) for the YO and CH diatomics, respectively, which are used to perform tests on the adiabatic and diabatic equivalence. The top panels show the diabats (solid lines) and adiabats (dashed lines). The bottom panels show the corresponding NAC (in the units of inverse Å) defining the transformations.

3.2 2-State Spectroscopic Models

As an illustration of the numerical equivalence between the adiabatic and diabatic representations used to compute the diatomic rovibronic solution, two model two-state electronic systems are investigated. We study YO and CH with their diabatic and adiabatic curves shown in Figure 3.1. The respective spectroscopic models input to our variational code Duo (see Section 2.3) are detailed below. We chose these systems for an initial analysis because they exhibit contrasting spectroscopic behavior, where their adiabatic and diabatic representations differ significantly. YO will be seen to have a strong NAC and weak DC characterised by a sharp avoided crossing, whereas CH contains a weak NAC and strong DC characterised by a smooth and broad avoided crossing. This behavior is mostly attributed to the energetic separation between the interacting states being small for YO and large for CH. Therefore, achieving equivalence for both YO and CH will demonstrate that the implementation of our diabatic Duo module to be robust for many different system types of varying degrees of NAC strength.

3.2.1 YO spectroscopic model

As an example of a two-state system with strongly bound electronic curves characterised by a narrow avoided crossing and a large NAC, we choose the *ab initio* PEC curves of the $B\,^2\Sigma^+$ and $D\,^2\Sigma^+$ states of YO from Smirnov et al.[230] with the NAC

from Brady et al. [172]. We model this YO system using the mathematical footing and theory from Section 2.5.1 of Chapter 2, which is summarised below.

We model the diabatic $B^2\Sigma^+$ and $D^2\Sigma^+$ PECs of YO using a simple Morse oscillator function given by

$$V(r) = T_e \ + \ (A_e - T_e)\left[1 - \exp\left(-b\left(r - r_e\right)\right)\right]^2, \tag{3.1}$$

where r_e is the equilibrium position, A_e is a dissociation asymptote, the expansion coefficient b controls the width of the potential well, and $A_e - V(r_e)$ is the dissociation energy. As is often done for strong NACs, we model the $[B^2\Sigma^+, D^2\Sigma^+]$ NAC of YO with a Lorentzian function given by

$$W_{12}^{(1)}(r) = \frac{1}{2}\frac{\gamma}{\gamma^2 + (r - r_c)^2}, \tag{3.2}$$

where γ is the HWHM parameter and r_c is its center defined to align with the crossing point of the diabatic curves. The model Morse oscillator PECs and lorentzian NAC are illustrated in Figure 3.2 where their functional parameters were obtained by a least squares fitting to the corresponding *ab initio* data, and are listed in Table 3.1. Accuracy of the fit at this stage is not important, since we only wish to test the equivalence of the adiabatic and diabatic representations, where only a consistent set of models is required.

For the Lorenztian model of the NAC, Eq. (3.2) can be easily integrated to yield the AtDT mixing-angle $\beta(r)$ given by (see also Eq.(2.56))

$$\beta(r) = \frac{\pi}{4} + \frac{1}{2}\arctan\left(\frac{r - r_c}{\gamma}\right), \tag{3.3}$$

where r_c is corresponds to the crossing point between the diabatic PECs and is obtained as numerical solution to $V_1^d = V_2^d$, which is listed in Table 3.1. It is required that the Lorentzian centroid r_c coincides with the diabatic crossing point otherwise the resulting adiabatic PECs and DC will become singular. This can be seen in the following expression for the two-state DC (from Eq.(2.59) of Section 2.5.1)

$$V_{12}^{(d)}(r) = \frac{1}{2}\tan(2\beta_{12}(r))(V_2^{(d)}(r) - V_1^{(d)}(r)), \tag{3.4}$$

where at the crossing point, the tangent function is singular $\tan(2\beta_{12}(r_c)) = \tan(\pi/2) = \infty$. However, the difference term in the diabatic potentials approaches zero at the crossing point, negating the singularity from the tangent term. There-

fore, if the crossing point differs from the Lorentzian center, where the mixing angle is computed as $\pi/4$, the DC becomes singular. This is also true for the adiabatic PECs, which are obtained from the diabatic potentials and DC as the eigenvalues of the diabatic electronic Hamiltonian (see Eqns.(2.60, 2.61, 2.62) in Section 2.5.1) which read

$$V_1^{\rm a}(r) = \frac{V_1^{\rm d}(r)+V_2^{\rm d}(r)}{2} - \frac{1}{2}\sqrt{[V_1^{\rm d}(r)-V_2^{\rm d}(r)]^2+4V_{12}^2(r)}, \tag{3.5}$$

$$V_2^{\rm a}(r) = \frac{V_1^{\rm d}(r)+V_2^{\rm d}(r)}{2} + \frac{1}{2}\sqrt{[V_1^{\rm d}(r)-V_2^{\rm d}(r)]^2+4W_{12}^2(r)}. \tag{3.6}$$

The YO DC curve is computed using Eq. (3.4) with the diabatic PECs and the mixing-angle computed via the parameters in Table 3.1. The adiabatic PECs of YO were computed as the eigenvalues of the diabatic electronic Hamiltonian given by Eqs. (3.5, 3.6). The model YO adiabatic PECs and DC are illustrated in Figure 3.2.

Finally, the second-order DDR **K** matrix is computed from Eq.(2.17) which, for a two-electronic state system, has only one unique element given by

$$\mathbf{K}_{2\times 2} = -\left(\mathbf{W}^{(1)}\right)^2 = \begin{pmatrix} \left(W_{12}^{(1)}\right)^2 & 0 \\ 0 & \left(W_{12}^{(1)}\right)^2 \end{pmatrix}. \tag{3.7}$$

Table 3.1: The molecular parameters defining the YO spectroscopic model

Parameter	$V_1^{\rm d}$	$V_2^{\rm d}$	$W_{12}^{(1)}$
$T_{\rm e}$, cm^{-1}	20700.000	20400.000	
$r_{\rm e}$, Å	1.890	2.035	
b, Å^{-1}	1.500	1.260	
$A_{\rm e}$, cm^{-1}	59220.000	59220.000	
γ, cm^{-1}			0.010
$r_{\rm c}$, Å			1.946

3.2.2 CH spectroscopic model

As an example of a weakly non-adiabatically coupled two-electronic state system characterised by a large energetic separation, we investigate the CH spectroscopic model corresponding to the $C^2\Sigma^+$ and $2^2\Sigma^+$ *ab initio* curves by van Dishoeck[231]. We model the diabatically bound $C^3\Pi$ state with a Morse oscillator Eq. (3.1), which is seen to have a diabatic well depth of about 16700 cm^{-1} (2.0705 eV). The $2^2\Sigma^+$ state is diabatically repulsive, much different to the YO two-state model, with the dissociation energy lower than that of the $C^2\Sigma^+$ state by about 10000 cm^{-1}. We

chose to model the $C^2\Sigma^+$ PEC using the following form

$$V(r) = D_e + C_4/r^4. \tag{3.8}$$

The NAC between the CH [$C^2\Sigma^+$, $2^2\Sigma^+$] states are modelled using the Lorentzian function of Eq. (3.2), where the Lorentzian parameters were chosen to match the NAC from van Dishoeck[231]. All parameters defining the CH [$C^2\Sigma^+$, $2^2\Sigma^+$] spectroscopic model are listed in Table 3.2. Similarly to YO, the value of the crossing point r_c is obtained as a numerical solution to $V_1^d = V_2^d$, the DC is determined via Eq.(3.4), and the adiabatic potentials are obtainted via diagonalisation of the diabatic CH electronic Hamiltonian.

Table 3.2: The molecular parameters defining the CH diabatic spectroscopic model

Parameter	V_1^d	V_2^d	$X^3\Sigma^-$	$W_{12}^{(1)}$
T_e, cm^{-1}	32500.000		0.000	
r_e, Å	1.120		1.120	
b, Å^{-1}	2.500		1.968	
A_e, cm^{-1}	49200.000	29374.000	39220.000	
C_4, Å^{-4}		18000.000		
γ, cm^{-1}				0.200
r_c, Å				1.657

3.3 Solving the Two-State Rovibronic Schrödinger Equations

The fully coupled rovibronic Schrödinger equation for the CH and YO doublet systems are solved using the variational code Duo, where the methodology in its solution is discussed in Section 2.3 of Chapter 2. As part of this work, the Duo kinetic energy operator was extended to include the first derivative component required for implementation of the NAC using the sinc-DVR representation[232]. The DBOC terms can be either provided as input or generated from the NAC using Eq. (2.16).

Demonstrating numerical equivalence between the adiabatic and diabatic representations of nuclear motion calculations, despite being the primary aim of my work, is not my only focus. Developing a tool which allows one to study the importance of different DDR terms on the computed spectroscopy would prove invaluable to any theoretical treatment of a diatomic system. Omission of DDR coupling terms is common practice, but their effect on the rovibronic energies, and therefore determination of a quantitative error on the rovibronic solution, is nontrivial. To address this, Duo allows the omission and inclusion of any combination of DDR couplings,

to which we define three levels of approximations to compare to: (A1) in the adiabatic model, both DDR terms are switched off ($W_{12}^{(1)} = K = 0$); (A2) in the adiabatic model, the diagonal DDR is switched off ($K = 0$), but the NAC is kept in; (A3) in the diabatic model, the diabatic coupling is set to zero ($V_{12} = 0$).

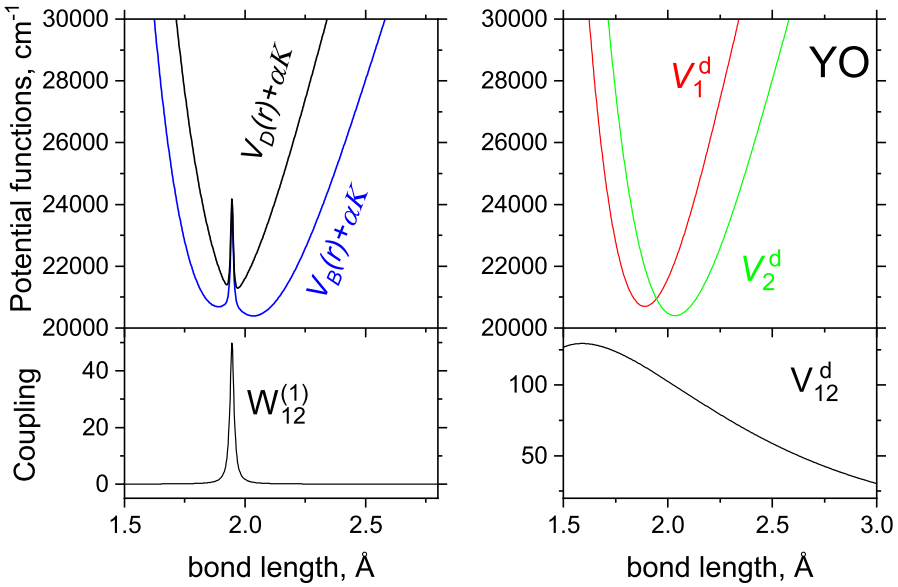

Figure 3.2: Full adiabatic (left) and diabatic (right) models of the $B^2\Sigma^+$ and $D^2\Sigma^+$ systems of YO. The top panels show the PECs, where the adiabatic PECs include the diagonal DDR correction αK and $\alpha = h/(8\pi^2 c\mu)$. The bottom panels show the corresponding coupling curves, NAC (left) and DC (right).

3.3.1 The YO solution

The vibronic energies ($J = 0.5$) of the coupled $B^2\Sigma^+$ and $D^2\Sigma^+$ systems are computed in both the adiabatic and diabatic representations as accurately as possible. This serves to establish a baseline while demonstrating the equivalence of the two representations. Although theoretical equivalence (i.e., identical results within numerical error) is expected between these representations, the practical realisation is subject to numerical convergence and other computational limitations. For instance, Duo employs a PEC-adapted vibrational basis set, constructed by solving the pure vibronic problem, which inherently differs depending on whether the adiabatic or diabatic representation is used. Therefore, both representations should exhibit different convergence behaviour.

The YO model curves detailed in Section 3.2.1 are presented in Figure 3.2, where the diagonal Born–Oppenheimer correction (DBOC) coupling (**K**) is added to the adiabatic PECs for clarity. Despite the significant differences between the

adiabatic and diabatic models – most notably a pronounced spike in the middle of the adiabatic PECs – Duo should yield identical eigenvalues and eigenfunctions, provided the calculations are fully converged.

The lowest twenty rovibronic energy term values ($J = 0.5$) computed using the two spectroscopic models are listed in Table 3.3. Despite the approximate Duo assigned quantum number labels being vastly different between the two calculations, the energies are indeed identical (within 2.5×10^{-5} cm^{-1}). Duo assigns quantum labels via the largest contribution from the corresponding basis sets, which in both cases are very different and so are their state interpretations, in which case states of matching energy enumerator n are compared.

Having established numerical equivalence, we now investigate the role of different non-adiabatic couplings within the YO model. Specifically, we analyse the impact of the three approximations outlined in Section 3.3 on the calculated rovibronic energy terms of YO (J=0.5). The effects of these approximations are summarised in Table 3.3, alongside results from the fully coupled models. For the adiabatic model, the omission of the DBOC coupling term (**K**, approximation A2) has the most significant influence, particularly on the $B^2\Sigma^+$ term values. By contrast, neglecting the off-diagonal diabatic coupling term ($V_{12}^{(\mathrm{d})} = 0$, approximation A3) in the diabatic model has a smaller impact. Quantitatively, approximation A2 yields a RMSE in the rovibronic energies (computed for the lowest twenty states) approximately 1.5 times larger than adiabatic approximation A1, and 10 times larger than the diabatic approximation A3. Nevertheless, it is evident that any simplification or omission of non-adiabatic couplings introduces significant errors, which are unacceptable for high-resolution spectroscopic applications. This is the central conclusion from this work, the exclusion of any non-adiabatic correction in models describing systems with electronic state crossings must be carefully evaluated, as such omissions can significantly compromise accuracy.

Out of the two representations, the adiabatic model is usually considered to be more complex to work with. Its curves have complex shapes with the model being very sensitive to the mutual consistency of the curves V_1^{a}, V_2^{a} and $W_{12}^{(1)}$ around the crossing point. The disadvantage of the diabatic representation is that it does not come out as a solution of the (adiabatic) electronic structure calculations and needs to be constructed either through a diabatisation approach[20,59–61,26,69–75,49] or approximated. However, it is clear for systems of strong NAC, then the diabatic representation offers a more physical model which is both more easily modeled and yields rovibronic energies less sensitive to the DC than the adiabatic model is to changes in the NACs.

Table 3.3: The rovibronic ($J = 0.5$) energy term values (cm^{-1}) of the $B^2\Sigma^+$ (B) and $D^2\Sigma^+$ (D) systems of YO computed using the adiabatic and diabatic representations. The energies are listed relative to the lowest $J = 0.5$ state. The root mean square error of the rovibronic energies computed via different approximations is given in the last line.

n	Adiabatic					Diabatic			
	$\tilde{E}$	$\tilde{E}$(DDRs=0)	$\tilde{E}(K=0)$	State	v	$\tilde{E}$	$\tilde{E}(V_{12}=0)$	State	v
1	0.000000	0.000000	0.000000	B	0	0.000000	0.000000	D	0
2	344.431810	347.928597	191.831751	B	1	344.431809	351.249676	B	0
3	561.079914	690.986320	492.221984	B	2	561.079921	549.732652	D	1
4	1009.133229	967.537324	983.098980	B	3	1009.133232	1002.246089	B	1
5	1108.354299	1132.062465	1129.463766	D	0	1108.354283	1095.516787	D	2
6	1612.539760	1553.296745	1777.897073	B	4	1612.539736	1637.352406	D	3
7	1688.323434	1897.761066	1868.635701	B	5	1688.323453	1647.646531	B	2
8	2179.350796	2008.167697	2345.749886	D	1	2179.350783	2175.239507	D	4
9	2297.569318	2465.488852	2396.923772	B	6	2297.569321	2287.451003	B	3
10	2718.929830	2689.784491	2839.568147	B	7	2718.929830	2709.178092	D	5
11	2928.147305	2925.374682	3115.611400	D	2	2928.147294	2921.659505	B	4
12	3247.771603	3395.227251	3377.138924	B	8	3247.771603	3239.168161	D	6
13	3559.124439	3442.432354	3666.238711	D	3	3559.124429	3550.272037	B	5
14	3772.447582	3862.695406	3963.866748	B	9	3772.447578	3765.209712	D	7
15	4181.801597	4167.979957	4373.535285	D	4	4181.801594	4173.288598	B	6
16	4295.897860	4333.054560	4472.298326	B	10	4295.897854	4287.302747	D	8
17	4783.958004	4805.617146	4913.118506	B	11	4783.958001	4790.709188	B	7
18	4829.238038	4866.961640	4961.045768	D	5	4829.238030	4805.447266	D	9
19	5320.626170	5275.859430	5497.071432	B	12	5320.626156	5319.643267	D	10
20	5417.844769	5552.275088	5610.459386	D	6	5417.844772	5402.533809	B	8
	...	...	...			...	...		
RMSE		97.968392	143.401905				14.339312		

3.3.2 Eigenfunctions and Reduced Density

It is instructive to compare the eigenfunctions $\varphi_i^{J,\tau}(r)$ of the adiabatic and diabatic solutions and different approximations. To this end we form reduced radial densities of the eigen-state in question. The eigenfunctions $\varphi_i^{J,\tau}$ computed by Duo are expanded in the basis set $|n\rangle$,

$$\varphi_i^{J,\tau} = \sum_{n=1}^{N} C_{i,n}^{J,\tau} |n\rangle \,, \tag{3.9}$$

where N is the basis size and $C_{i,n}^{J,\tau}$ are the expansion coefficients used to assign quantum numbers by largest contributions. $|n\rangle$ denotes the full basis (see Section 2.3 for details on this $\Lambda - S$ basis) $|n\rangle = |\text{state}, J, \Omega, \Lambda, S, \Sigma, v\rangle$. where 'state' is the electronic state, S is the total electron spin angular momentum, v is the vibrational quantum number, and Λ, Σ and Ω are the projections of electron orbital, spin, and total angular momentum along the internuclear axis, respectively. The reduced radial density $\rho_i^{J,\tau}(r)$ is then given by

$$\rho_i^{J,\tau}(r) = \sum_v \sum_k |C_{v,k}^{i,J,\tau}|^2 \, |\chi_v(r)|^2, \tag{3.10}$$

where $|k\rangle = |\text{state}, J, \Omega, \Lambda, S, \Sigma\rangle$ and $\chi_v(r)$ are the vibrational wavefunctions. The reduced density states are radial probability density functions averaged over all quantum numbers in $|n\rangle$. This is an efficient way of examining the behaviour of the wavefunctions without looking in a hyperdimensional space defined by quantum numbers $|n\rangle$.

Figure 3.3 shows selected reduced radial state densities of YO computed via the adiabatic and diabatic representations and approximations A1, A2, and A3. As expected from the energy comparisons of YO, the diabatic and adiabatic representations produce identical results, whereas the reduced densities quickly deviate when omitting the NAC and/or K corrections. It appears that omitting only the DBOC (approximation A2) yields significantly different reduced densities than when all NAC terms are removed from the calculation (approximation A1), at least concerning the lower energy levels. Furthermore, the diabatically computed reduced densities when omitting the DC (approximation A3) yields almost identical results than the fully coupled calculations. These results are consistent with the computed energy comparison in Section 3.3.1.

3.3.3 Adiabatic and diabatic solutions for CH

Our investigation now shifts to a system different to YO, the $C\,^2\Sigma^+$ and $2\,^2\Sigma^+$ states of CH which are depicted in Figure 3.4. In the adiabatic representation, these states are characterised by a large energy separation and a broad, weak NAC. Unlike YO, the DBOC term (**K**) does not introduce any spike-like features into the adiabatic PECs of CH. It can therefore be expected that the influence of the DBOC on the rovibronic solution to be less than that of YO. In the diabatic representation, the system consists of a bound and a repulsive state which cross at large internuclear distances and at high energies which – according to perturbation theory which predicts energy corrections inversely proportional to the energy difference – should not significantly influence the lower rovibronic states of $C\,^2\Sigma^+$. Regardless of the representation used, the region above the first dissociation channel (39220.0 cm^{-1}) is heavily (pre-)dissociated and should contain both pre-dissociative and continuum states. Duo is capable of computing both bound and continuum eigensolutions. The bound-state wavefunctions satisfy standard boundary conditions, decaying at both small and large distances. Continuum wavefunctions, also computed using the sinc-DVR method, by contrast satisfy the boundary conditions that enforce vanishing at the edges of the simulation box, along with their first derivatives[233]. To facilitate our analysis, (quasi-)bound and continuum states are distinguished by examining the wavefunction behaviour at the 'right' border r_{max}. Bound states vanish com-

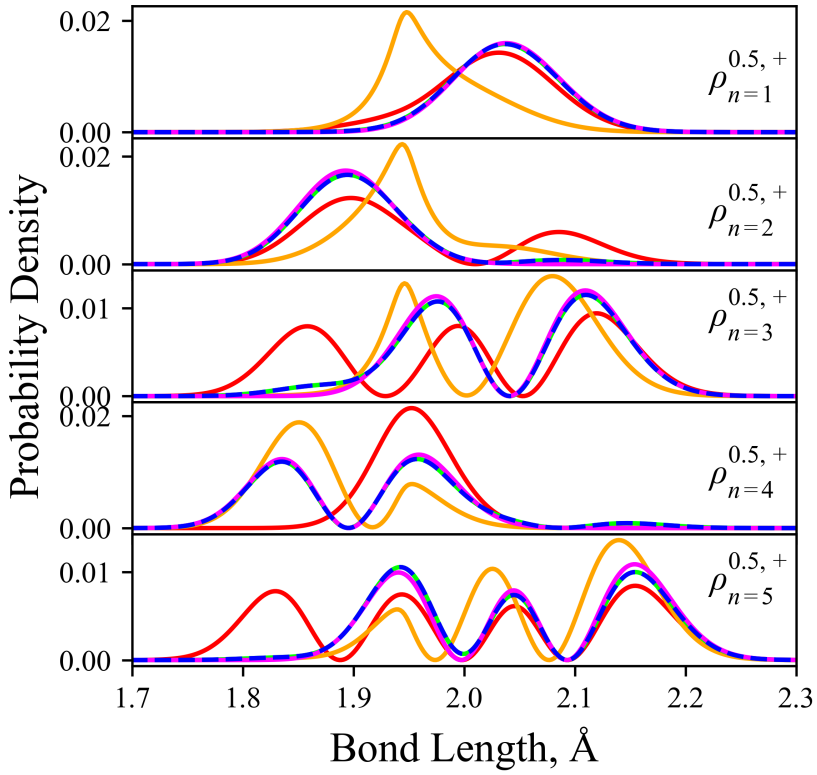

Figure 3.3: YO reduced density states for the lowest 5 bound levels with n being the energy enumerator given in Table 3.3. These reduced densities are illustrated and computed using different levels of theory: diabatic representation with DC (blue dotted); diabatic model with the DC turned off (magenta, A3); adiabatic representation with both the NAC and K correction included (lime green); adiabatic representation with NAC only (orange, A2); adiabatic representation with no correction (red, A1).

pletely at large distances, while continuum states exhibit oscillatory behavior for $r \to \infty$, with a non-zero density that extends to r_{max} [234].

The resulting bound state rovibronic energy term values are computed and listed in Table 3.4 for all five cases, including non-adiabatic and diabatic couplings with approximations as in the YO example. The full diabatic and adiabatic (bound) $C^2\Sigma^+$ energies are fully equivalent within 10^{-6} cm^{-1} (here shown up to the second decimal point). However, any degradation of the theory leads to significant changes in the calculated rovibronic energies of the $C^2\Sigma^+$ state, with the error quickly deteriorating already for $v = 2$. For example, removing the DC term, the diabatic solution becomes meaningless with many non-physical bound states above the first dissociation channel, non-existent in the case of the full treatment. A similar effect is caused by the omission of the NAC terms from the adiabatic picture with bound spurious $2^2\Sigma^+$ states being produced. Although the omission of the **K** term from

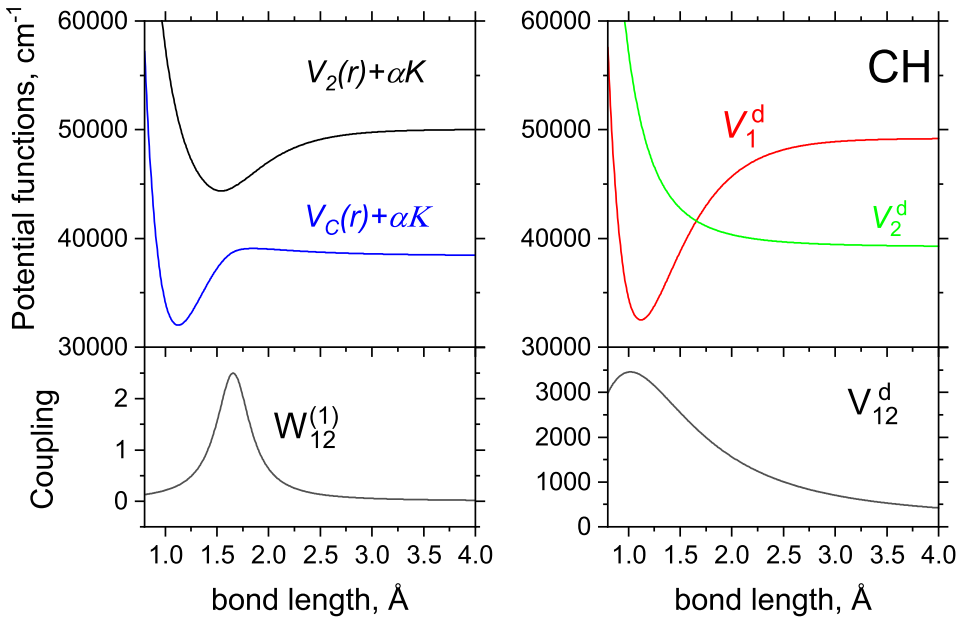

Figure 3.4: Full adiabatic (left) and diabatic (right) models of the $C\,^2\Sigma^+$ and $2\,^2\Sigma^+$ system of CH. The top panels show the PECs, where the adiabatic PECs include the diagonal DDR correction αK, where $\alpha = h/(8\pi^2 c\mu)$. The bottom panels show the corresponding coupling curves, NAC (left) and DC (right).

the adiabatic solution seems harmless for the topology of the corresponding PECs, even this case leads to a spurious $v = 0$ $2\,^2\Sigma^+$ state. Therefore, the conclusion is that every non-adiabatic term should be considered important, unless proven otherwise. The RMSE on the (six comparable) computed rovibronic CH energies for the diabatic approximation A3 is approximately 24 and 13.5 times larger than for adiabatic approximations A2 and A1, respectively. Therefore, molecular systems weakly coupled by a broad NAC with PECs of large energetic separation (consequently large DC) have an adiabatic representation that yields rovibronic energies less sensitive to the DDR terms compared to the corresponding diabatic representation.

The corresponding reduced densities for some lower lying bound states of CH ($C\,^2\Sigma^+$, $J = 0.5$) are shown in Figure 3.5 ($n = 1,2,3$). The low lying vibronic states of $C\,^2\Sigma^+$ are seen to be largely unaffected by the omission of the DDRs or DC since they are energetically well separated from the region of non-adiabatic interaction, in this case occurring near dissociation. However, the reduced densities of the $2\,^2\Sigma^+$ state ($n = 4$) quickly diverge when removing the NAC and/or **K** correction. The $2\,^2\Sigma^+$ state is adiabatically bound and diabatically unbound, where this drastic difference is seen in the reduced densities of Figure 3.5, and corresponds to

energy levels which arise from PECs of very different character. For example, in the diabatic case where the DC is omitted, the $n = 4$ state corresponds to the bound $C^2\Sigma^+(J = 0.5, +, v = 3)$ state whereas in the adiabatic A1 and A2 cases the $n = 4$ bound state corresponds to the bound $C^2\Sigma^+(J = 0.5, +, v = 0)$ state. In the cases where the DDRs and DC are fully accounted for, no fourth bound state exists since the couplings will push it into the quasi-bound region about the adiabatic potential hump of the $C^2\Sigma^+$ state. This quasi-bound nature begins to show itself in the reduced density of the adiabatic case with $\mathbf{K} = 0$ where small oscillations propagating to the right simulation border at 4 Å are seen.

Table 3.4: The rovibronic ($J = 0.5, 1.5$ and 2.5) bound energy term values (cm^{-1}) of the $C^2\Sigma^+$(C) and $2^2\Sigma^+$(2) systems of CH computed using the adiabatic and diabatic representations. The energies are listed relative to the lowest $J = 0.5$ state.

J	e/f	Adiabatic					Diabatic			
		State	v	$\tilde{E}$	$\tilde{E}$(DDRs=0)	$\tilde{E}(K=0)$	State	v	$\tilde{E}$	$\tilde{E}(V_{12}=0)$
0.5	e	C	0	0.00	0.00	0.00	C	0	0.00	0.00
0.5	e	C	1	2450.23	2448.12	2446.42	C	1	2450.23	2524.70
0.5	e	C	2	4617.30	4608.42	4601.48	C	2	4617.30	4822.76
0.5	e	2	0		11191.50	13607.15	C	3		6894.18
0.5	e	2	1		12464.33		C	4		8738.95
0.5	e	2	2		13549.98		C	5		10357.08
0.5	e	2	3		14449.75		C	6		11748.57
0.5	e	2	3				C	7		12913.41
0.5	e	2	3				C	8		13851.60
0.5	e	2	3				C	9		14563.15
0.5	f	2	2	27.83	27.82	27.82	C	6	27.83	28.08
0.5	f	2	3	2476.23	2474.10	2472.39	C	7	2476.23	2551.11
0.5	f	C	0	4641.14	4632.21	4625.24	C	8	4641.14	4847.45
0.5	f	2	1		11205.63	13620.21	C	9		6917.10
0.5	f	2	2		12478.11		C	0		8760.06
0.5	f	2	3		13562.86		C	1		10376.30
0.5	f	2	4		14461.35		C	2		11765.83
0.5	f	2	4				C	3		12928.61
0.5	f	2	4				C	4		13864.61
0.5	f	2	4				C	5		14573.78
				...	...	...	C	5	...	...
RMSE					5.29	9.42				126.45

3.3.4 Continuum solution of CH: photo-absorption spectra

In order to illustrate the equivalence of the continuum solution involving the repulsive $2^2\Sigma^+$ state of CH, we model a photoabsorption spectrum of the $X^2\Pi \rightarrow C^2\Sigma^+/2^2\Sigma^+$transitions, where we follow the recipe from Pezzella et al.[235], Tennyson et al.[236] for this analysis. For the $X^2\Pi$ state, we model its PEC using the Morse function in Eq. (3.1) with the parameters listed in Table 3.2. For the CH transition electric dipole moments $\bar{\mu}_{X,C} = \langle X^2\Pi | \mu | C^2\Sigma^+ \rangle$ and $\bar{\mu}_{X,2} = \langle X^2\Pi | \mu | 2^2\Sigma^+ \rangle$, we adopt the *ab initio* curves computed van Dishoeck[231] with an approximate

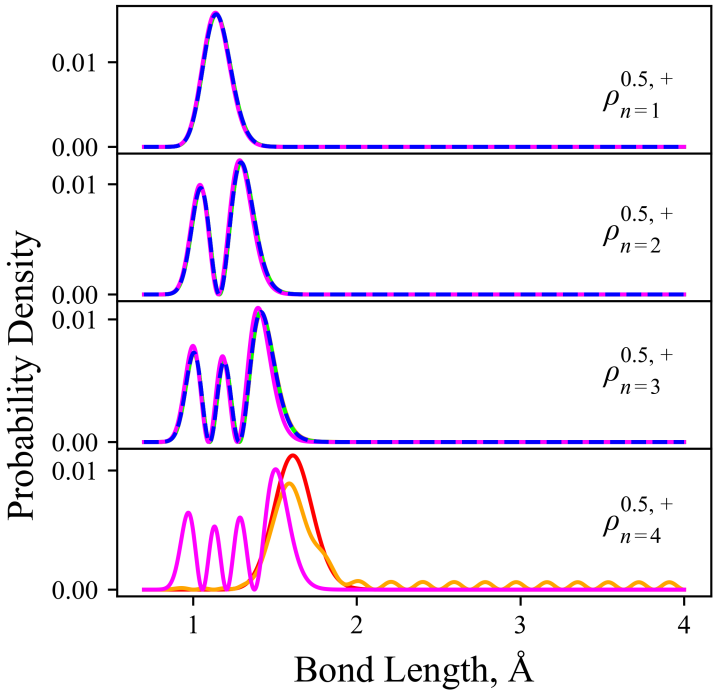

Figure 3.5: CH reduced density states for the lowest four bound rovibronic levels with n being the energy enumerator given by the row number in Table 3.4. Different levels of theory are used to compute these reduced densities and are illustrated: diabatic representation with DC (blue dotted); diabatic model with the DC turned off (magenta, A3); adiabatic representation with both the NAC and $K(r)$ correction included (lime green); adiabatic representation with NAC only (orange, A2); adiabatic representation with no correction (red, A1).

model using the following function

$$\bar{\mu}(r) = (c_0 + c_1\xi_p)(1-\xi_p), \tag{3.11}$$

where ξ_p is the Šurkus[178] variable given by

$$\xi_p = \frac{r^p - r^p_{\text{ref}}}{r^p + r^p_{\text{ref}}}. \tag{3.12}$$

The parameters defining the diabatic transition dipole moment (TDM) functions are listed in Table 3.5. The adiabatic TDM curves are obtained through the unitary AtDT transformation $\mathbf{U}(r)$

$$\bar{\boldsymbol{\mu}}^{\text{a}}(r) = \bar{\boldsymbol{\mu}}^{\text{d}}(r)\mathbf{U}^{\dagger} = (\bar{\mu}^{\text{a}}_1, \bar{\mu}^{\text{a}}_2) = \left(\bar{\mu}^{\text{d}}_1\cos(\beta) - \bar{\mu}^{\text{d}}_2\sin(\beta), \bar{\mu}^{\text{d}}_1\sin(\beta) + \bar{\mu}^{\text{d}}_2\cos(\beta)\right), \tag{3.13}$$

where the mixing-angle $\beta(r)$ is computed from Eq. (3.3) using the CH [$C^2\Sigma^+$, $2^2\Sigma^+$] Lorentzian NAC parameters in Table 3.2, and $\bar{\mu}_1^{\rm d}$, $\bar{\mu}_2^{\rm d}$ are the diabatic TDM curves $\langle X^2\Pi|\,\mu\,|C^2\Sigma^+\rangle$ and $\langle X^2\Pi|\,\mu\,|2^2\Sigma^+\rangle$, respectively. The full photodissociation system, in both the adiabatic and diabatic representations, is illustrated in Figure 3.6.

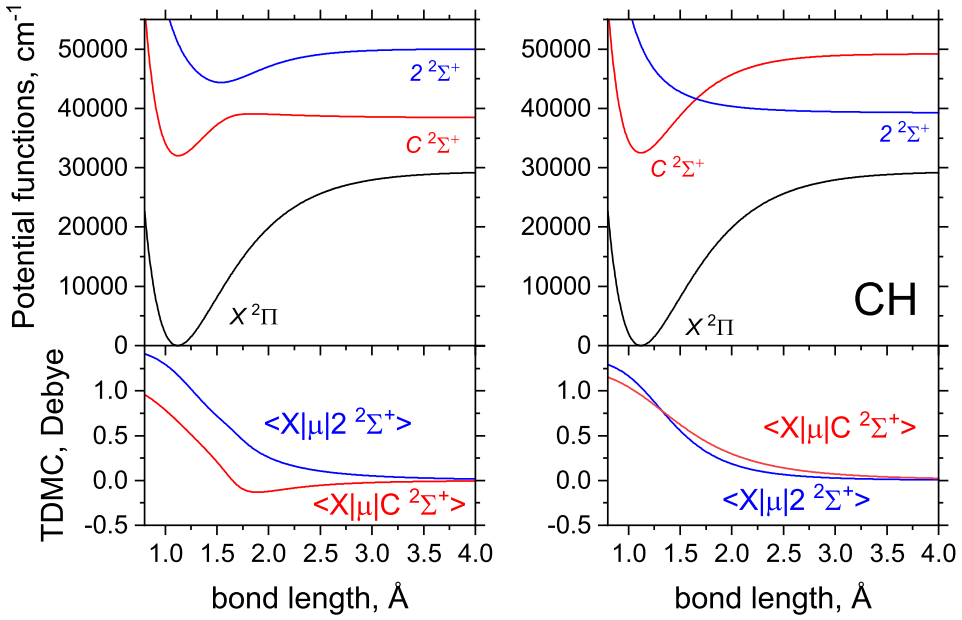

Figure 3.6: Adiabatic (left) and diabatic (right) models of the photo-absorption system of $X^2\Pi \rightarrow C^2\Sigma^+/2^2\Sigma^+$ of CH. The top panels show the PECs, adiabatic and diabatic, while the bottom panels show the corresponding transition dipole moment curves.

Table 3.5: The molecular parameters defining the CH diabatic transition dipole moment functions

Parameter	$\langle X^2\Pi\|\,\mu\,\|C^2\Sigma^+\rangle$	$\langle X^2\Pi\|\,\mu\,\|2^2\Sigma^+\rangle$
$r_{\rm ref}$, Å	1.4	1.27
p	4	5
c_0, Debye	0.71	0.85
c_1, Debye	0.09	0.17

Figure 3.7 illustrates the Duo computed photoabsorption spectrum of CH simulated at $T = 300$ K using the continuum solution of the coupled adiabatic and diabatic [$C^2\Sigma^+$, $2^2\Sigma^+$] system from the bound states of $X^2\Pi$. The continuum solution used a simulation box size 60 Å and 1600 sinc-DVR points to sample as many unbound states as possible in the Frank-Condon region of the ground state. For the cross sections, a Gaussian line profile of the half-width-at-half-maximum (HWHM)

equal to 50 cm^{-1} was used to redistribute the absorption intensities between the 'discrete' lines representing photo-absorption continuum (see Pezzella et al.[235] for details). The diabatic and adiabatic continuum wavefunctions are obtained identical, so the photo-absorption spectra in Figure 3.7 are indistinguishable. Figure 3.7 also illustrates effects of the non-adiabatic approximations on the photoabsorption spectra of CH. Removing the diagonal DDR ($K = 0$) results in a shift of the band by about -50 cm^{-1}, which can be understood since this DBOC term introduces a small barier at the avoided crossing which will shift energy levels. By contrast, setting both DDRs to zero leads to a significant drop of the absorption by a factor of ~ 4. This could be understood for multiple reasons. Firstly the wavefunction overlap will be different and will contribute to the observed intensity difference, where NACs mix the two state wavefunctions. To further illustrate the CH continuum system, Figure 3.8 illustrates exactly the reduced densities of one of the continuum states used in the photo-absorption simulations which are seen to be very different for the different approximations considered. Consequently, TDMs will become mixed through the intensity stealing mechanism, illustrative in the diabatic picture. The diabatic $\langle X^2\Pi | \mu | C^2\Sigma^+ \rangle$ TDM is ~ 2 times larger than the corresponding adiabatic TDM in the vertical region of the ground state, meaning a difference of approximately 4 times in the intensity which depends on the dipole moment squared. If the DC term from the diabatic model is removed, the bound absorption is observed to dominate in the Franck-Condon region (see Figure 3.6) and the photo-absorption contribution drops by two orders of magnitude and is therefore not visible on this scale.

3.4 Convergence

Since Duo uses a solution of the $J = 0$ uncoupled vibrational Schrödinger equation to form its vibrational basis set functions $\chi_v(r)$, it should be expected they should differ significantly whether the adiabatic or diabatic representation is used due to the PECs having different character. Therefore, one can also expect that the eigensolution convergence will be impacted by the choice of the representation.

The convergence of the $J = 0.5$ energy levels of the simplified YO and CH models are tested in the diabatic and adiabatic representations where all non-adiabatic effects encountered. Figure 3.9 illustrates the convergence of the lowest 20 $J = 0.5$ energies of YO and the $n = 5$ state of CH ($C^2\Sigma^+(J = 0.5, \pm)$). Illustrated is the difference of the i-th energy level $\tilde{E}_i$ to its converged value $\tilde{E}_i^{\text{cvg}}$ plotted as a function of vibrational basis size. The two systems show contrasting results. The diabatically computed YO ($D^2\Sigma^+$) energies converge very quickly for a smaller ba-

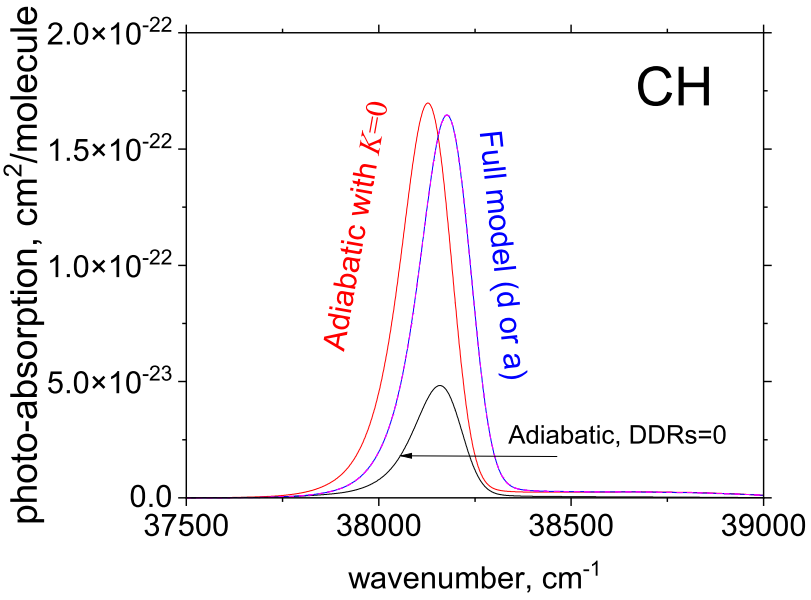

Figure 3.7: Photo-absorption spectra of CH at $T = 300$ K. The fully coupled adiabatic and diabatic calculations are shown with the blue line; the NAC=0 case is shown with the red line and the black line shows spectrum with all DDRs set to zero.

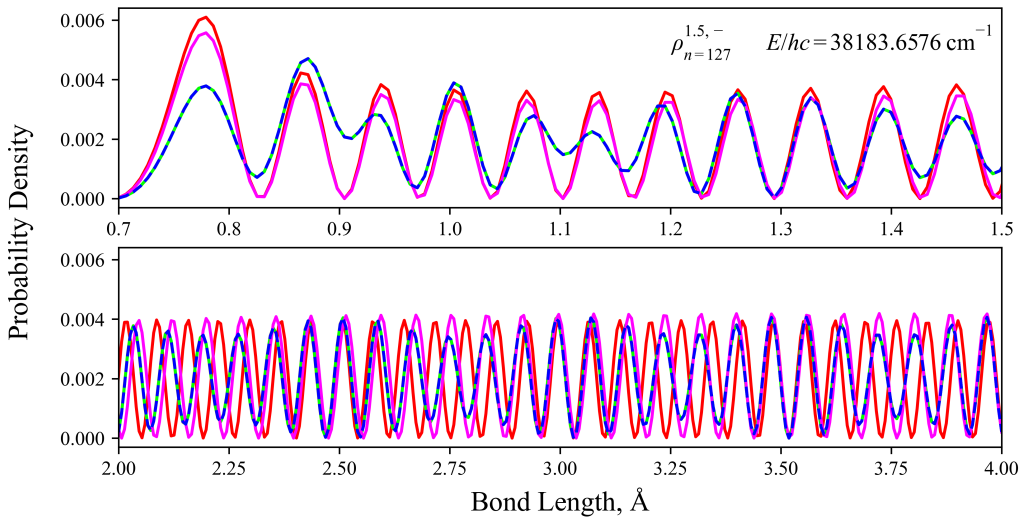

Figure 3.8: Reduced density of the continuum state corresponding to an energy of $hc \cdot 38183.6576\ \mathrm{cm}^{-1}$. Its transition with the $X\,^3\Sigma^-(J = 1.5, f, v = 0)$ state is positioned at the peak in the spectra of Figure (3.7). The reduced density state is illustrated and computed using different levels of theory: diabatic representation with DC (blue dotted); diabatic model with the DC turned off (magenta, A3); adiabatic representation with both the NAC and K correction included (lime green); adiabatic representation with NAC only (orange, A2); adiabatic representation with no correction (red, A1).

sis size of ~ 25 compared to the adiabatic representation where a much larger basis set of ~ 250 is required to achieve convergence. This is interesting since YO is a strongly NAC coupled system, where its diabatic representation, given its small DC, is a significantly more efficient representation of the nuclear dynamics for this system. For CH ($C^2\Sigma^+$) the adiabatic energies initially converge faster but the diabatic energies eventually converge to within 10^{-6} cm^{-1} for a basis size of ~ 25 as opposed to ~ 42 for the adiabatic energies.

Repeated tests on the adiabatic and diabatic vibrational energy convergence rates for numerous J levels were conducted, yielding the same conclusions as above for the $J = 0.5$ case for rotationally excited rovibronic levels.

This shows that there is not one representation that rules over the other, it depends on the character of the avoided crossing, specifically in its position, the shape of the potentials approaching the crossing, and the separation of the adiabatic PECs. It is therefore important to consider the system of study before choosing a representation, where all corrections must be included.

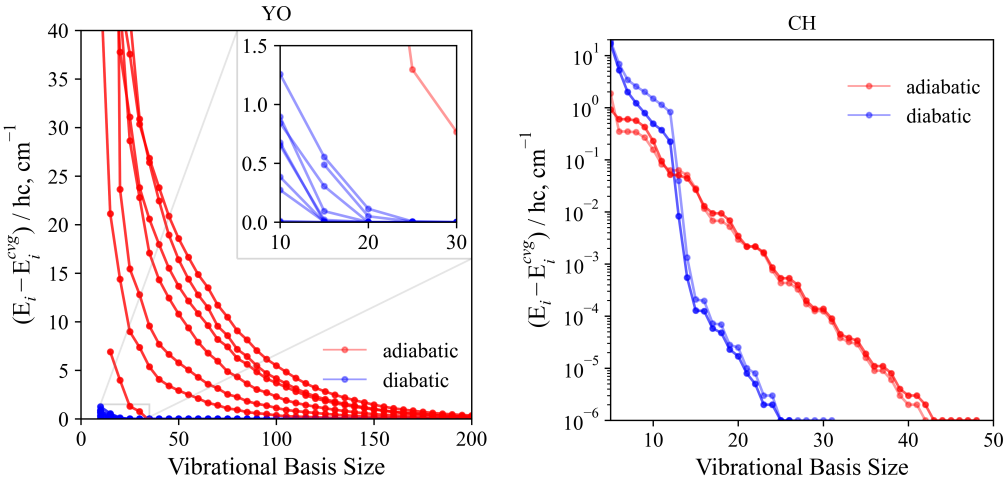

Figure 3.9: Convergence of the lowest 20 vibrational $J = 0$ energies of the $D^2\Sigma^+$ state of YO (left) and the C $^2\Sigma^+(v = 0, e/f)$ state of CH (right) are plotted, where the difference of the i-th vibrational level E_i to its converged value E_i^{cvg} is plotted as a function of vibrational basis size. A constant grid size of G$= 3001, 4001$ points for the sinc-DVR basis set was used for the YO and CH states, respectively. The diabatically computed energies for YO are observeed to converge much faster than the adiabatic ones, whereas for CH the opposite is true.

3.5 Numerical Equivalence for the General N-State Problem

So far in this chapter the two-state coupled diatomic system has been considered, where equivalence between the adiabatic and diabatic representations was shown for nuclear motion calculations as facilitated by the Duo code. I now extend our non-adiabatic treatment to any number of coupled electronic states and demonstrate that an exact AtDT can be determined, where the adiabatic and diabatic representations are shown to be rovibronically equivalent. The general N-state problem, and generation of the AtDT, is discussed rigorously in Section 2.5. The main challenges are now in the computation of a numerically exact AtDT which can remove all DDR couplings such that a strict diabatic representation which is rovibronically equivalent to the adiabatic representation can be made. Secondly, the obtained AtDT may not yield physical diabatic property curves, and so a regularising correction to the NACs is identified and computed using the HyAP method as described in Section 2.6.4.

The following sections of this chapter demonstrate, for the first time, numerical equivalency between the adiabatic and diabatic representations for multi-electronic-state coupled systems of diatomic molecules. Equivalency is demonstrated by direct application to the 3-state N_2 system, the 4-state CH system, and an artificially generated 10-state system with its PECs illustrated in figure 3.10. A regularising correction to the NACs of these systems is found such that the resulting diabatic property curves are physical, practical, converge to desirable asymptotic limits, and the spectroscopic model is made to be internally consistent. The importance of non-adiabatic coupling in these highly correlated systems are then investigated, where correct description of the complex non-adiabatic interactions and potential manifolds of these molecules will be valuable to many fields (see Section 3.1 for example uses). It is usually seen that highly excited electronic states of simple diatomics exhibit complex non-adiabatic behaviour and complex electronic structure[237], making the understanding of many coupled state systems and their interactions important. For example, molecules like C_2, CN, N_2 ($^3\Pi_u$, $^1\Sigma_g^+$ symmetry manifolds), SiC, Si_2, O_2, NO and their corresponding ions[238,239,237] exhibit these effects which motivates my work. Numerical equivalency will be first demonstrated on the extreme 10-state synthetic system, followed by an investigation of the impact of DDR terms in nuclear motion calculations for physical spectroscopic models of real molecular systems with fewer interacting states. Finally, the synthetic 10-state system is revisited to explore the effect of truncating the number of adiabatic states on the

computed rovibronic energy levels. The HyAP method is also applied to the system of study, where the effect of NAC regularisation on the computed rovibronic energy terms is investigated for the N_2 system.

The selection of CH and N_2 for construction of model 4-state and 3-state benchmarks is motivated by the contrasting extremes of their nonadiabatic behaviour. N_2 is characterised by strong, sharp NACs and avoided crossings between clearly bound PECs near their potential minima. In contrast, CH exhibits weak, wide NACs and broad avoided crossings near dissociation. Thus, I do not aim to provide empirically accurate data for these specific molecules, but use them as representative systems for numerical equivalence tests of non-adiabatic effects in diatomic molecules.

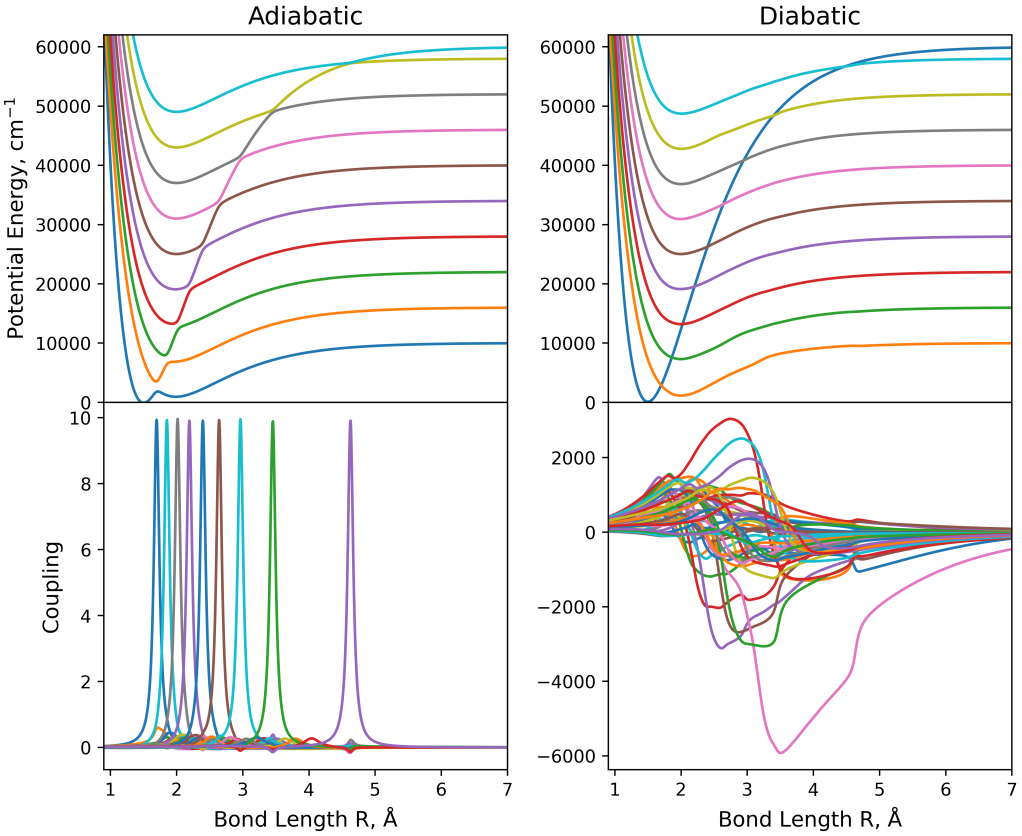

Figure 3.10: Illustration of the diabatisation of synthetic 10-state coupled system: Adiabatic PECs (top left), NACs (bottom left; regularised via the HyAP method), diabatic PECs (top right), and DCs (bottom right).

3.6 *N*-State Spectroscopic Models

It was shown that NACs are well described by a Lorentzian profile near the avoided crossing [170,171,165,166]. However, more flexibility is required in general. All NACs

in the following sections are modeled using a linear combination of a Lorentzian and a Gaussian distribution of equal width γ, peak position r_0, and amplitude N, giving a pseudo-Voigt profile[240,241] via

$$f(r) = mL(r;r_0,\gamma,N) + (1-m)G(r;r_0,\gamma,N) + \sum_i L(r;r_{0,i},\gamma_i,N_i), \tag{3.14}$$

where L is the Lorentzian function given by

$$L(r;r_0,\gamma,N) = \frac{N}{2}\frac{\gamma}{\gamma^2+(r-r_0)^2}, \tag{3.15}$$

and G is the Gaussian distribution given by

$$G(r;r_0,\gamma,N) = \frac{N}{2\gamma}\exp\left[-\ln(2)\left(\frac{r-r_0}{\gamma}\right)^2\right]. \tag{3.16}$$

The fraction of Lorentzian and Gaussian character contributing to $f(r)$ of Eq.(3.14) is controlled by the constant parameter m. For $m=1$, $f(r)$ reduces to a pure Lorentzian, and for $m=0$ a pure Gaussian. The summation of Lorentzian functions in Eq.(3.14) are used to model additional (perturbative) sharp peaks which are typically seen to be of lower magnitude to the rest of the profile. The width parameter γ is then modeled to vary sigmoidally to introduce skewness into the final profile[240,241] via

$$\gamma(r;\gamma_0,a,r_0) = \frac{2\gamma_0}{(1+e^{a(r-r_0)})}, \tag{3.17}$$

where γ_0 is a reference width and a is a skewness parameter when equal to zero ensures $\gamma=\gamma_0$.

All adiabatic potentials will be defined as a grid of points, to which the resulting diabatic PECs and DCs will be computed on the same grid of internuclear separations. The generation of the diabatic spectroscopic models will require a regularising correction to be computed for the NACs in question, such that the spectroscopic models are internally consistent (with desired properties discussed in Sections 2.5.2, 2.6.4, 2.7) and an AtDT which satisfies the physical boundary conditions discussed in Section 2.7 is constructed.

3.6.1 The N_2 Spectroscopic Model

Molecular nitrogen has been shown by numerous works to have complex electronic structure[227–229], of interest are the avoided crossings between the strongly coupled

Table 3.6: Function parameters of Eq.(3.14) for the NACs between the $1\,^1\Sigma_g^+$, $2\,^1\Sigma_g^+$, and $3\,^1\Sigma_g^+$ states of N_2.

	r_0 (Å)	γ (Å)	N	a	m	$r_{0,i}$ (Å)	γ_i (Å)	N_i
$\langle 1\,^1\Sigma_g^+ \vert \frac{d}{dr} \vert 2\,^1\Sigma_g^+ \rangle$	1.2272	0.0147	1.0273	0.0000	1.0000			
$\langle 2\,^1\Sigma_g^+ \vert \frac{d}{dr} \vert 3\,^1\Sigma_g^+ \rangle$	1.1151	0.0273	-1.0111	-11.8152	0.3927			
$\langle 1\,^1\Sigma_g^+ \vert \frac{d}{dr} \vert 3\,^1\Sigma_g^+ \rangle$	1.3073	0.2178	0.1629	-18.7122	-0.5968	0.0150	0.0300	0.0150
						1.097	1.0300	1.1400
						0.0065	0.013	0.0035

Table 3.7: Morphing parameters for the position dependent width parameters γ_{ij} of the switching functions in construction of the regularised N_2 AtDT solution ((see Eqns.(4.21, 2.77,2.76))). All functions have $\beta_2 = 0.1$, $\beta_4 = 0.02$, and $p = 4$.

	r_{ref} (Å)	γ_{ref} (Å)	B_0	B_1	B_2
γ_{12}	1.2130	7.9860	9.7618	-0.0691	-0.3258
γ_{13}	1.2391	5.3487	0.0589	-2.3842	0.3663
γ_{23}	1.2158	5.2183	1.1768	1.1938	1.8434

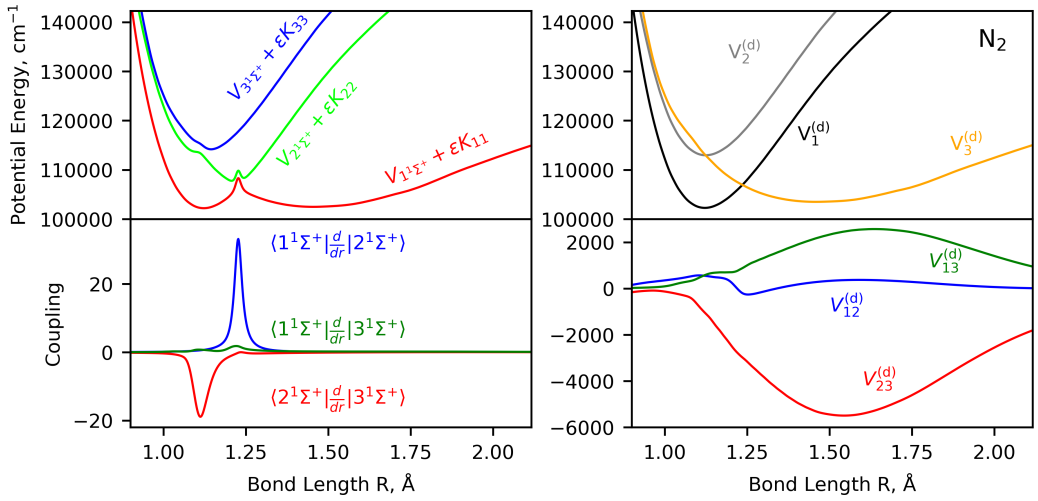

Figure 3.11: Illustration of the diabatisation of the N_2 [$1\,^1\Sigma_g^+$, $2\,^1\Sigma_g^+$, $3\,^1\Sigma_g^+$] system: Adiabatic PECs (top left), NACs (bottom left), diabatic PECs (top right), and DCs (bottom right). The DBOC corrections have been added to the adiabatic potentials, and are computed from multiplying the kinetic energy factor $\varepsilon = \frac{\hbar}{8\pi^2\mu c}$ by the diagonal elements of the **K** matrix.

$[1\,^1\Sigma_g^+, 2\,^1\Sigma_g^+, 3\,^1\Sigma_g^+]$ electronic states, characterised by bound PECs illustrated in Figure 3.11. The PECs and NACs for the $[1\,^1\Sigma_g^+, 2\,^1\Sigma_g^+, 3\,^1\Sigma_g^+]$ system studied here were taken from Gelfand et al.[227], where *ab initio* calculations were performed using MOLPRO at the MRCI/aug-cc-pVQZ level of theory, with orbitals optimised in preceding CASSCF calculations.

Upon inspection of the *ab initio* $2\,^1\Sigma_g^+$ and $3\,^1\Sigma_g^+$ PECs, the presented calculations omit interaction with higher energy states causing an avoided crossing in these PECs at $\sim 1.43 \times 10^5$ cm^{-1}. Therefore, the $2\,^1\Sigma_g^+$ and $3\,^1\Sigma_g^+$ PECs were extended smoothly to an energetically higher dissociation limit to effectively ignore interactions to the unresolved states. This extension is feasible since this interaction region is energetically well separated from the $[1\,^1\Sigma_g^+, 2\,^1\Sigma_g^+, 3\,^1\Sigma_g^+]$ avoided crossing system of interest here. Since the extension of the PECs were made arbitrarily, this introduces a source of inconsistency between the NACs obtained *ab initio* and the modified adiabatic potentials. This is not a problem, instead it then allows an interesting test on the HyAP NAC regularisation procedure, and is discussed later.

The NACs coupling the $[1\,^1\Sigma_g^+, 2\,^1\Sigma_g^+, 3\,^1\Sigma_g^+]$ states of N_2 are fitted to the *ab initio* curves of Gelfand et al.[227] using the pseudo-Voigt function of Eq.(3.14), and are illustrated in Figure 3.14. The fitted parameters are given in table 3.6. Only the $\langle 1\,^1\Sigma_g^+ | \frac{d}{dr} | 3\,^1\Sigma_g^+ \rangle$ (outer) NAC required additional perturbation by additional Lorentzian functions, creating a jagged pattern towards shorter bond lengths relative to the global peak of the distribution. This introduces significantly more mixing angle about the $[1\,^1\Sigma_g^+, 3\,^1\Sigma_g^+]$ axis towards shorter bond length as opposed to omitting the perturbation. I am not concerned about accuracy of the fit here since any inconsistencies will add a valuable metric to test the HyAP method.

With the adiabatic spectroscopic model of the N_2 $[1\,^1\Sigma_g^+, 2\,^1\Sigma_g^+, 3\,^1\Sigma_g^+]$ system defined, the AtDT and regularising NAC corrections are then computed via the HyAP method (see details in Section 2.6.1). Figure 3.12 illustrates the generator elements associated with the forward and backward evolved AtDT which are notably different, and therefore yield markedly different diabatisations. Overlaid are their linear combination which smoothly connects the forward and backward evolved AtDT solutions – satisfying the imposed short and long range boundary conditions while maximising the smoothness of the diabatic potential matrix with respect to the nuclear geometry. The linear combination is computed via Eq.(2.76), where the fitted switching functions are plotted in the bottom panel of Figure 3.12 and their optimised parameters given in Table 3.7. It is clear that the switching functions acting on the three generator elements are not necessarily similar. For example, the β_{12} switching function is a near pure sigmoid whereas a severely modified sigmoid is

optimised for the β_{13} element. The flexibility of the morphing function in Eq.(4.21) allows a unique morphology to be achieved, and is desirable for this problem since the exact shape of the switching function to maximise diabatic smoothness is not known *a priori* to the optimisation.

Figure 3.11 illustrates the diabatisation of the adiabatic N_2 spectroscopic model, where the DBOCs ($\varepsilon = \frac{\hbar}{8\pi^2\mu c}\mathbf{K}$) have been added to the adiabatic PECs (top left panel). The DBOCs are seen to introduce a significant potential barrier at the avoided crossing of the order $10^2 - 10^3$ cm^{-1}, therefore one should expect the DDR terms to be significant for the consistency and completeness of the model. This 3-state N_2 system is reminiscent of the 2-state YO system encountered earlier in this chapter. From the analysis on YO (and CH), it is clear that all DDR coupling terms are extremely important for the spectroscopic model and rovibronic calculations, neglecting these terms were shown to introduce gross errors into the accuracy of not only rovibronic energies but also their wavefunctions which will be relevant here for the 3-state case. Figure 3.11 also illustrates the three DCs coupling the N_2 [$1\,^1\Sigma_g^+$, $2\,^1\Sigma_g^+$, $3\,^1\Sigma_g^+$] states, which are seen to be simple, smooth functions of bond length with the exception at around the avoided crossing, where complex topology ensues. The DCs then tend towards 0 cm^{-1} towards both short and long range limits. The three diabatic PECs are simpler and smoother than their adiabatic counterparts, closely resembling a morse-oscillator function which showcases the advantages of the diabatic representation, where modelling is simpler.

3.6.1.1 The N_2 AtDT and Regularising Correction

Figure 3.13 illustrates the regularising corrections computed for the three NACs connecting N_2 [$1\,^1\Sigma_g^+$, $2\,^1\Sigma_g^+$, $3\,^1\Sigma_g^+$] using the HyAP method described in Section 2.6.4. The top panels compare the original (blue) and regularised (red) NACs, revealing complex differences in the spectroscopically important range of 0.7–3.0 Å. The bottom panels illustrate their difference, which corresponds to the regularising corrections applied to the NACs such that the diabatic PECs are made smooth. These corrections exhibit a non-standard dependence on nuclear geometry, as they are uniquely tailored to the adiabatic system in question, in this case ensuring consistency with the adiabatic PECs.

The magnitude of the regularising corrections are small relative to the associated NAC, which indicates the N_2 model to be nearly complete and internally consistent. An exception is for the $W_{13}^{(1)}$ NAC, which has a correction of a similar order of magnitude. However, this does not pose a significant issue due to the inherently low magnitude of $W_{13}^{(1)}$. Interestingly, a common bump is present in all regularis-

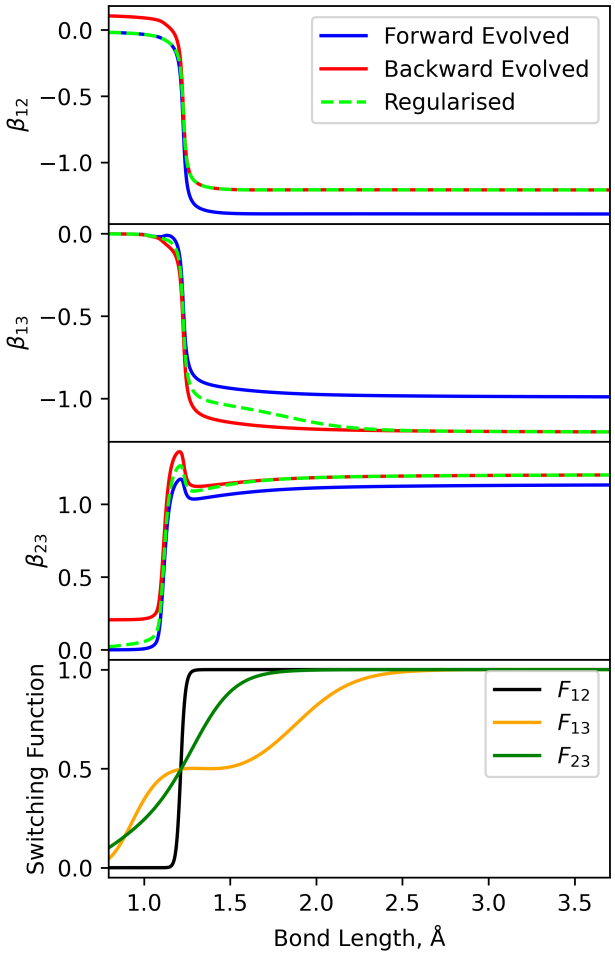

Figure 3.12: The matrix elements of the generator matrices for the forward- (blue) and backward- (red) evolved solutions for the N_2 AtDT can be seen in the top three panels. The regularised generator matrix (green dashed) is computed via Eq.(2.76) using the switching functions in the bottom panel. The switching functions have been optimised to maximise the smoothness of the diabatic potential matrix via minimisation of Eq.(2.81).

ing corrections at ~ 2 Å. This feature coincides with the region where the upper two adiabatic PECs have been manually extended to a higher dissociation, showing the method is reactive to such inconsistencies. This behaviour was not necessarily expected, however, the fact that the regularisation responds to the PEC extension confirms the close mutual consistency between the NACs and other molecular properties. Importantly, such consistency has been shown to be exploitable outside of not only the evolution solver, but also outside of *ab initio* calculations.

The AtDT that removes all radial DDR coupling has been determined for the N_2 $[1\,^1\Sigma_g^+, 2\,^1\Sigma_g^+, 3\,^1\Sigma_g^+]$ system, and therefore results in a strict diabatic representation of its spectroscopic model being found. The AtDT is illustrated in the top panel

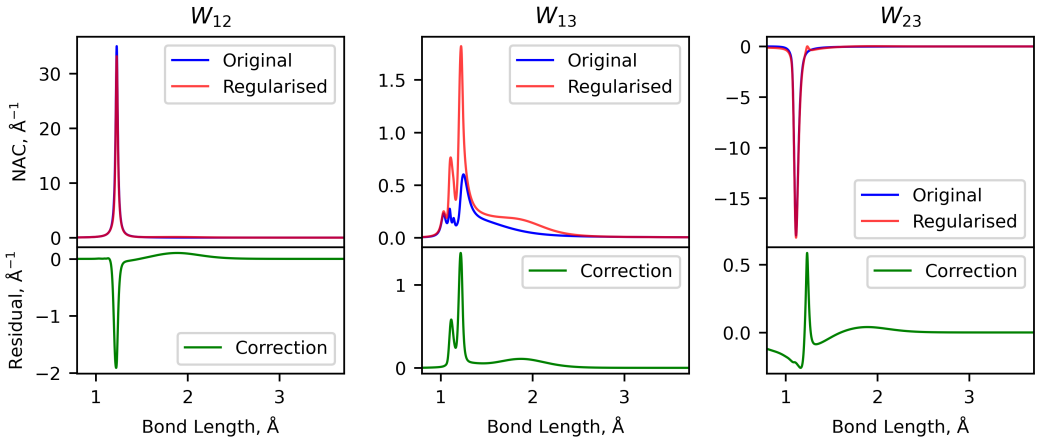

Figure 3.13: The original N_2 NACs (blue) are superimposed with the regularised NACs (red) found via the asymptotic-property-based-diabatisation method. The bottom panels show their difference as a function of bond length and corresponds to the regularising correction to the NACs.

of Figure 3.14 in an axis-angle representation, where solid lines depict the vector elements of the diabatising axis of rotation in the adiabatic basis. For example, $\mathscr{R}_{23}$ represents the axis in configuration space aligned with state 1 ($1\,^1\Sigma_g^+$). The black dashed line corresponds to the global mixing angle about the diabatisation axis. It is clear for this three-state system that the axis of rotation in Figure 3.14 varies with bond length. For the two-state problem, however, the AtDT is exactly solvable as the diabatising axis of rotation remains constant, and is the crux of the problem when extending to N-state systems (see Section 2.6). At short bond lengths, before the avoided crossing region, the global mixing angle begins at $\theta_{\text{global}} = 0^\circ$ indicating that there is no mixing between the electronic states. The mixing angle then evolves to $\theta_{\text{global}} = 120^\circ$ after the avoided crossings towards large stretches, consistent with a cyclic permutation of the three adiabatic eigenvectors. The solid curves in Figure 3.14 are color-coded to show the contributions of adiabatic basis vectors to the diabatic basis: red represents contribution by $|1\,^1\Sigma_g^+\rangle$, green by $|2\,^1\Sigma_g^+\rangle$, and blue by $|3\,^1\Sigma_g^+\rangle$. This visualization confirms that the diabatising transformation at the right boundary corresponds to a cyclic permutation and reflection, where some basis vectors acquire a phase of -1. The observed state transitions are from $r = 0 \to \infty$ are $1^+ \to 3^-$, $3^+ \to 2^+$, and $2^+ \to 1^-$, where the superscripts denote the phase of the eigenvector.

The bottom panel of Figure 3.14 illustrates the residual kinetic energy matrix computed via Eqs.(2.72, 2.83) after transformation of the AtDT, quantifying the accuracy of the solved N_2 AtDT. The residuals were computed using regularised

NACs and the AtDT determined by the HyAP method as input – which by construction exactly satisfies Eq.(2.49) – and demonstrates that all DDR couplings are removed completely to within $\sim 10^{-12}$ cm^{-1}. Tests on the accuracy of the evolution method itself have been made by computing the residual kinetic energy when substituting instead the original NACs and an evolved AtDT matrix into Eqs.(2.72, 2.83). The tests revealed that using the inverse transform sampling method presented in Section A.2 in conjunction with 50000 points yields the same accuracy as the exact approach detailed above. Thus, with a sensible grid, a numerically exact solution for the evolution of the AtDT is achievable. However, tests show that the accuracy of the computed NAC integral in Eq.(2.67) is the leading contribution to the error in the solved AtDT. Thus, use of methods with higher accuracy than the trapezium rule, or even analytical methods depending on the NAC functional forms, will yield an instant accuracy increase for prototypical evolution solutions.

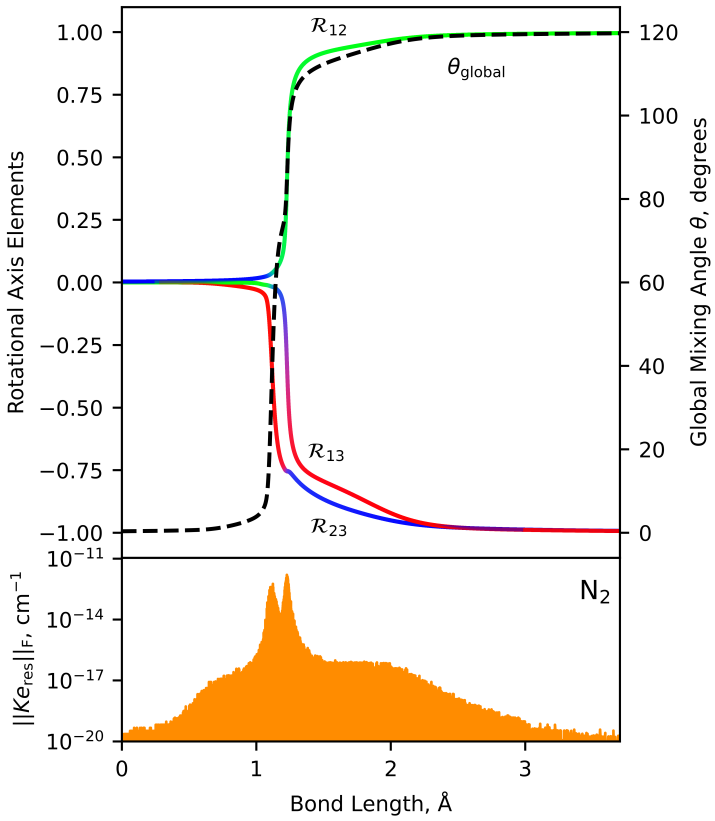

Figure 3.14: The AtDT for the N_2 [$1\,^1\Sigma_g^+$, $2\,^1\Sigma_g^+$, $3\,^1\Sigma_g^+$] 3-state system is illustrated in axis-angle representation (top panel), where the colored lines (see text for details) are the global rotation axis elements and the dotted line is the global mixing angle about the diabatising axis. The bottom panel shows the residual kinetic energy coupling after diabatisation via the Frobenius norm of the transformed adiabatic kinetic energy in Eqs.(2.72, 2.83).

Table 3.8: Function parameters of Eq.(3.14) for the NACs between the [$C^2\Sigma^+$, $2^2\Sigma^+$, $3^2\Sigma^+$, $4^2\Sigma^+$] states of CH. No perturbative Lorentzian's were used in the modelled NACs.

	r_0 (Å)	γ (Å)	N	a	m
$\langle C^2\Sigma^+\|\frac{d}{dr}\|2^2\Sigma^+\rangle$	1.6998	0.3114	0.9844	-2.1145	1
$\langle C^2\Sigma^+\|\frac{d}{dr}\|3^2\Sigma^+\rangle$	1.4283	0.3768	0.3033	-0.9984	0
$\langle C^2\Sigma^+\|\frac{d}{dr}\|4^2\Sigma^+\rangle$	1.8500	0.1900	-0.0500	-19.0000	1
$\langle 2^2\Sigma^+\|\frac{d}{dr}\|3^2\Sigma^+\rangle$	1.3384	0.2714	0.8468	-0.6660	1
$\langle 2^2\Sigma^+\|\frac{d}{dr}\|4^2\Sigma^+\rangle$	1.6450	0.2120	0.1775	1.1454	1
$\langle 3^2\Sigma^+\|\frac{d}{dr}\|4^2\Sigma^+\rangle$	2.0058	0.2051	0.8049	-0.6020	1

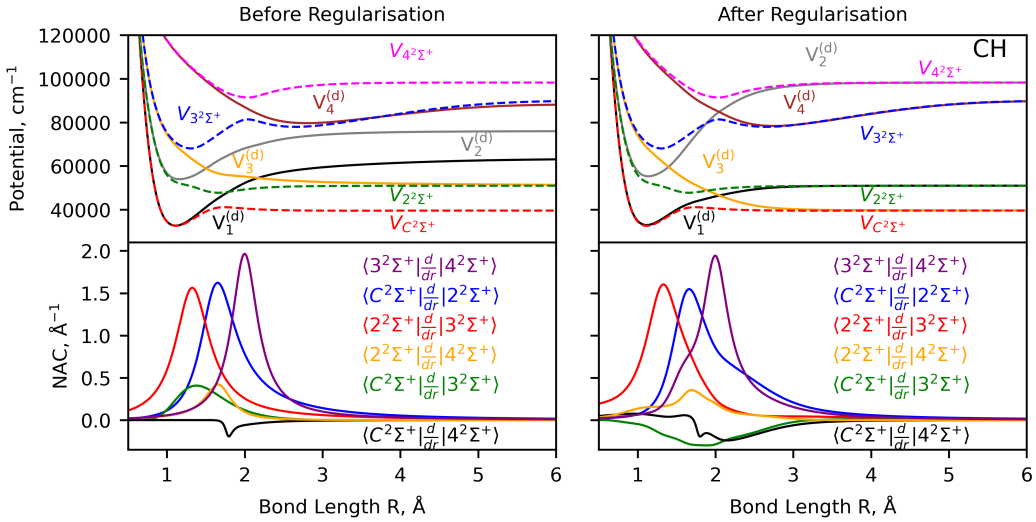

Figure 3.15: Illustration of the NAC regularisation on the subsequent diabatisation. The dashed lines plot the adiabatic potentials, where the diabatic PECs are plotted as solid lines in the top panels. The left panels depict the original, unregularised, NACs (bottom) and the resulting diabatic PECs, which are seen to correlate to different dissociation asymptotes. The right panels depict the regularised NACs (bottom) and the resulting diabatic PECs which are seen to be clearly bound or repulsive and correlate to the adiabatic asymptotes.

3.6.2 The CH Spectroscopic Model

The excited electronic states of CH has been studied *ab initio* by van Dishoeck [231] who show the $^2\Sigma^+$ manifold to exhibit multiple avoided crossings. The diabatisation of the two-state CH [$C^2\Sigma^+$, $2^2\Sigma^+$] system was studied earlier in this chapter, where the analysis of the different DDR coupling terms was based on our recent publication [38]. I now aim to extend our treatment to instead the lowest four $^2\Sigma^+$ electronic states [$C^2\Sigma^+$, $2^2\Sigma^+$, $3^2\Sigma^+$, $4^2\Sigma^+$]. To do this, I performed *ab initio* calculations for six NACs at the CASSCF level of theory using the weighted aug-cc-pwCVQZ basis sets via the MOLPRO quantum chemistry package [242]. Subse-

quently, the CH [$C\,^2\Sigma^+$, $2\,^2\Sigma^+$, $3\,^2\Sigma^+$, $4\,^2\Sigma^+$] potential energies were computed via the MRCI method using molecular orbitals optimised on the prior CASSCF calculations. The aug-cc-pwCVQZ basis set was chosen after confirming convergence in the computed potentials, lowering state energies in accordance with the variational principle.

To simplify the analysis, the PEC of the $4\,^2\Sigma^+$ state was modified to omit unresolved avoided crossings with higher-energy states at $r = 1.870$ Å and $r = 3.375$ Å. This adjustment was made to preserve the *ab initio* topology around the avoided crossing with the $3\,^2\Sigma^+$ state at $r = 1.95$ Å. The global description of the *ab initio* PEC for the $4\,^2\Sigma^+$ state, identified as $I^2\Sigma^+$, has been made by Kalemos et al.[243]. These modifications render the $4\,^2\Sigma^+$ PEC quasi-diabatic, ensuring it provides a practical diabatisation framework for this study while introducing controlled inconsistencies into the CH spectroscopic model which I aim to correct through the HyAP regularisation procedure. The $4\,^2\Sigma^+$ PEC was further extended smoothly to the C(^{1}P) + H dissociation limit and to shorter bond lengths using guidance from CASSCF calculations. Non-physical behaviour observed in the $\langle C\,^2\Sigma^+|\,\frac{d}{dr}\,|4\,^2\Sigma^+\rangle$ NAC near the region of non-convergence in the $4\,^2\Sigma^+$ PEC was modelled to replicate the *ab initio* character in the well-converged region and taper off to zero beyond this. This modification serves as a useful test for the regularisation method, and so its accuracy is not a concern at this stage. The $C\,^2\Sigma^+$, $2\,^2\Sigma^+$, and $3\,^2\Sigma^+$ states were also extrapolated for bond lengths ranging from $r = 0.5$ Å to $r = 1$ Å, as *ab initio* calculations of their PECs did not converge in this region.

Table 3.8 lists the fitted parameters of the asymmetric Lorentzian-Gaussian mixture in Eq.(3.14) to the *ab initio* calculations. The sources of inconsistency between the NACs and adiabatic PECs for the studied CH system will be from convergence issues in the corresponding MRCI calculations, the aforementioned modifications to the property curves, and incompleteness of the model (ignoring unresolved upper electronic states; truncation of the Born-Huang expansion of the wavefunction) which the proposed HyAP regularisation method aims to address through construction of a practical and physical diabatic representation.

3.6.2.1 The CH AtDT and Regularising Correction

With the adiabatic CH [$C\,^2\Sigma^+$, $2\,^2\Sigma^+$, $3\,^2\Sigma^+$, $4\,^2\Sigma^+$] spectroscopic model defined, the AtDT for this 4-state system is computed using the HyAP method detailed in Section 2.6.1 (for more details see the application to N_2 in Section 3.6.1). The residual kinetic energy coupling in the corresponding diabatic representation is computed via Eqs.(2.72, 2.83), resulting in a maximum error of 10^{-14} cm^{-1}– practically

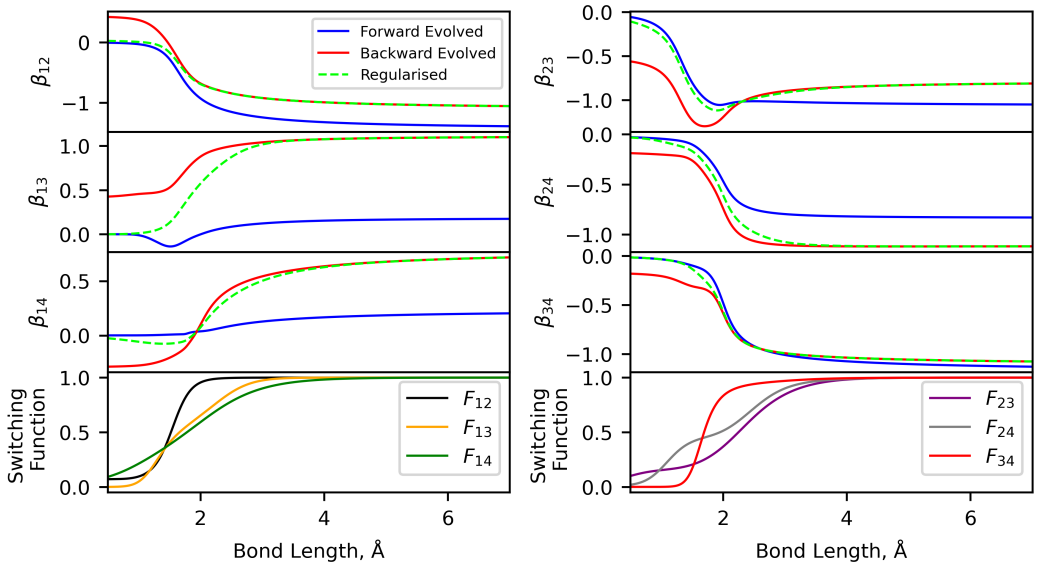

Figure 3.16: The matrix elements of the generator matrices for the forward- (blue) and backward- (red) evolved solutions for the CH AtDT can be seen in the top three panel rows. The regularised generator matrix (green dashed) is computed via Eq.(2.76) using the switching functions in the bottom panel. The switching functions have been optimised to maximise the smoothness of the diabatic potential matrix via minimisation of Eq.(2.81).

zero. Regularising corrections to the CH NACs were then computed by maximising the smoothness of the diabatic potential energy topology, and are shown in the bottom panels of Figure 3.15 as the differences between the original and corrected NACs (left and right panels). The generator matrix elements for the forward- and backward- evolved AtDTs are plotted as a function of bond length in Figure 3.16, exhibiting significant discrepancies. The largest deviations occur in the generator elements β_{13}, β_{14} and β_{23}, consistent with the distinct diabatic representations seen in Figure 2.6 and discussion presented in Section 2.6.1. The six switching functions and the corresponding linear combination of generator elements are illustrated in Figure 3.16, where Table 3.9 lists the optimised switching function parameters.

Figure 3.17 illustrates the adiabatic potentials of the CH [$C\,^2\Sigma^+$, $2\,^2\Sigma^+$, $3\,^2\Sigma^+$, $4\,^2\Sigma^+$] system and regularised NACs (left panels) with the corresponding diabatic representation (right panels). The DBOC terms have been added to the adiabatic PECs, and can be seen to introduce a minimal potential barrier unlike the YO and N_2 cases. The diabatic PECs appear as simple and smooth functions, with the $V_1^{(d)}$, $V_2^{(d)}$, and $V_4^{(d)}$ states showing bound, Morse-like behavior while the $V_3^{(d)}$ state is diabatically repulsive, crossing $V_1^{(d)}$ and $V_2^{(d)}$ to the C(^{1}P)+H dissociation limit. The DCs (bottom right panel) are seen to have complex behavior in the region of

	r_{ref} (Å)	γ_{ref} (Å)	B_0	B_1	B_2
γ_{12}	1.5236	4.5177	1.3523	0.8911	0.2793
γ_{13}	1.6616	3.6494	0.5642	-0.9450	-0.0686
γ_{14}	1.7811	1.8135	0.9224	-0.0029	0.0649
γ_{23}	2.2488	2.3498	0.9586	0.0436	-0.1269
γ_{24}	1.9488	2.1169	0.4680	0.0116	0.5909
γ_{34}	1.6929	1.9850	3.5388	-0.3588	-0.2925

Table 3.9: Functional parameters for switching functions (Eq.(2.77)) are listed, where morphing parameters to Eq.(4.21) in generation of a position dependent width γ_{ij} are given. These, in conjunction with the evolved AtDT solutions construct the regularised CH AtDT solution via Eq.(2.76). All functions have $\beta_2 = 0.1$, $\beta_4 = 0.02$, and $p = 4$.

avoided-crossing and are in general large in magnitude, reflecting the large separation in the adiabatic PECs at the avoided crossings.

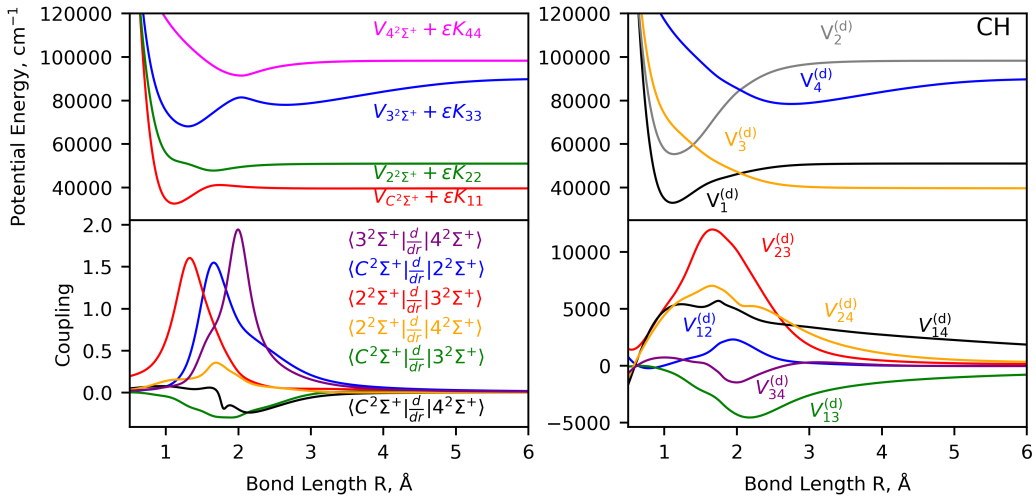

Figure 3.17: Illustration of the diabatisation of the CH $[C\,^2\Sigma^+, 2\,^2\Sigma^+, 3\,^2\Sigma^+, 4\,^2\Sigma^+]$ system: Adiabatic PECs (top left), NACs (bottom left), diabatic PECs (top right), and DCs (bottom right). The DBOC corrections have been added to the adiabatic potentials, and are computed from multiplying the kinetic energy factor $\varepsilon = \frac{\hbar}{8\pi^2\mu c}$ by the diagonal elements of the **K** matrix.

3.6.3 The 10-State Spectroscopic Model: A Web of Avoided Crossings

So far in this chapter a strict diabatic representation has been demonstrated to be possible for a 2-, 3-, and 4-state coupled system, where the AtDT ensured both the bound and continuum rovibronic solutions are preserved. The extension to the general N-state system would ideally have no limit to the number of states treated, N.

I now wish to test the adiabatic/diabatic equivalence on a significantly larger system, and to this end I generate a synthetic 10-state problem. The 10-state synthetic problem, X10 herein, was generated from the successive adiabatsations (diagonalisations) of 2-state systems between 10 neighboring Morse oscillator PECs via the method used to model the CH $[C\,^2\Sigma^+, 2\,^2\Sigma^+]$ system in Section 3.6.2. Lorentzian functions were used to initially model the 2-state NACs, where their magnitude was chosen to reflect the separation in the PECs. After the adiabatic PECs were generated, the outer-NACs $W_{ij}^{(1)}$ coupling states separated by one or more neighboring states ($|i-j| \geq 2$) were placed arbitrarily into the NAC $\mathbf{W}^{(1)}$ matrix. This arbitrariness is then a valuable metric to test the robustness of the HyAP method in generation of a physically meaningful diabatic representation. In essence, this "made-up" model of guessed NACs and PECs is the ultimate test on the HyAP regularisation scheme and numerical exactness of the computed AtDT. In total, the 10 electronic states are coupled by 45 NACs, yielding complex coupling pathways, where slight modification of one state will be "felt" by all other 9 states. The X10 model is not entirely guessed, however, but chosen to resemble the high energy electronic manifolds of molecules like C_2, CN, N_2 ($^3\Pi_u$ symmetry manifold), SiC, and Si_2 – which all possess a complicated web of adiabatic avoided crossings with a single deep diabatic potential well which crosses the entire potential web up to high dissociation limits[238,239]. Furthermore, this type of system is seen in the $^1\Sigma^+$ manifold of Alkali Hydride electronic structures[92,93,26]. Therefore, the results yielded from X10's diabatisation should emulate that of a real physical system.

Figure 3.10 illustrates the $^1\Sigma^+$ electronic manifold of the synthetic X10 system, where the NACs are regularised and subsequently a smooth and practical diabatic representation is generated using the HyAP method. The 45 DCs coupling the 10 diabatic states exhibit complex topology over the studied range of internuclear separation, where the diabatic PECs are seen to resemble smooth Morse oscillator functions. It is interesting to see a single bound electronic state pass through the web of potentials in a smooth manner, despite the complexity of the DCs, NACs, and adiabatic PECs. A significant portion of bound and continuum solutions for transitions connecting the ground adiabatic state are then reconstructed as transitions within the single diabatic bound well, where the rovibronic wavefunctions are expected to be equivalent to the adiabatic picture. The adiabatic/diabatic equivalence for the X10 system is studied later in this chapter.

Figure 3.18 illustrates the 45 forward- and backward- evolved AtDT generator elements of the X10 system and are seen to be complex functions of bond length. The two solutions also appear to differ significantly across all geometries, which

is to be expected since the NACs were arbitrarily chosen in generation of the adiabatic representation – therefore the evolution of the AtDT is not ensured to satisfy the proposed boundary conditions. The curves are plotted with nearly 2×10^4 grid points, and so the strange features seen are not due to numerical noise, but are real topological features of the AtDT. The linear combination of the forward- and backward- evolved elements are also overlaid in Figure 3.18, where the associated switching functions are optimised to ensure a smooth set diabatic PECs. The linear combination connects both solutions whilst maintaining their distinct topological features. With the extension to a 10-state coupled system emerges the possible complexity of the associated AtDT, where a physical, smooth diabatic representation is constructed using a very complex, non-smooth AtDT. Despite the challenges of dealing with such a complex system, I have demonstrated that the HyAP method can robustly produce sensible diabatisations regardless of system size.

3.7 Solving the *N*-State Rovibronic Schrödinger Equation

The fully coupled rovibronic Schrödinger equation for the 3-state N_2, 4-state CH, and 10-state X10 systems detailed above are solved using our variational code Duo, where the methodology in its solution is discussed in Section 2.3. As part of this work, we further extended the Duo kinetic energy operator to incorporate an arbitrary number of nonadiabatically coupled electronic states. Similarly to the 2-state system described earlier in this chapter, the DBOC terms can be either provided as input or generated from the NAC using Eq. (2.16).

Earlier in this chapter, it was demonstrated that rovibronic calculations for the 2-state system were consistent between the adiabatic and diabatic representations, even subject to the convergence (because of PEC-adapted vibronic basis set) or other numerical limitations. It was also shown that neither the adiabatic or diabatic model is better, but depends on the system studied. However, the coupled two-state system is an approximation, often justified by Hellman-Feynman theorem (see Section 2.2.1), to the exact system of an infinite number of coupled adiabatic states. The effect of couplings to higher energy states on the rovibronic energies, and hence wavefunctions, is tested in the following sections.

With the extension to *N*-states, further off-diagonal second-order DDR derivative couplings in the $\mathbf{K}$ matrix must be considered, which necessitates further approximate cases to be tested. Four approximations to the rovibronic solution are considered: I, the case when DBOCs are omitted from the adiabatic representation;

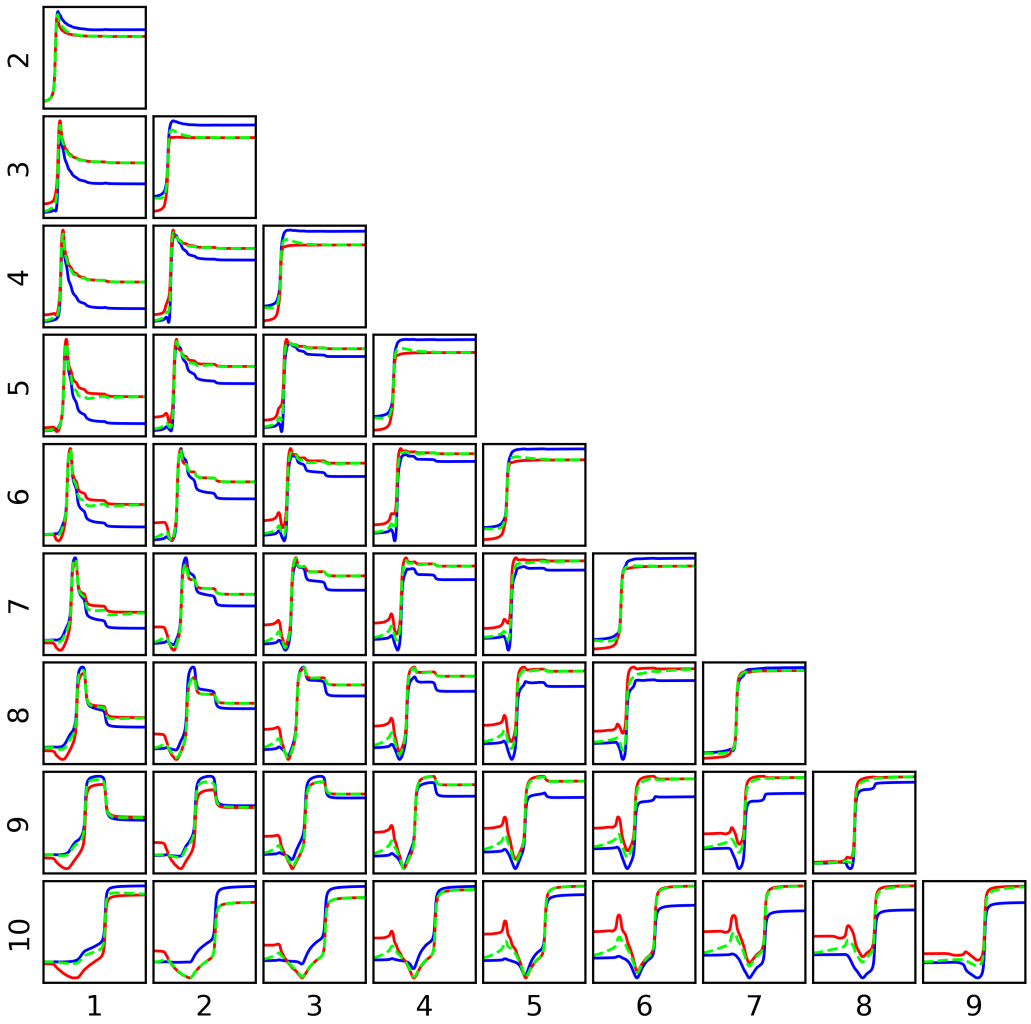

Figure 3.18: The 45 forward- and backward- generator elements of the 10-state system are plotted as blue and red lines, respectively. Overlaid in green are their linear combination corresponding to the regularised solution which is seen to connect the two solutions and satisfy the enforced boundary conditions. The curves are plotted between 1 Å and 7 Å, serving to illustrate the complexity of the 10-state solutions, where the numbers indicate the (row/column) element indices.

II, the case when all off-diagonal DDR couplings are omitted ($K_{i\neq j} = W_{ij}^{(1)} = 0$) from the adiabatic representation; III, the case when all DDR couplings (DBOC, off-diagonal DDRs) are omitted from the adiabatic representation; IV, the case when DCs are omitted from the diabatic representation.

It will be demonstrated in the following sections, and should be expected from the previous analyses in this chapter, that these approximations will significantly impact the computed spectroscopy, and as a result yield a quantum number labelling which becomes non-comparative between the different approximations. To this end, a combination of the energy enumeration, n, set of assigned quantum numbers, and character of the ("vibronic wavefunction") reduced density state (see 3.3.2 and Brady et al.[38] for more details) are studied, where only the closest matching states will have their energy compared. It has been discussed that state numbering leads to accurate assignments of the bound rovibronic levels, as summarised by the oscillation theorem[244–246] which states that *the i^{th} bound rovibronic eigenfunction has i internal nodes*, but breaks down in the strongly coupled case where the single state approximation is no longer valid.

3.7.1 The 10-State Solution

The bound-state rovibronic solutions for the X10 10-state system introduced in Section 3.6.3 are now analysed. Figure 3.10 illustrates the adiabatic and diabatic spectroscopic models constructed using the HyAP method. Examining the equivalence of rovibronic solutions between the adiabatic and diabatic representations is particularly interesting given the system's complexity. The intricate network of avoided crossings, characterised by 45 NACs, poses a significant computational challenge due to the extensive coupling between states, where any inconsistencies in the transformation should be pronounced in this complex system.

The lowest 1000 $J = 0$ rovibronic energies for the fully coupled 10-state system were computed in the adiabatic and diabatic representations, where selected $J = 0$ energies are listed in table 3.10. These $J = 0$ energy terms were selected to be near the avoided crossing regions over all 10 excited states to rigorously test the equivalence and diabatic module in Duo. Despite the large correlation in this highly coupled system, equivalence has been shown between the adiabatic and diabatic representations where a numerically exact AtDT has been found. This shows that one can model large systems for an arbitrary number of states in Duo without loss of strictness in the diabatic basis.

Table 3.10: Selected $J = 0$ rovibronic energy term values (in cm^{-1}) of the synthetic 10 coupled state state system computed within the adiabatic and diabatic representations using Duo. These states were chosen to be situated at the avoided crossing regions.

n	Adiabatic			Diabatic		
	$\tilde{E}$	State	v	$\tilde{E}$	State	v
7	1847.007771	$1^1\Sigma^+$	6	1847.007771	$2^1\Sigma^+$	3
8	2129.925260	$1^1\Sigma^+$	7	2129.925261	$2^1\Sigma^+$	4
9	2416.431857	$1^1\Sigma^+$	8	2416.431858	$2^1\Sigma^+$	5
30	6678.428517	$2^1\Sigma^+$	3	6678.428518	$3^1\Sigma^+$	0
32	6984.594060	$2^1\Sigma^+$	4	6984.594060	$3^1\Sigma^+$	1
35	7298.846922	$2^1\Sigma^+$	5	7298.846922	$3^1\Sigma^+$	2
114	12464.895630	$1^1\Sigma^+$	84	12464.895630	$1^1\Sigma^+$	13
115	12523.517670	$3^1\Sigma^+$	5	12523.517670	$2^1\Sigma^+$	80
116	12586.520910	$2^1\Sigma^+$	24	12586.520910	$3^1\Sigma^+$	20
247	18814.479740	$3^1\Sigma^+$	26	18814.479740	$4^1\Sigma^+$	21
249	18895.065350	$5^1\Sigma^+$	0	18895.065350	$5^1\Sigma^+$	0
251	18981.836630	$3^1\Sigma^+$	27	18981.836620	$4^1\Sigma^+$	22
253	19032.279350	$1^1\Sigma^+$	127	19032.279350	$1^1\Sigma^+$	21
426	25580.915070	$5^1\Sigma^+$	11	25580.915070	$6^1\Sigma^+$	2
427	25596.980210	$6^1\Sigma^+$	2	25596.980210	$6^1\Sigma^+$	3
435	25915.997070	$4^1\Sigma^+$	32	25915.997070	$5^1\Sigma^+$	27
662	33094.870560	$6^1\Sigma^+$	18	33094.870560	$5^1\Sigma^+$	98
663	33124.269800	$5^1\Sigma^+$	43	33124.269800	$3^1\Sigma^+$	160
664	33161.059010	$2^1\Sigma^+$	164	33161.059010	$6^1\Sigma^+$	37
669	33265.317660	$7^1\Sigma^+$	7	33265.317660	$7^1\Sigma^+$	8
949	40738.198500	$6^1\Sigma^+$	70	40738.198500	$7^1\Sigma^+$	62
950	40787.878880	$7^1\Sigma^+$	25	40787.878880	$1^1\Sigma^+$	54
958	40985.704660	$8^1\Sigma^+$	13	40985.704660	$6^1\Sigma^+$	110
1267	48624.059359	$9^1\Sigma^+$	20	48624.059359	$8^1\Sigma^+$	80
1270	48668.417006	$5^1\Sigma^+$	154	48668.417006	$3^1\Sigma^+$	217
1271	48684.060547	$1^1\Sigma^+$	241	48684.060547	$2^1\Sigma^+$	236
1272	48743.879213	$7^1\Sigma^+$	90	48743.879213	$8^1\Sigma^+$	81
1273	48769.629102	$3^1\Sigma^+$	202	48769.629102	$4^1\Sigma^+$	197
1276	48833.738010	$10^1\Sigma^+$	0	48833.738010	$10^1\Sigma^+$	0
1626	56637.515727	$10^1\Sigma^+$	32	56637.515727	$10^1\Sigma^+$	32
1627	56656.811037	$8^1\Sigma^+$	105	56656.811037	$9^1\Sigma^+$	96
1629	56677.102187	$7^1\Sigma^+$	138	56677.102187	$8^1\Sigma^+$	130
1648	57082.586039	$4^1\Sigma^+$	208	57082.586039	$5^1\Sigma^+$	205
1669	57491.954867	$9^1\Sigma^+$	61	57491.954867	$10^1\Sigma^+$	43
	...			...		

Table 3.11: The lowest 25 $J = 0$ rovibronic energies (to 2 decimal places) of the $1\,^1\Sigma_g^+$, $2\,^1\Sigma_g^+$, $3\,^1\Sigma_g^+$states of N_2 as computed within the adiabatic and diabatic representations using Duo. The rovibronic energies are computed in the adiabatic representation with the regularization correction to the NACs ($\boldsymbol{W}^{(1)} + \Delta$, see Eq.(2.84)) and without ($\boldsymbol{W}^{(1)}$).

n	$E(W^{(1)})$	$E(W^{(1)}+\Delta)$	ΔE	State	v
1	0	0	0	$1\,^1\Sigma_g^+$	0
2	457.78	458.17	-0.39	$1\,^1\Sigma_g^+$	1
3	693.56	693.58	-0.02	$1\,^1\Sigma_g^+$	2
4	1416.01	1416.29	-0.28	$1\,^1\Sigma_g^+$	3
5	2131.06	2133.37	-2.31	$1\,^1\Sigma_g^+$	4
6	2537.89	2548.85	-10.96	$1\,^1\Sigma_g^+$	5
7	2868.13	2863.40	4.73	$1\,^1\Sigma_g^+$	6
8	3549.80	3548.53	1.27	$1\,^1\Sigma_g^+$	7
9	4210.22	4213.43	-3.21	$1\,^1\Sigma_g^+$	8
10	4695.01	4687.04	7.97	$1\,^1\Sigma_g^+$	9
11	5133.73	5114.74	18.99	$1\,^1\Sigma_g^+$	10
12	5790.16	5781.04	9.12	$1\,^1\Sigma_g^+$	11
13	6479.41	6484.35	-4.94	$1\,^1\Sigma_g^+$	12
14	6779.06	6816.49	-37.43	$2\,^1\Sigma_g^+$	0
15	7213.41	7198.24	15.17	$1\,^1\Sigma_g^+$	13
16	7903.01	7894.19	8.82	$1\,^1\Sigma_g^+$	14
17	8583.09	8573.52	9.57	$1\,^1\Sigma_g^+$	15
18	8881.59	8898.94	-17.35	$2\,^1\Sigma_g^+$	1
19	9252.76	9251.95	0.81	$1\,^1\Sigma_g^+$	16
20	9904.98	9901.24	3.74	$1\,^1\Sigma_g^+$	17
21	10539.64	10532.84	6.8	$1\,^1\Sigma_g^+$	18
22	10877.91	10891.38	-13.47	$2\,^1\Sigma_g^+$	2
23	11141.61	11139.39	2.22	$1\,^1\Sigma_g^+$	19
24	11664.87	11660.10	4.77	$1\,^1\Sigma_g^+$	20
25	12082.38	12091.36	-8.98	$3\,^1\Sigma_g^+$	0
	...	...	...		

3.7.2 The Effect of Regularisation on Rovibronic Calculations

Understanding the relationship between changes in the DDR coupling terms and their impact on rovibronic energy levels is nontrivial. An effective regularisation procedure should correct the NACs such that any resulting changes in the molecule's spectral properties, particularly its rovibronic energy levels and wavefunctions, is less than the expected error in *ab initio* calculations. In the following section, I compare rovibronic energy levels computed with and without regularisation to assess the procedure's effectiveness.

3.7.2.1 Application to the 3-State N_2 System

The N_2 system presented in section 3.6.1 is treated rovibronically using the nuclear motion code Duo. To assess the impact of regularisation on the spectral properties, rovibronic energies were computed in the adiabatic representation using NACs with and without regularising corrections. Table 3.11 illustrates the computed rovibronic energies (quoted at two decimal places) relative to the zero-point energy of the $1\,^1\Sigma_g^+$ state, showing that the adiabatic calculations with regularisation introduces corrections similar to the expected error of MRCI calculations[247], typically of the order $1-10$ cm^{-1}, with a root mean square error of 10.2 cm^{-1}. Some energies, however, are minimally changed with a difference to the unregularised case of $\sim$ 1 cm^{-1}. I conclude that the HyAP method yields regularising NAC corrections which produce a sensible diabatic representation that preserves the physics of the system. Therefore, HyAP has been demonstrated to be a robust method for systems of different character and of arbitrary size.

3.7.3 The 3-State N_2 Solution

The rovibronic energies for the N_2 3-state system described in Section 3.6.1 are computed, where the adiabatic and diabatic spectroscopic models are illustrated in Figure 3.11. The NACs and hence AtDT have been regularised via the HyAP method (see Section 2.6.4). The DBOC coupling $K_{\rho\rho}$ has been added to the adiabatic PECs to demonstrate the significant difference between the adiabatic and diabatic models, where a large spike at the avoided crossing is seen in the adiabatic PECs. Regardless, one expects the two models to produce the same rovibronic eigenvalues and eigenfunctions, which this section aims to demonstrate.

The lowest 37 rovibronic energy term values ($J = 0$) computed using the adiabatic and diabatic N_2 [$1\,^1\Sigma_g^+$, $2\,^1\Sigma_g^+$, $3\,^1\Sigma_g^+$] models are listed in Table 3.12. It is clear that whilst the approximate quantum state numbers are very different for the

Table 3.12: The lowest 36 $J = 0$ rovibronic energy term values (cm^{-1}) of the $1\,^1\Sigma_g^+$, $2\,^1\Sigma_g^+$ and $3\,^1\Sigma_g^+$ states of N_2 computed within the adiabatic and diabatic representations using Duo (columns labeled with E). Varying degrees of approximations are used and are labeled: I is the case when DBOCs are omitted from the adiabatic representation; II is the case when all off-diagonal DDR couplings are omitted ($K_{i\neq j} = W_{ij}^{(1)} = 0$) from the adiabatic representation; III is the case when all DDR couplings (DBOC, off-diagonal DDRs) are omitted from the adiabatic representation; IV is the case when DCs are omitted from the diabatic representation. All energies are relative to the zero-point energies ($E_{\rm ZPE}$, including the electronic excitation) given at the bottom of each column. The bold numbers refer to states with difficult quantum number assignment (see text). The root mean square difference of the lowest n approximate and fully coupled rovibronic terms are computed for the energy ($E_{\rm rms}$) and radial reduced densities ($\rho_{\rm rms}$, see Eq.(3.18)).

n	Adiabatic						Diabatic			
	E	E(I)	E(II)	E(III)	State	v	E	E(IV)	State	v
1	0	0	0	0	1	0	0	491.132475	3	0
2	457.775275	434.700608	467.732785	449.719219	1	1	457.775275	0	1	0
3	693.564594	692.305891	694.208912	693.345881	1	2	693.564594	1147.153095	3	1
4	1416.011696	1405.993194	1419.423663	1412.727672	1	3	1416.011696	1841.288774	3	2
5	2131.061586	2063.317832	2141.838444	2102.127941	1	4	2131.061586	2531.370457	3	3
6	2537.890864	2343.138774	2607.762407	2464.898286	1	5	2537.890864	2135.104439	1	1
7	2868.126501	2816.769779	2917.159177	2907.742287	1	6	2868.126501	3211.1168	3	4
8	3549.801719	3411.324632	3621.012807	3561.954983	1	7	3549.801719	3887.928645	3	5
9	4210.218745	4012.169077	4323.406743	4182.424384	1	8	4210.218745	4576.045634	3	6
10	4695.005744	4466.6889	4889.466721	4757.112509	1	9	4695.005744	4220.679791	1	2
11	5133.725681	4916.044996	5394.712916	5374.479159	1	10	5133.725681	5276.230211	3	7
12	5790.155876	5622.044377	6086.615985	6042.50547	1	11	5790.155876	5974.586575	3	8
13	6479.408694	...	6814.520674	...	1	12	6479.408694	6668.763491	3	9
14	6779.063208	6312.321252	...	...	2	0	6779.063208	6272.449671	1	3
15	7213.410603	7161.506134	7480.056823	7376.437593	1	13	7213.410603	7357.065681	3	10
16	7903.009725	7866.377086	8070.548217	8027.394958	1	14	7903.009725	8032.029573	3	11
17	8583.091028	8515.760577	8701.901839	8681.313712	1	15	8583.091028	8695.766524	3	12
18	8881.592989	8770.025055	...	...	2	1	8881.592989	8297.308561	1	4
19	9252.763917	9147.869568	9381.767562	9335.855912	1	16	9252.763917	9349.303672	3	13
20	9904.981173	9794.810171	10057.131561	9984.600392	1	17	9904.981173	9994.943445	3	14
21	10539.639862	10440.512909	10692.735631	10624.650889	1	18	10539.639862	10629.690668	3	15
22	10877.912402	10683.076709	...	...	2	2	10877.912402	10289.060547	1	5
23	11141.610134	11029.361392	11292.145140		1	19	11141.610134	11254.067422	3	16
24	11664.870261	11932.753651	...	...	1	20	11664.870261	...	2	0
25	12082.377293	11479.032172	...	...	3	0	12082.377293	11867.937671	3	17
26	12541.173804	12441.239638	12528.326913	12499.508185	1	21	12541.173804	12470.756238	3	18
27	12881.431795	12750.503022	...	...	1	22	12881.431795	12244.598117	1	6
28	13129.244992	12993.67838	**13154.459922**	**13108.832369**	2	3	13129.244992	13061.272211	3	19
29	13562.8288	13491.249709	...	13706.292719	1	23	13562.828800	...	2	1
30	13934.090728	13852.417223	...	...	1	24	13934.090728	13640.028525	3	20
31	14380.132252	14292.754881	14335.152946	14291.510206	3	1	14380.132252	14205.528529	3	21
32	14762.541917	14689.50826	**14890.589468**	14863.83192	1	25	14762.541917	14205.528529	1	7
33	14987.484472	14889.542778	...	...	1	26	14987.484472	14757.424872	3	22
34	15431.979951	15365.047639	**15441.030728**	15423.319147	2	4	15431.979951	15294.675269	3	23
35	15776.743132	15692.664149	15988.978434	...	1	27	15776.743132	15816.839734	2	2
36	16094.15384	16038.826781	...	15968.690176	3	2	16094.153840	16322.968809	3	24
	...	...	...	...			...	...		
$E_{\rm ZPE}$	102834.749359	102834.412294	102834.810154	102834.492953			102834.749359	103364.634233		
$E_{\rm rms}$	n≤36	176.037033	138.544997	90.668019				333.288705		
$E_{\rm rms}$	n≤100	680.151000	407.768000	420.263000				492.621000		
$\rho_{\rm rms}$	n≤100	0.637000	1.434000	1.441000				0.755000		

adiabatic and diabatic representations, the state energies are identical to 10^{-6} cm^{-1}. Duo assigns quantum labels via the largest contribution from the corresponding basis sets, which in both cases are very different and so are their state interpretations, in which case states of matching energy enumeration are compared. Comparison of the adiabatic and diabatic reduced density states reveals that their wavefunctions are identical, confirming the comparison of rovibronic energies with the same energy enumeration is correct. In approximate cases, quantum numbers and energy enumeration fail as reliable state labels, requiring inspection of reduced density states for meaningful comparison with fully coupled cases. This inspection is done both visually and via studying the Euclidean distance between two reduced densities (see Eq.(3.18) below). The approximate solutions include many non-physical intermediate states (denoted by dots in the table). In some extreme cases, state assignment is too ambiguous for comparison. In some cases, highlighted in Table 3.12 in bold, only partial match of the radial densities can be established between approximate and fully coupled solutions.

Now that numerical equivalence has been demonstrated for the three-state problem, the significance of non-adiabatic coupling terms in the N_2 model can be assessed. Table 3.12 lists the rovibronic energies computed using approximations I, II, III, and IV (as described in Section 3.7). For the lowest energy levels, the exclusion of DCs (approximation IV) play a critical role in maintaining model accuracy. Omitting these couplings leads to significant discrepancies, with a root mean square error (RMSE) of 333.289 cm^{-1} compared to RMSE values for the adiabatic approximations: RMSE(I) = 176.037cm^{-1}, RMSE(II) = 138.545 cm^{-1}, RMSE(III) = 90.668 cm^{-1}.

This large discrepancy is primarily due to the unexpectedly strong DCs in this strongly non-adiabatic coupled system, which contradicts the earlier predictions in Section 3.3[38] which anticipate smaller DCs when NACs are large for the two state case of YO (see Section 3.3.1). The substantial differences between the adiabatic and diabatic potential minima leads to a swapping of the ground and first excited states (as seen for $n = 1$ and $n = 2$ in Table 3.12), introducing a systematic offset in the energy agreement. This effect is particularly relevant for the lowest energy levels, which are of significant spectroscopic importance and thus warrant careful analysis. Figure 3.19 illustrates how some of the approximations affect the computed energies of N_2 by comparing states approximated energies (adiabatic III and diabatic IV) to the "exact" values, i.e. computed with all associated couplings. It is clear that both approximations lead to strong deviations from the "exact" values with the diabatic case especially affected by the absence of the diabatic coupling.

It is interesting that despite the adiabatic zero-order approximation appearing to provide a more accurate and physically intuitive solution than in the the zero-order diabatic approximation, the convergence of the diabatic solution is faster for the latter, diabatic case.

In the region of the avoided crossing (states $n = 10 - 15$), neglecting NACs results in discrepancies comparable to those seen when the DCs are omitted, with energy differences from the fully coupled case on the order of 10^2 cm^{-1}. However, for states higher in energy than the crossing, the adiabatic approximations continue to break down as rovibronic energies deviate from the fully coupled case. When analysing the lowest 100 bound states, the RMSE increases significantly for adiabatic approximations (I, II, III), with the largest errors occurring when the DBOC is omitted. On the other hand, omitting the DCs results in a similar RMSE when more states are included. This suggests that the adiabatic representation for N_2 is less stable for highly excited states compared to the diabatic case.

Additionally, Table 3.12 highlights that the adiabatic approximation fails to capture certain states that are still present in the approximate diabatic case. Visual inspection of the reduced density states reveals that the wavefunctions in the adiabatic approximations struggle to reproduce the correct character seen in the fully coupled calculations. Deviation between the approximate and fully-coupled reduced density states are quantified by their Euclidean distance, defined as

$$d(\rho_i, \rho_j) = \int (\rho_i - \rho_j)^2 dr. \tag{3.18}$$

The RMSE of the Euclidean distance between the approximate and fully coupled reduced density states is twice as large for the adiabatic approximations than when the DCs are omitted from calculations. This indicates that wavefunctions computed in the approximate adiabatic representation differ significantly from those in the diabatic approximation IV, which may lead to inaccuracies in computed rovibronic intensities. Despite this, the induced errors via these approximations prove that for high resolution applications all non-adiabatic effects must be included.

While this analysis suggests the adiabatic representation is more reliable for the lower states, while the diabatic representation is more stable for higher states of the N_2 model, caution is needed when generalising these results. The comparison here is specific to this model, and further complexities must be considered. Notably, the sensitivity of the spectroscopy in each representation is an important factor. Testing the effect of varying the NACs revealed that small changes in their magnitudes led to substantial variations in the DCs, on the order of 10^4 cm^{-1}. A reduction of NAC

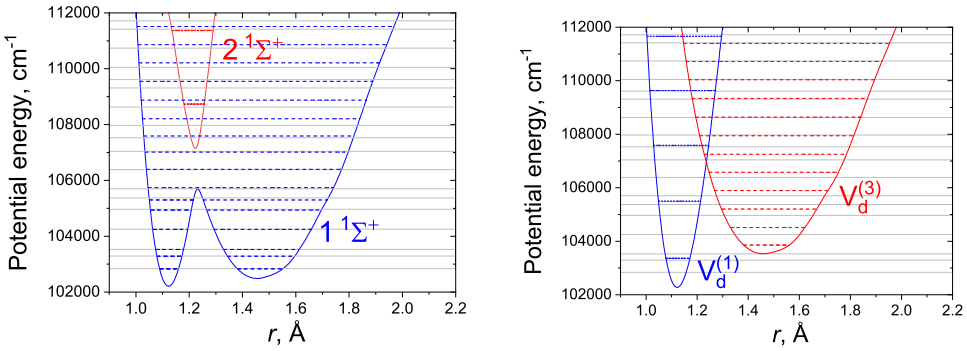

Figure 3.19: Illustration of the energy term values of the N_2 model ($J = 0$) system computed using the adiabatic approximation III (dashed, left panel) and diabatic approximation IV (dashed, right panel) compared to the corresponding "exact" solution (no approximations, solid gray lines, both panels) for the lowest 18 states.

magnitudes by 20% resulted in a corresponding change of 10^5 cm^{-1} in the DCs. Therefore, while the DCs in this system are strong, the N_2 spectroscopy is likely to be less sensitive to the diabatic representation.

3.7.4 The 4-State CH Solution

A rovibronic solution is computed for the CH 4-state system described in Section 3.6.2 using the adiabatic and diabatic representations of the spectroscopic model presented in Figure 3.17. The NACs have been regularised using the HyAP method to generate the diabatic representation. The DBOC correction terms have been added to the adiabatic PECs in Figure 3.17, which produce no obvious spike-like topologies in the region of avoided crossing.

The CH [$C\,^2\Sigma^+$, $2\,^2\Sigma^+$, $3\,^2\Sigma^+$, $4\,^2\Sigma^+$] system is different to the studied N_2 [$1\,^1\Sigma_g^+, 2\,^1\Sigma_g^+, 3\,^1\Sigma_g^+$] system in that, adiabatically, the CH PECs have large energetic separations, the NACs are weaker by an order of magnitude meaning no spike-like contributions from the DBOC terms, and diabatically the DCs are an order of magnitude greater. As described in Section 3.3, above the first CH dissociation channel (39220.0 cm^{-1}) is heavily (pre-)dissociated and contains (pre-)dissociative and continuum states which are separated from this analysis by removing wavefunctions which oscillate at the 'right' border $r_{\max} \to \infty$, whereas bound state wavefunctions vanish completely[234,233]. However, the continuum solution was shown to be equivalent through diabatisation in Section 3.3.4, where both continuum wavefunctions and photo-absorption spectra to these states are shown to be equivalent when computed using adiabatic and diabatic spectroscopic models. Therefore, only the bound

Table 3.13: The lowest 17 $J = 0.5$ e parity rovibronic energies of the [$C\,^2\Sigma^+$, $2\,^2\Sigma^+$, $3\,^2\Sigma^+$,$4\,^2\Sigma^+$] system of CH as computed within the adiabatic and diabatic representations using Duo. Varying degrees of approximations are used and are labeled: I is the case when DBOCs are omitted from the adiabatic representation; II is the case when all off-diagonal DDR couplings are omitted ($K_{i\neq j} = W^{(1)}_{ij} = 0$) from the adiabatic representation; III is the case when all DDR couplings (DBOC, off-diagonal DDRs) are omitted from the adiabatic representation; IV is the case when DCs are omitted from the diabatic representation. All energies are relative to the zero-point energies ($E_{\rm ZPE}$, including the electronic excitation) given at the bottom of each column. The root mean square difference of the approximate and fully coupled rovibronic terms are computed for the energy ($E_{\rm rms}$) and radial reduced densities ($\rho_{\rm rms}$, see Eq.(3.18)).

	Adiabatic						Diabatic			
	E	E(I)	E(II)	E(III)	State	v	E	E(IV)	State	v
	0	0	0	0	1	0	0	0	1	0
	2603.377370	2601.61	2603.91	2602.15	1	1	2603.377370	2636.14	1	1
	4945.843448	4939.04	4947.94	4941.15	1	2	4945.843448	5061.21	1	2
	16789.795532	16778.98		16773.52	2	3	16789.795532		1	10
	35292.621456	35251.74	35286.78	35245.85	3	0	35292.621456		2	4
	44373.500709	44372.59	44373.46	44372.55	3	5	44373.500709	44052.40	4	0
	45130.519202	45128.91	45130.66	45129.04	3	6	45130.519202	44832.40	4	1
	45858.509178	45855.77	45858.90	45856.16	3	8	45858.509178	45585.66	4	2
	46548.411670	46542.70	46548.79	46543.00	3	9	46548.411670	46313.23	4	3
	47255.394177	47247.31	47253.94	47246.11	3	11	47255.394177	47016.19	4	4
	47841.236755	47829.32	47841.29	47829.25	3	12	47841.236755	47695.43	4	5
	48329.046921		48326.19	48306.66	3	13	48329.046921	48351.65	2	12
	48752.567999	48738.67	48749.41	48735.75	3	14	48752.567999	48351.65	4	6
	49246.485508	49236.12	49245.62	49235.33	3	15	49246.485508	48985.97	4	7
	49754.863246	49743.51	49754.64	49743.26	3	16	49754.863246	49599.12	4	8
	50243.670156	50232.21	50243.28	50231.83	3	17	50243.670156	50188.72	4	9
	50724.086185	50714.07	50723.88	50713.92	3	18	50724.086185	50753.76	4	10
	...	...	...	...			...	...		
$E_{\rm ZPE}$	33961.631668	33960.58	33961.76	33960.71			33961.631668	34430.76		
$E_{\rm rms}$		13.11	1.94	15.40				191.07		
$\rho_{\rm rms}$		0.000919	0.000200	0.002045				0.516103		

state eigensolutions to the rovibronic Schrödinger equation for the CH problem will be studied here.

The lowest 17 bound $J = 0.5$ parity e rovibronic energy levels computed using both the adiabatic and diabatic CH models are listed in Table 3.13. The energy values match to within 5×10^{-8} cm^{-1} in both representations, confirming their equivalence for the 4-state system. A strict diabatic basis for the CH system has been established, yielding results that are numerically equivalent to the adiabatic model as computed using the Duo program. A comparison of rovibronic energies calculated via the approximate adiabatic and diabatic models indicates that the DCs play a critical role in ensuring model equivalence, both in terms of rovibronic energy and wavefunctions. Table 3.13 presents the RMSE for the studied bound states, showing that omitting the DCs results in a RMSE an order of magnitude higher than the approximate adiabatic calculations. Additionally, the approximate diabatic calculations yield significantly poorer reduced density states compared to the adiabatic approach, as reflected in the RMS of the Euclidean distance between the approximate and fully coupled reduced density states. Thus, the approximate adiabatic representation more accurately reproduces the spectroscopy of the CH system than the approximate diabatic representation. This aligns with the conclusion of Brady et al.[38], who studied the numerical equivalence of the CH [$C^2\Sigma^+$, $2^2\Sigma^+$] 2-state system and found that weakly non-adiabatic systems generate large DCs, making the adiabatic representation a more appropriate framework for modeling the spectroscopy. However, the induced errors via these approximations prove that for high resolution applications all non-adiabatic effects must be included.

The impact of these approximations on the energies of my model CH system are graphically illustrated in Figure 3.20 by plotting the states corresponding to the adiabatic approximation III and diabatic approximations IV and comparing them to the corresponding "exact" values (no approximation). While the adiabatic system of CH appears to be relatively immune for the absence of the couplings here, the diabatic zero-order approximation has a dramatic effect on the positions and even physical meaning of the computed states. Indeed, not only the approximated energies are very different, the very steep potential well of $V_1^{(d)}$, when not connected to the repulsive state $V_3^{(d)}$, yields additional bound states in the region above the adiabatic dissociation of the $C^2\Sigma^+$ state.

3.8 Validity of the 2-State Approximation

The two-state approximation refers to the coupling of only two adiabatic states, meaning the **K** matrix in Eq.(2.16) is diagonal and the DBOCs are given by the

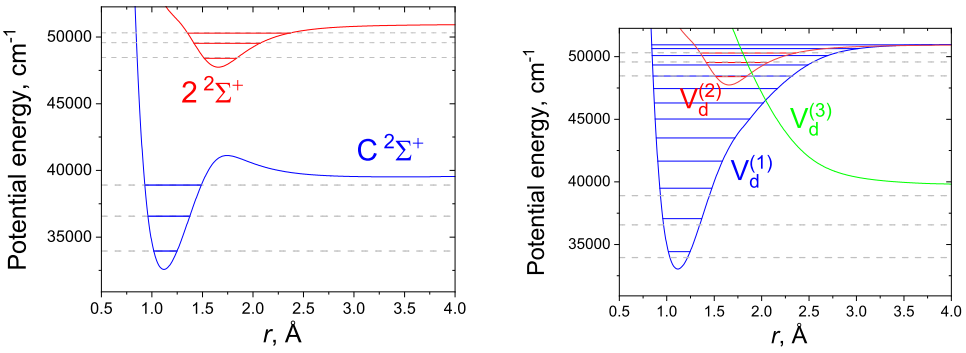

Figure 3.20: Illustration of the energy term values of my CH model system ($J = 0.5$, e) computed using the adiabatic approximation III (dashed, left panel) and diabatic approximation IV (dashed, right panel) compared to the corresponding "exact" solution (no approximations, solid gray lines, both panels) for the lowest 6 states.

NAC squared between states 1 and 2 (see Section 2.1). The two-state approximation is attractive since solution to Eq.(2.49) is analytic, and hence a diabatic representation is exactly known, where modelling of the full adiabatic or diabatic system is simple and requires only parameterisation of the NAC and two simple Morse and/or repulsive curves (see Section 2.5.1). The argument for such an approximation can be made via Hellman-Feynman theorem, which relates the difference in adiabatic energies to the NAC via (see Section 2.2.1 and Lengsfield and Yarkony [124], Saxe and Yarkony [125], Baer [46] for details)

$$W^{(1)}_{\alpha,\beta} = \frac{1}{E_\beta - E_\alpha}\left\langle \psi^a_\alpha \middle| \frac{d\hat{H}^{(a)}}{dr} \middle| \psi^a_\beta \right\rangle. \tag{3.19}$$

Hence, if states α and β are sufficiently well separated, i.e. $|E_\beta - E_\alpha| \gg 1$, then the DDR matrix elements are small $W^{(1)}_{\alpha,\beta} \ll 1$.

The DBOC $K_{\alpha,\beta} = \left\langle \frac{d\psi^a_\alpha}{dr} \middle| \frac{d\psi^a_\beta}{dr} \right\rangle$ can then be expressed in terms of the energy separation as follows

$$K_{\alpha,\beta} = \sum_\kappa^N \frac{1}{(E_\alpha - E_\kappa)(E_\kappa - E_\beta)}\left\langle \psi^a_\alpha \middle| \frac{d\hat{H}^{(a)}}{dr} \middle| \psi^a_\kappa \right\rangle \left\langle \psi^a_\kappa \middle| \frac{d\hat{H}^{(a)}}{dr} \middle| \psi^a_\beta \right\rangle \tag{3.20}$$

where the summation is over all adiabatic states and in the last line the Hellman-Feynman relation in Eq.(3.19) is inserted. It is evident that for the coupled two-electronic state system, states $|\psi^a_1\rangle$ and $|\psi^a_2\rangle$, the NAC elements coupling other states will be reduced by a factor of $\frac{1}{(E_\rho - E_\kappa)(E_\kappa - E_\rho)}$, for sufficiently well separated

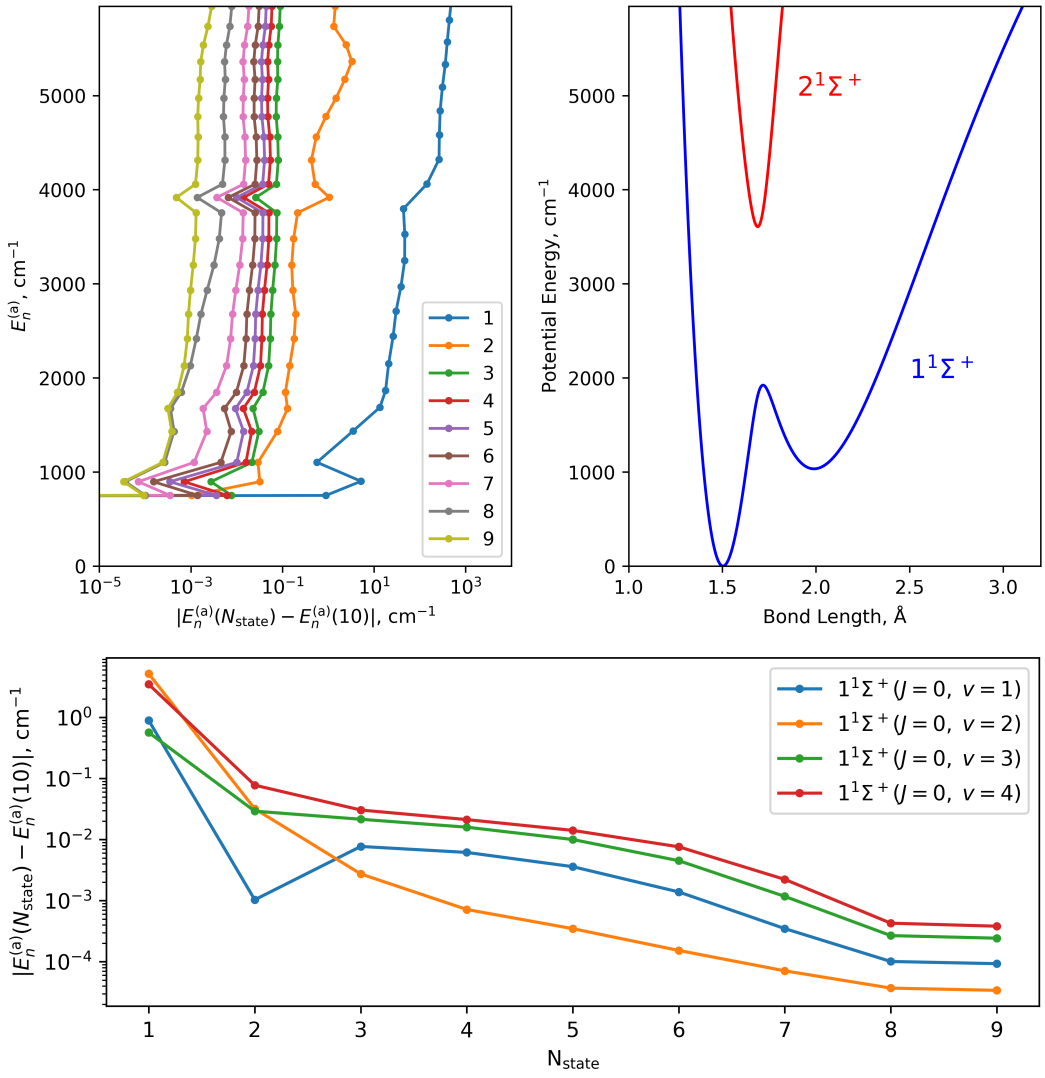

Figure 3.21: Illustration of the difference between the lowest 25 adiabatic rovibronic energy ($E_n^{(a)}$) in Table 3.10 computed with an N_{state} model and the fully-coupled 10-state model presented in section 3.6.3. The top left panel plots the energy level on the vertical axis vs. the discrepancy to the 10-state computed energy, where the states in question reside in the potential region shown in the top right panel. The bottom panel illustrates the energy discrepancy with increasing number of electronic states for the lowest 4 vibrational states of $1^1\Sigma^+$.

states from the coupled system $|\psi_1^a\rangle$ and $|\psi_2^a\rangle$ the summation is truncated yielding

$$K_{\rho,\rho} \approx -\left(W_{1,2}^{(1)}\right)^2. \tag{3.21}$$

To assess the validity of the two-state approximation, the lowest 25 rovibronic energy levels of the 10-state system described in Sections 3.6.3 and 3.7.1 are compared by progressively reducing the number of electronic states included in the nuclear motion calculations. Figure 3.21 shows the absolute differences between the n^{th} rovibronic energy level computed with an N_{state} model and the full 10-state adiabatic model with all DDR couplings, which is treated as the "true" reference for this system.

The most significant improvement occurs when moving from a single-state model to the two-state coupled system, reflected by an order-of-magnitude reduction in energy error, highlighting the critical role of non-adiabatic interactions. However, even for the lowest rovibronic states, the two-state model never agrees with the 10-state results to better than 10^{-2} cm^{-1}, indicating the necessity of incorporating additional non-adiabatic interactions from higher excited electronic states. Even the 9-state model does not achieve agreement with the 10-state reference within 10^{-3} cm^{-1}, which is insufficient for high-resolution spectroscopy.

Despite this argument being somewhat heuristic, it is evident that states separated by energies on the order of 10^4 cm^{-1} have a non-negligible impact on the ground-state energies. This can be attributed to the complex interactions between multiple different electronic states and results in a non-trivial correlation even among well-separated states. This challenges the straightforward application of the Hellmann-Feynman theorem to truncate the number of adiabatic states treated in rovibronic applications and highlights the need for further investigation, which tools like Duo now facilitate.

3.9 Applications of Diabatisation

This section outlines example use cases of our implemented diabatic module in the Duo program. So far this thesis has outlined both theoretical and numerical results in the construction of practical and exact diabatic representations for diatomic nuclear motion calculations, to which I now demonstrate its usefulness in the calculation of molecular line lists as in our recent works for the YO[172] (yttrium monoxide) and CO[248] (carbon monoxide) molecules.

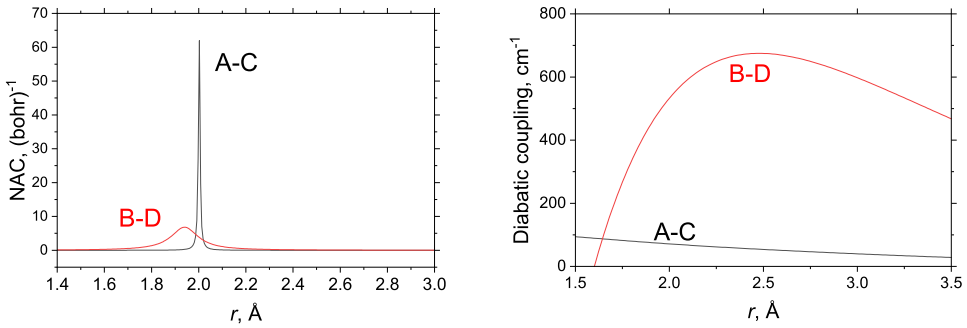

Figure 3.22: CASSCF NACs and empirical diabatic couplings $D(r)$ of YO, A–C and B–D.

3.9.1 $^{89}Y^{16}O$: The BRYTS Line List

The diabatic representation was employed in the construction of the BRYTS line list for $^{89}Y^{16}O$, $^{89}Y^{17}O$ and $^{89}Y^{18}O$. The line list covers the six lowest doublet electronic states: $X\,^2\Sigma^+$, $A\,^2\Pi$, $A'\,^2\Delta$, $B\,^2\Sigma^+$, $C\,^2\Pi$ and $D\,^2\Sigma^+$ up to 60 000 cm^{-1}. A previous *ab initio* study[230] provides the theoretical foundation for our refinement to spectroscopic data. This study employed a combination of multireference configuration interaction (MRCI) and coupled-cluster methods to compute potential energy curves (PECs), spin–orbit coupling curves (SOCs), electronic angular momentum curves (EAMCs), and (transition) electric dipole moment curves ((T)DMCs) for these six electronic states of YO.

Our collaborators extended this *ab initio* model to incorporate NACs for the $B\,^2\Sigma^+$, $D\,^2\Sigma^+$, and $A\,^2\Pi$, $C\,^2\Pi$ state pairs. These NACs were computed using the DDR procedure in MOLPRO[136] (see Section 2.2.2) at the complete active space self-consistent field (CASSCF) level of theory and are plotted in Figure 3.22. The *ab initio* calculations revealed that the $B\,^2\Sigma^+$, $D\,^2\Sigma^+$ and $A\,^2\Pi$, $C\,^2\Pi$ state pairs exhibit avoided crossings near their potential minima. Consequently, a careful treatment of non-adiabatic interactions was necessary to accurately reproduce the experimentally derived energy levels, as described below.

3.9.1.1 Refinement of the Diabatic Spectroscopic Model

We model the diabatic potentials for the $A\,^2\Pi$, $B\,^2\Sigma^+$, and $A\,^2\Pi$ state PECs using the Extended Morse Oscillator function (EMO)[249]. However, since the $C\,^2\Pi$ PEC lacks experimental data, we model its PEC with the Extended Hulburt-Hirschfelder (EHH) function[250,251] which was suggested to be more suitable for the description of the dissociation region[252]. Prior to refinement, the parameters describing the initial diabatic PECs were obtained by fitting the eigenvalues of the diabatic electronic Hamiltonian matrix to the *ab initio* PECs (see the ansatz diabatisation method in

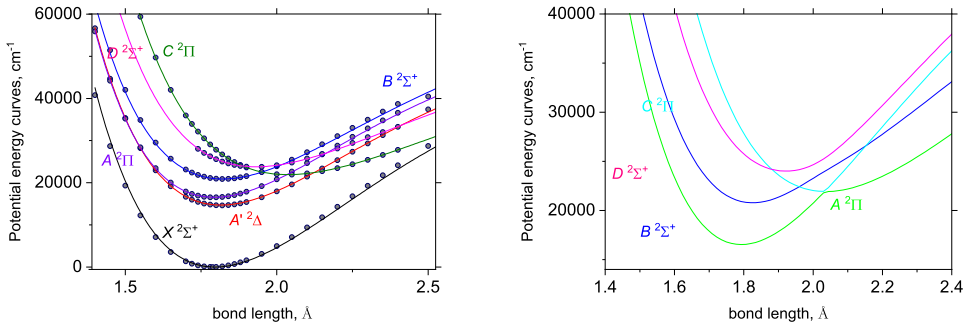

Figure 3.23: Refined (lines) and *ab initio* (points) PECs of YO: diabatic (left) and adiabatic (right).

Section 2.8.4). The DCs in this procedure are readily obtained from two diabatic PECs and a NAC via Eq.(2.59), where the NACs in this case were modelled by fitting Lorentzian functions to the *ab initio* computed curves. Figure 3.22 illustrates the CASSCF NACs and DCs for the $B\,^2\Sigma^+/D\,^2\Sigma^+$ and $A\,^2\Pi/C\,^2\Pi$ state pairs obtained by the methods described above. The $B\,^2\Sigma^+/D\,^2\Sigma^+$ DC has an asymmetric-Gaussian character, where ultimately the asymmetry in the DC is controlled by the difference $V_2^{(\mathrm{d})} - V_1^{(\mathrm{d})}$ if a symmetric NAC is used.

Figure 3.24 illustrates the available experimental $J = 0.5$ energy term values superimposed on the diabatic $B\,^2\Sigma^+/D\,^2\Sigma^+$ and $A\,^2\Pi/C\,^2\Pi$ PECs. Since the region about the avoided crossing of the $B\,^2\Sigma^+/D\,^2\Sigma^+$ system is well represented by experimental data, an inverse EMO function is used to model the DC between these states to introduce extra flexibility into the refinement of the coupled curves. Conversely, we model the $A\,^2\Pi/C\,^2\Pi$ DC via the diabatic PECs and a Lorentzian NAC via Eq.(2.59). The $B\,^2\Sigma^+$ vibronic energies of $v \geq 4$ are strongly affected by the diabatic coupling with the $D\,^2\Sigma^+$ state. Introduction of the diabatic coupling to the $B\,^2\Sigma^+$ states makes the shape of the PEC broader and pushes the positions of the $D\,^2\Sigma^+$ energies down. It is interesting to note that the $A\,^2\Pi$ state vibronic energies for $v = 11, 12, 13$ do not appear to be very perturbed by the presence of the close-by $C\,^2\Pi$ state, unlike the interaction of the B/D diabatic pair. This can be attributed to the difference in the corresponding DCs of the B/D and A/C pairs in Figure 3.22.

The diabatic spectroscopic model including PECs, DCs, and couplings (SOCs, EAMCs, initially computed *ab initio* via MRCI) was then tuned to experimentally determined energy levels obtained through the MARVEL algorithm (see Section 4.11.1 of Chapter 4 for details on the MARVEL algorithm). The refined (diabatic) PECs of YO are illustrated in Figure 3.23. The CCSD(T)/CBS *ab initio* energies from Smirnov et al.[230], shown with circles, appear to closely follow the refined

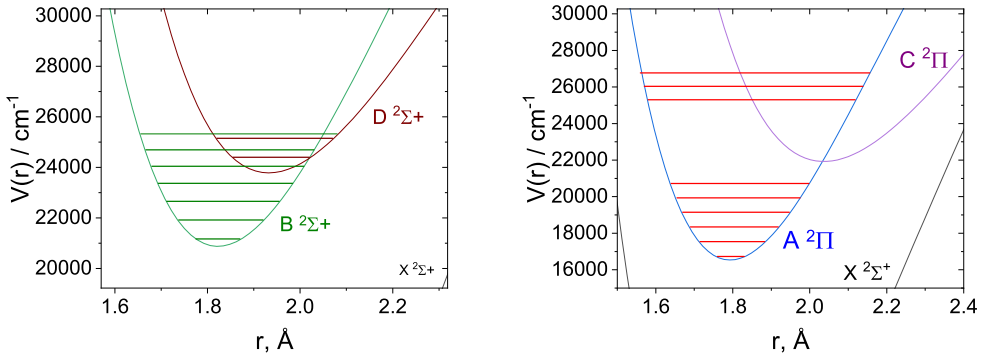

Figure 3.24: Diabatic PECs of the *B*/*D* and *A*/*C* pairs with the corresponding experimental energy term values ($J = 0.5$).

curves, indicating the excellent quality of the *ab initio* CCSD(T) PECs. The fitted DCs are then illustrated in Figure 3.22.

The results of the refinement are illustrated in Figure. 3.25, where |obs.-calc.| residuals are shown for the $A\,^2\Pi$, $D^2\Sigma^+$, and $B^2\Sigma^+$ electronic states. Some of the bands show clear systematic behavior of the residuals with respect to J, especially those that correspond to the synthetic data (derived via spectroscopic constants using PGOPHER[155]) or high resolution data (e.g. $A\,^2\Pi$ and some of the $B^2\Sigma^+$ vibrational systems), while others appear random with no particular structure (e.g. $v = 0$ of $B^2\Sigma^+$ and $D^2\Sigma^+$). The root-mean-square error achieved is 0.29 cm^{-1} for all 5906 energies (including the ground state and $A'^2\Delta$) covering J up to 142.5.

Given the sensitivity and significant impact of NACs (and DCs) on rovibronic energy levels, achieving the level of accuracy shown in Figure 3.25 is a challenging task. However, the inclusion of these couplings was crucial to attaining this precision, allowing us to achieve near-spectroscopic accuracy by accounting for the non-adiabatic effects.

3.9.1.2 Intensity Calculations

I diabatise our *ab initio* (T)DMCs using a combination of cubic-spline interpolation to smooth out the region around the avoided crossing and knowledge of the shape of the diabatised target curves. Figure 3.26 illustrates the property-based diabatising 'transformation' for the $\langle B^2\Sigma^+|\,\mu_z\,|X^2\Sigma^+\rangle$ and $\langle D^2\Sigma^+|\,\mu_z\,|X^2\Sigma^+\rangle$ transition dipole moment pairs, the effect being the two curves 'swap' beyond the avoided crossing and are now smooth. This method was employed because some computed coupling curves were incomplete, and this pragmatic, physics-driven approach provided a sensible solution. Additionally, since the avoided crossing positions predicted by *ab initio* CASSCF NACs, MRCI couplings, and CCSD(T) PECs may differ slightly,

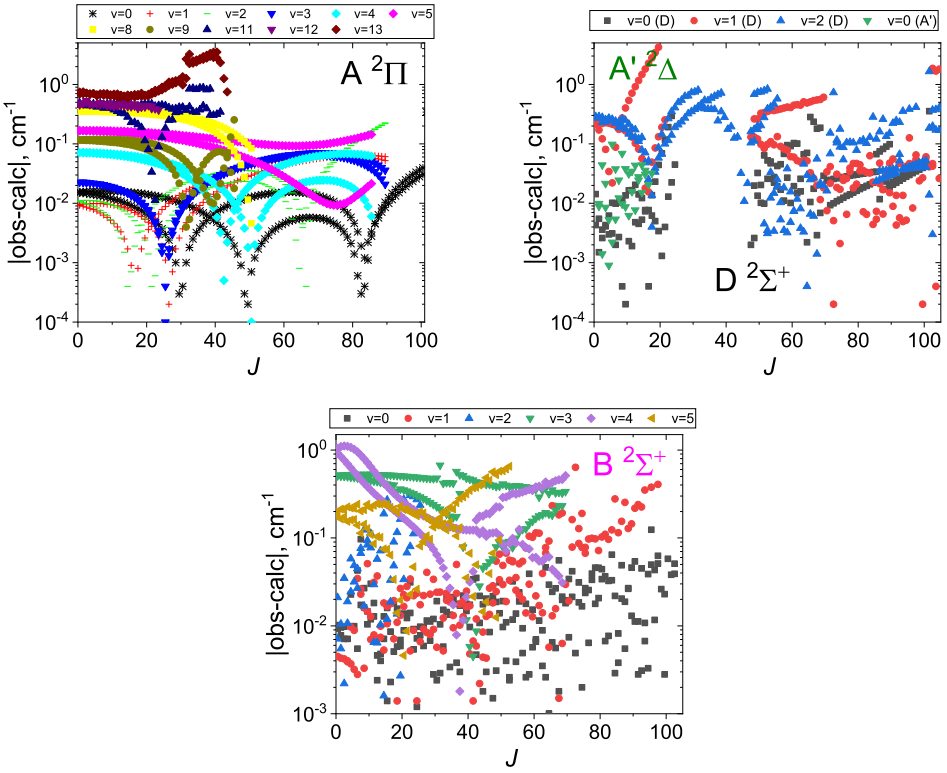

Figure 3.25: Observed minus calculated residuals for YO using the refined diabatic spectroscopic model for different vibronic states.

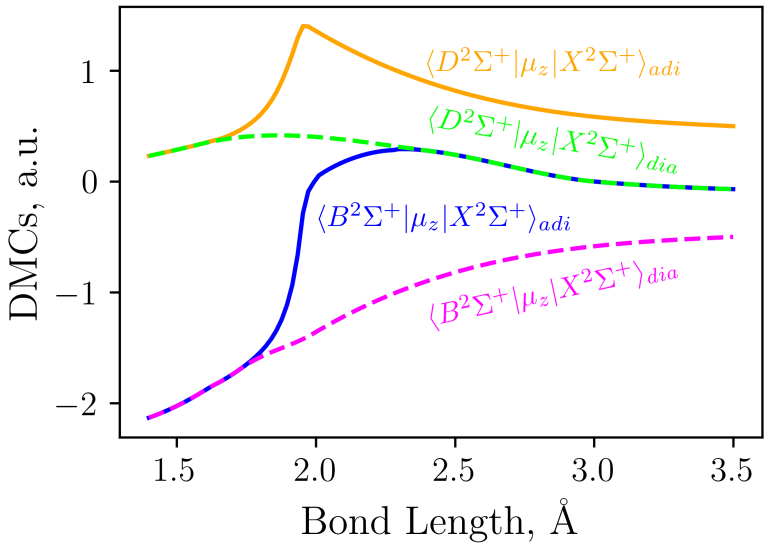

Figure 3.26: Example of the diabatisation (see text for details) of the adiabatic $\langle B^2\Sigma^+|\,\mu_z\,|X^2\Sigma^+\rangle$ and $\langle D^2\Sigma^+|\,\mu_z\,|X^2\Sigma^+\rangle$dipole moment pairs, where the $B^2\Sigma^+$ and $D^2\Sigma^+$ states exhibit an avoided crossing at $r \sim 1.81$ Å.

simply sketching the diabatic curves resolves any non-physical dipole oscillations that would arise from an inconsistent diabatisation using curves obtained at different theoretical levels – thus preventing strong artifacts in the computed diabatic intensities. The resulting computed intensities were validated against available spectroscopic data and show excellent agreement (see below).

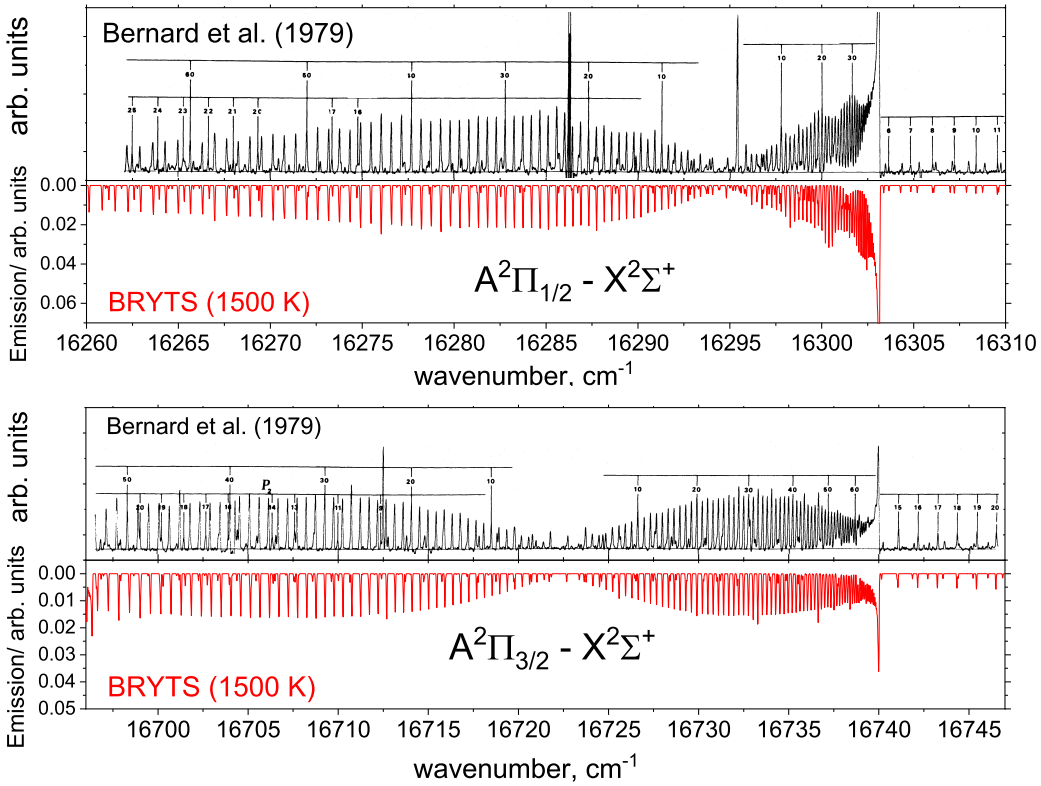

Figure 3.27: Comparison of our computed $A\,^2\Pi_{1/2} \leftarrow X^2\Sigma^+$ and $A\,^2\Pi_{3/2} \leftarrow X^2\Sigma^+$ $v = 0 \rightarrow 0$ rotational-electronic emission bands with those of Bernard et al.[253] (red lines), a measured spectrum using Fourier Transform Spectroscopy (upper displays). We compute our spectrum at a temperature of 1500 K to best match that of Bernard et al.[253]. A Gaussian line profile of 0.065 cm^{-1} was used with a resolution of 0.01 cm^{-1}. ©AAS. Reproduced with permission.

Figure 3.27 compares the experimental $A\,^2\Pi_{1/2} \leftarrow X^2\Sigma^+$ and $A\,^2\Pi_{3/2} \leftarrow X^2\Sigma^+$ $v = 0 \rightarrow 0$ emission bands measured by Bernard et al.[253] via Fourier Transform spectroscopy (black, extracted from their Figure 2) to our computed spectra (red). We simulate our spectra at the temperature of 1500 K to agree with the rotational structure of the experiment. Excellent agreement in both line position and band structure with the experiment is seen. Some discrepancies can be seen in the line intensities, but this could be due to assumptions about the temperature and line broadening. Generally, the magnitude of band head residuals $\Delta\tilde{\nu} = \tilde{\nu}_{\text{exp}} - \tilde{\nu}_{\text{calc}}$ correlates with the level of the rotational and vibrational excitations. The band heads

with J_{head} below 70.5 and $v \leq 8$ agree within ~ 0.1 cm^{-1}, which then degrades to about 0.5 cm^{-1} for $J_{\text{head}} \to 100.5$.

As in the previous YO *ab initio* study by Smirnov et al.[230], we present comparisons with the $B^2\Sigma^+ - X^2\Sigma^+$ and $D^2\Sigma^+ - X^2\Sigma^+$ absorption spectra from Zhang et al.[254], shown in Figure 3.28, now with improved agreement using the BRYTS line list. For further details, refer to the corresponding discussions in Smirnov et al.[230]. The experimental spectra were recorded in a heavily non-local thermodynamic equilibrium (non-LTE) environment, with rotational populations cooled to liquid nitrogen temperatures and vibrational populations remaining hot. This made comparisons to these bands challenging; however, we attempt to account for these non-LTE conditions by simulating the spectra with a rotational temperature of T_{rot} = 50K and a vibrational temperature of T_{vib} = 800K. We observe some intensity differences in the $D^2\Sigma^+ - X^2\Sigma^+$ absorption bands, but with good agreement in line positions. Due to the heavily non-LTE conditions, quantifying the accuracy of our computed bands is difficult.

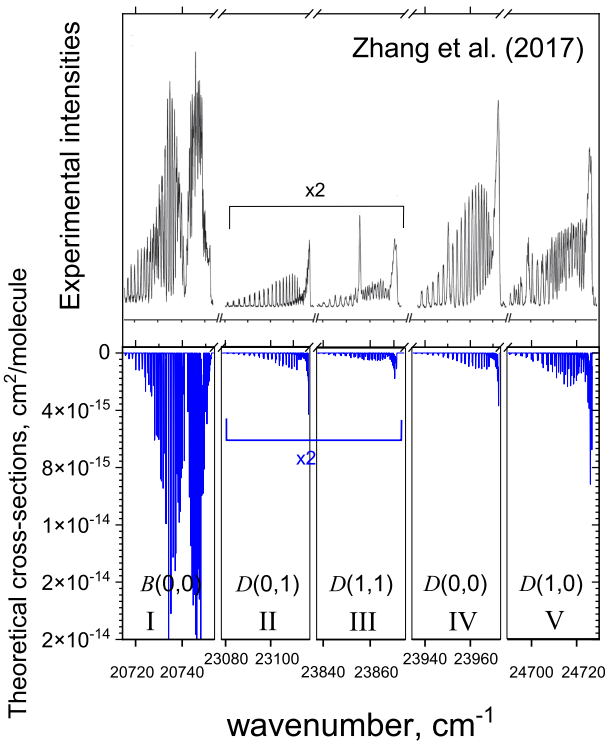

Figure 3.28: Comparison of our computed (bottom) $D^2\Sigma^+$–$X^2\Sigma^+$ absorption spectra to the measurements of Zhang et al.[254] (top). The simulations assumed a cold rotational temperature of T_{rot} = 50 K and a hot vibrational temperature of T_{vib} = 800 K. A Doppler line profile corresponding to T_{rot} = 50 K was used.

3.9.2 CO

Since, after hydrogen, CO is the second most abundant molecule in the universe[255,256], its spectrum is of astrophysical importance, e.g. for planetary atmospheres[257–259], interstellar space[260], exoplanetary and stellar atmospheres[261–266]. The CO spectrum is also important in plasma physics, laser physics, and combustion[267–269]. Indeed, some of the CO spectral bands are named after their signatures in plasmas. This means interpreting its spectral signature requires a thorough understanding of its absorption and emission properties, particularly of highly excited electronic states.

We report[270] a new accurate spectroscopic model for the ground and electronically-excited states of the CO molecule computed at the *ab initio* CASSCF/MRCI+Q level of theory. Of the investigated $A\,^1\Pi - X\,^1\Sigma^+$, $B\,^1\Sigma^+ - X\,^1\Sigma^+$, $C\,^1\Sigma^+ - X\,^1\Sigma^+$, and $E\,^1\Pi - X\,^1\Sigma^+$ band systems, I discuss here the $B\,^1\Sigma^+$ and $C\,^1\Sigma^+$ states which are characterised by multiple, near-vertical, avoided crossings. I then diabatise these states to obtain an accurate diabatic electronic structure model.

To the best of our knowledge, this is the first systematic theoretical spectroscopic study of highly excited states of the CO molecule.

3.9.2.1 Diabatisation

The highly excited states of CO exhibit strong nonadiabatic character, and so proper treatment of the non-Born-Oppenheimer effects must be taken into account for the accurate calculation of the CO UV spectroscopy. We identify three important states involved in the nonadiabatic coupling of the $^1\Sigma^+$ manifold, $B\,^1\Sigma^+$, $C\,^1\Sigma^+$, and $(IV)\,^1\Sigma^+$. The *ab initio* PECs of these three states are illustrated in Figure 3.29 which shows an avoided crossing between $C\,^1\Sigma^+/(IV)\,^1\Sigma^+$ at $r_c = 1.246$ Å and $B\,^1\Sigma^+/C\,^1\Sigma^+$at $r_c = 1.275$ Å. What is interesting about this system (and what makes it complex) is the near-vertical nature of the avoided crossings.

A proper treatment of the CO $[B\,^1\Sigma^+, C\,^1\Sigma^+, (IV)\,^1\Sigma^+]$ system would require *ab initio* calculation of the three NACs coupling these states, where a direct N-state diabatisation can be obtained through methods discussed extensively throughout this thesis. However, at the time of this project we lacked knowledge on the NAC calculations and on N-state diabatisations, and so we adopted the two-state property-based diabatisation approaches previously applied to the YO and CH systems in Section 3.2 (and also SO in Chapter 4). To do this, a two-step approach is required

- Perform a two-state diabatisation on the sub-manifold $[C\,^1\Sigma^+, (IV)\,^1\Sigma^+]$ to

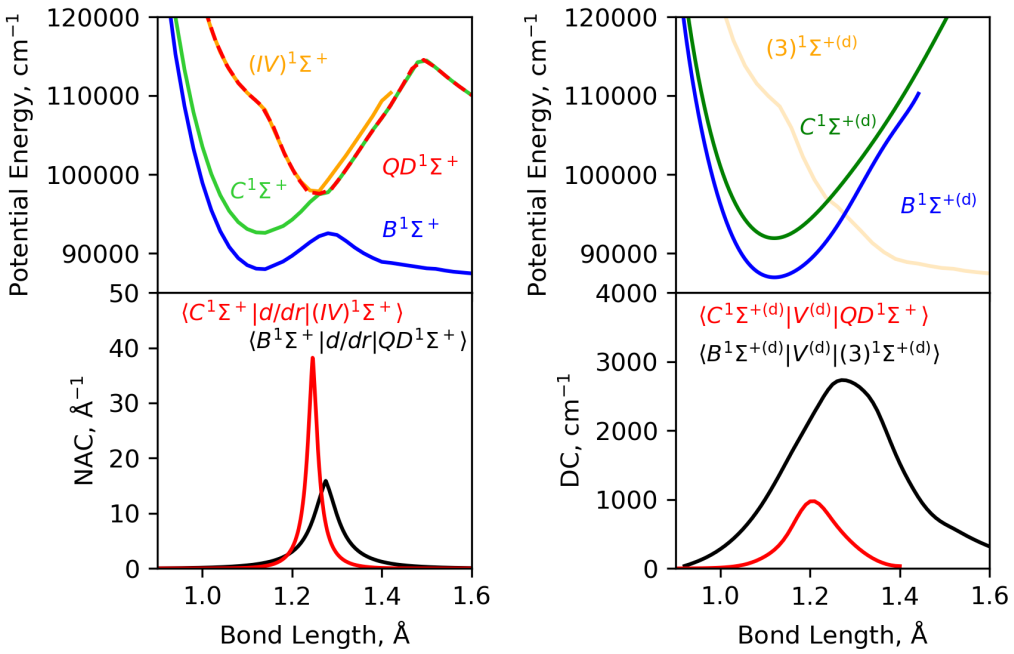

Figure 3.29: The *ab initio* PECs of the $B\,^1\Sigma^+$, $C\,^1\Sigma^+$, $(IV)^1\Sigma^+$ states are plotted as solid lines in the top left panel. A two step two-state property-based diabatisation (see text) yielded the optimised NACs shown in the bottom left plot, the diabatic PECs in the top right plot, and DCs in the bottom right plot. The diabatic model then serves the basis for rovibronic intensity calculations. The quasi-diabatic state $QD^1\Sigma^+$, the intermediary state for the applied two-step diabatisation approach, is plotted as a red dashed line in the top left panel.

yield quasi-diabatic states. The lowest quasi-diabatic state will be identified as the diabatic $C\,^1\Sigma^+$ state used in subsequent rovibronic calculations, and is illustrated in the top right panel of Figure 3.29.

- The upper quasi-diabatic state $QD^1\Sigma^+$, illustrated in the top left panel of Figure 3.29 (red dashed), will be used in a subsequent two-state diabatisation with the adiabatic $B\,^1\Sigma^+$ state. The lowest component of this second diabatisation is identified as the diabatic $B\,^1\Sigma^+$ state illustrated in Figure 3.29, and the upper diabatic state is now a repulsive curve.

Within both property-based diabatisations, NACs are optimised to yield the smoothest diabatic PECs, and can be seen plotted in Figure 3.29. The subsequent DCs are also illustrated in the bottom right panel of Figure 3.29.

Using these NACs, the transition DMCs connecting $X\,^1\Sigma^+$ with $B\,^1\Sigma^+$ and $C\,^1\Sigma^+$ are diabatised and are used in the intensity calculations in Section 3.9.2.2. The diabatic PECs are then fitted to experimentally derived energy levels. For more details, see discussions in Khalil et al.[270].

3.9.2.2 Intensity Calculations

As demonstrated throughout this chapter, the adiabatic and diabatic representations are exactly equivalent – yielding identical rovibronic energies, wavefunctions, and intensities – when all nonadiabatic couplings are fully encountered. However, adiabatic models often omit the NACs to reduce the computational cost of their integration and analytical fitting[271]. The adiabatic spectrum of CO has been computed using adiabatic PECs, TDMCs, with NACs omitted. The diabatic CO spectrum is computed including and excluding DCs. Comparisons of these spectra then reveal some interesting properties of the diabatic representation.

Figure 3.30 compares the adiabatically and diabatically computed $C\,^1\Sigma^+ - X\,^1\Sigma^+$ $v = 0 - 0$ band system with the experimental spectrum of Ubachs et al.[272]. There are noticeable differences between the adiabatically computed spectra and experiment: The (0-0) band peak shows a shift of about 0.137 nm in the line position, while the fundamental (1-0) peak position is shifted by about 0.187 nm (see Figure 20 of Khalil et al.[270]). The diabatic bands, however, show excellent agreement to the experimental band, with a line position difference < 0.0048 nm for the (0-0) peak and 0.0034 for the (1-0) peak. Even with omission of the DC, the computed diabatic band intensities generally agree well, but less than the fully coupled case due the strong DC (975.6121 cm^{-1}). Thus, the uncoupled diagonal diabatic potentials are a significantly better approximation to the spectroscopy of this system than the adiabatic representation with no NAC. In this case, it is clear the diabatic representation is a more physical representation than the adiabatic picture.

3.10 Summary

The work of this Chapter demonstrates the numerical equivalence of adiabatic and diabatic representations in nuclear motion calculations for multi-state diatomic systems, using Duo as a benchmark tool. I validate this equivalence for several systems, including N_2, CH, YO, and an artificial 10-state model, by comparing rovibronic energies and radial reduced densities computed in both representations. My results confirm that a strict diabatic representation – where all derivative couplings vanish – is achievable regardless of the number of states considered.

A key finding is the crucial role of NACs, DBOCs, and DCs in ensuring numerical consistency between the two representations. Omitting these terms leads to deviations of up to 10^2 cm^{-1}, making them essential for high-resolution spectroscopy. Notably, the diagonal derivative coupling, often neglected, is shown to significantly impact computed spectra. Moreover, I highlight the limitations of the

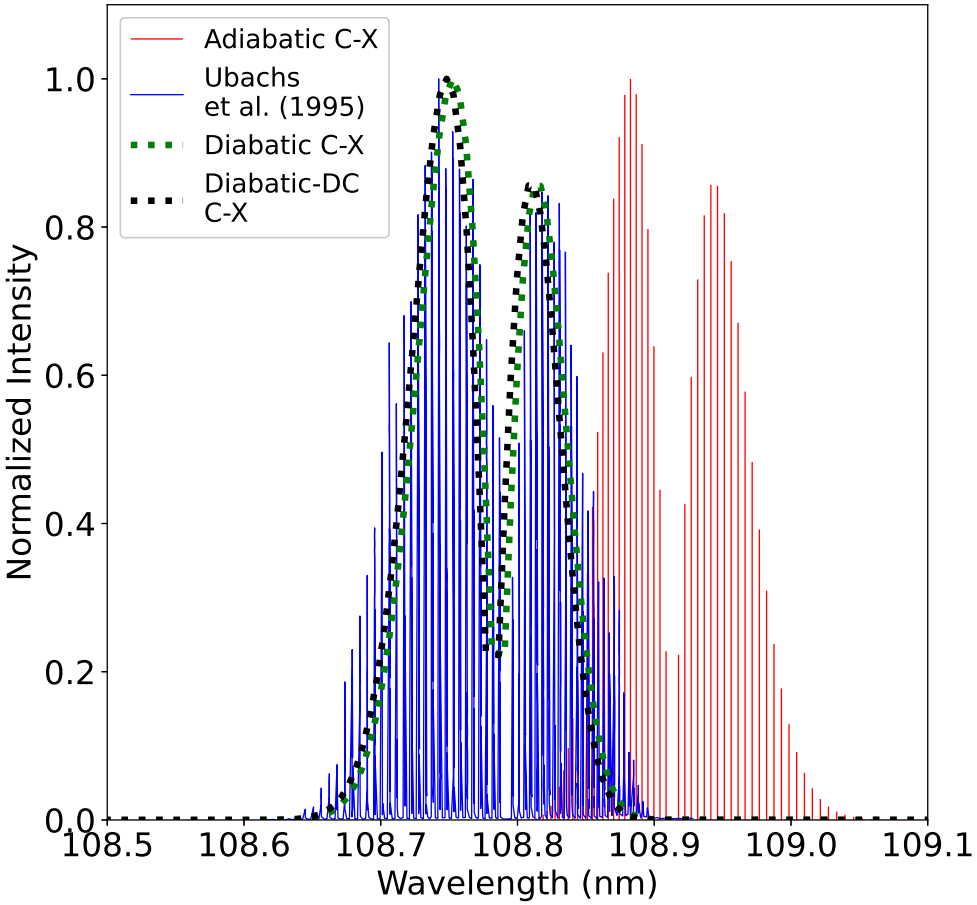

Figure 3.30: Comparison between the adiabatic and diabatic representations of the (0-0) $C\,^1\Sigma^+ - X\,^1\Sigma^+$ band and with Ubachs et al.[272] experiment.

commonly used two-state approximation, demonstrating that truncating the number of adiabatic states without quantitative validation introduces substantial errors, even when considering nine out of ten states in a multi-state model.

I further introduce a hybrid-asymptotic-property-based (HyAP) diabatisation scheme for N-state systems, applied here to N_2, CH, and a 10-state model, which ensures a smooth diabatic representation with sensible asymptotic behavior while maintaining exact equivalence to the adiabatic framework. The aim of developing HyAP was to allow the construction of practical, but accurate, diabatic states such that, for example, an efficient contracted rovibronic basis can be constructed to solve the fully coupled problem. Despite inherent challenges such as asymptotic misbehavior and topological discontinuities, these issues are mitigated through a

regularisation approach optimising switching functions on the exponential mapping of the AtDT – yielding regularised NACs. My method successfully removes all derivative couplings from the nuclear kinetic energy and provides a robust framework for modelling diatomic rovibronic spectra.

Beyond validating diabatic and adiabatic equivalency, the work presented in this chapter underscores that the preferable representation depends on the system: adiabatic models converge faster when NACs are small, whereas diabatic representations are more efficient for systems with strong NACs. The methodologies developed here lay the groundwork for extending these concepts to polyatomic molecules, where full removal of derivative couplings is not always possible.

The presented findings reinforce the importance of carefully considering all coupling terms and basis truncations in high-resolution molecular spectroscopy. The methodologies and benchmarks provided by Duo offer a reliable platform for future investigations into diabatisation strategies and non-adiabatic effects in molecular systems.

Chapter 4

A Spectroscopic Model and Rovibronic Line List for Sulfur Monoxide: SOLIS

4.1 Introduction

From the fiery hearts of volcanoes to the frosty depths of interstellar space, sulfur monoxide (SO) leaves its mark on a remarkably diverse range of environments. SO plays a key role as an intermediate in the oxidation of sulfur compounds, particularly within combustion processes, making it central to environmental chemistry due to its contribution to atmospheric acidification and pollution[273–277,141]. Its high reactivity and interactions with N_2 and O_2 further stress' its importance within atmospheric chemical reactions[141]. Astrophysically, SO was first detected by radio astronomy in the interstellar medium by means of rotational spectroscopy and was the first $^3\Sigma$ ground state molecule to be detected in outer space[278]. Additionally, SO was the first molecule observed using pure rotational transitions via microwave spectroscopy within its excited electronic states[279]. Since its first detection, SO has been observed in an array of astronomical environments. For example, in interstellar clouds[278,280], molecular clouds[281,282], planetary, and lunar atmospheres[283–286]. It is proposed by numerous studies that sulphur-bearing molecules, including SO, are important constituents of volcanic planetary atmospheres[287–289]. Consequently, SO is seen to play a role in many solar-system atmospheres, including that of Jupiter's moon Io[283,284] and of Venus[285,286]. SO's presence in planetary atmospheres could be linked with its presence within protoplanetary disks[290], where studies suggest sulphur-carrier based dust-formation channels may lead to planetary formation[291,292]. SO is now also expected to be present in regions where photochemistry is important. For example, the recent detection of SO_2 in the atmo-

sphere of the hot-Jupiter WASP-39b[293] suggests SO to be part of the photochemical production pathway of SO_2 and has been detected in this object[294]. It is in these studies that our SO line list, SOLIS, has been applied and is discussed later this chapter. Additionally, Zeeman splitting has been used to probe the magnetic fields of dense star-forming regions, such as the Orion molecular cloud, for field strengths $\geq 10^{-2}$ G[295,296] and its presence within warm chemistry's mean it is an excellent shock tracer[297,298]. Recently, our SO line list was utilised in a chemical evolution model which predicted detectable levels of SO in Type Ibc supernovae[1]. SO formation was determined to influence the ejecta's temperature and spectra, with the 8.7μm fundamental band feature a potential target for JWST observations. Experimentally, UV lasing has been demonstrated by SO[299,300], making it of spectroscopic interest.

Because of SO's diverse observational applications, an accurate description of its rovibronic structure is of central importance. The frontier orbitals of SO resemble that of carbon monoxide where the two π^* valence electrons mean SO has a $X\,^3\Sigma^-$ ground state similar to O_2 and S_2. Being isoelectronic with O_2, SO has two low-lying metastable $a\,^1\Delta$ and $b\,^1\Sigma^+$ states which are relatively short lived due to large spin-orbit coupling. To achieve a complete rovibronic description of SO, collaborator Gap-Sue Kim calculated *ab initio* potential energy curves (PECs), spin-orbit curves (SOCs), electronic angular momentum curves (EAMCs), and electric (transition) dipole moment curves ((T)DMCs) for the 13 lowest electronic states of SO ($X\,^3\Sigma^-$, $a\,^1\Delta$, $b\,^1\Sigma^+$, $c\,^1\Sigma^-$, $A'\,^3\Delta$, $A''\,^3\Sigma^+$, $A\,^3\Pi$, $B\,^3\Sigma^-$, $C\,^3\Pi$, $d\,^1\Pi$, $e\,^1\Pi$, $C'\,^3\Pi$, $(3)\,^1\Pi$) at an MRCI level of theory using aug-cc-pV5Z basis sets[13]. The relative phases of the the non-diagonal couplings and transition dipole moments provided are fully self-consistent[301] which is crucial for reproducible spectroscopic studies. Our *ab initio* curves are adiabatic as computed under the Born-Oppenheimer approximation[2] and so the spatially degenerate states $e\,^1\Pi$, $(3)\,^1\Pi$ and $C\,^3\Pi$, $C'\,^3\Pi$ exhibit avoided crossings due to their shared symmetries, where non-adiabatic effects play important role (see Chapter 2 for details). I obtain a set of NACs, and therefore a diabatisation, for the two mentioned 2-state systems via the property-based diabatisation method, where I explored – for the first time during my PhD – the use of diabatic and adiabatic curves in rovibronic calculations. It is in the spectroscopic characterisation of SO where my journey into studying diatomic non-adiabatic interactions begun.

The literature also contains many theoretical studies of SO[302–323,307,324], the most comprehensive, and one I compare to often, being Yu and Bian[312] who give spectroscopic constants on all electronic states considered here (except $(3)\,^1\Pi$) com-

puted through internally contracted multireference configuration interaction (ic-MRCI) methods using aug-cc-pV5Z basis sets. Another important theoretical work is by Sarka and Nanbu [325] who study the UV region of SO non-adiabatically where they compute PECs, DMCs, and non-adiabatic couplings (NACs) for the $X\,^3\Sigma^-$, $A\,^3\Pi$, $B\,^3\Sigma^-$, $C\,^3\Pi$, $C'\,^3\Pi$, $(3)^3\Sigma^-$, $(4)^3\Pi$, and $(5)^3\Pi$ states at a MRCI-F12+Q level of theory using aug-cc-pV(5+d)Z basis sets. Sarka and coworkers [325] are also the first to compute cross-sections for SO down to 190 nm in the UV.

Experimentally, the SO spectrum for the $X\,^3\Sigma^-$ $a\,^1\Delta$, $b\,^1\Sigma^+$, $A\,^3\Pi$– at low vibrational excitation's – $B\,^3\Sigma^-$, and $C\,^3\Pi$ electronic states has been studied by numerous works, where I provide a full analysis of the experimental coverage on SO in Section 4.12. SO's electronic transitions were first reported by Martin (1932) [326], and has since been subject to pure rotational [327,328], electronic [329–331], and rovibrational [332–334] spectroscopic studies. The pure rotational transitions within several vibrational states in the ground $X\,^3\Sigma^-$ electronic state have been measured in the terahertz [139,335], far infrared [336,337], and microwave regions [328,338,339]. More recently, Bernath et al. [340,341] produced empirical line lists for SO's $b\,^1\Sigma^+$–$X\,^3\Sigma^-$, $a\,^1\Delta$–$X\,^3\Sigma^-$, $X\,^3\Sigma^-$, and $a\,^1\Delta$ rovibronic bands. For most of these recorded spectra, SO was studied in non-local thermodynamic equilibrium (non-LTE) conditions, and so only relative intensities are available at best. Currently, to the best of my knowledge, only Heays et al. [140] have provided absolute spectral intensities for SO. However, measurements of state lifetimes provide information on Einstein A coefficients and hence transition dipole moments [342]. Experimental lifetimes for the $b\,^1\Sigma^+$, $A\,^3\Pi$ and $B\,^3\Sigma^-$ states have been measured [343–345], and provide a valuable benchmark for my intensity calculations (see 4.14.1).

In this chapter I present the largest compilation of experimental transition data and derived self-consistent empirical rovibrational energy levels for $^{32}S^{16}O$ to date. The derived energy levels where obtained through use of the MARVEL (Measured-Active-Rotational-Vibrational-Energy-Levels) spectroscopic network algorithm, to which the $^{32}S^{16}O$ data is formatted based on the MARVEL format [156]. The *ab initio* spectroscopic model [13] can then be refined to the determined empirical energies to produce a hot semi-empirical line list SOLIS for $^{32}S^{16}O$ as part of the ExoMol project [53,54]. The SOLIS line list supplements existing spectroscopic line list data for SO which are limited in coverage. For example, spectroscopic databases CDMS [346] and NIST [347] databases contain data covering the microwave region only. HITRAN [348] considers relatively low vibrational excitations for transitions between electronic states $X\,^3\Sigma^-$, $a\,^1\Delta$ and $b\,^1\Sigma^+$ only. The SOLIS line list is compared to the existing spectra data in Section 4.14.5.

4.2 Computational Details

Initially, internally-contracted multi-reference configuration interaction (icMRCI) *ab initio* calculations for the 13 lowest singlet and triplet states of SO correlating with S(^{3}P) + O(^{3}P), S(^{1}D) + O(^{3}P) and S(^{1}D) + O(^{1}D) were performed by collaborator Gap-Sue Kim using MOLPRO[349] with aug-cc-pV5Z basis sets[350,351]. Molecular orbitals were optimised using prior obtained state-averaged complete active space self-consistent field (CASSCF) calculations. Under C_{2V} point group symmetry all *ab initio* calculations started with 14 (8σ, $3\pi_x$, $3\pi_y$) orbitals which included 6 closed (4σ, $1\pi_x$, $1\pi_y$) orbitals. The active space occupying 12 active electrons consisted of 8 (5σ–8σ,2π,3π) valence orbitals. The PECs, including the 8 bound states $X\,^3\Sigma^-$, $a\,^1\Delta$, $b\,^1\Sigma^+$, $c\,^1\Sigma^-$, $A''\,^3\Sigma^+$, $A'\,^3\Delta$, $A\,^3\Pi$, and $B\,^3\Sigma^-$ are shown in Figure 4.1, as well as the adiabatic $e\,^1\Pi$ - $(3)\,^1\Pi$ and $C\,^3\Pi$ - $C'\,^3\Pi$ systems. The EAMC, SOCs (both diagonal and non-diagonal), DMCs (diagonal and transition) computed are shown in Figures. 4.2 – 4.6 in the original adiabatic representation as computed by MOLPRO 2015[349] (left) and the diabatic representation (right). Further discussion of the diabatisation is given in the next section.

I note here that I later performed further *ab initio* calculations with the same theory method and active space described above to supplement the *ab initio* model. Additional $\langle b\,^1\Sigma^+|\,\mathrm{SO}_x\,|A\,^3\Pi\rangle$, $\langle a\,^1\Delta|\,\mathrm{SO}_x\,|A\,^3\Pi\rangle$, $\langle e\,^1\Pi|\,\mathrm{SO}_z\,|A\,^3\Pi\rangle$ (diabatised), $\langle d\,^1\Pi|\,\mathrm{SO}_z\,|A\,^3\Pi\rangle$, and $\langle c\,^1\Sigma^-|\,\mathrm{SO}_x\,|A\,^3\Pi\rangle$ spin-orbit couplings are computed, originally missing in the initial set of calculations. These SOCs were identified as either important upon refinement of the *ab initio* model to our MARVEL dataset, in study of the $b\,^1\Sigma^+$–$X\,^3\Sigma^-$band intensity, or required for completeness.

Table 4.1 lists the quantum numbers used to label the electronic states in the following sections. All electronic states of SO studied in this chapter are either triplet ($S=1$) or singlet ($S=0$) multiplets in the Σ^- ($\Lambda=0$), Σ^+ ($\Lambda=0$), Π ($\Lambda=1$), and Δ ($\Lambda=2$) manifolds.

Quantum Number	Description
$2S+1$	The spin-multiplicity with total electron spin S
Λ	Electronic orbital AM projection
Σ	Electronic spin AM projection
$\Omega=\Lambda+\Sigma$	The total electronic AM projection
$\pm$	Planar reflection symmetry about the internuclear axis

Table 4.1: Quantum numbers used in description of the molecular term symbol $^{2S+1}\Lambda^{\pm}_{\Omega}$. 'AM' refers to angular momentum and its projection is onto the internuclear axis.

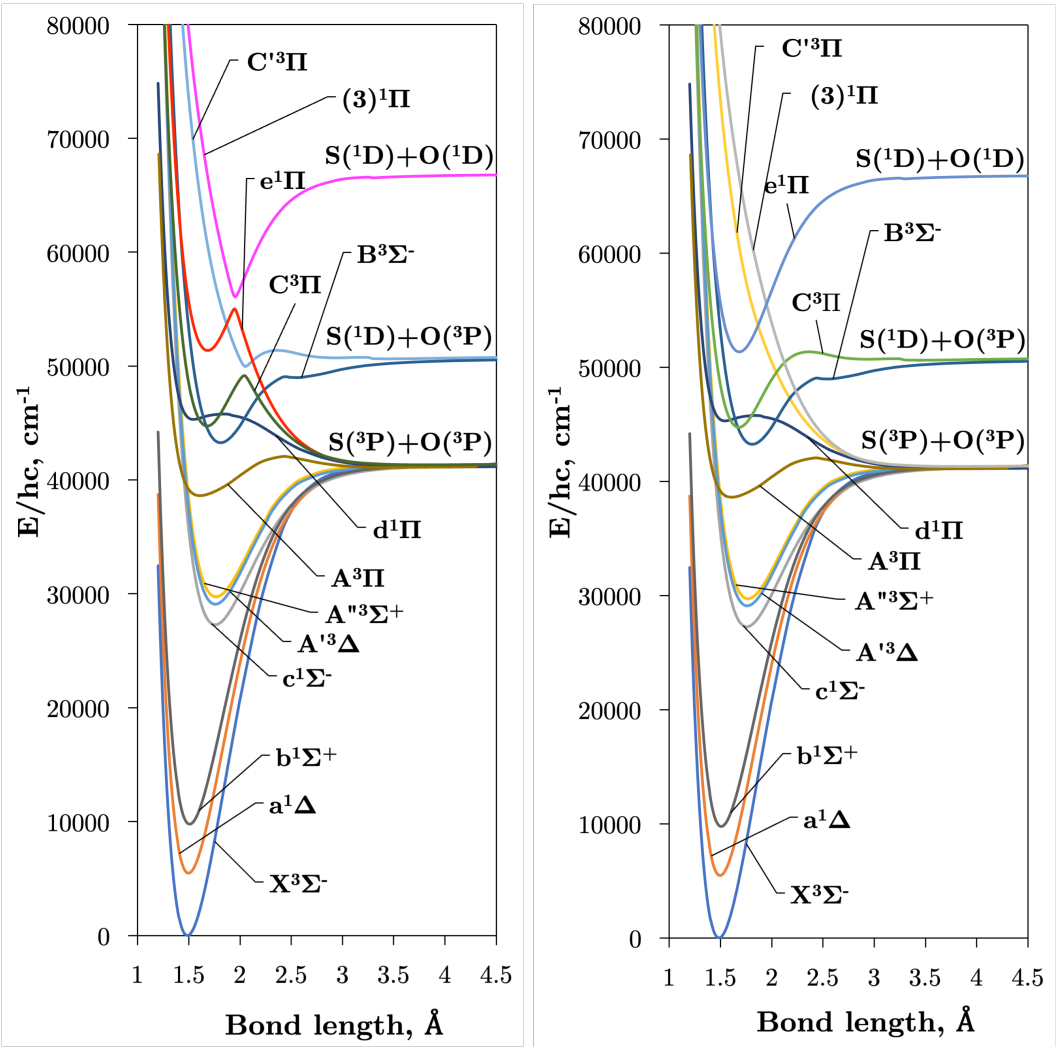

Figure 4.1: Plots of our 13 adiabatic (left) and diabatised (right) *ab initio* PECs covering the first 7 triplet and 6 singlet electronic states up to 80,000 cm^{-1}.

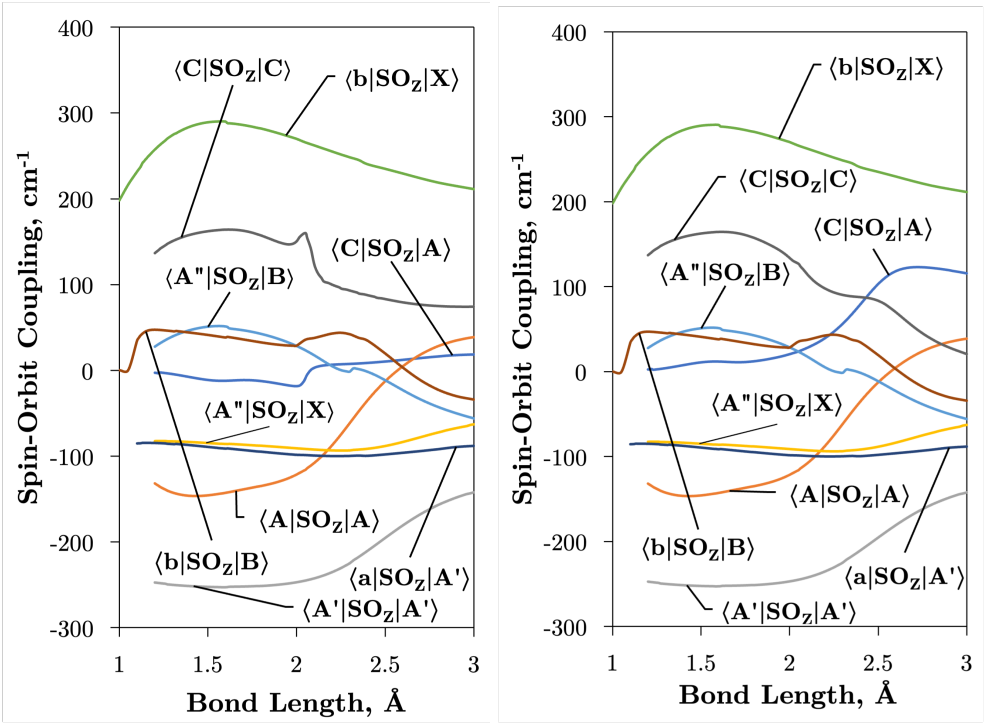

Figure 4.2: Adiabatic (left) and diabatic (right) *ab initio* spin-orbit curves between states of the same Λ as a function of bond length.

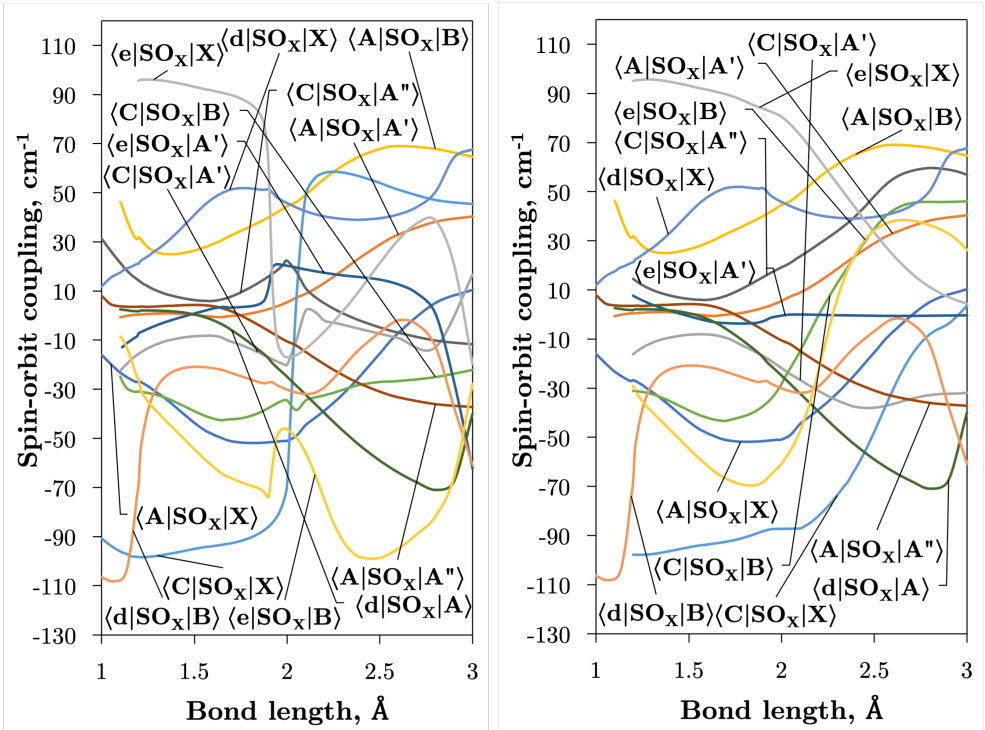

Figure 4.3: *Ab initio* spin-orbit MOLRPO matrix elements in the adiabatic (left) and diabatic (top right) representations between states of different values of Λ as a function of bond length.

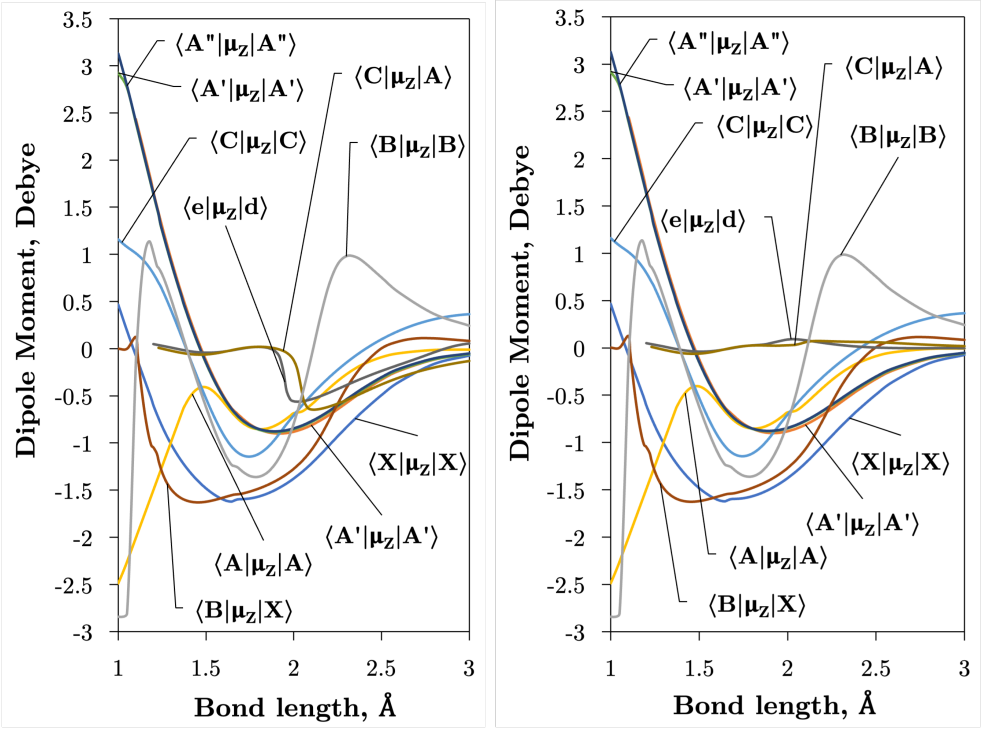

Figure 4.4: Adiabatic (left) and diabatic (right) *ab initio* (transition) dipole moment matrix elements between states of the same symmetry (Λ and multiplicity).

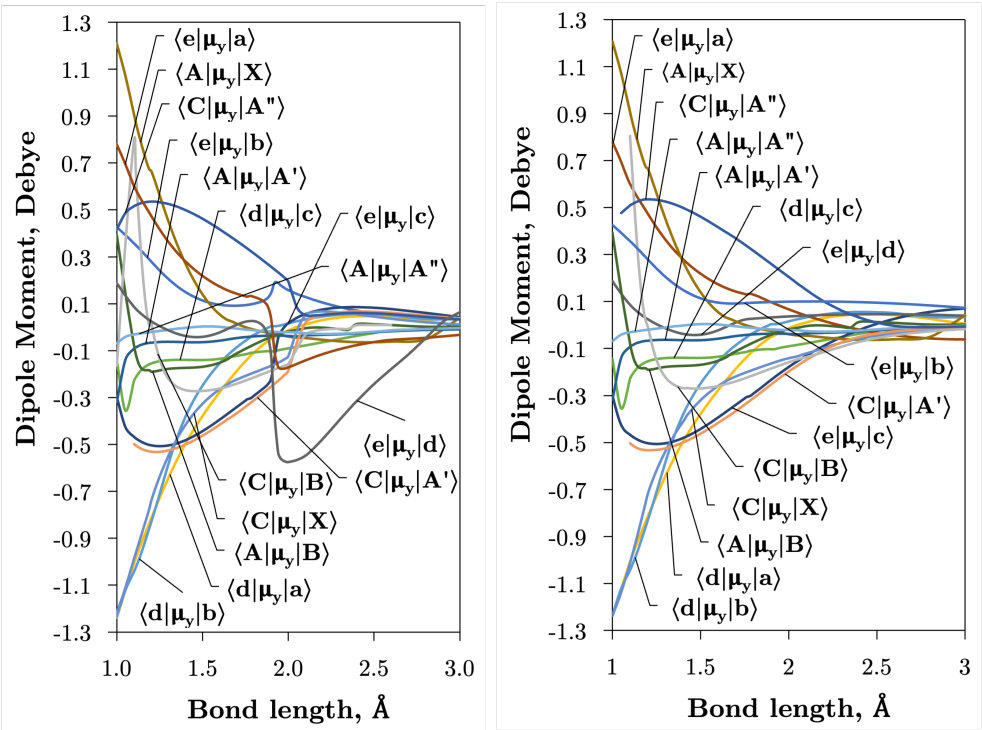

Figure 4.5: Adiabatic (left) and diabatic (right) *ab initio* transition dipole moment curves (Debye) between states of different symmetry as a function of the bond length.

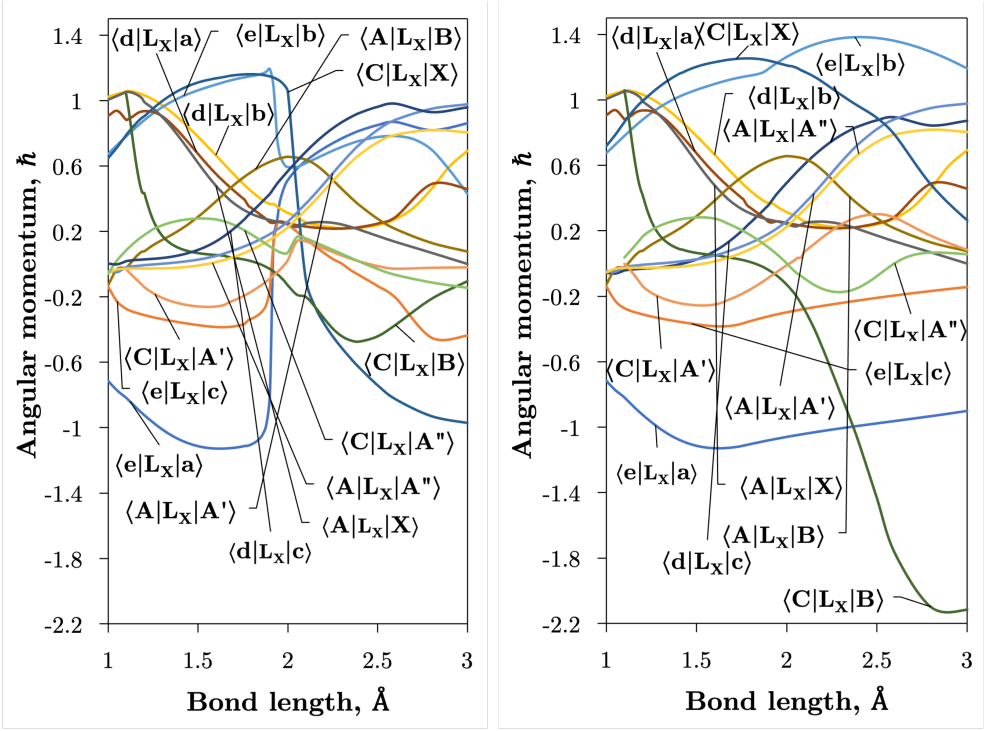

Figure 4.6: *Ab initio* electronic angular momentum curves in the adiabatic (left) and diabatic (right) representation plotted as a function of bond length. L_x means the cartesian x-component of the electronic angular momentum.

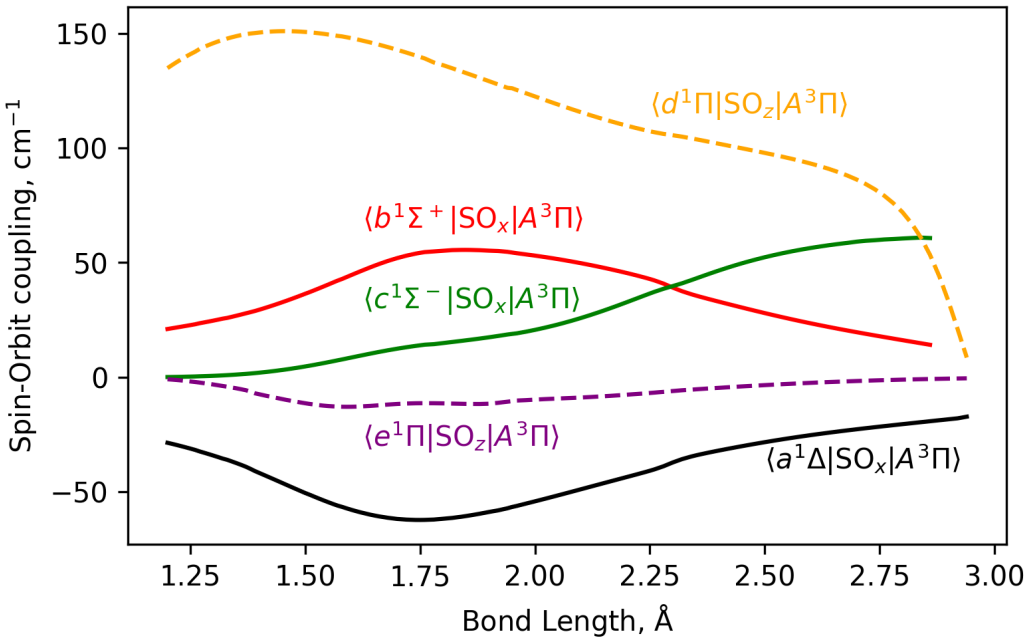

Figure 4.7: Additional computed *ab initio* SOCs (see text for details).

4.3 Diabatisation

A detailed description of the theory and methodology behind diabatisation can be found in Chapter 2, however, this section discusses a different formulation of the NAC used in the property-based diabatisation of the $e\,^1\Pi$ - $(3)^1\Pi$ and $C\,^3\Pi$ - $C'\,^3\Pi$ 2-state systems. Specifically, Section 2.5.1 of Chapter 2 details the theory behind 2-state diabatisations, where below the application of the theory directly within our SO model is summarised.

4.3.1 Analytical NACs and the 2-State AtDT

The transformation from the adiabatic to the diabatic representation is described by a unitary matrix U, which is parametrically dependent on the NAC term,

$$\mathbf{U}(\beta(r)) = \begin{bmatrix} \cos(\beta(r)) & -\sin(\beta(r)) \\ \sin(\beta(r)) & \cos(\beta(r)) \end{bmatrix}, \tag{4.1}$$

where the mixing angle $\beta(r)$ is obtained by integrating the functional form of the non-adiabatic derivative coupling $W_{12}(r) := \langle \psi_1 | \frac{d}{dr} | \psi_2 \rangle$ [164–166,20]

$$\beta(r) = \int_{-\infty}^{r} W_{12}(r')dr' \tag{4.2}$$

with $|\psi_1\rangle$ and $|\psi_2\rangle$ being the lower and upper energy electronic wavefunctions in the adiabatic representation. The lower limit of the integral here is $-\infty$ rather than 0 because the functional forms of the NAC extend over all regions of the independent variable r. As will be seen below, the functional forms are not zero for $r \leq 0$, this is simply an artifact of the approximation made when representing the NAC with a mathematical function. In all practical use cases, this is not a problem where I wish to simply parametrise the NAC, mixing angle, and subsequently the AtDT.

Writing the two-state electronic Hamiltonian in terms of the adiabatic potential energy curves $V_1^{\mathrm{a}}(r)$ and $V_2^{\mathrm{a}}(r)$,

$$\mathbf{V}^{\mathrm{a}}(r) = \begin{pmatrix} V_1^{\mathrm{a}}(r) & 0 \\ 0 & V_2^{\mathrm{a}}(r) \end{pmatrix}, \tag{4.3}$$

The diabatic electronic Hamiltonian is obtained by applying the unitary transforma-

tion $\mathbf{U}(\beta(r))$,

$$\mathbf{V}^{\mathrm{d}}(r) = \mathbf{U}^{\dagger}\mathbf{V}^{\mathrm{a}}(r)\mathbf{U} = \begin{pmatrix} V_1^{\mathrm{d}}(r) & V_{12}^{\mathrm{d}}(r) \\ V_{12}^{\mathrm{d}}(r) & V_2^{\mathrm{d}}(r) \end{pmatrix} = \begin{bmatrix} V_1^{\mathrm{a}}\cos^2\beta + V_2^{\mathrm{a}}\sin^2\beta & \frac{1}{2}(V_2^{\mathrm{a}} - V_1^{\mathrm{a}})\sin(2\beta) \\ \frac{1}{2}(V_2^{\mathrm{a}} - V_1^{\mathrm{a}})\sin(2\beta) & V_1^{\mathrm{a}}\sin^2\beta + V_2^{\mathrm{a}}\cos^2\beta \end{bmatrix}, \quad (4.4)$$

where the superscripts 'd' and 'a' refer to the diabatic and adiabatic bases, respectively, and the off-diagonal elements $V_{12}^{\mathrm{d}}(r)$ are the DCs. The reverse transformation is obtained by diagonalising the diabatic electronic Hamiltonian.

The NAC can be computed via quantum-chemistry methods from the electronic wavefunctions, as done by Sarka and Nanbu[325] for SO. It is approximately symmetrical with a cusp at the crossing point r_{c}. Alternatively, the NAC curves are modeled using, e.g. a Lorentzian[26], as given by

$$W_{ij}(r) = W_{ij}^{\mathrm{Lo}}(r;\alpha,r_{\mathrm{c}}) = \frac{1}{2}\frac{\alpha}{1+\alpha^2(r-r_{\mathrm{c}})^2}, \quad (4.5)$$

where α is the inverse half-width-at-half-maximum (HWHM), or a Laplacian

$$W_{ij}(r) = W_{ij}^{\mathrm{La}}(r;\gamma,r_{\mathrm{c}}) = \frac{\pi}{4\gamma}\exp\left[-\frac{|r-r_{\mathrm{c}}|}{\gamma}\right], \quad (4.6)$$

where γ is a damping constant related to the FWHM, superscripts 'Lo' and 'La' mean Lorentzian and Laplacian respectively, and the normalisation $\int_{-\infty}^{\infty} W_{12}(r)\,dr = \pi/2$ is applied. Figure 4.8 illustrates the $C\,^3\Pi$ –$C'\,^3\Pi$ NAC modelled in this work using a Lorentzian and Laplacian function. The mixing angle $\beta(r)$, determined through Eq. (4.2), ranges from 0 to $\pi/2$ going through $\pi/4$ at the crossing point $r = r_{\mathrm{c}}$ which can also be seen in Figure 4.8.

The Lorentzian was shown to provide a good description of the *ab initio* NACs around the crossing point[170,171,165,166] (see Figure 4.8) but diverges at large distances r from r_{c} causing improper shaped diabatic PECs by decaying too slowly[165,166,170,352]. It has been discussed that some damping functions can be introduced to correct the Lorentzian's slow decay using properties such as dipole moments, but determination of their fitting parameters is both difficult and requires extra calculations[170,26]. Laplacians underestimate NACs far in the wings and overestimate them near the crossing point[165]. One can show that NACs have an overlap dependence on the internuclear separation[170,353], r, which is given properly by a Laplacian[165]. The undesirable features of these NAC models can be mitigated by

their combination [165,166,170,352] to which I base my diabatisation procedure of SO on. The used method of augmenting the Lorentzian with a Laplacian is discussed in section 4.3.2.

4.3.2 Mixing Angle from a Geometric Average of DCs

The 'property based diabatisation' method [20] is explored below (see discussions in Chapter 1 and Section 2.8.5 of Chapter 2), where diabatic potentials are constructed using the condition of having no avoiding crossing, which I define as to minimise their second derivatives in the vicinity of the crossing point r_c:

$$\mathscr{F} = \sum_r \frac{d^2 V_i^{\mathrm{d}}(r)}{dr^2} \to 0, \tag{4.7}$$

hence creating the smoothest PECs $V_1^{\mathrm{d}}(r)$ and $V_2^{\mathrm{d}}(r)$. This is, however, easily generalisable to any diabatic property, such as dipoles. Section 4.3.3 details the algorithmic implementation of my property-based diabatisation.

In order to mitigate the undesirable properties of the Lorentzian and Laplacian functional forms of Eqns. (4.5,4.6), I follow the approach by An and Baeck [165] and represent the mixing angle β of Eq.(4.2) by the following combination of the mixing angles determined from the Lorentzian and Laplacian NACs (Eq.(4.2)), $\beta^{\mathrm{Lo}}(r)$ and $\beta^{\mathrm{La}}(r)$

$$\beta_{ij}^{\mathrm{ga}}(r) = \frac{1}{2}\arcsin\left(\sqrt{\sin(2\beta_{ij}^{\mathrm{Lo}}(r))\sin(2\beta_{ij}^{\mathrm{La}}(r))}\right), \tag{4.8}$$

where the 'ga' superscript refers to the geometrically averaged diabatic mixing angle (See Figure 4.8), the Lorentzian derived mixing angle $\beta^{\mathrm{Lo}}(r)$ is given by

$$\beta_{ij}^{\mathrm{Lo}}(r) = \frac{\pi}{4} + \frac{1}{2}\arctan(\alpha(r - r_c)), \tag{4.9}$$

and the Laplacian derived mixing angle $\beta^{\mathrm{La}}(r)$ is given by

$$\beta_{ij}^{\mathrm{La}}(r) = \begin{cases} \frac{\pi}{4}\exp(\frac{r-r_c}{\gamma}), & r < r_c \\ \frac{\pi}{4}, & r = r_c \\ \frac{\pi}{2} - \frac{\pi}{2}\exp(-\frac{r-r_c}{\gamma}), & r > r_c \end{cases}. \tag{4.10}$$

Equation (4.8) must not be taken as the geometric average of β^{Lo} and β^{La}, but rather originates from the simple geometric average of V_{12}^{Lo} and V_{12}^{La} [165]. From Eq.(16) of

An and Baeck [165], the following is obtained

$$\begin{aligned} V_{12}^{\mathrm{ga}} &= \sqrt{V_{12}^{\mathrm{d,Lo}} \cdot V_{12}^{\mathrm{d,La}}} \\ &= \sqrt{\frac{1}{2}(V_2^{\mathrm{a}} - V_1^{\mathrm{a}})\sin(2\beta^{\mathrm{Lo}}) \cdot \frac{1}{2}(V_2^{\mathrm{a}} - V_1^{\mathrm{a}})\sin(2\beta^{\mathrm{La}})} \\ &= \frac{1}{2}(V_2^{\mathrm{a}} - V_1^{\mathrm{a}})\sqrt{\sin(2\beta^{\mathrm{Lo}})\sin(2\beta^{\mathrm{La}})} \\ &= \frac{1}{2}(V_2^{\mathrm{a}} - V_1^{\mathrm{a}})\sin(2\beta^{\mathrm{av}}) \end{aligned}$$

where in the second line the matrix elements given in Eq.(4.4) are substituted. Comparing the last two lines, one can recover Eq.(4.8), the mixing angle that corresponds to the geometrically averaged DC is then

$$\begin{aligned} \sin(2\beta^{\mathrm{av}}) &= \sqrt{\sin(2\beta^{\mathrm{Lo}})\sin(2\beta^{\mathrm{La}})} \\ \rightarrow \beta^{\mathrm{av}} &= \frac{1}{2}\arcsin\left(\sqrt{\sin(2\beta^{\mathrm{Lo}})\sin(2\beta^{\mathrm{La}})}\right), \end{aligned}$$

which corresponds to Eq. (15) of An and Baeck [165]. An and Baeck [165] also showed that an optimal relation between the parameters α and γ exists which given by

$$\alpha \times \gamma = 1.397 \tag{4.11}$$

providing maximal overlap between the Lorentzian and Laplacian functions over the bond length.

Where my method diverges from that of An and Baeck [165] is in the determination of the crossing point r_{c} and the Lorentzian parameter α. An and Baeck [165] obtained r_{c} and α through fitting a Lorentzian to a NAC computed with MOLPRO. Instead, I determine a set of parameters $\{r_{\mathrm{c}}, \alpha\}$ by fulfilling the condition given in Eq.(4.7), to which the Laplacian parameter γ is instantly obtained through Eq.(4.11). Using the theory in section 4.3.1 and Eq.(4.8) the AtDT $\mathbf{U}^{\mathrm{ga}}$ corresponding to the 'geometrically averaged' NAC is found. With this the diabatic potential energies and DC elements can be obtained through the simple matrix transformation in Eq.(4.4). The diabatic PECs for SO can be seen in Figure 4.1 and a close-up of the avoided crossings between the $e\,^1\Pi$ – $(3)^1\Pi$ and $C\,^3\Pi$ – $C'\,^3\Pi$ states of SO superimposed with their DCs, V_{ij}^{ga}, and NACs, W_{ij}^{ga}, are illustrated in Figure 4.9.

Figure 4.9 shows that the pair of singlet states are coupled more strongly than the triplet states, and also reveals the DCs to be slightly asymmetric. This is to be expected since the DCs depend on the difference $V_2^{\mathrm{a}} - V_1^{\mathrm{a}}$ which can be asymmet-

rical in nature (see examples in Chapter 3). One sees an effect of this especially in the DC between the triplet states where the adiabatic PEC turning points are offset to each other by ~ 0.01 Å.

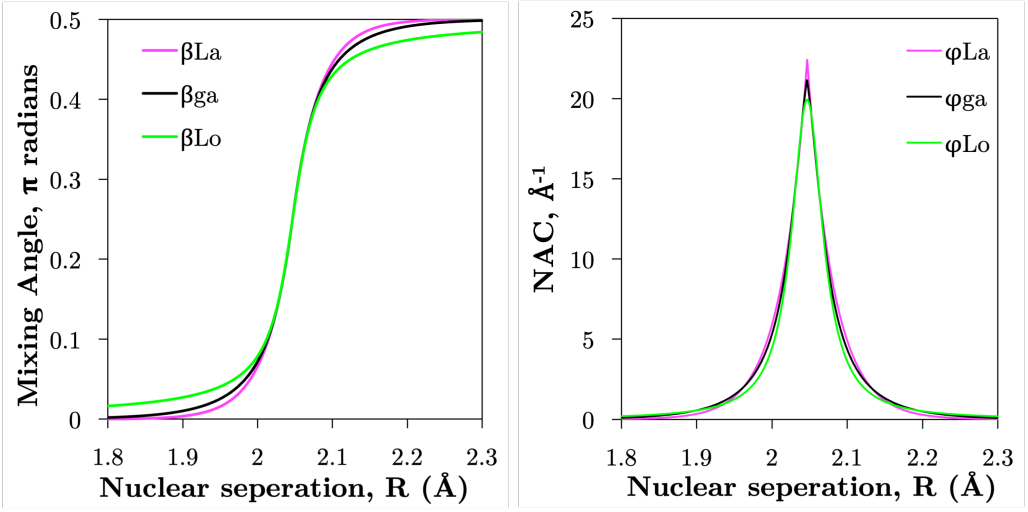

Figure 4.8: Comparison of example NACs (W_{ij}) and corresponding diabatic mixing angles (β) between the Lorentzian ('Lo'), Laplacian ('La'), and geometrically averaged ('ga') cases as described in the text. These curves are computed for the $C\,^3\Pi$ and $C'\,^3\Pi$ non-adiabatic interaction (see section 4.4 and Figure 4.1).

4.3.3 Diabatisation Procedure

To diabatise adiabatic couplings such as spin-orbit, or dipoles, one requires the operation of the AtDT given in Eq.(4.1). For some coupling, ζ, considering two adiabatically interacting states $|1\rangle$ and $|2\rangle$, the transformation for non-diagonal couplings $\langle i|\,\zeta\,|k\rangle$, where $i \in \{1,2\}$ and $k \neq 1,2$, from the adiabatic ('a') to the diabatic ('d') representation can be found as follows

$$\begin{bmatrix} \langle 1|\,\zeta\,|k\rangle \\ \langle 2|\,\zeta\,|k\rangle \end{bmatrix}^{d} = \mathbf{U}^{\dagger} \begin{bmatrix} \langle 1|\,\zeta\,|k\rangle \\ \langle 2|\,\zeta\,|k\rangle \end{bmatrix}^{a}. \tag{4.12}$$

To diabatise diagonal couplings one requires inclusion of the off-diagonal counterparts, which transforms similarly to the elecronic Hamiltonian as,

$$\mathscr{D}^{\mathrm{d}} = \begin{bmatrix} \langle 1|\,\zeta\,|1\rangle^{\mathrm{d}} & \langle 1|\,\zeta\,|2\rangle^{\mathrm{d}} \\ \langle 2|\,\zeta\,|1\rangle^{\mathrm{d}} & \langle 2|\,\zeta\,|2\rangle^{\mathrm{d}} \end{bmatrix} = \mathbf{U}^{\dagger} \begin{bmatrix} \langle 1|\,\zeta\,|1\rangle^{a} & \langle 1|\,\zeta\,|2\rangle^{a} \\ \langle 2|\,\zeta\,|1\rangle^{a} & \langle 2|\,\zeta\,|2\rangle^{a} \end{bmatrix} \mathbf{U} = \mathbf{U}^{\dagger} \mathscr{D}^{\mathrm{a}} \mathbf{U}$$

The computational procedure for performing the diabatisation is straightforward, and is based on the heuristic that the diabatisation should result in smoothly varying potential energy curves that are twice differentiable due to the properties of the

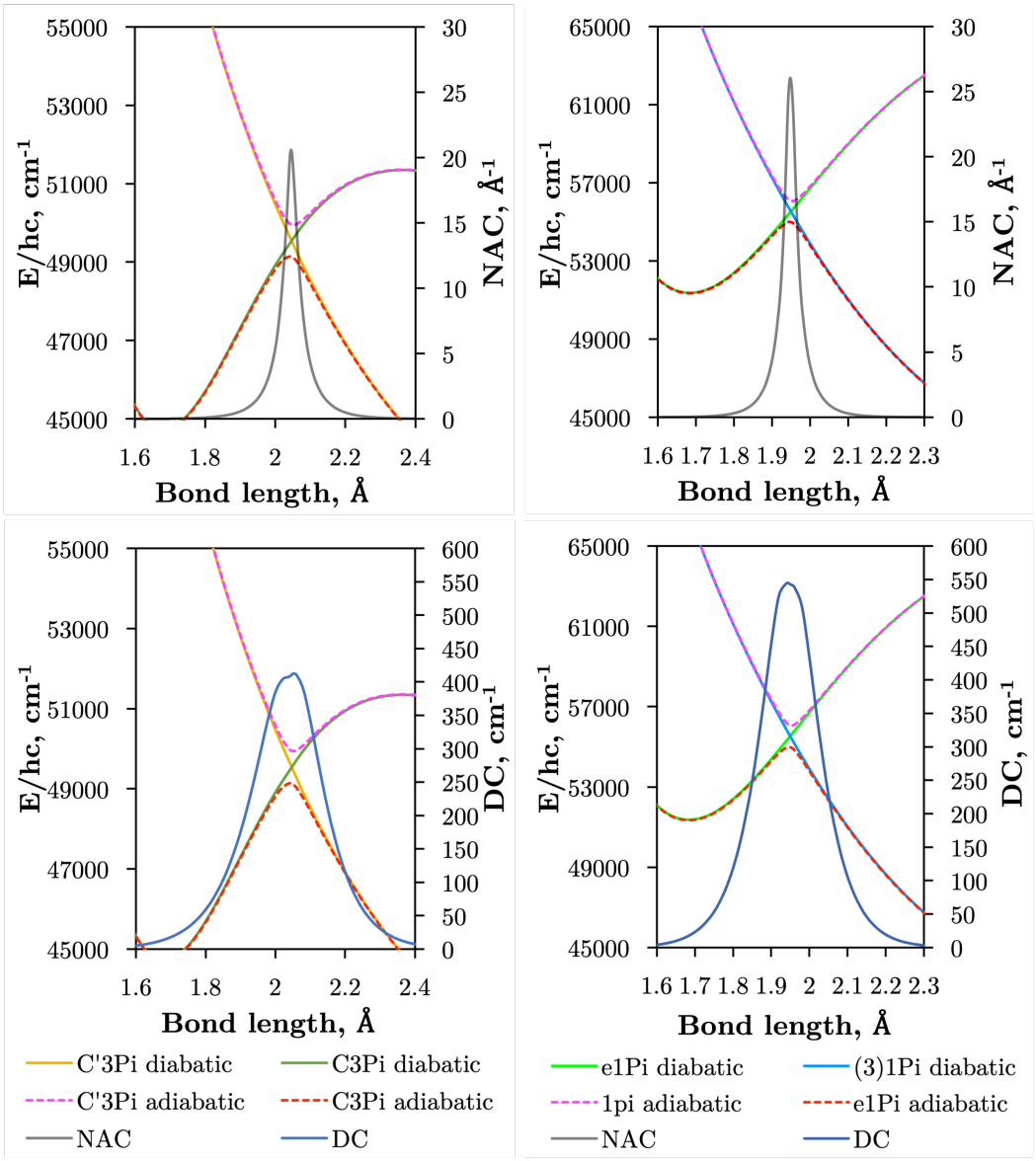

Figure 4.9: Illustration of the avoided crossings between $e\,^1\Pi$ - $(3)^1\Pi$ and (right panels) and $C\,^3\Pi$ - $C'\,^3\Pi$ states of SO (left panels) are shown, where adiabatic PECs are presented as dashed lines and diabatic ones in solid lines. Superimposed are the DCs (V_{12}^{ga}, bottom panels), and NACs (W_{ij}^{ga}, top panels).

wave function and derivatives. For a function represented by a discrete grid of points V_i at geometries r_i, gradients are calculated via finite differences and the task of satisfying this criterion is approximated by minimising the sum of second derivatives of the function.

To achieve this I optimise the parameters of an arbitrary NAC function, $W(r;\{p\})$. The parameters $\{p\}$ are typically: a central geometry r_{c}, and a characteristic width ω (see e.g Equations (4.5) and (4.6)). The NAC function, in turn,

parameterises the transformation from the adiabatic potential energy operators $\mathbf{V}_i^{\mathrm{a}}$ to the diabatic potential energy operators $\mathbf{V}_i^{\mathrm{d}}$ at each geometry i, as described by Equation (4.4).

The optimisation itself is easy to achieve using any commonly available optimisation libraries. I use the Julia programming language and the open-source Optim library's `Optim.minimizer` function to minimise the following loss function using the Nelder-Mead method[195,196]

$$L(\omega, r_{\mathrm{c}}; \{\mathbf{V}_i^{\mathrm{a}}\}, \{r_i\}) = 2 \sum_{i=2}^{N-1} \frac{\mathbf{V}_{i+1}^{\mathrm{d}}(r_i - r_{i-1}) - \mathbf{V}_i^{\mathrm{d}}(r_{i+1} - r_{i-1}) + \mathbf{V}_{i-1}^{\mathrm{d}}(r_{i+1} - r_i)}{(r_{i+1} - r_i)(r_{i+1} - r_{i-1})(r_i - r_{i-1})}$$

where the terms of the summation are simply central finite difference second derivatives of the diabatic potential energy operator.

The integration of the NAC function to obtain the mixing angle β_i at each geometry is obtained by adaptive Gauss-Kronrod quadrature using the `QuadGK.jl` library.

Empirically, I find that an initial guess for the characteristic width ω with the correct order of magnitude suffices for the optimiser to converge. However, the procedure is somewhat more sensitive to the initial guess for the central geometry r_{c}, as a result a convenience function that attempts to detect the central geometry by searching for the largest absolute value of the second order derivatives of the adiabatic operators is provided.

Table 4.2 provides values for the optimised NAC parameters $\alpha, \gamma, r_{\mathrm{c}}$ used to diabatise the energy degenerate pairs $e\,^1\Pi$ – $(3)\,^1\Pi$ and $C\,^3\Pi$ – $C'\,^3\Pi$, which are visualised in Figure 4.9. The effect of diabatisation is seen to smooth the PECs, as enforced by Eq.(4.7) with no avoided-crossing. The non-Born-Oppenheimer dynamics, initially manifested in the nuclear kintetic energy, has been rotated into the potential and coupling terms connecting the non-adiabatically interacting states. As a result, PECs are produced that can be more easily modelled using analytical forms in the diabatic representation. This facilitates their refinement to experimental data in Section4.13.1, aligning with the ExoMol project's goal of producing empirically accurate line lists.

4.4 *Ab initio* Potential Energy Curves

Figure 4.1 presents *ab initio* PECs of the 13 lowest energy electronic states of SO. The $C\,^3\Pi$ state exhibits an avoided crossing at $r \sim 2.05$ Å due to a non-adiabatic

Table 4.2: Optimised parameters α (inverse Lorentzian HWHM), γ (Laplacian damping parameter), and r_c (avoided crossing/centroid position) for the Lorentzian and Laplacian NACs used to diabatise the $e\,^1\Pi$ and $C\,^3\Pi$ state PECs (see Figure 4.1).

State	α	γ	r_c (Å)
$e\,^1\Pi$	52.422	0.027	1.949
$C\,^3\Pi$	39.859	0.035	2.047

coupling with the $C'\,^3\Pi$, which lends a dissociative character to the $C\,^3\Pi$ in the long-range region. Similarly, the $e\,^1\Pi$ state exhibits an avoided crossing at 1.95 Å, due to the singlet state $(3)^1\Pi$[312]. These non-adiabatic interactions produce large gradients in coupling curves connecting these states within the region of the avoided crossing, as shown for EAMCs, SOC, and DMCs in Figures. 4.2–4.6. The equilibrium geometry of the $C\,^3\Pi$ state also lies very close in energy to those of the $d\,^1\Pi$ and $B\,^3\Sigma^-$ states, and so one can expect perturbations in the energy levels around their minima which was reported and confirmed experimentally by Liu et al.[354]. It is worth noting that the $A'\,^3\Delta$ and $A''\,^3\Sigma^+$ states lie very close across the range of nuclear geometries included in these calculations, but do not cross.

Table 4.3 compares the equilibrium potential energies, T_e (cm^{-1}), equilibrium bond lengths, r_e (Å), and dissociation energies, D_e (eV), of the 11 lowest singlet and triplet states of SO determined directly from the *ab initio* adiabatic PECs presented in Figure 4.1 to both calculations[325,312,311,355,302] and experiment[340,356,357,355,358]. The calculations[312,311,355,302] use a MRCI/cc-aug-pV5Z level of theory, whereas the *ab initio* calculation by Sarka and Nanbu[325] use a MRCI-F12+Q/cc-aug-pV(5+d)Z level of theory. The experimentally derived spectroscopic constants where obtained via Photoion-Photoelectron Coincidence[357], Multiphoton Ionization[355], and Ar + SO_2 afterglow[358] spectroscopies as well as from the recent analysis by Bernath et al.[340].

Our bond lengths show good agreement to both theoretical and empirical values, with better agreement to experiment than previous calculations for the $b\,^1\Sigma^+$, $A\,^3\Pi$, and $d\,^1\Pi$ states. Worse agreements are seen for our T_e values, the most accurate being $T_e(A\,^3\Pi)$, $T_e(C\,^3\Pi)$, and $T_e(e\,^1\Pi)$ within 152 cm^{-1}, 210 cm^{-1}, and 338 cm^{-1} of experiment respectively. Lastly, worse agreements are seen between our *ab initio* dissociation energies to both experiment and calculations, to which we underestimate. It is apparent that our dissociation asymptotes are the major source of inaccuracy in our *ab initio* SO model and probably arise because we do not include sulfur specific diffuse d orbitals in our basis set during *ab initio* calculations. This is not a major problem, however, since I refine the PECs to the available spectroscopic

data later in Section 4.13.1, mitigating inaccuracies present in the current *ab initio* curves. I note that the reported r_e values by Bernath et al.[340] in Table 4.3 were derived from the $B_{v=0}$ rotational constant, and show close agreements to within 0.006 Å and 0.002 Å to our bond lengths for the $a\,^1\Delta$ and $b\,^1\Sigma^+$ respectively. Our fundamental vibrational energy of the $X\,^3\Sigma^-$ state is found approximately 30 cm^{-1} too high from the experiment, which is to be expected with MRCI calculations, and provides insight to the accuracy of the other computed states and couplings, which will also require empirical tuning.

The intersections between states of different symmetries obtained in our calculations can be seen in Figure 4.10. The $d\,^1\Pi$ and $C\,^3\Pi$ states cross at 1.59 and 1.82 Å, $d\,^1\Pi$ and $B\,^3\Sigma^-$ at 1.64 and 2.20 Å, both agreeing with the intersection locations of 1.62 and 1.80 Å and 1.60 and 2.14 Å, respectively, provided by Yu et al. (2011)[312]. The intersection of the $e\,^1\Pi$ with the $B\,^3\Sigma^-$ state occurs at 2.4 Å in our calculations, somewhat larger than the value of 2.3 Å reported by Yu et al. (2011)[312]. Since the $e\,^1\Pi$ and $d\,^1\Pi$ states become repulsive at 1.92 Å and 1.9 Å respectively, crossings beyond these geometries provide potential predissociation pathways for the $C\,^3\Pi$ and $B\,^3\Sigma^-$ states. Yu and Bian[312] also show that the $C'\,^3\Pi$ state crosses the $B\,^3\Sigma^-$ state at 2.25 Å, to which they state predissociation of $B\,^3\Sigma^-$ through this $C'\,^3\Pi$ state is possible. Sarka and Nanbu[325] also give intersections $R(C,B) = 1.57, 2.21$ Å as opposed to our values of $R(C,B) = 1.67, 2.18$ Å.

Lastly, I report further crossings between the $c\,^1\Sigma^-$, $A'\,^3\Delta$, and $A''\,^3\Sigma^+$ states and the $A\,^3\Pi$ and $d\,^1\Pi$ states of SO at $r(c,A) = 1.46$ Å, $r(A',A) = 1.48$ Å, $r(A'',A) = 1.50$ Å, $r(c,d) = 1.40$ Å, $r(A',d) = 1.42$ Å, and $r(A'',d) = 1.43$ Å. These crossings agree with those reported by Yu and Bian[312] between $c\,^1\Sigma^-$, $A'\,^3\Delta$, and $A''\,^3\Sigma^+$with $A\,^3\Pi$ in the region 1.47–1.51 Å and crossings between $c\,^1\Sigma^-$, $A'\,^3\Delta$, $A''\,^3\Sigma^+$ with $d\,^1\Pi$ in the region 1.42–1.45 Å.

Table 4.3: Comparison of our *ab initio* equilibrium potential energies T_e (cm^{-1}), dissociation energies D_e (eV), and equilibrium geometries r_e (Å) to the values from the literature. Parameters next to bold state symbols correspond to the *ab initio* PECs calculated in this study.

State	T_e (cm^{-1})	D_e (eV)	r_e (Å)	State	T_e (cm^{-1})	D_e (eV)	r_e (Å)
$\boldsymbol{X}\,^3\boldsymbol{\Sigma}^-$	0	5.1253	1.4821	$\boldsymbol{A'}\,^3\boldsymbol{\Delta}$	29097.8878	1.503	1.7571
Calc.[312]	0	5.418	1.4865	Calc.[312]	29828	1.72	1.7649
Expt.[356]		5.429	1.481	$\boldsymbol{B}\,^3\boldsymbol{\Sigma}^-$	43255.0097	0.9212	1.8121
Calc.[325]	0	5.475	1.4925	Calc.[325]	41706.5886	1.4022	1.7868
Expt.[357]			1.481	Calc.[312]	41314	1.387	1.782
Calc.[311]			1.481	Expt.[357]	41629	1.410[359]	1.775
Calc.[302]			1.493	Calc.[302]	41206		1.794
$\boldsymbol{a}\,^1\boldsymbol{\Delta}$	5479.8013	4.4486	1.4979	$\boldsymbol{d}\,^1\boldsymbol{\Pi}$	45309.0766	0.0587	1.545
Calc.[312]	5936	4.682	1.4945	Calc.[312]	44166	0.189	1.5475
Expt.[356]	5873	4.647	1.4919	Expt.[355]	43902	0.195	1.5303
Calc.[302]	5883		1.502	Calc.[302]	44975	0.059	1.723
Expt.[340]			1.4920	Calc.[355]	44471	0.14	1.553
$\boldsymbol{b}\,^1\boldsymbol{\Sigma}^+$	9774.1938	3.9154	1.5057	$\boldsymbol{A''}\,^3\boldsymbol{\Sigma}^+$	29731.2077	1.4417	1.765
Calc.[312]	10548	4.112	1.5062	Calc.[312]	30495	1.637	1.7701
Expt.[356]	10510	4.137	1.5001	Expt.[358]	30692		
Calc.[302]	10576		1.514	Calc.[302]	30025		1.776
Expt.[340]			1.5035	$\boldsymbol{C}\,^3\boldsymbol{\Pi}$	44719.2593	0.5489	1.6786
$\boldsymbol{A}\,^3\boldsymbol{\Pi}$	38607.6737	0.4246	1.6079	Calc.[312]	44033	0.609	1.6692
Calc.[325]	38879.2948	0.6441	1.5946	Calc.[325]	44909.0901	0.6027	1.6727
Calc.[312]	38334	0.665	1.6196	Expt.[355]	44381		1.654
Expt.[356]	38455	0.662	1.609	Calc.[302]	44038		1.681
Calc.[311]	38880		1.613	$\boldsymbol{e}\,^1\boldsymbol{\Pi}$	51347.9346	0.4524	1.6864
Calc.[302]	38931		1.719	Calc.[312]	51224	0.45	1.6826
$\boldsymbol{c}\,^1\boldsymbol{\Sigma}^-$	27274.9752	1.7679	1.7571	Expt.[355]	51558		1.6774
Calc.[312]	28544	1.879	1.7617	Calc.[302]	51258		1.685

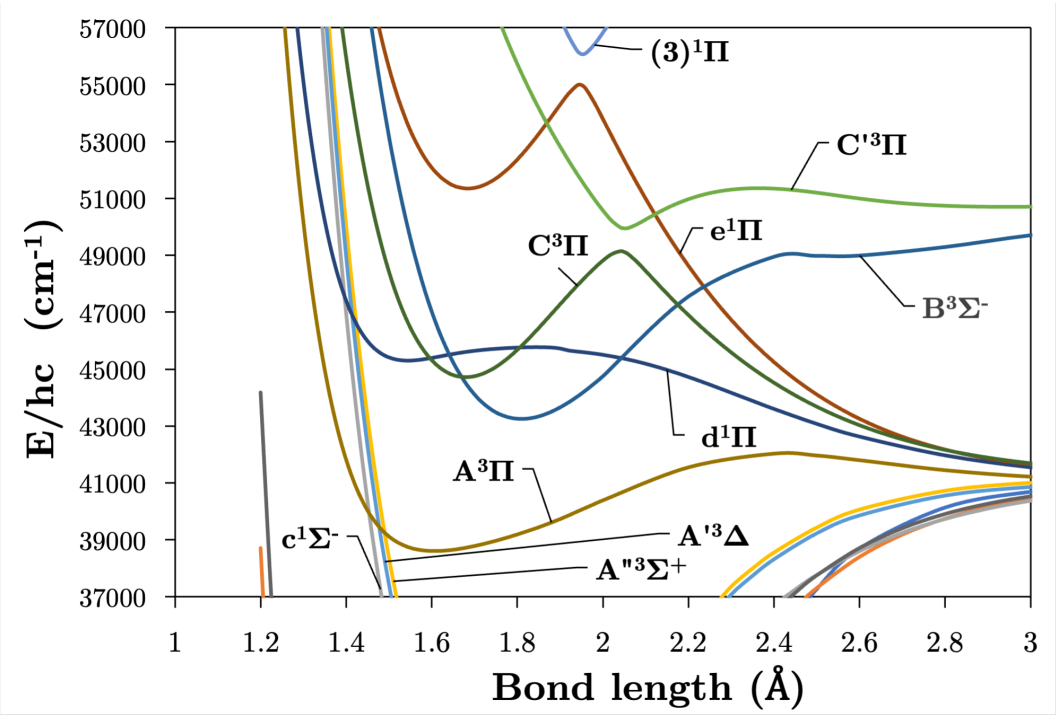

Figure 4.10: Our *ab initio* PECs in the region 37,000 – 57,000 cm^{-1} showcasing the various state crossings.

4.5 *Ab initio* Spin-Orbit and Electronic Angular Momentum Curves

Figures 4.2 and 4.3 plot the z (SO_z) and x (SO_x) components of the spin-orbit curves of SO over nuclear geometries where the former couple states of same Λ (projection of the electronic angular momentum) and the latter couple states of different Λ values. One sees again that the effect of diabatisation is to smooth out the curves over r, where avoided crossings in the adiabatic picture create steep gradients around the avoided crossing. An example of the diabatisation process can be seen for the $\langle e\,^1\Pi|\,SO_x\,|X\,^3\Sigma^-\rangle$ and $\langle(3)^1\Pi|\,SO_x\,|X\,^3\Sigma^-\rangle$ pair in Figure 4.11. Spin-orbit matrix elements at the avoided crossing geometries are important in determining the possible spin-orbit induced predissociation mechanisms that occur between states of different spin multiplicity[312]. Referring to the spin-orbit couplings $\langle e\,^1\Pi|\,SO_x\,|B\,^3\Sigma^-\rangle$ and $\langle d\,^1\Pi|\,SO_x\,|B\,^3\Sigma^-\rangle$ in Figure 4.3 with the magnitudes of approximately 90 and 20–30 cm^{-1}, respectively, the predissociation of the $B\,^3\Sigma^-$ state through $d\,^1\Pi$ is likely to be very weak, but will be stronger through the $e\,^1\Pi$ state. The construction of diabatic SOCs will hence influence the description of pre-dissociation pathways between states of different symmetry.

Figure 4.6 shows the EAMCs of SO both in the adiabatic and diabatic representations, where their relative phases are carefully maintained according with their *ab initio* values[301]. Without this, using couplings and any other non-diagonal properties in rovibronic calculations become meaningless. The phase of the EAMCs often changes after the crossing point, lending different long-range total angular momenta of the S+O atomic system important in dissociation mechanisms.

4.6 *Ab initio* Dipole Moment Curves

Figures 4.4 and 4.5 plot the z- and y-components of the dipole moments coupling states of same and different symmetry (Λ and multiplicity) respectively. The corresponding μ_x components can be always reconstructed from μ_y using their symmetry properties. It is again evident that the effect of diabatisation is to smooth out the curves over r, where the DMCs tend to zero in the long range limit now with no steep gradients around the avoided crossing regions.

The vibronic intensities are directly affected by the derivatives of the dipole moment with respect to the internucelar separation, r. Since adiabatic curves are prone to strong, steep-gradient variations around avoided crossings, even small inaccuracies in *ab initio* calculations (including the position of the crossing and the corresponding NAC) can lead to large errors in spectral properties of the molecule.

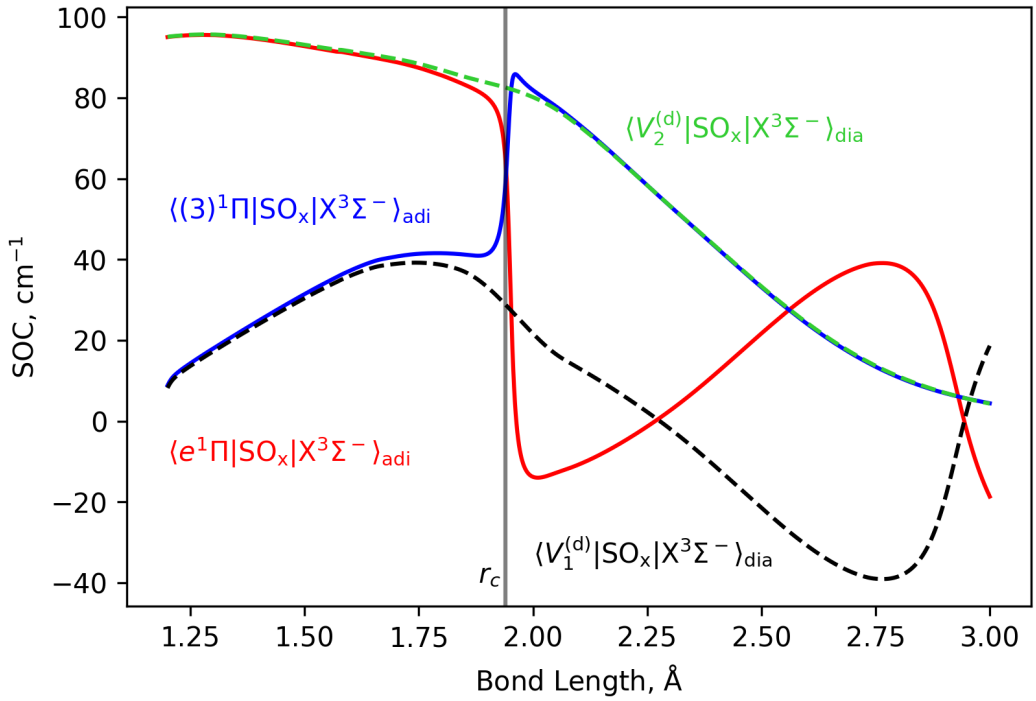

Figure 4.11: Example diabatisation of the adiabatic $\langle e^1\Pi|SO_x|X^3\Sigma^-\rangle$ (red) and $\langle(3)^1\Pi|SO_x|X^3\Sigma^-\rangle$ (blue) SOCs which are seen to have steep topology at the region of avoided crossing r_c highlighted by the vertical line. The corresponding diabatic SOCs (black and green dotted lines) are seen to have smooth topology, and are simple curves of nuclear geometry, ideal for modelling.

Table 4.4: Σ values (total spin angular momentum projection onto the internuclear axis) for the bra and ket electronic states of the SOCs presented in Figures [4.2, 4.3, 4.7].

SO coupling	bra Σ	ket Σ	SO coupling	bra Σ	ket Σ
$\langle A\,^3\Pi\|\,SO_x\,\|X\,^3\Sigma^-\rangle$	0	1	$\langle e\,^1\Pi\|\,SO_x\,\|X\,^3\Sigma^-\rangle$	0	1
$\langle A\,^3\Pi\|\,SO_x\,\|A'\,^3\Delta\rangle$	0	1	$\langle e\,^1\Pi\|\,SO_x\,\|B\,^3\Sigma^-\rangle$	0	1
$\langle C\,^3\Pi\|\,SO_x\,\|A'\,^3\Delta\rangle$	0	1	$\langle C\,^3\Pi\|\,SO_x\,\|A''\,^3\Sigma^+\rangle$	0	1
$\langle A\,^3\Pi\|\,SO_x\,\|B\,^3\Sigma^-\rangle$	0	1	$\langle e\,^1\Pi\|\,SO_x\,\|A'\,^3\Delta\rangle$	0	1
$\langle C\,^3\Pi\|\,SO_x\,\|X\,^3\Sigma^-\rangle$	0	1	$\langle d\,^1\Pi\|\,SO_x\,\|X\,^3\Sigma^-\rangle$	0	1
$\langle C\,^3\Pi\|\,SO_x\,\|B\,^3\Sigma^-\rangle$	0	1	$\langle d\,^1\Pi\|\,SO_x\,\|B\,^3\Sigma^-\rangle$	0	1
$\langle A\,^3\Pi\|\,SO_x\,\|A''\,^3\Sigma^+\rangle$	0	1	$\langle b\,^1\Sigma^+\|\,SO_z\,\|X\,^3\Sigma^-\rangle$	0	0
$\langle d\,^1\Pi\|\,SO_x\,\|A'\,^3\Delta\rangle$	0	1	$\langle a\,^1\Delta\|\,SO_z\,\|A'\,^3\Delta\rangle$	0	0
$\langle A'\,^3\Delta\|\,SO_z\,\|A'\,^3\Delta\rangle$	1	1	$\langle A\,^3\Pi\|\,SO_z\,\|A\,^3\Pi\rangle$	1	1
$\langle A''\,^3\Sigma^+\|\,SO_z\,\|X\,^3\Sigma^-\rangle$	1	1	$\langle A''\,^3\Sigma^+\|\,SO_z\,\|B\,^3\Sigma^-\rangle$	1	1
$\langle C\,^3\Pi\|\,SO_z\,\|A\,^3\Pi\rangle$	1	1	$\langle C\,^3\Pi\|\,SO_z\,\|C\,^3\Pi\rangle$	1	1
$\langle b\,^1\Sigma^+\|\,SO_z\,\|B\,^3\Sigma^-\rangle$	0	0	$\langle b\,^1\Sigma^+\|\,SO_x\,\|A\,^3\Pi\rangle$	0	1
$\langle a\,^1\Delta\|\,SO_x\,\|A\,^3\Pi\rangle$	0	1	$\langle c\,^1\Sigma^-\|\,SO_x\,\|A\,^3\Pi\rangle$	0	1
$\langle d\,^1\Pi\|\,SO_z\,\|A\,^3\Pi\rangle$	0	1	$\langle e\,^1\Pi\|\,SO_z\,\|A\,^3\Pi\rangle$	0	1

For example, the adiabatic $\langle C^3\Pi|\,\mathrm{DM}\,|X^3\Sigma^-\rangle$ dipole moment has a steep gradient at around 2 Å which can be expected to be due to the avoiding crossing between $C^3\Pi$ and $C'^3\Pi$ states, therefore the $C^3\Pi$–$X^3\Sigma^-$ electronic band is expected to be sensitive to the quality of its adiabatic description. The diabatic representation can also be sensitive to the quality of the corresponding curves, but to a significantly lesser extend due to their smooth character. Of course, the adiabatic and diabatic representations are equivalent (as demonstrated in Chapter 3) but one should still expect the two representations to offer different behaviours when subject to the accuracy of the calculation. For example, whether convergence has been achieved and numerical precision of mathematical operations such as the derivative or diagonalisation which depend on the choice of grid spacing.

Comparison with the $\langle A^3\Pi|\,\mu_x\,|X^3\Sigma^-\rangle$, $\langle C^3\Pi|\,\mu_x\,|X^3\Sigma^-\rangle$, and $\langle B^3\Sigma^-|\,\mu_z\,|X^3\Sigma^-\rangle$ transition dipoles provided by Sarka and Nanbu[325] shows excellent agreements up to dissociation, with values ({ours,Sarka and Nanbu[325]}) at the ground state equilibrium geometry $R_e(X^3\Sigma^-) = 1.48$ Å of $\{0.16, 0.18\}$ Debye, $\{0.333, 0.337\}$ Debye, $\{1.623, 1.633\}$ Debye, respectively.

4.7 Nuclear Motion Calculations

Duo[103] is a general purpose variational code that solves the rovibronic Schrödinger equation for diatomics while allowing an arbitrary number of couplings between various electronic states including spin-spin, spin-orbit, spin-rotation, and rotational Born-Oppenheimer breakdown curves. It is assumed one has solved the Schrödinger equation for the electronic motion *a priori* in order to obtain PECs, SOCs, EAMCs, (T)DMCs etc. for the electronic states in question. These curves can be supplied to the program as either a grid of *ab initio* points, or in an analytical form. After solving the Schrödinger equation for the nuclear motion Duo obtains eigenstates and energies for the good quantum numbers J (total angular momentum), and τ (parity); other quantum numbers are assigned on the basis of the largest coefficient in the basis set. The eigenfunctions are used to compute transition line strengths and Einstein A coefficients in order to obtain a complete spectroscopy for the system in question. A detailed methodology of Duo is given by Yurchenko et al.[103] and is discussed in Section 2.3 of Chapter 2.

In our original publication[13], we did not include non-adiabatic couplings (NACs) in the rovibronic Duo calculations. At the time, I was new to non-adiabatic nuclear motion and did not fully appreciate the importance of these couplings on the rovibronic solution and computed spectroscopy. However, it is interesting to compare the computed spectra using adiabatic and diabatic curves, as the differ-

ent models are expected to have different convergence characteristics and efficacy in representing the spectroscopy. Their comparison serves as an example in the importance of a proper non-adiabatic treatment since one expects the diabatic and adiabatic spectrum to be exactly equivalent.

4.8 The *ab initio* SO Spectrum

Using the diabatic spectroscopic model I produce an *ab initio* rovibronic spectrum of SO for the system involving the lowest 11 singlet and triplet electronic states of SO covering the wavelength range up to 147 nm. The vibrational sinc-DVR basis set was defined for a grid of 701 internuclear geometries in the range 0.6–6.0 Å. I select 58, 58, 49, 11, 31, 41, 27, 27, 14, 20, and 36 vibrational wavefunctions for the $X\,^3\Sigma^-$, $a\,^1\Delta$, $b\,^1\Sigma^+$, $A\,^3\Pi$, $B\,^3\Sigma^-$, $c\,^1\Sigma^-$, $A''\,^3\Sigma^+$, $A'\,^3\Delta$, $C\,^3\Pi$, $d\,^1\Pi$, and $e\,^1\Pi$, respectively, to form the contracted vibronic basis. In total 15 364 624 Einstein A coefficients between 119 600 bound rovibronic states were computed with a maximum total rotational quantum number $J_{\max} = 180$ and used to simulate rovibronic absorption spectra at a given temperature using the program ExoCross[360]. Figure

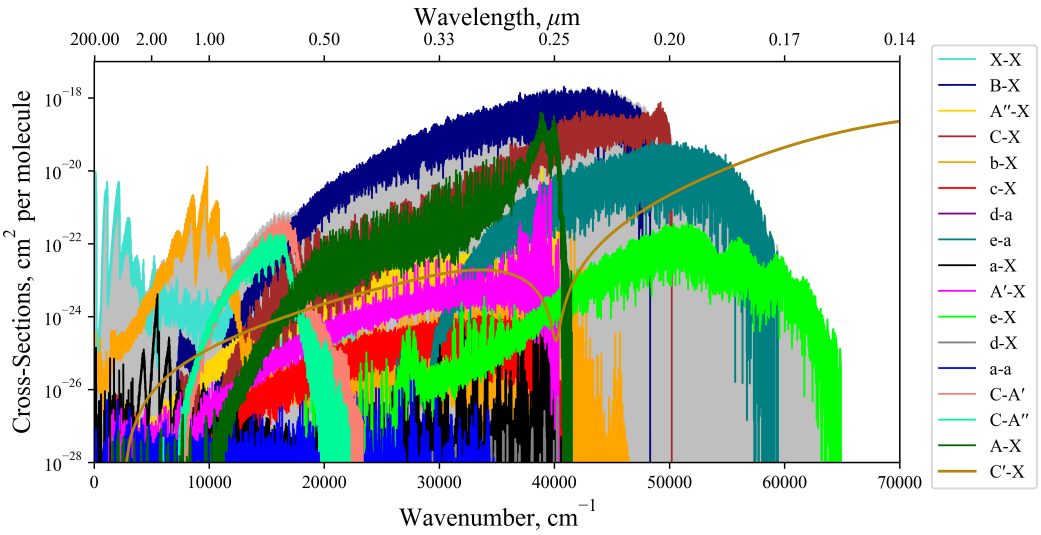

Figure 4.12: Dipole allowed and forbidden components of the *ab initio* absorption spectrum simulated with the diabatic model at 5000 K connecting the $X\,^3\Sigma^-$, $a\,^1\Delta$, $A'\,^3\Delta$, and $A''\,^3\Sigma^+$states. The $C'\,^3\Pi$ continuum is also plotted in gold. The absorption lines are modelled using Gaussian profiles with a HWHM of 0.6 cm^{-1} in the bound cases, and 300 cm^{-1} for the continuum band.

4.12 shows an absorption rovibronic spectrum of SO computed at 5000 K with all bands plotted using different colours, both electric dipole-allowed and forbidden. The spectrum is modelled at a high temperature for a visual aid since at this temperature there is a good separation between different electronic bands. The grey shaded

region in Figure 4.12 marks the total SO bound-bound absorption at 5000 K, which is mostly traced by the strongest bands with the exception for the region between 12000-17000 cm^{-1}. Hence, weaker bands, e.g. ones that break dipole selection rules, have negligible contribution to the total SO opacity and will be less important for low resolution studies such as in astrophysical observations.

The non-bound diabatic states such as $C'^{3}\Pi$ and $(3)^{1}\Pi$ are excluded from the bound-bound spectra simulations. Tests show that the effect of the unbound states on the bound-bound spectra is negligible, and vice versa, the continuum spectra are negligibly affected by the bound electronic states and therefore can be treated separately.

The continuum spectra of the unbound diabatic $C'^{3}\Pi$ state is computed using the stabilisation method[235] and is shown in Figure 4.12 plotted in gold overlaying the bound-bound spectrum to demonstrate its contribution to the total SO opacity. For the continuum state a larger basis set of 5000 wavefunctions was used. The structure energetically above (below) the 'dip' at 41200 cm^{-1} is due to absorption to unbound $C'^{3}\Pi$ states above (below) the $S(^{1}D)+O(^{3}P)$ dissociation. The $X^{3}\Sigma^{-} \rightarrow C'^{3}\Pi$ continuum band continues to 100000 cm^{-1}, peaking at ~78000 cm^{-1} which corresponds to the Frank-Condon region (vertical transitions) from states localised around the minima of $X^{3}\Sigma^{-}$.

I note that the dipole-forbidden bands in Figure 4.12 are not computed using quadrupole or magnetic dipole moments, which have very weak intensities, but rather intensities are 'stolen' from other transitions. This intensity stealing propagates through the mixture of electronic wave-functions via couplings such as SOCs and EAMCs. For example, the spin-forbidden $c^{1}\Sigma^{-}$–$X^{3}\Sigma^{-}$ band occurs due to the overlap between the $c^{1}\Sigma^{-}$ wavefunction both with $e^{1}\Pi$ and $d^{1}\Pi$ wavefunctions through the EAM couplings, and then with $X^{3}\Sigma^{-}$ through a secondary mixing via $\langle e^{1}\Pi|\,SO_{x}\,|X^{3}\Sigma^{-}\rangle$ and $\langle d^{1}\Pi|\,SO_{x}\,|X^{3}\Sigma^{-}\rangle$ to produce an effective, direct dipole moment, which dominates over the weaker magnetic and quadrupole moment mechanisms.

Absolute intensities for every rovibronic transitions are computed between the lowest 11 diabatic singlet and triplet states of SO covering the entire spectroscopic range down to 147 nm, where the avoided crossings have been studied. I note that the only other study with similar coverage into the UV on SO is from the theoretical work by Sarka and Nanbu[325] who compute cross sections in the 190–300 nm wavelength region. However, our spectroscopic model is both more complete and phase consistent (phases carefully reconstructed, see 4.5), whereas Sarka and Nanbu[325] do not provide any phases.

4.8.1 Experimental Coverage of the *ab initio* SO Spectrum

Currently within the literature a small fraction of the SO spectrum has been measured experimentally covering only the $X\,^3\Sigma^-$, $a\,^1\Delta$, $b\,^1\Sigma^+$, $A\,^3\Pi$, $B\,^3\Sigma^-$, and $C\,^3\Pi$ states. Figure 4.13 reviews the spectroscopic coverage of SO from 24 experimental sources from the literature. Figure 4.12 shows our model to supplement the experimental data over the whole spectral range. In particular, we cover the SO spectrum above 40000 cm^{-1} and 12000–16000 cm^{-1} where no measurements have been taken for any electronic state. I also plot the available HITRAN[361] SO line list containing data on the first three electronic states $X\,^3\Sigma^-$, $a\,^1\Delta$, and $b\,^1\Sigma^+$. Our *ab initio* model is able to extend the HITRAN coverage up to dissociation at 40000 cm^{-1}.

The aim of Section 4.13.1 is to refine our *ab initio* SO model to the experimental transition frequencies from these sources and to produce an empirically accurate line list for SO.

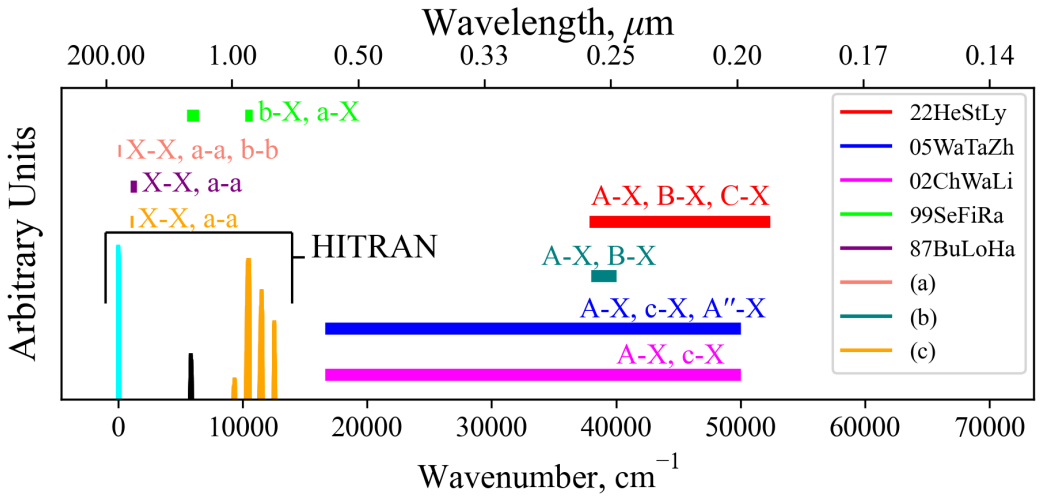

Figure 4.13: Coverage of experimental measurements for 24 sources illustrated by horizontal bars covering the spectral regions measured, where the named works[140,141,331,362] include some spectral data, mostly with relative intensities: (a) 14 sources[363,139,296,364–366,336,367,368,328,337,369,339,335,346] cover $X\,^3\Sigma^- \rightarrow X\,^3\Sigma^-$, $a\,^1\Delta \rightarrow a\,^1\Delta$, $b\,^1\Sigma^+ \rightarrow b\,^1\Sigma^+$ for 0-125 cm^{-1}; (b) 3 experimental sources[330,370,371] cover the $A\,^3\Pi \rightarrow X\,^3\Sigma^-$ and $B\,^3\Sigma^- \rightarrow X\,^3\Sigma^-$ bands for 38000–39800 cm^{-1}; (c) 2 experimental sources[332,334] cover the $X\,^3\Sigma^- \rightarrow X\,^3\Sigma^-$ and $a\,^1\Delta \rightarrow a\,^1\Delta$ bands for 1040–1125 cm^{-1}.

4.9 Effect of Diabatisation on the Computed Spectra

In theory, the adiabatic and diabatic representations should yield identical results, provided that the corresponding NACs and DCs are included. However, due to

the computational cost of computing NACs through proper *ab initio* methods, it is not common practice to include NACs in adiabatic models. Without definition of the NAC, non-Born-Oppenheimer interactions are effectively removed. In our original work[13] we omitted the NAC terms to study the effect of these non-Born-Oppenheimer interactions on the computed spectroscopy when compared to a complete diabatic model. Our results show that these interactions are important not just for energies and wavefunctions (see Chapter 3), but also in the computed intensities. In this section I analyse the importance of the non-adiabatic couplings between the [$C\,^3\Pi$, $C'\,^3\Pi$] and [$e\,^1\Pi$, $(3)\,^1\Pi$] systems when computing the (absorption) spectra of SO.

As discussed in our two-state adiabatic-diabatic equivalence study[38] and in Chapter 3, when the NAC is strong, the DC tends to be small in magnitude. A heuristic can be made where one can consider the diabatic representation without DCs to more efficiently represent the physics of the studied electronic structure than an adiabatic representation without treatment of NACs. To test this, the fully coupled Schrödinger equation is solved for the diabatic $C'\,^3\Pi$ state for two cases which include (case A) or exclude (case B) the upper $C'\,^3\Pi$ state and its (electronic/diabatic) coupling to the $C\,^3\Pi$ state. The results showed that the $C\,^3\Pi$–$X\,^3\Sigma^-$bound-bound spectrum is minimally influenced by the coupling to the $C'\,^3\Pi$ state. This could be due to a combination of: the Frank-Condon region corresponding to transitions from the $X\,^3\Sigma^-$ to levels of a heavily bound character in the $C\,^3\Pi$ state; a small DC between the $C\,^3\Pi$ and $C'\,^3\Pi$. Figure 4.14 illustrates the vibrational energy levels of the diabatic $C\,^3\Pi$, fully bound below its dissociation limit of 50700 cm^{-1}.

Figure 4.15 illustrates the importance of the non-adiabatic effects when modeling the spectra consisting of transitions to states around the avoiding crossings for the $X\,^3\Sigma^- \rightarrow C\,^3\Pi$ and $a\,^1\Delta \rightarrow e\,^1\Pi$ bound-bound absorption bands (panel a), and the $X\,^3\Sigma^- \rightarrow C'\,^3\Pi$ continuum absorption band (panel b). The adiabatic spectra were computed with the NACs excluded and compared to the diabatic spectra with the non-adiabatic effects fully encountered. Each spectra has been modeled at a temperature of 5000 K – such that hot bands are populated, aiding my comparisons below – with Gaussian profiles of a 0.6 cm^{-1} half-width-at-half-maximum (HWHM) for the bound-bound spectra and a HWHM of 300 cm^{-1} for continuum bands.

Great differences between the bound-bound spectra in panel (a) of Figure 4.15 are seen towards both the high and low energy regions. In the high energy region the adiabatic spectral bands terminate abruptly at the avoided crossings whereas

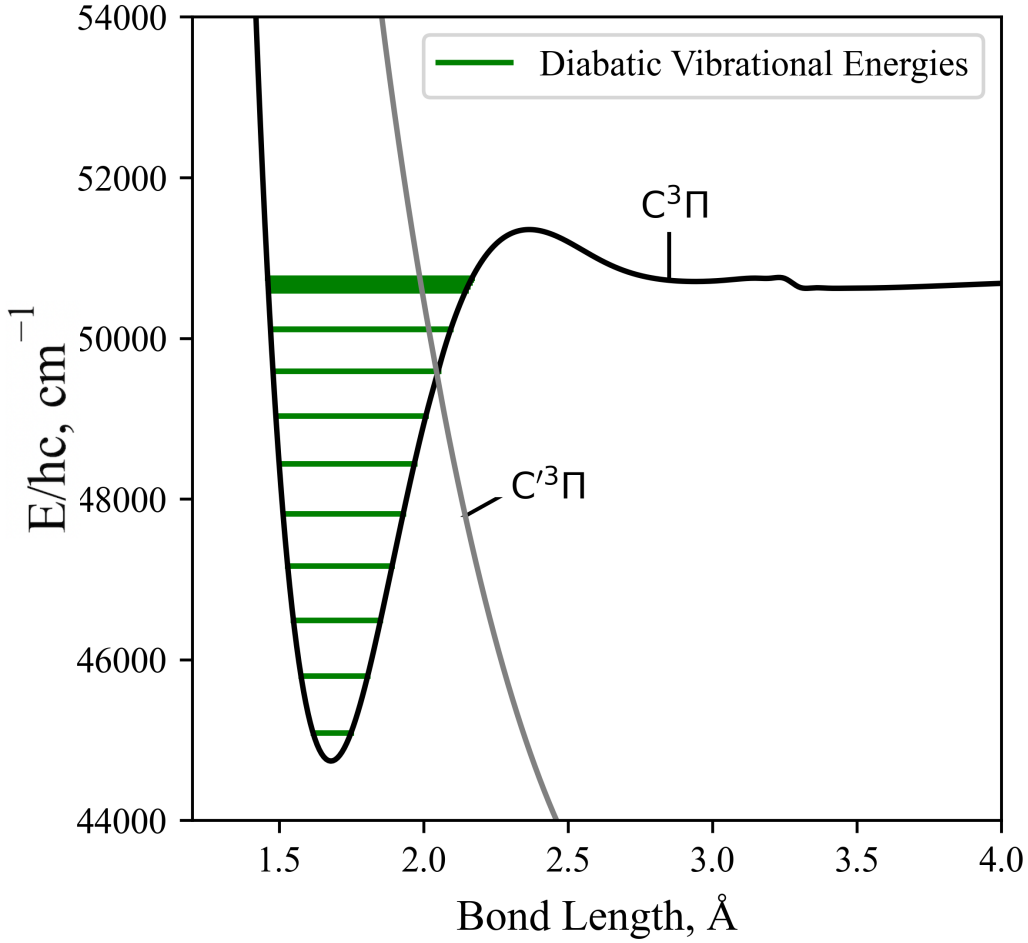

Figure 4.14: The computed Duo diabatic vibronic energies of the $C^3\Pi$ superimposed upon the $C^3\Pi$ and $C'^3\Pi$ PECs. The secondary and tertiary 'bumps' at R = 2.42, 3.30 Å are due to an avoided crossing and numerical noise, respectively.

the diabatic bands continue to the diabatically correlated dissociation asymptotes $S(^1D)+O(^3P)$ & $S(1^1D)+O(^1D)$ (see Figure 4.1). The diabatisation extends these bands by at least a few thousand wavenumbers because of the availability of higher rovibrational states in the deeper diabatic potential wells. For purely bound-bound calculations, the adiabatically computed bands have lower intensities compared to the diabatic spectrum which can be attributed to the increased repulsive character of the adiabatic PECs on the right hand side of the crossing points present. Due to the tunneling through the potential barriers, the adiabatic wavefunctions 'leak' to the continuum region thus resulting in reduction of the intensity of their bound absorption spectra.

The most interesting feature from Figure 4.15 is the extension of the $a^1\Delta \rightarrow$

$e\,^1\Pi$ band beyond the stronger $X\,^3\Sigma^- \rightarrow C\,^3\Pi$ band at $E/hc > 50000$ cm^{-1}. Although being relatively weak, this band is not covered by stronger bands and therefore may be observable in the $\sim 0.18-0.2$ μm region, a result only predicted when using a full non-adiabatic theoretical treatment.

The low intensity regions are very sensitive to changes in the *ab initio* model and will be also affected by the changes in the shape of couplings between the adiabatic and diabatic representations. The hump-like structure in the $C\,^3\Pi$–$X\,^3\Sigma^-$ band at around 10,000 cm^{-1} is absent in the adiabatic spectrum because of the unavailability of vibrational states above the avoided crossing. For example, the brightest transitions within this hump for the $C\,^3\Pi$–$X\,^3\Sigma^-$ band connect the $v = 13$ state which is energetically above the avoided crossing in the adiabatic PEC.

I note that these regions negligibly contribute to the total SO opacity and so are not important for the SO model, but will be important for other systems where non-adiabatic effects occur in the spectroscopically important regions.

Panel (b) of Figure 4.15 presents a similar analysis for the continuum $X\,^3\Sigma^- \rightarrow C'\,^3\Pi$ band, which would include an additional bound structure towards longer wavelengths if the NAC is not included in the adiabatic model since the $C'\,^3\Pi$ PEC in this representation is bound. However, the adiabatic $X\,^3\Sigma^- \rightarrow C'\,^3\Pi$ bound feature is orders of magnitude weaker than the continuum bands presented here and an analysis on the change of character of bound-bound absorption bands with diabatisation is already provided above. The $X\,^3\Sigma^- \rightarrow C'\,^3\Pi$ continuum bands for transitions to unbound $C'\,^3\Pi$ states above the $S(^1D) + O(^3P)$ dissociation converge between both representations, since the non-adiabatic effects are far away from the peak at $\sim$78000 cm^{-1} corresponding to vertical transitions from the electronic ground state. However, if the avoided crossing occurred vertically above the $X\,^3\Sigma^-$ minima, one would expect non-adiabatic effects to have a greater contribution to the continuum cross sections.

From the comparison above, I show that neglecting NACs within an adiabatic model can lead to drastic differences in the physics gleamed from the computed spectra.

4.10 Conclusions on the *ab initio* Analysis of SO

In this work, multireference methods of electronic structure theory combined with a diabatisation procedure were used to compute a fully diabatic model for the transient diatomic molecule sulphur monoxide. The model includes 25 spin-orbit, 29 (transition) dipole moment, and 18 electronic angular momentum curves for the $X\,^3\Sigma^-$, $a\,^1\Delta$, $b\,^1\Sigma^+$, $A\,^3\Pi$, $B\,^3\Sigma^-$, $c\,^1\Sigma^-$, $A''\,^3\Sigma^+$, $A'\,^3\Delta$, $C\,^3\Pi$, $d\,^1\Pi$, and $e\,^1\Pi$ elec-

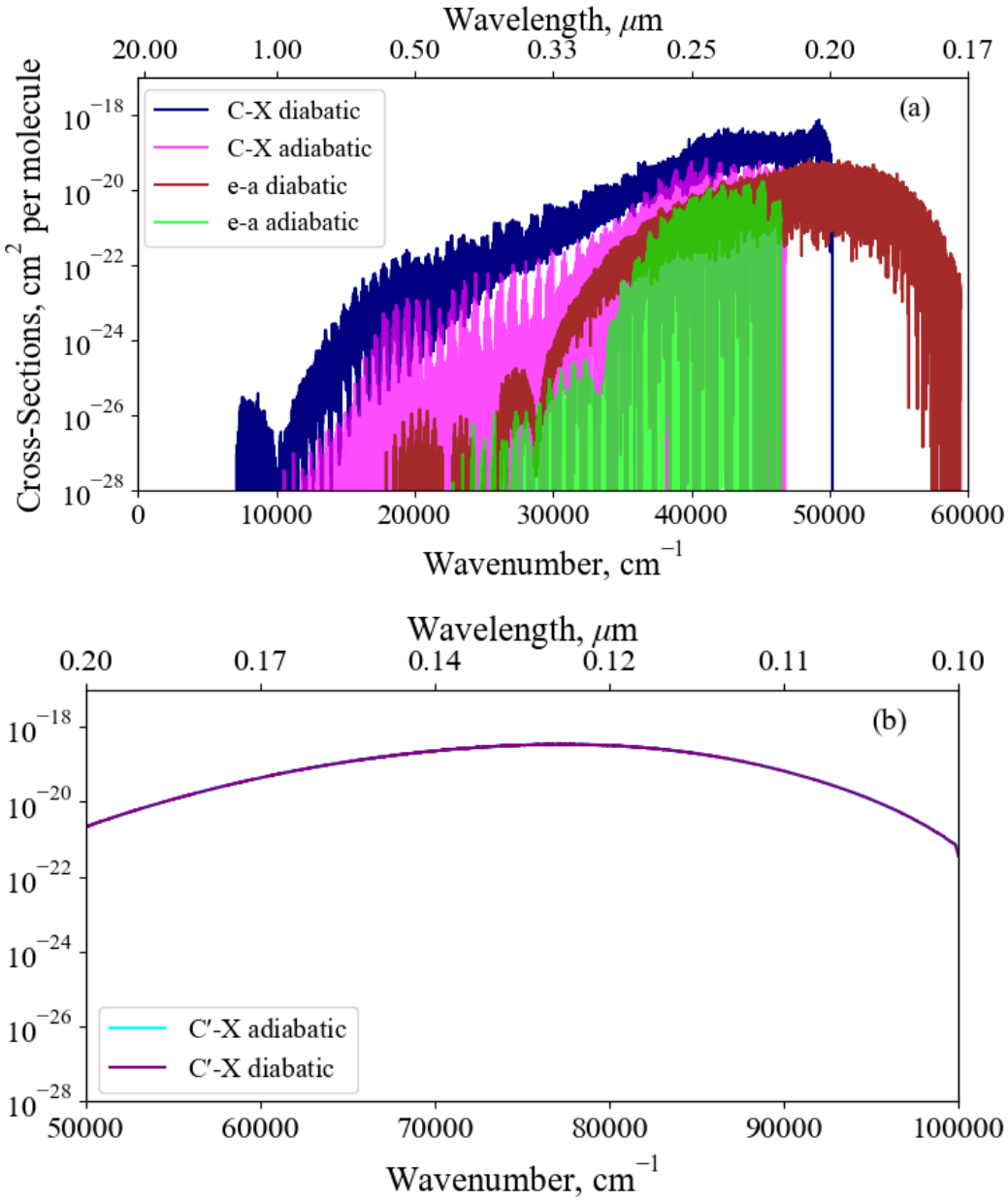

Figure 4.15: A comparison between the $X\,^3\Sigma^- \rightarrow C\,^3\Pi$, $a\,^1\Delta \rightarrow e\,^1\Pi$, and $X\,^3\Sigma^- \rightarrow C'\,^3\Pi$ band spectra computed with an adiabatic model with no NAC and a diabatic model. These bands are dipole allowed and are expected to be observable, great differences are seen between the spectra at the dissociation, highlighting the importance of proper non-adiabatic treatment. Each spectra has been modeled at a temperature of 5000 K with Guassian line profiles of a 0.6 cm^{-1} HWHM.

tronic states of SO and were produced *ab initio* via CASSCF and MRCI methods using aug-cc-pV5Z basis sets. These curves were then used to compute the nuclear motion via solving the fully-coupled Schrödinger equation with the Duo program.

A further two electronic states ($C'^3\Pi$ and $(3)^1\Pi$) were computed along with their couplings, which are essential to forming the diabatic representation.

The property-based diabatisation procedure I use is a computationally low cost method to reconstruct the non-adiabatic couplings without additional quantum chemistry calculations *a priori* to nuclear motion calculations.

To assess the importance of non-adiabatic effects for the spectroscopy of SO, spectra computed in the diabatic and adiabatic representations, without definition of NACs, are compared. The most notable difference is the absence of the UV spectrum above ~ 50000 cm^{-1} because of the illusionary predissociation from the adiabatic PECs. It was also observed that adiabatically computed bound absorption bands to have lower intensities than the diabatic counterparts. It is therefore important to treat NACs for systems where these non-adiabatic interactions occur in spectroscopically important regions since they have drastic effects on the computed spectroscopy.

All coupling curves of SO are defined with self-consistent relative phases, which is crucial for spectral calculations[301]. Therefore our spectroscopic model of SO provides a comprehensive and extensive theoretical baseline, which is the first fully reproducible spectroscopic description of SO longer than 147 nm. Since the existing spectroscopic data on SO only covers $X^3\Sigma^-$, $a^1\Delta$, $b^1\Sigma^+$, $A^3\Pi$, $B^3\Sigma^-$, and $C^3\Pi$ our *ab initio* model can be used as a benchmark for future rovibronic methods and calculations.

4.11 Building a Semi-Empirical Hot Line List for SO

The topic of the following sections will be to build a (hot) semi-empirical line list as part of the ExoMol project[53,54] for SO through the refinement of our *ab initio* model (see Sections 4.2 – 4.10) to experimental transition data, where I expect to reduce the shift in line positions relative to experiment. The final SO line list will have applications primarily in the atmospheric modelling of exoplanets[287–289] and cool stars. Further applications of this empirical SO line list will be in shock zone modeling[372,297,298], SO lasing systems[299,300], and spectroscopy of Venus[285,286] and Io[283,284].

The following sections in this chapter will be organised as follows. Sections 4.11.1 and 4.11.2 summarise the theoretical background behind the generation of a self-consistent set of empirical rovibronic energy levels, quantum number assignments, and uncertainties. Section 4.12 details the experimental transition frequency database curated from the literature, where their inversion to a set of empirically determined rovibronic energies and associated uncertainties is analysed. Section

5.2.4 details the SO spectroscopic model used for refinement to the MARVEL energies, where the refinement process, the resulting accuracy of the final computed rovibronic energy terms, and the MARVELisation of the SO line list are discussed. Section 4.14 details the intensity calculations, opacities, and comparisons between our calculated and experimental spectra. Finally, Section 4.16 discusses the works in which our SO line list was used, where the main results are presented from these studies.

4.11.1 The MARVEL Procedure

The critical evaluation of experimental transition data and formation of a self-consistent set of rovibronic energy levels is done through the MARVEL procedure[156,373] which is built on the concept of spectroscopic networks (SN)[374,375]. Through a weighted linear least squares protocol, MARVEL inverts the information contained within transition data to form a set of associated energy levels and uncertainties. This procedure is built on the simple idea of matrix inversion, for example, consider a list of N_t transition frequencies and the following matrix equation

$$\mathbf{A}\vec{E} = \vec{T} \tag{4.13}$$

where $\vec{T}$ is an N_t-dimensional vector of transition frequencies with index j, $\vec{E}$ is an N_E-dimensional vector of unique energy levels with index i, and the matrix $\mathbf{A}$ maps the energy level index i to transition index j. Inversion of $\mathbf{A}$ thus yields the vector of energy levels. The same procedure is done for the associated uncertainties of the transitions obtained by experiment.

Self consistency within the energy levels is then achieved through an iterative re-weighting algorithm which adjusts (increases) the uncertainties in the line positions to an optimised uncertainty σ_{opt} until they agree with the rest of the network.

The inverted MARVEL energy levels form nodes of a SN, which are linked by transitions, to which the validation of experimental information can be done on all data simultaneously using elements of network theory. The final energy level uncertainties in the SN are obtained through combining the optimal MARVEL uncertainties of all transitions connecting a given energy level. This study used a new implementation, MARVEL 4, which uses a bootstrap method to determine uncertainties in the empirical energy levels it determines[376]. I used 100 iterations with the bootstrap method to determine the uncertainties in our empirical MARVEL energy levels.

4.11.2 Quantum Numbers

The rovibronic energy levels of $^{32}S^{16}O$ were assigned using the vibrational and rotational quantum numbers v and J, respectively, rotationless parity τ (e/f) and, in line with Hund's case-(a) coupling scheme, sublevels denoted by the fine structure F_{2S+1}. For the following definition of quantum numbers, triplet and singlet multiplets were assigned only, different formulae's would entail for systems with half integer spins. For $J \geq \Lambda + S$, the fine structure, F_{2S+1}, is defined for triplet electronic states via

$$\begin{aligned} F_1 &= N + S, \\ F_2 &= N, \\ F_3 &= N - S, \end{aligned} \tag{4.14}$$

where singlet states have no spin projection (i.e. F_2) and the total angular momentum excluding electronic and nuclear spin is labelled N. For linear molecules such as diatomics, levels with parity $+(-1)^J$ and $-(-1)^J$ are labelled e and f levels, respectively, and their relation to the $\pm$ parities are given in Table 4.5. Thus, assignment of every experimental rovibrational transition was done using the $v, J, e/f, F$ quantum numbers and standard spectroscopic notation for electronic states. For nuclear motion calculations the quantum numbers Λ, Σ, and Ω were used to assign electronic states, which are the projection of orbital, spin, and total angular momentum on the bond axis, respectively, in additional to the state labels $X\,^3\Sigma^-$, $A\,^3\Pi$, $b\,^1\Sigma^+$ etc. For the $X\,^3\Sigma^-$ and $B\,^3\Sigma^-$ states the spin-parity sub-levels in increasing energy order are

$$\begin{aligned} (F_1, e) &: \Lambda = 0,\ \Sigma = 0,\ \Omega = 0, \\ (F_2, f) &: \Lambda = 0,\ \Sigma = 1,\ \Omega = 1, \\ (F_3, e) &: \Lambda = 0,\ \Sigma = 1,\ \Omega = 1, \end{aligned} \tag{4.15}$$

whereas for the regular $A\,^3\Pi$ there is lambda-doubling, yielding

$$\begin{aligned} (F_1, e/f) &: \Lambda = 1,\ \Sigma = -1,\ \Omega = 0, \\ (F_2, e/f) &: \Lambda = 1,\ \Sigma = \ \ 0,\ \Omega = 1, \\ (F_3, e/f) &: \Lambda = 1,\ \Sigma = +1,\ \Omega = 2 \end{aligned} \tag{4.16}$$

Table 4.5: Relation between the e/f and $\pm$ parities for linear molecules.

e/f	J	$\pm$
e	even	$+$
e	odd	$-$
f	even	$-$
f	odd	$+$

and for the inverted $C\,^3\Pi$ the sublevels increase in energy with decreasing Ω

$$\begin{aligned}(F_1, e/f) &: \Lambda = 1,\ \Sigma = +1,\ \Omega = 2,\\ (F_2, e/f) &: \Lambda = 1,\ \Sigma = \ \ 0,\ \Omega = 1,\\ (F_3, e/f) &: \Lambda = 1,\ \Sigma = -1,\ \Omega = 0.\end{aligned} \tag{4.17}$$

Rigorous electric-dipole selection rules hold here, and can be summarised as $+ \leftrightarrow -$, $\Delta J = \pm 1$ $(e \leftrightarrow e, f \leftrightarrow f)$, and $\Delta J = 0$ $(e \leftrightarrow f, 0 \not\leftrightarrow 0)$.

4.12 The Experimental Transition Database

4.12.1 Outline

Table 4.6 summarises the experimental transition data included within our MARVEL analysis where each study is conveniently labelled with a tag including the first two digits of the year of publication and letters of the names of the first three authors in the form 'YYAaBbCc'. Table 4.6 includes the spectral coverage of each study, the associated quantum number coverage of their assignments, and the mean uncertainty of their results. I compiled a total of 50 106 transitions, of which 49 613 are non-redundant, from 29 experimental sources covering the $X\,^3\Sigma^-$, $a\,^1\Delta$, $b\,^1\Sigma^+$, $A\,^3\Pi$, $B\,^3\Sigma^-$ and $C\,^3\Pi$ electronic states of SO for rovibrational excitation's $J \leq 69$, $v \leq 30$.

4.12.2 General Comments

A crucial limitation of the experimental data set for SO (Table 4.6) is in the vibrational state coverage of the lower electronic states. Transitions to/within states beyond the third vibrational excitation for $X\,^3\Sigma^-$, $a\,^1\Delta$, $b\,^1\Sigma^+$, and $A\,^3\Pi$ are severely lacking. Some vibrational transition data involving states beyond $v > 3$ are available, but inclusion of these within our MARVEL analysis often led to fragmented SNs.

Our literature review found that no transitions have been measured associated with the vibrational ground state of the $B\,^3\Sigma^-$ state, which makes it difficult to constrain its PEC minima during refinement of the spectroscopic model. The impact of

this missing data is then amplified since the $B^3\Sigma^-$ and $C^3\Pi$ energies exhibit many mutual perturbations because of their overlapping potentials and strong coupling. To correctly model the perturbations one requires accurate positioning of the potentials corresponding to the resonating states relative to each other, which is made difficult because of the absence of data connecting to the $B^3\Sigma^-(v=0)$ state.

Isotopologues of SO have been experimentally measured by several sources covering $^{33}S^{16}O$[369,139,140], $^{34}S^{16}O$[335,366,377,328,139,141,367,140], $^{32}S^{17}O$[369], $^{32}S^{18}O$[369,335,366,377,141,367] and the rare isotopologue $^{36}S^{16}O$[140,369]. Few studies measure transitions within excited electronic states for these isotopologues, where Klaus et al.[335] measured the $a^1\Delta$ and $b^1\Sigma^+$ states, Yamamoto[328] measured the $b^1\Sigma^+$ state, and Heays et al.[140] measured the higher $A^3\Pi$, $B^3\Sigma^-$, and $C^3\Pi$ electronic states. Low vibronic excitation is typically measured with similar J coverage as the main $^{32}S^{16}O$ isotopologue.

4.12.3 Source Specific Comments

(a). A significant problem faced during data analysis is that several literature sources[378–380,330,371] did not provide obvious uncertainties on their line measurements, which is important for their validation within the MARVEL protocol (Section 4.11.1). I thus had to estimate their uncertainties through combination difference (CD) tests to other data in our database with known uncertainties where possible. Initial uncertainties for these sources were assumed to be 0.05 cm^{-1} and manually increased with successive MARVEL runs until the data gave satisfactory CD relations with other sources. In the case of blended lines, their uncertainties were increased by a factor of $\sqrt{2}$ relative to the non-blended data which often resulted in their validation. As a result of this the source uncertainties were estimated to be 0.02 cm^{-1}[371], 0.4 cm^{-1}[381,382], 0.05 cm^{-1}[380] and 0.2 cm^{-1}[330].

(b). Another issue with the experimental transition data is the significant proportion of blended lines that are reported, such in the measurements by Colin[380], [330], Clyne and Tennyson[370], Burkholder et al.[141], Kanamori et al.[334] and Bogey et al.[339]. To account for potential inaccuracy in their assignments the blended lines were given a lower weight in our SN model (see comment (a) above).

(c). Experimental sources[383,332,368,334,328,371,369,339,335,363] provide transition data in high vibrational states which were removed from the MARVEL SN (see Section 4.12.2).

(d). 15MaHiMo[139] provide much data on SO isotopologues with determined isotopically invariant parameters as well as other various constants for the lowest 7 vibrational states.

(e). 87BuLoHa[141] contains a misprint in Table 1 column 5, the SO ($X\,^3\Sigma^-$, $v = 1-0$, $R(18)$) line should be 1108.81665 cm^{-1}, not 1008.81665 cm^{-1}.

(f). 88KaTiHi[334] provide 60 SO ($a\,^1\Delta$, $v = 3-4, 4-5$) transitions. If high vibrational data for SO becomes available these would be a prime source for inter-vibrational transition data to supplement our MARVEL dataset.

(g). A discrepancy in the CDMS data for the $X\,^3\Sigma^-$, $v = 1$ state of SO was found. The lowest $v = 1$ state energy had to be shifted by 26.4559 cm^{-1}. Furthermore, a shift of 6.478 cm^{-1} was found in the $a\,^1\Delta$, $v = 0$ CDMS data of SO, where the source of error may come from use of a high uncertainty $v = 0-0$ band center[384]. The relative energies between CDMS levels within the same vibrational levels are unaffected, hence the transition wavenumbers are correct, but were corrected before being used in analyses involving MARVEL.

(h). 22HeStLy[140] perform high-resolution FUV Fourier-transform photoabsorption spectroscopy and provide the only published UV transition data covering the $C\,^3\Pi \leftarrow X\,^3\Sigma^-$ and $B\,^3\Sigma^-$ ($v = 4 \ldots 30$) $\leftarrow X\,^3\Sigma^-$. Because of the large overlap and spin-orbit coupling (SOC) between the $B\,^3\Sigma^-$ and $C\,^3\Pi$ states, many perturbations are present within the experimental data which appear to be assigned accurately. They also provide transition data for the isotopologues ^{33}S^{16}O and ^{36}S^{16}O.

(i). 99SeFiRa[331] provide 74 $b\,^1\Sigma^+ - X\,^3\Sigma^-$ magnetic dipole transitions, which have the same selection rules as for electric dipole transitions except from the parity changing rule. I do not include these in our MARVEL network.

(j). I chose to omit the 540 $A\,^3\Pi$ ($v' = 2$)$-X\,^3\Sigma^-$ ($v'' = 0$) transitions measured by Colin[380] for two reasons: (1) they produced many conflicts with the more comprehensive and more accurate data by Heays et al.[140]; (2) use of MARVELised energies generated including these data for refining our spectroscopic model proved very difficult; abnormalities in the energy structure were prescribed to be due to the poor data which did not occur when using the equivalent MARVELised data from Heays et al.[140].

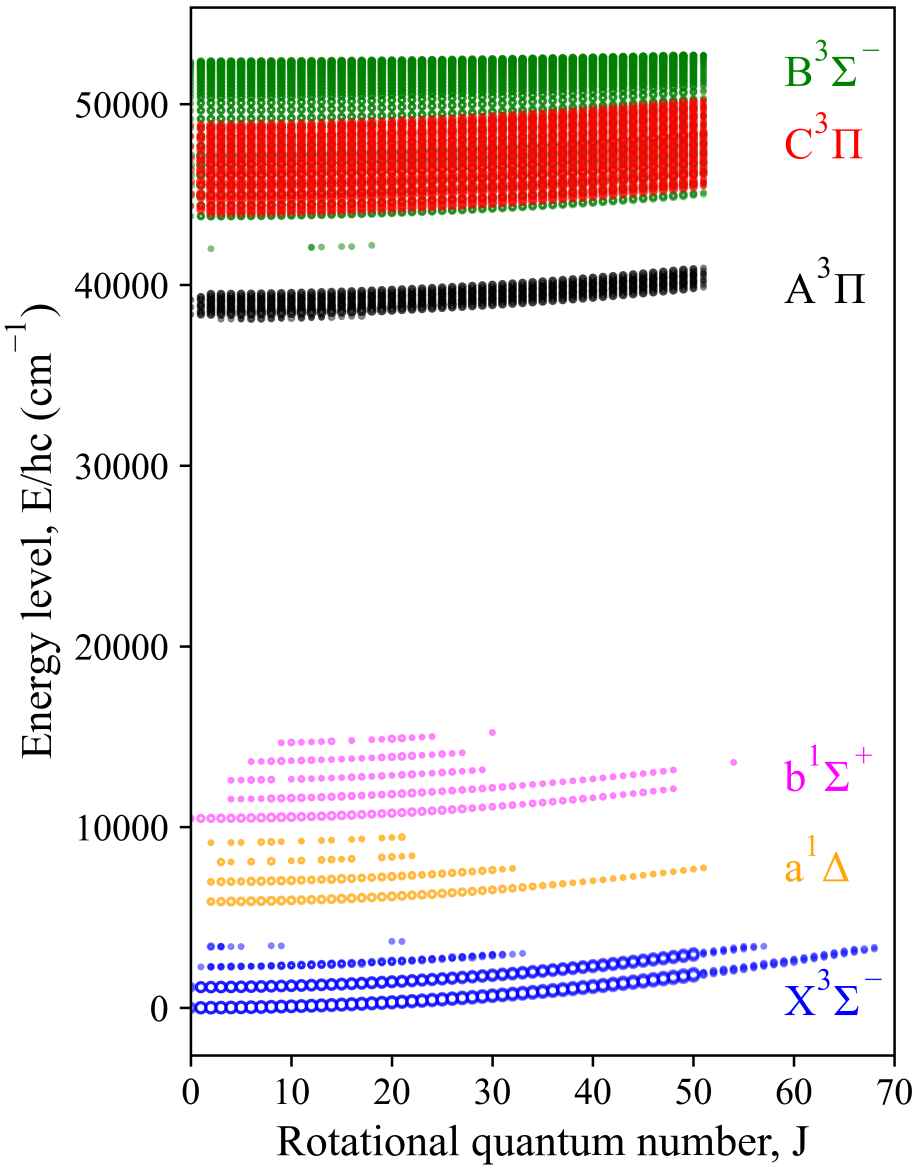

Figure 4.16: Our generated MARVEL energies plotted against the angular momentum quantum number J for the $X\,^3\Sigma^-$, $a\,^1\Delta$, $b\,^1\Sigma^+$, $A\,^3\Pi$, $B\,^3\Sigma^-$, and $C\,^3\Pi$ states. The vertical structure within each electronic state corresponds to the different vibrational levels. The size of the plot markers are directly proportional to the number of combination differences to that level in the SN.

Table 4.6: The experimental data sources included in the final MARVEL analysis and their spectroscopic coverage. TAG denotes the identifier used to label the data sources throughout this paper, V/T describes the number of validated or included (V) data using the MARVEL procedure described in Section 4.11.1 relative to the total number of provided transitions (T), and the final column cross-references source specific comments (Comm) in Section 4.12.3.

TAG	Source	Range (cm^{-1})	El. states	J	v	$\bar{\sigma}$ (cm^{-1})	V/T	Comm
64PoLi	364	0.435-2.2	*X*-*X*	0-3	0-0	1.07×10^{-5}	5/5	
64WiGoSa	365	2.87-5.74	*X*-*X*	1-4	0-0	1.67×10^{-5}	6/6	
69Colin	380	38672.94-39086.99	*A*-*X*	0-34	0-2	0.06	0/514	(a),(b),(j)
71BoMa	378	11354.43-11606.78	*b*-*X*	5-96	0-2	0.40	154/227	(a)
72BoMa	379	12265.5-12625.29	*b*-*X*	8-32	0-4	0.40	123/165	(a)
74Tiemann	366	1.21-4.31	*X*-*X*	1-4	0-0	8.64×10^{-8}	6/6	
76ClDe	336	4.26-11.6	*X*-*X*, *a*-*a*	0-9	0-0	4.50×10^{-5}	28/28	
82Colin	330	38255.26-39499.71	*A*-*X*	1-34	0-1	0.21	246/275	(a),(b)
82WoAmBe	333	3368.19-3386.30	*X*-*X*	1-9	0-3	2.00×10^{-3}	28/28	
82WuMoYe	383	23696.68-40816.33	*B*-*X*	0-0	1-19	2.00×10^{-4}	0/9	(c)
82Tiemann	367	1.21-9.89	*X*-*X*	1-9	0-0	3.53×10^{-5}	5/5	
85KaBuKa	332	1041.95-1116.20	*X*-*X*	1-44	0-6	2.14×10^{-3}	50/94	(c)
86ClTe	370	38051.24-38108.07	*A*-*X*	1-24	0-0	0.15	74/87	(b)
87BuLoHa	141	1051.89-2296.98	*X*-*X*, *a*-*a*	0-47	0-2	1.64×10^{-3}	560/562	(b),(e)
87EnKaHi	368	10.9-12.8	*a*-*a*	7-9	0-5	9.00×10^{-7}	12/24	(c)
88KaTiHi	334	1022.14-1121.26	*a*-*a*	2-41	0-5	2.01×10^{-3}	82/144	(b),(c),(f)
92LoSuOg	338	0.435-0.435	*X*-*X*	1-1	0-0	6.67×10^{-7}	0/1	
93Yamamoto	328	2.8-15.4	*b*-*b*	1-11	0-8	5.89×10^{-7}	42/42	(c)
94CaClCo	337	19-62.8	*X*-*X*, *a*-*a*	9-45	0-0	1.46×10^{-4}	33/33	
94StCaPo	371	39619.44-40280.32	*A*-*X*, *B*-*X*	1-26	0-5.	0.03	85/237	(a),(c)
96KlSaBe	369	19.7-34.4	*X*-*X*	12-25	0-7	3.76×10^{-6}	45/71	(c)
97BoCiDe	339	11.7-31.2	*a*-*a*, *b*-*b*	8-22	0-13	1.40×10^{-6}	81/143	(b),(c)
97KlBeWi	335	9.94-35.4	*a*-*a*, *b*-*b*	6-25	0-7	4.43×10^{-6}	41/55	(c)
99SeFiRa	331	5792.97-10566.42	*a*-*X*, *b*-*X*	0-50	0-2	0.01	813/890	(i)
03KiYa	363	1.11-2.8	*b*-*b*	0-2	0-22	6.67×10^{-8}	30/30	(c)
15MaHiMo	139	0.435-83.8	*X*-*X*	0-60	0-0	2.08×10^{-6}	110/110	(d)
17CaLaCo	296	2.87-28.1	*X*-*X*	0-20	0-0	6.67×10^{-5}	19/19	
CDMS	346	0.43-125.40	*X*-*X*, *a*-*a*	0-69	0-1	3.97×10^{-2}	860/862	(g)
22HeStLy	140	37856.62-52350.40	*A*-*X*, *B*-*X*, *C*-*X*	0-51	0-30	0.05	45434/45434	(h)

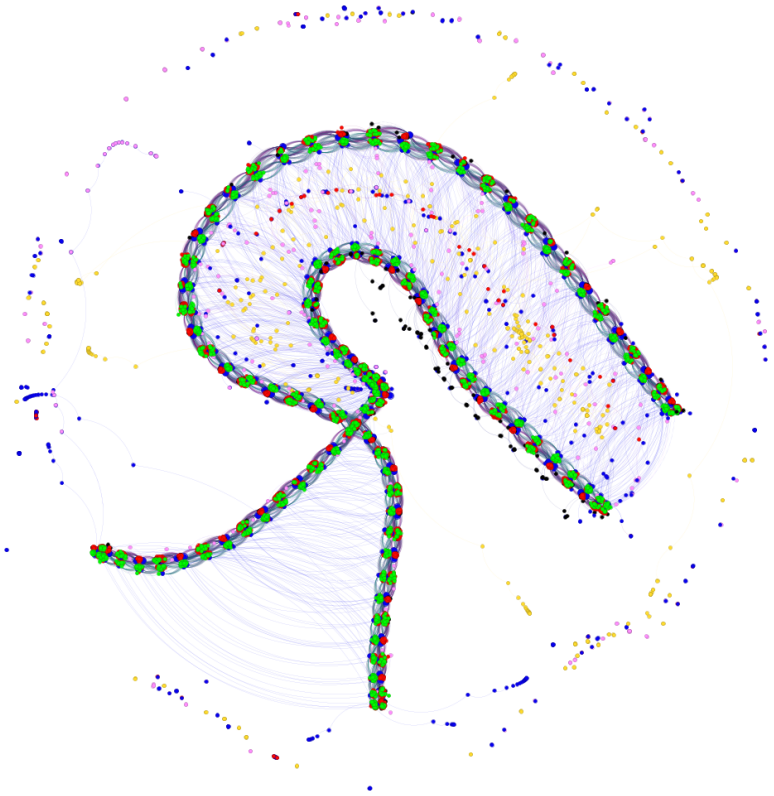

Figure 4.17: Illustration of the MARVEL spectroscopic network of SO. The coloured circles are nodes corresponding to energy levels and the connecting lines are transitions. The size of the nodes are proportional to the number of experimental transitions from that level. The colours correspond to different electronic states: blue for $X\,^3\Sigma^-$, pink for $b\,^1\Sigma^+$, yellow for $a\,^1\Delta$, red for $B\,^3\Sigma^-$, and green for $C\,^3\Pi$.

4.12.4 MARVELisation of the Experimental Transition Data

The $^{32}S^{16}O$ spectroscopic network was built through input of 50 106 rovibronic transitions into MARVEL from the 29 data sources outlined in Table 4.6. 546 transitions were invalidated since their optimised uncertainties did not satisfy the validation condition $\sigma_{opt} - \sigma_{exp} < 0.05$ cm^{-1}. Invalidation of transition data can be due to multiple reasons, errors in their quantum number assignment, in their measurement, in the digitization of their scanned data tables (especially in old papers), and simply because they are not self-consistent with the rest of the network. The latter is the most common cause of invalidation but since they usually connect few levels they are invalidated if the aforementioned reasons are not the cause. The invalidated transitions are removed from the MARVEL network but are kept in the MARVEL input file with a negative wavenumber transition frequency. I note

590 transitions were excluded not because of invalidation through the MARVEL procedure and are detailed in comments (i) and (j) in Section 4.12.3.

The majority of transitions that were invalidated are for lines connecting $v > 3$ (69%) because of the lack of inter-vibrational data energetically above $v > 3$ which, if included, resulted in the fragmentation of our central SN and the invalidation of otherwise seemingly reliable data sources. There are a lack of measurements of rotational transitions within these higher vibrational states. It was found that keeping data for $v \leq 3$ produced the largest set of self consistent energy levels and hence SN. For $v \leq 3$ the experimental source that provided the most invalidated transitions is by Colin[380] (44%) who measured the only $A\,^3\Pi \rightarrow X\,^3\Sigma^-$ $v = 2 \rightarrow 0$ band transitions, which is important for the refinement of the $A\,^3\Pi$ potential energy curve (PEC). Colin[380] measured $^{32}S^{16}O$ in emission by means of flash photolysis of sulphur bearing gases using a medium resolution quartz spectrograph. They provide no direct uncertainty on their line positions, but provide an uncertainty for their $X\,^3\Sigma^- \rightarrow B\,^3\Sigma^-$ bandheads of ± 1 cm^{-1} obtained in their absorption study. If one uses this value as a metric for their line position uncertainties, then it is to be expected that data coming from Colin[380] should be treated with caution, consequently leading to much of their data being invalidated. The majority of the remaining invalidated $v \leq 3$ data comes from Colin[330] and Stuart et al.[371] (21% and 22%, respectively) who measure $X\,^3\Sigma^- \rightarrow A\,^3\Pi$ and $X\,^3\Sigma^- \rightarrow B\,^3\Sigma^-$ transition bands, respectively.

As a result of the critical evaluation of the experimental transition data, we invert and provide optimised uncertainties for 8558 rovibrational energy levels for $^{32}S^{16}O$ which forms a fully self-consistent SN. Figure 4.16 plots the MARVEL energies versus the rotational quantum number J, where a large gap in the $\sim$15 000-37 000 cm^{-1} region exists, corresponding to missing highly excited vibrational data in the $X\,^3\Sigma^-$, $a\,^1\Delta$, and $b\,^1\Sigma^+$ states and any experimental coverage of the intermediate electronic states $c\,^1\Sigma^-$, $A'\,^3\Delta$, and $A''\,^3\Sigma^+$. For the higher vibrational energy levels of each electronic state there are also gaps in the rotational structure.

Figure 4.17 illustrates the $^{32}S^{16}O$ MARVEL spectroscopic network as a graph of nodes and edges. The graph was generated using the GEPHI software package[385] and the force-directed layout algorithm[386]. Each node is arranged based on its connectivity in the network and is agnostic to the quantum number labelling. Two strand structures are seen to form a ladder-like object which starts at low J at the right and increases in J along to the bottom left. Each rung on this ladder usually corresponds to an alternating parity state, where clusters at the rung have structure depending on the vibrational state. The nodes forming a ring at the outer perimeter

of the network correspond to states with minimal connection to the main network, and form strands with usually a single connecting node to the main network. These states (typically $a\,^1\Delta$ states) therefore will have minimal combination differences. Please note this is just an artistic illustration of the network and contains no information on the energies.

4.13 The Spectroscopic Model

To produce the final semi-empirical line list for $^{32}S^{16}O$ the *ab initio* spectroscopic model presented in Sections 4.3–4.10 (see also our study Brady et al.[13]) is used as a theoretical baseline for refinement to our MARVELised energy levels. Sections 4.2 and 4.3 overviews the details of the *ab initio* model and Section 4.13.1 details the method used to refine it.

4.13.1 Refinement

I refined our model to the IR/Vis region by fitting to the $X\,^3\Sigma^-$, $a\,^1\Delta$, $b\,^1\Sigma^+$, and $A\,^3\Pi$ energies only. Only the minimum number of states and couplings required are included such that the computed energies for these states agree with the MARVEL energies. The refined model includes PECs and couplings connecting the $X\,^3\Sigma^-$, $a\,^1\Delta$, $b\,^1\Sigma^+$, $A\,^3\Pi$, $B\,^3\Sigma^{-\dagger}$, $A'\,^3\Delta^\dagger$, $A''\,^3\Sigma^{+\dagger}$, $e\,^1\Pi^\dagger$ states, see Figure 4.18, where potentials for states labelled with a '†' superscript are not refined; these are included solely for their couplings within our model, but their dipoles are kept *ab initio*. These couplings, despite not being the dominant contributions to the energies of the $X\,^3\Sigma^-$, $a\,^1\Delta$, $b\,^1\Sigma^+$ and $A\,^3\Pi$ states, will redistribute intensities according to the intensity stealing mechanism (see Sections 4.15 and 5.2).

Firstly, I found that including the $c\,^1\Sigma^-$ and $d\,^1\Pi$ states within the model had negligible effect on the energies of the states of interest, and so they were omitted. Secondly, the inclusion of the $C\,^3\Pi$ state proved problematic and only worsened the fit. Because the $B\,^3\Sigma^-$ and $C\,^3\Pi$ PECs have large overlap and strong mutual couplings, their MARVEL energies include many perturbations. This is because the $B\,^3\Sigma^-$ and $C\,^3\Pi$ states resonate due to their close proximity, where an example resonance is plotted in Figure 4.19 between the $^{32}S^{16}O$ MARVEL $B\,^3\Sigma^-(v=6)$ and $C\,^3\Pi(v=1)$ rotational energies. To accurately reproduce these resonances in our spectroscopic model, careful modelling of the rotational trajectories leading into the resonances are required, where the vibrational energy levels need to be very accurate in this region. Any inaccuracies in this region will yield a resonance which occurs at both different energies and J, producing Obs.-Calc. of the order $10-100$ cm^{-1}. Additionally, both the $B\,^3\Sigma^-$ and $C\,^3\Pi$ states exhibit multiple avoided crossings with

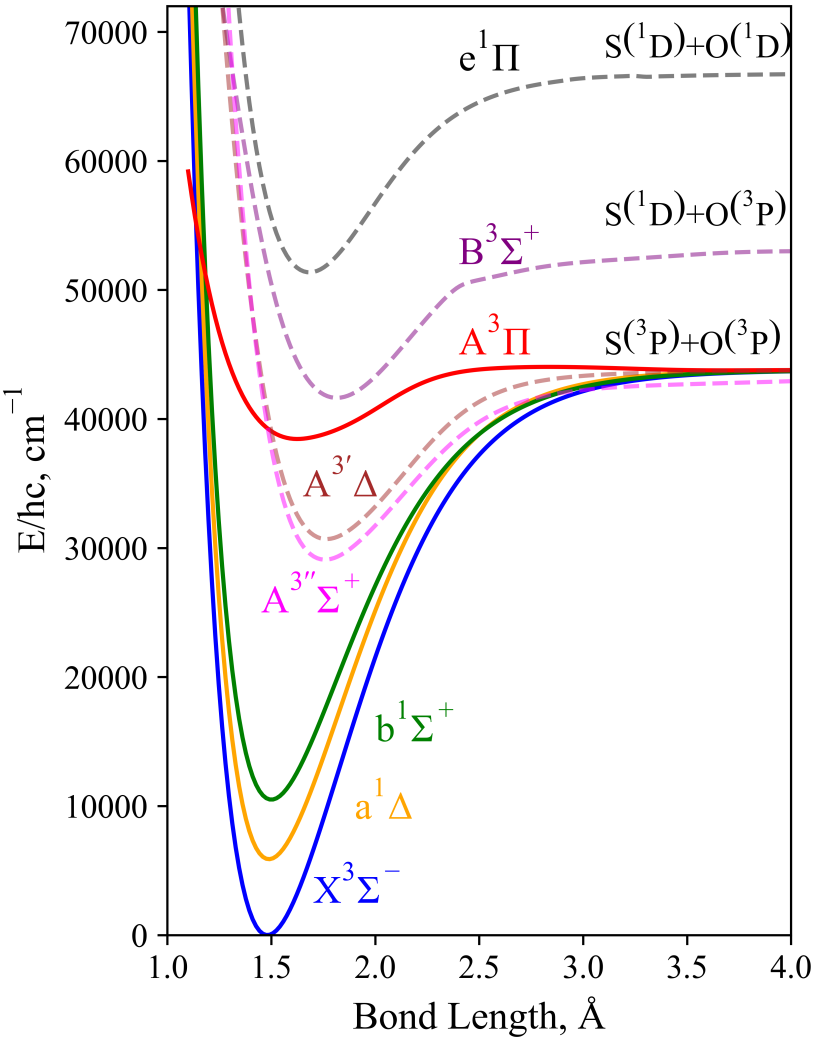

Figure 4.18: Potential energy curves of states included within our spectroscopic model of SO. The solid lines correspond to the potentials refined to MARVEL data, dashed lines correspond to states included within our model but have not been refined, where couplings to these states are essential for the accuracy of the $X\,^3\Sigma^-$, $a\,^1\Delta$, $b\,^1\Sigma^+$, and $A\,^3\Pi$ energies and band intensities.

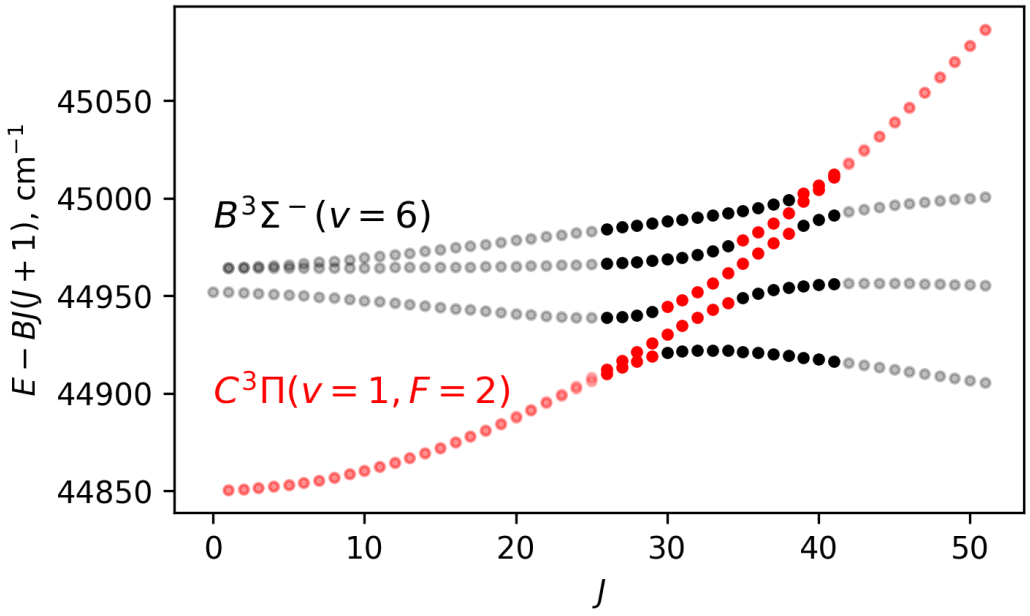

Figure 4.19: Rotational progression of the $^{32}S^{16}O$ MARVEL $B^3\Sigma^-(v=6)$ and $C^3\Pi(v=1)$ energies are plotted and deperturbed by a rotational constant of $B = 0.47$ cm^{-1}. The high opacity region marks the resonance of between these states, where the state trajectories with J appear to continue along the other state trajectories. This demonstrates the excellent assignment by Heays et al.[140] and the complicated task of fitting our model to these resonances.

upper electronic states, complicating their energy structuring. Furthermore, due to the lack of important experimental data and consequent lack of proper constraint on the $B^3\Sigma^-$ PEC minimum, efforts to include the UV region within my fit proved too difficult to do satisfactorily. Therefore the $C^3\Pi$ state is removed entirely from the model, but found including the $B^3\Sigma^-$, now without resonances with $C^3\Pi$, improved the fit of the $X^3\Sigma^-$, $a^1\Delta$, $b^1\Sigma^+$, and $A^3\Pi$ energies without being a major contribution to the accuracy of our model. My initial efforts to fit the UV model constrained the $B^3\Sigma^-$ PEC enough such that expectation values of its couplings to other states in our model were sensible. Furthermore, the current need for the IR/Vis SO line list means we leave work on the UV model to a future study when the appropriate data becomes available.

Refinement of the *ab initio* model is facilitated through Duo, a general purpose variational code that solves the rovibronic Schrödinger equation for diatomic molecules. A description of the methodologies used in Duo is given by Yurchenko et al.[159] and are discussed in Section 2.3.1 of Chapter 2. The refinement process goes as follows: (1) represent PECs, SOCs, EAMCs, DMCs, and other empirically fitted couplings such as rotational Born-Oppenheimer breakdown, spin-spin, and

spin-rotational curves with analytical forms; (2) compute energy levels using Duo through solving the rovibronic Schrödinger equation with curves defined; (3) fit parameters of the analytical functions such that the computed energy levels agree with the MARVEL energies.

Before refinement, the MARVEL energy level quantum number assignments need to be converted to the Duo quantum numbers J, τ, v, Λ, Σ, and Ω (see Section 4.11.2 and Table 4.1). Next, the i-th MARVEL energy was given a weight equal to

$$w_i = |\log_{10}(\sigma_i^{\text{opt}})| \times n_i^{\text{CD}}. \tag{4.18}$$

where σ_i^{opt} is its optimised uncertainty and n_i^{CD} is the number of combination differences/frequency of occurrence within the transition database. This weight is used in the Duo fitting procedure meaning energy levels with large uncertainty and a low number of combination differences will have less effect on the optimisation. Next, a running number must be defined to enumerate the global order of the energy levels calculated by Duo. These should agree with MARVEL's energy ordering for lower v and J numbers, but for higher energy states where Duo's calculated energies deviate significantly from the MARVEL data, the ordering of states between the two can differ. The running number I employ increases by 1 per vibrational excitation and by 100 per each electronic state, for example the running numbers for $X\,^3\Sigma^-(v=1)$ and $a\,^1\Delta(v=2)$ are 1 and 102, respectively. This produced a sensible enumeration that effectively separated the energy levels and provided correct assignments of the calculated energy levels.

4.13.1.1 Potential energy, spin–orbit, electronic angular momentum curves

I represent all PECs using the Extended Morse Oscillator (EMO) function[249] which has the form

$$V(r) = V_{\text{e}} + (A_{\text{e}} - V_{\text{e}}) \left(1 - \exp\left[-\left(\sum_{i=0}^{N} a_i \xi_p(r)^i\right)(r - r_{\text{e}})\right]\right)^2, \tag{4.19}$$

where $D_{\text{e}} = A_{\text{e}} - V_{\text{e}}$ is the dissociation energy, V_{e} is the potential minimum and A_{e} is the asymptote, a_i are the expansion coefficients, r_{e} is the equilibrium bond length, and $\xi_p(r)$ is the so called Šurkus variable[178] given by

$$\xi_p(r) = \frac{r^p - r_{\text{e}}^p}{r^p + r_{\text{e}}^p} \tag{4.20}$$

with p as an integer parameter to allow for a better convergence at large bond lengths values and effectively controls the "variability"/"responsiveness" of the polynomial with r. The $X\,^3\Sigma^-$, $a\,^1\Delta$, $b\,^1\Sigma^+$, $A\,^3\Pi$, $A'\,^3\Delta$, and $A''\,^3\Sigma^+$ states dissociate to the same asymptote S(^{3}P) + O(^{3}P), which was initially set at 5.429 eV as reported by Huber and Herzberg[356] and then floated during my fits, which converged to a nearby value of 5.42895 eV. The $B\,^3\Sigma^-$ state adiabatically correlates to S(^{1}D) + O(^{3}P) which was set to a value of 6.5731 eV (53015.86 cm^{-1}) as determined through atomic energies from the NIST atomic database. I shifted the PECs to the $X\,^3\Sigma^-$ minimum such that $V_e(X\,^3\Sigma^-) = 0$ cm^{-1}. Since only the $X\,^3\Sigma^-$, $a\,^1\Delta$, $b\,^1\Sigma^+$, $A\,^3\Pi$, $B\,^3\Sigma^-$ and $C\,^3\Pi$ have experimental transition data to refine their PECs to, the *ab initio* PECs for the $A''\,^3\Sigma^+$, and $A'\,^3\Delta$ were fitted to the EMO function given in Eq. (4.19) using 10 expansion parameters which ensured accurate representation of their shape as given by *ab initio* calculations. Once the EMO functions were fitted, I could then tune their dissociation assymptotes to the 5.429 eV limit[356]. The T_e value for the $A''\,^3\Sigma^+$ state was fixed to 30 692 cm^{-1} as provided by Norwood and Ng[357]. We chose not to tune the $e\,^1\Pi$ *ab initio* PEC because it has a strong influence on the computed $X\,^3\Sigma^-$, $a\,^1\Delta$, $b\,^1\Sigma^+$, and $A\,^3\Pi$ energies and negatively effects the refinement when altering its potential. This negative effect is due to: (1) The shapes of the PEC would be destroyed in tuning the T_e and D_e values; (2) the $e\,^1\Pi$ state has been diabatised[13], so tuning its PEC would change the avoided crossing morphology and hence a new diabatisation of the spectroscopic model would be required; without experimental data covering $e\,^1\Pi$ we chose to keep the diabatised *ab initio* potential values.

During the refinement, the *ab initio* $B\,^3\Sigma^-$ PEC by Sarka and Nanbu[325] was used instead of the PEC from our recent *ab initio* work[13]. The latter did not employ (the extended) sulphur specific diffuse d-orbital functions in the basis set, which led to the underestimation of the S(^{3}P) + O(^{3}P), S(^{1}D) + O(^{3}P) and S(^{1}D) + O(^{1}D) dissociation asymptotes. Particularly, the omission of these d-orbitals negatively effected the $B\,^3\Sigma^-$ PEC the most (see Table 4.3). The adiabatic character of the $B\,^3\Sigma^-$ PEC was modelled by diagonalising a 2×2 matrix of diabatic potentials and corresponding diabatic coupling yielding the adiabatic potentials as the associated eigenvalues[13].

The *ab initio* SOCs and EAMCs were morphed from the grid representation to a Šurkus-like expansion[176,177] given by

$$F(r) = \sum_{i=0}^{N} B_i z^i(r)(r-\xi_p) + \xi_p B_\infty, \tag{4.21}$$

where B_i are the expansion coefficients, B_∞ is usually taken as zero in-order to prevent the expansion from diverging towards $r \to \infty$, and z is a damped displacement coordinate given by

$$z(r) = (r - r_e)\exp[-\beta_2(r - r_e)^2 - \beta_4(r - r_e)^4], \tag{4.22}$$

where β_2 and β_4 are damping constants which prevent large oscillations of the function asymptotes which are not well constrained by the data.

4.13.1.2 Empirical Rotational Born-Oppenheimer Breakdown, Spin-Spin, Spin-Rotational Curves

The phenomenological spin-spin (SS) couplings and the empirical spin-rotation (SR) couplings of the triplet $X\,^3\Sigma^-$, $A\,^3\Pi$, and $B\,^3\Sigma^-$ states were fitted to account for additional Ω-splitting and to allow for additional variation of J, respectively, not described by the *ab initio* model[159,107]. Additionally, rotational Born-Oppenheimer breakdown (BOB) curves for all but the $B\,^3\Sigma^-$ state were fitted to correct for the electron un-coupling to the nuclear motion. This produced additional J^2 dependence in the residuals of the rovibronic energies, and can be thought of as a correction to the position-dependent rotational mass. Some SS, SR, and BOB couplings are modelled using Eq.(4.22) and some using a Šurkus polynomial expansion given by

$$F(r) = (1 - \xi_p)\sum_{i=0}^{N} a_i \xi_p^i + \xi_p a_\infty. \tag{4.23}$$

This greatly enhanced the accuracy of the finalised spectroscopic model.

4.13.2 Accuracy of the Refined Model

Figure 4.20 illustrates the Observed minus Calculated (Obs.-Calc.) energy residuals as a function of the rotational quantum number J, and provides a metric on the accuracy of our model to reproduce our MARVELised energies (see Section 4.12). Most of the highly scattered energy levels have no combination differences with other sources, and so are effectively removed from the fit by setting their weight to 10^{-6}. I fit 100% of 512 $X\,^3\Sigma^-$ ($J \leq 69$) energy levels with a total root-mean-square (rms) error of 3.13×10^{-3} cm^{-1}, 99% of 244 $a\,^1\Delta$ ($J \leq 52$) energy levels with a rms error of 1.08×10^{-3} cm^{-1}, 95% of 206 $b\,^1\Sigma^+$ ($J \leq 64$) energy levels with a total rms error of 0.27 cm^{-1}, and 78% of 1262 $A\,^3\Pi$ ($J \leq 34$) energy levels with a rms error of 0.24 cm^{-1}. The above rms errors were calculated after filtering outliers from our dataset which heavily influenced the rms, such as the scattered data of $b\,^1\Sigma^+(v = 3,4)$, the $A\,^3\Pi(v = 2, J \geq 35)$ states, and a single data point of $a\,^1\Delta$.

Elks and Western[343] provide rotational constants for the $A\,^3\Pi$ ($v = 4-13$) states fitted to their 1+1 resonances enhanced multiphoton ionisation spectra. I used these constants to compute low J ($J \leq 5$) energies via PGOPHER[155]. These energies to our knowledge are the only ones covering the highly excited vibronic states of $A\,^3\Pi$ and so we use them to constrain the $A\,^3\Pi$ potential up to its dissociation. The black points in figure 4.20 for $J \leq 5$ (see label (a)) indicates the vibrational dependence in the residuals of these PGOPHER levels, which I managed to fit all within $\sim$4.5 cm^{-1}. Doing this allowed for a more physical description of the effective position dependent correction to the rotational mass for the $A\,^3\Pi$ state by constraining the potential gradient, and ultimately led to higher accuracy in the associated computed lifetimes (see Section 4.14.1).

Generally, the $b\,^1\Sigma^+$ data are of high quality and are reproduced by our model to within $\sim 10^{-4} - 10^{-3}$ cm^{-1} with the exception of high scatter within the MARVELised $b\,^1\Sigma^+(v = 3,4)$ energies. This scatter can be seen in Figure 4.20 around the label (b). One striking feature in Figure 4.20 is of the $A\,^3\Pi$ ($v = 2$) Obs.-Calc. residuals, which, despite many attempts to model correctly, are poorly recovered in the model. A smooth, but rapid increase in the MARVEL energies with J of this band to $\sim$35 cm^{-1} at $J = 51$ is seen. It could be postulated that a dark state pushes these energies upwards, some candidates being the $c\,^1\Sigma^-$, $A''\,^3\Sigma^+$, and $A'\,^3\Delta$ which cross through the $A\,^3\Pi$ potential, however all attempts to correctly position their PECs relative to the $A\,^3\Pi$ failed to reproduce this behaviour. No published data on the crossing states exists, but it is entirely possible that a correct description of these electronic potentials could resolve this issue, and some empirical data could be used to constrain their curves better than blindly varying their positions.

Some residual J-dependence can be seen for the $X\,^3\Sigma^-$ and $b\,^1\Sigma^+$ states, where the former is due to J-dependent Ω-splitting and parity splitting within the $|\Omega| = 1$ levels, and the latter is due to vibrational dependence in the effective rotational centre not being fully accounted for. However, the residuals to the MARVEL energies are all $\leq 10^{-2}$ cm^{-1} which means the model should extrapolate well to higher J.

One major problem faced during the refinement was with the spin-orbit splitting of the $A\,^3\Pi$ energies, where experiment[380,330] predicts regular Ω energy ordering, whereas multiple *ab initio* calculations reveal the $\langle A\,^3\Pi|\,\mathrm{SO}_z\,|A\,^3\Pi\rangle$ SOC to have a negative phase, suggesting irregular Ω energy ordering. Analysis by Colin[380] shows the Λ-doubling (LD) to be $\sim$1.2 cm^{-1} in the lowest energy Ω state with slight dependence on J, small doubling in the middle component which varies with $J(J+1)$ and zero splitting for the highest component state. To decide whether to adopt the irregular Ω energy ordering suggested by *ab initio* calculations or the

experimental assignment with a change in phase of the $\langle A\,^3\Pi|\,\mathrm{SO}_z\,|A\,^3\Pi\rangle$ SOC, the e/f parity splitting of the $A\,^3\Pi$ energies were studied since this would confirm what Λ-doubling matrix elements to adopt. It was found that the slightly J-dependant $\sim$1.2 cm^{-1} parity splitting in the lowest energy state could only be resolved via the following Λ-doubling element

$$\hat{\mathscr{H}}_{\mathrm{LD}} = \frac{1}{2}\alpha^{\mathrm{LD}}_{opq}(r)(\hat{S}^2_+ + \hat{S}^2_-) \tag{4.24}$$

with the Λ-doubling constant being consistent with the Brown and Merer[160] convention $\alpha^{\mathrm{LD}}_{opq} = o^{\mathrm{LD}} + p^{\mathrm{LD}} + q^{\mathrm{LD}}$ for a regular Ω energy ordering, i.e. the splitting is between states of $\Delta\Sigma = \pm 2$ which is only possible for a triplet state if $\Omega = 0$. If one adopted an irregular assignment scheme with $\Omega = 2$ for the lowest energy state, then one could not correctly model the J-dependence of the splitting since the element in Eq.(4.24) would be zero. The experimental assignment was thus adopted and the sign of the computed $\langle A\,^3\Pi|\,\mathrm{SO}_z\,|A\,^3\Pi\rangle$ SOC was changed. This should not break the phase consistency of the model since it is a diagonal coupling.

4.13.3 Dipole Moment Curves

We use the accurate *ab initio* ground state dipole moment function from Bernath et al.[341] who calculate with an ic-MRCI+Q level of theory including the Davidson corrections, scalar relativistic contributions using the exact 2-component (X2C) relativistic Hamiltonian, and aug-cc-pCV6Z-X2C basis sets. All other DMCs are computed at a level of theory described in Section 4.2. Within nuclear motion and intensity calculations, these dipoles are originally represented as a grid of *ab initio* points on the Duo defined grid, however one sees a flattening of both the IR $X\,^3\Sigma^-$–$X\,^3\Sigma^-$ band spectrum and its variation of TDMC with vibrational excitation. The source of this nonphysical flattening has been discussed by Medvedev et al.[387,388], Medvedev and Ushakov[389] who identify numerical noise as the culprit. This noise comes from the interpolation of the given MOLPRO dipole grid points onto the Duo defined grid. One can try to increase the precision of their transition moments from double to quadruple precision, but this seldom fixes the problem with any appreciable magnitude. The most effective method found is to represent the input dipole moments analytically. For the $X\,^3\Sigma^-$ DMC, the following 'irregular DMC' form proposed by Medvedev and Ushakov[389] was adopted

$$\mathscr{D}_{\mathrm{irreg}}(r) = \chi(r; c_2, \ldots, c_6)\sum_{i=0}^{6} b_i T_i(z(r)) \tag{4.25}$$

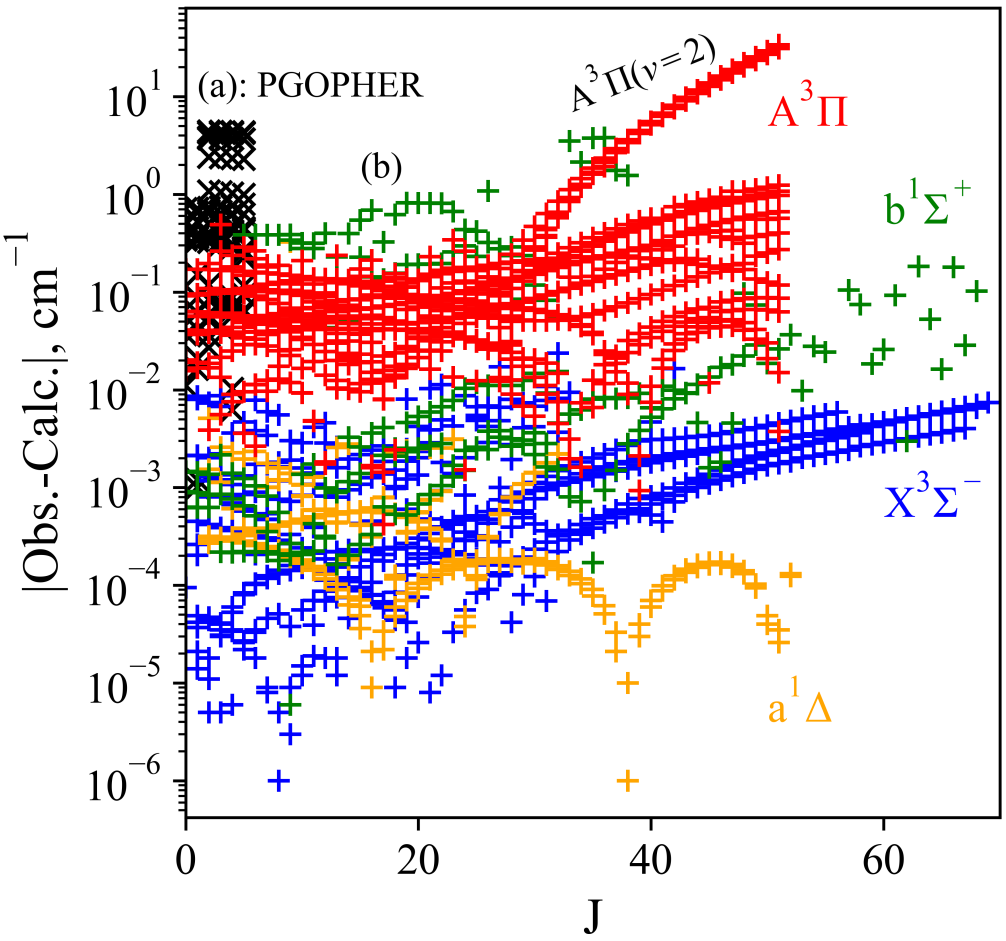

Figure 4.20: Visual representation of the difference between MARVEL (Obs.) and Duo calculated (Calc.) energy levels as a function of J for the $X\,^3\Sigma^-$, $a\,^1\Delta$, $b\,^1\Sigma^+$, and $A\,^3\Pi$ states. (a) The Black crosses compare computed PGOPHER energies to the calculated Duo ones; (b) high scatter present in the MARVELised $b\,^1\Sigma^+(v=3,4)$ levels; ($A\,^3\Pi(v=2)$) the Obs.-Calc. structure in the red points increases rapidly towards higher J's (see text).

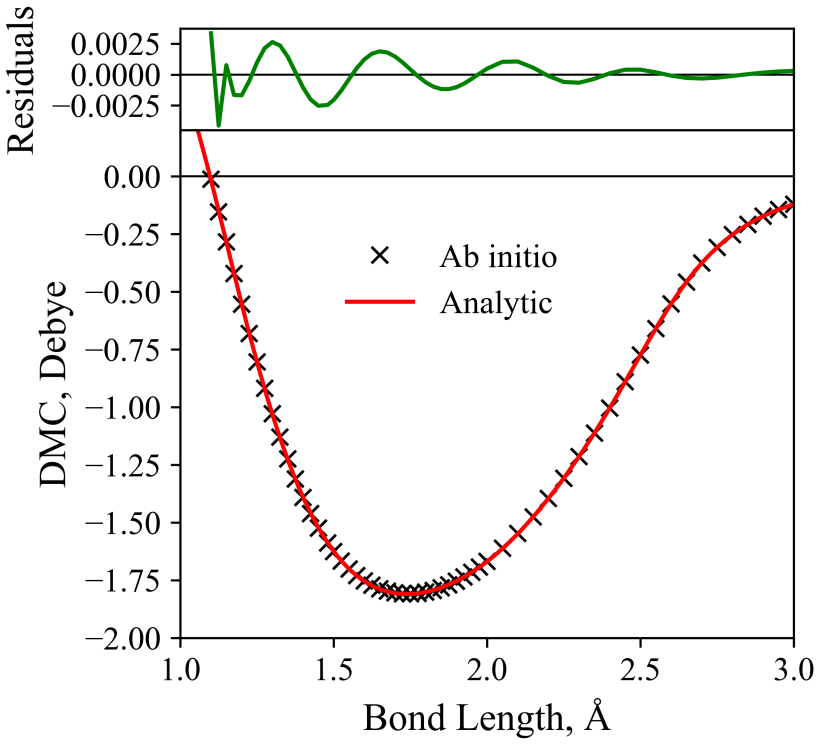

Figure 4.21: The *ab initio* $X\,^3\Sigma^-$ DMC provided by Bernath et al.[341], computed at an ic-MRCI+Q level of theory with full relativistic corrections using aug-cc-pCV6Z-X2C basis sets, is shown (black crosses) superimposed with my fitted analytical form using Eq. 4.25 (red line). The residuals to the *ab initio* DMC of the fit are shown in the top panel (green line).

Where T_i are Chebyshev polynomials of the first kind, b_i are summation coefficients to be fit, $z(r)$ is a reduced variable in bond length similar to the damped polynomial coordinate in Eq.(4.22) and is given by,

$$z(r) = 1 - 2e^{-c_1 r}, \tag{4.26}$$

which maps the $r \in [0,\infty]$ interval to the $z \in [-1,1]$ reduced interval, and finally $\chi(r;c_2,...,c_6)$ is an r-dependent term parametrically dependent on 5 c_k parameters to be fitted and is given by

$$\chi(r;c_2,...,c_6)\frac{(1-e^{-c_2 r})^3}{\sqrt{(r^2-c_3^2)^2+c_4^2}\sqrt{(r^2-c_5^2)^2+c_6^2}}.$$

Our fitted $X\,^3\Sigma^-$ DMC is illustrated with its residual to the *ab initio* DMC in Figure 4.21.

The irregular DMC has the desirable properties of quickly converging to the

correct long-range limit, having enough parameters (13) to ensure an accurate description of the full range in bond length with minimal local oscillations, and yields a straight Normal Intensity Distribution Law (NIDL)[389,390,387].

The desired NIDL is a major constraint on the model DMC, where the logarithm of the vibrational overtone TDM (intensity) should evolve linearly with the square root of the upper state energy over the harmonic frequency, or $\sqrt{v' + \frac{1}{2}}$. The $v' - 0$ TDM was computed up to dissociation for the $X\,^3\Sigma^-$ using both the grid defined dipole and the fitted analytical form, where Figure 4.22 shows their behaviour. The expected linear form of the NIDL is shown on Figure 4.22 as a gray line which is seen to have greater agreement to the TDM computed using the analytical $X\,^3\Sigma^-$ DMC compared to the calculation using the grid interpolated DMC. At the $v' = 8$ overtone the grid interpolated DMC causes an non-physical flattening of the intensities at $\sim 10^{-6}$ Debye, whereas a departure from the straight NIDL at $v' = 16$ when using the analytical form is seen – flattening at $\sim 10^{-14}$ Debye. The analytically represented $X\,^3\Sigma^-$ DMC therefore provides a more physically meaningful behaviour of the vibrational overtone TDM but still departs from the expected NIDL at high overtones where the intensities are much lower and therefore less important since they will be 'washed out' by higher intensity bands[389,387,390].

4.14 Line List

We produce a semi-empirical rovibronic line list SOLIS for $^{32}S^{16}O$ covering the $X\,^3\Sigma^-$, $a\,^1\Delta$, $b\,^1\Sigma^+$ and $A\,^3\Pi$ electronic states, where a system involving couplings between $X\,^3\Sigma^-$, $a\,^1\Delta$, $b\,^1\Sigma^+$, $A\,^3\Pi$, $B\,^3\Sigma^-$, $A''\,^3\Sigma^+$, $A'\,^3\Delta$, and $e\,^1\Pi$ defines our spectroscopic model. The SOLIS line list covers wavelengths down to 222.22 nm. Illustrations of the spectra simulated with the new line list are presented in Figures 4.25 and 4.26.

For nuclear motion calculations a vibrational sinc-DVR basis set was defined for a grid of 301 internuclear geometries in the range 0.6–6.0 Å. Fifty eight vibrational wavefunctions were then selected for the $X\,^3\Sigma^-$, $a\,^1\Delta$, $b\,^1\Sigma^+$, $A\,^3\Pi$, $B\,^3\Sigma^-$, $A''\,^3\Sigma^+$, $A'\,^3\Delta$, and $e\,^1\Pi$ states to form the contracted vibronic basis. In total 7 008 190 Einstein A coefficients between 84 114 bound rovibronic states were computed with a maximum total rotational quantum number $J_{max} = 250$.

The PEC of the $A\,^3\Pi$ state implies that predissociative and continuum states should exist for the region above dissociation. To this end, these states have been removed from the line list through checking the character of the wavefunctions at the 'right' simulation border r_{max} in our Duo model where unbound states tend to oscillate at $r \to \infty$ with a non-zero density around r_{max}[234]. The presented line list

Table 4.7: Extract from the states file of the line list for SO.

i	Energy (cm^{-1})	g_i	J	unc	τ	Parity	State	v	Λ	Σ	Ω	Ma/Ca	Energy (cm^{-1})
733	12277.658473	5	2	0.302298	0.068323	+ e	a1Delta	6	2	0	2	Ca	12277.658473
734	12576.55717	5	2	0.01039	0.0067518	+ e	b1Sig+	2	0	0	0	Ma	12576.558535
735	12824.746272	5	2	0.603962	0.025301	+ e	X3Sig-	12	0	0	0	Ca	12824.746272
736	12836.684546	5	2	0.603962	0.025272	+ e	X3Sig-	12	0	1	1	Ca	12836.684546
737	13297.933546	5	2	0.352298	0.059146	+ e	a1Delta	7	2	0	2	Ca	13297.933546
738	13602.425655	5	2	0.165193	0.0069414	+ e	b1Sig+	3	0	0	0	PS	13601.834707
739	13810.582705	5	2	0.653962	0.023019	+ e	X3Sig-	13	0	0	0	Ca	13810.582705
740	13822.57783	5	2	0.653962	0.022993	+ e	X3Sig-	13	0	1	1	Ca	13822.57783

i: State counting number.
$\tilde{E}$: State energy term values in cm^{-1}, MARVEL or Calculated (DUO).
g_i: Total statistical weight, equal to $g_{ns}(2J+1)$.
J: Total angular momentum.
unc: Uncertainty, cm^{-1}.
τ: Lifetime (s^{-1}).
$+/-$: Total parity.
e/f: Rotationless parity.
State: Electronic state.
v: State vibrational quantum number.
Λ: Projection of the electronic angular momentum.
Σ: Projection of the electronic spin.
Ω: Projection of the total angular momentum, $\Omega = \Lambda + \Sigma$.
Label: 'Ma' is for MARVEL, 'Ca' is for Calculated, and 'PS' is for predicted shift.
Energy: State energy term values in cm^{-1}, Calculated (DUO).

Table 4.8: Extract from the transitions file of the line list for SO.

f	i	A_{fi} (s^{-1})	$\tilde{\nu}_{fi}$
37557	36527	2.7817E-01	5199.704942
37204	36852	2.7817E-01	5199.704945
32098	32422	1.2080E+00	5199.713048
21055	22048	3.3851E-06	5199.718029
60350	61047	2.8777E-04	5199.728151
45755	46561	4.3835E-01	5199.728902

f: Upper state counting number;
i: Lower state counting number;
A_{fi}: Einstein-A coefficient in s^{-1};
$\tilde{\nu}_{fi}$: transition wavenumber in cm^{-1}.

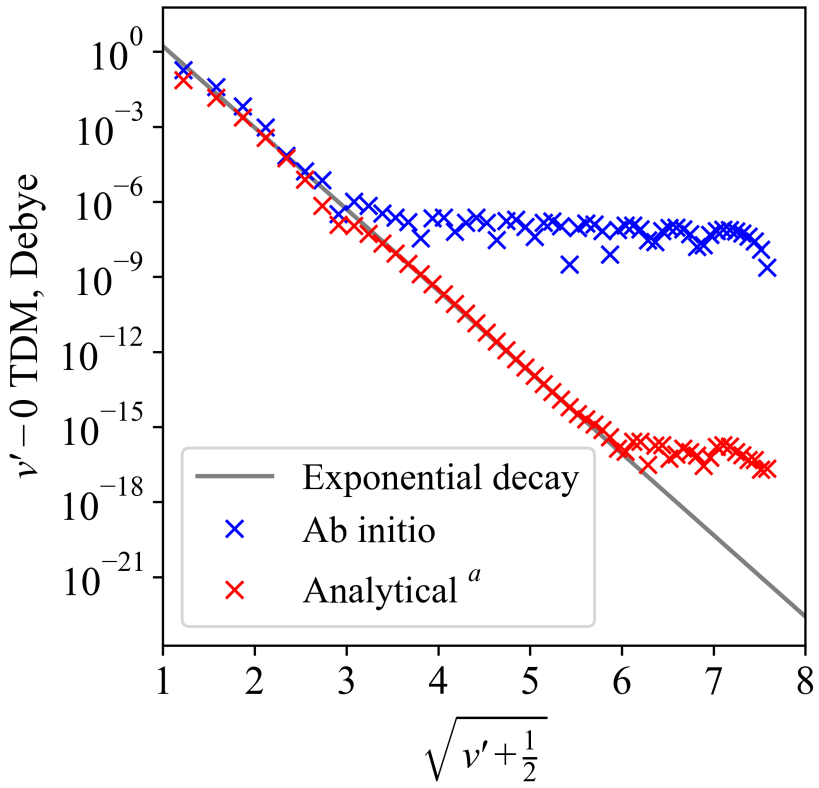

Figure 4.22: $v'-0$ overtone TDMs are plotted on a log scale vs. $\sqrt{v'+\frac{1}{2}}$ and are computed using the grid interpolated *ab initio* DMC of[341] (shown as blue crosses) and the fitted analytical model DMC (Eq. (4.25), shown as red crosses). A simple exponential decay is shown for comparison which simulates the correct NIDL behaviour.

therefore only contains bound to bound transitions only.

The calculated energies in the `.states` file are 'MARVELised' which involves replacing them with the MARVEL ones. For levels that are not covered by the MARVEL SN, the predicted shift method of Bowesman et al.[391] was used to MARVELise them. Predicted shifts work by fitting the Obs.-Calc. trends as functions of J for each 'state', v and Ω energy band to then interpolate gaps within the MARVEL network or extrapolating to higher J.

The SOLIS line list is available in the ExoMol database in the form of a States (`.states`) and Transition (`.trans`) files, with extracts shown in Tables 4.7 and 4.8 respectively. Uncertainties for the energy levels where either taken directly as the MARVEL ones where available, or otherwise computed using the following

empirical formulae

$$\sigma(\text{state}, J, v) = \Delta T + \Delta\omega\, v + \Delta B\, J(J+1), \tag{4.27}$$

where σ is the energy uncertainty for a given state and ΔT, $\Delta\omega$, ΔB are state dependent parameters given in Table 4.9. ΔT were found by taking twice the standard deviation of the total Obs.-Calc. of each electronic state (see Figure 4.20) after outliers were removed by selecting states outside of this two standard-deviation threshold, where the standard deviation was computed again.

Table 4.9: State dependent parameters (in cm^{-1}) of Eq. (4.27) used to estimated uncertainties for the calculated states of $^{32}\text{S}^{16}\text{O}$ where MARVEL uncertainties were not available.

State	ΔT	$\Delta\omega$	ΔB
$X\,^3\Sigma^-$	0.003363	0.05	0.0001
$a\,^1\Delta$	0.001698	0.05	0.0001
$b\,^1\Sigma^+$	0.368965	0.05	0.0001
$A\,^3\Pi$	2.835039	0.05	0.0001

4.14.1 Intensity Scaling: Dipoles and Lifetimes

There are only a few recorded experimental values for electric dipole moments, lifetimes, and no direct intensity measurements for many electronic states of SO which can be used to constrain our *ab initio* dipoles. Lifetimes are useful to constrain dipole moments via the relation

$$\frac{1}{\tau_u} = \sum_l A_{ul} \propto |\langle u|\,\mu_\sigma\,|\tilde{l}\rangle|^2, \tag{4.28}$$

where $|\tilde{l}\rangle$ is the dominant ro-vibronic state contributing to the lifetime of the level $|u\rangle$, $\sigma = 0, \pm 1$ denotes a tensorial dipole component. So a scaling in lifetime $\tilde{\tau} = \xi\tau$ would correspond to an approximate scaling in dipole moment to the dominant lower state of $1/\sqrt{\xi}$.

Previous Stark measurements[364,338] have determined the ground state dipole to be $\mu_0^X = 1.55(2)$ D[364] and 1.52(2) D[338], slightly smaller than my computed vibrational transition moment of $|\langle X\,^3\Sigma^-, v=0|\,\mu_0\,|X\,^3\Sigma^-, v=0\rangle| = 1.588$ D. I scale our $X\,^3\Sigma^-$ dipole to the value of 1.535 D averaged from the two Stark measurements, which I note is the dipole moment adopted by CDMS[346] where the same averaging was done. Wildt et al.[392] measure the radiative lifetime of the $b\,^1\Sigma^+(v=0)$ state through time-resolved measurements of the $b\,^1\Sigma^+ \rightarrow X\,^3\Sigma^-$ emission band

and provide a lifetime of $\tau = 6.8 \pm 0.4$ ms. To achieve this lifetime, I scale our $\langle b\,^1\Sigma^+ | \mu_0 | b\,^1\Sigma^+ \rangle$ dipole by a factor of 0.7401.

Saito[279] determines the $a\,^1\Delta$ dipole moment to be 1.336 ± 0.045 D through Stark measurements, larger than my computed transition moment $|\langle a\,^1\Delta, v = 0 | \mu_0 | a\,^1\Delta, v = 0 \rangle| = 1.184$ D. I scale our $a\,^1\Delta$ dipole by a factor of 1.1282 to reproduce the measured transition moment.

Radiative lifetimes of the $A\,^3\Pi$ state for $v' = 0-13$ were measured by Elks and Western[343] by laser induced fluorescence and for $v' = 0-6$ by Clyne and Liddy[393]. Figure 4.23 shows the experimentally determined lifetimes as a function of v' with the theoretically predicted values by Borin and Ornellas[311], Fulscher et al.[321], and those computed by our model superimposed in red. Since Elks and Western[343] quote their lifetimes to a lower uncertainty and for a large vibrational coverage, their lifetimes were chosen to be modelled. Modelling these lifetimes proved to be difficult, the characteristic sharp drop in lifetime from $v' = 0$ and $v' = 1$ was very sensitive to multiple factors: (1) the position of the $\langle A\,^3\Pi | \mu_{\pm 1} | X\,^3\Sigma^- \rangle$ dipole relative to the respective PECs; (2) the crossing point of the dipole with zero; (3) the local gradient of the dipole around the zero crossing point. Initial attempts to reproduce the experimental lifetimes were made using our *ab initio* dipole, various *ab initio* dipoles from the literature[321,325,305], and the empirical dipole from Elks and Western[343] which all failed to produce lifetimes that agreed with experiment.

Firstly, I was able to reproduce the lifetimes of Elks and Western[343] using a linear dipole function. Albeit being nonphysical, it provided important constraints on the short range position and the gradient around the equilibrium geometry. This linear dipole function was then combined with the MRCI-F12+Q/aug-cc-pV(5+d)Z dipole computed by Sarka and Nanbu[325] at larger values of r into a single smooth curve. Despite a slight change in the shape of the *ab initio* dipole, Figure 4.23 shows that my semi-empirically fitted $\langle A\,^3\Pi | \mu_{\pm 1} | X\,^3\Sigma^- \rangle$ dipole yields lifetimes which are much closer to the experimentally determined lifetimes by Elks and Western[343] than other theoretical predictions.

4.14.2 Partition Function

The molecular partition function (PF) for $^{32}S^{16}O$ is computed from our semi-empirical line list using the equation

$$Q(T) = \sum_i g_i^{\text{tot}} e^{-\frac{c_2 \tilde{E}_i}{T}} \tag{4.29}$$

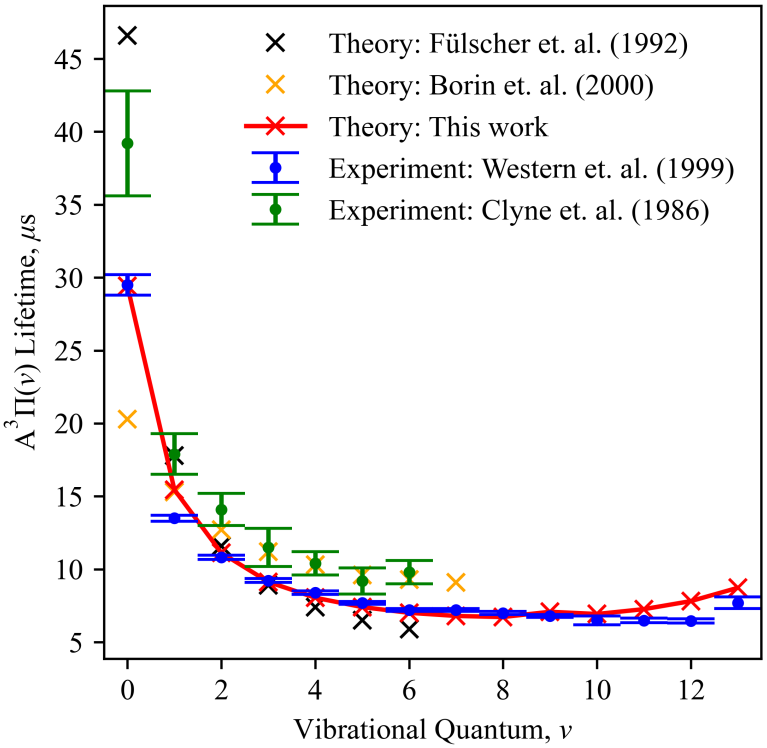

Figure 4.23: The $A\,^3\Pi$ lifetimes as a function of v' are shown from experimental[343,370] and theoretical[311,321] sources with my computed lifetimes overlaid in red.

where c_2 is the second radiation constant, $\tilde{E}_i$ is the rovibronic energy term value in wavenumbers, $g_i^{\rm tot} = g_{\rm ns}(2J_i+1)$ is the total state degeneracy which includes the nuclear weight spin-statistic $g_{\rm ns}$ ($g_{\rm ns}$ = 1 for $^{32}S^{16}O$) where a 1 K temperature step is used. Figure 4.24 compares our computed PF to the PFs of Sauval and Tatum[394], Barklem and Collet[395], CDMS[346], and HITRAN[396] who compute their PF from the line lists produced by Bernath et al.[340,341]. As the nuclear spin degeneracy is one, no PFs need to be scaled to the physics convention of nuclear statistical weights, which ExoMol uses. Figure 4.24 shows that all PFs agree for $500 \lesssim T \lesssim 2000$ K; for all temperatures our computed PF continues to agree with that of Barklem and Collet[395], where our computed PF is generally lower than theirs up to 0.1% at 5000 K; the CDMS PF agrees to within 1% of all PFs up to its cutoff at 300 K; the PF of Sauval and Tatum[394] is larger than the rest of the PFs at low temperatures up to 500 K and at 5000 K their PF is 3.4% lower than our computed PF; the HITRAN PF begins to deviate from the other PFs at $\sim$ 2000 K, where at 5000 K it is lower than ours by 17%. This behaviour of HITRAN PFs has been noted previously[397].

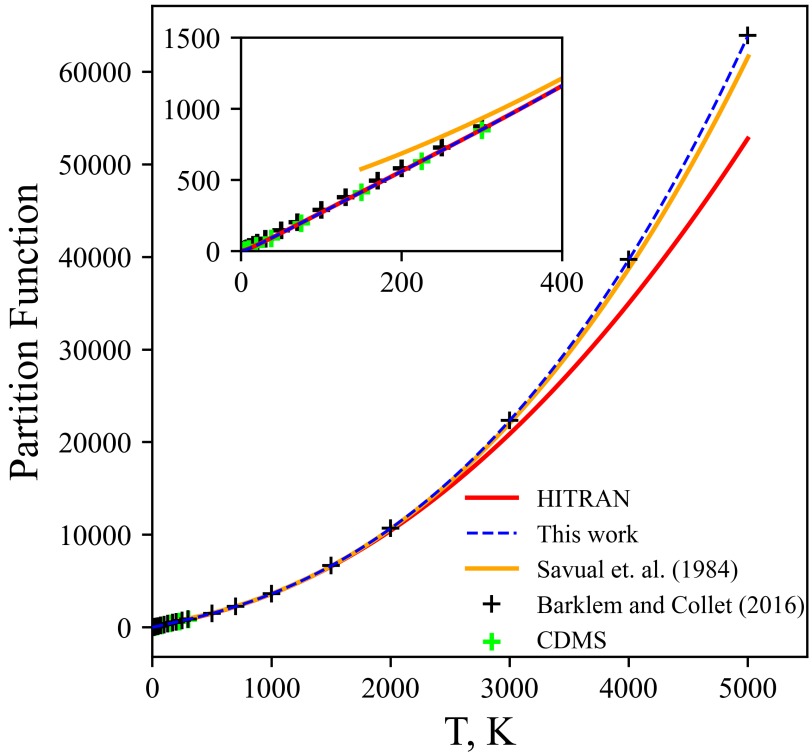

Figure 4.24: Comparison between our partition function and those produced by HITRAN[396], Sauval and Tatum[394], Barklem and Collet[395] and CDMS[346].

4.14.3 SO opacities

We follow the ExoMolOP procedure of Chubb et al.[398] and generate molecular opacities for SO using the SOLIS line list for four exoplanetary atmosphere retrieval codes ARCiS[399], TauREx[400], NEMESIS[401] and petitRADTRANS[402] on an extensive grid of temperatures and pressures. The opacities are provided as part of the SO ExoMol dataset.

4.14.4 Simulated spectra

Program ExoCross[360] was used to simulate rovibronic absorption spectra as a function of temperature using SOLIS. Figure 4.25 illustrates the dipole allowed and forbidden electronic bands connecting $X\,^3\Sigma^-$ to $X\,^3\Sigma^-$, $a\,^1\Delta$, $b\,^1\Sigma^+$, and $A\,^3\Pi$ which are shown as different colours. The total computed SO opacity is also shown in Figure 4.25 as a grey region. Here, lines are simulated with a Gaussian line profile of HWHM 0.6 cm^{-1}. The forbidden band intensities are stolen through mixing of the electronic wavefunctions through couplings such as SOCs, DMCs, and EAMCs resulting in non-zero dipole matrix elements, which I note provides a stronger mechanism here than their corresponding magnetic dipole or electric

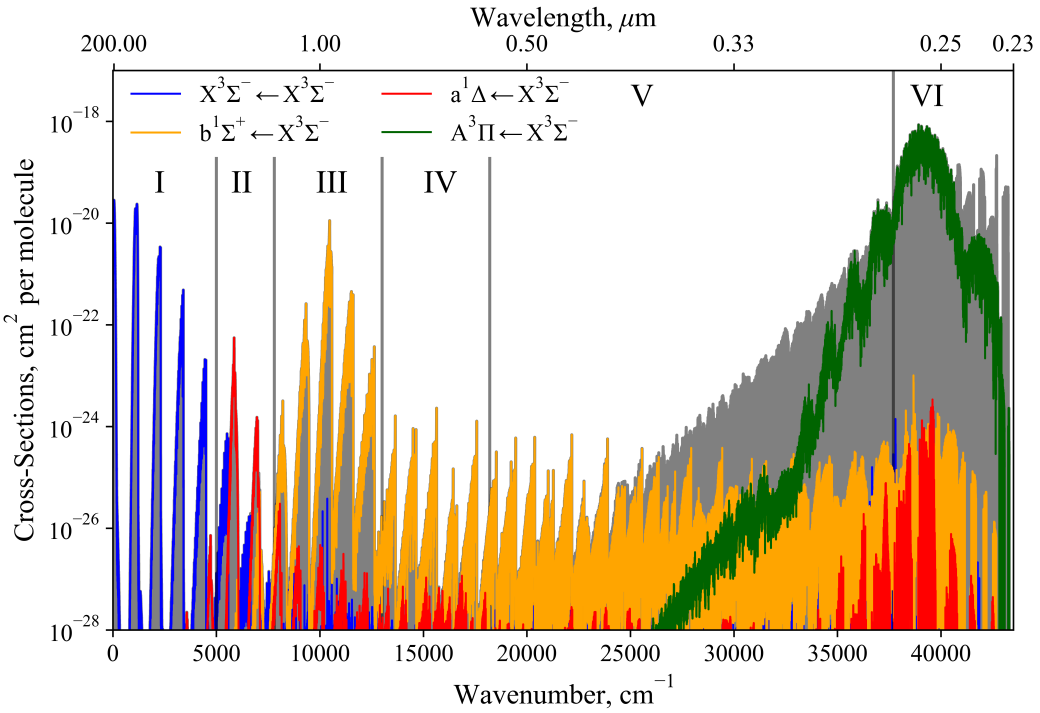

Figure 4.25: Dipole allowed and forbidden components of the absorption spectrum simulated with our semi-empirical model at 1000 K connecting $X\,^3\Sigma^-$ with $X\,^3\Sigma^-$, $a\,^1\Delta$, $b\,^1\Sigma^+$, and $A\,^3\Pi$. Regions of spectral importance are marked with roman numerals and are detailed in the text. The grey shaded region marks the total SO opacity computed with our model at 1000 K.

quadrupole couplings. Figure 4.26 shows the temperature variation of the simulated total SO opacity which has a strong effect on the UV/Vis cross-sections. The greatest temperature variation can be seen in the 18 000-35 000 cm^{-1} region (V) where the $X\,^3\Sigma^- \rightarrow B\,^3\Sigma^-$ band begins to dominate opacity. Again, lines are simulated with a Gaussian line profile of HWHM 0.6 cm^{-1}. It is clear the IR/NIR spectrum is largely unaffected by the increase of temperature except from the expected rotational broadening. Below I comment on the spectral regions marked by I-VI illustrated in Figure 4.25.

(I) The IR ∼0–5000 cm^{-1} region is dominated by the $X\,^3\Sigma^- \leftarrow X\,^3\Sigma^-$ electronic band peaking at $\sim 3 \times 10^{-20}$ cm^2 per molecule.

(II) The ∼5000–7800 cm^{-1} NIR region shows strong $a\,^1\Delta \leftarrow X\,^3\Sigma^-$ band features, even for room temperature spectra, but $X\,^3\Sigma^- \leftarrow X\,^3\Sigma^-$ lines are expected to be still observable here.

(III) The ∼7800–13000 cm^{-1} NIR region is dominated by strong $b\,^1\Sigma^+ \leftarrow X\,^3\Sigma^-$ band absorption for all temperatures, and is almost as strong as the dipole allowed $X\,^3\Sigma^- \leftarrow X\,^3\Sigma^-$ band spectrum because of large intensity stealing mecha-

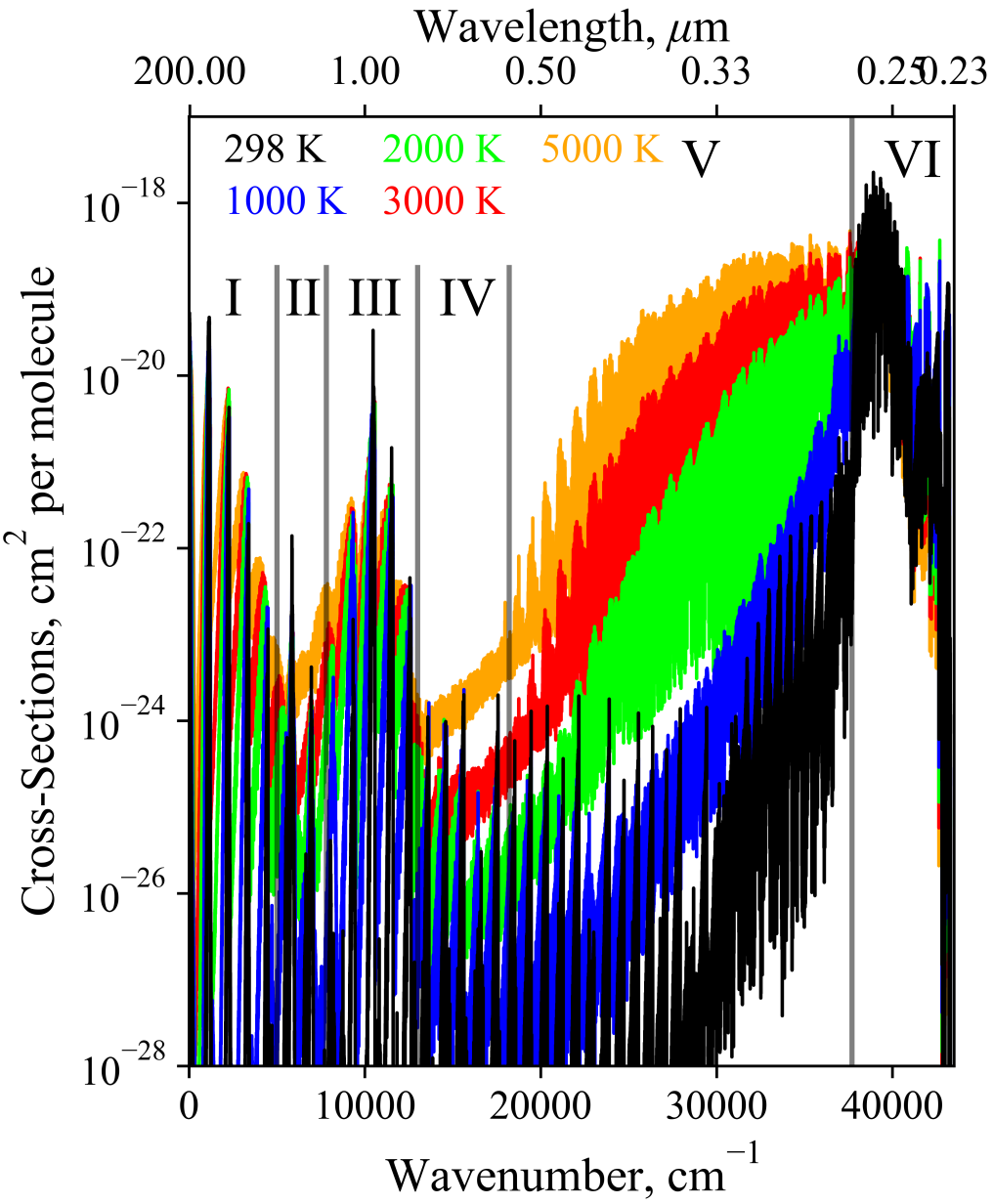

Figure 4.26: The total absorption spectrum of SO simulated with our semi-empirical model for different temperatures ranging from 298 K to 5000 K. It is seen that the intensity deviation is greatest in region *V* around 18 000-35 000 cm^{-1} where the $B^3\Sigma^- \leftarrow X^3\Sigma^-$ band begins to dominate opacity.

nism facilitated through the strong $\langle b\,^1\Sigma^+|\,\mu_z\,|X\,^3\Sigma^-\rangle$ SOC.

(IV) The Vis ∼13000–18200 cm^{-1} region shows a flat feature due to $A\,^3\Pi\leftarrow X\,^3\Sigma^-$ band absorption which becomes prominent for temperatures above 3000 K. However, since the $C\,^3\Pi$ state is removed from our spectroscopic model, the $C\,^3\Pi\leftarrow A'\,^3\Delta$ and $C\,^3\Pi\leftarrow A''\,^3\Sigma^+$ band intensities were not computed, although we previously predicted them to be strong in this region[13].

(V) The Vis/UV ∼18200–37700 cm^{-1} region is largely uncovered at high accuracy by our spectroscopic model since it is dominated by the $B\,^3\Sigma^-\leftarrow X\,^3\Sigma^-$ and lesser $C\,^3\Pi\leftarrow X\,^3\Sigma^-$ electronic bands which become major sources of SO opacity for temperatures above 1000 K. I am currently working on the UV SO line list for a future study which will accurately cover this region. However, for lower temperatures the $A\,^3\Pi\leftarrow X\,^3\Sigma^-$ and $b\,^1\Sigma^+\leftarrow X\,^3\Sigma^-$ bands become more important which are recovered accurately by our line list.

(VI) The UV ∼37700–43500 cm^{-1} region has a strong $A\,^3\Pi\leftarrow X\,^3\Sigma^-$ band feature which should be observable at all temperatures.

4.14.5 Comparisons to experimental spectra

There are few recorded experimental spectra of ^{32}S^{16}O with large coverage and almost none with absolute intensity measurements. However, relative intensities are usually provided[403,141,331,362]. The only study to my knowledge that provides measured absolute intensities is the recent study by Heays et al.[140] on the $A\,^3\Pi-X\,^3\Sigma^-$ band, which I compare to (also $B\,^3\Sigma^--X\,^3\Sigma^-$ and $C\,^3\Pi-X\,^3\Sigma^-$bands which I do not compare to).

The forbidden band intensities computed here are through the intensity stealing mechanism which works through mixing of electronic state wavefunctions through couplings such as SOCs. We do not compute magnetic dipole intensities, which are much weaker for the bands of interest than the redistributed intensities which we compute. For example, the diagonal $\langle b\,^1\Sigma^+|\,\mu_z\,|b\,^1\Sigma^+\rangle$ and $\langle X\,^3\Sigma^-|\,\mu_z\,|X\,^3\Sigma^-\rangle$ dipoles produce $b\,^1\Sigma^+\leftarrow X\,^3\Sigma^-$ band intensities a factor of $\sim 10-1000$ times stronger at the band peak than the corresponding magnetic dipole intensities. Therefore, magnetic dipole transitions are omitted from our line list. An illustration of the intensity stealing mechanism for this band is given in Section 4.15.

4.14.5.1 HITRAN

HITRAN produces empirical SO line lists which have been produced by fitting spectroscopic models to experimentally derived spectroscopic constants, lifetimes, and rotational branching ratios (ratios in perpendicular and parallel transition moments, see below discussion). Therefore, I will compare to this data since it

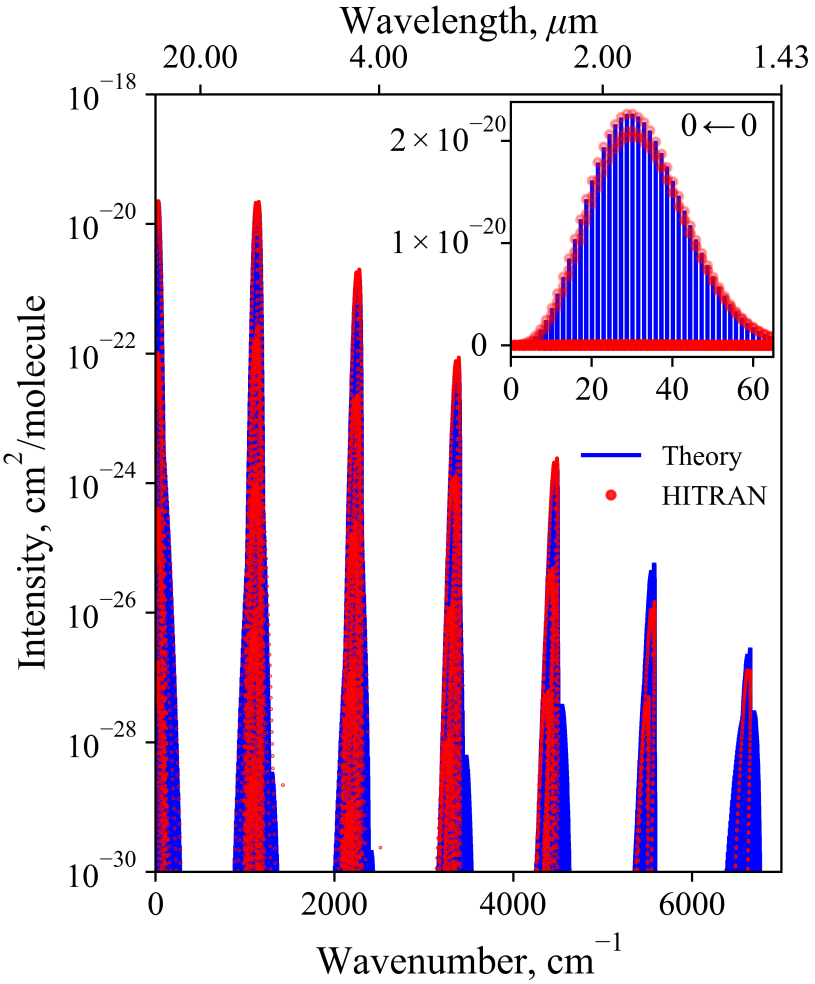

Figure 4.27: Comparison between the theoretical and HITRAN $X\,^3\Sigma^- \rightarrow X\,^3\Sigma^-$ rovibrational band for 0-7000 cm^{-1}. I simulate the spectra using a temperature of 296 K and scale the intensities by the fractional isotopologue abundance of 0.9479[348].

is the closest comparison of rovibronic intensities to experimental data for the $X\,^3\Sigma^- - X\,^3\Sigma^-$, $b\,^1\Sigma^+ - X\,^3\Sigma^-$, and $a\,^1\Delta - X\,^3\Sigma^-$ electronic bands.

HITRAN[348] provides empirical line list data on the first three electronic states of SO $X\,^3\Sigma^-$, $a\,^1\Delta$, and $b\,^1\Sigma^+$ to which I compare our theoretical spectra to. The HITRAN intensities for the $X\,^3\Sigma^- \leftarrow X\,^3\Sigma^-$ band were originally presented by Bernath et al.[341] and the forbidden $b\,^1\Sigma^+ \leftarrow X\,^3\Sigma^-$ and $a\,^1\Delta \leftarrow X\,^3\Sigma^-$ bands are from Bernath et al.[340]. In both studies, fitted spectroscopic constants from the literature were used to predict line positions, transition moments were obtained using LeRoy's LEVEL program[404] which assumes the single state approximation, and their line lists were computed using PGOPHER[155]. Bernath et al.[340] used the Ω-representation (see Section 5.2.1 in Chapter 5) to allow for the single state ap-

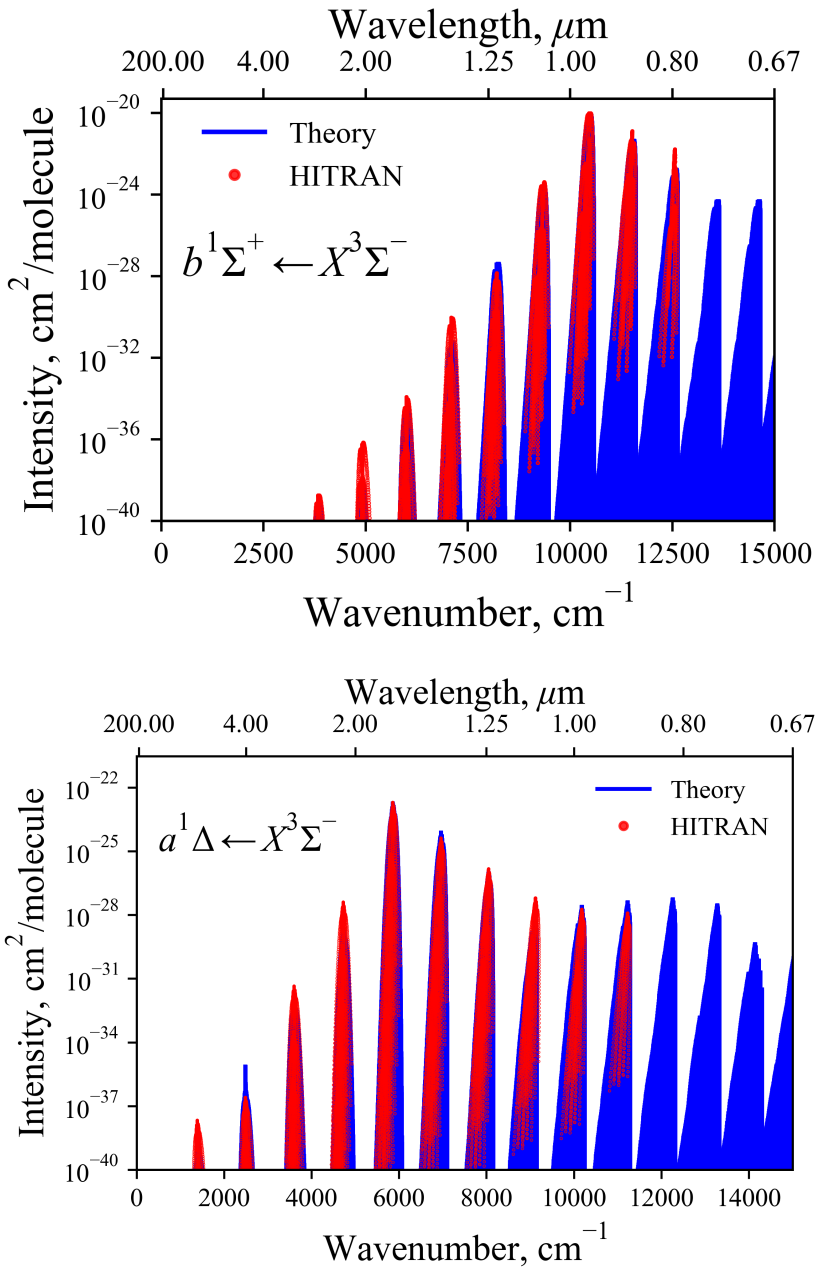

Figure 4.28: Comparison between the theoretical and HITRAN $X\,^3\Sigma^- \rightarrow b\,^1\Sigma^+$ (top) and $X\,^3\Sigma^- \rightarrow a\,^1\Delta$ (bottom) absorption spectrum for 0-15000 cm^{-1}. I simulate the spectra using a temperature of 296 K and scale the intensities by the fractional isotopologue abundance of 0.9479[348].

proximation – in line with LEVEL[404] – such that the forbidden band intensity are computed from effective dipoles between single Ω-states, the so-called parallel and perpendicular transition moments. This is as opposed to the non-approximate intensity stealing mechanism via mixing of electronic wavefunctions through, e.g. SOCs, as we do. Perpendicular and parallel electronic transition moments between the spin-orbit states $b0^+ - X0^+$, $b0^+ - X1$, and $a2 - X1$ were computed by Bernath et al.[340] at an ic-MRCI/aug-cc-pCVQZ-DK level of theory and were scaled to the experimentally determined values by Setzer et al.[331]. The HITRAN $X\,^3\Sigma^- \leftarrow X\,^3\Sigma^-$ intensities were computed using the *ab initio* ground state expectation dipole moment computed by Bernath et al.[341] at a ic-MRCI+Q/ACV6Z-X2C/ED+Q level of theory.

In all comparisons below, I scale our computed intensities with the $^{32}S^{16}O$ isotopologue abundance 0.947926 given by HITRAN[348]. Figure 4.27 presents a comparison between our semi-empirical $X\,^3\Sigma^- \leftarrow X\,^3\Sigma^-$ rovibronic spectrum, where I compute stick spectrum using a temperature of 296 K, and the empirical HITRAN line list[341]. A good agreement in both the line positions and band structure are seen, where band intensities agree up to the fifth hot band at ~ 4500 cm^{-1} where I compute higher intensities relative to the HITRAN data. The $0 \leftarrow 0$ band agrees extremely well which can be seen in the sub plot of Figure 4.27. The agreement in intensities confirms our methodology since the HITRAN dipole was also scaled to the same experimental values discussed in Section 4.14.1. The discrepancy in intensities towards hotter bands can be attributed to the difference in the DMCs as well as the wavefunctions used to calculate the transition probabilities.

Figure 4.28 compares my computed $b\,^1\Sigma^+ \leftarrow X\,^3\Sigma^-$ spectrum simulated at a temperature of 296 K to the empirical HITRAN[348] $b\,^1\Sigma^+ \leftarrow X\,^3\Sigma^-$ line list[340]. For this comparison, the magnetic dipole transitions present in the HITRAN line list are filtered out, since we only calculate electric dipole transitions. The selection rules for magnetic dipole branches are the same except they follow the non-parity changing rule. Our model is seen to supplement the HITRAN line list at both the higher and lower wavenumber regions (< 4000 cm^{-1} and > 12500 cm^{-1}) where line positions, band structure and intensities generally show good agreement. This is to be expected since the HITRAN $b\,^1\Sigma^+ \leftarrow X\,^3\Sigma^-$ dipoles were scaled to the same experimental values for the $b\,^1\Sigma^+$ lifetime as I do. For vibrational bands energetically below ~ 7500 cm^{-1} the two spectra begin to deviate from each other, where SOLIS tends to be slightly lower than the HITRAN intensities. However, this is below the standard HITRAN intensity threshold of 10^{-30} cm^2/molecule, and so these bands are typically of less importance. For intensities above the threshold, good

agreement is seen in line with the methodologies used.

I also compare to the forbidden $a\,^1\Delta \leftarrow X\,^3\Sigma^-$ band in Figure 4.28 to the theoretical HITRAN line list at 296 K. The transitions here are all electric dipole in nature. It is evident that the electronic band structures agrees well between the peak band up to the penultimate hot band before the HITRAN terminus at $\sim$11000 cm^{-1} with the largest intensity deviation being between vibronic bands outside the 5000–8500 cm^{-1} spectral range. The low energy bands $<$4500 cm^{-1} all sit below the 10^{-30} cm^2/molecule intensity threshold, which are less important spectroscopically. Differences in the band intensity are difficult to disentangle since $a\,^1\Delta \leftarrow X\,^3\Sigma^-$ is a dipole forbidden band where intensities are accumulated through 'intensity stealing' mechanism via multiple coupling channels in our model.

The general agreement with SOLIS and the empirical HITRAN line list confirms that no fundamental physics is missing, since both approaches produce similar spectra using different methodologies. Furthermore, Bernath et al.[340] scale their $b\,^1\Sigma^+ \leftarrow X\,^3\Sigma^-$ effective dipoles using the same lifetime provided by Setzer et al.[331] as I did, whereas the $a\,^1\Delta \leftarrow X\,^3\Sigma^-$ band has no reliable experimental dipoles or lifetimes to scale the *ab initio* dipoles to except the indirect $a\,^1\Delta$– $a\,^1\Delta$ dipole moment presented by Saito[279], which was used for scaling only in SOLIS. Agreement for the latter band then confirm the good quality of the PECs, SOCs, and (T)DMCs used.

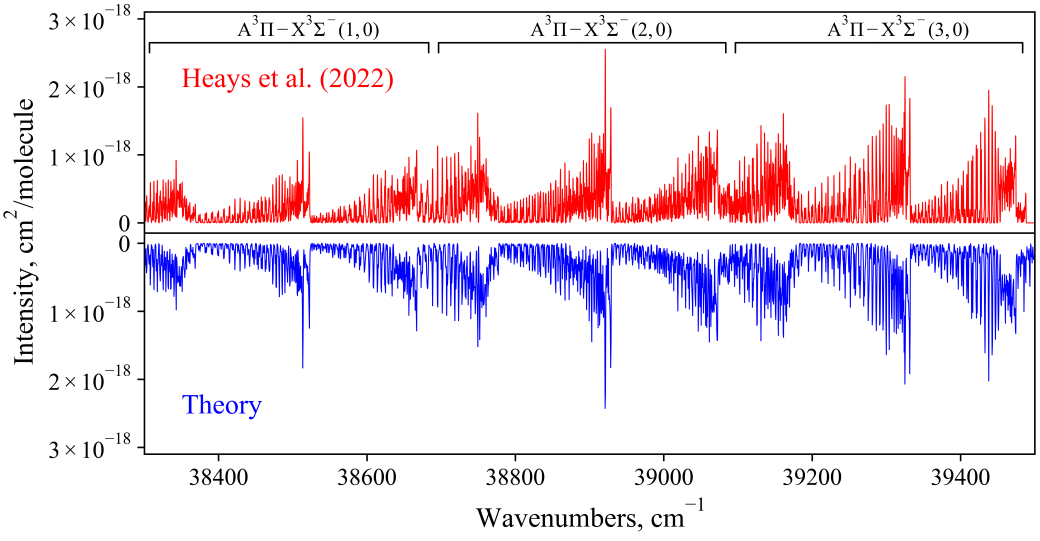

Figure 4.29: Comparison of the absorption $A\,^3\Pi(v' = 1,2,3)$–$X\,^3\Sigma^-(v'' = 0)$ band computed from our spectroscopic model, to the cross sections generated using the empirical line list of Heays et al.[140], which was fitted band-by-band to their measured spectra.

4.14.5.2 A–X Bands

The recent study by Heays et al.[140] measured, in high resolution, the FUV $A\,^3\Pi - X\,^3\Sigma^-$ band via Fourier-transform spectroscopy up to the $(v', v") = (3,0)$ band for $J \leq 51$; the $B\,^3\Sigma^- - X\,^3\Sigma^-$ and $C\,^3\Pi - X\,^3\Sigma^-$ bands were also measured but I do not compare to these here. Heays et al.[140] present an empirical line list where effective Hamiltonian spectroscopic constants were fitted band-by-band to their measured spectrum, providing quantum number assignments and oscillator strengths for each assigned transition. Their coupled-band models reproduce the experimentally measured line positions, intensities, and widths to within 5% uncertainty. With this, I converted their line list to the ExoCross format to compute corresponding cross-sections, which is then compared to. For all spectra simulations a temperature of T = 360 K and Gaussian line broadening of HWHM 0.3 cm^{-1} was used. Figure 4.29 shows the comparison between the $A\,^3\Pi(v' = 1,2,3) - X\,^3\Sigma^-(v'' = 0)$ band intensities computed from our model in blue (bottom panel) and the simulated band intensities of Heays et al.[140] in red (top panel). Excellent agreement in line positions, intensities, and band structure is seen, where a mirror plot was chosen since overlaying the spectra made it hard to distinguish between them since they agree so well.

I am confident that our model correctly reproduces the experimental spectra for the $A\,^3\Pi(v' = 1,2,3) - X\,^3\Sigma^-(v'' = 0)$ band, confirming the good quality of our PECs, (T)DMCs, and couplings to other states.

Table 4.10: The largest expansion coefficients for the $X\,^3\Sigma^-$ and $b\,^1\Sigma^+$ wavefunctions in the Ω representation. The column headers with a subscript 'Duo' are the computed Duo-states which have components in the basis states given as rows due to spin-orbit coupling.

Basis	$\lvert X\,^3\Sigma^-_{0+}\rangle_{Duo}$	$\lvert b\,^1\Sigma^+_0+\rangle_{Duo}$	$\lvert X\,^3\Sigma^-_{+1}\rangle_{Duo}$	$\lvert X\,^3\Sigma^-_{1-}\rangle_{Duo}$
$\lvert X\,^3\Sigma^-_{-1}\rangle$	0	0	0.99999	0
$\lvert X\,^3\Sigma^-_{+1}\rangle$	0	0	0	0.99999
$\lvert A\,^3\Pi_{+1}\rangle$	0	0	0	-0.00119
$\lvert A\,^3\Pi_{-1}\rangle$	0	0	0.00119	0
$\lvert X\,^3\Sigma^-_{0+}\rangle$	-0.99964	-0.02670	0	0
$\lvert b\,^1\Sigma^+_{0+}\rangle$	0.02669	-0.99964	0	0
$\lvert A\,^3\Pi_{0+}\rangle$	0.00121	-0.00093	0	0
$\lvert A\,^3\Pi_{0-}\rangle$	-0.00121	0.00093	0	0

4.15 Intensity Stealing Mechanism for the $b\,^1\Sigma^+ \rightarrow X\,^3\Sigma^-$ Band

Dipole forbidden transitions can arise through multiple mechanisms, such as through the magnetic dipole moment (MDM), quadrupole moment, and from intensity stealing. Intensity stealing propagates through the mixture of electronic state wave-functions via couplings such as SOCs and EAMCs, where contributions to the forbidden intensities are derived through taking dipole matrix elements in the eigenstates of the diagonalised Hamiltonian constructed from the coupled $\Lambda - \Sigma$ basis. To understand these intensity contributions to the $X\,^3\Sigma^- \rightarrow b\,^1\Sigma^+$ band an analysis was conducted on the Duo computed electronic state wavefunctions corresponding to the eigensolutions of the diagonalised Hamiltonian which included SOCs, EAMCs, and DMCs for the full 11 state system described in Section 4.2 plus additional $\langle b\,^1\Sigma^+|\,\mathrm{SO}_x\,|A\,^3\Pi\rangle$, and $\langle a\,^1\Delta|\,\mathrm{SO}_x\,|A\,^3\Pi\rangle$ couplings. The contributions to the $X\,^3\Sigma^-$ and $b\,^1\Sigma^+$ computed wavefunctions in the Ω representation are shown in Table 4.10 which gives the expansion coefficients C_n of the wavefunctions in the eigenbasis of the diagonalised Hamiltonian

$$\Psi_\Omega^{J,\tau} = \sum_n C_n^{J,\tau}\,|n\rangle \tag{4.30}$$

where J is the rotational quantum number, τ is the parity, and n represents the full set of quantum numbers $|n\rangle = |\mathrm{State}, J, \Omega, \Lambda, S, \Sigma, v\rangle$. Because of a large SOC between the $X\,^3\Sigma^-$ and $b\,^1\Sigma^+$ states, it is seen that they share sizeable contributions in their final mixed wavefunctions of their corresponding unmixed basis states. The amount of intensity stealing will then distribute itself through subsequent coupling of the dipole operators in the new mixed state basis. To this end, consider the parallel and perpendicular transition dipole moments (TDMs) which couple $\Omega = 0^+ - 0$ and $\Omega = 0^+ - 1$ states, respectively. In spherical tensor form they read, considering the $X\,^3\Sigma^-$ and $b\,^1\Sigma^+$ states,

$$\mu_0 = \langle b^1\Sigma_0^+|\,\mu_z\,|X^3\Sigma_0^-\rangle \tag{4.31}$$

$$\mu_1 = \pm\langle b^1\Sigma_0^+|\,2^{-1/2}(\mu_x \mp i\mu_y)\,|X^3\Sigma_{\pm1}^-\rangle \tag{4.32}$$

The experimental measurement and analysis by Setzer et al.[331] of the $b\,^1\Sigma^+ \rightarrow X\,^3\Sigma^-$ emission band and work by Bernath et al.[340] shows the μ_0 and $\mu_{\pm1}$ TDMs to be of the same order of magnitude. However, comparing the $b\,^1\Sigma^+ \rightarrow X\,^3\Sigma^-$ $v = 0 - 0$ band measured by Setzer et al.[331] to our semi-empirical line list and the HITRAN empirical line list show disagreements in the P- and R- branch ratios where

experiment predicts the P- branch to have the most intensity within the band. Considering the intensity stealing mechanism, cross-examining Eqs.(4.31,4.32) with Table 4.10 reveals that intensity stealing is different for the perpendicular and parallel transitions and therefore the branch ratios for these transitions. This could explain the experimental observation in Setzer et al.[331] that the P- and R- branch ratios are different. In an attempt to understand this discrepancy, my analysis on the mixed $X\,^3\Sigma^-$ and $b\,^1\Sigma^+$ state wavefunctions reveals that the competition between the $\langle b\,^1\Sigma^+|\,\mu_z\,|b\,^1\Sigma^+\rangle$ and $\langle X\,^3\Sigma^-|\,\mu_z\,|X\,^3\Sigma^-\rangle$ DMCs provides the dominant contributions to μ_0, as facilitated through the large $\langle b\,^1\Sigma^+|\,\mathrm{SO}_z\,|X\,^3\Sigma^-\rangle$ spin-orbit coupling, where $\langle b\,^1\Sigma^+|\,\mu_z\,|b\,^1\Sigma^+\rangle$ subtracts from $\langle X\,^3\Sigma^-|\,\mu_z\,|X\,^3\Sigma^-\rangle$ and can be seen in Figure 4.30 as the reduction of intensity between the red and blue spectra. μ_1, however, has leading contributions from the $\langle A\,^3\Pi|\,\mu_x\,|X\,^3\Sigma^-\rangle$ dipole as facilitated through the $\langle b\,^1\Sigma^+|\,\mathrm{SO}_x\,|A\,^3\Pi\rangle$ and $\langle X\,^3\Sigma^-|\,\mathrm{SO}_x\,|A\,^3\Pi\rangle$ couplings. It is found that the perpendicular TDM μ_1 is responsible for the P- R- branch asymmetry ($P > R$) as seen in the Fourier transform spectroscopy by Setzer et al.[331] whereas the parallel TDM μ_0 produces the opposite branch ratios ($P < R$). However, when considering only a vibrationless expansion for the wavefunctions, that is $v = 0$, the μ_1 TDM is very weak producing much lower intensities than the parallel transition moment and as a result the $b\,^1\Sigma^+ \rightarrow X\,^3\Sigma^-$ band has a $P < R$ branch ratio. When considering a larger vibrational basis ($v = 20$) the P- R- branch ratio becomes more sensitive to changes in DMCs and SOCs. From this analysis is is evident that the vibrational TDMs have an effect on the rovibrational band intensity distribution in favour of the P- R- branch ratio as seen in Setzer et al.[331].

I therefore speculate that further coupling to an unresolved $^3\Pi$ state could resolve the seen branch asymmetries. Somogyi et al.[405] show that coupling to highly excited Π states is crucial in proper reproduction of the IR branch ratios. However, since I have achieved a good fit to the empirical energy levels, this problem is left for a future study.

4.16 Application of the $^{32}S^{16}O$ Line List

The $^{32}S^{16}O$ line list, SOLIS, has been utilised in several astrophysical studies. Its creation was the focus of my master's project with Sergey Yurchenko and continued through the early years of my PhD. Since then, we have made SOLIS available for various chemical modelling studies, where it has contributed to advancing our understanding of sulfur chemistry in astrophysical environments. This section provides a brief overview of key applications of the line list, highlighting its scientific impact.

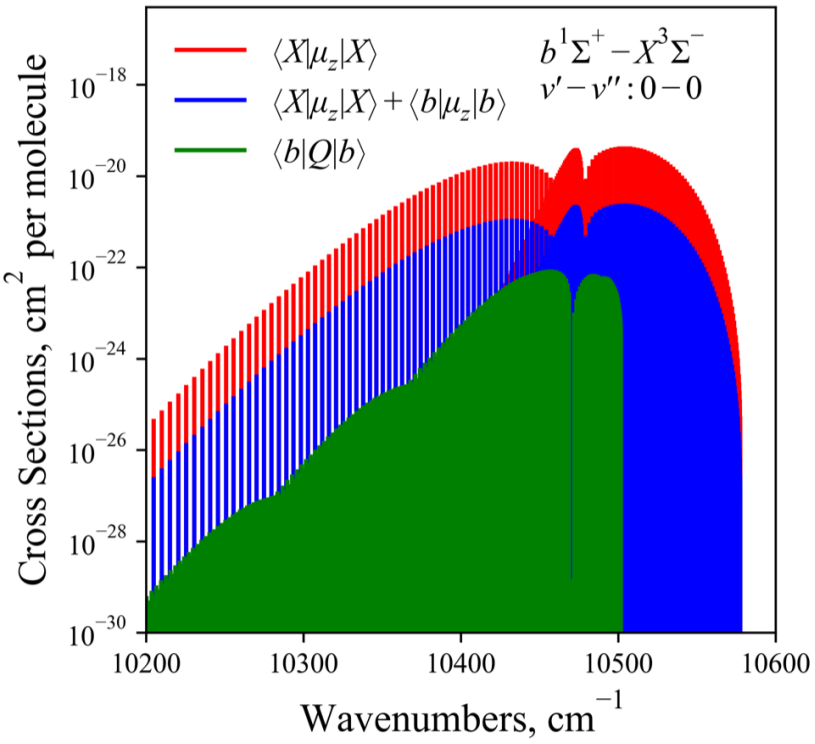

Figure 4.30: Visualisation of the different contributions to the forbidden $X\,^3\Sigma^- \rightarrow b\,^1\Sigma^+$ band intensities. 'Q' refers to the magnetic dipole moment, where the green spectra are due to magnetic dipole transitions, which is orders of magnitude weaker than the intensity stealing mechanism.

4.16.1 The molecular Chemistry of Type Ibc Supernovae (Liljegren, S. et al.[1])

Liljegren, S. et al.[1] coupled a chemical kinetic network into the non local thermal equilibrium (NLTE) spectral synthesis code SUMO to study the spectral evolution of Type Ic SN in the 100–600 days time range. In this code, four species – CO, SiO, SiS, and SO – participate in NLTE cooling of the modeled stripped envelope SNe gas to achieve self-consistency between the molecule formation and the temperature. As a result, predicted molecular formation masses are computed over the studied epochs and their effect on the temperature and optical spectra of these stripped envelope SNe are studied. Some key results for $^{32}S^{16}O$ in these environments include:

- **$^{32}S^{16}O$ formation in SNe ejecta**: At $\sim$ 350 days SO becomes abundant where its fundamental band, blended with the SiO fundamental, contributes significantly in the 7–10 μm region. At these epochs, the SNe ejecta densities can be contrained by the emerging $^{32}S^{16}O$ emission – a promising epoch for

the first SO detection in an SNe.

- **$^{32}S^{16}O$ nucleosynthesis tracer**: SO forms mainly in the O/Si/S zone of the SNe ejecta, and holds a promising tracer species for neon burning.
- **$^{32}S^{16}O$ detectability**: It is predicted that $^{32}S^{16}O$ should be detectable in the mid-IR via the JWST/MIRI telescope.

4.16.2 Photochemistry in the Atmosphere of WASP-39b

The SOLIS line list for $^{32}S^{16}O$ has played a role in advancing our understanding of exoplanet atmospheres, particularly in the study of WASP-39b. Two major studies utilised the line list to investigate the presence and photochemical role of SO (mainly SO_2) in the atmosphere of this Saturn-mass exoplanet. These studies provide the first unambiguous detection of sulfur photochemistry in an exoplanetary atmosphere, with implications for planetary chemistry, atmospheric metallically, and exoplanet characterization.

4.16.2.1 Photochemically Produced SO_2 in WASP-39b (Tsai et al.[148])

This study provides the first detection of SO_2 in an exoplanet atmosphere through JWST transmission observations using NIRSpec PRISM (2.7σ) and G395H (4.5σ). A strong spectral feature at 4.05 μm is identified to be produced via SO_2. This detection was particularly interesting since the proposed source of SO_2 was explained as a photochemical product of hydrogen sulfide (H_2S) oxidation, rather than as an equilibrium chemistry species. Key findings include:

- **SO_2 as a tracer of metallically**: The inferred SO_2 abundance suggested a 10× solar metallically atmosphere, making SO_2 a new indicator of bulk atmospheric composition.
- **Photochemical pathways**: The study demonstrated that UV-driven oxidation of sulfur leads to SO_2 production, revealing the complexity of sulfur chemistry in hot exoplanetary environments.
- **Predicted additional spectral features**: The work suggested that SO and SO_2 should also exhibit strong features in the ultraviolet and infrared, motivating further observations.

The SO line list contributed to this study by providing accurate spectroscopic data in transmission spectroscopy models (in addition to other molecular species) in confirmation of the presence of SO_2.

4.16.2.2 Sulfur Dioxide in the Mid-Infrared Spectrum of WASP-39b (Powell et al.[406])

Building upon the initial detection of SO_2 by Tsai et al.[148], this study[406] used JWST/MIRI LRS observations to detect additional SO_2 absorption features at 7.7 μm and 8.5 μm, further confirming the role of photochemistry in WASP-39b's atmosphere. Major results include:

- **SO_2 spectral features in the mid-infrared**: The study identified broad SO_2 absorption bands, in agreement with photochemical model predictions.
- **Consistency with prior detections**: The retrieved SO_2 abundance (0.5–25 ppm) was consistent with previous near-infrared findings, reinforcing the photochemical origin of SO_2.
- **Detection of SO**: A weak feature at ~ 9 μm was identified as a possible SO signature with a 2.5 σ detection (as predicted by Liljegren, S. et al.[1] in Section 4.16.1), though further observations are needed for confirmation. The presence of stronger SO_2 features in this region mask SO, but the retrievals do not rule out SO's presence, which is consistent in the photochemical models of sulfur bearing species in a UV-driven oxidation scheme.

The SOLIS opacities were included in the ARCiS retrievals, where its weak-to-moderate detection further supports the proposed photochemical production schemes of SO_2 – improving constraints on WASP-39b's atmospheric chemistry.

4.17 Summary

A semi-empirical SOLIS line list for $^{32}S^{16}O$ is constructed starting from the refinement of the *ab initio* spectroscopic model[13] presented in Sections 4.2-4.10 to empirically derived MARVEL energy levels. As part of the line list creation, a MARVEL analysis of 29 experimental transition sources resulted in a self-consistent set of 8558 rotation-vibration energy levels ($J \leq 69$ and $v \leq 3$) for the $X\,^3\Sigma^-$, $a\,^1\Delta$, $b\,^1\Sigma^+$, $A\,^3\Pi$, $B\,^3\Sigma^-$, $C\,^3\Pi$ electronic states, where 48 972/50 106 experimental transitions were validated. The SOLIS SO line list now supplements existing ExoMol line lists for SO_2[407] and SO_3[408].

The $X\,^3\Sigma^-$ state expectation value of the dipole moment operator was fitted to an analytical form and shown to improve the non-physical flattening of the vibrational transition moment and NIDL compared to using the grid interpolated form of the DMC. This resulted in the physical exponential decay of the $X\,^3\Sigma^- \rightarrow X\,^3\Sigma^-$ IR spectral band.

Comparison of the simulated rovibronic spectrum of $^{32}S^{16}O$ to experiment/HITRAN show good agreements in both positions and intensities. However, inspection of the $v = 0 \rightarrow 0$ of the forbidden $b\,^1\Sigma^+ \rightarrow X\,^3\Sigma^-$ band revealed disagreeing P- and R- branch ratios to experiment, where tuning of the spectroscopic model showed no proper inversion of the branch intensities. Analysis of the electronic wavefunctions revealed that the band intensities are dominated by competing diagonal X and b DMCs, which contribute to the parallel transition moment. The weaker perpendicular transition moment was shown to produce intensities of the desired P- and R- branch ratio, but was much weaker than the parallel transition component to the intensities. Analysis on the basis set revealed the branch ratio to be more sensitive when including a larger vibrational basis, but still does not produce the desired branch ratio. I speculate that coupling to unresolved, highly excited Π states should contribute to the desired branch ratios, which is left to a future work.

The future work includes extension to the UV region with the $B\,^3\Sigma^- \leftarrow X\,^3\Sigma^-$ and $C\,^3\Pi \leftarrow X\,^3\Sigma^-$ electronic bands, and production of photodissociation cross sections and rates.

The SOLIS line list has a wide range of applications, spanning environmental chemistry to astrophysics. In atmospheric science, it facilitates the study of sulfur monoxide (SO) and its role in processes such as acid rain formation and pollution. In astrophysics, SOLIS enables the investigation of SO across diverse environments, including interstellar clouds, planetary atmospheres, and supernovae. It contributes to our understanding of planetary formation and evolution, the dynamics of star-forming regions, and the chemical composition of celestial bodies. Additionally, SOLIS can be used in the study of SO's photochemistry, its potential as a shock tracer, and its suitability for observational studies with telescopes like the James Webb Space Telescope (JWST). Notably, SOLIS has been used in detecting sulfur dioxide (SO_2) in the exoplanet WASP-39b, marking the first unambiguous observation of UV-driven photochemistry in a hot exoplanetary atmosphere Tsai et al. [148]. Its mid-infrared fundamental band feature has also been identified in WASP-39b by Powell et al. [147], and it has been recognized as an abundant molecular species in the oxygen/silicon/sulfur neon-burning zones of supernova ejecta [1].

Chapter 5

Additional Research and Contributions

The preceding chapters have detailed the primary research projects and major findings of my doctoral studies. This chapter complements that work by documenting additional research activities, collaborative projects, and preliminary results. While not forming the core focus of the thesis, these endeavors represent significant contributions and highlight potential avenues for future investigation. This chapter encompasses both collaborative efforts and independent explorations, including work that has not yet reached full publication readiness, with the aim of providing a complete overview of my research activities during my PhD.

5.1 Collisional Broadening of Molecular Rovibronic UV Lines

My initial PhD research trajectory focused on the effects of pressure broadening on UV/visible spectral lines, a different direction from the nonadiabatic effects in diatomic molecules that ultimately formed the core of this thesis. A key early collaborative project, undertaken with visiting collaborator Jeanna Buldyreva – during her six-month tenure with the ExoMol group at UCL – involved calculating high-level *ab initio* interaction potentials for excited states of diatom-diatom and diatom-atom collisions. These potentials were intended to be used, via phase-shift theory, to estimate pressure broadening coefficients. This is the topic of this section, with a focus on my contribution being the *ab initio* calculations (for more details see Buldyreva et al.[409]).

Our recent article[409] aims to meet the burning need for high-resolution pressure-induced line-shape parameters in the UV/visible regions for hot-temperature industrial and atmospheric applications as well as current and future

space missions[410–413]. In this article, phase-shift theory is examined in its historical context, tested, and revisited using accurate numerical potentials and advanced trajectory models.

Within the mean-thermal-velocity approximation (MTVA), the phase-shift-theory formulae for collisional linewidth γ and shift δ (in s^{-1}) are[414–418]

$$\gamma = N\bar{v}\int_0^{\infty}[1-\cos\eta(b)]\,bdb\,, \tag{5.1}$$

$$\delta = N\bar{v}\int_0^{\infty}\sin\eta(b)bdb \tag{5.2}$$

with N denoting the number of molecules per unit volume, $\bar{v}$ standing for the mean thermal velocity and $\eta(b)$ being the phase shift induced in the radiation by a collision of impact parameter b. The phase shift $\eta(b)$ represents an accumulation of the frequency displacements $\Delta\omega$ (in rad s^{-1}) at time t through the trajectory:

$$\eta(b) = \int_{-\infty}^{+\infty}\Delta\omega dt \tag{5.3}$$

and $\Delta\omega$ itself is determined by the intermolecular interactions inversely proportional to the n-th powers of the intermolecular distance r.

The theoretical approach developed by Hindmarsh and coauthors[419] suggested a realistic treatment of Eq.(5.3) via a combination of both attractive and repulsive forces in a Lennard-Jones 12-6 form

$$\eta(b) = \int_{-\infty}^{+\infty}\left[\frac{\Delta C'_{12}}{r^{12}(t)} - \frac{\Delta C'_{6}}{r^{6}(t)}\right]dt\,, \tag{5.4}$$

where the parameters $\Delta C_{12} = \hbar\Delta C'_{12}$ and $\Delta C_6 = \hbar\Delta C'_6$ refer to the differences between the Lennard-Jones intermolecular *isotropic* potential parameters for the final and initial states of the transition considered.

The relatively straightforward formulae for linewidth/shift calculations above rely on a simplified representation of the isotropic intermolecular interaction by a 12-6 Lennard-Jones form, which enables analytic integration for the phase shift $\eta(b)$ and converged numerical integrations over the collision parameter for the linewidth γ and shift δ. However, it was found that the Lennard-Jones parameters to be extremely sensitive to the choice of the intermolecular-distance interval and strongly influence the computed linewidth and shift. Therefore, in the frame of the MTVA adopted for simplicity, a numerical integration was attempted on the *ab initio* computed difference $\Delta V(r) = V_f(r) - V_i(r)$ of the isotropic interaction poten-

tials in the final 'f' and initial 'i' electronic states of the active molecule to get the phase-shift dependence on b (for straight line trajectories)

$$\eta(b) = \frac{2}{\bar{v}} \int_0^\infty \frac{\Delta V(r)}{\sqrt{1-(b/r)^2}} dr \,. \tag{5.5}$$

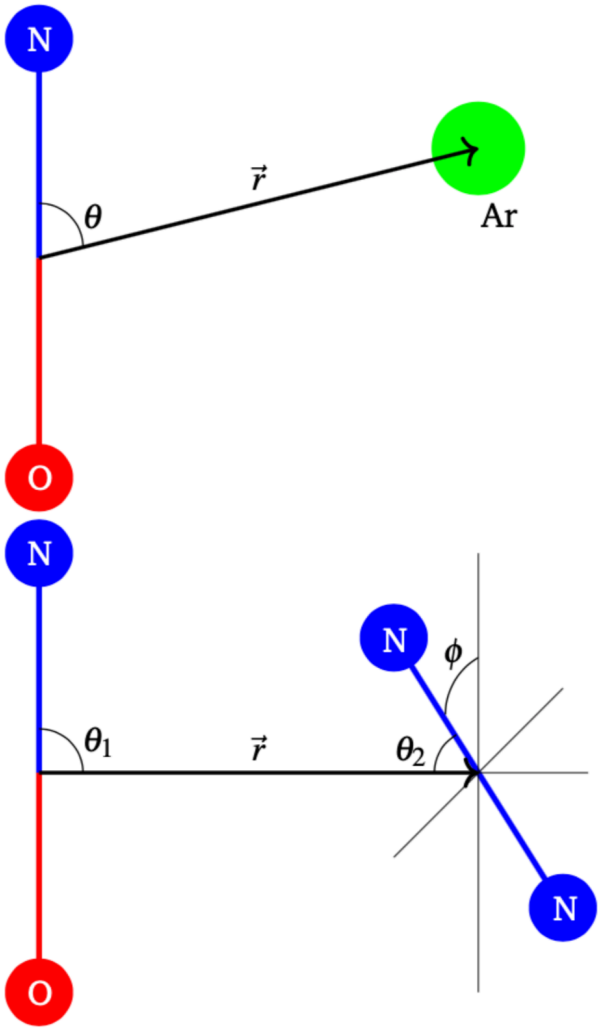

Figure 5.1: Collision geometry and Jacobi coordinates for NO perturbed by Ar and N_2.

5.1.1 *Ab initio* Calculations of Intermolecular Interaction Potentials

The general considerations presented above are supported below by calculations for some test systems. To choose them, the availability of experimental data up to high temperatures (see Table 1 of Buldyreva et al.[409]) and representativity of various leading interactions was taken into account. NO and OH with the permanent dipole

moments differing by an order of magnitude (0.158 D[420] and 1.668 D[421], respectively) were chosen as active molecules whereas Ar and N_2 – a rare-gas atom and a non-polar molecule with the quadrupole as its leading multipole – were taken as perturbers. With these combinations, the behaviour of the active molecule with weak and strong dipoles and the role of dispersion/induction and electrostatic interactions were probed.

Inter-molecular potential energy surfaces (PES) of the complexes NO-Ar, NO-N_2, OH-Ar and OH-N_2 were computed *ab initio* using the MOLPRO quantum chemistry package[136] at the coupled-cluster level of theory CCSD(T): RCCSD(T)/aug-cc-pV(X+d)z (spin-restricted) or UCCSD(T)/aug-cc-pV(X+d)z (spin-unrestricted), where X=T,Q[422]. Since CCSD(T) is a single reference theory, the T1 diagnostic[423] for all ground and excited state calculations was checked against both the 0.044 and 0.02 criteria (criteria $\mathscr{C}_1$ and $\mathscr{C}_2$, herein) suggested by Rienstra-Kiracofe et al.[424] and by Lee and Taylor[423], respectively, where T1 values larger than this indicate the need for a multireference electron correlation procedure. The corresponding inter-atomic distances were fixed at their equilibrium values, while the distance and orientation between the radiator (NO or OH) and perturber were varied over sets of grid points in Jacobi coordinates: $\{r,\theta\}$ for collisions with Ar or $\{r,\theta_1,\theta_2,\phi\}$ for collisions with N_2 (see Fig. 5.1).

For collisions with Ar, the isotropic parts of the PESs corresponding to the ground and excited electronic states were extracted with the use of expansions over series of l^{th} rank Legendre polynomials P_l:

$$V(r,\theta) = \sum_l V_l(r)\, P_l(\cos(\theta)) \,,$$

where $V_l(r)$ are the radial potential terms with $l = 0$ giving the isotropic component. For collisions with N_2, the approach of limiting geometries for homonuclear-heteronuclear diatoms (A_2-BC) was used[425] and the isotropic term was

$$V(r) = \frac{1}{18}\{4V_H(r) + V_{L_1}(r) + V_{L_2}(r) + 2[V_{T_1}(r) + V_{T_2}(r) + 2(V_{T_3}(r) + V_X(r))]\} \,,$$

where the indices on the potentials in the right hand side indicate the contributing geometries (see[425] for more details). The isotropic parts were further fitted by 12-6 Lennard-Jones expressions (see Eq. 5.4).

I note here that within the phase-shift theory the accuracy of the final computed broadening parameters is limited to not the quality of *ab initio* PESs but rather the theory itself. Phase-shift theory is an approximate frame whereby semi-classical

methods for modelling the collision processes are made, such as the notion of a classical trajectory and the lack of rotation-vibration effects accounted for. Furthermore, I fit the isotropic interaction potential derived from my *ab initio* PESs to a simple Lennard-Jones form, so any inaccuracies introduced by choice of quantum chemistry theory will not effect the computed broadening parameters with any appreciable magnitude since errors introduced by the Lennard-Jones approximation will be greater. What phase-shift theory allows us to do is derive values for the line broadening parameters for a general system of active molecule involved in an electronic transition and perturber.

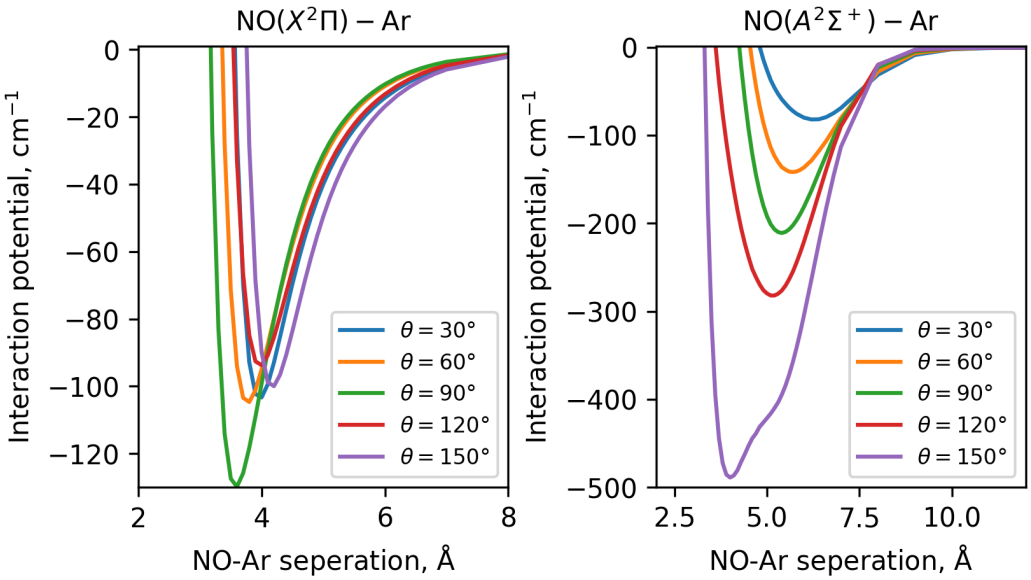

Figure 5.2: *Ab initio* RCCSD(T)/aug-cc-pV(t+d)z computed interaction potentials for the NO(X)-Ar and NO(A)-Ar complexes as a function of the NO-Ar separation r in Figure 5.1. The interaction potentials are plotted for different scattering angles θ (see also Figure 5.1) plotted in different colours.

5.1.1.1 NO-Ar

The interaction PESs of the NO-Ar complex were computed for the ground $X^2\Pi$ and first excited $A^2\Sigma^+$ electronic states of NO. The radiator was approximated by a rigid rotor with equilibrium bond lengths $r_e(X) = 1.15077$ Å and $r_e(A) = 1.06434$ Å. Due to the computational costs of the RCCSD(T)/aug-cc-pV(X+d)z level of theory (X=T,Q), a grid of 62 intermolecular distances NO–Ar (2–15 Å) and only 5 angles (30, 60, 90, 120 and 150 degrees) between the inter-molecular distance vector and the NO molecular axis equal to were considered, providing 310 points in total. The *ab initio* computed interaction potentials are illustrated in Figure 5.2.

The T1 diagnostic never exceeded values of 0.017 and 0.032 for the ground- and excited-state calculations, respectively, both less than the $\mathscr{C}_1$ and $\mathscr{C}_2$ criteria. This confirms that the computed wavefunctions are described well by a single reference determinant and that there is minimal multireference character.

When introducing the Ar atom from non-linear geometries the X $^2\Pi$ ground state of NO is lowered in symmetry, creating a symmetric A' and antisymmetric A'' state of the NO-Ar complex within the C_s point group. This lowering in symmetry means that NO(A $^2\Sigma^+$)–Ar is no longer the lowest A' symmetry state. An advantage of this system is that its weak interaction does not break the orthogonality of NO's molecular orbitals, meaning that one can converge a CCSD(T)/aug-cc-pV(X+d)z (X = T,Q) calculation to the excited NO(A)–Ar state through rotation of the electron orbitals centered on the active molecule. I rotated the outer electron orbital of NO obtained via an initial restricted Hartree-Fock (RHF) calculation which was then used in a second RHF calculation preceding the actual RCCSD(T) calculation. Testing was done using a CASSCF+icMRCI (Complete Active Space Self-Consistent Field[426] + internally-contracted Multi-Reference Configuration Interaction[427]) approach and the aug-cc-pV(X+d)z (X=T,Q) basis sets, however strange results were often obtained where multiple discontinuities are seen over the potential minimum, especially within the excited-state PES. The RCCSD(T) calculations, however, produced more stable results with a lower dissociation energy, in accordance with the values predicted by Holmes-Ross and Lawrance[428], Tsuji et al.[429], Alexander[430] and Sumiyoshi and Endo[431].

5.1.1.2 NO-N_2

Similar to the NO-Ar case, the ground- and first-excited-state PESs of the NO-N_2 complex were calculated at the RCCSD(T)/cc-pV(Q+d)z level of theory using MOLPRO[136]. The T1 diagnostic never exceeded 0.022 and 0.017, respectively, both less than the 0.044 criterion[424] for all ground- and excited-state calculations, confirming minimal multireference character. The *ab initio* computed interaction potentials are illustrated in Figure 5.3.

Seven leading configurations of NO–N_2 geometry were taken into account: two linear L, three perpendicular T, a parallel H, and the X configurations. As for NO-Ar, the near linear geometries of the excited state were the most difficult to converge and the UCCSD(T)/aug-cc-pV(X+d)z (X = T, Q) level of theory was found to help said convergence.

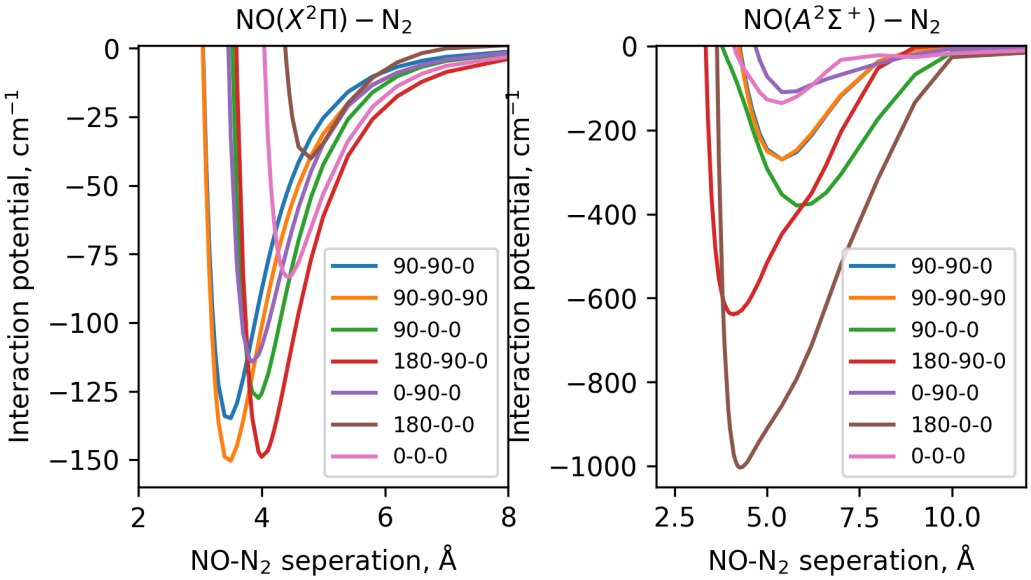

Figure 5.3: *Ab initio* RCCSD(T)/aug-cc-pV(Q+d)z computed interaction potentials for the NO(X)-N_2 and NO(A)-N_2 complexes as a function of the NO-N_2 separation r in Figure 5.1. The interaction potentials are plotted for different scattering angle configurations $\{\theta_1, \theta_2, \phi\}$ (see also Figure 5.1) plotted in different colours.

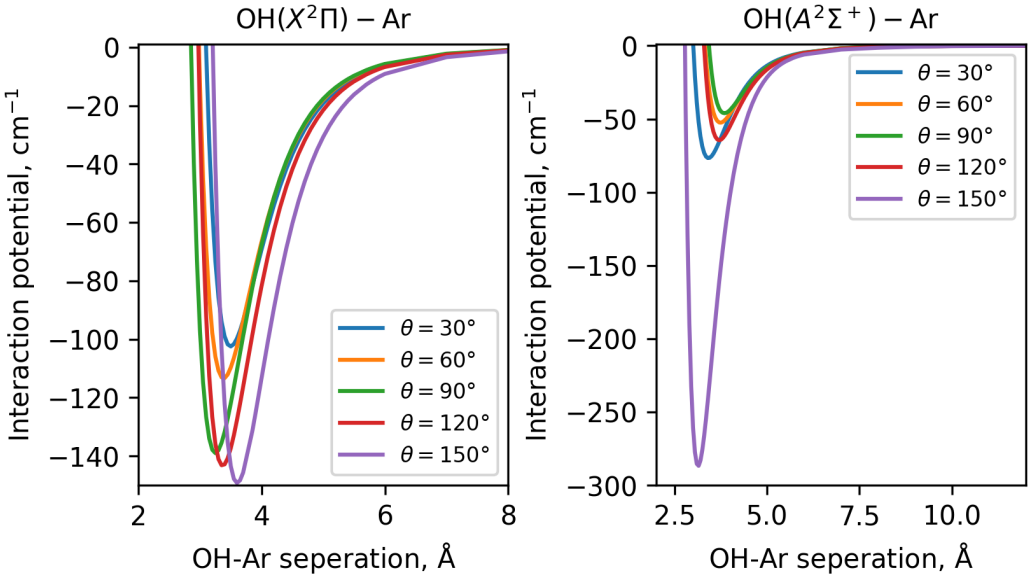

Figure 5.4: *Ab initio* UCCSD(T)/aug-cc-pVQz computed interaction potentials for the OH(X)-Ar and OH(A)-Ar complexes as a function of the OH-Ar separation r in Figure 5.1. The interaction potentials are plotted for different scattering angles θ (see also Figure 5.1) plotted in different colours.

5.1.1.3 OH-Ar

For all geometries of the OH(X)–Ar complex, the UCCSD(T)/aug-cc-pVQz (ground electronic state) and MRCI/aug-cc-pV5z (excited electronic state) levels of theory were used. The T1 diagnostic (both for the ground and electronic states) on average gave 0.004 and only 9 points of which exceeded the 0.044 criterion[424] at a value of 0.075. For the first electronically excited state $A^2\Sigma^+$, electronic orbitals were rotated as for NO-Ar. However, convergence to the correct energy was not reached, which was checked by studying the difference in ground and excited coupled cluster energies for the complex at a 15 Å separation. A CASSCF+icMRCI approach was then used to compute the excited state PES using the larger aug-cc-pV5Z basis sets. The *ab initio* computed interaction potentials are illustrated in Figure 5.4.

A grid of intermolecular distances corresponding to the range 2–15 Å and the angles between the intermolecular distance vector and the OH molecular axis equal to 10–180 degrees in 10 degree steps provided 1275 points in total.

The ground and first excited electronic states of OH are the same as NO, when introducing the Ar atom from non-linear geometries, the ground X $^2\Pi$ state of OH is seen to lift degeneracy and is energetically lowered, creating a symmetric A' and antisymmetric A'' state of the OH-Ar complex within the C_s point group.

5.1.2 Results: Pressure Broadening Parameters

To assess the reliability of phase-shift theory for representative molecular systems, we selected NO and OH as active molecules, with Ar and N_2 as perturbers, chosen for their distinct dipole moments and interaction types. These systems have also been extensively studied experimentally across various temperatures.

Lennard-Jones parameters for linewidth and shift calculations were derived from quantum chemistry calculations of the potential energy surfaces of ground and excited electronic states, as detailed in Section 5.1.1. When the interaction potential deviated significantly from the Lennard-Jones form, we prioritised the repulsive-wall regions, which are dominant at high temperatures. For instance, NO-Ar showed improved line-shape predictions with this approach. Generally, linewidth and shift coefficients at 295 K and 2700/2800 K were underestimated by about 30%, with a notable 44% underestimate for NO-N_2 at 2700 K. Prediction accuracy was similar for NO perturbed by Ar and N_2, while limited OH data prevented definitive conclusions. Overall, phase-shift theory provided underestimated values with uncertainties under 50%, making it suitable for order-of-magnitude estimates.

To reduce sensitivity to the Lennard-Jones fit region, we also applied a numerical representation of the potential difference ΔV for NO-Ar, with extrapolation for small r values. While extrapolation type had little impact on linewidths, shifts were severely underestimated. Thus, refining the potential alone within the traditional phase-shift theory proved ineffective.

Next, we explored trajectory model improvements using mean-thermal-velocity approximations. Parabolic and exact curved trajectories were tested for NO-Ar and NO-N_2. Results varied significantly, suggesting that further trajectory refinements are necessary to match experimental data.

For detailed quantitative discussions on the derived pressure broadening line shape parameters, please refer to Buldyreva et al. [409].

5.2 A True Ω Representation: Spin-Orbit Induced Non-Adiabatic Effects

Similarly to the (a)diabatising transformation, the transformation to what we call the $\Omega-$representation has been widely used[340,432,433] to simplify the treatment of spin-orbit coupling (SOC) in rovibronic calculations. SOC is a fundamental interaction in molecular systems, especially for highly excited electronic states, giving rise to the fine structure of rovibronic energy levels, reaction pathways between otherwise non-interacting states[434,435] (e.g. interstate crossings between singlets and triplets), and making dark states bright through the intensity stealing mechanism[436,437,13,341] (spin-orbit mixing). The transformation to the $\Omega-$representation, known as the state interacting method[432,433], aims to remove the SOC by diagonalisation of the Breit-Pauli SO-Hamiltonian together with the electronic Hamiltonian,

$$\mathbf{U}_{\Omega}^{\dagger}\left(\mathbf{V}+\mathbf{H}_{\mathrm{SO}}\right)\mathbf{U}_{\Omega}=\mathbf{V}_{\Omega}, \tag{5.6}$$

where $\mathbf{U}_{\Omega}$ is the unitary diagonalising transformation to the $\Omega-$representation, $\mathbf{H}_{\mathrm{SO}}$ is the Breit-Pauli spin-orbit Hamiltonian[157,438,439,433], yielding effective potentials for each SO-component as the diagonal elements of $\mathbf{V}_{\Omega}$. It has become an established method, where it is assumed that removal of the SOC decouples the molecular system transforming it to a single state representation. Single state representations are desirable not only because of their simplicity, but also because they can be readily used in LeRoy's LEVEL program[404], together with generated effective transition dipole moments (synonymous with the intensity stealing mechanism for forbidden bands, see Section 5.2.4.2), to compute transition intensities[340].

However, like the AtDT transformation, transforming to the Ω−representation ("adiabatic") introduces strong NAC terms and complex bond length dependence in molecular properties, such as spin, which are otherwise constant in the $\Lambda - S$ representation (as in Eq.(2.33) and Section 2.3). Although many spectroscopic studies[440,340,441] appear to overlook the need to transform the vibrational and rotational kinetic energy operators accordingly, the resulting non-adiabatic coupling terms and bond-length dependence are not entirely unrecognised, particularly in the context of ultracold physics[442–444]. Given my expertise in the full nonadiabatic treatment of the rovibronic problem, and the widespread use of the state-interacting method for generating single-state approximations to molecular spectroscopy, I found this representation problem particularly compelling.

We are currently developing a numerical comparison of the conventional $\Lambda - S$ representation and the Ω-representation, examining the challenges of using the single-state approximation for molecular spectroscopy. This work is ongoing, and I plan to submit our findings soon. Consequently, this section highlights the current progress and initial results from this project, reflecting the significant time and effort dedicated to its development.

5.2.1 Transformation to the Ω−representation

In this thesis, a 'true' Ω−representation is built by transforming all terms of the rovibronic molecular Hamiltonian in Eq.(2.9), where the impact of neglecting SOC-induced NAC terms on the rovibronic solution are investigated. But first, a theoretical framework for the Ω-representation must be developed, where each term is studied. For the remainder of this section I study the fully spin-orbit coupled rovibronic Schrödinger equation, where all NAC terms arising from the decoupling of electronic and nuclear motion are omitted for simplicity. One has, in the usual $\Lambda - S$ basis

$$\hat{\mathbf{H}}_{\text{tot}}\vec{\chi} = \left[-\frac{\hbar^2}{2\mu}\frac{\overrightarrow{d^2}}{dr^2} + \hat{\mathbf{H}}_{\text{rot}} + \boldsymbol{V}(r) + \hat{\mathbf{H}}_{\text{SO}} \right] \vec{\chi} = E_i\vec{\chi}, \tag{5.7}$$

where $\hat{\mathbf{H}}_{\text{rot}}$ is defined in Eq.(2.32) as the rotational Hamiltonian operator.

Transformation of the $\Lambda - S$ basis in Eq.(2.33) to the Ω representation after diagonalisation of Eq.(5.6) results in the following

$$\underbrace{|\text{state}, \Lambda, S, \Sigma\rangle}_{\Lambda - S \text{ representation, } |n\rangle} \rightarrow \underbrace{|\text{state}, \Omega\rangle}_{\Omega \text{ representation, } |m\rangle} . \tag{5.8}$$

Where one now considers a Hund's case (c) type basis where the total electronic AM projection quantum number Ω is approximately conserved. Since SOC couple states of the same Ω, it is evident that the SO-Hamiltonian is diagonal in the Ω−basis. Currently, the electronic and SO Hamiltonian has been transformed, however each term of Eq.(5.7) requires transformation by $\mathbf{U}_\Omega$ to maintain consistency between the $\Lambda - S$ and Ω representations. Particularly, the unitary transformation of the vibrational nuclear kinetic energy operator has been discussed extensively in Chapter 2, particularly in Section 2.4 for the derivation of the AtDT condition Eq.(2.49). Therefore, in matrix notation, the transformed Ω−representation of the total molecular Hamiltonian reads

$$\hat{\mathbf{H}}_{\text{tot},\Omega} = -\frac{\hbar^2}{2\mu}\left(\frac{\overrightarrow{d^2}}{dr^2} + (\mathbf{W}_\Omega)^2 - \left[\frac{\overleftarrow{d}}{dr}\mathbf{W}_\Omega - \mathbf{W}_\Omega\frac{\overrightarrow{d}}{dr}\right]\right) + \mathbf{V}_\Omega + \frac{\hbar^2}{2\mu r^2}\mathbf{U}_\Omega\mathbf{R}^2\mathbf{U}_\Omega^\dagger, \tag{5.9}$$

where $\mathbf{V}_\Omega$ is defined in Eq.(5.6) and $\mathbf{W}_\Omega$ is a skew-symmetric matrix, analogous to the NAC matrix, containing radial nuclear momentum couplings between states of the same Ω quantum number. Therefore, the spin-orbit induced NAC matrix $\mathbf{W}_\Omega$ is related to the Ω−transformation similarly to Eq.(2.48) via

$$\mathbf{U}_\Omega\frac{d\mathbf{U}_\Omega^\dagger}{dr} = \mathbf{W}_\Omega. \tag{5.10}$$

All that is left to study is the transformation of the rotational part to the Ω−representation. This task is slightly more complicated due to the selection rules arising in the different AM operator terms of Eq.(2.32), and so I will derive the AM matrix elements for a simple example system in the following section.

state	Λ	Σ	Ω
$^1\Sigma^+$	0	0	0
$^3\Sigma^-$	0	0	0
	0	±1	±1

Table 5.1: Possible components of electronic AM projection Λ Σ, and Ω for $^3\Sigma^-$ and $^1\Sigma^+$ electronic states.

5.2.2 Transforming the Rotational Hamiltonian: $^3\Sigma^-$–$^1\Sigma^+$ Transition

This section serves not only as a theoretical exercise, but also for debugging purposes in our implementation of the Ω−representation in our nuclear motion code

	$\vert^3\Sigma^-,0,1,0\rangle$	$\vert^1\Sigma^+,0,0,0\rangle$	$\vert^3\Sigma^-,0,1,-1\rangle$	$\vert^3\Sigma^-,0,1,1\rangle$
$\langle^3\Sigma^-,0\vert$	ω_{11}	ω_{12}	0	0
$\langle^1\Sigma^+,0\vert$	ω_{21}	ω_{22}	0	0
$\langle^3\Sigma^-,-1\vert$	0	0	1	0
$\langle^3\Sigma^-,1\vert$	0	0	0	1

Table 5.2: Overlap integrals between the Ω and $\Lambda-S$ basis functions of a $^3\Sigma^-$ and a $^1\Sigma^+$ state given by the rows and columns. $\omega_{i,j}$ are elements of the diagonalising Ω−transformation $\mathbf{U}_\Omega$. Here I specify the ordering of states in increasing Ω quantum number, given by the ordering of rows and columns above.

Duo. I study the transformed matrix elements of the Rotational Hamiltonian of Eq.(2.32) for the simple example of a two-state $^3\Sigma^-$–$^1\Sigma^+$ system. Table 5.1 shows all possible values of electronic AM projections Λ Σ, and Ω for this test system, showing that only the $\Omega=0$ component is coupled by SOC. I use the subscript notation to denote the Ω value, for example $^3\Sigma_0^-$ corresponds to a state with $\Lambda=0$, $S=1$, and $\Omega=0$. Any basis vector with this notation means it is evaluated in the Ω−representation.

Transforming the matrix elements of a general operator $\hat{\mathbf{P}}$ from the $\Lambda-S$ to the Ω−representation can be done as follows

$$\langle \text{state}',\Omega'|\,\hat{\mathbf{P}}\,|\text{state}'',\Omega''\rangle = \sum_{i,j}\Big[\langle \text{state}',\Omega'|\text{state}_i,\Lambda_i,S_i,\Sigma_i\rangle\langle \text{state}_j,\Lambda_j,S_j,\Sigma_j|\text{state}'',\Omega''\rangle \times\langle \text{state}_i,\Lambda_i,S_i,\Sigma_i|\,\hat{\mathbf{P}}\,|\text{state}_j,\Lambda_j,S_j,\Sigma_j\rangle\Big]\,\delta_{\Omega';\Lambda_i+\Sigma_i}\delta_{\Omega'';\Lambda_j+\Sigma_j}, \tag{5.11}$$

where only the non-rotational part of the rovibronic basis set Eq.(2.33) is considered, i and j denote counting indices over all quantum numbers Λ,S,Σ and the 'state' label (or equivalently, matrix element indices of the $\Lambda-S$ basis), and the Kronecker delta's indicate that the Ω−transformation couples only states of the same Ω quantum number. The wavefunction overlaps will then contain combinations of the Ω−transformation matrix elements, computed on each point of the bond length grid. Therefore, additional bond-length dependence is introduced into the transformed matrix elements, such as molecular AM properties like spin which is constant in the $\Lambda-S$ representation.

$\hat{\mathbf{S}}^2$

The matrix elements of the $\hat{\mathbf{S}}^2$ spin angular momentum operator in the $\Lambda-S$ representation are

$$\langle S,\Sigma|\,\mathbf{S}^2\,|S,\Sigma\rangle = S(S+1)\hbar^2, \tag{5.12}$$

and so the selection rules couple states of same spin S and its projection Σ. The non-vanishing $\Omega-$representation matrix elements are then given by

$$\begin{aligned}
\langle {}^3\Sigma_0^- | \mathbf{S}^2 | {}^3\Sigma_0^- \rangle &= 2\omega_{11}^2\hbar^2 \\
\langle {}^1\Sigma_0^+ | \mathbf{S}^2 | {}^1\Sigma_0^+ \rangle &= 2\omega_{21}^2\hbar^2 \\
\langle {}^1\Sigma_0^+ | \mathbf{S}^2 | {}^3\Sigma_0^- \rangle &= 2\omega_{21}\omega_{11}\hbar^2 = \langle {}^3\Sigma_0^- | \mathbf{S}^2 | {}^1\Sigma_0^+ \rangle
\end{aligned} \tag{5.13}$$

where $\omega_{ij}(r)$ are the matrix elements of the diagonalising $\Omega-$transformation and are related to the overlap integrals given in Table 5.2.

$\hat{\mathbf{S}}_z$

The matrix elements of the $\hat{\mathbf{S}}_z$ spin angular momentum operator in the $\Lambda-S$ representation are

$$\langle S,\Sigma | \mathbf{S}_z | S,\Sigma \rangle = \Sigma\hbar, \tag{5.14}$$

and so the selection rules couple states of same spin S and its projection Σ. The non-vanishing $\Omega-$representation matrix elements are then given by

$$\begin{aligned}
\langle {}^3\Sigma_{-1}^- | \mathbf{S}^2 | {}^3\Sigma_{-1}^- \rangle &= -\hbar \\
\langle {}^3\Sigma_1^+ | \mathbf{S}^2 | {}^3\Sigma_1^- \rangle &= \hbar
\end{aligned} \tag{5.15}$$

$\hat{\mathbf{S}}_\pm$

The matrix elements of the $\hat{\mathbf{S}}_\pm$ spin angular momentum operator in the $\Lambda-S$ representation are

$$\langle S,\Sigma\pm 1 | \mathbf{S}_\pm | S,\Sigma \rangle = [S(S+1)-\Sigma(\Sigma\pm 1)]^{\frac{1}{2}}\hbar, \tag{5.16}$$

and so the selection rules couple states same spin S and its projection differing by 1 quantum ($\Delta\Sigma = \pm 1$). The non-vanishing $\Omega-$representation matrix elements are then given by

$$\begin{aligned}
\langle {}^3\Sigma_0^- | \mathbf{S}_- | {}^3\Sigma_1^- \rangle &= \omega_{11} \sqrt{2\hbar^2} \\
\langle {}^1\Sigma_0^+ | \mathbf{S}_- | {}^3\Sigma_1^- \rangle &= \omega_{21} \sqrt{2\hbar^2} \\
\langle {}^3\Sigma_{-1}^- | \mathbf{S}_- | {}^3\Sigma_0^- \rangle &= \omega_{11} \sqrt{2\hbar^2} \\
\langle {}^3\Sigma_{-1}^- | \mathbf{S}_- | {}^1\Sigma_0^- \rangle &= \omega_{21} \sqrt{2\hbar^2} \\
\langle {}^3\Sigma_0^- | \mathbf{S}_+ | {}^3\Sigma_{-1}^- \rangle &= \omega_{11} \sqrt{2\hbar^2} \\
\langle {}^1\Sigma_0^+ | \mathbf{S}_+ | {}^3\Sigma_{-1}^- \rangle &= \omega_{21} \sqrt{2\hbar^2} \\
\langle {}^3\Sigma_1^- | \mathbf{S}_+ | {}^3\Sigma_0^- \rangle &= \omega_{11} \sqrt{2\hbar^2} \\
\langle {}^3\Sigma_1^- | \mathbf{S}_+ | {}^1\Sigma_0^- \rangle &= \omega_{21} \sqrt{2\hbar^2}
\end{aligned} \tag{5.17}$$

$\hat{\mathbf{L}}_\pm$

The matrix elements of the $\hat{\mathbf{L}}_{\pm 1}$ orbital angular momentum operator in the $\Lambda - S$ representation are

$$\langle L, \Lambda \pm 1 | \mathbf{L}_\pm | L, \Lambda \rangle = \langle L, \Lambda \pm 1 | \mathbf{L}_x | L, \Lambda \rangle \pm i \langle L, \Lambda \pm 1 | \mathbf{L}_y | L, \Lambda \rangle \tag{5.18}$$

and so the selection rules couple states of same electronic orbital angular momenta L (states with the same dissociation limit) and its projection differing by one quanta $\Delta\Lambda = \pm 1$. For a ${}^3\Sigma^- - {}^1\Sigma^+$ transition all elements of the electronic orbital AM ladder operator are zero since $\Lambda = 0$ in both states. To transform $\hat{\mathbf{L}}_\pm$ one can simply transform the $\mathbf{L}_x$ matrix via $\mathbf{U}_\Omega$ transformation.

5.2.3 Transformation of the electric Dipole Moment

The light intensity seen from a molecular transition is due to interaction with the dipole moment in the laboratory frame. However, since one solves nuclear motion in the molecule-fixed frame, the molecule-fixed coordinates of the dipole moment must be transformed to the lab-frame. It can be shown[107] that the electric dipole moment is calculated as

$$\begin{aligned}
&\langle \text{state}, \Lambda, S, \Sigma | \langle \text{state}, v | \langle J, \Omega, M | \mu_{\mathbf{R}_\lambda} | \text{state}', \Lambda', S', \Sigma' \rangle | \text{state}', v' \rangle | J', \Omega', M' \rangle \\
&\quad = \sum_{t=0,\pm 1} (-1)^{\lambda - t} \langle \text{state}, v | \langle \text{state}, \Lambda | \mu_{\mathbf{r}_t} | \text{state}', \Lambda' \rangle | \text{state}', v' \rangle \\
&\qquad \times \langle S, \Sigma | S', \Sigma' \rangle \langle J, \Omega, M | D^1_{-\lambda\, -t} | J', \Omega', M' \rangle ,
\end{aligned} \tag{5.19}$$

where $\mathbf{R}_\lambda$ is the lab-fixed spherical tensor coordinate which is related to the molecular-fixed spherical coordinates r_t by the rotation matrix $D^1_{-\lambda -t}$ via

$$\mathbf{R}_\lambda = \sum_{t=0,\pm 1} (-1)^{\lambda - t} \mathbf{D}^1_{-\lambda -t} \mathbf{r}_t . \tag{5.20}$$

Therefore, $\mu_{\mathbf{r}_t}$ represents the usual transition dipole moment operator in the molecule-fixed frame, where its electronic elements are computed in quantum chemistry programs such as MOLPRO [136]. Next, the transition dipole moment above is transformed to the $\Omega-$representation, using the transformation of the form given by Eq.(5.11), yielding

$$\begin{aligned}
&\langle \text{state}, \Omega | \langle \text{state}, v | \langle J, \Omega, M | \, \mu_{\mathbf{R}_\lambda} \, | \text{state}', \Omega' \rangle | \text{state}', v' \rangle | J', \Omega', M' \rangle \\
&\quad = \sum_{t,i,j} (-1)^{\lambda - t} \langle \text{state}, \Omega | \text{state}_i, \Lambda_i, S_i, \Sigma_i \rangle \langle \text{state}_j, \Lambda_j, S_j, \Sigma_j | \text{state}', \Omega' \rangle \\
&\qquad \times \langle \text{state}, v | \langle \text{state}_i, \Lambda_i | \, \mu_{\mathbf{r}_t} \, | \text{state}_j, \Lambda_j \rangle | \text{state}', v' \rangle \\
&\qquad \times \delta_{S_i, S_j} \delta_{\Sigma_i, \Sigma_j} \delta_{\Omega, \Lambda_i + \Sigma_i} \delta_{\Omega', \Lambda_j + \Sigma_j} \\
&\qquad \times (-1)^{M' - \Omega'} [(2J+1)(2J'+1)]^{1/2} \begin{pmatrix} J' & J & 1 \\ -M' & M & -\lambda \end{pmatrix} \begin{pmatrix} J' & J & 1 \\ -\Omega' & \Omega & -t \end{pmatrix},
\end{aligned} \tag{5.21}$$

where the elements of the rotation matrix $D^1_{-\lambda -t}$ are given explicitly in terms of the Wigner 3-j symbols in the last line. The transition dipole moment in the $\Omega-$representation is then slightly more complicated since the summation is not only over spatial degrees of freedom, but also in the $\Lambda - S$ states with matrix element indices given by i and j. Summing over the i, j indices (the resolution of the identity in the $\Lambda - S$ basis) then yields the transition dipole moments in the $\Omega-$representation

$$\begin{aligned}
\langle \text{state}, \Omega | \, \mu_{\mathbf{r}_t} \, | \text{state}', \Omega' \rangle = \sum_{i,j} &\langle \text{state}, \Omega | \text{state}_i, \Lambda_i, S_i, \Sigma_i \rangle \langle \text{state}_j, \Lambda_j, S_j, \Sigma_j | \text{state}', \Omega' \rangle \\
&\times \langle \text{state}_i, \Lambda_i | \, \mu_{\mathbf{r}_t} \, | \text{state}_j, \Lambda_j \rangle \, \delta_{\Omega, \Lambda_i + \Sigma_i} \delta_{\Omega', \Lambda_j + \Sigma_j} .
\end{aligned} \tag{5.22}$$

Therefore, for a ${}^3\Sigma^- - {}^1\Sigma^+$ transition the $\Omega-$representation transition dipole elements read

$$\begin{aligned}
\langle {}^3\Sigma^-, 0 | \, \mu_{\mathbf{r}_t} \, | {}^3\Sigma^-, 0 \rangle = \omega_{11}^2 \, &\langle {}^3\Sigma^-, \Lambda = 0 | \, \mu_{\mathbf{r}_t} \, | {}^3\Sigma^-, \Lambda = 0 \rangle \\
&+ \omega_{12}^2 \, \langle {}^1\Sigma^+, \Lambda = 0 | \, \mu_{\mathbf{r}_t} \, | {}^1\Sigma^+, \Lambda = 0 \rangle ,
\end{aligned} \tag{5.23}$$

$$\langle {}^3\Sigma^-,-1|\,\mu_{\mathbf{r}_t}\,|{}^3\Sigma^-,-1\rangle = \langle {}^3\Sigma^-,\Lambda=0|\,\mu_{\mathbf{r}_t}\,|{}^3\Sigma^-,\Lambda=0\rangle\,, \tag{5.24}$$

$$\langle {}^3\Sigma^-,1|\,\mu_{\mathbf{r}_t}\,|{}^3\Sigma^-,1\rangle = \langle {}^3\Sigma^-,\Lambda=0|\,\mu_{\mathbf{r}_t}\,|{}^3\Sigma^-,\Lambda=0\rangle\,, \tag{5.25}$$

$$\begin{aligned}\langle {}^1\Sigma^+,0|\,\mu_{\mathbf{r}_t}\,|{}^1\Sigma^+,0\rangle = \omega_{21}^2\,\langle {}^3\Sigma^-,\Lambda=0|\,\mu_{\mathbf{r}_t}\,|{}^3\Sigma^-,\Lambda=0\rangle \\ +\,\omega_{22}^2\,\langle {}^1\Sigma^+,\Lambda=0|\,\mu_{\mathbf{r}_t}\,|{}^1\Sigma^+,\Lambda=0\rangle\,,\end{aligned} \tag{5.26}$$

$$\begin{aligned}\langle {}^3\Sigma^-,0|\,\mu_{\mathbf{r}_t}\,|{}^1\Sigma^+,0\rangle = \omega_{11}\omega_{21}\,\langle {}^3\Sigma^-,\Lambda=0|\,\mu_{\mathbf{r}_t}\,|{}^3\Sigma^-,\Lambda=0\rangle \\ +\,\omega_{12}\omega_{22}\,\langle {}^1\Sigma^+,\Lambda=0|\,\mu_{\mathbf{r}_t}\,|{}^1\Sigma^+,\Lambda=0\rangle\,.\end{aligned} \tag{5.27}$$

It is evident in Eq.(5.27) that a transition dipole moment arises between the two spin multiplets in the Ω−representation, where transitions between states such as ${}^3\Sigma^-$ and ${}^1\Sigma^+$ are spin-forbidden in the $\Lambda-S$ representation meaning no direct transition dipole moment (TDM) exists. Spin-orbit coupling (SOC) introduces spin-orbit mixing that leads to the dipole forbidden transition intensity. This works by mixing the two states wavefunctions where, subsequently, components of the diagonal dipole moments are effectively "borrowed", enabling transitions that would otherwise be forbidden – the intensity-stealing mechanism.

Conveniently, in the Ω-representation forbidden transitions become directly allowed due to SO-induced mixing, with new selection rules being $\Delta\Omega = 0, \pm 1$. These are classified as parallel or perpendicular transitions based on the orientation of the transition dipole moment relative to the internuclear axis[445]. For the perpendicular transition, this is made possible through further interaction with, for example, a ${}^3\Pi$ state[172].

5.2.4 Spectroscopic Model of a ${}^3\Sigma^- - {}^1\Sigma^+$ System

x I now present an example artificial two-state electronic system coupled by SOC, where the rovibronic solution will be studied in both the $\Lambda-S$ and Ω representation.

I model two bound potential energy curves that intersect near their minima to ensure that the Ω-transformation significantly impacts low-lying bound states, thereby highlighting the consequences of omitting DDR terms in subsequent analyses. I assign the two states as a triplet-singlet system with term symbols $X^3\Sigma^-$ and $b^1\Sigma^+$, where transitions between them are dipole/spin-forbidden. The $\Lambda-S$

	V_X	V_b	W_{bX}
T_e	0.0000	2000.0000	
A_e	42056.0000	27000.0000	
r_e	1.2100	1.2400	
b	1.9000	2.3000	
r_c			1.4529
γ			0.0100

Table 5.3: Molecular parameters for the two-state model.

potentials were modeled using simple Morse oscillator functions of the form

$$V(r) = T_e + (A_e - T_e)[1 - \exp(-b(r - r_e))]^2, \tag{5.28}$$

where $V(r_e) = T_e$ is the minimum energy, A_e is the dissociation asymptote, b is a parameter controlling the width of the well, and r_e is the minimum position. Using the methodology presented by Brady et al.[38] (see also Section 2.5.1), the SOC is modeled like their diabatic coupling (DC), where combination of two potentials and a NAC define the SOC (DC) via

$$SO_{bX}(r) = \frac{1}{2}\tan\left(2\beta_{bX}(r)\right)(V_b - V_X), \tag{5.29}$$

where $\beta_{bX}(r)$ is the mixing angle of the Ω-transformation, defined by the corresponding SO-induced NAC W_{bX} by the cumulative integral.

$$\beta(r) = \beta_0 + \int_0^r W_{\Omega,bX} dr. \tag{5.30}$$

I model the SO-induced NAC W_{bX} with a Lorentzian function of the form

$$W_{bX}(r) = \frac{1}{2}\frac{\gamma}{\gamma^2 + (r - r_c)^2}, \tag{5.31}$$

where γ is the half-width at half-maximum (HWHM) and r_c defines the centroid position which is set to the crossing geometry of the V_X and V_b $(\Lambda - S)$ potentials. The mixing angle β_{bX}, is then

$$\beta_{bX}(r) = \frac{\pi}{4} + \frac{1}{2}\arctan\left(\frac{r - r_c}{\gamma}\right). \tag{5.32}$$

The parameters for the potential and NAC curves for this two-state coupled system are given in Table 5.3.

Figure 5.5 illustrates the Ω and $\Lambda - S$ curves for the spectroscopic model defined here, where the DBOC-like diagonal corrections to the Ω-potentials have been added and are seen to create huge spike-like barriers. It is therefore expected these SO-induced NAC terms will be important in the final rovibronic solution. The Ω potentials are computed via the eigenvalues of the resulting diagonalisation in Eq.(5.6). The three SO-components of the $X^3\Sigma^-$ state are seen as solid lines in the top left panel of Figure 5.5, where the degenerate $X_{\pm 1}$ terms are seen to not interact with the b_0 state, following the SO-selection rules, but an avoided crossing is exhibited between the b_0 and X_0 Ω-states with a NAC centered at the avoided crossing.

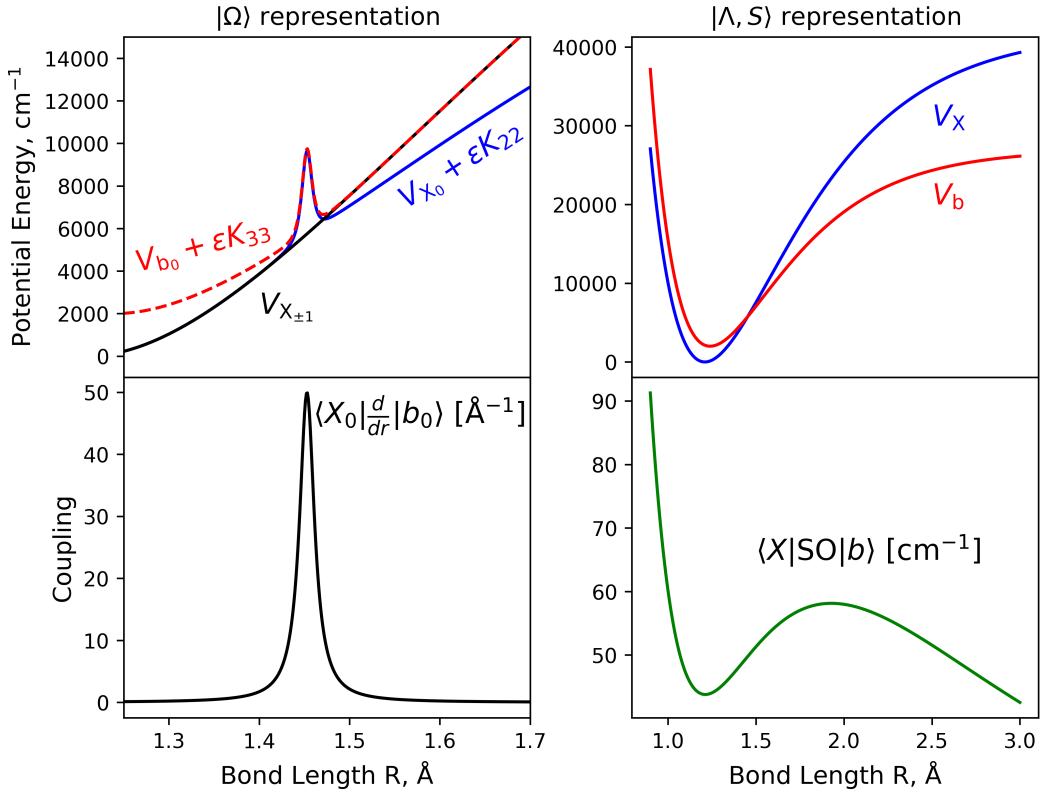

Figure 5.5: Illustration of the potentials (top panels) and associated couplings (bottom panels) of the two-state coupled system in the Ω-representation (left panels) and $\Lambda - S$ representation (right panels). The DBOC-like corrections have been added to the Ω potentials, and are computed from multiplying the kinetic energy factor $\varepsilon = \frac{\hbar}{8\pi^2\mu c}$ by the diagonal elements of the $\mathbf{W}^2$ matrix in Eq.(2.17).

5.2.4.1 The Rovibronic Solution

With the spectroscopic model defined in Section 5.2.4, the rovibronic basis, either in the $\Lambda - S$ or Ω representation (see section 5.2.1), is used to construct the fully

coupled rovibronic Hamiltonian. The Hamiltonian is then diagonalised to yield a set of rovibronic energies and wavefunctions. A full non-adiabatic module has been implemented in our rovibronic code Duo to incorporate the NACs arising from the transformation of the vibrational nuclear kinetic energy. All functionality of Duo, previously implemented exclusively in the $\Lambda - S$ representation, has now been extended to operate in the Ω representation, where all terms of the Hamiltonian are transformed.

The lowest twenty $J = 0$ energy levels are calculated for the presented two-state system to demonstrate the equivalence between the $\Lambda - S$ and Ω representations, as well as the impact of omitting induced NAC terms on the rovibronic solutions. These energies are computed with high accuracy to avoid limitations stemming from basis set convergence issues. Since the vibronic wavefunctions are optimised for the respective potentials, differences between the two representations are naturally expected.

To evaluate the impact of NAC terms, rovibronic energies are computed under three levels of approximation: (A) omitting all NAC terms ($\mathbf{W}_\Omega = 0$, $(\mathbf{W}_\Omega)^2 = 0$); (B) omitting only the DBOC-like correction term ($(\mathbf{W}_\Omega)^2 = 0$); and (C) omitting spin-orbit coupling (SOC) in the $\Lambda - S$ representation. The results are summarised in Table 5.4. The Ω representation, when including all NAC terms, produces identical energies to the fully coupled $\Lambda - S$ representation, confirming their equivalence as expected. However, omission of any NAC terms introduces significant errors, with maximal deviations on the order of 10^2 cm^{-1}. For high-resolution applications, NAC terms must be included, as they are crucial for maintaining equivalence between the $\Lambda - S$ and Ω representations. Brady et al.[38] show that omission of any NAC terms also leads to drastic differences seen in the computed rovibronic wavefunctions, therefore since I have demonstrated this in the energies it can be assumed the wavefunctions will also be significantly effected.

Interestingly, omitting SOC in the $\Lambda - S$ representation results in much smaller errors than in the Ω representation, with maximum differences below 10 cm^{-1}. Therefore, transformation to the Ω representation should be treated with caution, as omitting induced NAC terms is not a reliable approximation. The Duo program now supports testing various approximations in non-adiabatic effects, providing a robust tool for quantitatively studying the impact of these approximations on rovibronic energy calculations.

Table 5.4: The lowest 25 $J = 0$ rovibronic energies of the presented two-state system computed within the $\Lambda - S$ and Ω representations using Duo. Varying degrees of approximations are used and described in the text.

n	Ω representation					$\Lambda - S$ representation			
	E	E(A)	E(B)	State	v	E	E(C)	State	v
1	0	0	0	X_0	0	0	0	X	0
2	968.345455	968.354306	968.304973	X_0	1	968.345455	968.485302	X	1
3	1924.867208	1925.231078	1924.429095	X_0	2	1924.867208	1925.554298	X	2
4	1966.978286	1966.596190	1966.928886	b_0	0	1966.978286	1964.514372	b	0
5	2859.629394	2864.714731	2857.087255	b_0	1	2859.629394	2862.363719	b	1
6	2875.718441	2870.521034	2872.441660	X_0	3	2875.718441	2871.206988	X	3
7	3743.883880	3746.544245	3724.749937	b_0	2	3743.883880	3743.483993	b	2
8	3806.823099	3803.674870	3770.379262	X_0	4	3806.823099	3805.443372	X	4
9	4608.585135	4613.974883	4461.643064	b_0	3	4608.585135	4607.875192	b	3
10	4729.337869	4722.247604	4550.730178	X_0	5	4729.337869	4728.263448	X	5
11	5456.318936	5473.798714	5106.378331	b_0	4	5456.318936	5455.537318	b	4
12	5640.676959	5618.439714	5300.498571	X_0	6	5640.676959	5639.667218	X	6
13	6287.255096	6338.303861	5976.212596	X_0	7	6287.255096	6286.470370	b	5
14	6540.670439	6477.847087	6238.527487	b_0	5	6540.670439	6539.654681	X	7
15	7101.433679	7214.262671	6971.996148	X_0	8	7101.433679	7100.674348	b	6
16	7429.278037	7295.604841	7280.802461	b_0	6	7429.278037	7428.225842	X	8
17	7898.869553	8091.348144	7867.479901	X_0	9	7898.869553	7898.149252	b	7
18	8306.484602	8092.493363	8276.551687	b_0	7	8306.484602	8305.380717	X	9
19	8679.569862	8870.870473	8521.679569	X_0	10	8679.569862	8678.895083	b	8
20	9172.282642	8960.013008	9041.823978	b_0	8	9172.282642	9171.119361	X	10

5.2.4.2 Spin-Orbit Mixing: Visualising the Intensity Stealing Mechanism

Spin-orbit coupling (SOC) introduces spin-orbit mixing that leads to dipole forbidden transition intensity. In the Λ-S representation, transitions between states such as $X^3\Sigma^-$ and $b^1\Sigma^+$ are spin-forbidden, meaning no direct transition dipole moment (TDM) exists between them. However, SOC mixes the wavefunctions of these states where components of the diagonal dipole moments are effectively "borrowed", enabling transitions that would otherwise be forbidden – the intensity-stealing mechanism.

Conveniently, in the Ω-representation forbidden transitions become directly allowed due to SO-induced mixing, with new selection rules being $\Delta\Omega = 0, \pm 1$. These are classified as parallel or perpendicular transitions based on the orientation of the transition dipole moment relative to the internuclear axis[445]. The TDMs in this representation can be derived by applying the unitary $\Omega-$transformation to the dipole moment matrix in Section 5.2.3.

Figure 5.6 illustrates the dipole moment curves in both representations. Interestingly, the effective $b_0 - X_0$ dipole (with subscripts being the Ω value) exhibits a Lorentzian-like character in regions of strong SOC-induced non-adiabatic coupling (NAC). In this region, the molecular wavefunctions are nearly equal superpositions

of the Λ-S states, allowing the emergence of transition dipole moments. Outside these regions, the states behave analogously to the Λ-S representation, where transitions are dipole spin-forbidden and thus TDMs vanish. Diagonal dipole moments show an avoided crossing in regions of strong SOC, reminiscent of adiabatic property behavior during avoided crossings between states of identical symmetry.

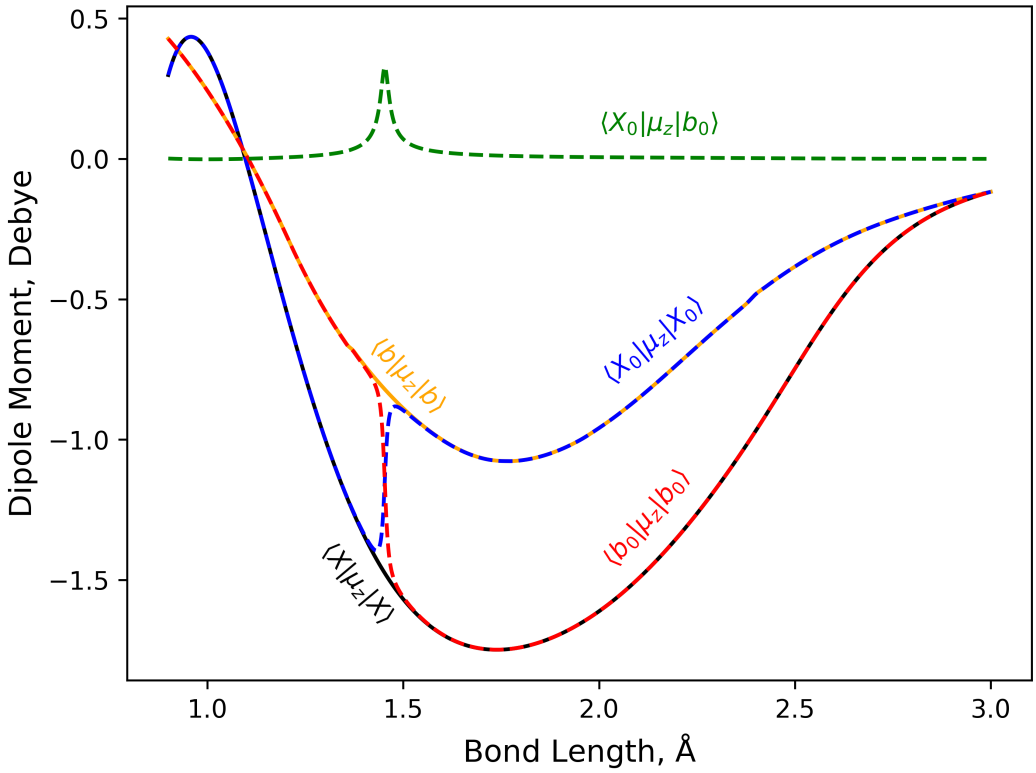

Figure 5.6: Dipole moment curves in the Λ-S and Ω representations. The effective $b_0 - X_0$ dipole moment reveals SOC-driven intensity-stealing, while diagonal dipoles illustrate avoided crossings as in the adiabatic representation of the electronic Hamiltonian.

5.2.4.3 Transformation of the Rotational Hamiltonian

Transformation of the rotational kinetic energy Hamiltonian (see Section 5.2.2) is necessary to maintain consistency between the $\Lambda - S$ and Ω representations. A key example is the spin operator, $\hat{\mathbf{S}}$. In the Λ-S representation, $\hat{\mathbf{S}}$ eigenvalues are constants, since spin is treated as a conserved quantum number. However, the Ω-representation introduces a bond-length dependence to spin properties. Figure 5.7 illustrates the spin evolution as a function of bond length. At short internuclear distances, where NAC is weak, the b state is predominantly singlet and the X state is predominantly triplet, consistent with the Λ-S description. As the bond length

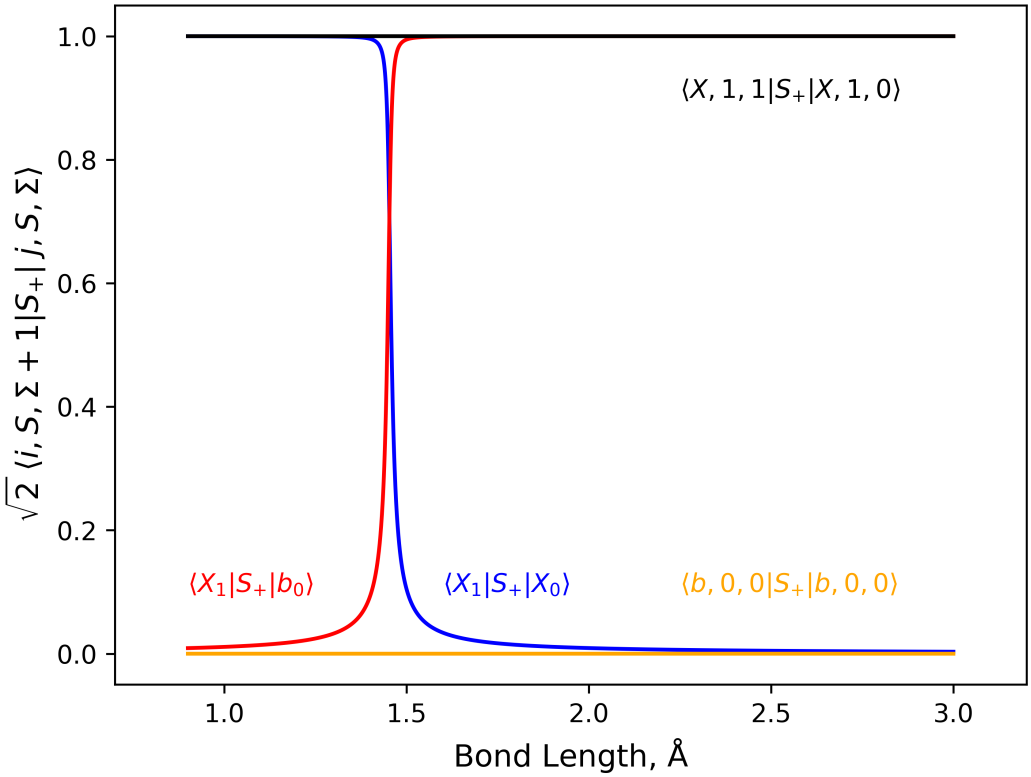

Figure 5.7: Illustrations of the spin eigenvalues as a function of bond length in the Ω-representation. SOC-induced mixing swaps spin multiplicities between the b and X states, highlighting the emergence of a transition dipole moment. The correpsonding constant spins in the $\Lambda - S$ representation are also shown.

increases, SOC-driven mixing (or NAC) leads to state spin multiplicities swapping over the avoided crossing.

This spin evolution explains the emergence of transition dipole moments in regions of strong mixing, where both b and X states exhibit significant singlet-triplet contributions, satisfying spin selection rules. While the Ω-representation provides insight into spin-orbit mixing and the generation of transition dipole moments, it introduces complexity into the spectroscopic model. Properties such as spin and angular momentum acquire a nuclear geometry dependence, resulting in complex topologies for important quantities like the dipole moment. Accurately treating the true Ω-representation requires careful treatment, as small changes in the avoided crossing topology of the SO-component potentials can significantly alter spin curves and dipole moments (if one was to remain consistent). By contrast, the Λ-S representation simplifies modeling, requiring only the treatment of potentials and SOC terms. Constant spin properties can then be hard-programmed and require no treatment beyond their initial computation, making it a more practical

choice for applications demanding accuracy and consistency.

5.2.5 Conclusions

A 'true' Ω−representation is presented, whereby all terms of the rovibronic molecular Hamiltonian are transformed with the diagonalisation of the spin-orbit and potential matrix. In this representation, spin-orbit couplings vanish, however strong non-adiabatic couplings ensue and a bond length dependence is introduced into molecular properties such as spin which are constant in the $\Lambda - S$ representation.

I show that omitting spin-orbit-induced NAC terms (common in many studies) introduces significant errors in computed rovibronic energies and that they are crucial for the equivalence between the Ω and $\Lambda - S$ representations. Thus, for high-resolution applications, all NAC terms must be included, or their omission should be rigorously tested using tools like the Duo program.

The bond-length dependence of molecular properties, such as spin, introduces complex topologies in the Ω−representation. While spin-orbit mixing can provide insights, such as understanding forbidden band intensities through effective transition dipole moments, treating these effects (fitting analytical forms, integrating property curves, etc.) is computationally challenging. Refining Ω−representation potentials for spectroscopic models requires careful adjustment of molecular properties such as spin and dipole moments to maintain consistency. This is difficult even for a two-state model and becomes impractical for larger systems.

I conclude that the Ω−representation, while often perceived as simpler, can be more complex and challenging to implement accurately. It is highly sensitive to the topology of property curves and often less practical than the spin-orbit coupled $\Lambda - S$ representation. An exact decoupling scheme is not rigorously achievable, where *simplification of one part of the Hamiltonian leads to the complication of another*.

5.3 An *Ab initio* study on Potassium Hydride

Alkali hydride molecules have long been a subject of interest in both experimental and theoretical chemistry[446–454]. Despite their seemingly simple diatomic structure (MH, where M represents an alkali metal), these compounds present significant challenges. These challenges arise from a combination of factors: strong electron correlation effects (particularly core-valence interactions); the ionic character of the ground state ($M^+ + H^-$) which dissociates into neutral atomic fragments (M + H), leading to avoided crossings between electronic states; and the large-amplitude, highly anharmonic nuclear motion resulting from the light hydrogen atom. For

heavier alkali metals like potassium, relativistic effects also become important. These factors combine to make accurate *ab initio* calculations computationally demanding and complicate experimental investigations due to the molecules' high reactivity and complex spectra.

The ionic-to-neutral transition during dissociation necessitates a charge-transfer process, manifesting as an avoided crossing, making a diabatic representation particularly insightful. Previous studies on LiH[454–456], for example, highlight the benefits of the diabatic approach for understanding non-Born-Oppenheimer effects, such as collision-induced transitions[457–459], vibronic shifts[460,460–462], and vibronic non-radiative lifetimes[461,462]. Furthermore, the diabatic framework can be used to improve the accuracy of *ab initio* calculations by mitigating the difficulties associated with accurately computing the electron affinity of hydrogen due to basis set limitations, a significant source of error in determining ground-state binding energies of alkali hydrides[454]. For these reasons, KH could be a benchmark molecule for theoretical chemistry, where proven advantages of the diabatic representation for LiH motivates extension to KH.

While KH has been studied theoretically[451,463,450,447,463–468] and experimentally[469–473], a comprehensive spectroscopic line list, crucial for its potential astrophysical detection, is currently lacking. To the best of our knowledge, existing *ab initio* calculations focus primarily on potential energy curves and dipole moments, without fully addressing all relevant couplings (e.g. spin-orbit, electronic angular momentum). This work presents a full spectroscopic model for KH, addressing this gap. It is speculated that potassium containing molecules should contribute to the absorption in astrophysical plasmas[474], but the astrophysical detection of KH – the simplest potassium molecule – has yet to been done. The KH line list will then be important for its potential future detection.

This section details the *ab initio* electronic structure calculations for the KH diatomic, where I obtain PECs for the lowest lying singlet and triplet states and their SOCs, EAMCs, and TDMCs. My aim is to provide an accurate and thorough *ab initio* spectroscopic model to be used in subsequent refinement to a future MARVEL network of rovibronic energy levels. I also aim to produce a strong theoretical baseline for the study of NACs for the ionic molecule, where a diabatic representation is discussed above to be potentially insightful for the resulting nuclear motion.

While this research was completed as part of my doctoral work, time limitations prevented its publication. The results are now ready for manuscript preparation, and I plan to submit them for publication in the near future.

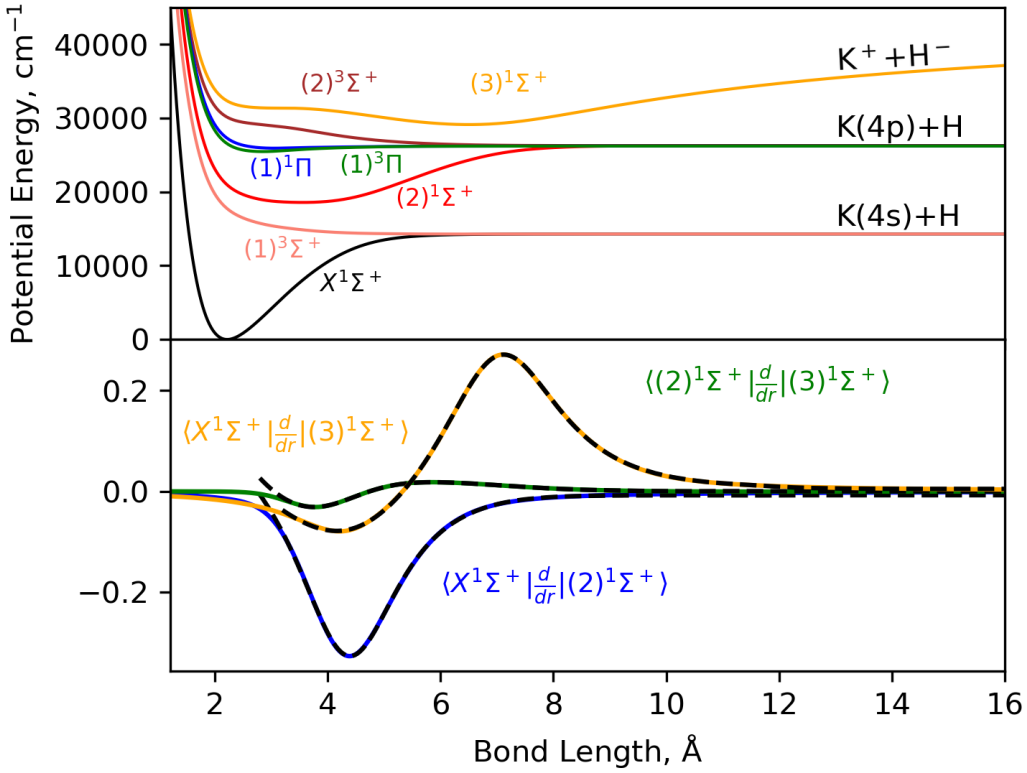

Figure 5.8: Illustration of the *ab initio* calculated adiabatic PECs of the energetcially lowest 7 singlet and triplet states of KH (top panel). The bottom panel plots the CASSCF computed NACs in the $^1\Sigma^+$ manifold as dashed lines and their fitted analytical forms to Eq.(5.33) – which show excellent agreement.

5.3.1 Calculation Details

Internally-contracted multi-reference configuration interaction (icMRCI) *ab initio* calculations for the lowest 7 singlet and triplet electronic states of KH correlating to the K($4s$)+H, K($4p$)+H, and ionic K^++H^- dissociation limits were performed using MolPro[104] with aug-cc-pVQZ-X2C basis sets, using molecular orbitals obtained from state-averaged complete active space self-consistent field (CASSCF) calculations. Under C_{2v} point group symmetry, all *ab initio* calculations were done using the occupied orbital space (8,3,3,0) across the A1, B1, B2 and A2 irreducible representations, respectively, with corresponding core orbitals (5,1,1,0).

Potential Energy Curves: The potential energy curves (PECs) for the electronic states $X^1\Sigma^+$, $(2)^1\Sigma^+$, $(3)^1\Sigma^+$, $(1)^3\Sigma^+$, $(2)^3\Sigma^+$, $(1)^1\Pi$, and $(1)^3\Pi$ were computed and are shown in Figure 5.8. Except for the $(1)^3\Sigma^+$ and $(2)^3\Sigma^+$ states, which are clearly unbound, the remaining five states are bound. However, the $(1)^1\Pi$ and $(1)^3\Pi$ states exhibit very shallow potential wells. Notably, the potentials extend significantly at large bond lengths. An avoided crossing structure is observed in the

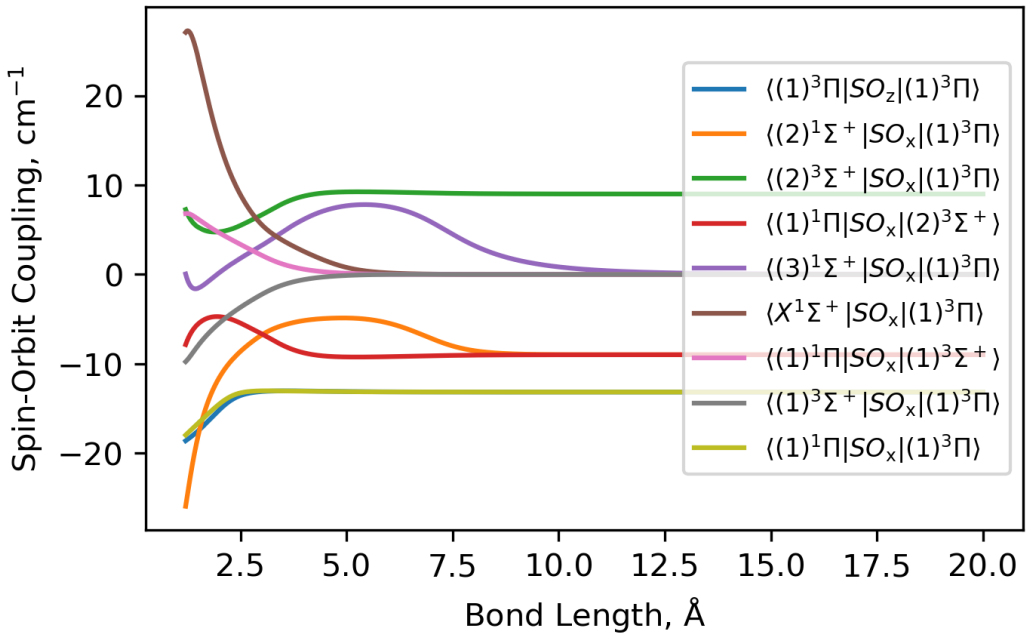

Figure 5.9: Illustration of my *ab initio* SOCs coupling the states of KH considered here. SO$_x$ denotes the cartesian x -component of the SO operator, coupling states of different symmetry, while SO$_z$ denotes the z-component which couples states of the same symmetry.

$^1\Sigma^+$ manifold, where the ground state appears ionic. The diabatic counterpart of this state extends toward the ionic limit in the $(3)^1\Sigma^+$ state. These avoided crossings are indicative of a charge-transfer process, leading to the progression from ionic to neutral character in $X^1\Sigma^+$, contributing to the wide extension of these potentials. Additionally, three non-adiabatic couplings (NACs) between the $[X^1\Sigma^+, (2)^1\Sigma^+, (3)^1\Sigma^+]$ system were computed at the CASSCF level of theory using the DDR procedure (see Section 2.2.2), as illustrated in the bottom panel of Figure 5.8.

Spin-Orbit: Figure 5.9 illustrates all non-zero computed spin-orbit couplings between the electronic states of interest. Only one diagonal SO_z term is present, and couples the $(1)^3\Pi$ state. It is clear that the SOCs appear to be simple functions of bond length, and correlate to different asymptotes corresponding to the spin-orbit interaction in the atomic fragments. The spin-orbit interactions are weak for KH, and so minimal splitting of the total angular momentum Ω states is expected.

Electronic Angular Momentum (EAM): Figure 5.10 illustrates the computed cartesian x-component of the (non-diagonal) EAM couplings between all electronic states of interest. Some coupling curves are seen to show strange ungulations in their topology, consistent with the adiabatic character of properties in the vicinity of avoided crossings. Again, the EAM couplings correlate to different asymptotes

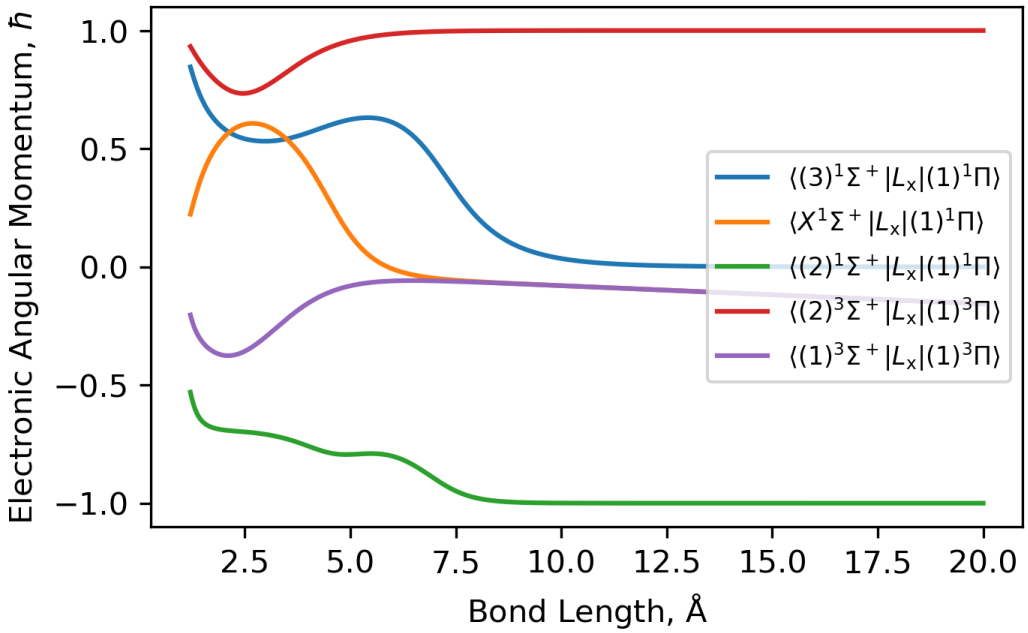

Figure 5.10: Illustration of my *ab initio* EAMCs coupling the states of KH considered here. L_x denotes the x-component of the electronic angular momentum operator, which couples states of different symmetry.

corresponding to the EAM of the atomic fragments.

Dipole Moment Couplings (DMCs): Figure 5.11 illustrates the computed DMCs between all electronic states of interest. The top panel shows the diagonal z-component of the dipole oeprator coupling states of the same symmetry (Λ and S), and the bottom panel plots the off-diagonal x-component of the DM operator coupling states of different symmetry. One striking feature is the $\langle(3)^1\Sigma^+|\mu_z|(3)^1\Sigma^+\rangle$ DMC, which becomes linear in bond length, consistent with the ionic nature of the $(3)^1\Sigma^+$ state in this region. Generally, the DMCs appear to be strong, which could be lent to the ionic nature of the KH electronic structure, where any non-zero asymptotes corresponds to strong atomic transitions in the potassium atom.

5.3.2 A Flexible Functional Form for NACs

From Eq.(3.14) in Chapter 3, the three computed NACs of KH in Figure 5.8 (dashed lines) were fitted (solid lines) using a linear combination of a Lorentzian and a Gaussian distribution of equal width γ, peak position r_0, and amplitude N, giving a pseudo-Voigt profile[240,241] via

$$f(r) = mL(r;r_0,\gamma,N) + (1-m)G(r;r_0,\gamma,N) + \sum_i L(r;r_{0,i},\gamma_i,N_i), \tag{5.33}$$

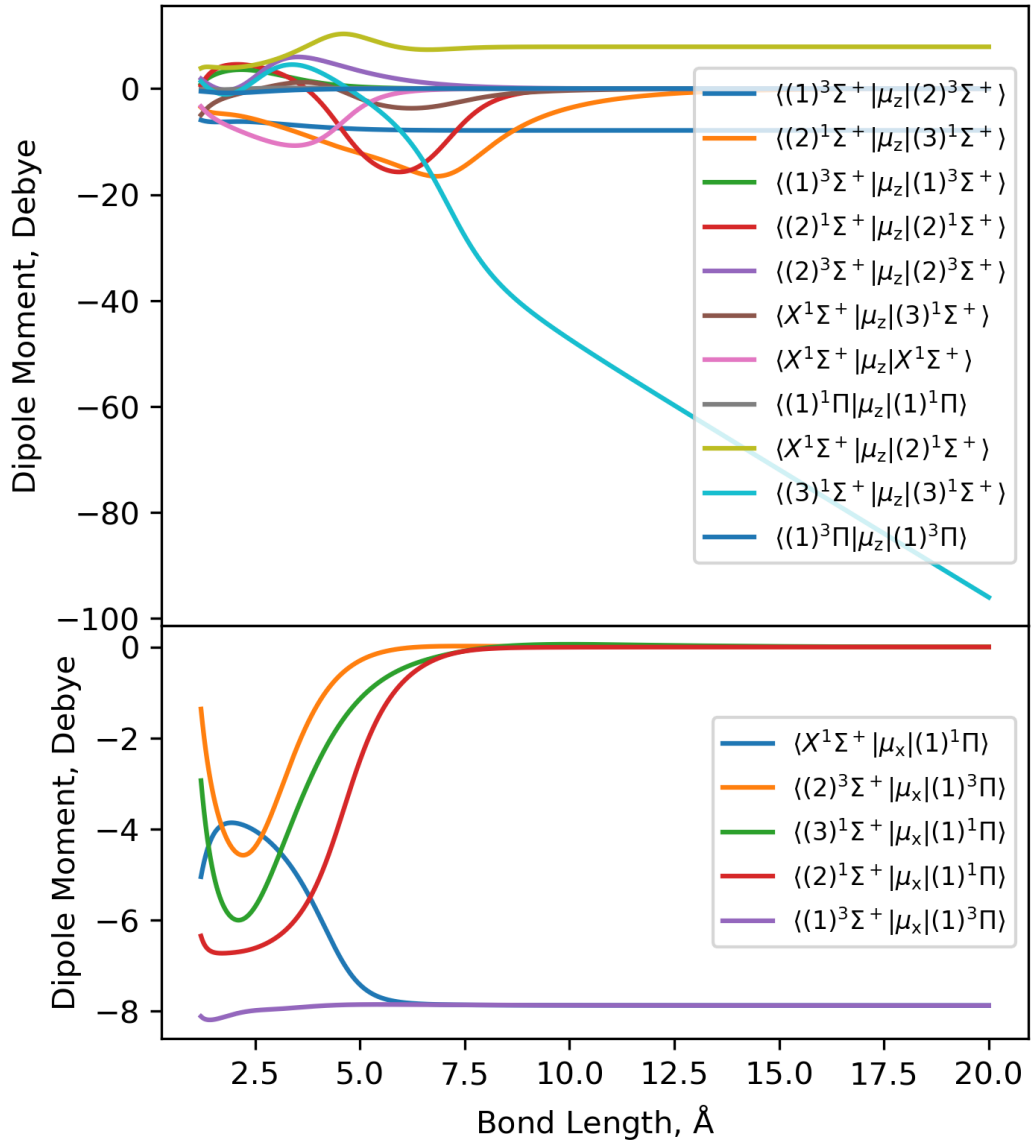

Figure 5.11: Illustration of my *ab initio* (T)DMCs coupling the states of KH considered here. μ_x denotes the cartesian x-component of the dipole operator, coupling states of different symmetry, while μ_z denotes the z-component which couples states of the same symmetry. It is clear that the $(3)^1\Sigma^+$ state is ionic due to its linear DMC with bond length (top pane, light blue).

where L is the Lorentzian function given by

$$L(r;r_0,\gamma,N) = \frac{N}{2}\frac{\gamma}{\gamma^2+(r-r_0)^2}, \tag{5.34}$$

and G is the Gaussian distribution given by

$$G(r;r_0,\gamma,N) = \frac{N}{2\gamma}\exp\left(-\ln(2)\left(\frac{r-r_0}{\gamma}\right)^2\right). \tag{5.35}$$

The fraction of Lorentzian and Gaussian character contributing to $f(r)$ of Eq.(5.33) is controlled by the constant parameter m. For $m=1$, $f(r)$ reduces to a pure Lorentzian, and for $m=0$ a pure Gaussian. The summation of Lorentzian functions in Eq.(5.33) are used to model additional (perturbative) sharp peaks which are typically seen to be of lower magnitude to the rest of the profile. The width parameter γ is then modeled to vary sigmoidally to introduce skewness into the final profile[240,241] via

$$\gamma(r;\gamma_0,a,r_0) = \frac{2\gamma_0}{(1+e^{a(r-r_0)})}, \tag{5.36}$$

where γ_0 is a reference width and a is a skewness parameter when equal to zero ensures $\gamma=\gamma_0$.

This functional form fits the *ab initio* NACs extremely well with a root mean square error for the A/B coupling to be RMS($X^1\Sigma^+,(2)^1\Sigma^+$) = 0.0008 Å^{-1}, RMS($X^1\Sigma^+,(3)^1\Sigma^+$) = 0.0001 Å^{-1}, and RMS($(2)^1\Sigma^+,(3)^1\Sigma^+$) = 0.0008 Å^{-1}. Similar fitting accuracy was also seen for the N_2 and CH cases in Chapter 3, indicating there may be physics in the skewed profile. It would be interesting to study the expected functional dependence of the NAC on the nuclear coordinate, r, where one could attempt to represent the electronic wavefunctions in a simple basis (such as GTO), and derive the corresponding NAC computed using the finite difference/density overlap schemes within the CASSCF theory level. My initial insights would be that the skewness is due to coupling to other electronic states, i.e. an effect not captured in a two-state approximation, and the reference width γ_0 should depend on the adiabatic separation (or DC) and the gradient of the diabatic potentials at the avoided crossing (as seen for the two-state YO and CH systems in Chapter 3).

Chapter 6

Conclusions

This thesis focuses on improving diatomic molecular line list production, essential for high-resolution spectroscopy, by enhancing the underlying spectroscopic models used in the variational nuclear motion code Duo. Specifically, it addresses the increasing importance of non-adiabatic effects, particularly in the UV region. The following sections summarise the major contributions and results from each chapter of this thesis, and conclude on potential future works.

6.1 Summary

Chapter 2 presents a reformulation of existing diabatisation theory for systematic benchmarking of non-adiabatic effects within the Duo rovibronic code. While the underlying physics of non-adiabatic (radial) electron-nuclear coupling and its inclusion in nuclear motion are well-established[123,49,48,41,475], this thesis provides a novel, consolidated framework within a rovibronic context, establishing the theoretical foundation for subsequent analysis of the adiabatic to diabatic transformation – the AtDT. Specifically, this work integrates: (1) the Hermitian formulation of the non-adiabatic coupling terms within the vibronic Schrödinger equation; (2) a complete description of the non-adiabatic nuclear kinetic energy Hamiltonian using only the first derivative term (NAC); (3) an examination of the condition for a strict AtDT, comparing to other similar conditions to highlight solution difficulties; (4) solutions for the AtDT in two-, three-, and N-state cases, with discussions on the theory and practical applications for constructing contracted vibronic basis sets for nuclear motion; and (5) quantitative and qualitative comparisons of different AtDT solution methods.

The primary result of Chapter 2 is the development of a novel regularisation (and diabatisation) method, hybrid-asymptotic-property-based diabatisation (HyAP), for NACs. To construct spectroscopic models with advantageous con-

vergence properties, accurate descriptions of relevant spectroscopy, and simplified property curves for analytical and numerical treatment, this method leverages asymptotic conditions on the AtDT and NACs inspired by two-state property based diabatisation approaches. Both the mathematical framework and algorithmic implementation of the HyAP method, with detailed discussions on its motivation, are presented and benchmarked.

Chapter 3 implements the diabatisation methodologies developed in Chapter 2 within Duo for real molecular systems. A key achievement of this thesis is the establishment of Duo as a unique and powerful tool for benchmarking non-adiabatic effects in rovibronic calculations. By demonstrating, for the first time, numerical rovibronic equivalence between adiabatic and diabatic representations across both two-state and N-state systems – defined as the exact reproduction of rovibronic energies and wavefunctions – this work validates Duo as a robust platform for quantitatively assessing the impact of different non-adiabatic coupling terms (equivalently, DDR terms). This equivalence is demonstrated across a range of systems, including two-state YO and CH, the three-state N_2, the four-state CH, and an artificial 10-state model. Through this, a comprehensive benchmarking of various NAC terms, including off-diagonal and diagonal (DBOCs) contributions, as well as diabatic couplings (DCs), is conducted, revealing their critical role in achieving numerical consistency. Our findings emphasise the impact of all DDR terms, including the diagonal DDR couplings, often omitted, on spectral accuracy and highlight the limitations of two-state approximations, underscoring the necessity of rigorous validation when truncating adiabatic states for spectroscopic modelling. This novel application of Duo represents a significant contribution, offering a reliable method for evaluating non-adiabatic effects in molecular systems.

Despite the exactness of the computed AtDT through evolution methods, issues such as asymptotic misbehavior, topological non-smoothness of diabatic properties, and non-coincidence of imposed ideal AtDT boundary conditions were observed, stemming from improper NACs input to the solver. These inconsistencies, often obscured in the adiabatic representation but evident upon diabatisation, can arise from factors like differing theory levels in *ab initio* calculations, convergence errors, post-processing adjustments, or truncation of the Born-Oppenheimer state manifold. My pragmatic goal was to create a smooth diabatic representation suitable for controlling bound rovibronic molecular spectroscopy through efficient contracted rovibronic bases. To achieve this, I developed (in Chapter 2) the HyAP regularisation approach that optimises switching functions connecting AtDT solutions evolving from different boundary conditions. This connection yields a regularising

correction to the NACs, ensuring an AtDT that evolves between desired boundary conditions while establishing a smooth diabatic representation. The HyAP method minimises artificiality in the regularised NACs by leveraging underlying electronic structure data to guide the correction, combining the accuracy of direct diabatisation with the practicality of property-based approaches. HyAP is applied to N_2, CH, and a 10-state model, and was shown to successfully produce smooth diabatic representations with sensible asymptotic behavior while subsequently maintaining exact equivalence to the adiabatic framework. The HyAP method's validity was demonstrated by comparing rovibronic energy levels of the N_2 system with and without NAC regularisation. The resulting energy level differences were consistent with expected *ab initio* errors. Furthermore, the regularising corrections were significantly smaller than the substantial NAC terms for both N_2 and CH, confirming the method's robustness and reliability. In essence, the HyAP method provides a robust framework for constructing diabatic spectroscopic models for the modeling of diatomic rovibronic spectra, effectively mitigating challenges associated with NAC inconsistencies and ensuring the generation of physically meaningful and computationally efficient diabatic representations.

Beyond demonstrating equivalency, our work highlights system-dependent advantages between adiabatic or diabatic representations, emphasising the importance of considering NACs in model selection. The methodologies and benchmarks established in Chapter 3 lay a foundation for extending these concepts to polyatomic molecules, where full derivative coupling removal is not always feasible. Ultimately, this research reinforces the necessity of meticulous consideration of non-adiabatic coupling terms and basis truncations in high-resolution molecular spectroscopy, positioning Duo as a reliable tool for future diabatisation and non-adiabatic effect investigations.

Chapter 4 describes the development of a semi-empirical line list for the $^{32}S^{16}O$ radical. The project began with the calculation of an extensive *ab initio* spectroscopic model[13] for the 13 lowest-energy singlet and triplet electronic states of SO ($X\,^3\Sigma^-$, $a\,^1\Delta$, $b\,^1\Sigma^+$, $c\,^1\Sigma^-$, $A'\,^3\Delta$, $A''\,^3\Sigma^+$, $A\,^3\Pi$, $B\,^3\Sigma^-$, $C\,^3\Pi$, $d\,^1\Pi$, $e\,^1\Pi$, $C'\,^3\Pi$, $(3)\,^1\Pi$). These calculations included potential energy curves (PECs), spin-orbit curves (SOCs), electronic angular momentum curves (EAMCs), and electric (transition) dipole moment curves ((T)DMCs), all performed at the MRCI level of theory using aug-cc-pV5Z basis sets. The computed *ab initio* curves are adiabatic, as they were obtained under the Born-Oppenheimer approximation[2]. Consequently, states with the same symmetry, such as $e\,^1\Pi$, $(3)\,^1\Pi$ and $C\,^3\Pi$, $C'\,^3\Pi$, exhibit avoided crossings due to non-adiabatic interactions. These effects, which play a crucial role

in the computed spectroscopy, are discussed in Chapters 2 and 3. To address these non-adiabatic interactions, I derived a set of NAC terms for these two-state pairs using a property-based diabatisation procedure. Notably, this study marks the first time during my PhD that I explored the use of both diabatic and adiabatic curves in rovibronic calculations – an investigation that initiated my journey into the study of diatomic non-adiabatic interactions.

Following the development of an *ab initio* spectroscopic model for $^{32}S^{16}O$, Chapter 4 presents the most comprehensive compilation of experimental transition data and self-consistent empirical rovibrational energy levels for $^{32}S^{16}O$ to date. These energy levels were derived using the MARVEL (Measured-Active-Rotational-Vibrational-Energy-Levels) spectroscopic network algorithm[156,373]. Subsequently, I refined our initial *ab initio* spectroscopic model[13] to compute rovibronic energies that best reproduce these empirically determined energy levels, ultimately producing an accurate semi-empirical line list, SOLIS, for $^{32}S^{16}O$ as part of the ExoMol project[53,54].

The SOLIS line list supplements existing spectroscopic line lists for SO, which are currently limited in spectroscopic coverage. For instance, the CDMS[346] and NIST[347] databases provide only microwave spectral data, while HITRAN[348] includes transitions between the $X\,^3\Sigma^-$, $a\,^1\Delta$, and $b\,^1\Sigma^+$ electronic states but only for relatively low vibrational excitations. A detailed comparison of the SOLIS line list with existing spectral data is provided in Section 4.14.5.

As discussed in Chapter 4, the SOLIS line list serves a broad range of applications, extending from astrophysics to environmental chemistry. In atmospheric research, it provides valuable data for examining sulfur monoxide and its involvement in processes like acid rain formation and pollution. In the field of astrophysics, SOLIS supports the exploration of SO across various environments, including interstellar clouds, planetary atmospheres, and supernovae. Particularly, the $^{32}S^{16}O$ line list can be used to further our understanding of planetary evolution, atmospheric chemistry, and star-forming regions. Moreover, SOLIS proves useful in studying the photochemical behaviour of SO, its potential as a tracer of shock regions, and its observability using instruments such as the James Webb Space Telescope (JWST). Notably, the line list has contributed to the detection of sulfur dioxide (SO_2) in the atmosphere of the exoplanet WASP-39b, marking a major milestone as the first clear observation of UV-driven sulfur photochemistry in a hot exoplanet atmosphere[148]. Additionally, the mid-infrared fundamental band feature of SO was identified in WASP-39b[147], and it has been recognised as a prominent molecular species in the oxygen/silicon/sulfur neon-burning zones within supernova ejecta[1].

Chapter 5 presents additional research undertaken during my doctoral studies, complementing the primary projects discussed in previous chapters. These efforts include investigations into phase-shift theory for UV spectral line pressure broadening, the development of an exact Ω-representation for rovibronic calculations, and a comprehensive *ab initio* study of the KH alkali hydride diatomic.

To assess the reliability of phase-shift theory, NO and OH were studied with Ar and N_2 as perturbers, where their interaction potentials were computed using coupled cluster methods with MOLPRO. While the theory systematically underestimated linewidth and shift values, it remained suitable for order-of-magnitude estimates. Refining the interaction potentials within the framework proved insufficient, highlighting the need for methodological improvements beyond traditional phase-shift theory.

Chapter 5 also details a significant theoretical advancement, which was the implementation of a 'true' Ω-representation for rovibronic calculations. By diagonalising the spin-orbit and electronic Hamiltonian, this approach eliminated the spin-orbit couplings but introduced strong non-adiabatic couplings into the nuclear kinetic energy and complex bond-length-dependent properties. My study demonstrated that neglecting spin-orbit-induced NAC terms significantly worsens rovibronic energy predictions more so than simply omitting spin-orbit couplings in the conventional $\Lambda - S$ representation for the studied toy model. Maintaining a self-consistent Ω-representation model is particularly challenging due to the introduced complex bond-length dependence of molecular properties like spin, which must align with the associated NACs and potentials.

Additionally, a detailed *ab initio* study of the KH alkali hydride molecule was conducted to (1) address the data gap in the ExoMol database by producing a rovibronic line list, and (2) explore the non-adiabatic charge-transfer dynamics in its electronic ground state, particularly the ionic-to-neutral transition. High-level *ab initio* calculations, including potential energy curves, spin-orbit couplings, transition dipole moments, and NACs for the lowest seven singlet and triplet states, were performed using ic-MRCI theory with aug-cc-pVQZ-X2C basis sets in MOLPRO. This spectroscopic model provides a strong foundation for future refinements and the development of a KH line list, which will support its potential astrophysical detection and enhance our understanding of potassium-containing molecules in astrophysical environments.

6.2 Future Work

With the successful implementation of non-adiabatic effects and a diabatic module within the Duo diatomic rovibronic code, extension to polyatomic systems, which are expected to be important[476–478], would be a natural avenue for future research. Polyatomic non-adiabatic interactions are much more complex due to the increased number of nuclear degrees of freedom, where cross derivative terms prevent all non-adiabatic couplings from being removed exactly – yielding quasi-diabatic representations[48,40,89,479]. Specifically, the longitudinal NAC term is removable, whereas the transverse NAC term is non-removable in general, but can be minimised[479]. Diatomic systems are simple in the sense that the AtDT, with definition of the NACs and a boundary condition, is unique. Polyatomics, on the other hand, have infinitely many integration paths to choose in solution of the AtDT, which for evolution methods typically gives rise to path ordered integrals[46], meaning the AtDT is not unique. The next problem is finding a suitable platform to test rovibronic equivalence in the adiabatic and quasi-diabatic representations. My colleague Armando Perri, and his collaborator Alexander Mitrushchenkov, are currently exploring diabatic and adiabatic modules in the EVEREST[480] triatomic rovibronic program – an ideal platform for the testing of triatomic adiabatic and diabatic rovibronic equivalence in the near future. I would be interested in exploring new diabatisation methodolgies in the construction of physical, sensible, and rovibronically advantageous diabatic representations (e.g. in the construction of contracted basis sets) for polyatomic systems – similar to HyAP.

Chapter 4 focused on refining a spectroscopic model for SO in the IR/Vis region by fitting to the $X\,^3\Sigma^-$, $a\,^1\Delta$, $b\,^1\Sigma^+$, and $A\,^3\Pi$ energy levels only. While this approach yielded accurate rovibronic calculations for these states, the SOLIS line list is largely incomplete, particularly in the UV region. This is because of the exclusion of the $C\,^3\Pi$, $B\,^3\Sigma^-$, $d\,^1\Pi$, and $e\,^1\Pi$ states, which introduced complexities in maintaining an accurate spectroscopic model in this region, such as strong couplings and resonances, particularly between the $B\,^3\Sigma^-$ and $C\,^3\Pi$ states. These states also exhibited complex adiabatic topology due to avoided crossing with other electronic states. Future work should prioritise extending the SO model to incorporate these UV states. The application of the developed diabatic methodologies in this thesis to fit the UV line list would significantly enhance the model's accuracy and predictive power in this region, which is crucial for astrophysical applications. Furthermore, the inclusion of UV states, in particular diabatically dissociative $C'^3\Pi$ and $(3)^1\Pi$ states, would enable the computation of photodissociation cross sections,

a critical data source for understanding the photochemical processes in astrophysical environments[235,481–483]. The UV spectral region of sulfur bearing molecules is of particular importance in astrophysics, where photodissociation plays a key role in the chemical evolution of interstellar clouds[484–486] and more recently in planetary atmospheres with the first unambiguous detection of (UV) photochemically driven sulfur chemistry of sulfur bearing molecules in an exoplanetary atmosphere[148,147]. Therefore, a comprehensive model describing both the IR/Vis and UV regions would provide a more complete and accurate description of the SO spectroscopy, offering valuable insights for astrophysical studies.

Section 5.2 of Chapter 5 details the theory and implementation of a true Ω-representation within the Duo rovibronic code. This work is currently unpublished due to ongoing challenges in demonstrating exact equivalence between intensities computed in the Ω- and $\Lambda - S$-representations. While rovibronic energies and radial reduced densities are precisely reproduced, and external transformations confirm the accuracy of DMCs in the Ω-representation, I believe convergence issues are the primary source of discrepancy. The Ω-representation demands an exceptionally large number of grid points ($\sim 2000 - 3000$) and contracted vibronic basis functions (~ 1000). Furthermore, numerical noise in the integration of near-discontinuous property curves may lead to non-exponential decaying vibronic transition moments (premature flattening), similar to observations in the $X\,^3\Sigma^-$ state of SO in Chapter 4. I am actively debugging these issues, aiming to establish exact rovibronic equivalence in energies, wavefunctions, and intensities between the Ω- and $\Lambda - S$-representations. This is particularly important as the Ω-representation is often used in the single-state approximation within the widely used LEVEL program[404] for computing forbidden band intensities[340,432,433], and I wish to quantify the errors introduced by this commonly employed approximation.

For future work, extending the Ω-representation to diagonalise all quantities independent of the rotational quantum J, such as spin-orbit couplings (SOCs), electronic angular momentum couplings, spin angular momentum, e.t.c., would be interesting. This could potentially allow for a more simplified model, where non-adiabatic couplings and transformed PECs would completely define the vibronic spectroscopy. However, as I now have experience with the Ω-representation, this new representation is not guaranteed to be advantageous or simple. Regardless, it would be a novel and interesting project for a future work.

Section 5.3 of Chapter 5 details the calculation of an *ab initio* spectroscopic model for the potassium hydride molecule. An important future work would be to collect and critically evaluate experimental transition frequency data with the

MARVEL algorithm to produce a set of empirically determined energy levels and uncertainties. From this, the *ab initio* KH spectroscopic model can be fitted to reproduce the MARVEL energies, similarly to the SO line list generation in Chapter 4. This would allow for the accurate prediction of the KH spectrum, where a full KH line list may be crucial for the first astrophysical detection of KH.

Finally, the diabatisation methodologies, in determination of an AtDT, presented throughout this thesis are currently implemented in an external JULIA program, DIABATOM-PRO. The results from DIABATOM-PRO are then fed into the Duo code to compute adiabatic and diabatic rovibronic solutions. However, Duo can currently model adiabatic PECs by definition of a set of diabats and DCs, for the N-state case, or two PECs and a NAC for a two-state system. Current efforts to try and reformulate the AtDT condition of Eq.(2.49) in terms of a linear algebra problem, whereby coefficients of some basis are found to solve the differential equation would allow a potentially numerically efficient method to perform N-state diabatisations on-the-fly within the Duo program. So far, I have identified that such a DVR method exists for solving this first order differential matrix equation, where efficiency considerations are currently being tested.

Appendix A

Technical Programmatic and Theoretical Details on N-state Diabatisation

A.1 Matrix Exponentiation

A.1.1 The 3-State Problem

The problem of matrix exponentiation, required for the exponential line-integral propagator method of solving Eq. (2.49), is now addressed for the specific case of a 3-state system. The AtDT for a 3-state system resembles a 3D rotation matrix, and has some useful properties I wish to exploit.

For three-dimensional systems, Euler angles are often less convenient due to their non-unique parameterisation and their susceptibility to Gimbal lock (where a degree of freedom is lost when two of the three rotation axes align). Instead, an angle-axis representation can provide a more straightforward solution, which can be derived using the Rodrigues rotation formula[487,488]. This formula offers a closed-form solution that is a quadratic polynomial in the generator matrix $\boldsymbol{\beta}$ (see Eq.(2.51) for a 2-state example)

$$\mathbf{U} = e^{\boldsymbol{\beta}} = \boldsymbol{I} + \frac{\sin(\alpha)}{\alpha}\boldsymbol{\beta} + \frac{1-\cos(\alpha)}{\alpha^2}\boldsymbol{\beta}^2, \tag{A.1}$$

where the generator $\boldsymbol{\beta} \in \mathfrak{so}(N)$ is a 3×3 skew-symmetric matrix and is discussed in Appendix B, α is the global angle of the rotation and is computed from the Frobenius norm of the upper triangle elements of $\boldsymbol{\beta}$ (or equivalently from its eigenvalue)

via

$$\alpha(r) = \sqrt{\sum_{i<j}^{3} \boldsymbol{\beta}_{ij}^2(r)}. \tag{A.2}$$

Eq.(A.1) provides an analytical way to find the exponential mapping of $\boldsymbol{\beta}$ which removes numerical error in its computation and reduces computational time during the evolution of $\mathbf{U}$. Rodriguez formular is a generalisation of Eulers equation for 2×2 matrix exponentials as the simple rotation matrix in Eq.(2.54).

Rodrigues formular also provides a convenient way to find the generator from the non-exponentiated matrix $\mathbf{U}$. I present the relations for completeness here:

$$\boldsymbol{\beta} = \frac{\alpha}{2\sin(\alpha)}(\mathbf{U} - \mathbf{U}^\dagger), \tag{A.3}$$

where the global angle α can be computed from the trace of $\mathbf{U}$ as follows

$$Tr(\mathbf{U}) = 1 + 2\cos(\alpha) \;\rightarrow\; \alpha = \arccos\left(\frac{Tr(\mathbf{U}) - 1}{2}\right). \tag{A.4}$$

A.1.2 The N-State Problem

The treatment is now generalised to systems of dimension $N > 3$, where a closed form of the matrix exponential is not necessarily available. Numerical methods are then used to compute the exponential mapping of the skew-symmetric matrices $\boldsymbol{\beta}$ in an efficient and generalisable manner. One powerful approach uses the spectral decomposition, which generalises Euler's formula for rotations and extends the Rodrigues formula (Eq.(A.1)) to higher dimensions. I will summarise the spectral decomposition method here since it yields intuitive results, for more details please see the book by Higham[489].

To compute the matrix exponential of a skew-symmetric matrix $\boldsymbol{\beta}$, consider its spectral decomposition

$$\boldsymbol{\beta} = \boldsymbol{T}\boldsymbol{\Lambda}\boldsymbol{T}^\dagger, \tag{A.5}$$

where $\mathbf{T}$ is a unitary and $\boldsymbol{\Lambda}$ is a diagonal matrix with elements being either zero (for odd dimensional matrices) or imaginary eigenvalue pairs $\pm i\lambda_i$. Exponentiation is then simple since the exponential of $\boldsymbol{\Lambda}$ remains diagonal and simply exponentiates the diagonal elements. However, while this decomposition yields a simple method to computing the exponential, it does not yield an obvious geometric interpretation.

Instead, I use the Schur decomposition[489], which gives a block-diagonal form

when considering the spectrum of skew-symmetric matrices

$$\boldsymbol{\beta} = \boldsymbol{T}\boldsymbol{Q}\boldsymbol{T}^{\dagger}, \tag{A.6}$$

where **T** is again unitary and **Q** is block diagonal given by

$$\boldsymbol{Q} = \begin{pmatrix} 0 & \tilde{\lambda}_1 & 0 & 0 & \cdots \\ -\tilde{\lambda}_1 & 0 & 0 & 0 & \cdots \\ 0 & 0 & 0 & \tilde{\lambda}_2 & \cdots \\ 0 & 0 & -\tilde{\lambda}_2 & 0 & \cdots \\ \vdots & \vdots & \vdots & \vdots & \ddots \end{pmatrix}, \tag{A.7}$$

where $\tilde{\lambda}_i$ is the i^{th} unique eigenvalue multiplied by the imaginary number. Then, the exponential of $\boldsymbol{\beta}$ is related to the exponential of $\boldsymbol{Q}$ by

$$e^{\boldsymbol{\beta}} = \boldsymbol{T}e^{\boldsymbol{Q}}\boldsymbol{T}^{\dagger} = \boldsymbol{T}\begin{pmatrix} \cos\tilde{\lambda}_1 & \sin\tilde{\lambda}_1 & 0 & 0 & \cdots \\ -\sin\tilde{\lambda}_1 & \cos\tilde{\lambda}_1 & 0 & 0 & \cdots \\ 0 & 0 & \cos\tilde{\lambda}_2 & \sin\tilde{\lambda}_2 & \cdots \\ 0 & 0 & -\sin\tilde{\lambda}_2 & \cos\tilde{\lambda}_2 & \cdots \\ \vdots & \vdots & \vdots & \vdots & \ddots \end{pmatrix}\boldsymbol{T}^{\dagger} \tag{A.8}$$

which can be derived by analysis of the odd and even powers of the Taylor expansion of $\exp(\boldsymbol{Q})$. The exponential $\exp(\boldsymbol{Q})$ matrix then has the geometric interpretation of representing a set of independent plane rotations by a rotation given by the eigenvalues of $\boldsymbol{\beta}$.

A.2 A (Nearly Monte-Carlo) Method of determining the Nuclear Geometry Grid

This section details a physics-driven approach for selecting a suitable nuclear geometry grid for the AtDT evolution. The impact of grid choice on the AtDT accuracy will now be discussed, where the following aspects are found to be important:

- **Density in Strong Coupling Regions**: A fine grid spacing of $\sim 10^{-5}$ Å is required where non-adiabatic interactions are strong. For N_2 (Section 3.6.1), this ensures residual kinetic energy matrix norms below 10^{-8} cm^{-1}, yielding comparable adiabatic and diabatic rovibronic energies. However, this metric is system-dependent and should be tested (e.g., with Duo, Section 2.3.1).

- **Trajectory Considerations**: Sensible evolution into strongly coupled regions can impact the resulting diabatisation. NACs are modeled with functional forms vanishing at $|r| \to \infty$, requiring a large configuration space ($r \in [-1000, 1000]$ Å). While negative bond lengths lack physical meaning, they facilitate a smooth transition into the physical region, preventing discontinuities in short-bond regions. Although these regions are not spectroscopically important, they affect how the AtDT evolution unfolds into the spectroscopically relevant regions. A cleanly initialized evolution is desirable, akin to two-state system treatments, where the mixing angle is determined by integrating the NAC function from $-\infty$. This highlights the inherent approximation in choosing NAC functional forms, though this is not an issue for most practical applications.

- **Grid Efficiency**: A uniformly dense grid across a wide range is inefficient. To enable on-the-fly diabatisation and interactive spectroscopic modelling, a non-uniform grid is required – sparse in outer regions and denser where NACs are strongest.

- **Transition Profile**: The rate at which the grid transitions from sparse to dense impacts AtDT accuracy. Optimising both accuracy and efficiency (minimising points) is non-trivial. While an adaptive grid was tested to dynamically optimise solution accuracy, it proved inefficient for my use cases.

With the above points in mind, I now turn to inverse transform sampling[490] which is a Monte Carlo method (MCM)[491] for generating random samples from any probability distribution function (PDF) given its cumulative distribution function (CDF). The PDF is defined as the probability density of the continuous variable x given by $\rho(x)$, and the CDF is then defined as the integral of the PDF via

$$C(x) = \int_{-\infty}^{x} \rho(x')dx'. \tag{A.9}$$

MCM inverse transform sampling works by generating a random number $Y \in [0,1]$, then inverting the CDF to map Y to the independent variable of the PDF, x, i.e.

$$x = C^{-1}(Y). \tag{A.10}$$

Figure A.1 visualises the MCM inverse transform sampling method by chosing the PDF, (x) to be a Gaussian distribution. This then allows the generation of a grid sample, X, that is distributed according to the PDF of the studied system, and is ideal

for efficiently generating non-uniformly spaced geometry grids for the evolution of the AtDT in Eq.(2.67).

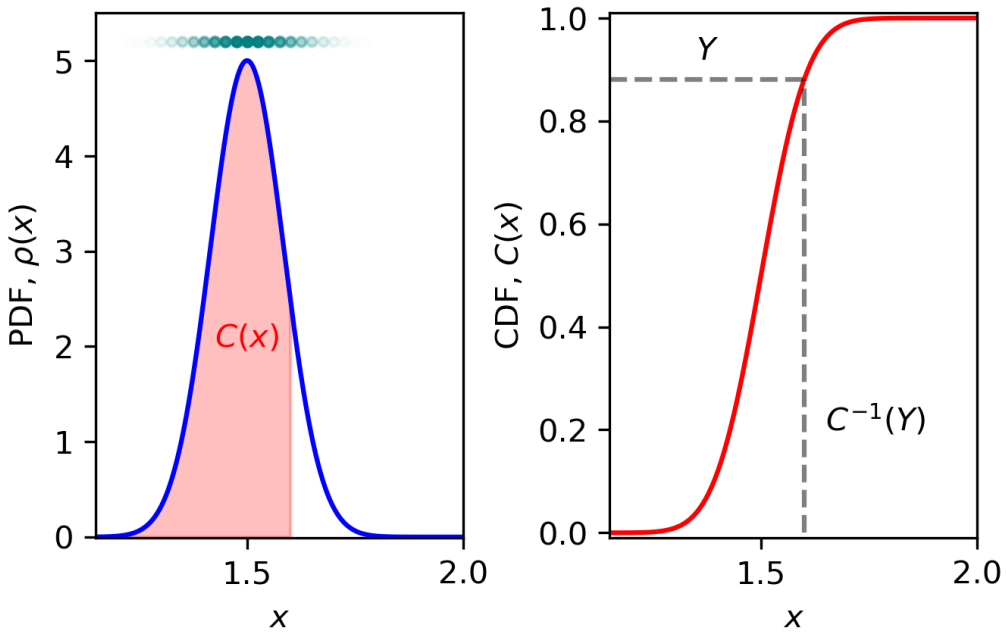

Figure A.1: Illustration of inverse transform sampling, where the left panel plots the PDF $\rho(x)$ and the right panel the CDF $C(x)$ computed via Eq.(A.9). A value Y is chosen to sample the CDF and is inverted to yield the corresponding independent variable $x = C^{-1}(Y)$. Repeated inverse transform sampling of the CDF will then yield a set of x values which are distributed according to the PDF, and are visualised by the teal dots above the PDF. The denser regions corresponds to a high frequency of points being sampled where the probability density is highest, and reduces for regions further from the PDF peak.

To use this MCM inverse transform sampling method, one requires computation of the CDF, which needs definition of a PDF. In the case of generating a nuclear geometry grid to perform the AtDT evolution Eq.(2.67) on, the NAC matrix $\mathbf{W}^{(1)}$ contains important information about the interaction strength as a function of the bond length – defining the propagator. Multiple options are available to construct a PDF from $\mathbf{W}^{(1)}$, two examples being the eigenvalues of $\mathbf{W}^{(1)}$ or the Frobenius norm of $\mathbf{W}^{(1)}$ via Eq.(2.83). The eigenvalues will contain information about the instantaneous axis of diabatisation and the angle of rotation, where for 3-state systems the Frobenius norm is equivalent to the positive eigenvalue of $\mathbf{W}^{(1)}$. However, for $N-$state systems, multiple unique eigenvalues are realised, making definition of a single PDF ambiguous. Instead, the Frobenius norm of $\mathbf{W}^{(1)}$ is proposed to yield a metric for the NAC strength of a given system. This norm can then be considered a PDF since NACs are assumed to be bounded functions of the nuclear geometry (see

discussion in Section 2.7), and the norm is then a positive bounded function. The following form of the PDF is then used

$$\rho(r) = ||\mathbf{W}^{(1)}||_{\Delta}, \tag{A.11}$$

where the operator $||\cdot||_{\Delta}$ is the Frobenius norm of the upper triangle given by Eq.(2.83), r is the nuclear geometery (bond length), and its integration then yields the following CDF

$$C(r) = \int_{-\infty}^{r} ||\mathbf{W}^{(1)}||_{\Delta}(r')dr', \tag{A.12}$$

which can be normalised to the interval $[0,1]$. From the above CDF, inverse transform sampling can be employed to yield a set of grid points r. Instead of randomly sampling the above CDF as in Monte-Carlo methods, I instead sample with a grid of n equally spaced points between 0 and 1, and invert them through Eq.(A.10). Now the only meta-parameter that requires definition is simply the number of points, where the non-linearity of the grid structure is constructed through the proposed sampling scheme.

Figure A.2 illustrates a set of three model NACs corresponding to the NACs coupling the 3-state N_2 $^1\Sigma^+$ manifold discussed in Section 3.6.1 and the associated PDF and CDF computed via Eqns.(A.11,A.12). The PDF is a double peaked distribution corresponding to the strong NACs $W_{12}^{(1)}$ and $W_{23}^{(1)}$, where the computed CDF has a structure which reflects this. As a consequence, it should be expected that the nuclear geometries computed via the inverse transform sampling of this CDF to cluster around the peaks of the bimodal distribution. Figure A.3 visualises the resulting nuclear geometry grid where indeed the grid becomes very dense at the region of strong NAC with a separation of $\sim 10^{-6}$ Å, and becomes sparse for extended geometries – the ideal behaviour of a non-linear geometry grid for evolution of the AtDT. An AtDT is then computed via a forward evolution using the three N_2 NACs in Figure A.2 via Eq.(2.67). The corresponding residual diabatised kinetic energy matrix is computed. Figure A.4 plots the convergence of the maximal residual kinetic energy Frobenius norm with the number of points used to construct the nuclear configuration grid via inverse transform sampling. It is observed that at $\sim 5 \times 10^4$ points the accuracy of the evolution solution has converged to a maximal norm of $\sim 5 \times 10^{-12}$ cm^{-1}. It is interesting to see that only ~ 7500 points is required to yield a maximal error of 10^{-8} cm^{-1} whereas my manual efforts required 53000 points. Thus, the inverse transform sampling method is an efficient and physics driven procedure to compute a non-linear grid to be used in the com-

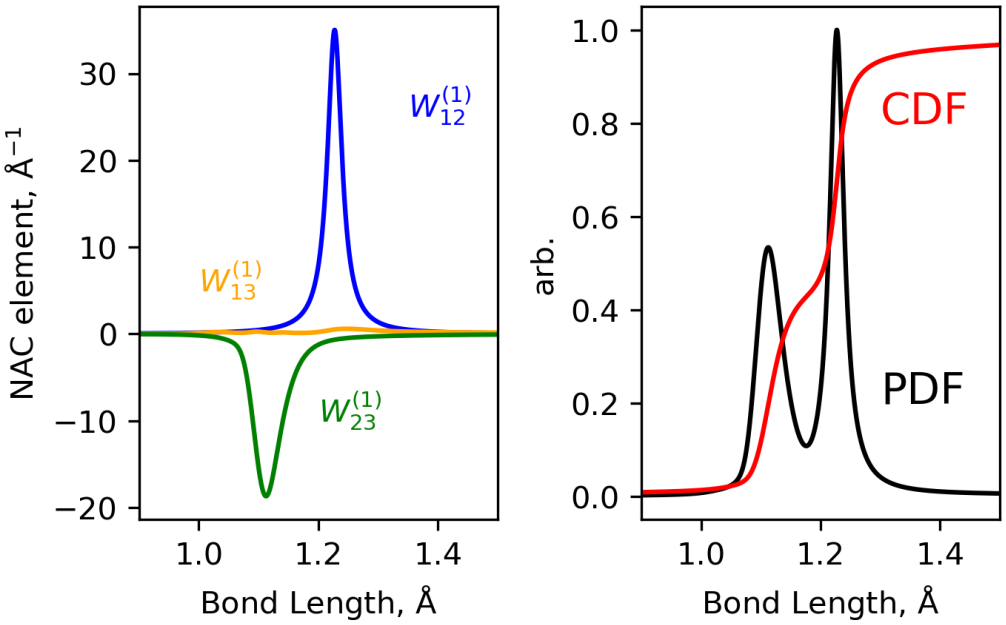

Figure A.2: Illustration of an example 3-state system NAC elements (taken from the N_2 system discussed in Section 3.6.1), where the corresponding Frobenius norm of this NAC matrix is computed via Eq.(2.83) and is plotted on the right panel in black. The corresponding CDF is computed via integration of the PDF via Eq.(A.12) and is plotted in red (right panel).

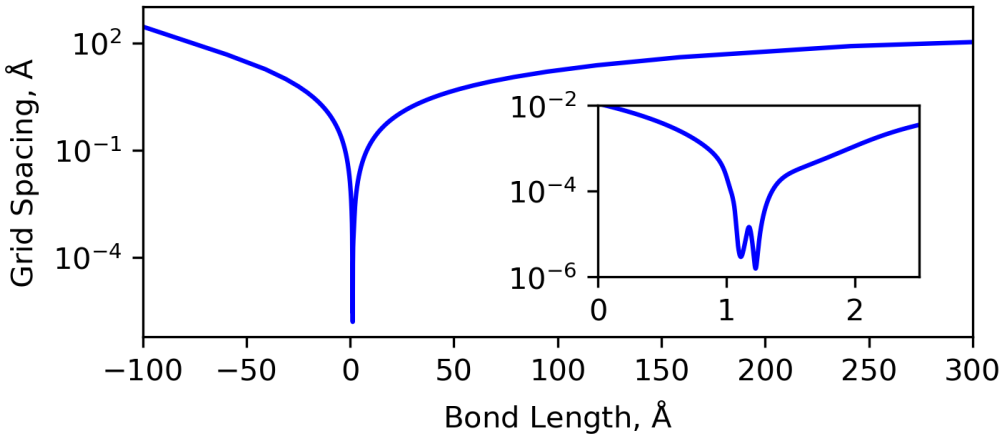

Figure A.3: Illustration of the computed nuclear geometry grid via the inverse transform sampling method applied to the CDF in Figure A.2, where grid spacing is plotted as a function of the grid position. In the region of strong NAC interaction the grid is dense, and exhibits structure reflecting the strength of $\mathbf{W}^{(1)}$.

putation of the AtDT via the evolution method, which requires no optimisation and only the definition of the number of points.

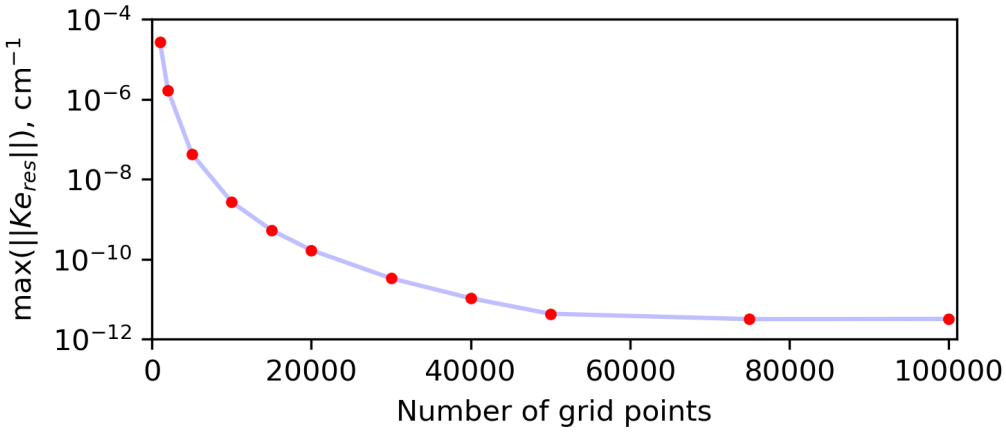

Figure A.4: Convergence of the maximal error as a function of the number of points used to generate a nuclear geometry grid via the inverse transform sampling method. The error is identified as the maximal Frobenius norm of the residual kinetic enerrgy matrix after diabatisation (see Eqns.(2.72,2.73)) of the 3-state N_2 system in Figure A.2.

Appendix B

Generator Representation of The AtDT

This appendix summarises the mathematical framework behind what this thesis refers to as the 'generator representation of the AtDT' and why this approach is desirable. Specifically, this thesis is concerned with Lie groups in the context of rotation matrices (the AtDT) and the corresponding Lie algebras, which serve as their generators. A Lie group is a smooth, differentiable N-dimensional manifold. Although the elements of a Lie group do not necessarily form a vector space, its associated Lie algebra defines a tangent space that is a (flat) vector space of dimension $N(N-1)/2$. As a result, the Lie algebra is generally simpler to analyse than the corresponding Lie group (rotation matrices) and captures most of the group's properties, thus motivating the use of this representation in my analysis.

I do not claim that the following sections are new mathematical developments, I try to briefly detail aspects relating to Lie theory in the context of rotations and NACs. For more details please refer to the excellent books of Stillwell[492], Rossman[493], and Gilmore[494].

B.1 The Special-Orthogonal Group

The AtDT can be considered a (unitary) rotation matrix which rotates the adiabatic frame to the diabatic frame, an object which belongs to the special orthogonal group of dimension N, $SO(N)$.[1] Rotation matrices are orthogonal matrices since they satisfy the following relation

$$\mathbf{R}^T\mathbf{R} = \mathbf{I}, \tag{B.1}$$

[1]Here I continue the derivations with the set of orthogonal matrices, but in general this thesis typically refers to the AtDT as being unitary. This does not change the conclusions, however, and should be noted.

which has the property of preserving vector norms upon action on a vector space $\mathbb{R}^N$. For example, consider the length, l, of a vector $\vec{v} \in \mathbb{R}^N$ in Euclidean-N space

$$\vec{v}^T \cdot \vec{v} = l^2, \tag{B.2}$$

rotating this vector by action of $\mathbf{R}$ yields the following scalar product

$$\vec{v}^T \, \mathbf{R}^T \cdot \, \mathbf{R} \, \vec{v} = \vec{v}^T \cdot \mathbf{I} \, \vec{v} = l^2, \tag{B.3}$$

showing that the orthogonal matrices $\mathbf{R}$ are norm preserving, and thus represent proper rotations. Now, noting that the determinant of products equals the product of determinants, one yields

$$\det(\mathbf{R}^T \mathbf{R}) = \det(\mathbf{R})^2 = \det(\mathbf{I}) = 1, \tag{B.4}$$

and therefore the determinant of orthogonal matrices is then

$$\det(\mathbf{R}) = \pm 1. \tag{B.5}$$

Ignoring the case when the determinant is -1, which represent reflections, the orthogonal matrix is said to be *special* when its determinant is $+1$, representing rotations. Therefore, considering only rotations, the AtDT can be considered to belong to the $SO(N)$ group.

It can briefly be confirmed that $SO(N)$ forms a group with the operation being matrix multiplication. Firstly, matrix multiplication is associative and therefore the group is closed since the product of two rotation matrices is a rotation matrix. Secondly, the $SO(N)$ group contains the identity element $\mathbf{I}$. Lastly, since each element $\mathbf{R} \in SO(N)$ has a non-zero determinant, its inverse exists – as the transpose.

B.2 Generators of Rotation

I now turn the discussion towards the so-called generator of the rotation $\mathbf{R} \in SO(N)$. Consider the following exponential map of some matrix κ

$$\mathbf{R} = e^{\kappa}. \tag{B.6}$$

In order for this to coincide with a rotation, i.e. $\mathbf{R} \in SO(N)$, then κ must posess certain properties. Recalling the orthogonality condition

$$\mathbf{R}^T\mathbf{R} = \left(e^{\kappa}\right)^T e^{\kappa} = e^{\kappa^T} e^{\kappa} = \mathbf{I}. \tag{B.7}$$

If κ and its transpose commutes, then the product of exponentials can be simplified as an exponentiated summation

$$\mathbf{R}^T\mathbf{R} = e^{\kappa^T+\kappa} = \mathbf{I}. \tag{B.8}$$

In order for the above exponential to equal the identity, it is required κ to be an antisymmetric matrix, i.e.

$$\kappa^T + \kappa = 0 \quad \rightarrow \quad \kappa^T = -\kappa. \tag{B.9}$$

It can be quickly checked whether a skew-symmetric matrix and its transpose commute

$$\left[\kappa^T, \kappa\right] = \kappa^T\kappa - \kappa\kappa^T = -\kappa^2 + \kappa^2 = 0, \tag{B.10}$$

supporting the step from Eq.(B.7) to Eq.(B.8) where commutativity was assumed. Therefore, $\exp(\kappa)$ is orthogonal. Finally, it is required to show that $\exp(\kappa)$ has determinant $+1$, making it special. Recalling the general definition of the determinant

$$\det(\mathbf{A}) = \prod_i \lambda_i, \tag{B.11}$$

where λ_i are the eigenvalues of $\mathbf{A}$. Recalling the trace invariance to similarity transformations, considering the diagonalising transformation $\mathbf{P}$,

$$Tr(\mathbf{PAP}^{-1}) = Tr(\mathbf{P}^{-1}\mathbf{PA}) = Tr(\mathbf{IA}) = Tr(\mathbf{A}) = \sum_i \lambda_i, \tag{B.12}$$

for any square matrix $\mathbf{A}$, where the cyclic nature of the trace has been used and also

$$Tr(\mathbf{PAP}^{-1}) = Tr(\mathbf{D}) = \sum_i \lambda_i, \tag{B.13}$$

where $\mathbf{D}$ is the diagonalised form of $\mathbf{A}$. Considering the trace of the exponential matrix,

$$Tr(e^{\kappa}) = e^{Tr(\kappa)} = e^{\sum_i \tilde{\lambda}_i} = \prod_i e^{\tilde{\lambda}_i}, \tag{B.14}$$

where $\tilde{\lambda}_i$ are the eigenvalues of κ. However, $\exp(\tilde{\lambda}_i)$ are the eigenvalues of the exponential matrix $\exp(\kappa)$. Comparison with Eq.(B.11) reveals that the following relation holds

$$\det(\mathbf{R}) = e^{Tr(\kappa)}. \tag{B.15}$$

Finally, knowing that κ is skew-symmetric, its trace is zero, the determinant of the exponential matrix is indeed 1 via

$$\det(\mathbf{R}) = \det(e^{\kappa}) = e^{0} = 1, \tag{B.16}$$

thus proving that $SO(N)$ Lie groups are connected to skew-symmetric matrices by the exponential map.

The (real) skew-symmetric matrix κ has its diagonal elements equaling zero, and its off-diagonal elements coming in $\pm$ pairs giving rise to skew-symmetry. Therefore, for an $N \times N$ rotation matrix $\mathbf{R}$ with N^2 elements, the corresponding skew-symmetric matrix κ has $N(N-1)/2$ unique elements. One sees how the exponential mapping nicely transforms the rotation to a representation with fewer parameters, simplifying the problem. In fact, a subset of skew-symmetric matrices $\mathbf{S}_\mu$ can be defined which represent infinitesimal rotations about the μ^{th} axis and has elements given by

$$\left(\mathbf{S}_\mu\right)_{ij} = \varepsilon_{\mu ij} = \begin{cases} +1, & \text{even index permutations} \\ -1, & \text{odd index permutations} \\ 0, & \text{otherwise} \end{cases} \tag{B.17}$$

where $\varepsilon_{\mu ij}$ is the Levi-Civita symbol. The skew-symmetric matrix in Eq.(B.6) can then be represented by the following linear combination

$$\kappa(r) = \sum_\mu \mathfrak{a}_\mu(r)\mathbf{S}_\mu, \tag{B.18}$$

where $\mathfrak{a}_\mu$ are in general scalar functions, in the case of the diatomic AtDT, of internuclear separation r. The skew-symmetric matrices $\mathbf{S}_\mu$ have a special meaning, they are the infinitesimal generators of the rotation $\mathbf{R}$, and form a vector space. It can be quickly proved that $\mathbf{S}_\mu$ forms a vector space since the addition operation and scalar product between any $\mathbf{S}_\mu$ matrix is also skew-symmetric. Thus, $\mathbf{S}_\mu$ constitute the basis for a (flat) vector space [2]. For example, in the $N = 2$ case, only one

[2] This is a powerful property of the skew-symmetric matrices, and allows linear combinations of skew-symmetric matrices in generation of a new AtDT in the HyAP method (see section 2.6.1) since

skew-symmetric matrix exists, that is

$$\mathbf{S}_3 = \begin{pmatrix} 0 & 1 \\ -1 & 0 \end{pmatrix}. \tag{B.19}$$

In the $N = 3$ case, there are $N(N-1)/2 = 3$ generator elements as follows,

$$\mathbf{S}_3 = \begin{pmatrix} 0 & 1 & 0 \\ -1 & 0 & 0 \\ 0 & 0 & 0 \end{pmatrix}, \quad \mathbf{S}_2 = \begin{pmatrix} 0 & 0 & -1 \\ 0 & 0 & 0 \\ 1 & 0 & 0 \end{pmatrix}, \quad \mathbf{S}_1 = \begin{pmatrix} 0 & 0 & 0 \\ 0 & 0 & 1 \\ 0 & -1 & 0 \end{pmatrix}. \tag{B.20}$$

κ then represents the generator matrix of a finite rotation, a linear combination of the generator basis $\mathbf{S}_\mu$.

B.3 Lie Algebras

The previous section (B.2) showed that the generator of a rotation is a skew-symmetric matrix, which, when exponentiated, yields the rotation matrix. It was also seen that generators form a vector space. It can be shown that this vector space is in fact the tangent space to $SO(N)$ by considering Eqns.(2.49,2.48,2.43) which have the form

$$\frac{d\mathbf{R}}{dr} = \mathbf{R}\Omega(r), \tag{B.21}$$

where $\mathbf{R} \in SO(N)$ is a rotation matrix parametrically dependent on some parameter r, and Ω is a skew-symmetric matrix. Evaluating the above equation at the identity $\mathbf{R}(r = r_0) = \mathbf{I}$

$$\frac{d\mathbf{R}(r_0)}{dr} = \Omega(r_0). \tag{B.22}$$

Thus, at the identity, the tangent space of $SO(N)$ corresponds to all possible $N \times N$ skew-symmetric matrices $\Omega(r_0)$. Another way of showing this is in the Taylor expansion of the rotation matrix near the identity

$$\mathbf{R} \approx \mathbf{I} + \frac{d\mathbf{R}(\mathbf{r_0})}{dr}(r - r_0) + \mathscr{O}(r^2) \qquad |r - r_0| \ll 1, \tag{B.23}$$

and the exponential series

$$e^{\kappa} \approx \mathbf{I} + \kappa + \mathscr{O}(\kappa^2). \tag{B.24}$$

Direct comparison shows the skew-symmetric matrix κ represents the tangent of $\mathbf{R}$ at the identity. Therefore, the entire set of $N \times N$ skew-symmetric matrices form

addition algebra is allowed.

the tangent space of $SO(N)$ – this is exactly the Lie algebra $\mathfrak{so}(N)$ of the Lie group $SO(N)$. The tangent space therefore represents a space of angular "velocities" that all points on the $SO(N)$ group manifold can have when passing through the identity. In conclusion, the generator representation of a rotation matrix is equivalent to representation by the Lie algebra ($\kappa \in \mathfrak{so}(N)$).

For completeness, Lie algebras are required to be closed under the Lie bracket operation, which in this case is the commutator. Consider the transposed commutator between two skew-symmetric matrices **A** and **B**

$$([\mathbf{A},\mathbf{B}])^T = (\mathbf{AB})^T - (\mathbf{BA})^T = \mathbf{B}^T\mathbf{A}^T - \mathbf{A}^T\mathbf{B}^T = \mathbf{BA} - \mathbf{AB} = -[\mathbf{A},\mathbf{B}]\,. \quad \text{(B.25)}$$

Therefore, the commutator between two skew-symmetric matrices is itself skew-symmetric, proving that skew-symmetric matrices are closed under the commutator – a Lie algebra.

B.4 Example Generator for the 2D Problem

To illustrate the generator, the simplest case of $N = 2$ is now considered.[3] Recalling from section B.2 that there exists only one Lie algebra element for the two-dimensional problem, $\mathbf{S}_3$ (see Eq.(B.19)), the rotation matrix is

$$\mathbf{R}(\theta) = e^{\theta\mathbf{S}_3} = \cos(\theta)\mathbf{I} + \sin(\theta)\mathbf{S}_3 = \begin{pmatrix} \cos(\theta) & \sin(\theta) \\ -\sin(\theta) & \cos(\theta) \end{pmatrix} \quad \text{(B.26)}$$

where θ is the angle of rotation and is a scalar quantity. [4] One can separate the even and odd power terms of the exponential series to give the trigonometric representation of the rotation matrix, where the above is a generalisation of Euler's formulae to matrices. The $SO(2)$ manifold in this case is $2-$dimensional and can be thought of as a circle where the $x-$ and $y-$ values are the sin and cos of the angle θ. θ then parameterises the trajectory 'arc' of the rotation through the $SO(2)$ manifold. The tangent to this circle then represents the angular velocity of the rotation and corresponds to the generator, or Lie algebra, which indeed is a $1-$dimensional object. Figure B.1 illustrates this pictorially. At the identity ($\theta = 0$), the derivative of the

[3] An example application of generator representation of the AtDT for a 2-state system is discussed in section 2.5.1

[4] In general the parameterisation of $\mathbf{R} \in SO(N)$ in the tangent space $\mathfrak{so}(N)$ is a $N-$dimensional vector quantity, with elements $\mathfrak{a}_{mn}(r)$ as in Eq.(B.18).

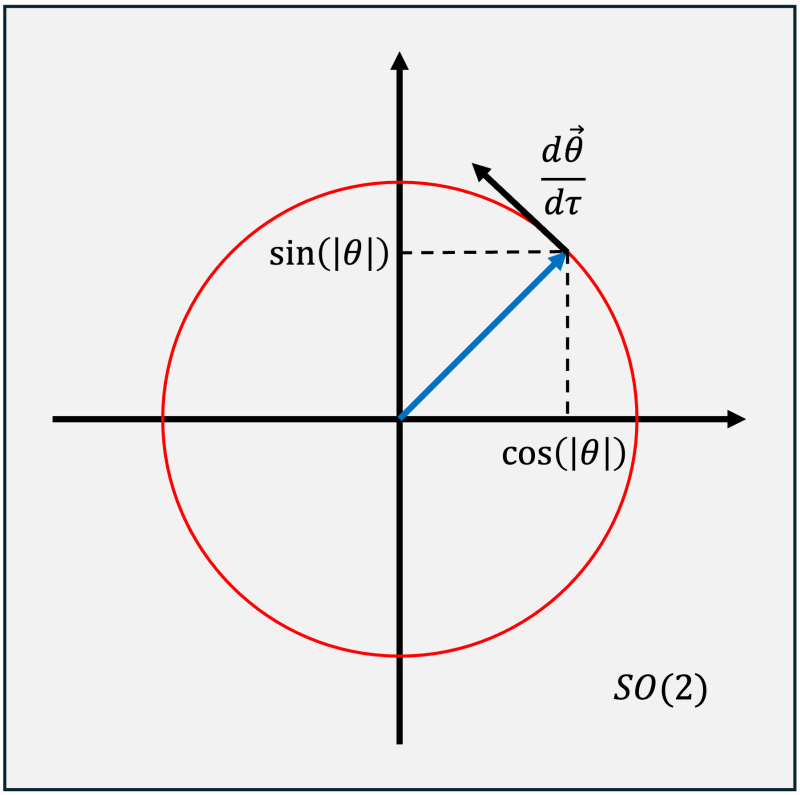

Figure B.1: Simplified visualisation of the $SO(2)$ group manifold with Lie group relating to the 1D angular velocity.

rotation is then easily computed from above as

$$\frac{d\mathbf{R}(\theta=0)}{dr} = \begin{pmatrix} 0 & 1 \\ -1 & 0 \end{pmatrix} \frac{d\theta}{dr} = \frac{d\theta}{dr}\mathbf{S}_3. \tag{B.27}$$

This equation looks similar to Eqns.(2.49,2.53), and indeed the NAC is equivalent to the angular velocity of the diabatic frame relative to the adiabatic frame in the diatomic Hilbert space. It is then clear that NACs have a deep connection to coordinate transformations, or more specifically, rotational dynamics, and the abstract Lie algebras of these tranfromations. This, however, was foreshadowed when deriving the conditions for transforming to a strictly diabatic representation in section 2.4. Lie algebras, or generators, then form a sensible representation of the AtDT, and motivates the methodology not only used extensively in this thesis, but also in the literature[495].

Bibliography

[1] Liljegren, S., Jerkstrand, A., Barklem, P. S., Nyman, G., Brady, R., and Yurchenko, S. N. The molecular chemistry of type ibc supernovae and diagnostic potential with the james webb space telescope. *Aston. and Astr.*, 674: A184, 2023. doi:10.1051/0004-6361/202243491.

[2] M. Born and R. Oppenheimer. Zur Quantentheorie der Molekeln. *Annalen der Physik*, 389(20):457–484, 1927. doi:10.1002/andp.19273892002.

[3] Andrew J. Orr-Ewing. Photodissociation and reaction dynamics. *Phys. Chem. Chem. Phys.*, 21:13878–13879, 2019. doi:10.1039/C9CP90164G.

[4] M. Pezzella, S. N. Yurchenko, and J. Tennyson. A method for calculating temperature-dependent photodissociaiton cross sections and rates. *Phys. Chem. Chem. Phys.*, 23:16390–16400, 2021. doi:10.1039/D1CP02162A.

[5] M. Pezzella, S. N. Yurchenko, and J. Tennyson. ExoMol photodissociation cross sections I – HCl and HF. *Mon. Not. R. Astron. Soc.*, 514:4413–4425, 2022. doi:10.1093/mnras/stac1634.

[6] M. Pezzella, G. Mitev, S. N. Yurchenko, J. Tennyson, and A. O. Mitrushchenkov. A time-independent, variational method for studying the photodissociation of triatomic molecules. *Phys. Chem. Chem. Phys.*, 26: 27519–27529, 2024. doi:10.1039/D4CP02771J.

[7] G. B. Mitev, M Pezzella, C A Bowesman, Jingxin Zhang, S. N. Yurchenko, and J. Tennyson. ExoMol Photodissociation Cross Sections – II: Continuum Absorption and Predissociation Spectra for the Hydroxyl Radical. *Mon. Not. R. Astron. Soc.*, 539:3732–3740, 2025. doi:10.1093/mnras/staf729.

[8] Jacob N Israelachvili. *Intermolecular and Surface Forces*. Academic Press, San Diego, CA, third edition, Dec 2010. doi:10.1016/C2009-0-21560-1.

[9] Anthony Stone. *The Theory of Intermolecular Forces*. Oxford University Press, Jan 2013. ISBN 9780199672394. doi:10.1093/acprof:oso/9780199672394.001.0001.

[10] Ilya G Kaplan. *Intermolecular interactions*. Wiley Series in Theoretical Chemistry. Wiley-Blackwell, Hoboken, NJ, April 2006. doi:10.1002/047086334X.

[11] David R. Yarkony. Diabolical conical intersections. *Rev. Mod. Phys.*, 68: 985–1013, Oct 1996. doi:10.1103/RevModPhys.68.985.

[12] J Von Neumann and Eugene Wigner. On the behaviour of eigenvalues in adiabatic processes. In *Quantum Chemistry: Classic Scientific Papers*, pages 25–31. World Scientific, 2000.

[13] R. P. Brady, S. N. Yurchenko, G.-S. Kim, W. Somogyi, and J. Tennyson. An ab initio study of the rovibronic spectrum of sulphur monoxide (SO): Diabatic vs. adiabatic representation. *Phys. Chem. Chem. Phys.*, 24(39):24076–24088, 2022. ISSN 1463-9084. doi:10.1039/D2CP03051A.

[14] Michael S. Schuurman and Albert Stolow. Dynamics at Conical Intersections. *Ann. Rev. Phys. Chem.*, 69(1):427–450, 2018. doi:10.1146/annurev-physchem-052516-050721.

[15] Benjamin G. Levine and Todd J. Martínez. Isomerization Through Conical Intersections. *Ann. Rev. Phys. Chem.*, 58(1):613–634, May 2007. doi:10.1146/annurev.physchem.57.032905.104612.

[16] Jacob Whitlow, Zhubing Jia, Ye Wang, Chao Fang, Jungsang Kim, and Kenneth R. Brown. Simulating conical intersections with trapped ions, 2023.

[17] Ahren W. Jasper, Chaoyuan Zhu, Shikha Nangia, and Donald G. Truhlar. Introductory lecture: Nonadiabatic effects in chemical dynamics. *Faraday Discuss.*, 127:1–22, 2004. doi:10.1039/B405601A.

[18] Spiridoula Matsika and Pascal Krause. Nonadiabatic Events and Conical Intersections. *Ann. Rev. Phys. Chem.*, 62(1):621–643, 2011. doi:10.1146/annurev-physchem-032210-103450.

[19] Yinan Shu, B. Scott Fales, Wei-Tao Peng, and Benjamin G. Levine. Understanding Nonradiative Recombination through Defect-Induced Con-

ical Intersections. *J. Phys. Chem. Lett.*, 8(17):4091–4099, 2017. doi:10.1021/acs.jpclett.7b01707.

[20] Tijs Karman, Matthieu Besemer, Ad van der Avoird, and Gerrit C. Groenenboom. Diabatic states, nonadiabatic coupling, and the counterpoise procedure for weakly interacting open-shell molecules. *J. Chem. Phys.*, 148: 094105, 2018. doi:10.1063/1.5013091.

[21] Tijs Karman, Ad van der Avoird, and Gerrit C. Groenenboom. Communication: Multiple-property-based diabatization for open-shell van der Waals molecules. *J. Chem. Phys.*, 144(12):121101, 2016. doi:10.1063/1.4944744.

[22] Qianli Ma, Jacek Kłos, Millard H. Alexander, Ad van der Avoird, and Paul J. Dagdigian. The interaction of OH ($X^2\Pi$) with H_2: Ab initio potential energy surfaces and bound states. *J. Chem. Phys.*, 141(17):174309, 2014. doi:10.1063/1.4900478.

[23] Jacek Kłos, Qianli Ma, Millard H. Alexander, and Paul J. Dagdigian. The interaction of NO($X\ ^2\Pi$) with H_2: Ab initio potential energy surfaces and bound states. *J. Chem. Phys.*, 146(11):114301, 2017. doi:10.1063/1.4977992.

[24] Tim de Jongh, Tijs Karman, Sjoerd N. Vogels, Matthieu Besemer, Jolijn Onvlee, Arthur G. Suits, James O. F. Thompson, Gerrit C. Groenenboom, Ad van der Avoird, and Sebastiaan Y. T. van de Meerakker. Imaging diffraction oscillations for inelastic collisions of NO radicals with He and D_2. *J. Chem. Phys.*, 147(1):013918, 2017. doi:10.1063/1.4981023.

[25] Marcin Kolbuszewski, James S Wright, and Robert J Buenker. Avoided crossings in potential curves of BF^{2+}: A study of models for bonding in diatomic dications. *J. Chem. Phys.*, 102:7519–7529, 1995. doi:10.1063/1.469083.

[26] Hans-Joachim Werner and Wilfried Meyer. MCSCF study of the avoided curve crossing of the two lowest $^1\Sigma^+$ states of LiF. *J. Chem. Phys.*, 74(10): 5802–5807, 1981. doi:10.1063/1.440893.

[27] M Šimsová-Zámecníková, P Soldán, and Magnus Gustafsson. Formation of NaCl by radiative association in interstellar environments. *Astron. Astrophys.*, 664:A5, 2022. doi:10.1051/0004-6361/202142965.

[28] L. Wolniewicz and K. Dressler. The EF and GK $^1\Sigma_g^+$ states of hydrogen: Adiabatic calculation of vibronic states in H_2, HD, and D_2. *J. Mol. Spectrosc.*, 67(1-3):416–439, sep 1977. doi:10.1016/0022-2852(77)90050-9.

[29] K. Dressler, R. Gallusser, P. Quadrelli, and L. Wolniewicz. The EF and GK $^1\Sigma_g^+$ states of hydrogen: Calculation of nonadiabatic coupling. *J. Mol. Spectrosc.*, 75(2):205–219, may 1979. doi:10.1016/0022-2852(79)90117-6.

[30] K. Dressler and L. Wolniewicz. Improved adiabatic corrections for the $B^1\Sigma_u^+$, $C^1\Pi_u$, and $D^1\Pi_u$ states of the hydrogen molecule and vibrational structures for H_2, HD, and D_2 . *J. Chem. Phys.*, 85(5):2821–2830, sep 1986. doi:10.1063/1.451040.

[31] P. Quadrelli, K. Dressler, and L. Wolniewicz. Nonadiabatic coupling between the EF+GK+H $^1\Sigma_g^+$, I $^1\Pi_g$, and J $^1\Delta_g$ states of the hydrogen molecule. Calculation of rovibronic structures in H_2, HD, and D_2. *J. Chem. Phys.*, 92(12): 7461–7478, jun 1990. doi:10.1063/1.458181.

[32] L. Wolniewicz and K. Dressler. Nonadiabatic energy corrections for the vibrational levels of the B and B' $^1\Sigma_u^+$ states of the H_2 and D_2 molecules. *J. Chem. Phys.*, 96(8):6053–6064, apr 1992. doi:10.1063/1.462647.

[33] L. Wolniewicz and K. Dressler. Adiabatic potential curves and nonadiabatic coupling functions for the first five excited $^1\Sigma_g^+$ states of the hydrogen molecule. *J. Chem. Phys.*, 100(1):444–451, jan 1994. doi:10.1063/1.466957.

[34] S. Yu and K. Dressler. Calculation of rovibronic structures in the lowest nine excited $^1\Sigma_g^+ + ^1\Pi_g + ^1\Delta_g$ states of H_2, D_2, and T_2. *J. Chem. Phys.*, 101(9): 7692–7706, nov 1994. doi:10.1063/1.468263.

[35] Ralph Jaquet and Werner Kutzelnigg. Non-adiabatic theory in terms of a single potential energy surface. The vibration–rotation levels of and. *Chem. Phys.*, 346(1-3):69–76, May 2008. ISSN 03010104. doi:10.1016/j.chemphys.2008.02.068. URL https://linkinghub.elsevier.com/retrieve/pii/S0301010408001663.

[36] Krzysztof Pachucki and Jacek Komasa. Nonadiabatic corrections to the wave function and energy. *J. Chem. Phys.*, 129(3):034102, 07 2008. doi:10.1063/1.2952517.

[37] Krzysztof Pachucki and Jacek Komasa. Nonadiabatic corrections to rovibrational levels of H_2. *J. Chem. Phys.*, 130(16):164113, 04 2009. doi:10.1063/1.3114680.

[38] Ryan P. Brady, Charlie Drury, Sergei N. Yurchenko, and Jonathan Tennyson. Numerical Equivalence of Diabatic and Adiabatic Representations in Diatomic Molecules. *J. Chem. Theory Comput.*, 20(5):2127–2139, 2024. doi:10.1021/acs.jctc.3c01150.

[39] W. D. Hobey and A. D. McLachlan. Dynamical Jahn-Teller Effect in Hydrocarbon Radicals. *J. Chem. Phys.*, 33(6):1695–1703, 12 1960. doi:10.1063/1.1731485.

[40] C. Alden Mead and Donald G. Truhlar. Conditions for the definition of a strictly diabatic electronic basis for molecular systems. *J. Chem. Phys.*, 77 (12):6090–6098, 1982. doi:10.1063/1.443853.

[41] Ahren W. Jasper, Brian K. Kendrick, C. Alden Mead, and Donald G. Truhlar. *Non-Born-Oppenheimer Chemistry: Potential Surfaces, Couplings, and Dynamics*, pages 329–391. World Scientific, 2004. doi:10.1142/9789812565426_0008.

[42] John B. Delos. Theory of electronic transitions in slow atomic collisions. *Rev. Mod. Phys.*, 53:287–357, Apr 1981. doi:10.1103/RevModPhys.53.287.

[43] Michael Baer. Topological effects in molecular systems: an attempt towards a complete theory. *Chem. Phys.*, 259(2-3):123–147, sep 2000. doi:10.1016/S0301-0104(00)00193-2.

[44] Michael Baer and Alexander Alijah. Quantized non-adiabatic coupling terms to ensure diabatic potentials. *Chem. Phys. Lett.*, 319(5-6):489–493, mar 2000. doi:10.1016/S0009-2614(00)00195-0.

[45] Michael Baer. Introduction to the theory of electronic non-adiabatic coupling terms in molecular systems. *Phys. Rep.*, 358(2):75–142, feb 2002. doi:10.1016/S0370-1573(01)00052-7.

[46] Michael Baer. *Beyond Born-Oppenheimer: electronic nonadiabatic coupling terms and conical intersections*. John Wiley & Sons, 2006. doi:10.1002/0471780081.

[47] Felix T. Smith. Diabatic and Adiabatic Representations for Atomic Collision Problems. *Phys. Rev.*, 179:111–123, Mar 1969. doi:10.1103/PhysRev.179.111.

[48] David R. Yarkony, Changjian Xie, Xiaolei Zhu, Yuchen Wang, Christopher L. Malbon, and Hua Guo. Diabatic and adiabatic representations: Electronic structure caveats. 1152:41–52, 2019. doi:10.1016/j.comptc.2019.01.020.

[49] Zoltan Varga, Kelsey A. Parker, and Donald G. Truhlar. Direct diabatization based on nonadiabatic couplings: the N/D method. *Phys. Chem. Chem. Phys.*, 20:26643–26659, 2018. doi:10.1039/C8CP03410A.

[50] Wissem Zrafi N. Mabrouk and H. Berriche. Theoretical study of the LiNa molecule beyond the Born-Oppenheimer approximation: adiabatic and diabatic potential energy curves, radial coupling, adiabatic correction, dipole moments and vibrational levels. *Mol. Phys.*, 118(3):e1605098, 2020. doi:10.1080/00268976.2019.1605098.

[51] Michael Baer. Integral equation approach to atom-diatom exchange processes. *Physics Reports*, 178(3):99–143, jun 1989. doi:10.1016/0370-1573(89)90137-3.

[52] Sergei N Yurchenko, Ryan P Brady, Jonathan Tennyson, Alexander N Smirnov, Oleg A Vasilyev, and Victor G Solomonik. ExoMol line lists – LIII: empirical rovibronic spectra of yttrium oxide. *Mon. Not. R. Astron. Soc.*, 527 (3):4899–4912, 10 2023. ISSN 0035-8711. doi:10.1093/mnras/stad3225.

[53] Jonathan Tennyson and Sergei N. Yurchenko. ExoMol: Molecular line lists for exoplanet and other atmospheres. *Mon. Not. R. Astron. Soc.*, 425:21–33, 2012. doi:10.1111/j.1365-2966.2012.21440.x.

[54] Jonathan Tennyson, Sergei N. Yurchenko, Ahmed F. Al-Refaie, Victoria H.J. Clark, Katy L. Chubb, Eamon K. Conway, Akhil Dewan, Maire N. Gorman, Christian Hill, A.E. Lynas-Gray, Thomas Mellor, Laura K. McKemmish, Alec Owens, Oleg L. Polyansky, Mikhail Semenov, Wilfrid Somogyi, Giovanna Tinetti, Apoorva Upadhyay, Ingo Waldmann, Yixin Wang, Samuel Wright, and Olga P. Yurchenko. The 2020 release of the ExoMol database: molecular line lists for exoplanet and other hot atmospheres. *J. Quant. Spectrosc. Radiat. Transf.*, 255:107228, 2020. doi:10.1016/j.jqsrt.2020.107228.

[55] Jonathan Tennyson, Sergei N. Yurchenko, Jingxin Zhang, Charles A. Bowesman, Ryan P. Brady, Jeanna Buldyreva, Katy L. Chubb, Robert R. Gamache, Maire N. Gorman, Elizabeth R. Guest, Christian Hill, Kyriaki Kefala, A. E. Lynas-Gray, Thomas M. Mellor, Laura K. McKemmish, Georgi B. Mitev, Irina I. Mizus, Alec Owens, Zhijian Peng, Armando N. Perri, Marco Pezzella, Oleg L. Polyansky, Qianwei Qu, Mikhail Semenov, Oleksiy Smola, Andrei Solokov, Wilfrid Somogyi, Apoorva Upadhyay, Samuel O. M. Wright, and Nikolai F. Zobov. The 2024 release of the ExoMol database: molecular line lists for exoplanet and other hot atmospheres. *J. Quant. Spectrosc. Radiat. Transf.*, 326:109083, 2024. doi:10.1016/j.jqsrt.2024.109083.

[56] Yinan Shu, Zoltan Varga, Antonio Gustavo Sampaio de Oliveira-Filho, and Donald G. Truhlar. Permutationally Restrained Diabatization by Machine Intelligence. *J. Chem. Theory Comput.*, 17(2):1106–1116, 2021. doi:10.1021/acs.jctc.0c01110.

[57] R. P. Brady. A strict and internally consistent diabatic representation for coupled N-state diatomics: A hybrid asymptotic-property-based diabatization method. *J. Chem. Phys.*, 162(17):174105, 05 2025. ISSN 0021-9606. doi:10.1063/5.0260594.

[58] Ryan P. Brady. Exact Rovibronic Equivalence of the Adiabatic and Diabatic Representations of N-coupled State Diatomic Systems. *J. Comput. Chem.*, 2025. Submitted to the Journal of Computational Chemistry.

[59] R. P. Brady, S. N. Yurchenko, G.-S. Kim, W. Somogyi, and J. Tennyson. An *ab initio* study of the rovibronic spectrum of sulphur monoxide (SO): diabatic vs. adiabatic representation. *Phys. Chem. Chem. Phys.*, 24:24076–24088, 2022. doi:10.1039/D2CP03051A.

[60] Xiaolei Zhu and David R. Yarkony. On the Construction of Property Based Diabatizations: Diabolical Singular Points. *J. Phys. Chem. A*, 119(50): 12383–12391, 2015. doi:10.1021/acs.jpca.5b07705.

[61] Chad E. Hoyer, Xuefei Xu, Dongxia Ma, Laura Gagliardi, and Donald G. Truhlar. Diabatization based on the dipole and quadrupole: The DQ method. *J. Chem. Phys.*, 141(11):114104, 2014. doi:10.1063/1.4894472.

[62] Chad E. Hoyer, Kelsey Parker, Laura Gagliardi, and Donald G. Truhlar. The DQ and DQΦ electronic structure diabatization methods: Valida-

tion for general applications. *J. Chem. Phys.*, 144(19):194101, 05 2016. doi:10.1063/1.4948728.

[63] A.J. Dobbyn and P.J. Knowles. A comparative study of methods for describing non-adiabatic coupling: Diabatic representation of the 1Sigma +/1Pi HOH and HHO conical intersections. *Mol. Phys.*, 91(6):1107–1124, 1997. doi:10.1080/002689797170842.

[64] A Macias and A Riera. Calculation of diabatic states from molecular properties. *J. Phys. B: At. Mol. Phys.*, 11(16):L489, aug 1978. doi:10.1088/0022-3700/11/16/003.

[65] Gerhard Hirsch Carlo Petrongolo and Robert J. Buenker. Diabatic representation of the $\tilde{A}^2A_1$ and $\tilde{B}^2B_2$ conical intersection in NH_2 . *Mol. Phys.*, 70(5): 825–834, 1990. doi:10.1080/00268979000101381.

[66] M. Boggio-Pasqua, A. I. Voronin, Ph. Halvick, J.-C. Rayez, and A. J. C. Varandas. Coupled ab initio potential energy surfaces for the two lowest $^2A'$ electronic states of the C_2H molecule. *Mol. Phys.*, 98(23):1925–1938, 2000. doi:10.1080/00268970009483396.

[67] V. C. Mota, P. J. S. B. Caridade, and A. J. C. Varandas. Toward the modeling of the NO_2 ($^2A''$) manifold. *Intern. J. Quantum Chem.*, 111(14):3776–3785, 2011. doi:10.1002/qua.22907.

[68] F George D. Xavier and A. J. C. Varandas. Modelling adiabatic cusps in via 2 $\times$ 2 diabatic matrix. *Mol. Phys.*, 119(10):e1904157, 2021. doi:10.1080/00268976.2021.1904157.

[69] Klaus Ruedenberg and Gregory J. Atchity. A quantum chemical determination of diabatic states. *J. Phys. Chem.*, 99(5):3799–3803, 1993. doi:10.1063/1.466125.

[70] G. J. Atchity and K. Ruedenberg. Global potential energy surfaces for the lowest two 1 A $'$ states of ozone. *Theor. Chem. Acc.*, 96(3):176–194, aug 1997. doi:10.1007/s002140050220.

[71] Hisao Nakamura and Donald G. Truhlar. The direct calculation of diabatic states based on configurational uniformity. *J. Chem. Phys.*, 115(22):10353–10372, 2001. doi:10.1063/1.1412879.

[72] H. Nakamura and D. G. Truhlar. Direct diabatization of electronic states by the fourfold way. II. Dynamical correlation and rearrangement processes. *J. Chem. Phys.*, 117:5576–5593, 2002. doi:10.1063/1.1500734.

[73] Hisao Nakamura and Donald G. Truhlar. Extension of the fourfold way for calculation of global diabatic potential energy surfaces of complex, multiarrangement, non-Born-Oppenheimer systems: Application to HNCO(S0,S1). *J. Chem. Phys.*, 118(15):6816–6829, 2003. doi:10.1063/1.1540622.

[74] Xuefei Xu, Ke R. Yang, and Donald G. Truhlar. Diabatic Molecular Orbitals, Potential Energies, and Potential Energy Surface Couplings by the 4-fold Way for Photodissociation of Phenol. *J. Chem. Theory Comput.*, 9(8):3612–3625, aug 2013. doi:10.1021/ct400447f.

[75] J.E. Subotnik, S. Yeganeh, R.J. Cave, and M.A. Ratner. Constructing diabatic states from adiabatic states: Extending generalized Mulliken-Hush to multiple charge centers with Boys localization. *J. Chem. Phys.*, 129(24):244101, 2008. doi:10.1063/1.3042233.

[76] Michael Baer. Adiabatic and diabatic representations for atom-molecule collisions: Treatment of the collinear arrangement. *Chem. Phys. Lett.*, 35(1):112–118, 1975. doi:10.1016/0009-2614(75)85599-0.

[77] Michael Baer. Adiabatic and diabatic representations for atom-diatom collisions: Treatment of the three-dimensional case. *Chem. Phys.*, 15(1):49–57, 1976. ISSN 0301-0104. doi:10.1016/0301-0104(76)89006-4.

[78] Michael Baer. Electronic non-adiabatic transitions derivation of the general adiabatic-diabatic transformation matrix. *Mol. Phys.*, 40(4):1011–1013, 1980. doi:10.1080/00268978000102091.

[79] Philippe Halvick and Donald G. Truhlar. A new diabatic representation of the coupled potential energy surfaces for Na(3p2P)+H2→Na(3s2S)+H2 or NaH+H. *J. Chem. Phys.*, 96(4):2895–2909, 02 1992. ISSN 0021-9606. doi:10.1063/1.461986.

[80] C.A. Nicolaides, N.C. Bacalis, and Y. Komninos. Theory for the direct construction of diabatic states and application to the He^+ $2\,^2\Sigma_g^+$ spectrum. *Chem. Phys. Lett.*, 192(5):486–492, 1992. ISSN 0009-2614. doi:10.1016/0009-2614(92)85503-3.

[81] L S Cederbaum, J Schirmer, and H D Meyer. Block diagonalisation of Hermitian matrices. *J. Phys. A: Math. Gen.*, 22(13):2427, jul 1989. doi:10.1088/0305-4470/22/13/035. URL https://dx.doi.org/10.1088/0305-4470/22/13/035.

[82] N. Wittenbrink, F. Venghaus, D. Williams, and W. Eisfeld. A new approach for the development of diabatic potential energy surfaces: Hybrid block-diagonalization and diabatization by ansatz. *J. Chem. Phys.*, 145(18), 2016. doi:10.1063/1.4967258.

[83] D.M.G. Williams and W. Eisfeld. Neural network diabatization: A new ansatz for accurate high-dimensional coupled potential energy surfaces. *J. Chem. Phys.*, 149(20), 2018. doi:10.1063/1.5053664.

[84] D.M.G. Williams and W. Eisfeld. Complete Nuclear Permutation Inversion Invariant Artificial Neural Network (CNPI-ANN) Diabatization for the Accurate Treatment of Vibronic Coupling Problems. *J. Phys. Chem. A*, 124(37): 7608–7621, 2020. doi:10.1021/acs.jpca.0c05991.

[85] D.M.G. Williams, A. Viel, and W. Eisfeld. Diabatic neural network potentials for accurate vibronic quantum dynamics - The test case of planar NO_3. *J. Chem. Phys.*, 151(16), 2019. doi:10.1063/1.5125851.

[86] Yafu Guan, David R. Yarkony, and Dong H. Zhang. Permutation invariant polynomial neural network based diabatic ansatz for the (E + A) × (e + a) Jahn-Teller and Pseudo-Jahn-Teller systems. *J. Chem. Phys.*, 157(1):014110, 07 2022. ISSN 0021-9606. doi:10.1063/5.0096912.

[87] F. Venghaus and W. Eisfeld. Block-diagonalization as a tool for the robust diabatization of high-dimensional potential energy surfaces. *J. Chem. Phys.*, 144(11), 2016. doi:10.1063/1.4943869.

[88] R.J. Cave and J.F. Stanton. Block diagonalization of the equation-of-motion coupled cluster effective Hamiltonian: Treatment of diabatic potential constants and triple excitations. *J. Chem. Phys.*, 140(21), 2014. doi:10.1063/1.4880757.

[89] Yinan Shu, Zoltan Varga, Siriluk Kanchanakungwankul, Linyao Zhang, and Donald G. Truhlar. Diabatic States of Molecules. *J. Phys. Chem. A*, 126: 992–1018, 2022. doi:10.1021/acs.jpca.1c10583.

[90] Wolfgang Domcke, David R Yarkony, and Horst Köppel. *Conical intersections: Electronic structure, dynamics & spectroscopy*. Advanced Series In Physical Chemistry. World Scientific Publishing, Singapore, Singapore, apr 2004.

[91] H. Köppel, W. Domcke, and L. S. Cederbaum. *Multimode Molecular Dynamics Beyond the Born-Oppenheimer Approximation*, pages 59–246. John Wiley & Sons, Ltd, 1984. doi:10.1002/9780470142813.ch2.

[92] Thomas F. O'Malley. Diabatic States of Molecules- Quasistationary Electronic States. volume 7 of *Advances in Atomic and Molecular Physics*, pages 223–249. Academic Press, 1971. doi:10.1016/S0065-2199(08)60361-9.

[93] R.K. Janev. Nonadiabatic Transitions Between Ionic and Covalent States. volume 12 of *Advances in Atomic and Molecular Physics*, pages 1–37. Academic Press, 1976. doi:10.1016/S0065-2199(08)60041-X.

[94] Hans-Joachim Werner, Peter J. Knowles, Gerald Knizia, Frederick R. Manby, and Martin Schütz. Molpro: a general-purpose quantum chemistry program package. *WIREs Comput. Mol. Sci.*, 2:242–253, 2012. doi:10.1002/wcms.82.

[95] Gareth W. Richings and Graham A. Worth. Multi-state non-adiabatic direct-dynamics on propagated diabatic potential energy surfaces. *Chem. Phys. Lett.*, 683:606–612, 2017. doi:10.1016/j.cplett.2017.03.032.

[96] Gareth W. Richings and Graham A. Worth. A Practical Diabatisation Scheme for Use with the Direct-Dynamics Variational Multi-Configuration Gaussian Method. *J. Phys. Chem. A*, 119(50):12457–12470, 2015. doi:10.1021/acs.jpca.5b07921.

[97] B. D. Esry and H. R. Sadeghpour. Split diabatic representation. *Phys. Rev. A*, 68:042706, Oct 2003. doi:10.1103/PhysRevA.68.042706.

[98] Hai-mei Shi, Guang-hai Guo, and Zhi-gang Sun. Numerical convergence of the Sinc discrete variable representation for solving molecular vibrational states with a conical intersection in adiabatic representation. *Chinese J. Chem. Phys.*, 32:333, 2019. doi:10.1063/1674-0068/cjcp1812275.

[99] I. Harold Zimmerman and Thomas F. George. Numerical comparison between electronically adiabatic and diabatic representations for

collinear atom-diatom collisions. *J. Chem. Phys.*, 63:2109–2114, 1975. doi:10.1063/1.431550.

[100] D. A. Little and J. Tennyson. An R-matrix study of singlet and triplet continuum states of N_2. *J. Phys. B: At. Mol. Opt. Phys.*, 47:105204, 2014. doi:10.1088/0953-4075/47/10/105204.

[101] D. A. Little, K. Chakrabarti, I. F. Schneider, and J. Tennyson. The dissociative recombination of N_2^+: an ab initio study. *Phys. Rev. A*, 90:052705, 2014. doi:10.1103/PhysRevA.90.052705.

[102] M. V. Volkov, S. L. Yakovlev, E. A. Yarevsky, and N. Elander. Adiabatic versus diabatic approach to multichannel Coulomb scattering for mutual neutralisation reaction $H^+ + H^- \rightarrow H_2^* \rightarrow H(1)+H(n)$. *Chem. Phys.*, 462:57–64, 2015. doi:10.1016/j.chemphys.2015.07.008.

[103] Sergei N. Yurchenko, Lorenzo Lodi, Jonathan Tennyson, and Andrey V. Stolyarov. Duo: A general program for calculating spectra of diatomic molecules. *Comput. Phys. Commun.*, 202:262 – 275, 2016. doi:10.1016/j.cpc.2015.12.021.

[104] Hans-Joachim Werner, Peter J. Knowles, Frederick R. Manby, Joshua A. Black, Klaus Doll, Andreas Heßelmann, Daniel Kats, Andreas Köhn, Tatiana Korona, David A. Kreplin, Qianli Ma, III Miller, Thomas F., Alexander Mitrushchenkov, Kirk A. Peterson, Iakov Polyak, Guntram Rauhut, and Marat Sibaev. The Molpro quantum chemistry package. *J. Chem. Phys.*, 152 (14):144107, 04 2020. ISSN 0021-9606. doi:10.1063/5.0005081.

[105] F. Neese. The orca program system. *WIRES Comput. Molec. Sci.*, 2(1): 73–78, 2012. doi:10.1002/wcms.81.

[106] Daniel G. A. Smith, Lori A. Burns, Andrew C. Simmonett, Robert M. Parrish, Matthew C. Schieber, Raimondas Galvelis, Peter Kraus, Holger Kruse, Roberto Di Remigio, Asem Alenaizan, Andrew M. James, Susi Lehtola, Jonathon P. Misiewicz, Maximilian Scheurer, Robert A. Shaw, Jeffrey B. Schriber, Yi Xie, Zachary L. Glick, Dominic A. Sirianni, Joseph Senan O'Brien, Jonathan M. Waldrop, Ashutosh Kumar, Edward G. Hohenstein, Benjamin P. Pritchard, Bernard R. Brooks, III Schaefer, Henry F., Alexander Yu. Sokolov, Konrad Patkowski, III DePrince, A. Eugene, Uğur Bozkaya,

Rollin A. King, Francesco A. Evangelista, Justin M. Turney, T. Daniel Crawford, and C. David Sherrill. Psi4 1.4: Open-source software for high-throughput quantum chemistry. *J. Chem. Phys.*, 152(18):184108, 05 2020. ISSN 0021-9606. doi:10.1063/5.0006002.

[107] H Kato. Energy-levels and line-intensities of diatomic-molecules – application to alkali-metal molecules. *Bull. Chem. Soc. Japan*, 66:3203–3234, 1993. doi:10.1246/bcsj.66.3203.

[108] Reza Islampour and Mahsasadat Miralinaghi. An extensive study of transformation of the diatomics hamiltonian operator from laboratory- to body-fixed frame. *Intern. J. Quantum Chem.*, 115(8):510–522, 2015. doi:10.1002/qua.24881.

[109] Brian T Sutcliffe. The separation of electronic and nuclear motion in the diatomic molecule. *Theor. Chem. Acc.*, 118(3):563–571, aug 2007.

[110] Sergei N. Yurchenko, Lorenzo Lodi, Jonathan Tennyson, and Andrey V. Stolyarov. Duo: A general program for calculating spectra of diatomic molecules. *Comput. Phys. Commun.*, 202:262–275, 2016. doi:10.1016/j.cpc.2015.12.021.

[111] Russell T. Pack and Joseph O. Hirschfelder. Separation of rotational coordinates from the n electron diatomic schrödinger equation. *J. Chem. Phys.*, 49 (9):4009 – 4020, 1968. doi:10.1063/1.1670711.

[112] P.R. Bunker. The electronic isotope shift in diatomic molecules and the partial breakdown of the born-oppenheimer approximation. *J. Mol. Spectrosc.*, 28(4):422–443, 1968. ISSN 0022-2852. doi:10.1016/0022-2852(68)90176-8.

[113] Nobuhiro Yamanaka. Calculation of mass polarization for the and states in li-like ions. *J. Phys. B: At. Mol. Opt. Phys.*, 32(6):1597, mar 1999. doi:10.1088/0953-4075/32/6/020. URL https://dx.doi.org/10.1088/0953-4075/32/6/020.

[114] Max Born and K. Huang. Dynamical theory of crystal lattices. 1954. URL https://api.semanticscholar.org/CorpusID:59567814.

[115] V Fock. Näherungsmethode zur lösung des quantenmechanischen mehrkörperproblems. *Eur. Phys. J. A*, 61(1-2):126–148, January 1930.

[116] A. Szabo and N.S. Ostlund. *Modern Quantum Chemistry: Introduction to Advanced Electronic Structure Theory*. Dover Books on Chemistry. Dover Publications, first edition, 1996. ISBN 9780486691862.

[117] Björn O. Roos. The complete active space scf method in a fock-matrix-based super-ci formulation. *Intern. J. Quantum Chem.*, 18(S14):175–189, 1980. doi:10.1002/qua.560180822.

[118] Daniel S. Levine, Diptarka Hait, Norm M. Tubman, Susi Lehtola, K. Birgitta Whaley, and Martin Head-Gordon. Casscf with extremely large active spaces using the adaptive sampling configuration interaction method. *J. Chem. Theory Comput.*, 16(4):2340–2354, 2020. doi:10.1021/acs.jctc.9b01255.

[119] Hans-Joachim Werner and Peter J. Knowles. An efficient internally contracted multiconfiguration–reference configuration interaction method. *J. Chem. Phys.*, 89(9):5803–5814, 11 1988. ISSN 0021-9606. doi:10.1063/1.455556.

[120] Peter J. Knowles and Hans-Joachim Werner. Internally contracted multiconfiguration-reference configuration interaction calculations for excited states. *Theor. Chim. Acta.*, 84(1–2):95–103, October 1992. ISSN 1432-2234. doi:10.1007/bf01117405.

[121] Rodney J. Bartlett and Monika Musiał. Coupled-cluster theory in quantum chemistry. *Rev. Mod. Phys.*, 79:291–352, Feb 2007. doi:10.1103/RevModPhys.79.291.

[122] Ajith Perera, Young Choon Park, and Rodney J. Bartlett. How coupled-cluster theory is solving the electron correlation problem. In Manuel Yáñez and Russell J. Boyd, editor, *Comprehensive Computational Chemistry (First Edition)*, pages 18–46. Elsevier, Oxford, first edition edition, 2024. ISBN 978-0-12-823256-9. doi:10.1016/B978-0-12-821978-2.00137-9.

[123] Joachim Römelt. A Hermitean reformulation of the Born-Oppenheimer nonadiabatic coupling terms for diatomic molecules. *Intern. J. Quantum Chem.*, 24:627–631, 1983. doi:10.1002/qua.560240609.

[124] III Lengsfield, Byron H. and David R. Yarkony. On the evaluation of nonadiabatic coupling matrix elements for MCSCF/CI wave functions using analytic derivative methods. III. Second derivative terms. *J. Chem. Phys.*, 84(1): 348–353, 01 1986. doi:10.1063/1.450144.

[125] Paul Saxe and David R. Yarkony. On the evaluation of nonadiabatic coupling matrix elements for MCSCF/CI wave functions. IV. Second derivative terms using analytic gradient methods. *J. Phys. Chem.*, 86(1):321–328, 01 1987. doi:10.1063/1.452621.

[126] Joachim Römelt. A Hermitean reformulation of the Born-Oppenheimer nonadiabatic coupling terms for diatomic molecules. *Intern. J. Quantum Chem.*, 24(6):627–631, 1983. doi:10.1002/qua.560240609.

[127] H Hellmann. Zur rolle der kinetischen elektronenenergie for die zwischenatomaren kröfte. *Eur. Phys. J. A*, 85(3-4):180–190, March 1933.

[128] R P Feynman. Forces in molecules. *Phys. Rev.*, 56(4):340–343, August 1939.

[129] Shervin Fatehi, Ethan Alguire, Yihan Shao, and Joseph E. Subotnik. Analytic derivative couplings between configuration-interaction-singles states with built-in electron-translation factors for translational invariance. *J. Chem. Phys.*, 135(23):234105, 12 2011. ISSN 0021-9606. doi:10.1063/1.3665031.

[130] Rami Gherib, Liyuan Ye, Ilya G. Ryabinkin, and Artur F. Izmaylov. On the inclusion of the diagonal Born-Oppenheimer correction in surface hopping methods. *J. Chem. Phys.*, 144(15):154103, 04 2016. doi:10.1063/1.4945817.

[131] Peter Habitz and Christian Votava. The Hellmann–Feynman theorem for approximate wave functions and its application to nonadiabatic coupling matrix elements with the aid of a coupled Hartree–Fock method. *J. Chem. Phys.*, 72 (10):5532–5539, 05 1980. ISSN 0021-9606. doi:10.1063/1.438971.

[132] Andrei V Stolyarov and Mark S Child. Analog of the Hellmann-Feynman theorem in multichannel quantum-defect theory. *Phys. Rev. A*, 63(5), April 2001. doi:10.1103/PhysRevA.63.052510.

[133] Seung Kyu Min, Federica Agostini, Ivano Tavernelli, and E. K. U. Gross. Ab initio nonadiabatic dynamics with coupled trajectories: A rigorous approach to quantum (de)coherence. *The Journal of Physical Chemistry Letters*, 8(13): 3048–3055, 2017. doi:10.1021/acs.jpclett.7b01249.

[134] Basile F. E. Curchod and Todd J. Martínez. Ab initio nonadiabatic quantum molecular dynamics. *Chemical Reviews*, 118(7):3305–3336, 2018. doi:10.1021/acs.chemrev.7b00423.

[135] John C. Tully. Nonadiabatic molecular dynamics. *Intern. J. Quantum Chem.*, 40(S25):299–309, 1991. doi:10.1002/qua.560400830.

[136] Hans-Joachim Werner, Peter J. Knowles, Frederick R. Manby, Joshua A. Black, Klaus Doll, Andreas Heßelmann, Daniel Kats, Andreas Köhn, Tatiana Korona, David A. Kreplin, Qianli Ma, Thomas F. Miller, Alexander Mitrushchenkov, Kirk A. Peterson, Iakov Polyak, Guntram Rauhut, and Marat Sibaev. The Molpro quantum chemistry package. *J. Chem. Phys.*, 152: 144107, 2020. doi:10.1063/5.0005081.

[137] R. Hassaine, D. Talbi, R. P. Brady, J. Zs. Mezei, J. Tennyson, and I. F. Schneider. Theoretical study of the excited states of NeH and of their non-adiabatic couplings: A preliminary for the modeling of the dissociative recombination of NeH^+. *J. Chem. Phys.*, 162(13):134302, 04 2025. doi:10.1063/5.0261152.

[138] S. F. Boys and Alfred Charles Egerton. Electronic wave functions - i. a general method of calculation for the stationary states of any molecular system. *Proceedings of the Royal Society of London. Series A. Mathematical and Physical Sciences*, 200(1063):542–554, 1950. doi:10.1098/rspa.1950.0036.

[139] M. A. Martin-Drumel, F. Hindle, G. Mouret, A. Cuisset, and J. Cernicharo. A complete spectroscopic characterization of SO and its isotopologues up to the terahertz domain. *Astron. J.*, 799:115, 2015. doi:10.1088/0004-637X/799/2/115.

[140] A. N. Heays, G. Stark, J. R. Lyons, N. de Oliveira, B. R. Lewis, and S. T. Gibson. Ultraviolet photoabsorption in the b $^3\sigma^-$ - x $^3\sigma^-$ and c $^3\pi$ - x$^3\sigma^-$ band systems of so sulphur isotopologues. *Mol. Phys.*, 121:e2153092, 2022. doi:10.1080/00268976.2022.2153092.

[141] J. B. Burkholder, E. R. Lovejoy, P. D. Hammer, C. J. Howard, and M. Mizushima. High-resolution infrared Fourier-transform spectroscopy of SO in the $X^3\Sigma^-$ and $a^1\Delta$ electronic states. *J. Mol. Spectrosc.*, 124:379–392, 1987. doi:10.1016/0022-2852(87)90148-2.

[142] J. Tennyson and B. T. Sutcliffe. On the rovibrational levels of the H_3^+ and H_2D^+ molecules. *Mol. Phys.*, 51:887–906, 1984. doi:10.1080/00268978400100591.

[143] J. Tennyson and B. T. Sutcliffe. A calculation of the rovibrational spectra of the H_3^+, H_2D^+ and HD_2^+ molecules. *Mol. Phys.*, 56:1175–1183, 1985. doi:10.1080/00268978500102981.

[144] J. Tennyson and B. T. Sutcliffe. The infrared spectra of H_3^+ and its isotopomers – a challenge to theory and experiment. *J. Chem. Soc.*, 82:1151–1162, 1986. doi:10.1039/F29868201151.

[145] S. Miller and J. Tennyson. First principles calculation of the molecular constants of H_3^+, H_2D^+, D_2H^+ and D_3^+. *J. Mol. Spectrosc.*, 126:183–192, 1987. doi:10.1016/0022-2852(87)90089-0.

[146] P Drossart, J-P Maillard, J Caldwell, S J Kim, J K G Watson, W A Majewski, J Tennyson, S Miller, S K Atreya, J T Clarke, J H Waite, Jr, and R Wagener. Detection of h3+ on jupiter. *Nature*, 340(6234):539–541, August 1989.

[147] Diana Powell, Adina D Feinstein, Elspeth K H Lee, Michael Zhang, Shang-Min Tsai, Jake Taylor, James Kirk, Taylor Bell, Joanna K Barstow, Peter Gao, Jacob L Bean, Jasmina Blecic, Katy L Chubb, Ian J M Crossfield, Sean Jordan, Daniel Kitzmann, Sarah E Moran, Giuseppe Morello, Julianne I Moses, Luis Welbanks, Jeehyun Yang, Xi Zhang, Eva-Maria Ahrer, Aaron Bello-Arufe, Jonathan Brande, S L Casewell, Nicolas Crouzet, Patricio E Cubillos, Brice-Olivier Demory, Achrène Dyrek, Laura Flagg, Renyu Hu, Julie Inglis, Kathryn D Jones, Laura Kreidberg, Mercedes López-Morales, Pierre-Olivier Lagage, Erik A Meier Valdés, Yamila Miguel, Vivien Parmentier, Anjali A A Piette, Benjamin V Rackham, Michael Radica, Seth Redfield, Kevin B Stevenson, Hannah R Wakeford, Keshav Aggarwal, Munazza K Alam, Natalie M Batalha, Natasha E Batalha, Björn Benneke, Zach K Berta-Thompson, Ryan P Brady, Claudio Caceres, Aarynn L Carter, Jean-Michel Désert, Joseph Harrington, Nicolas Iro, Michael R Line, Joshua D Lothringer, Ryan J MacDonald, Luigi Mancini, Karan Molaverdikhani, Sagnick Mukherjee, Matthew C Nixon, Apurva V Oza, Enric Palle, Zafar Rustamkulov, David K Sing, Maria E Steinrueck, Olivia Venot, Peter J Wheatley, and Sergei N Yurchenko. Sulfur dioxide in the mid-infrared transmission spectrum of WASP-39b. *Nature*, 626(8001):979–983, February 2024. doi:https://doi.org/10.1038/s41586-024-07040-9.

[148] Shang-Min Tsai, Elspeth K H Lee, Diana Powell, Peter Gao, Xi Zhang, Julianne Moses, Eric Hébrard, Olivia Venot, Vivien Parmentier, Sean Jordan,

Renyu Hu, Munazza K Alam, Lili Alderson, Natalie M Batalha, Jacob L Bean, Björn Benneke, Carver J Bierson, Ryan P Brady, Ludmila Carone, Aarynn L Carter, Katy L Chubb, Julie Inglis, Jérémy Leconte, Michael Line, Mercedes López-Morales, Yamila Miguel, Karan Molaverdikhani, Zafar Rustamkulov, David K Sing, Kevin B Stevenson, Hannah R Wakeford, Jeehyun Yang, Keshav Aggarwal, Robin Baeyens, Saugata Barat, Miguel de Val-Borro, Tansu Daylan, Jonathan J Fortney, Kevin France, Jayesh M Goyal, David Grant, James Kirk, Laura Kreidberg, Amy Louca, Sarah E Moran, Sagnick Mukherjee, Evert Nasedkin, Kazumasa Ohno, Benjamin V Rackham, Seth Redfield, Jake Taylor, Pascal Tremblin, Channon Visscher, Nicole L Wallack, Luis Welbanks, Allison Youngblood, Eva-Maria Ahrer, Natasha E Batalha, Patrick Behr, Zachory K Berta-Thompson, Jasmina Blecic, S L Casewell, Ian J M Crossfield, Nicolas Crouzet, Patricio E Cubillos, Leen Decin, Jean-Michel Désert, Adina D Feinstein, Neale P Gibson, Joseph Harrington, Kevin Heng, Thomas Henning, Eliza M-R Kempton, Jessica Krick, Pierre-Olivier Lagage, Monika Lendl, Joshua D Lothringer, Megan Mansfield, N J Mayne, Thomas Mikal-Evans, Enric Palle, Everett Schlawin, Oliver Shorttle, Peter J Wheatley, and Sergei N Yurchenko. Photochemically produced SO2 in the atmosphere of WASP-39b. *Nature*, 617(7961):483–487, May 2023.

[149] Peter F. Bernath. Mollist: Molecular line lists, intensities and spectra. *Journal of Quantitative Spectroscopy and Radiative Transfer*, 240:106687, 2020. ISSN 0022-4073. doi:10.1016/j.jqsrt.2019.106687.

[150] R. Guardiola and J. Ros. On the numerical integration of the Schrödinger equation in the finite-difference schemes. *J. Comp. Phys.*, 45(3): 374–389, 1982. ISSN 0021-9991. doi:https://doi.org/10.1016/0021-9991(82)90110-3. URL https://www.sciencedirect.com/science/article/pii/0021999182901103.

[151] John R. Lund and Bruce V. Riley. A Sine-Collocation Method for the Computation of the Eigenvalues of the Radial Schrödinger Equation. *IMA J. Numer. Anal.*, 4:83–98, 1984. doi:10.1093/imanum/4.1.83.

[152] Andrew U. Hazi and Howard S. Taylor. Stabilization method of calculating resonance energies: Model problem. *Phys. Rev. A*, 1:1109–1120, Apr 1970. doi:10.1103/PhysRevA.1.1109. URL https://link.aps.org/doi/10.1103/PhysRevA.1.1109.

[153] V. A. Mandelshtam, T. R. Ravuri, and H. S. Taylor. Calculation of the density of resonance states using the stabilization method. *Phys. Rev. Lett.*, 70: 1932–1935, Mar 1993. doi:10.1103/PhysRevLett.70.1932. URL https://link.aps.org/doi/10.1103/PhysRevLett.70.1932.

[154] Zlatko Bacic and Jack Simons. Resonance energies and lifetimes from stabilization-based methods. *J. Chem. Phys.*, 86(7):1192–1200, 1982. doi:10.1021/j100396a027.

[155] Colin M. Western. PGOPHER: A program for simulating rotational, vibrational and electronic spectra . *J. Quant. Spectrosc. Radiat. Transf.*, 186:221–242, 2017. doi:10.1016/j.jqsrt.2016.04.010.

[156] T. Furtenbacher, A. G. Császár, and J. Tennyson. MARVEL: measured active rotational-vibrational energy levels. *J. Mol. Spectrosc.*, 245:115–125, 2007. doi:10.1016/j.jms.2007.07.005.

[157] Christel M. Marian. Spin-orbit coupling in molecules. In K B Lipkowitz and D B Boyd, editors, *Rev. Comput. Chem.*, volume 17, pages 99–204. John Wiley & Sons, Inc., 2001.

[158] W.G. Richards, H.P. Trivedi, and D.L. Cooper. *Spin-orbit Coupling in Molecules*. International series of monographs on chemistry. Clarendon Press, 1981. ISBN 9780198556145.

[159] Sergei N. Yurchenko, Lorenzo Lodi, Jonathan Tennyson, and Andrey V. Stolyarov. Duo: A general program for calculating spectra of diatomic molecules. *Comput. Phys. Commun.*, 202:262 – 275, 2016. doi:http://dx.doi.org/10.1016/j.cpc.2015.12.021. URL http://www.sciencedirect.com/science/article/pii/S0010465516000023.

[160] J M Brown and A J Merer. Lambda-type doubling parameters for molecules in Π-electronic states of triplet and higher multiplicity. *J. Mol. Spectrosc.*, 74:488–494, 1979. doi:10.1016/0022-2852(79)90172-3.

[161] G. Herzberg. *Molecular Spectra and Molecular Structure: Spectra of diatomic molecules*. Molecular Spectra and Molecular Structure. Van Nostrand, 1950. URL https://books.google.co.uk/books?id=hwwJAQAAIAAJ.

[162] John M. Brown and Alan Carrington. *Rotational Spectroscopy of Diatomic Molecules*. Cambridge University Press, 2003.

[163] C. Alden Mead and Donald G. Truhlar. Conditions for the definition of a strictly diabatic electronic basis for molecular systems. *J. Chem. Phys.*, 77: 6090–6098, 1982. doi:10.1063/1.443853.

[164] David Simah, Bernd Hartke, and Hans-Joachim Werner. Photodissociation dynamics of H2S on new coupled ab initio potential energy surfaces. *J. Chem. Phys.*, 111(10):4523–4534, 1999. doi:10.1063/1.479214.

[165] Heesun An and Kyoung Koo Baeck. A practical and efficient diabatization that combines Lorentz and Laplace functions to approximate nonadiabatic coupling terms. *J. Chem. Phys.*, 143(19):194102, 2015. doi:10.1063/1.4935607.

[166] K.K. Baeck and H. An. Practical approximation of the non-adiabatic coupling terms for same-symmetry interstate crossings by using adiabatic potential energies only. *J. Chem. Phys.*, 146:064107, 2017. doi:10.1063/1.4975323.

[167] Mark W Spong, Seth Hutchinson, and M Vidyasagar. *Robot modeling and control*. John Wiley & Sons, Nashville, TN, 2 edition, February 2020.

[168] Bruno Siciliano, Lorenzo Sciavicco, Luigi Villani, and Giuseppe Oriolo. *Robotics: Modelling, Planning and Control*. Advanced Textbooks in Control and Signal Processing. Springer, London, England, 1 edition, November 2008. ISBN 1846286417.

[169] Akshit Lunia, Ashley Stevens, Cavender Holt, Rhyan Morgan, Joshua Norris, Shailendran Poyyamozhi, and Yehua Zhong. *Modeling, Motion Planning, and Control of Manipulators and Mobile Robots*. Open Textbooks, n.d. URL https://opentextbooks.clemson.edu/wangrobotics/chapter/chapter-1-introduction/.

[170] A. J. C. Varandas. Accurate ab initio potential energy curves for the classic Li-F ionic-covalent interaction by extrapolation to the complete basis set limit and modeling of the radial nonadiabatic coupling. *J. Chem. Phys.*, 131 (12):124128, 2009. doi:10.1063/1.3237028.

[171] T. Mondal and A. J. C. Varandas. The Jahn-Teller effect in the triply degenerate electronic state of methane radical cation. *J. Chem. Phys.*, 135(17): 174304, 2011. doi:10.1063/1.3658641.

[172] Ryan P Brady, Sergei N Yurchenko, Jonathan Tennyson, and Gap-Sue Kim. ExoMol line lists - LVI. The SO line list, MARVEL analysis of experimental transition data and refinement of the spectroscopic model. *Mon. Not. R. Astron. Soc.*, 527:6675–6690, 2023. doi:10.1093/mnras/stad3508.

[173] Jonathan Tennyson, Sergei N. Yurchenko, Jingxin Zhang, Charles A. Bowesman, Ryan P. Brady, Jeanna Buldyreva, Katy L. Chubb, Robert R. Gamache, Maire N. Gorman, Elizabeth R. Guest, Christian Hill, Kyriaki Kefala, A.E. Lynas-Gray, Thomas M. Mellor, Laura K. McKemmish, Georgi B. Mitev, Irina I. Mizus, Alec Owens, Zhijian Peng, Armando N. Perri, Marco Pezzella, Oleg L. Polyansky, Qianwei Qu, Mikhail Semenov, Oleksiy Smola, Andrei Solokov, Wilfrid Somogyi, Apoorva Upadhyay, Samuel O.M. Wright, and Nikolai F. Zobov. The 2024 release of the ExoMol database: Molecular line lists for exoplanet and other hot atmospheres. *J. Quant. Spectrosc. Radiat. Transf.*, 326:109083, 2024. doi:10.1016/j.jqsrt.2024.109083.

[174] H Hellmann. Zur Rolle der kinetischen Elektronenenergie für die zwischenatomaren Kröfte. *Eur. Phys. J. A*, 85(3-4):180–190, mar 1933.

[175] R P Feynman. Forces in molecules. *Phys. Rev.*, 56(4):340–343, aug 1939.

[176] Laxmi Prajapat, Pawel Jagoda, Lorenzo Lodi, Maire N. Gorman, Sergei N. Yurchenko, and Jonathan Tennyson. ExoMol molecular line lists - XXIII. Spectra of PO and PS. *Mon. Not. R. Astron. Soc.*, 472:3648–3658, 2017. doi:10.1093/mnras/stx2229. URL `http://dx.doi.org/10.1093/mnras/stx2229`.

[177] S. N. Yurchenko, Frances Sinden, Lorenzo Lodi, Christian Hill, Maire N. Gorman, and J. Tennyson. ExoMol Molecular linelists – XXIV: A new hot line list for silicon monohydride, SiH. *Mon. Not. R. Astron. Soc.*, 473:5324–5333, 2018. doi:10.1093/mnras/stx2738.

[178] A. A. Šurkus, R. J. Rakauskas, and A. B. Bolotin. The generalized potential-energy function for diatomic-molecules. *Chem. Phys. Lett.*, 105:291–294, 1984. doi:10.1016/0009-2614(84)85032-0.

[179] Alexander Dalgarno, R. McCarroll, and David Robert Bates. Adiabatic coupling between electronic and nuclear motion in molecules. *Proceedings of the Royal Society of London. Series A. Mathematical and Physical Sciences*, 237(1210):383–394, 1956. doi:10.1098/rspa.1956.0184.

[180] S. E. Butler. Radial couplings for charge transfer. *Phys. Rev. A*, 23:1–9, Jan 1981. doi:10.1103/PhysRevA.23.1. URL https://link.aps.org/doi/10.1103/PhysRevA.23.1.

[181] L. Wolniewicz and K. Dressler. Adiabatic potential curves and nonadiabatic coupling functions for the first five excited $^1\Sigma_g^+$ states of the hydrogen molecule. *J. Chem. Phys.*, 100(1):444–451, 01 1994. doi:10.1063/1.466957.

[182] L. Wolniewicz, T. Orlikowski, and G. Staszewska. $^1\Sigma_u$ and $^1\Pi_u$ states of the hydrogen molecule: Nonadiabatic couplings and vibrational levels. *J. Mol. Spectrosc.*, 238(1):118–126, 2006. ISSN 0022-2852. doi:10.1016/j.jms.2006.04.020.

[183] A. Riera. Elimination of asymptotic couplings in molecular dynamics. *Chem. Phys. Lett.*, 232(5):457–462, 1995. ISSN 0009-2614. doi:10.1016/0009-2614(94)01389-D.

[184] W. R. Thorson and J. B. Delos. Theory of near-adiabatic collisions. II. Scattering coordinate method. *Phys. Rev. A*, 18:135–155, Jul 1978. doi:10.1103/PhysRevA.18.135.

[185] J. B. Delos. Quantum theory of slow atomic collisions. *Intern. J. Quantum Chem.*, 24(S17):37–48, 1983. doi:10.1002/qua.560240806.

[186] Marvin H. Mittleman and Hsiang Tai. Low-Energy Atom-Atom Scattering: Corrections to the He-He Interaction. *Phys. Rev. A*, 8:1880–1891, Oct 1973. doi:10.1103/PhysRevA.8.1880.

[187] Laurence A. Nafie. Adiabatic molecular properties beyond the Born-Oppenheimer approximation. Complete adiabatic wave functions and vibrationally induced electronic current density. *J. Chem. Phys.*, 79(10):4950–4957, 11 1983. ISSN 0021-9606. doi:10.1063/1.445588.

[188] Xuezhi Bian, Yanze Wu, Tian Qiu, Zhen Tao, and Joseph E. Subotnik. A semiclassical non-adiabatic phase-space approach to molecular translations

and rotations: Surface hopping with electronic inertial effects. *J. Chem. Phys.*, 161(23):234114, 12 2024. ISSN 0021-9606. doi:10.1063/5.0242673.

[189] A. Macías and A. Riera. Ab initio quantum chemistry in the molecular model of atomic collisions. *Physics Reports*, 90(5):299–376, 1982. ISSN 0370-1573. doi:10.1016/0370-1573(82)90173-9.

[190] Hyun-Jin Kim, Chun-Woo Lee, and Yeon-Joo Cheong. Transition of the Rydberg series from the spectroscopic to the united atom region in LiH. *J. Phys. B: At. Mol. Opt. Phys.*, 49(23):235101, nov 2016. doi:10.1088/0953-4075/49/23/235101.

[191] A Macias, A Riera, P J Salas, and V H Ponce. United-atom limit of radial couplings between molecular wavefunctions. *J. Phys. B: At. Mol. Phys.*, 20 (2):295, jan 1987. doi:10.1088/0022-3700/20/2/013.

[192] B.C. Hall. *Lie Groups, Lie Algebras, and Representations: An Elementary Introduction*. Graduate Texts in Mathematics. Springer, 2003. ISBN 9780387401225.

[193] Sergio Blanes and Fernando Casas. On the convergence and optimization of the baker–campbell–hausdorff formula. *Linear Algebra and its Applications*, 378:135–158, 2004. ISSN 0024-3795. doi:10.1016/j.laa.2003.09.010.

[194] Ryan P Brady, Sergei N Yurchenko, Jonathan Tennyson, and Gap-Sue Kim. ExoMol line lists – LVI. The SO line list, MARVEL analysis of experimental transition data and refinement of the spectroscopic model. *Mon. Not. R. Astron. Soc.*, 527(3):6675–6690, 11 2023. ISSN 0035-8711. doi:10.1093/mnras/stad3508.

[195] Jeff Bezanson, Alan Edelman, Stefan Karpinski, and Viral B Shah. Julia: A fresh approach to numerical computing. *SIAM Review*, 59(1):65–98, 2017. doi:10.1137/141000671. URL https://epubs.siam.org/doi/10.1137/141000671.

[196] Patrick Kofod Mogensen, John Myles White, Asbjørn Nilsen Riseth, Tim Holy, Miles Lubin, Christof Stocker, Andreas Noack, Antoine Levitt, Christoph Ortner, Blake Johnson, Dahua Lin, Kristoffer Carlsson, Yichao Yu, Christopher Rackauckas, Josua Grawitter, Alex Williams, Ben Kuhn, Benoît Legat, Jeffrey Regier, cossio, Ron Rock, Thomas R. Covert, Benoit Pasquier,

Takafumi Arakaki, Alexey Stukalov, Andrew Clausen, Arno Strouwen, and Benjamin Deonovic. JuliaNLSolvers/Optim.jl: v1.7.2, August 2022. URL https://zenodo.org/record/7019119.

[197] Ryan P. Brady. Total Rovibronic Equivalence of the Adiabatic and Diabatic Representations of N-coupled State Diatomic Systems. *J. Chem. Phys.*, 2025. Submitted to the Journal of Computational Chemistry.

[198] V. P. Goranskii and E. A. Barsukova. Comparative spectral analysis of the peculiar red novae V838 Mon and V4332 Sgr in quiescence after their outbursts. *Astron. Rep.*, 51:126–142, 2007. doi:10.1134/S1063772907020072.

[199] T. Kaminski, M. Schmidt, R. Tylenda, M. Konacki, and M. Gromadzki. KECK/HIRES spectroscopy of V838 monocerotis in october 2005. *Astrophys. J. Suppl.*, 182:33–50, 2009. doi:10.1088/0067-0049/182/1/33.

[200] P. S. Murty. New identifications of YO and CeO in R-Cygni. *Astrophys. Lett.*, 23:7–9, 1982. URL http://adsabs.harvard.edu/pdf/1982ApL....23....7M.

[201] P. S. Murty. PI-gruis: Molecular identifications and spectral classification. *Astrophys. Space Sci.*, 94:295–305, 1983. doi:10.1007/BF00653719.

[202] J. M. Badie, L. Cassan, and B. Granier. Temperature of the gas phase in solar processes from simulation of the YO fluorescence spectra for A(2)Pi(1/2)-X-2 Sigma(+), A(2)Pi(3/2)-X-2 Sigma(+), B-2 Sigma(+)-X-2 Sigma(+) systems. *Eur. Phys. J.-Appl. Phys*, 32:61–64, 2005. doi:10.1051/epjap:2005070.

[203] J. M. Badie, L. Cassan, B. Granier, S. Agudelo Florez, and F. Chejne Janna. Gas temperature measurements in high concentration solar furnace environments: Evidence of nonequilibrium effects. *J. Sol. Energy Eng. Trans.-ASME*, 129:412–415, 2007. doi:10.1115/1.2769718.

[204] J. M. Badie, L. Cassan, and B. Granier. Solar induced fluorescence of YO: gas phase temperature measurements in solar processes. *Eur. Phys. J.-Appl. Phys*, 29:111–114, 2005. doi:10.1051/epjap:2004202.

[205] Mark Yeo, Matthew T. Hummon, Alejandra L. Collopy, Bo Yan, Boerge Hemmerling, Eunmi Chae, John M. Doyle, and Jun Ye. Rotational state microwave mixing for laser cooling of complex diatomic molecules. *Phys.*

Rev. Lett., 114:223003, 2015. doi:10.1103/PhysRevLett.114.223003. URL https://doi.org/10.1103/PhysRevLett.114.223003.

[206] Alejandra L. Collopy, Shiqian Ding, Yewei Wu, Ian A. Finneran, Loic Anderegg, Benjamin L. Augenbraun, John M. Doyle, and Jun Ye. 3D Magneto-Optical Trap of Yttrium Monoxide. *Phys. Rev. Lett.*, 121:213201, 2018. doi:10.1103/PhysRevLett.121.213201.

[207] Alejandra L. Collopy, Matthew T. Hummon, Mark Yeo, Bo Yan, and Jun Ye. Prospects for a narrow line MOT in YO. *New J. Phys*, 17:055008, 2015. doi:10.1088/1367-2630/17/5/055008.

[208] Goulven Quéméner and John L. Bohn. Shielding Σ 2 ultracold dipolar molecular collisions with electric fields. *Phys. Rev. A*, 93:012704, 2016. doi:10.1103/PhysRevA.93.012704. URL https://doi.org/10.1103/PhysRevA.93.012704.

[209] Skip Williams, David S. Green, Srinivasan Sethuraman, and Richard N. Zare. Detection of trace species in hostile environments using degenerate four-wave mixing: methylidyne radical (CH) in an atmospheric-pressure flame. *J. Am. Chem. Soc.*, 114:9122–9130, 1992. doi:10.1021/ja00049a053.

[210] Philippe Versailles, Graeme M.G. Watson, Antonio C.A. Lipardi, and Jeffrey M. Bergthorson. Quantitative CH measurements in atmospheric-pressure, premixed flames of C_1-C_4 alkanes. *Combust.*, 165:109–124, 2016. doi:10.1016/j.combustflame.2015.11.001.

[211] D. L. Lambert. The abundances of the elements in the solar photosphere - VIII. Revised abundances of carbon, nitrogen and oxygen. *Mon. Not. R. Astron. Soc.*, 182:249–272, 1978. doi:10.1093/mnras/182.2.249.

[212] F. Mélen, N. Grevesse, A.J. Sauval, C.B. Farmer, R.H. Norton, H. Bredohl, and I. Dubois. A new analysis of the vibration-rotation spectrum of CH from solar spectra. *J. Mol. Spectrosc.*, 134:305–313, 1989. doi:10.1016/0022-2852(89)90317-2.

[213] N. Grevesse, D.L. Lambert, A.J. Sauval, E.F. van Dishoeck, C.B. Farmer, and R.H. Norton. Vibration-rotation bands of CH in the solar infrared spectrum and the solar carbon abundance. *Astron. Astrophys.*, 242:488–495, 1991.

[214] Maria Womack, Barry L. Lutz, and R. Mark Wagner. Pre- and Postperihelion Abundances of Gas and Dust in Comet Halley. *Astrophys. J.*, 433:886, 1994. doi:10.1086/174697.

[215] P. Swings and L. Rosenfeld. Considerations Regarding Interstellar Molecules. *Astrophys. J.*, 86:483–486, 1937. doi:10.1086/143880.

[216] M. Jura and D. M. Meyer. An optical measurement of the population inversion of the ground state Lambda doublet of interstellar CH. *Astrophys. J.*, 294:238–241, 1985. doi:10.1086/163292.

[217] William B. Somerville and Ian A. Crawford. Observations of molecules in diffuse interstellar clouds. *J. Chem. Soc. Faraday Trans.*, 89:2261–2268, 1993. doi:10.1039/FT9938902261.

[218] D.J. Lien. A reanalysis of the interstellar CH abundance. *Astrophys. J.*, 284: 578–588, 1984. doi:10.1086/162440.

[219] Gordon J. Stacey, J. B. Lugten, and R. Genzel. Detection of Interstellar CH in the Far-Infrared. *Astrophys. J.*, 313:859, 1987. doi:10.1086/165025.

[220] Hong-Peng Jia and Elsje Alessandra Quadrelli. Mechanistic aspects of dinitrogen cleavage and hydrogenation to produce ammonia in catalysis and organometallic chemistry: relevance of metal hydride bonds and dihydrogen. *Chem. Soc. Rev.*, 43:547–564, 2014. doi:10.1039/C3CS60206K.

[221] Yongwen Ren, Chang Yu, Xinyi Tan, Qianbing Wei, Zhao Wang, Lin Ni, Linshan Wang, and Jieshan Qiu. Strategies to activate inert nitrogen molecules for efficient ammonia electrosynthesis: current status, challenges, and perspectives. *Energy Environ. Sci.*, 15:2776–2805, 2022. doi:10.1039/D2EE00358A.

[222] Antonio José Martín, Tatsuya Shinagawa, and Javier Pérez-Ramírez. Electrocatalytic Reduction of Nitrogen: From Haber-Bosch to Ammonia Artificial Leaf. *Chem*, 5(2):263–283, 2019. ISSN 2451-9294. doi:10.1016/j.chempr.2018.10.010.

[223] Darrell F Strobel. Chemistry and evolution of Titan's atmosphere. *Planet Space Sci.*, 12:244–244, 1982.

[224] R.R. Meier, James A.R. Samson, Y. Chung, E.-M. Lee, and Z.-X. He. Production of N^{+*} from $N_2 + h\nu$: Effective EUV emission yields from laboratory and dayglow data. *Planet Space Sci.*, 39(8):1197–1207, 1991. doi:10.1016/0032-0633(91)90171-6.

[225] Richard P Wayne. *Chemistry of atmospheres*. Oxford University Press, London, England, 3 edition, mar 2000.

[226] David C Knauth, B-G Andersson, Stephan R McCandliss, and H Warren Moos. The interstellar N_2 abundance towards HD 124314 from far-ultraviolet observations. *Nature*, 429(6992):636–638, jun 2004.

[227] Natalia Gelfand, Ksenia Komarova, Francoise Remacle, and Raphael D. Levine. On the Energy-specific Photodissociation Pathways of $^{14}N_2$ and $^{14}N^{15}N$ Isotopomers to N Atoms of Different Reactivity: A Quantum Dynamical Perspective. *Astrophys. J.*, 948(1):58, may 2023. doi:10.3847/1538-4357/acbef8.

[228] Natalia Gelfand, Francoise Remacle, and Raphael D. Levine. Recombination of N Atoms in a Manifold of Electronic States Simulated by Time-Reversed Nonadiabatic Photodissociation Dynamics of N_2. *J. Phys. Chem. Lett.*, 14 (19):4625–4630, 2023. doi:10.1021/acs.jpclett.3c00666.

[229] Junming Zhao Zhi Qin and Linhua Liu. Radiative transition probabilities between low-lying electronic states of N_2. *Mol. Phys.*, 117(18):2418–2433, 2019. doi:10.1080/00268976.2018.1562579.

[230] Alexander N. Smirnov, Victor G. Solomonik, Sergei N. Yurchenko, and Jonathan Tennyson. Spectroscopy of YO from first principles. *Phys. Chem. Chem. Phys.*, 21:22794–22810, 2019. doi:10.1039/C9CP03208H. URL http://dx.doi.org/10.1039/C9CP03208H.

[231] Ewine F. van Dishoeck. Photodissociation processes in the CH molecule. *J. Chem. Phys.*, 86:196–214, 1987. doi:10.1063/1.452610.

[232] Joseph Lo and Bernie D. Shizgal. Spectral convergence of the quadrature discretization method in the solution of the Schrödinger and Fokker-Planck equations: Comparison with sinc methods. *J. Chem. Phys.*, 125:194108, 2006. doi:10.1063/1.2378622.

[233] Marco Pezzella, Jonathan Tennyson, and Sergei N. Yurchenko. ExoMol photodissociation cross-sections - I. HCl and HF. *Mon. Not. R. Astron. Soc.*, 514: 4413–4425, 2022. doi:10.1093/mnras/stac1634.

[234] Sergei N Yurchenko, Emma Nogué, Ala'a A A Azzam, and Jonathan Tennyson. ExoMol line lists - XLVII. Rovibronic spectrum of aluminium monochloride (AlCl). *Mon. Not. R. Astron. Soc.*, 520(4):5183–5191, 2022. doi:10.1093/mnras/stac3757.

[235] Marco Pezzella, Sergei N. Yurchenko, and Jonathan Tennyson. A method for calculating temperature-dependent photodissociation cross sections and rates. *Phys. Chem. Chem. Phys.*, 23:16390–16400, 2021. doi:10.1039/D1CP02162A.

[236] J. Tennyson, M. Pezzella, Jingxin Zhang, and S. N. Yurchenko. Data structures for photoadsorption within the ExoMol project. *RASTI*, 2:231–237, 2023. doi:10.1093/rasti/rzad014.

[237] Forrest R. Gilmore. Potential energy curves for N_2, NO, O_2 and corresponding ions. *J. Quant. Spectrosc. Radiat. Transf.*, 5:369–389, 1965. doi:10.1016/0022-4073(65)90072-5.

[238] Jun Jiang, Hong-Zhou Ye, Klaas Nauta, Troy Van Voorhis, Timothy W. Schmidt, and Robert W. Field. Diabatic Valence-Hole States in the C_2 Molecule: "Putting Humpty Dumpty Together Again". *J. Phys. Chem. A*, 126:3090–3100, 2022. doi:10.1021/acs.jpca.2c00495.

[239] Jun Jiang. Diabatic Valence-Hole Concept. *J. Phys. Chem. A*, 128(17):3253–3265, 2024. doi:10.1021/acs.jpca.4c00289.

[240] Vitaly I. Korepanov and Daria M. Sedlovets. An asymmetric fitting function for condensed-phase Raman spectroscopy. *Analyst*, 143(11):2674–2679, 2018. doi:10.1039/C8AN00710A.

[241] Martin Schmid, Hans-Peter Steinrück, and J. Michael Gottfried. A new asymmetric Pseudo-Voigt function for more efficient fitting of XPS lines. *Surface and Interface Analysis*, 46(8):505–511, 2014. doi:10.1002/sia.5521.

[242] H. J. Werner, P. J. Knowles, R. Lindh, F. R. Manby, and M. Schütz. MOLPRO, a package of ab initio programs, 2010. see `http://www.molpro.net/`.

[243] Apostolos Kalemos, Aristides Mavridis, and Aristophanes Metropoulos. An accurate description of the ground and excited states of CH. *J. Chem. Phys.*, 111(21):9536–9548, 12 1999. doi:10.1063/1.480285.

[244] V. I. Pupyshev, E. A. Pazyuk, A. V. Stolyarov, M. Tamanis, and R. Ferber. Analogue of oscillation theorem for nonadiabatic diatomic states: application to the $A^1\Sigma^+$ and $b^3\Pi$ states of KCs. *Phys. Chem. Chem. Phys.*, 12:4809–4812, 201. doi:10.1039/B918384A.

[245] V. Pupyshev, E. Pazyuk, Andrey Stolyarov, Maris Tamanis, and Ruvin Ferber. On Oscillation Theorem for Two-Component Schrödinger Equation. *arXiv*, July 2009. doi:10.48550/arXiv.0907.1380.

[246] L.D. Landau and E.M. Lifshitz. *Quantum Mechanics*. Pergamon Press, New York, 1965.

[247] Vladimir Yu. Makhnev, Aleksandra A. Kyuberis, Nikolai F. Zobov, Lorenzo Lodi, Jonathan Tennyson, and Oleg L. Polyansky. High accuracy ab initio calculations of rotational–vibrational levels of the hcn/hnc system. *J. Phys. Chem. A*, 122(5):1326–1343, 2018. doi:10.1021/acs.jpca.7b10483.

[248] Malathe Khalil, Salman Mahmoud, Ryan P. Brady, Mubarak Almehairbi, Marko Gacesa, Sergei N. Yurchenko, Jonathan Tennyson, Amal Al Ghaferi, and Nayla El-Kork. Theoretical investigation of the $A\,^1\Pi - X\,^1\Sigma^+$, $B\,^1\Sigma^+ - X\,^1\Sigma^+$, $C\,^1\Sigma^+ - X\,^1\Sigma^+$, $D'\,^1\Sigma^+ - X\,^1\Sigma^+$ and $E\,^1\Pi - X\,^1\Sigma^+$. *Phys. Chem. Chem. Phys.*, 27:2783–2801, 2024. doi:10.1039/D4CP03418J.

[249] E G Lee, J Y Seto, T Hirao, P F Bernath, and R J Le Roy. FTIR emission spectra, molecular constants, and potential curve of ground state GeO. *J. Mol. Spectrosc.*, 194:197–202, 1999. doi:10.1006/jmsp.1998.7789.

[250] Hugh M. Hulburt and Joseph O. Hirschfelder. Potential Energy Functions for Diatomic Molecules. *J. Chem. Phys.*, 9:61–69, 1941. doi:10.1063/1.1750827.

[251] V.G. Ushakov, M. Semenov, S.N. Yurchenko, A. Yu. Ermilov, and E.S. Medvedev. Improved potential-energy and dipole-moment functions of the ground electronic state of phosphorus nitride. *J. Mol. Spectrosc.*, page 111804, 2023. doi:10.1016/j.jms.2023.111804.

[252] Gabriele Cazzoli, Lino Cludi, and Cristina Puzzarini. Microwave spectrum of (PN)-N-14 and (PN)-N-15: Spectroscopic constants and molecular structure. *J. Molec. Struct. (THEOCHEM)*, 780-81:260–267, 2006. doi:10.1016/j.molstruc.2005.07.010.

[253] A. Bernard, R. Bacis, and P. Luc. Fourier-transform spectroscopy: Extensive analysis of the A2-PI–X2-SIGMA+ and B2-SIGMA+–X2-SIGMA+ systems of yttrium-oxide. *Astrophys. J.*, 227:338–348, 1979. doi:10.1086/156736.

[254] Deping Zhang, Qiang Zhang, Boxing Zhu, Jingwang Gu, Bingbing Suo, Yang Chen, and Dongfeng Zhao. High-resolution electronic spectra of yttrium oxide (YO): The D-X transition. *J. Chem. Phys.*, 146:114303, 2017. doi:10.1063/1.4978335.

[255] P. M. Solomon and William Klemperer. The Formation of Diatomic Molecules in Interstellar Clouds. , 178:389–422, December 1972. doi:10.1086/151799.

[256] Y. P. Viala, C. Letzelter, M. Eidelsberg, and F. Rostas. The photodissociation of interstellar CO. , 193(1-2):265–272, March 1988.

[257] M. H. Bortner, R. H. Kummler, and L. S. Jaffe. Carbon monoxide in the earth's atmosphere. *Water, Air, and Soil Pollution*, 3(1):17–52, March 1974. ISSN 1573-2932. doi:10.1007/BF00282725. URL 10.1007/BF00282725.

[258] A.C. Vandaele, A. Mahieux, S. Chamberlain, B. Ristic, S. Robert, I.R. Thomas, L. Trompet, V. Wilquet, and J.L. Bertaux. Carbon monoxide observed in venus' atmosphere with soir/vex. *Icarus*, 272: 48–59, 2016. ISSN 0019-1035. doi:10.1016/j.icarus.2016.02.025. URL https://www.sciencedirect.com/science/article/pii/S0019103516000944.

[259] R.T. Clancy, D.O. Muhleman, and B.M. Jakosky. Variability of carbon monoxide in the mars atmosphere. *Icarus*, 55(2):282–301, 1983. ISSN 0019-1035. doi:10.1016/0019-1035(83)90083-0. URL https://www.sciencedirect.com/science/article/pii/0019103583900830.

[260] A. A. Penzias, P. M. Solomon, K. B. Jefferts, and R. W. Wilson. Carbon Monoxide Observations of Dense Interstellar Clouds. , 174:L43, May 1972. doi:10.1086/180945.

[261] H. Olofsson, P. Bergman, K. Eriksson, and B. Gustafsson. Carbon stars with episodic mass loss: observations and models of molecular emission from detached circumstellar shells. , 311:587–615, July 1996.

[262] Quinn M. Konopacky, Travis S. Barman, Bruce A. Macintosh, and Christian Marois. Detection of carbon monoxide and water absorption lines in an exoplanet atmosphere. *Science*, 339:1398–1401, 2013. doi:10.1126/science.1232003.

[263] Jean-Michel Désert, Alain Lecavelier des Etangs, Guillaume Hébrard, David K. Sing, David Ehrenreich, Roger Ferlet, and Alfred Vidal-Madjar. Search for Carbon Monoxide in the Atmosphere of the Transiting Exoplanet HD 189733b. *Astrophys. J.*, 699(1):478–485, July 2009. doi:10.1088/0004-637X/699/1/478.

[264] Paolo Giacobbe, Matteo Brogi, Siddharth Gandhi, and et al. Five carbon- and nitrogen-bearing species in a hot giant planet's atmosphere. *Nature*, 592 (7855):205–208, 2021. doi:10.1038/s41586-021-03381-x.

[265] A. W. Mantz and J.-P. Maillard. Emission spectra with a high resolution Fourier transform spectrometer: CO spectra and their astrophysical importance. *J. Mol. Spectrosc.*, 53:466–478, 1974. doi:10.1016/0022-2852(74)90083-6.

[266] Meng Zhang and Deheng Shi. Transition properties of the x1+, i1, a1, d1, b1+, and a3 states of carbon monoxide. *Computational and Theoretical Chemistry*, 1202:113302, 2021. doi:10.1016/j.comptc.2021.113302.

[267] Yanjun Du, Keishiro Tamura, Sampson Moore, Zhimin Peng, Tomohiro Nozaki, and Peter J. Bruggeman. Co(¡i¿b¡/i¿ ¡sup¿1¡/sup¿i£¡sup¿+¡/sup¿→¡i¿a¡/i¿ ¡sup¿1¡/sup¿i) angstrom system for gas temperature measurements in co¡sub¿2¡/sub¿ containing plasmas. *PLASMA CHEMISTRY AND PLASMA PROCESSING*, 37:29–41, 2017. doi:10.1007/s11090-016-9759-5.

[268] Sean D. McGuire, Augustin C. Tibere-Inglesse, Pierre B. Mariotto, Brett A. Cruden, and Christophe O. Laux. Measurements and modeling of co 4th

positive (a-x) radiation. *J. Quant. Spectrosc. Radiat. Transf.*, 245:106855, 2020. doi:10.1016/j.jqsrt.2020.106855.

[269] Shota Yamada, Yuki Morita, Atsushi Nezu, and Hiroshi Akatsuka. Nonequilibrium characteristics in the rotational temperature of co excited states in microwave discharge co¡sub¿2¡/sub¿ plasma. *JAPANESE JOURNAL OF APPLIED PHYSICS*, 60:046005, 2021. doi:10.35848/1347-4065/abee04.

[270] Malathe Khalil, Salman Mahmoud, Ryan P. Brady, Mubarak Almehairbi, Marko Gacesa, Sergei N. Yurchenko, Jonathan Tennyson, Amal Al Ghaferi, and Nayla El-Kork. Theoretical investigation of the a1–x1+, b1+–x1+, c1+–x1+, and e1–x1+ transitions of the co molecule. *Phys. Chem. Chem. Phys.*, 27:2783–2801, 2025. doi:10.1039/D4CP03418J.

[271] S. N. Yurchenko, L. Lodi, J. Tennyson, and A. V. Stolyarov. Duo: a general program for calculating spectra of diatomic molecules. *Comput. Phys. Commun.*, 202:262–275, 2016. doi:10.1016/j.cpc.2015.12.021.

[272] W. Ubachs, P.C. Hinnen, P. Hansen, S. Stolte, W. Hogervorst, and P. Cacciani. Laser spectroscopic studies of thec1+,v= 0 andv= 1 states of co. *J. Mol. Spectrosc.*, 174(2):388–396, 1995. doi:10.1006/jmsp.1995.0010.

[273] A. G. Gaydon. *Spectroscopy and combustion theory*. Chapman and Hall, Ltd., London, 2 edition, 1948.

[274] Michael Wang. Fuel cycle analysis of conventional and alternative fuel vehicles. In Cutler J. Cleveland, editor, *Encyclopedia of Energy*, pages 771–789. Elsevier, New York, 2004. doi:https://doi.org/10.1016/B0-12-176480-X/00195-9.

[275] George D. Thurston. Outdoor air pollution: Sources, atmospheric transport, and human health effects. In Stella R. Quah, editor, *International Encyclopedia of Public Health (Second Edition)*, pages 367–377. Academic Press, Oxford, second edition edition, 2017. doi:https://doi.org/10.1016/B978-0-12-803678-5.00320-9.

[276] Xiaochuan Pan. Sulfur oxides⋆. In Jerome Nriagu, editor, *Encyclopedia of Environmental Health (Second Edition)*, pages 823–829. Elsevier, Oxford, second edition edition, 2019. doi:https://doi.org/10.1016/B978-0-12-409548-9.11333-8.

[277] X. Pan. Sulfur oxides: Sources, exposures and health effects. In J.O. Nriagu, editor, *Encyclopedia of Environmental Health*, pages 290–296. Elsevier, Burlington, 2011. doi:https://doi.org/10.1016/B978-0-444-52272-6.00069-6.

[278] C. A. Gottlieb and J. A. Ball. Interstellar sulfur monoxide. *Astrophys. J.*, 184:L59–L64, 1973. doi:10.1086/181288.

[279] S Saito. Microwave spectrum of SO radical in first electronically excited state, 1DELTA. *J. Chem. Phys.*, 53:2544–2545, 1970. doi:10.1063/1.1674365.

[280] C. A. Gottlieb, E. W. Gottlieb, M. M. Litvak, J. A. Ball, and H. Penfield. Observations of interstellar sulfur monoxide. *Astrophys. J.*, 219:77–94, 1978. URL http://adsabs.harvard.edu/pdf/1978ApJ...219...77G.

[281] C. Codella and D. Muders. SO observations towards Bok globules. *Mon. Not. R. Astron. Soc.*, 291:337–344, 1997. doi:10.1093/mnras/291.2.337.

[282] G A Blake, E C Sutton, C R Masson, and T G Phillips. Molecular Abundances in OMO-1 - The Chemical-Composition of Interstellar Molecular Clouds and the Influence of Massive Star Formation. *Astron. J.*, 315:621–645, 1987. doi:10.1086/165165.

[283] E Lellouch. Urey Prize Lecture - Io's atmosphere: Not yet understood. *Icarus*, 124(1):1–21, 1996. doi:10.1006/icar.1996.0186.

[284] I. de Pater, H. Roe, J. R. Graham, D. F. Strobel, and P. Bernath. Detection of the forbidden SO a $^1\Delta \rightarrow$ X $^3\Sigma^-$ rovibronic transition on Io at 1.7 μm. *Icarus*, 156:296–301, 2002. doi:10.1006/icar.2001.6787.

[285] C. Y. Na, L. W. Esposito, and T. E. Skinner. International ultraviolet explorer observation of Venus SO_2 and SO. *J. Geophys. Res. Atmos.*, 95:7485–7491, 1990. doi:10.1029/JD095iD06p07485.

[286] D. A. Belyaev, Franck Montmessin, Jean-Loup Bertaux, Arnaud Mahieux, A. A. Fedorova, O. I. Korablev, Emmanuel Marcq, Yuk L. Yung, and Xi Zhang. Vertical profiling of SO_2 and so above Venus' clouds by SPICAV/SOIR solar occultations. *Icarus*, 217:740–751, 2012. doi:10.1016/j.icarus.2011.09.025.

[287] Mikhail Yu. Zolotov and Bruce Jr. Fegley. Volcanic production of sulfur monoxide (so) on io. *Icarus*, 132:431–434, 1998. doi:10.1006/ICAR.1998.5906.

[288] Richard Hobbs, Paul B Rimmer, Oliver Shorttle, and Nikku Madhusudhan. Sulfur chemistry in the atmospheres of warm and hot Jupiters. *Mon. Not. R. Astron. Soc.*, 506:3186–3204, 2021. doi:10.1093/mnras/stab1839.

[289] Vladimir A. Krasnopolsky. A photochemical model for the Venus atmosphere at 47-112 km. *Icarus*, 218(1):230–246, 2012. doi:10.1016/j.icarus.2011.11.012.

[290] S. Pacheco-Vazquez, A. Fuente, M. Agundez, C. Pinte, T. Alonso-Albi, R. Neri, J. Cernicharo, J. R. Goicoechea, O. Berne, L. Wiesenfeld, R. Bachiller, and B. Lefloch. Chemical composition of the circumstellar disk around AB Aurigae. *Astron. Astrophys.*, 578, 2015. doi:10.1051/0004-6361/201425347.

[291] Jacob C. Laas and Paola Caselli. Modeling sulfur depletion in interstellar clouds. *Astron. Astrophys.*, 624:A108, APR 22 2019. doi:10.1051/0004-6361/201834446.

[292] Thomas H. G. Vidal, Jean-Christophe Loison, Adam Yassin Jaziri, Maxime Ruaud, Pierre Gratier, and Valentine Wakelam. On the reservoir of sulphur in dark clouds: chemistry and elemental abundance reconciled. *Mon. Not. R. Astron. Soc.*, 469:435–447, 2017. doi:10.1093/mnras/stx828.

[293] Z. Rustamkulov, D. K. Sing, S. Mukherjee, E. M. May, J. Kirk, E. Schlawin, M. R. Line, C. Piaulet, A. L. Carter, N. E. Batalha, J. M. Goyal, M. López-Morales, J. D. Lothringer, R. J. MacDonald, S. E. Moran, K. B. Stevenson, H. R. Wakeford, N. Espinoza, J. L. Bean, N. M. Batalha, B. Benneke, Z. K. Berta-Thompson, I. J. M. Crossfield, P. Gao, L. Kreidberg, D. K. Powell, P. E. Cubillos, N. P. Gibson, J. Leconte, K. Molaverdikhani, N. K. Nikolov, V. Parmentier, P. Roy, J. Taylor, J. D. Turner, P. J. Wheatley, K. Aggarwal, E. Ahrer, M. K. Alam, L. Alderson, N. H. Allen, A. Banerjee, S. Barat, D. Barrado, J. K. Barstow, T. J. Bell, J. Blecic, J. Brande, S. Casewell, Q. Changeat, K. L. Chubb, N. Crouzet, T. Daylan, L. Decin, J. Désert, T. Mikal-Evans, A. D. Feinstein, L. Flagg, J. J. Fortney, J. Harrington, K. Heng, Y. Hong, R. Hu, N. Iro, T. Kataria, E. M.-R. Kempton, J. Krick, M. Lendl, J. Lillo-Box, A. Louca, J. Lustig-Yaeger, L. Mancini, M. Mansfield, N. J. Mayne,

Y. Miguel, G. Morello, K. Ohno, E. Palle, D. J. M. Petit dit de la Roche, B. V. Rackham, M. Radica, L. Ramos-Rosado, S. Redfield, L. K. Rogers, E. L. Shkolnik, J. Southworth, J. Teske, P. Tremblin, G. S. Tucker, O. Venot, W. C. Waalkes, L. Welbanks, X. Zhang, and S. Zieba. Early Release Science of the exoplanet WASP-39b with JWST NIRSpec PRISM. *Nature*, 614: 659–663, 2023. doi:10.1038/s41586-022-05677-y.

[294] S-M Tsai et al. Photochemically produced SO_2 in the atmosphere of WASP-39b. *Nature Astron.*, 617:483–487, 2023. doi:10.1038/s41586-023-05902-2.

[295] F. O. Clark and D. R. Johnson. Magnetic-fields in Orion molecular cloud from Zeeman effect in SO. *Astrophys. J.*, 191:L87–L91, 1974. doi:10.1086/181556.

[296] Gabriele Cazzoli, Valerio Lattanzi, Sonia Coriani, Juergen Gauss, Claudio Codella, Andres Asensio Ramos, Jose Cernicharo, and Cristina Puzzarini. Zeeman effect in sulfur monoxide A tool to probe magnetic fields in star forming regions. *Astron. Astrophys.*, 605:A20, 2017. doi:10.1051/0004-6361/201730858.

[297] L. Chernin and C. Masson. Observations of SO and SiO in the outflow from NGC-2071. *Astrophys. J.*, 403:L21–L24, 1993. doi:10.1086/186712.

[298] M. Y. Amin, M. S. Elnawawy, and M. A. Elshalaby. Shock waves and the chemical structure of interstellar clouds. *Astrophys. Space Sci.*, 185:277–294, 1991. doi:10.1007/BF00643194.

[299] H. C. Miller, K. Yamasaki, J. E. Smedley, and S. R. Leone. An optically pumped ultraviolet-laser on SO($B^3\Sigma^-$-$X^3\Sigma^-$). *Chem. Phys. Lett.*, 181:250–254, 1991. doi:10.1016/0009-2614(91)90362-D.

[300] B. C. Stuart, S. M. Cameron, and H. T. Powell. SO($A^3\Pi \leftarrow X^3\Sigma^-$) saturation by narrow and broad-band KRF excitation. *Chem. Phys. Lett.*, 191:273–278, 1992. doi:10.1016/0009-2614(92)85300-Y.

[301] Andrei T. Patrascu, Christian Hill, Jonathan Tennyson, and Sergei N. Yurchenko. Study of the electronic and rovibronic structure of the $X^2\Sigma^+$, $A^2\Pi$, and $B^2\Sigma^+$ states of AlO. *J. Chem. Phys.*, 141:144312, 2014. doi:10.1063/1.4897484.

[302] A. C. Borin and F. R. Ornellas. The lowest triplet and singlet electronic states of the molecule SO. *Chem. Phys.*, 247:351–364, 1999. doi:10.1016/S0301-0104(99)00229-3.

[303] A. Boca and B. Friedrich. Fine structure, alignment, and orientation of $^{32}S^{16}O$ and $^{16}O^{18}O$ molecules in congruent electric and magnetic fields. *J. Chem. Phys.*, 112:3609–3619, 2000. doi:10.1063/1.480514.

[304] P. A. Denis and O. N. Ventura. Density functional investigation of atmospheric sulfur chemistry. I. Enthalpy of formation of HSO and related molecules. *Intern. J. Quantum Chem.*, 80:439–453, 2000. doi:10.1002/1097-461X(2000)80:3<439::AID-QUA14>3.0.CO;2-O.

[305] Yanan Feng and Zunlue Zhu. Dipole-allowed transitions between the $X^3\Sigma^-$, $A'^3\Delta$, $A''^3\Sigma^+$, $A^3\Pi$, $B^3\Sigma^-$, and $C^3\Pi$ states of the sulfur monoxide radical. *J. Quant. Spectrosc. Radiat. Transf.*, 234:98–107, 2019. doi:10.1016/j.jqsrt.2019.05.032.

[306] R. N. Dixon, P. W. Tasker, and G. G. Balintkurti. Ground and low-lying excited potential curves of SO: Pseudopotential multi-structure valence-bond calculation. *Mol. Phys.*, 34:1455–1471, 1977. doi:10.1080/00268977700102661.

[307] F. R. Ornellas and A. C. Borin. The hidden facet of the C-3 Pi state of SO. *Mol. Phys.*, 94:139–145, 1998. doi:10.1080/002689798168420.

[308] R. Klotz, C. M. Marian, S. D. Peyerimhoff, B. A. Hess, and R. J. Buenker. Study of the dependence of spin-orbit matrix-elements on AO basis set composition for inner and valence shells: Results for the multiplet splitting of $X^3\Sigma^-$ and $C^3\Pi$ of SO and $X^2\Pi$ in SO+. *Chem. Phys.*, 76:367–383, 1983. doi:10.1016/0301-0104(83)85219-7.

[309] C. M. Andreazza and E. P. Marinho. Formation of SO, SO^+, and S_2 by radiative association. *Astrophys. J.*, 624:1121–1125, 2005. doi:10.1086/429234.

[310] F. Lique, A. Spielfiedel, M.-L. Dubernet, and N. Feautrier. Rotational excitation of sulfur monoxide by collisions with helium at low temperature. *J. Chem. Phys.*, 123:134316, 2005. doi:10.1063/1.2004994.

[311] A. C. Borin and F. R. Ornellas. A theoretical investigation of the A (II)-I-3 – X $^3\Sigma^-$ transition in SO. *Chem. Phys. Lett.*, 322:149–156, 2000. doi:10.1016/S0009-2614(00)00406-1.

[312] Le Yu and Wensheng Bian. Extensive Theoretical Study on Electronically Excited States and Predissociation Mechanisms of Sulfur Monoxide Including Spin-Orbit Coupling. *J. Comput. Chem.*, 32:1577–1588, 2011. doi:10.1002/jcc.21737.

[313] Jie-min Wang, Heng-qiang Feng, Jin-feng Sun, De-heng Shi, and Zun-lue Zhu. Spectroscopic Parameters of X $^3\Sigma^-$, a $^1\Delta$, and A $^3\Delta$ Electronic States of SO Radical. *Chin. J. Chem. Phys.*, 25:533–539, 2012. doi:10.1088/1674-0068/25/05/533-539.

[314] F. D. Wayne. Origin of variation with vibrational and rotational state of fine-structure constants in O2, SO and S2. *Chem. Phys. Lett.*, 31:97–101, 1975. doi:10.1016/0009-2614(75)80066-2.

[315] W. C. Swope, Y. P. Lee, and H. F. Schaefer. Sulfur oxide: Low-lying bound molecular electronic states of SO. *J. Chem. Phys.*, 71:3761–3769, 1979. doi:10.1063/1.438783.

[316] G. Theodorakopoulos, S. D. Peyerimhoff, and R. J. Buenker. Abinitio configuration-interaction study of the $X^3\Sigma^-$,$a^1\Delta$ and 1-SIGMA+ states of SO and S-2. *Chem. Phys. Lett.*, 81:413–420, 1981. doi:10.1016/0009-2614(81)85641-2.

[317] P. Mathies, F. O. Sladky, and B. M. Rode. A quantum chemical investigation of CO, NF, SO, CF-2 and their combination products. *J. Molec. Struct. (THEOCHEM)*, 7:335–340, 1982. doi:10.1016/0166-1280(82)80072-9.

[318] R. Klotz, C. M. Marian, S. D. Peyerimhoff, B. A. Hess, and R. J. Buenker. Calculation of spin-forbidden radiative transitions using correlated wavefunctions: Lifetimes of B1-SIGMA-+, A1-DELTA-states in O2, S2 and SO. *Chem. Phys.*, 89:223–236, 1984. doi:10.1016/0301-0104(84)85311-2.

[319] A. Balaban, G. R. Demare, and R. A. Poirier. Abinitio study of neutral O_2, SO, S_2, C_2H_2 and their monocations and dications. *J. Molec. Struct. (THEOCHEM)*, 52:103–119, 1989. doi:10.1016/0166-1280(89)80027-2.

[320] K. A. Peterson and R. C. Woods. An abinitio study of the 24 electron radicals PF, SO, NCl, SF^+, ClO^+, SiF^-, PO^-, NS^-, and CCl^- in their $X^3\Sigma^-$ electronic states. *J. Chem. Phys.*, 93:1876–1888, 1990. doi:10.1063/1.459065.

[321] M. P. Fulscher, M. Jaszunski, B. O. Roos, and W. P. Kraemer. A restricted active space self-consistent field and multireference configuration-interaction study of the lifetime of the $A^3\Pi$ state of SO. *J. Chem. Phys.*, 96:504–512, 1992. doi:10.1063/1.462487.

[322] Peter F. Bernath and Dror M. Bittner. Line list for the $a^1\delta$-$x^3\sigma^-$ transition of so: Assignment of the 1.69 micron feature on io. *J. Quant. Spectrosc. Radiat. Transf.*, 240:106686, 2020. ISSN 0022-4073. doi:10.1016/j.jqsrt.2019.106686.

[323] C. W. Bauschlicher and A. Ricca. Atomization energies of SO and SO(2): Basis set extrapolation revisited. *J. Phys. Chem. A*, 102:8044–8050, 1998. doi:10.1021/jp9819691.

[324] B. S. Jursic. Theoretical study of the atomization energy and geometry of sulfur dioxide and sulfur monoxide. *J. Molec. Struct. (THEOCHEM)*, 467: 187–193, 1999. doi:10.1016/S0166-1280(98)00484-9.

[325] Karolis Sarka and Shinkoh Nanbu. Total Absorption Cross Section for UV Excitation of Sulfur Monoxide. *J. Phys. Chem. A*, 123:3697–3702, 2019. doi:10.1021/acs.jpca.9b01921.

[326] E. V. Martin. The band spectrum of sulphur monoxide. *Phys. Rev.*, 41:167–193, 1932. doi:10.1103/PhysRev.41.167.

[327] T. Klaus, S. P. Belov, A. H. Saleck, G. Winnewisser, and E. Herbst. Rotational spectrum of SO in the terahertz region. *J. Mol. Spectrosc.*, 168: 235–247, 1994. doi:10.1006/jmsp.1994.1274.

[328] Satoshi Yamamoto. The microwave spectrum of SO in the $b^1\Sigma^+$ electronic state. *Chem. Phys. Lett.*, 212:113–117, 1993. doi:10.1016/0009-2614(93)87117-L.

[329] R Colin. $b^1\Sigma^+$-$X^3\Sigma^-$ BAND SYSTEM OF SO. *Can. J. Phys.*, 46:1539–1546, 1968. doi:10.1139/p68-480. URL https://doi.org/10.1139/p68-480.

[330] R. Colin. Spectrum of SO. Evidence for a new $^(3)\Delta$ state. *J. Chem. Soc. Faraday Trans.*, 78:1139–1147, 1982. doi:10.1039/F29827801139.

[331] K. D. Setzer, E. H. Fink, and D. A. Ramsay. High-Resolution Fourier-transform study of the b(1)Sigma(+)-¿ X (3)Sigma(-) and a(1)Delta -¿ X (3)Sigma(-) transitions of SO. *J. Mol. Spectrosc.*, 198:163–174, 1999. doi:10.1006/jmsp.1999.7943.

[332] H. Kanamori, J. E. Butler, K. Kawaguchi, C. Yamada, and E. Hirota. Infrared diode-laser kinetic spectroscopy of transient molecules produced by excimer laser photolysis: Application to the SO radical. *J. Mol. Spectrosc.*, 113:262–268, 1985. doi:10.1016/0022-2852(85)90135-3.

[333] M. Wong, T. Amano, and P. Bernath. Observation of the v=3[-0 band of SO(X3DELTA-) with a difference frequency laser. *J. Chem. Phys.*, 77:2211–2213, 1982. doi:10.1063/1.444006.

[334] H. Kanamori, E. Tiemann, and E. Hirota. Infrared diode-laser spectroscopy of SO in the $a^1\Delta state generated by the photolysis of Cl_2SO$ AT 193 nm. *J. Chem. Phys.*, 89:621–624, 1988. doi:10.1063/1.455237.

[335] T. Klaus, S. P. Belov, and G. Winnewisser. Submillimeter-wave rotational spectra of SO isotopomers in the electronic states a(1)Delta and b(1)Sigma(+). *J. Mol. Spectrosc.*, 186:416–421, 1997. doi:10.1006/jmsp.1997.7450.

[336] W. W. Clark and F. C. Delucia. MIcrowave-spectrum and rotational structure of DELTA-1 and SIGMA-3 electronic states of sulfur monoxide. *J. Mol. Spectrosc.*, 60:332–342, 1976. doi:10.1016/0022-2852(76)90136-3.

[337] G. Cazzoli, L. Cludi, G. Cotti, C. D. Esposti, and L. Dore. Far-infrared spectrum of SO in the (3)SIGMA and (1)Triangle electronic states. *J. Mol. Spectrosc.*, 167:468–471, 1994. doi:10.1006/jmsp.1994.1251.

[338] F. J. Lovas, R. D. Suenram, T. Ogata, and S. Yamamoto. Microwave-spectra and electric-dipole moments for low-J levels of interstellar radicals: SO, C2S, C3S, C-HC3, CH2CC, and C-C3H2. *Astrophys. J.*, 399:325–329, 1992. doi:10.1086/171928.

[339] M. Bogey, S. Civis, B. Delcroix, C. Demuynck, A. F. Krupnov, J. Quiguer, M. Y. Tretyakov, and A. Walters. Microwave spectrum up to 900 GHz of SO created in highly excited states by electric discharge and UV-laser photolysis. *J. Mol. Spectrosc.*, 182:85–97, 1997. doi:10.1006/jmsp.1996.7218.

[340] Peter F. Bernath, Ryan Johnson, and Jacques Liévin. Line lists for the b $^1\sigma^+$–x $^3\sigma^-$ and a $^1\delta$–x $^3\sigma^-$ transitions of so. *J. Quant. Spectrosc. Radiat. Transf.*, 272:107772, 2021. ISSN 0022-4073. doi:10.1016/j.jqsrt.2021.107772.

[341] Peter F. Bernath, Ryan Johnson, and Jacques Liévin. Line lists for X $^3\Sigma^-$ and a $^1\Delta$ vibration-rotation bands of SO. *J. Quant. Spectrosc. Radiat. Transf.*, page 108317, 2022. doi:10.1016/j.jqsrt.2022.108317.

[342] Jonathan Tennyson, Kelsey Hulme, Omree K Naim, and Sergei N Yurchenko. Radiative lifetimes and cooling functions for astrophysically important molecules. *J. Phys. B: At. Mol. Opt. Phys.*, 49:044002, 2016.

[343] J. M. F. Elks and C. M. Western. The A (II)-I-3 state of SO. *J. Chem. Phys.*, 110:7699–7706, 1999. doi:10.1063/1.478681.

[344] W. H. Smith. Absolute transition probabilities for some electronic states of CS, SO and S2. *J. Quant. Spectrosc. Radiat. Transf.*, 9:1191–1199, 1969. doi:10.1016/0022-4073(69)90106-X.

[345] K. Yamasaki, F. Taketani, S. Tomita, K. Sugiura, and I. Tokue. Collision-free lifetimes of SO(B $^3\Sigma^-, v' = 0, 1$, and 2) and vibrational level dependence of deactivation by He. *J. Phys. Chem. A*, 107:2442–2447, 2003. doi:10.1021/jp027129a.

[346] C. P. Endres, S. Schlemmer, P. Schilke, J. Stutzki, and H. S. P. Müller. The Cologne Database for Molecular Spectroscopy, CDMS, in the Virtual Atomic and Molecular Data Centre, VAMDC. *J. Mol. Spectrosc.*, 327:95–104, 2016. doi:10.1016/j.jms.2016.03.005.

[347] A. Kramida, Yu. Ralchenko, J. Reader, and NIST ASD Team. NIST atomic spectra database (version 5.10). [Online], 2022. URL https://physics.nist.gov/asd. [Accessed on Tue Apr 04 2023].

[348] I. E. Gordon, L. S. Rothman, R. J. Hargreaves, R. Hashemi, E. V. Karlovets, F. M. Skinner, E. K. Conway, C. Hill, R. V. Kochanov, Y. Tan, P. Wcisło, A. A. Finenko, K. Nelson, P. F. Bernath, M. Birk, V. Boudon, A. Campargue, K. V. Chance, A. Coustenis, B. J. Drouin, J.–M. Flaud, R. R. Gamache, J. T. Hodges, D. Jacquemart, E. J. Mlawer, A. V. Nikitin, V. I. Perevalov, M. Rotger, J. Tennyson, G. C. Toon, H. Tran, V. G. Tyuterev, E. M. Adkins, A. Baker, A. Barbe, E. Canè, A. G. Császár, A. Dudaryonok, O. Egorov,

A. J. Fleisher, H. Fleurbaey, A. Foltynowicz, T. Furtenbacher, J. J. Harrison, J.–M. Hartmann, V.–M. Horneman, X. Huang, T. Karman, J. Karns, S. Kassi, I. Kleiner, V. Kofman, F. Kwabia–Tchana, N. N. Lavrentieva, T. J. Lee, D. A. Long, A. A. Lukashevskaya, O. M. Lyulin, V. Yu. Makhnev, W. Matt, S. T. Massie, M. Melosso, S. N. Mikhailenko, D. Mondelain, H. S. P. Müller, O. V. Naumenko, A. Perrin, O. L. Polyansky, E. Raddaoui, P. L. Raston, Z. D. Reed, M. Rey, C. Richard, R. Tóbiás, I. Sadiek, D. W. Schwenke, E. Starikova, K. Sung, F. Tamassia, S. A. Tashkun, J. Vander Auwera, I. A. Vasilenko, A. A. Vigasin, G. L. Villanueva, B. Vispoel, G. Wagner, A. Yachmenev, and S. N. Yurchenko. The HITRAN2020 molecular spectroscopic database. *J. Quant. Spectrosc. Radiat. Transf.*, 277:107949, 2022. doi:10.1016/j.jqsrt.2021.107949.

[349] H. J. Werner, P. J. Knowles, G. Knizia, F. R. Manby, M. Schütz, P. Celani, W. Györffy, D. Kats, T. Korona, R. Lindh, A. Mitrushenkov, G. Rauhut, K. R. Shamasundar, T. B. Adler, R. D. Amos, A. Bernhardsson, A. Berning, D. L. Cooper, M. J. O. Deegan, A. J. Dobbyn, F. Eckert, E. Goll, C. Hampel, A. Hesselmann, G. Hetzer, T. Hrenar, G. Jansen, C. Köppl, Y. Liu, A. W. Lloyd, R. A. Mata, A. J. May, S. J. McNicholas, W. Meyer, M. E. Mura, A. Nicklass, D. P. O'Neill, P. Palmieri, D. Peng, K. Pflüger, R. Pitzer, M. Reiher, T. Shiozaki, H. Stoll, A. J. Stone, R. Tarroni, T. Thorsteinsson, and M. Wang. Molpro, version 2015.1, a package of ab initio programs. http://www.molpro.net, 2015.

[350] Thom H. Dunning Jr. Gaussian basis sets for use in correlated molecular calculations. I. The atoms boron through neon and hydrogen . *J. Chem. Phys.*, 90:1007–1023, 1989. doi:10.1063/1.456153.

[351] D E Woon and T H Dunning. Gaussian-basis sets for use in correlated molecular calculations .3. the atoms aluminum through argon. *J. Chem. Phys.*, 98: 1358–1371, 1993. doi:10.1063/1.464303.

[352] A. J. C. Varandas. Erratum: "Accurate ab initio potential energy curves for the classic Li-F ionic-covalent interaction by extrapolation to the complete basis set limit and modeling of the nonadiabatic coupling" [J. Chem. Phys. 131, 124128 (2009)]. *J. Chem. Phys.*, 135(11):119902, 2011. doi:10.1063/1.3641404.

[353] A.J.C. Varandas. A simple, yet reliable, direct diabatization scheme.

The $^1\sigma_g^+$ states of c2. *Chem. Phys. Lett.*, 471(4):315–321, 2009. doi:10.1016/j.cplett.2009.02.028.

[354] Ching-Ping Liu, Nicola L. Elliott, Colin M. Western, Yuan-Pern Lee, and Reginald Colin. The B $^3\Sigma^-$ state of the SO radical. *J. Mol. Spectrosc.*, 238: 213–223, 2006. doi:10.1016/j.jms.2006.05.005.

[355] C. P. Archer, J. M. F. Elks, and C. M. Western. The C $^3\Pi$, d $^1\Pi$, and e $^1\Pi$ states of SO. *J. Chem. Phys.*, 112:6293–6300, 2000. doi:10.1063/1.481190.

[356] K. P. Huber and G. Herzberg. *Molecular Spectra and Molecular Structure IV. Constants of Diatomic Molecules*. Van Nostrand Reinhold Company, New York, 1979. doi:10.1007/978-1-4757-0961-2. URL https://doi.org/10.1007/978-1-4757-0961-2.

[357] K. Norwood and C.Y. Ng. Photoion-photoelectron coincidence spectroscopy of the transient molecules SO and S_2O. *Chem. Phys. Lett.*, 156:145–150, 1989. doi:10.1016/S0009-2614(89)87110-6.

[358] H. M. Wang, X. S. Tang, S. K. Zhou, W. J. Zhang, and Y. N. Chu. Spectroscopic observation of electronically excited SO (A $'^3\Sigma^+$). *Chem. Phys. Lett.*, 407:78–82, 2005. doi:10.1016/j.cplett.2005.03.063.

[359] B. Rosen. *Spectroscopic Data Relative to Diatomic Molecules*. Tables internationales de constantes selectionnees. Elsevier Science, 2013.

[360] Sergei N. Yurchenko, Ahmed F. Al-Refaie, and Jonathan Tennyson. ExoCross: a general program for generating spectra from molecular line lists. *Astron. Astrophys.*, 614:A131, 2018. doi:10.1051/0004-6361/201732531.

[361] L. S. Rothman, I. E. Gordon, Y. Babikov, A. Barbe, D. Chris Benner, P. F. Bernath, M. Birk, L. Bizzocchi, V. Boudon, L. R. Brown, A. Campargue, K. Chance, E. A. Cohen, L. H. Coudert, V. M. Devi, B. J. Drouin, A. Fayt, J.-M. Flaud, R. R. Gamache, J. J. Harrison, J.-M. Hartmann, C. Hill, J. T. Hodges, D. Jacquemart, A. Jolly, J. Lamouroux, R. J. Le Roy, G. Li, D. A. Long, O. M. Lyulin, C. J. Mackie, S. T. Massie, S. Mikhailenko, H. S. P. Müller, O. V. Naumenko, A. V. Nikitin, J. Orphal, V. Perevalov, A. Perrin, E. R. Polovtseva, C. Richard, M. A. H. Smith, E. Starikova, K. Sung, S. Tashkun, J. Tennyson, G. C. Toon, Vl. G. Tyuterev, and G. Wagner. The *HITRAN* 2012 molecular spectroscopic database. *J. Quant. Spectrosc. Radiat. Transf.*, 130:4 – 50, 2013. doi:10.1016/jqsrt.2013.07.002.

[362] H. M. Wang, X. S. Tang, H. Y. Han, J. Q. Li, S. K. Zhou, W. J. Zhang, and Y. A. Chu. Emission spectrum of SO (A $^{\prime 3}\Sigma^{+}$) generated in the reaction of Ar ($P_3(0,2)$) with SO_2. *Chin. J. Chem. Phys.*, 18:670–674, 2005. doi:10.1088/1674-0068/18/5/670-674.

[363] E. Kim and S. Yamamoto. Fourier transform millimeter-wave spectroscopy of CS(X $^1\Sigma^+$) and SO(b $^1\Sigma^+$) in highly excited vibrational states. *J. Mol. Spectrosc.*, 219:296–304, 2003. doi:10.1016/S0022-2852(03)00027-4.

[364] F. X. Powell and D. R. Lide. Microwave spectrum of SO radical. *J. Chem. Phys.*, 41:1413–1419, 1964. doi:10.1063/1.1726082.

[365] M. Winnewisser, W. Gordy, Kvln Sastry, and R. L. Cook. Millimeter wave spectroscopy of unstable molecular species. 2. Sulfur monoxide. *J. Chem. Phys.*, 41:1687–1691, 1964. doi:10.1063/1.1726146.

[366] E. Tiemann. Isotope dependence of the rotational constant of sulfur monoxide in the $X^3\Sigma^-$ ground state. *J. Mol. Spectrosc.*, 51:316–320, 1974. doi:10.1016/0022-2852(74)90059-9.

[367] E. Tiemann. Isotope shifts of the molecular parameters in the $X^3\Sigma^-$ state of sulfur monoxide. *J. Mol. Spectrosc.*, 91:60–71, 1982. doi:10.1016/0022-2852(82)90030-3.

[368] Y. Endo, H. Kanamori, and E. Hirota. Submillimeter-wave spectroscopy of $a^1\Delta$ SO in excited vibrational-states produced by 193-nm photolysis of Cl2SO. *Chem. Phys. Lett.*, 141:129–132, 1987. doi:10.1016/0009-2614(87)80105-7.

[369] T. Klaus, A. H. Saleck, S. P. Belov, G. Winnewisser, Y. Hirahara, M. Hayashi, E. Kagi, and K. Kawaguchi. Pure rotational spectra of SO: Rare isotopomers in the 80-GHz to 1.1-THz region. *J. Mol. Spectrosc.*, 180:197–206, 1996. doi:10.1006/jmsp.1996.0243.

[370] M. A. A. Clyne and P. H. Tennyson. $A^3\Pi$ and $B^3\Sigma^-$ excited-states of the SO radical. Part 3. The 0-0 band spectrum of the $A^3\Pi_1$-$X^3\Sigma^-$ transition. *J. Chem. Soc. Faraday Trans.*, 82:1315–1325, 1986. doi:10.1039/f29868201315.

[371] B. C. Stuart, S. M. Cameron, and H. T. Powell. Production, excitation, and laser dynamics of sulfur monoxide. *J. Phys. Chem.*, 98:11499–11511, 1994. doi:10.1021/j100095a035.

[372] Rafael Bachiller. BIPOLAR MOLECULAR OUTFLOWS FROM YOUNG STARS AND PROTOSTARS. *Ann. Rev. Astron. Astrophys*, 34(1):111–154, 1996. doi:10.1146/annurev.astro.34.1.111.

[373] T. Furtenbacher and A. G. Császár. MARVEL: measured active rotational-vibrational energy levels. II. Algorithmic improvements. *J. Quant. Spectrosc. Radiat. Transf.*, 113:929–935, 2012.

[374] T. Furtenbacher and A. G. Császár. The role of intensities in determining characteristics of spectroscopic networks. *J. Molec. Struct. (THEOCHEM)*, 1009:123 – 129, 2012. doi:10.1016/j.molstruc.2011.10.057.

[375] A. G. Császár and T. Furtenbacher. Spectroscopic networks. *J. Mol. Spectrosc.*, 266:99 – 103, 2011. doi:10.1016/j.jms.2011.03.031.

[376] J. Tennyson, T. Furtenbacher, S. N. Yurchenko, and A. G. Császár. Empirical rovibrational energy levels for nitrous oxide. *J. Quant. Spectrosc. Radiat. Transf.*, 316:108902, 2024. doi:10.1016/j.jqsrt.2024.108902.

[377] M. Bogey, C. Demuynck, and J. L. Destombes. Millimeter wave spectrum of SO in highly excited vibrational-states: Vibrational and isotopic dependence of molecular-constants. *Chem. Phys.*, 66:99–104, 1982. doi:10.1016/0301-0104(82)88010-5.

[378] A.M. Bouchoux, J. Marchand, and J. Janin. Contribution à l'étude du système $b^1\Sigma^+ X^3\Sigma^-$ de la molécule SO. *Spectra Chimica Acta A*, pages 1909–1915, 1971. ISSN 0584-8539. doi:10.1016/0584-8539(71)80244-1.

[379] Mme A.-M. Bouchoux and M.J. Marchand. Structure de rotation des bandes [2,0], [3,1] et [4,2] du systeme $b^1\Sigma^+$-$X^3\Sigma^-$3 de SO. *Spectra Chimica Acta A*, 28:1771–1773, 1972. ISSN 0584-8539. doi:10.1016/0584-8539(72)80147-8.

[380] R. Colin. Spectrum of SO: Analysis of $B^3\Sigma^-$-$X^3\Sigma^-$ and $A^3\Pi$-$X^3\Sigma^-$ band systems. *Can. J. Phys.*, 47:979–994, 1969. doi:10.1139/p69-122. URL https://doi.org/10.1139/p69-122.

[381] A. M. Bouchoux, J. Marchand, and J. Janin. Contribution à l'étude du système $b^1\Sigma^+ X^3\Sigma^-$ de la molécule SO. *Spectra Chimica Acta A*, A 27:1909–1915, 1971. doi:10.1016/0584-8539(71)80244-1.

[382] A. M. Bouchoux, J. Marchand, and J. Janin. Vibration temperature of SO radical in hydrogen sulfide oxygen flame. *Cr. Acad. Sci. B Phys.*, 274:256, 1972.

[383] K. T. Wu, H. Morgner, and A. J. Yencha. SO($B^3\Sigma^-$,$A^3\Pi$-$X^3\Sigma^-$) emission from low-temperature rare gas-sulfur dioxide afterglows. *Chem. Phys.*, 68: 285–292, 1982. doi:10.1016/0301-0104(82)87035-3.

[384] M. Bielefeld, G. Elfers, E. H. Fink, H. Kruse, J. Wildt, R. Winter, and F. Zabel. *J. Photochem.*, 25(2-4):419–438, 1984. doi:10.1016/0047-2670(84)87043-4.

[385] Mathieu Bastian, Sebastien Heymann, and Mathieu Jacomy. Gephi: An open source software for exploring and manipulating networks. 2009. URL http://www.aaai.org/ocs/index.php/ICWSM/09/paper/view/154.

[386] Mathieu Jacomy, Tommaso Venturini, Sebastien Heymann, and Mathieu Bastian. Forceatlas2, a continuous graph layout algorithm for handy network visualization designed for the gephi software. *PLOS ONE*, 9(6):1–12, 06 2014. doi:10.1371/journal.pone.0098679. URL 10.1371/journal.pone.0098679.

[387] Emile S. Medvedev, Vladimir V. Meshkov, Andrey V. Stolyarov, and Iouli E. Gordon. Peculiarities of high-overtone transition probabilities in carbon monoxide revealed by high-precision calculation. *J. Chem. Phys.*, 143: 154301, 2015. doi:10.1063/1.4933136.

[388] Emile S. Medvedev, Vladimir V. Meshkov, Andrey V. Stolyarov, Vladimir G. Ushakov, and Iouli E. Gordon. Impact of the dipole-moment representation on the intensity of high overtones. *J. Mol. Spectrosc.*, 330:36–42, 2016. doi:10.1016/j.jms.2016.06.013.

[389] Emile S. Medvedev and Vladimir G. Ushakov. Irregular semi-empirical dipole-moment function for carbon monoxide and line lists for all its isotopologues verified for extremely high overtone transitions. *J. Quant. Spectrosc. Radiat. Transf.*, 288:108255, 2022. doi:10.1016/j.jqsrt.2022.108255.

[390] E. S. Medvedev. Towards understanding the nature of the intensities of overtone vibrational transitions. *J. Chem. Phys.*, 137:174307, 2012. doi:10.1063/1.4761930.

[391] C. A. Bowesman, Meiyin Shuai, Sergei N. Yurchenko, and Jonathan Tennyson. A high resolution line list for AlO. *Mon. Not. R. Astron. Soc.*, 508: 3181–3193, 2021. doi:10.1093/mnras/stab2525.

[392] J. Wildt, E. H. Fink, R. Winter, and F. Zabel. Radiative lifetime and quenching of SO($b^1\Sigma^+, v' = 0$). *Chem. Phys.*, 80:167–175, 1983. doi:10.1016/0301-0104(83)85177-5.

[393] M. A. A. Clyne and J. P. Liddy. $A^3\Pi$ and $B^3\Sigma^-$excited states of the SO radical. 2. Lifetimes of vibrational levels of the A-state and quenching rates. *J. Chem. Soc. Faraday Trans.*, 78:1127–1138, 1982. doi:10.1039/f29827801127.

[394] A. J Sauval and J. B. Tatum. A set of partition functions and equilibrium constants for 300 diatomic molecules of astrophysical interest. *Astrophys. J. Suppl.*, 56:193–209, 1984. doi:10.1086/190980.

[395] P. S. Barklem and R. Collet. Partition functions and equilibrium constants for diatomic molecules and atoms of astrophysical interest. *Astron. Astrophys.*, 588:A96, 2016. doi:10.1051/0004-6361/201526961.

[396] R. R. Gamache, C. Roller, E. Lopes, I. E. Gordon, L. S. Rothman, O. L. Polyansky, N. F. Zobov, A. A. Kyuberis, J. Tennyson, S N Yurchenko, A. G. Császár, T. Furtenbacher, Xinchuan Huang, David W. Schwenke, Timothy J. Lee, B J Drouin, S. A. Tashkun, V. I. Perevalov, and R V. Kochanov. Total Internal Partition Sums for 167 isotopologues of 53 molecules important in planetary atmospheres: application to HITRAN2016 and beyond. *J. Quant. Spectrosc. Radiat. Transf.*, 203:70–87, 2017. doi:10.1016/j.jqsrt.2017.03.045.

[397] Rong Wang, U. Balciunaite, Juncai Chen, Cheng Yuan, A. Owens, and J. Tennyson. NASA polynomial representation of molecular specific heats. *J. Quant. Spectrosc. Radiat. Transf.*, 306:108617, 2023. doi:10.1016/j.jqsrt.2023.108617.

[398] K. L. Chubb, M. Rocchetto, S. N. Yurchenko, M. Min, I. Waldmann, J. K. Barstow, P. Molliére, A. F. Al-Refaie, M. Phillips, and J. Tennyson. The ExoMolOP Database: Cross-sections and *k*-tables for Molecules of Interest in High-Temperature Exoplanet Atmospheres. *Astron. Astrophys.*, 646:A21, 2020. doi:10.1051/0004-6361/202038350.

[399] Michiel Min, Chris W. Ormel, Katy Chubb, Christiane Helling, and Yui Kawashima. The ARCiS framework for exoplanet atmospheres - Modelling philosophy and retrieval. *Astron. Astrophys.*, 642:A28, 2020. doi:10.1051/0004-6361/201937377.

[400] A. F. Al-Refaie, Q. Changeat, I. P. Waldmann, and G. Tinetti. TauREx 3: A Fast, Dynamic, and Extendable Framework for Retrievals. *Astrophys. J.*, 917:37, 2021. doi:10.3847/1538-4357/ac0252.

[401] P. G. J. Irwin, N. A. Teanby, R. de Kok, L. N. Fletcher, C. J. A. Howett, C. C. C. Tsang, C. F. Wilson, S. B. Calcutt, C. A. Nixon, and P. D. Parrish. The NEMESIS planetary atmosphere radiative transfer and retrieval tool. *J. Quant. Spectrosc. Radiat. Transf.*, 109:1136 – 1150, 2008. doi:10.1016/j.jqsrt.2007.11.006.

[402] P. Mollière, J. P. Wardenier, R. van Boekel, Th. Henning, K. Molaverdikhani, and I. A. G. Snellen. petitRADTRANS - A Python radiative transfer package for exoplanet characterization and retrieval. *Astron. Astrophys.*, 627:A67, 2019. doi:10.1051/0004-6361/201935470.

[403] Y. N. Chu, H. M. Wang, J. Q. Li, P. Cheng, and D. Z. Cao. Emission observation for electronically excited state SO(c $^1\Sigma^-$) in gas phase. *Chem. Phys. Lett.*, 366:147–152, 2002. doi:10.1016/S0009-2614(02)01525-7.

[404] R. J. Le Roy. LEVEL: A Computer Program for Solving the Radial Schrödinger Equation for Bound and Quasibound Levels. *J. Quant. Spectrosc. Radiat. Transf.*, 186:167 – 178, 2017. doi:10.1016/j.jqsrt.2016.05.028.

[405] Wilfrid Somogyi, Sergey N Yurchenko, and Gap-Sue Kim. An ab initio spectroscopic model of the molecular oxygen atmospheric and infrared bands. *Phys. Chem. Chem. Phys.*, 26(43):27419–27430, November 2024.

[406] Diana Powell, Adina D. Feinstein, Elspeth K. H. Lee, Michael Zhang, Shang-Min Tsai, Jake Taylor, James Kirk, Taylor Bell, Joanna K. Barstow, Peter Gao, Jacob L. Bean, Jasmina Blecic, Katy L. Chubb, Ian J. M. Crossfield, Sean Jordan, Daniel Kitzmann, Sarah E. Moran, Giuseppe Morello, Julianne I. Moses, Luis Welbanks, Jeehyun Yang, Xi Zhang, Eva-Maria Ahrer, Aaron Bello-Arufe, Jonathan Brande, S. L. Casewell, Nicolas Crouzet, Patricio E. Cubillos, Brice-Olivier Demory, Achrène Dyrek, Laura Flagg, Renyu

Hu, Julie Inglis, Kathryn D. Jones, Laura Kreidberg, Mercedes López-Morales, Pierre-Olivier Lagage, Erik A. Meier Valdés, Yamila Miguel, Vivien Parmentier, Anjali A. A. Piette, Benjamin V. Rackham, Michael Radica, Seth Redfield, Kevin B. Stevenson, Hannah R. Wakeford, Keshav Aggarwal, Munazza K. Alam, Natalie M. Batalha, Natasha E. Batalha, Björn Benneke, Zach K. Berta-Thompson, Ryan P. Brady, Claudio Caceres, Aarynn L. Carter, Jean-Michel Désert, Joseph Harrington, Nicolas Iro, Michael R. Line, Joshua D. Lothringer, Ryan J. MacDonald, Luigi Mancini, Karan Molaverdikhani, Sagnick Mukherjee, Matthew C. Nixon, Apurva V. Oza, Enric Palle, Zafar Rustamkulov, David K. Sing, Maria E. Steinrueck, Olivia Venot, Peter J. Wheatley, and Sergei N. Yurchenko. Sulphur dioxide in the mid-infrared transmission spectrum of WASP-39b. *Nature*, 626:979–983, 2024. doi:10.1038/s41586-024-07040-9.

[407] D. S. Underwood, J. Tennyson, S. N. Yurchenko, Xinchuan Huang, David W. Schwenke, Timothy J. Lee, S. Clausen, and A. Fateev. ExoMol line lists XIV: A line list for hot SO_2. *Mon. Not. R. Astron. Soc.*, 459:3890–3899, 2016. doi:10.1093/mnras/stw849.

[408] D. S. Underwood, J. Tennyson, S. N. Yurchenko, S. Clausen, and A. Fateev. ExoMol line lists XVII: A line list for hot SO_3. *Mon. Not. R. Astron. Soc.*, 462:4300–4313, 2016. doi:10.1093/mnras/stw1828.

[409] Jeanna Buldyreva, Ryan P. Brady, Sergei N. Yurchenko, and Jonathan Tennyson. Collisional broadening of molecular rovibronic lines. *J. Quant. Spectrosc. Radiat. Transf.*, 313:108843, 2024. ISSN 0022-4073. doi:https://doi.org/10.1016/j.jqsrt.2023.108843.

[410] Fredrik R. Westlye, Benjamin A. K. Hartz, Anders Ivarsson, Alexander Fateev, and Sonnik Clausen. Evaluation of spectral radiative properties of gases in high-pressure combustion. *J. Quant. Spectrosc. Radiat. Transf.*, 280: 108089, 2022. doi:10.1016/j.jqsrt.2022.108089.

[411] M. Pavanello, L. Adamowicz, A. Alijah, N. F. Zobov, I. I. Mizus, O. L. Polyansky, J. Tennyson, T. Szidarovszky, A. G. Császár, M. Berg, A. Petrignani, and A. Wolf. Precision measurements and computations of transition energies in rotationally cold triatomic hydrogen ions up to the mid-visible spectral range. *Phys. Rev. Lett.*, 108:023002, 2012. doi:10.1103/PhysRevLett.108.023002.

[412] L. Anisman, K. L. Chubb, Q. Changeat, B. Edwards, S. N. Yurchenko, J. Tennyson, and G. Tinetti. Cross-sections for heavy atmospheres: H_2O self-broadening. *J. Quant. Spectrosc. Radiat. Transf.*, 283:108146, 2022. doi:10.1016/j.jqsrt.2022.108146.

[413] Jonathan J. Fortney, Tyler D. Robinson, Shawn Domagal-Goldman, Anthony D. Del Genio, Iouli E. Gordon, Ehsan Gharib-Nezhad, Nikole Lewis, Clara Sousa-Silva, Vladimir Airapetian, Brian Drouin, Robert J. Hargreaves, Xinchuan Huang, Tijs Karman, Ramses M. Ramirez, Gregory B. Rieker, Jonathan Tennyson, Robin Wordsworth, Sergei N Yurchenko, Alexandria V Johnson, Timothy J. Lee, Chuanfei Dong, Stephen Kane, Mercedes Lopez-Morales, Thomas Fauchez, Timothy Lee, Mark S. Marley, Keeyoon Sung, Nader Haghighipour, Tyler Robinson, Sarah Horst, Peter Gao, Der you Kao, Courtney Dressing, Roxana Lupu, Daniel Wolf Savin, Benjamin Fleury, Olivia Venot, Daniela Ascenzi, Stefanie Milam, Harold Linnartz, Murthy Gudipati, Guillaume Gronoff, Farid Salama, Lisseth Gavilan, Jordy Bouwman, Martin Turbet, Yves Benilan, Bryana Henderson, Natalie Batalha, Rebecca Jensen-Clem, Timothy Lyons, Richard Freedman, Edward Schwieterman, Jayesh Goyal, Luigi Mancini, Patrick Irwin, Jean-Michel Desert, Karan Molaverdikhani, John Gizis, Jake Taylor, Joshua Lothringer, Raymond Pierrehumbert, Robert Zellem, Natasha Batalha, Sarah Rugheimer, Jacob Lustig-Yaeger, Renyu Hu, Eliza Kempton, Giada Arney, Mike Line, Munazza Alam, Julianne Moses, Nicolas Iro, Laura Kreidberg, Jasmina Blecic, Tom Louden, Paul Molliere, Kevin Stevenson, Mark Swain, Kimberly Bott, Nikku Madhusudhan, Joshua Krissansen-Totton, Drake Deming, Irina Kitiashvili, Evgenya Shkolnik, Zafar Rustamkulov, Leslie Rogers, and Laird Close. The Need for Laboratory Measurements and Ab Initio Studies to Aid Understanding of Exoplanetary Atmospheres, 2019. arXiv:1905.07064.

[414] E. Lindholm. *Arkiv. Mat. Astron. Fysik.*, 32:17, 1945.

[415] H.M. Foley. The pressure broadening of spectral lines. *Phys. Rev.*, 69(11): 616–628, 1946. doi:10.1103/physrev.69.616.

[416] M. Mizushima. The theory of pressure broadening and its application to microwave spectra. *Phys. Rev.*, 83:94–103, 1951.

[417] H. Cybulski, A. Bielski, R. Ciurylo, J. Szudy, and R. Trawinski. Power-law temperature dependence of collision broadening and shift of atomic and

molecular rovibronic lines. *J. Quant. Spectrosc. Radiat. Transf.*, 120:90–103, 2013.

[418] R G Breene. *The Shift and Shape of Spectral Lines*. Pergamon, Oxford, 1961.

[419] W R Hindmarsh, A D Petford, and G. Smith. Interpretation of collision broadening and shift in atomic spectra. *Proc. R. Soc. London A*, 297:296–304, 1967.

[420] D E Stogryn and A P Stogryn. Molecular multipole moments. *Mol. Phys.*, 11:371–393, 1966.

[421] W. L. Meerts and A. Dymanus. Electric dipole moments of OH and OD by molecular beam electric resonance. *Chem. Phys. Lett.*, 23:45–47, 1973.

[422] P J Knowles, C Hampel, and H-J Werner. Coupled-cluster theory for high-spin, open-shell reference wave-functions. *J. Chem. Phys.*, 99:5219–5227, 1993. doi:10.1063/1.465990.

[423] T. J. Lee and P. R. Taylor. A Diagnostic for determining the quality of single-reference electron correlation methods. *Intern. J. Quantum Chem.*, 36:199–207, 1989. doi:10.1002/qua.560360824.

[424] Jonathan C. Rienstra-Kiracofe, Wesley D. Allen, and Henry F. Schaefer. The $C_2H_5 + O_2$ Reaction Mechanism: High-Level ab Initio Characterizations. *J. Phys. Chem. A*, 104(44):9823—-9840, 2000. doi:10.1021/jp001041k.

[425] Patricia R.P. Barreto, Ana Claudia P.S. Cruz, Rodrigo L.P. Barreto, Federico Palazzetti, Alessandra F. Albernaz, Andrea Lombardi, Glauciete S. Maciel, and Vincenzo Aquilanti. The spherical-harmonics representation for the interaction between diatomic molecules: The general case and applications to COCO and COHF. *Journal of Molecular Spectroscopy*, 337:163–177, 2017. doi:10.1016/j.jms.2017.05.009.

[426] Björn O. Roos. *The Complete Active Space Self-Consistent Field Method and its Applications in Electronic Structure Calculations*, pages 399–445. John Wiley & Sons, Ltd, 1987. ISBN 9780470142943. doi:https://doi.org/10.1002/9780470142943.ch7. URL https://onlinelibrary.wiley.com/doi/abs/10.1002/9780470142943.ch7.

[427] K. R. Shamasundar, G. Knizia, and H.-J. Werner. A new internally contracted multi-reference configuration interaction method. *J. Chem. Phys.*, 135:054101, 2011.

[428] Heather L. Holmes-Ross and Warren D. Lawrance. The binding energies of NO–Rg (Rg = He, Ne, Ar) determined by velocity map imaging. *J. Chem. Phys.*, 135:014302, 2011. doi:10.1063/1.3601924.

[429] Kazuhide Tsuji, Kazuhiko Shibuya, and Kinichi Obi. Bound–bound A $^2\Sigma^+$- –X $^2\Pi$ transition of NO–Ar van der Waals complexes. *J. Phys. Chem.*, 100 (8):5441–5447, 04 1994. doi:10.1063/1.467161.

[430] Millard H. Alexander. A new, fully ab initio investigation of the ArNO ($X^2\Pi$) system. II. Bound states of the Ar–NO complex. *J. Phys. Chem.*, 111(16): 7435–7439, 10 1999. doi:10.1063/1.480067.

[431] Yoshihiro Sumiyoshi and Yasuki Endo. Intermolecular potential energy surface of Ar–NO. *J. Phys. Chem.*, 127:184309, 2007. doi:10.1063/1.2798760.

[432] Pavel Pokhilko, Evgeny Epifanovsky, and Anna I. Krylov. General framework for calculating spin–orbit couplings using spinless one-particle density matrices: Theory and application to the equation-of-motion coupled-cluster wave functions. *J. Chem. Phys.*, 151(3):034106, 07 2019. ISSN 0021-9606. doi:10.1063/1.5108762.

[433] ANDREAS BERNING, MARCUS SCHWEIZER, HANS-JOACHIM WERNER, PETER J. KNOWLES, and PAOLO PALMIERI. Spin-orbit matrix elements for internally contracted multireference configuration interaction wavefunctions. *Molecular Physics*, 98(21):1823–1833, 2000. doi:10.1080/00268970009483386.

[434] Thomas J. Penfold, Etienne Gindensperger, Chantal Daniel, and Christel M. Marian. Spin-vibronic mechanism for intersystem crossing. *Chemical Reviews*, 118(15):6975–7025, 2018. doi:10.1021/acs.chemrev.7b00617.

[435] Sebastian Mai, Philipp Marquetand, and Leticia González. Non-adiabatic and intersystem crossing dynamics in so2. ii. the role of triplet states in the bound state dynamics studied by surface-hopping simulations. *J. Chem. Phys.*, 140(20):204302, 05 2014. ISSN 0021-9606. doi:10.1063/1.4875036.

[436] Yu Ru Chih, Yu-Ting Lin, Chi-Wei Yin, and Yuan Jang Chen. High intrinsic phosphorescence efficiency and density functional theory modeling of ru(ii)-bipyridine complexes with π-aromatic-rich cyclometalated ligands: Attributions of spin–orbit coupling perturbation and efficient configurational mixing of singlet excited states. *ACS Omega*, 7(51):48583–48599, 2022. doi:10.1021/acsomega.2c07276.

[437] Stephen R. Wilson and Richard Bramley. The electronic spectra of 10, 10-dimethylanthracen-9-one crystals: Spin-Orbit/vibronic coupling in the $^3n\pi^\ddagger$ states. *Chemical Physics*, 67(1):119–132, 1982. ISSN 0301-0104. doi:10.1016/0301-0104(82)88064-6.

[438] W.G. Richards, H.P. Trivedi, and D.L. Cooper. *Spin-orbit Coupling in Molecules*. International series of monographs on chemistry. Clarendon Press, 1981. ISBN 9780198556145.

[439] Reza Islampour and Mahsasadat Miralinaghi. An extensive study of transformation of the diatomics hamiltonian operator from laboratory- to body-fixed frame. *Intern. J. Quantum Chem.*, 115(8):510–522, 2015. doi:10.1002/qua.24881.

[440] Lidan Xiao, Qinghui Wei, Siyaolitu An, Boris F. Minaev, and Bing Yan. Transition properties of the spin- forbidden a4-x2 systems in the no, po and ps molecules. *J. Quant. Spectrosc. Radiat. Transf.*, 320:108979, 2024. ISSN 0022-4073. doi:https://doi.org/10.1016/j.jqsrt.2024.108979.

[441] Cristina Sanz-Sanz and Graham A. Worth. The strong-field control of IBr photodissociation re-visited. *Phys. Chem. Chem. Phys.*, pages –, 2025. doi:10.1039/D5CP02054A.

[442] Michał Tomza, Filip Pawłowski, Małgorzata Jeziorska, Christiane P. Koch, and Robert Moszynski. Formation of ultracold sryb molecules in an optical lattice by photoassociation spectroscopy: theoretical prospects. *Phys. Chem. Chem. Phys.*, 13:18893–18904, 2011. doi:10.1039/C1CP21196J.

[443] Michał Tomza, Wojciech Skomorowski, Monika Musiał, Rosario González-Férez, Christiane P. Koch, and Robert Moszynski. Interatomic potentials, electric properties and spectroscopy of the ground and excited states of the rb2 molecule: ab initio calculations and effect of a non-resonant field*. *Mol. Phys.*, 111(12-13):1781–1797, 2013. doi:10.1080/00268976.2013.793835.

[444] Michał Tomza, Michael H. Goerz, Monika Musiał, Robert Moszynski, and Christiane P. Koch. Optimized production of ultracold ground-state molecules: Stabilization employing potentials with ion-pair character and strong spin-orbit coupling. *Phys. Rev. A*, 86:043424, Oct 2012. doi:10.1103/PhysRevA.86.043424.

[445] Peter F. Bernath, Ryan Johnson, and Jacques Lievin. Line lists for the b(1)Sigma(+)-X-3 Sigma(-) and a(1) Delta-X-3 Sigma(-) transitions of SO. *J. Quant. Spectrosc. Radiat. Transf.*, 272:107772, 2021. doi:10.1016/j.jqsrt.2021.107772.

[446] F Gemperle and FX Gadea. Beyond born–oppenheimer spectroscopic study for the c state of lih. *J. Chem. Phys.*, 110(23):11197–11205, 1999.

[447] Hyo Sug Lee, Yoon Sup Lee, and Gwang-Hi Jeung. Singlet and triplet σ+ excited states of nah and kh: undulating potential energy curves. *Chemical Physics Letters*, 325(1-3):46–52, 2000.

[448] William C Stwalley, Warren T Zemke, and Sze Cheng Yang. Spectroscopy and structure of the alkali hydride diatomic molecules and their ions. *Journal of physical and chemical reference data*, 20(1):153–187, 1991.

[449] William C Stwalley and Warren T Zemke. Spectroscopy and structure of the lithium hydride diatomic molecules and ions. *Journal of physical and chemical reference data*, 22(1):87–112, 1993.

[450] GH Jeung, JP Daudey, and JP Malrieu. Inclusion of core-valence correlation effects in pseudopotential calculations. ii. k2 and kh lowest σ+ potential curves from valence-correlated wavefunctions. *Journal of Physics B: Atomic and Molecular Physics*, 16(5):699, 1983.

[451] Vanesa M Garcıa, Rosa Caballol, and Jean P Malrieu. Treatment of core-valence correlation effects through difference-dedicated configuration interaction: Application to the lowest electronic states of k, rb, kh, rbh, and k 2. *J. Chem. Phys.*, 109(2):504–511, 1998.

[452] G Chambaud and B Lévy. Cah* potential curves: a simple theoretical treatment of intershell effects. *J. Phys. B: At. Mol. Opt. Phys.*, 22(20):3155, 1989.

[453] Bruno Lepetit, M Le Dourneuf, Jean-Michel Launay, and FX Gadea. Quantum dynamics of the collinear cshh system. *Chemical physics letters*, 135 (4-5):377–380, 1987.

[454] A Boutalib and FX Gadea. Ab initio adiabatic and diabatic potential-energy curves of the lih molecule. *J. Chem. Phys.*, 97(2):1144–1156, 1992.

[455] FX Gadea and A Boutalib. Computation and assignment of radial couplings using accurate diabatic data for the lih molecule. *J. Phys. B: At. Mol. Opt. Phys.*, 26(1):61, 1993.

[456] Hamid Berriche and Florent Xavier Gadea. Ab initio adiabatic and diabatic permanent dipoles for the low-lying states of the lih molecule. a direct illustration of the ionic character. *Chemical physics letters*, 247(1-2):85–88, 1995.

[457] H Croft, AS Dickinson, and FX Gadéa. A theoretical study of mutual neutralization in li+ h collisions. *J. Phys. B: At. Mol. Opt. Phys.*, 32(1):81, 1999.

[458] H Croft, AS Dickinson, and FX Gadea. Rate coefficients for the li+/h- and li-/h+ mutual neutralization reactions. *Monthly Notices of the Royal Astronomical Society*, 304(2):327–329, 1999.

[459] AS Dickinson and FX Gadea. Lih formation by radiative association in li++ h- collisions. *Monthly Notices of the Royal Astronomical Society*, 318(4): 1227–1231, 2000.

[460] FX Gadea, F Gemperle, H Berriche, P Villarreal, and G Delgado Barrio. Vibronic shifts for lih in x and a states. *J. Phys. B: At. Mol. Opt. Phys.*, 30 (12):L427, 1997.

[461] FX Gadéa, H Berriche, Octavio Roncero, Pablo Villarreal, and Gerardo Delgado Barrio. Nonradiative lifetimes for lih in the a state using adiabatic and diabatic schemes. *J. Chem. Phys.*, 107(24):10515–10522, 1997.

[462] F Gemperle and FX Gadea. Breakdown of the born-oppenheimer approach fora diatomic molecule: Lih in the d state. *Europhysics Letters*, 48(5):513, 1999.

[463] Neji Khelifi, Brahim Oujia, and Florent Xavier Gadea. Ab initio adiabatic and diabatic energies and dipole moments of the kh molecule. *J. Chem. Phys.*, 116(7):2879–2887, 02 2002. ISSN 0021-9606. doi:10.1063/1.1436467.

[464] D. C. Jain and P. Sah. Potential-energy curves of the excited states of alkali hydride molecules. *J. Chem. Phys.*, 38(7):1553–1557, 04 1963. ISSN 0021-9606. doi:10.1063/1.1776919.

[465] Neji Khelifi, Brahim Oujia, and Florent Xavier Gadea. Dynamic couplings, radiative and nonradiative lifetimes of the a1+ and c1+ states of the kh molecule. *Journal of Physical and Chemical Reference Data*, 36(1):191–202, 02 2007. ISSN 0047-2689. doi:10.1063/1.2432887.

[466] Neji Khelifi, Brahim Oujia, and Florent Xavier Gadea. Dynamic study: Radiative and nonradiative lifetimes for vibrational levels of the a 1+ and c 1+ states of the alkali hydride kh. *Journal of Russian Laser Research*, 27:575–600, 2006.

[467] Neji Khelifi. First and second derivative of the wave function of the 1 σ+ states of the kh molecule. *Physical Review A—Atomic, Molecular, and Optical Physics*, 83(4):042502, 2011.

[468] Yukiumi Kita, Ryo Maezono, Masanori Tachikawa, Mike D Towler, and Richard J Needs. Ab initio quantum monte carlo study of the binding of a positron to alkali-metal hydrides. *J. Chem. Phys.*, 135(5), 2011.

[469] Marc Giroud and Odette Nedelec. Spectroscopy of the nah, nad, kh, and kd x 1σ+ ground state by laser excited fluorescence in a high frequency discharge. *J. Chem. Phys.*, 73(9):4151–4155, 1980.

[470] Adam C. Beiler. The molecular spectrum of potassium hydride. *ProQuest Dissertations and Theses*, page 104, 1941. URL https://www.proquest.com/dissertations-theses/molecular-spectrum-potassium-hydride/docview/2912974511/se-2. Copyright - Database copyright ProQuest LLC; ProQuest does not claim copyright in the individual underlying works; Last updated - 2024-01-11.

[471] G. M. Almy and C. D. Hause. The spectrum of potassium hydride. *Phys. Rev.*, 42:242–266, Oct 1932. doi:10.1103/PhysRev.42.242.

[472] Nathan N. Haese, Di-Jia Liu, and Robert S. Altman. The infrared spectrum of kh. *J. Chem. Phys.*, 81(9):3766–3773, 11 1984. ISSN 0021-9606. doi:10.1063/1.448176. URL 10.1063/1.448176.

[473] Xuefeng Wang and Lester Andrews. Infrared spectra and theoretical calculations of kh and (kh)2 in solid hydrogen. *The Journal of Physical Chemistry A*, 111(49):12260–12265, 2007. doi:10.1021/jp0745889.

[474] Vladimir A. Srećković, Milan S. Dimitrijević, and Ljubinko M. Ignjatović. Absorption caused by potassium molecules in astrophysical plasmas: Data needed for modeling. *Advances in Space Research*, 71(2):1252–1259, 2023. ISSN 0273-1177. doi:10.1016/j.asr.2022.07.084.

[475] I. W. M. Smith. Morse franck-condon factors and r-centroids for so $b^3\sigma^-$-$x^3\sigma^-$ system. *J. Quant. Spectrosc. Radiat. Transf.*, 8:1437–1441, 1968. doi:10.1016/0022-4073(68)90119-2.

[476] AD Bykov, SS Voronina, and MM Makogon. Water vapor absorption band nearby 270 nm: intensity borrowing mechanism translated by ab malikova, edited by yu. f. arshinov. *ATMOSPHERIC AND OCEANIC OPTICS C/C OF OPTIKA ATMOSFERY I OKEANA*, 16(11):912–915, 2003.

[477] David W. Schwenke. Beyond the potential energy surface: ab initio corrections to the bornoppenheimer approximation for h2o. *J. Phys. Chem. A*, 105 (11):2352–2360, 2001. doi:10.1021/jp0032513.

[478] Jaime Suárez, L. Méndez, and I. Rabadán. Nonadiabatic Quantum Dynamics Predissociation of H_2O+($\tilde{B}\ ^2B_2$). *J. Phys. Chem. Lett.*, 6(1):72–76, 2015. doi:10.1021/jz5022894.

[479] Ravinder Abrol and Aron Kuppermann. An optimal adiabatic-to-diabatic transformation of the 1 $2A'$ and 2 $2A'$ states of H3. *J. Chem. Phys.*, 116(3): 1035–1062, jan 2002. doi:10.1063/1.1419257.

[480] Alexander O. Mitrushchenkov. A new general Renner-Teller (including $\varepsilon \geq 1$) spectroscopic formalism for triatomic molecules. *J. Chem. Phys.*, 136: 024108, 2012. doi:10.1063/1.3672162.

[481] Olivia Venot, Marco Rocchetto, Shaun Carl, Aysha Roshni Hashim, and Leen Decin. INFLUENCE OF STELLAR FLARES ON THE CHEMICAL COMPOSITION OF EXOPLANETS AND SPECTRA. *Astrophys. J.*, 830:77, 2016. doi:10.3847/0004-637x/830/2/77.

[482] Benjamin Fleury, Murthy S. Gudipati, Bryana L. Henderson, and Mark Swain. Photochemistry in Hot H_2-dominated Exoplanet Atmospheres. *Astrophys. J.*, 871:158, 2019. doi:10.3847/1538-4357/aaf79f.

[483] Mahmuda Afrin Badhan, Eric T. Wolf, Ravi Kumar Kopparapu, Giada Arney, Eliza M.-R. Kempton, Drake Deming, and Shawn D. Domagal-Goldman.

Stellar Activity Effects on Moist Habitable Terrestrial Atmospheres around M Dwarfs . *Astrophys. J.*, 887:34, 2019. doi:10.3847/1538-4357/ab32e8.

[484] Valentine Wakelam, Emeric Bron, Stephanie Cazaux, Francois Dulieu, Cécile Gry, Pierre Guillard, Emilie Habart, Liv Hornekær, Sabine Morisset, Gunnar Nyman, Valerio Pirronello, Stephen D. Price, Valeska Valdivia, Gianfranco Vidali, and Naoki Watanabe. H_2 formation on interstellar dust grains: The viewpoints of theory, experiments, models and observations. *Molecular Astrophysics*, 9:1–36, 2017. ISSN 2405-6758. doi:10.1016/j.molap.2017.11.001.

[485] D. J. Hollenbach and A. G. G. M. Tielens. Dense photodissociation regions (pdrs). *Annual Review of Astronomy and Astrophysics*, 35(Volume 35, 1997): 179–215, 1997. doi:10.1146/annurev.astro.35.1.179.

[486] D. J. Hollenbach and A. G. G. M. Tielens. Photodissociation regions in the interstellar medium of galaxies. *Rev. Mod. Phys.*, 71:173–230, Jan 1999. doi:10.1103/RevModPhys.71.173.

[487] Olinde Rodrigues. Des lois géométriques qui régissent les déplacements d'un système solide dans l'espace, et de la variation des coordonnées provenant de ces déplacements considérés indépendamment des causes qui peuvent les produire. *Journal de mathématiques pures et appliquées*, 5:380–440, 1840.

[488] Kun Wang and Jian S. Dai. The dual euler-rodrigues formula in various mathematical forms and their intrinsic relations. *Mechanism and Machine Theory*, 181:105184, 2023. ISSN 0094-114X. doi:10.1016/j.mechmachtheory.2022.105184.

[489] Nicholas J. Higham. *Functions of Matrices*. Society for Industrial and Applied Mathematics, 2008. doi:10.1137/1.9780898717778. URL https://epubs.siam.org/doi/abs/10.1137/1.9780898717778.

[490] Ying Liang, Wazir Muhammad, Gregory R Hart, Bradley J Nartowt, Zhe J Chen, James B Yu, Kenneth B Roberts, James S Duncan, and Jun Deng. A general-purpose monte carlo particle transport code based on inverse transform sampling for radiotherapy dose calculation. *Sci. Rep.*, 10(1):9808, June 2020.

[491] Nicholas Metropolis and S. Ulam. The monte carlo method. *Journal of the American Statistical Association*, 44(247):335–341, 1949. doi:10.1080/01621459.1949.10483310.

[492] John Stillwell. *Naive Lie Theory*. Springer New York, 2008. ISBN 9780387782157. doi:10.1007/978-0-387-78214-0.

[493] Wulf Rossmann. *Lie groups: an introduction through linear groups*, volume 5. Oxford University Press, USA, 2006.

[494] Robert Gilmore. *Lie groups, Lie algebras, and some of their applications*. Courier Corporation, 2006.

[495] Viktor Szalay, Dominika Viglaska, and Michael Rey. Internal- and rho-axis systems of molecules with one large amplitude internal motion: The geometry of rho. *J. Chem. Phys.*, 149(24):244118, 12 2018. ISSN 0021-9606. doi:10.1063/1.5056217.